

nature

INTERRED IN AFRICA

Remains represent the continent's earliest known burial of a modern human

Unwanted extras

The race to assess if ingesting microplastics can cause harm

Social skills

Artificial intelligence needs to learn to collaborate

Warming warning

Paris climate target is key to avoiding sharp rise in land-ice loss



Nature.2021.05.08

[Sat, 08 May 2021]

- [This Week](#)
- [News in Focus](#)
- [Books & Arts](#)
- [Opinion](#)
- [Work](#)
- [Research](#)
- [Amendments & Corrections](#)

| [Next section](#) | [Main menu](#) |

Donation

| [Next section](#) | [Main menu](#) |

This Week

- **[India, Brazil and the human cost of sidelining science](#)** [04 May 2021]
Editorial • Governments that ignore or delay acting on scientific advice are missing out on a crucial opportunity to control the pandemic.
- **[Good research begins long before papers get written](#)** [29 April 2021]
Editorial • Publishers are redoubling their commitment to transparency and reproducibility — but they can't bring about change alone.
- **[Indian government should heed its scientists on COVID](#)**
[30 April 2021]
World View • Researchers have spoken out against policies that have exacerbated the country's coronavirus crisis. Policymakers must listen.
- **[A surface stays frost-free by showing water drops no mercy](#)**
[29 April 2021]
Research Highlight • A bio-inspired material forces water droplets to jump into the void — and thus prevents ice formation.
- **[The world's northernmost bird is a clock-watcher](#)** [29 April 2021]
Research Highlight • Ptarmigan that live far above the Arctic Circle generate circadian rhythms, despite summer's eternal sunshine.
- **[A smart genome scan could help scratch the itch for new antifungal drugs](#)** [28 April 2021]
Research Highlight • Genome mining uncovers how a fungus makes a chemical agent against others of its kind.
- **[Dim stars that have failed at fusion are masters of spin](#)** [27 April 2021]
Research Highlight • Three brown dwarfs whirl on their axes at a dizzying rate that might be close to the celestial speed limit for these bodies.
- **[Warming seas brought an eerie calm to a stormy region](#)** [29 April 2021]
Research Highlight • In July 2020, the Western North Pacific was hit by a record-breaking number of typhoons: zero.

- **Meat lovers worldwide pay climate little heed** [26 April 2021]
Research Highlight • People are eating more poultry and fish — but they're not giving up their hamburgers.
- **Animals' bright colours don't lie: eat me and you'll be sorry** [27 April 2021]
Research Highlight • An analysis of a score of species that includes frogs and insects shows that colouration is an 'honest' signal of toxicity.

| [Next section](#) | [Main menu](#) | [Previous section](#) |

EDITORIAL

04 May 2021

India, Brazil and the human cost of sidelining science

Governments that ignore or delay acting on scientific advice are missing out on a crucial opportunity to control the pandemic.



A COVID care centre in New Delhi. India has been recording 400,000 cases and more than 3,500 deaths a day from COVID-19. Credit: Imtiyaz Khan/Anadolu Agency/Getty

Last week, Brazil's total death toll from COVID-19 passed 400,000. In India, the pandemic is taking around 3,500 lives every day and has prompted

a global response, with offers of oxygen, ventilators, intensive-care beds and more. Although these two countries are thousands of miles apart, the crises in both are the result of political failings: their leaders have either failed or been slow to act on researchers' advice. This has contributed to an unconscionable loss of life.

Brazil's biggest failing is that its president, Jair Bolsonaro, has consistently mischaracterized COVID-19 as a "little flu" and has [refused to follow scientific advice in setting policy](#), such as enforcing mask-wearing and limiting contact between people.



[Indian government should heed its scientists on COVID](#)

India's leaders have not acted as decisively as was needed. They have, for example, allowed — and, in some cases, encouraged — large gatherings. Such a situation isn't new. As we saw during the administration of former US president Donald Trump, ignoring evidence of the need to maintain physical distancing to combat COVID-19 has catastrophic consequences. The United States has recorded more than 570,000 deaths from the disease — still the world's largest COVID-19 death toll in absolute terms.

As *Nature* reports in a [World View article](#), India's leaders became complacent after daily COVID-19 cases peaked at nearly 96,000 in September before slowly declining— to around 12,000 at the beginning of

March. During this time, businesses reopened. Large gatherings followed, including protests against controversial new farm laws that brought thousands of farmers to New Delhi's borders. Election rallies and religious gatherings also continued during March and April.

Data difficulties

And India has other problems. One is that it's not easy for scientists to access data for COVID-19 research. That, in turn, prevents them from providing accurate predictions and evidence-based advice to the government. Even in the absence of such data, researchers warned the government last September to be cautious about relaxing COVID-19 restrictions ([*Lancet* 396, 867; 2020](#)). And as late as the start of April, they warned that a second wave could see 100,000 COVID-19 cases a day by the end of the month.

On 29 April, more than 700 scientists wrote to Prime Minister Narendra Modi, asking for better access to data such as COVID-19 test results and clinical outcomes of patients in hospitals (see go.nature.com/3vc1svt), as well as a large-scale genome-surveillance programme to identify new variants (see go.nature.com/3vd7fak). The following day, Krishnaswamy Vijayraghavan, the government's principal scientific adviser, [acknowledged these concerns](#) and clarified the ways in which researchers outside the government can access these data. This move has been welcomed by the letter's signatories, but they have told *Nature* that some aspects of data access remain unclear.



'We are being ignored': Brazil's researchers blame anti-science government for devastating COVID surge

A letter of protest shouldn't have been necessary in the first place. By identifying themselves, the signatories took a risk: in the past, the Modi government has not reacted well to researchers organizing to question its policies. Two years ago, a letter from more than 100 economists and statisticians urging an end to political interference in official statistics was not well received by officials. The letter was written after the resignations of senior officials from India's National Statistical Commission over what they saw as interference in the timing of the release of government data.

It's never good when research communities have a difficult relationship with their national governments. But this can be fatal in the middle of a pandemic — when decisions need to be swift and evidence-based. By sidelining their scientists, the governments of Brazil and India have missed out on a crucial opportunity to reduce the loss of life.

During a pandemic, we all need our governments to succeed. However, it's difficult to make good decisions quickly, more so with incomplete information — which is why health data need to be both accurate and accessible to researchers and clinicians. Denying or obscuring such access risks prolonging the pandemic.

Nature **593**, 7-8 (2021)

doi: <https://doi.org/10.1038/d41586-021-01166-w>

Jobs from Nature Careers

- - - [All jobs](#)
 - - [Postdoc \(f/m/d\) – Molecular mechanisms of translation in yeast –](#)

[Max Planck Institute for Biophysical Chemistry \(MPIBPC\)](#)
[Göttingen, Germany](#)
[JOB POST](#)
 - [Laboratory Research Scientist - Cancer Epigenetics Laboratory](#)

[Francis Crick Institute](#)
[London, United Kingdom](#)
[JOB POST](#)
 - [PhD student \(m/f/div\) in MS-based proteomics of small proteins](#)

[Max Planck Institute of Biophysics \(MPIBP\)](#)
[Frankfurt am Main, Germany](#)
[JOB POST](#)

■ **Senior/Laboratory Research Scientist**

Francis Crick Institute

London, United Kingdom

JOB POST

This article was downloaded by **calibre** from <https://www.nature.com/articles/d41586-021-01166-w>

| [Section menu](#) | [Main menu](#) |

EDITORIAL

29 April 2021

Good research begins long before papers get written

Publishers are redoubling their commitment to transparency and reproducibility — but they can't bring about change alone.



Many researchers are keen to improve transparency and reproducibility in science. Publishers have designed a new reporting framework to help. Getty

In 2013, *Nature* began asking the authors of life-sciences papers to provide extra information in a bid to tackle the pressing problem of poor reproducibility in research. According to one survey of *Nature* authors conducted in 2016–17, [86% of respondents](#) considered poor reproducibility to be a growing challenge in the life sciences.

Researchers in these fields are now asked to use a structured reporting summary for their manuscript submissions. Among other things, the checklist requires authors to state whether their experimental findings have been replicated; how they determined an appropriate sample size; whether they randomized samples; and whether data have been assessed by researchers who did not know which group they were assessing.

Such a checklist, which is provided to peer reviewers and published with each life-sciences paper, has helped to improve transparency in the reporting of research^{1,2}. But editors from many journals and researchers recognize that there is still work to be done.



Checklists work to improve science

In 2017, a group met to discuss how such a systematic approach to transparency and reproducibility could be improved and adopted across more journals. The result is the MDAR (Materials Design Analysis Reporting) Framework, which has just been published³.

The MDAR initiative is the result of an effort by editors at *Science*, Cell Press, the Public Library of Science, *eLife*, Wiley and in the Nature Portfolio, working with experts in reproducibility and research improvement. The objective is to encourage more-detailed disclosures in four areas of life-sciences manuscripts: materials (such as reagents,

laboratory animals and model organisms); data; analysis (including code and statistics); and reporting (adhering to discipline-specific guidelines).

Nature's standards cover most of the MDAR initiative's objectives, but there are plans for further alignment. At the same time, the group is encouraging other journals beyond the founding members to sign up.

Publishers are not the only important players in this arena, however. A key test will be the extent to which funders and universities also support the new framework. Any initiative that improves transparency and reproducibility should be welcomed. But MDAR comes at a time when some of Europe's largest funders have announced plans to reduce what they regard as burdens and bureaucracy in research. The European Commission, for example, is undertaking a review of its pharmaceuticals legislation, partly in an effort to reduce red tape. And the UK government has appointed Adam Tickell, vice-chancellor of the University of Sussex in Brighton, to lead a review with the explicit aim of reducing red tape for researchers.

For these funders, such measures are designed, in part, to remove perceived obstacles to innovation and competitiveness in science. But if the result is reduced funding for research management and administrative support — which are essential to the success of implementing quality measures — that will have an impact on efforts to improve transparency and reproducibility.

All of those involved — funders, publishers and research managers and administrators — need to be on the same page in this respect. Europe's national and regional funders, in particular, must not forget that efforts to enhance transparency and reproducibility are fundamental to the scientific process — and to scientific integrity — and are far from being red tape.



Equality and diversity efforts do not ‘burden’ research

Fortunately, many researchers appreciate this. In a pilot study in 2019, [the MDAR checklist was tested](#) by 33 journal editors and 211 authors working on 289 manuscripts. Most respondents from both groups said they found the expanded checklist helpful. And in response to *Nature*’s 2016–17 survey, some three-quarters of respondents said that they would use the journal’s checklist to some extent, whether or not they were planning to submit their draft to a *Nature* journal.

In a parallel and welcome development, researchers and publishers, including the *Nature* journals, are embracing a format called [Registered Reports](#) in which scientists submit a detailed plan for a research project, including the question or questions being asked, study design and methodology. If editors approve it for peer review, and reviewers think the proposal is sufficiently robust, the journal commits to publishing the work, regardless of the outcome.

All participants involved in the research process know that good research starts long before papers get written. Progress in science comes not with the sparkle of glitter or the crash of cymbals, but in carefully crafted prose after years of deliberations, experimental testing and continuous refinement. The MDAR Framework is one such achievement. The time has come for science institutions to catch up with the growing desire among researchers for

greater transparency and reproducibility. MDAR won't solve everything, but, if it can make research more reliable, then it will go some way towards achieving its promise.

Nature **593**, 8 (2021)

doi: <https://doi.org/10.1038/d41586-021-01167-9>

References

1. 1.
Hair, K. *et al. Res. Integr. Peer Rev.* **4**, 12 (2019).
2. 2.
The NPQIP Collaborative group *BMJ Open Sci.* **3**, e000035 (2019).
3. 3.
Macleod, M. *et al. Proc. Natl Acad. Sci. USA* **118**, e2103238118 (2021).

Jobs from Nature Careers

- - - [All jobs](#)
 - - [**Postdoc \(f/m/d\) – Molecular mechanisms of translation in yeast –**](#)
[Max Planck Institute for Biophysical Chemistry \(MPIBPC\)](#)
[Göttingen, Germany](#)

JOB POST

- Laboratory Research Scientist - Cancer Epigenetics Laboratory

Francis Crick Institute

London, United Kingdom

JOB POST

- PhD student (m/f/div) in MS-based proteomics of small proteins

Max Planck Institute of Biophysics (MPIBP)

Frankfurt am Main, Germany

JOB POST

- Senior/Laboratory Research Scientist

Francis Crick Institute

London, United Kingdom

JOB POST

This article was downloaded by **calibre** from <https://www.nature.com/articles/d41586-021-01167-9>

WORLD VIEW

30 April 2021

Indian government should heed its scientists on COVID



Researchers have spoken out against policies that have exacerbated the country's coronavirus crisis. Policymakers must listen.

- [T. V. Padma](#) 0

1. [T. V. Padma](#)

1. T. V. Padma is a science journalist based in New Delhi. Twitter: [@tvpadma](#)

[View author publications](#)

You can also search for this author in [PubMed](#) [Google Scholar](#)

The world stands aghast at the COVID-19 crisis in India. There have been more than 300,000 new cases per day for the past week; hospitals are full; oxygen supplies are short; and cremation sites are unable to keep pace.

On 29 April, many of India's leading scientists signed an [open letter to Prime Minister Narendra Modi](#), blaming the country's inability to control infections on, in large part, "epidemiological data not being systematically collected and released". Furthermore, they argue that even though the Indian Council of Medical Research has been collecting data from COVID-19 diagnostic tests since early in the pandemic, it has made those data inaccessible, except to certain experts in government.

This collective stance is commendable; the government should not respond by dismissing concerns and criticism as anti-national. Rather, it should make sure that data are collected and made accessible.

As late as March, the government repeatedly boasted that results from serological surveys and from India's main computer model predicting disease spread showed that the country was in the "endgame" of the pandemic. By then, shopping centres, restaurants and theatres had reopened across the country. On the borders of Delhi, farmers held protests against new farm laws. Government ministers lauded large political rallies. And as millions gathered at the Kumbh Mela festival in April, the chief minister of the state of Uttarakhand declared that the Ganges River, considered holy by Hindus, would protect everyone from the coronavirus. Already India's cases were booming; by 27 April, the daily tally passed 353,000 cases, a global record.



India's massive COVID surge puzzles scientists

For months, individual epidemiologists, virologists, immunologists and public-health experts had been warning that the fight against the pandemic was not over, that better data were needed and precautionary measures were warranted. They went unheard. Their arguments did not fit the government's narrative that the pandemic was under control. Biophysicist Gautam Menon, for example, has consistently argued against flawed assumptions in the national model's simulations, and decried the fact that there were no epidemiologists in the committee overseeing them.

Throughout 2020, Anthony Fauci, director of the US National Institute of Allergy and Infectious Diseases, firmly stated sobering facts that ran counter to anti-science messages from the administration of then-president Donald Trump. In Brazil, [scientists spoke against President Jair Bolsonaro's anti-science stand](#). Governments do not always heed researchers, and in countries such as India, science chiefs could lose their jobs for dissent. This means that many are more comfortable toeing the government line than 'doing a Fauci'. Indian scientific academies continue their head-in-the-sand approach, making no statements on superspread events or data access. But it is important for high-profile researchers and societies to speak up.

Even as the government endorsed and encouraged gatherings in recent months, there were reports of second waves and new variants in other

countries. Cases were surging in Manaus, Brazil, where there had been reason to think herd immunity had been reached. By the end of March, a consortium of Indian biology labs had found that the B.1.1.7 variant, first identified in the United Kingdom, was spreading fast in the state of Punjab. And a new worrisome strain (now called B.1.617) was spreading in India's worst-hit state, Maharashtra.



Intolerance and funding concern Indian scientists ahead of election

Public-health experts had been calling for better data and preventive measures, but they have long been overlooked by the government. Their findings highlight social failings such as poor people's lack of access to safe working conditions, health facilities and even sanitation — topics that counter India's desired image.

The current situation is certainly even worse than described. The majority of recorded infections and deaths are in relatively well-off urban areas, whose residents have access to private health care. The extent of devastation in rural India, where around 66% of the nation's 1.4 billion people live, is still largely unknown. And official data and peer-reviewed research do not capture the despondence I feel hearing of news colleagues battling COVID-19 in intensive care — or, worse, succumbing — or friends' frantic 20-hour search for a hospital bed. My Whatsapp and Twitter

feeds are full of urgent pleas for beds, ventilators, oxygen, remdesivir and the like — and now, updates on deaths.

Many countries are struggling with successive waves of outbreaks, and have taken questionable decisions on border control, testing, contact tracing and reopening. India has not learnt from others' disasters, even though its researchers pointed to Manaus as a precautionary tale.

It is time for India's policymakers to trust those with relevant expertise, to make sure the necessary data are collected and available, and to accept the value of scientific findings, even if they do not fit the government narrative. Indian citizens are dying because of flawed policies, alongside government unwillingness to acknowledge or act on unwelcome implications from informed analyses.

The open letter is welcome, coming from scientists' frustration and despair at the tragedy. But scientific administrators and academies need to make even stronger statements. And the government must show that it is listening, by getting them access to the data needed to curb this devastating second wave.

Nature **593**, 9 (2021)

doi: <https://doi.org/10.1038/d41586-021-01140-6>

Jobs from Nature Careers

- - - [All jobs](#)
 - - [Postdoc \(f/m/d\) – Molecular mechanisms of translation in yeast –](#)

[Max Planck Institute for Biophysical Chemistry \(MPIBPC\)](#)

[Göttingen, Germany](#)

[JOB POST](#)

- [Laboratory Research Scientist - Cancer Epigenetics Laboratory](#)

[Francis Crick Institute](#)

[London, United Kingdom](#)

[JOB POST](#)

- [PhD student \(m/f/div\) in MS-based proteomics of small proteins](#)

[Max Planck Institute of Biophysics \(MPIBP\)](#)

[Frankfurt am Main, Germany](#)

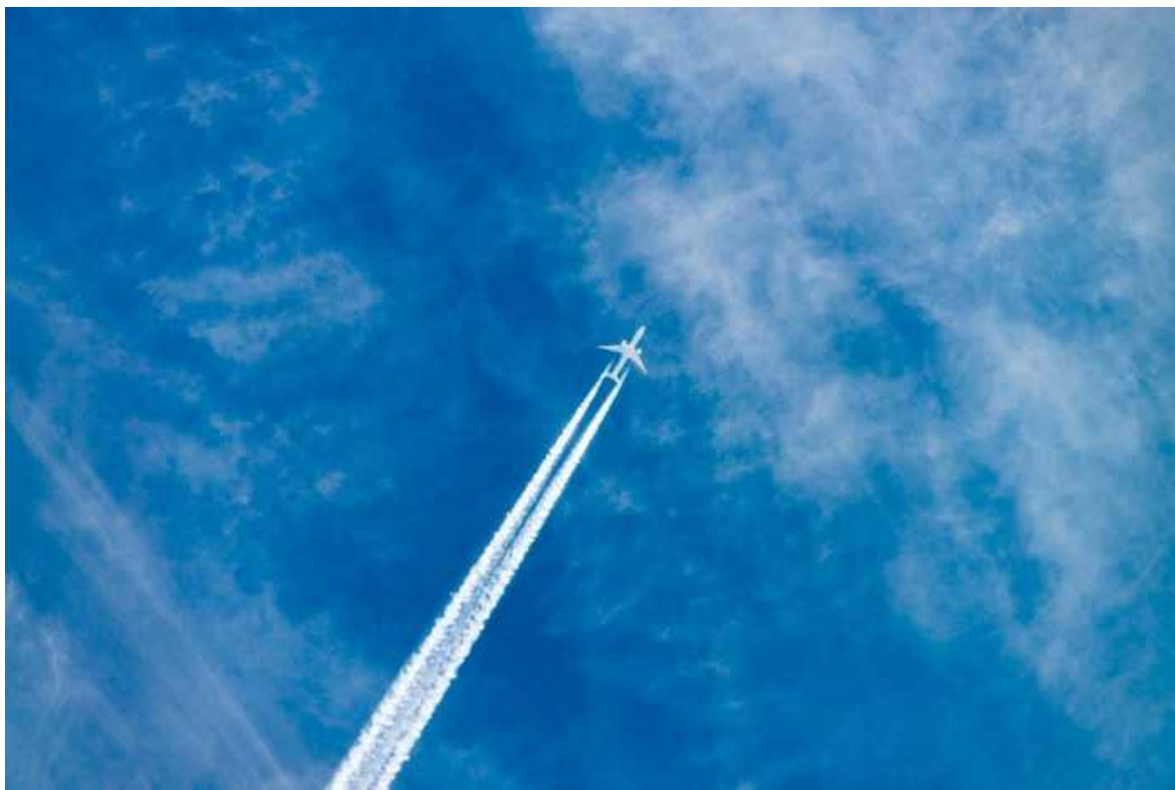
[JOB POST](#)

- [Senior/Laboratory Research Scientist](#)

[Francis Crick Institute](#)

[London, United Kingdom](#)

[JOB POST](#)



Water can't get a grip on a newly fabricated material, which might one day help to prevent ice build-up on aeroplane wings. Credit: Getty

Materials science

29 April 2021

A surface stays frost-free by showing water drops no mercy

A bio-inspired material forces water droplets to jump into the void — and thus prevents ice formation.

A textured material repels water so well that any droplets that condense on its surface vault off almost immediately, standing no chance of turning into dangerous ice.

Keeping people safe on wintry pavements and ensuring that planes stay ice-free requires surfaces that thwart frost formation. Wheat plants offer clues for doing the job: the structure of their leaves causes small droplets of dew to merge. The resulting, larger droplets spontaneously propel themselves off the leaf, keeping the foliage clean and dry.

Ximin He at the University of California, Los Angeles, Zhiyuan He at the University of Chinese Academy of Sciences in Beijing and their colleagues drew on this phenomenon to fight frost. The researchers deposited a layer of nanoparticles onto copper in a porous pattern that mimicked the wheat leaf's texture. The pattern forces water droplets on the material to merge and jump off within milliseconds, which not only keeps the material dry but also maximizes its ability to absorb solar energy.

Under artificial sunlight, the material stayed dry and kept its surface temperature above freezing even amid humid surroundings at -50°C .

[Proc. Natl Acad. Sci. USA \(2021\)](#)

- [Materials science](#)
-

This article was downloaded by **calibre** from <https://www.nature.com/articles/d41586-021-01144-2>



Minding the diary: the Svalbard ptarmigan relies on its internal clock to know when it's mating season. Credit: Vincent Legrand/AGAMI Photo Agency/Alamy

Physiology

29 April 2021

The world's northernmost bird is a clock-watcher

Ptarmigan that live far above the Arctic Circle generate circadian rhythms, despite summer's eternal sunshine.

No bird spends its life farther north than the Svalbard ptarmigan, which passes deepest winter in perpetual darkness and high summer bathed in 24-

hour sunlight. But it seems that even the ptarmigan has a light-sensitive internal clock, which tells it when the breeding season has arrived.

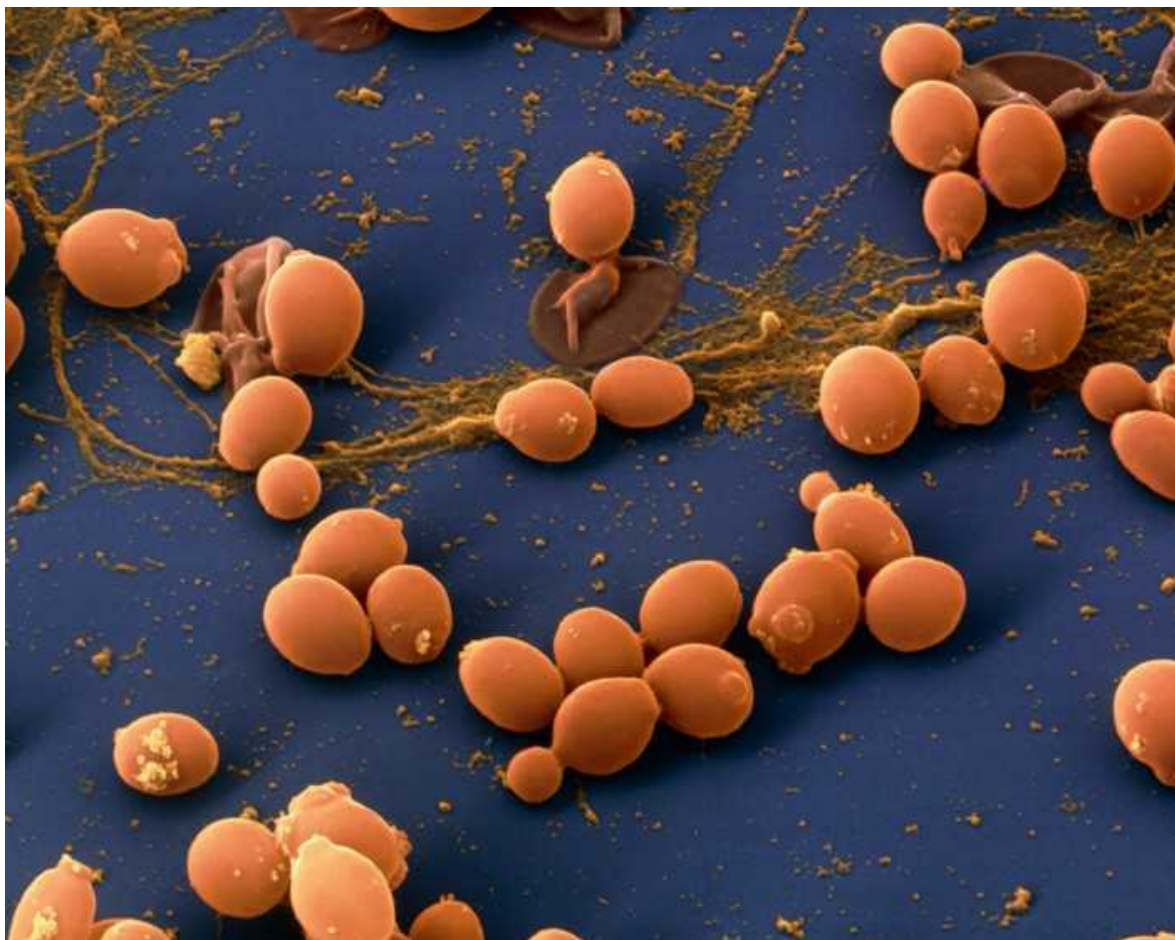
Most birds have an inner clock that prompts them to perform specific tasks at specific times of day. But in summer, Svalbard ptarmigan (*Lagopus muta hyperborea*) live under a midnight sun, and their activity during a 24-hour period doesn't follow a consistent pattern.

Nevertheless, David Hazlerigg, Alexander West and their colleagues at the University of Tromsø in Norway found that key genes for establishing 24-hour rhythms are active in the brain of the ptarmigan, which uses this daily 'circadian' clock to time seasonal events. In birds kept constantly in the light, genes linked to reproduction became active, and the birds increased their activity in preparation for mating. The researchers' experiments suggest that 14 hours after sunrise, the birds' internal clocks 'check' whether the Sun is still up.

Curr. Biol. (2021)

- Physiology
-

This article was downloaded by **calibre** from <https://www.nature.com/articles/d41586-021-01124-6>



Using an algorithm they developed, researchers identified a fungus that makes a chemical weapon against infectious fungi such as *Candida albicans* (pictured). Credit: Eye of Science/Science Photo Library

Biochemistry

28 April 2021

A smart genome scan could help scratch the itch for new antifungal drugs

Genome mining uncovers how a fungus makes a chemical agent against others of its kind.

The key to creating new antifungal drugs might be hiding in the genomes of fungi that need to protect themselves from their own chemical weapons.

To defend itself against other fungi, *Penicillium restrictum* makes a molecule called restricticin, which blocks a crucial fungal enzyme. Shutting down the enzyme can curb the growth of fungi, such as *Candida albicans*, that infect humans.

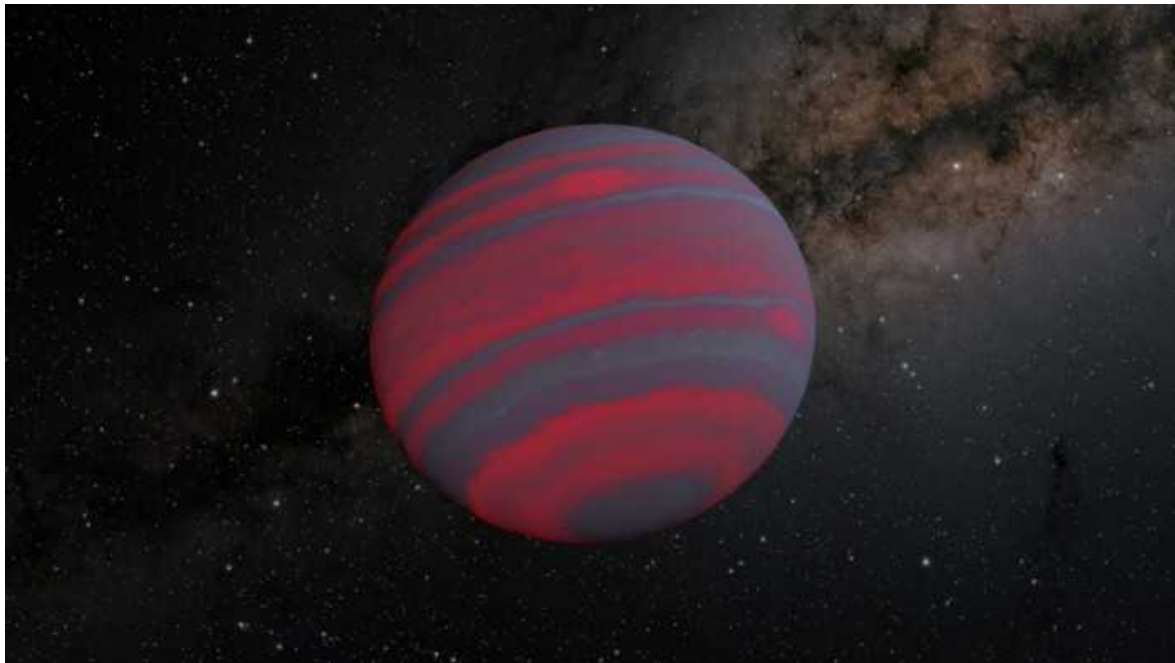
How *P. restrictum* makes restricticin has been unknown, but Yi Tang at the University of California, Los Angeles, and his colleagues realized that any fungus that makes restricticin would also need to protect itself from its own poison. They suspected that the fungal genes that encode restricticin might sit close to genes for a restricticin-resistant version of its target enzyme.

The researchers built a genome-mining algorithm to look for genes encoding a resistant enzyme near clusters of genes that could potentially make restricticin. The algorithm led to the discovery of the biosynthetic pathway for restricticin — and showed that the compound is also produced by other species of fungus. The authors hope that their genome-mining method will lead to the identification of other naturally occurring antifungal substances.

[J. Am. Chem. Soc. \(2021\)](#)

- [Biochemistry](#)

This article was downloaded by **calibre** from <https://www.nature.com/articles/d41586-021-01137-1>



A rapidly spinning brown dwarf (pictured, artist's impression) tends to have narrow atmospheric bands; the faster the spin, the thinner the bands. Credit: NASA/JPL-Caltech

Astronomy and astrophysics

27 April 2021

Dim stars that have failed at fusion are masters of spin

Three brown dwarfs whirl on their axes at a dizzying rate that might be close to the celestial speed limit for these bodies.

Astronomers have caught three brown dwarfs spinning at the fastest rates ever recorded for these objects, which are sometimes described as ‘failed stars’.

Brown dwarfs are celestial objects with masses that fall between those of large, Jupiter-like planets and the smallest ordinary stars. They are cooler and dimmer than ordinary stars because they are too small to sustain long-term nuclear fusion.

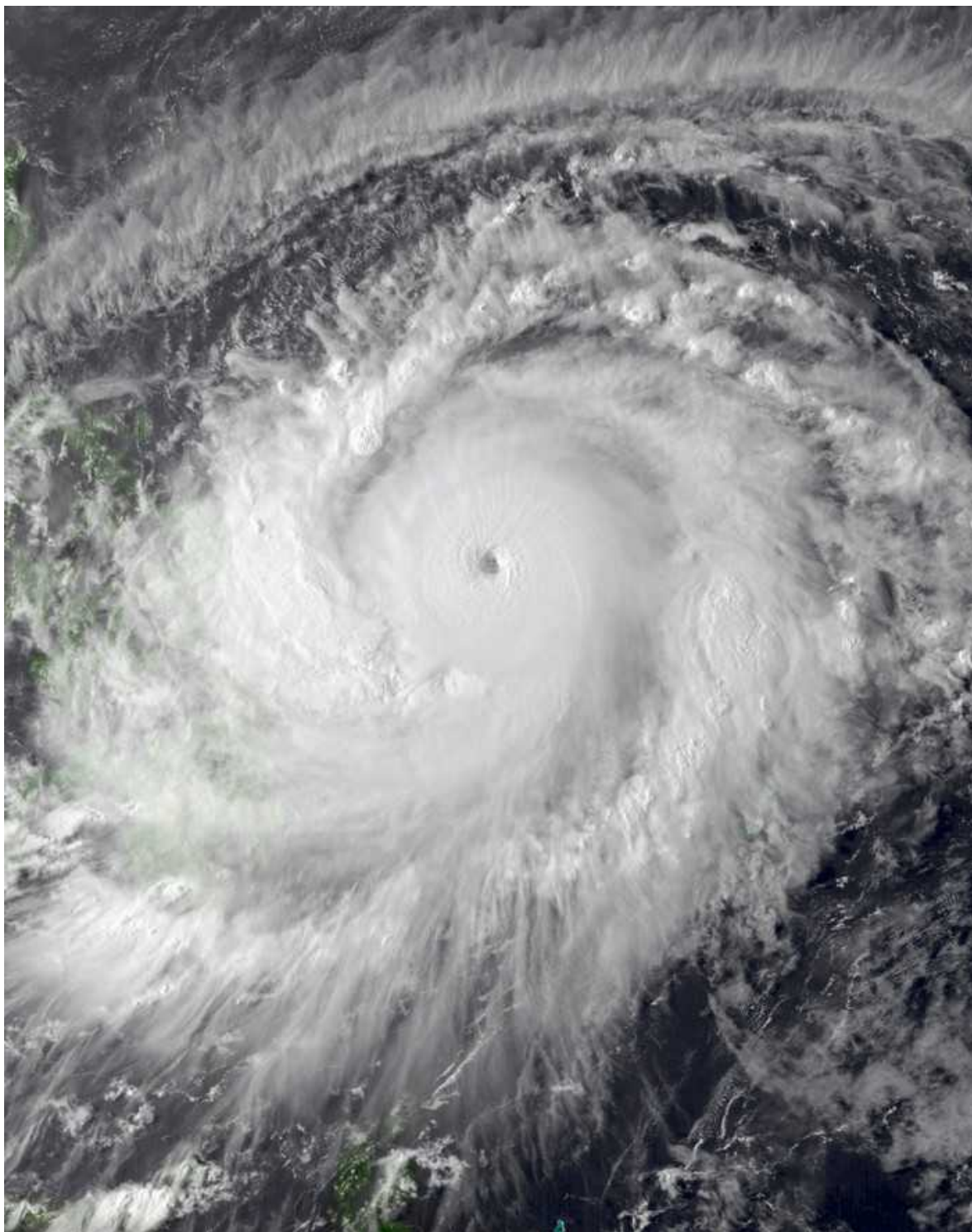
Megan Tannock at the University of Western Ontario in London, Canada, and her collaborators analysed nearly 80 brown dwarfs with regular variations in their brightness and light spectrum. Such variations are produced when brighter spots on the stars' surfaces come in and out of view as the stars rotate. Measuring the period of such variations gives an accurate estimate of how fast a star is spinning.

The authors found that 3 of the brown dwarfs had record-short rotation periods, ranging from 1 hour and 5 minutes to 1 hour and 14 minutes. The similarity between the periods suggests that the objects might be moving at close to a maximum speed limit, beyond which they would break apart.

Astron. J. (2021)

- Astronomy and astrophysics

This article was downloaded by **calibre** from <https://www.nature.com/articles/d41586-021-01122-8>



Typhoon Surigae looms over the Western North Pacific in mid-April 2021. Such storms, normally common in the region, were notably absent in July 2020. Credit: NASA via Wikimedia Commons

Climate sciences

29 April 2021

Warming seas brought an eerie calm to a stormy region

In July 2020, the Western North Pacific was hit by a record-breaking number of typhoons: zero.

Unusually balmy Indian Ocean temperatures were a major reason for the total lack of Pacific typhoons in July 2020 — an unprecedented absence in 55 years of record-keeping.

Like hurricanes in the Atlantic Ocean, typhoons in the Northwestern Pacific can wreak destruction on coastal areas. But in July last year, not one typhoon made its way through the region. Such a deficit has not been recorded since satellites began monitoring tropical cyclone activity in 1965.

Liguang Wu at Fudan University in Shanghai and Chao Wang at Nanjing University of Information Science and Technology, both in China, and their colleagues analysed oceanic and atmospheric data in search of an explanation for the calmer-than-normal skies. They found that surface temperatures in the Indian Ocean in July 2020 were the highest on record, leading to a high-pressure atmospheric system that suppressed typhoon formation. Anomalous ocean temperatures in the Atlantic and Pacific oceans also contributed.

Because climate change is warming the Indian Ocean faster than other tropical waters, the authors say, this lack of typhoons might become more common in future.

[*Geophys. Res. Lett. \(2021\)*](#)

- [Climate sciences](#)
-

This article was downloaded by **calibre** from <https://www.nature.com/articles/d41586-021-01145-1>

| [Section menu](#) | [Main menu](#) |



Large-scale facilities such as this feedlot in Floresville, Texas, help to meet the global appetite for beef and other red meat, which remains strong despite the growing consumption of chicken and fish. Credit: Daniel Acker/Bloomberg/Getty

Agriculture

26 April 2021

Meat lovers worldwide pay climate little heed

People are eating more poultry and fish — but they're not giving up their hamburgers.

Global consumption of poultry and seafood, which are relatively climate-friendly, has grown since the early 1960s — but that growth has not suppressed people's hunger for red meat.

The production of meats such as beef and pork releases large amounts of heat-trapping gases compared with the production of poultry and seafood. Richard York at the University of Oregon in Eugene looked at 50 years of global food-consumption data to find out how people's dietary choices have changed and found that the consumption of poultry and seafood increased between 1961 and 2013. But consumption of beef and other meats has not fallen, despite growing evidence that eating less of it would be beneficial for both the climate and human health.

Consumption patterns might have changed since 2013, the last year for which data were available, York cautions. But to seriously reduce greenhouse-gas emissions — and the number of animals raised in industrial facilities — people would need to shift to a customary diet with a minimum of animal-based foodstuffs.

[Nature Sustain. \(2021\)](#)

- [Agriculture](#)

This article was downloaded by **calibre** from <https://www.nature.com/articles/d41586-021-01091-y>.



Truth in advertising: a poison dart frog's loud colours send the message that it is toxic if eaten. Credit: Getty

Evolution

27 April 2021

Animals' bright colours don't lie: eat me and you'll be sorry

An analysis of a score of species that includes frogs and insects shows that colouration is an 'honest' signal of toxicity.

The bright colours of animals such as poison dart frogs act as a warning signal, telling predators that the humble creatures pack a noxious punch.

Now, an analysis of the results of multiple scientific studies shows that the most eye-catching animals also tend to be the most toxic.

Scientists have long known that an animal's colourful markings can signal its toxicity, but it has not been clear whether variations in colour indicate differences in toxicity levels. Thomas White at the University of Sydney and Kate Umbers at Western Sydney University in Richmond, both in Australia, examined 24 studies that together assessed the colouring and toxicity of more than 20 species, taking in insects, amphibians and gastropods, a group of animals that includes snails and slugs.

The researchers found that specific features of warning signals — including brightness, hue and saturation — were more pronounced in animals with stronger or more abundant chemical defences than in those with lower levels of defence. The relationship holds at all scales: between individuals, populations and species.

This suggests that warning markings are a reliable indicator of how well defended animals are. The findings could help scientists to understand the function and evolution of warning signals, the authors say.

[Proc. R. Soc. B \(2021\)](#)

- [Evolution](#)

This article was downloaded by **calibre** from <https://www.nature.com/articles/d41586-021-01123-7>

News in Focus

- **[One billion COVID vaccines, psychedelic sensor and COVID transmission halved](#)** [05 May 2021]
News Round-Up • The latest science news, in brief.
- **[‘We are being ignored’: Brazil’s researchers blame anti-science government for devastating COVID surge](#)** [27 April 2021]
News • Researchers say that President Jair Bolsonaro’s administration has undermined science during an epic public-health crisis.
- **[Malaria vaccine shows promise — now come tougher trials](#)** [26 April 2021]
News • Preliminary results suggest the vaccine is up to 77% effective in young children, but researchers await larger studies.
- **[What’s next for physics’ standard model? Muon results throw theories into confusion](#)** [23 April 2021]
News • Anomalies to fundamental theory have physicists trying to concoct new explanations.
- **[How a historic funding boom might transform the US National Science Foundation](#)** [23 April 2021]
News • Proposed budget increases for the research funding agency could bolster US innovation efforts, but some worry this will change the agency’s mission.
- **[Key COVID research hit by cut to UK foreign-aid budget](#)** [29 April 2021]
News • UK scientists buffeted by uncertainty as the pandemic’s economic fallout reduces research funds.
- **[One million coronavirus sequences: popular genome site hits mega milestone](#)** [23 April 2021]
News • GISAID’s impressive effort to understand the spread of COVID-19 has seen scientists upload sequences from most nations on Earth.
- **[Microplastics are everywhere — but are they harmful?](#)** [04 May 2021]
News Feature • Scientists are rushing to study the tiny plastic specks that are in marine animals — and in us.

- **Fevers are plaguing the oceans — and climate change is making them worse** [05 May 2021]

News Feature • Sudden marine heatwaves can devastate ecosystems, and scientists are scrambling to predict when they will strike.

| [Next section](#) | [Main menu](#) | [Previous section](#) |

NEWS ROUND-UP

05 May 2021

One billion COVID vaccines, psychedelic sensor and COVID transmission halved

The latest science news, in brief.



A Nepalese man receives a COVID-19 vaccine at Lukla near Mount Everest in the Himalayas.

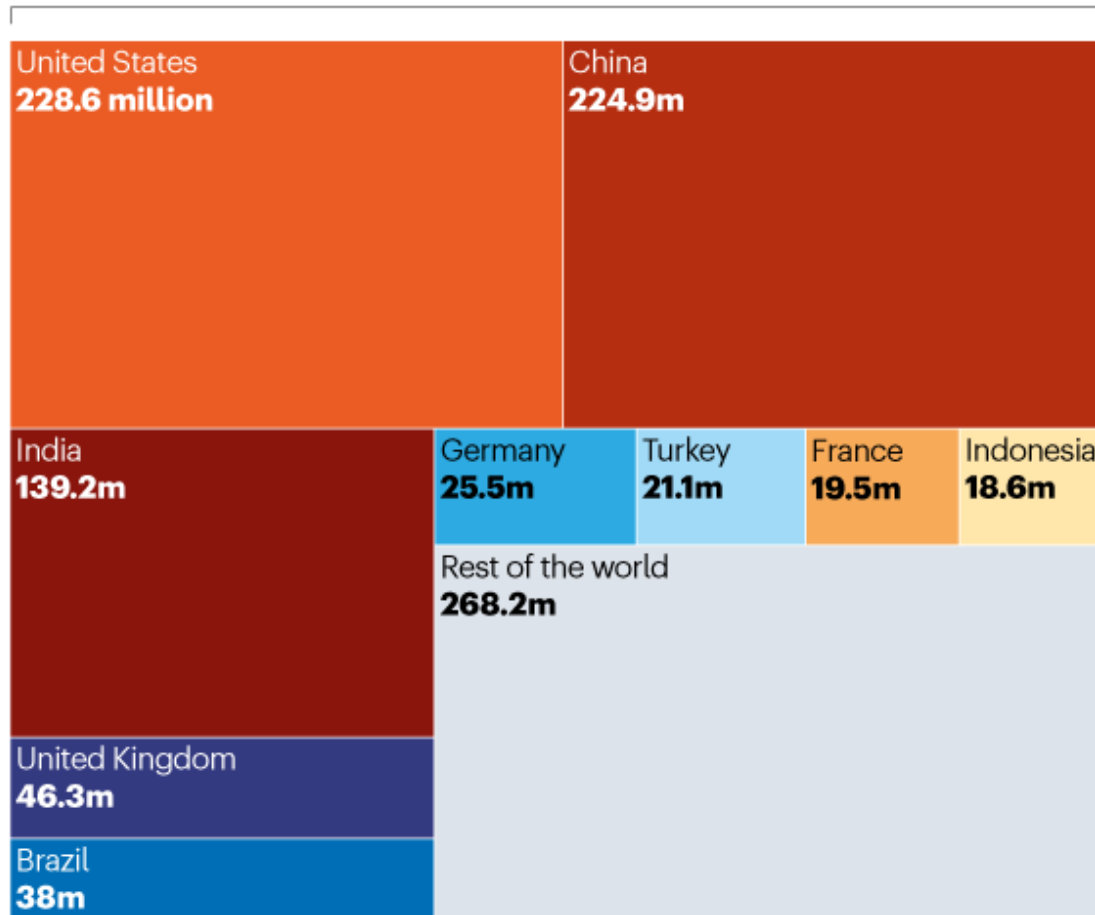
Who got the first billion COVID vaccinations?

The world has reached the milestone of administering [one billion doses of COVID-19 vaccines](#), just four months after the World Health Organization (WHO) approved the first vaccine for emergency use, and roll-outs began in countries such as the United States and the United Kingdom. The speed at which they have been administered is remarkable, but unequal distribution of the vaccinations highlights global disparities, say researchers (see ‘Divided by doses’).

DIVIDED BY DOSES

More than three-quarters of all doses of COVID-19 vaccines given so far have been administered in just ten nations. People in more than 170 other nations and territories have had to share the remainder.

Total vaccine doses administered as of 25 April **1.03 billion**



©nature

Source: Our World in Data

“It is an unprecedented scientific achievement. Nobody could have imagined that, within 16 months of the identification of a new virus, we would have vaccinated one billion people worldwide,” says Soumya Swaminathan, the WHO’s chief scientist, based in Geneva, Switzerland.

As of 27 April, 1.06 billion doses had been given to 570 million people, which means that about 7.3% of the world’s population of 7.79 billion have received at least one dose. But scientists say that more than 75% of the world’s population will need to be vaccinated to bring the pandemic under control.



Crystals of the neurotransmitter serotonin (polarized light). Psychedelic drugs bind to serotonin receptors in the brain. Credit: Michael W. Davidson/Science Photo Library

Sensor seeks out psychedelic drugs without the trip

Scientists in search of psychedelic drug treatments have developed a way to determine whether a molecule is likely to cause hallucinations, without testing it on people or animals. Using their approach, the researchers identified a psychedelic-like molecule that had no hallucinogenic properties but showed antidepressant activity in mice ([C. Dong et al. Cell https://doi.org/gjtmmt, 2021](#)).

Growing evidence suggests that psychedelic compounds might be able to treat illnesses such as post-traumatic stress disorder, but it's unclear whether there is a way to harness their therapeutic properties without the trippy side effects.

It is almost impossible to predict whether a potential drug will cause hallucinations before it is tested. To address this, a team led by neuroscientists David Olson and Lin Tian at the University of California, Davis, designed a [fluorescent biosensor](#) based on the structure of a brain receptor for the neurotransmitter serotonin (crystals pictured), which is targeted by psychedelics. When compounds bind to the sensor, it changes shape, which affects the intensity of light emitted. This can be used to predict the effect the compound would have on a real serotonin receptor, making it “a radar for hallucinogenic potential”, Tian says.



A healthcare worker prepares a dose of the AstraZeneca COVID-19 vaccine for a woman in Hasland, UK. Credit: Oli Scarff/AFP/Getty

One dose of COVID vaccine nearly halves transmission risk

A single dose of the COVID-19 vaccine made by either Pfizer or AstraZeneca cuts a person's risk of transmitting SARS-CoV-2 to their closest contacts by as much as half, according to an analysis of more than 365,000 households in the United Kingdom.

Although the vaccines have been shown to reduce COVID-19 symptoms and serious illness, their ability to prevent coronavirus transmission has been unclear. Kevin Dunbar, Gavin Dabrera and their colleagues at Public Health England in London looked for cases in which someone became infected with SARS-CoV-2 after receiving a dose of either vaccine ([R. J. Harris et al. Preprint at Knowledge Hub https://go.nature.com/3e3iu1i; 2021](#)). They then assessed how often those individuals transmitted the virus to household contacts.

The team found that people who had been vaccinated for at least 21 days could still test positive for the virus. But viral transmission from these individuals to others in their households was 40–50% lower than transmission in households in which the first person to test positive had not been vaccinated. Results for the two vaccines were similar.

Nature **593**, 13 (2021)

doi: <https://doi.org/10.1038/d41586-021-01141-5>

Jobs from Nature Careers

- - - [All jobs](#)
 - - [Postdoc \(f/m/d\) – Molecular mechanisms of translation in yeast –](#)

Max Planck Institute for Biophysical Chemistry (MPIBPC)
Göttingen, Germany

JOB POST
 - [Laboratory Research Scientist - Cancer Epigenetics Laboratory](#)

Francis Crick Institute
London, United Kingdom

JOB POST
 - [PhD student \(m/f/div\) in MS-based proteomics of small proteins](#)

Max Planck Institute of Biophysics (MPIBP).

Frankfurt am Main, Germany

JOB POST

▪ **Senior/Laboratory Research Scientist**

Francis Crick Institute

London, United Kingdom

JOB POST

This article was downloaded by **calibre** from <https://www.nature.com/articles/d41586-021-01141-5>

| [Section menu](#) | [Main menu](#) |

NEWS

27 April 2021

‘We are being ignored’: Brazil’s researchers blame anti-science government for devastating COVID surge

Researchers say that President Jair Bolsonaro’s administration has undermined science during an epic public-health crisis.

- [Luke Taylor](#)
 1. Luke Taylor
[View author publications](#)

You can also search for this author in [PubMed](#) [Google Scholar](#)



COVID-19 deaths have peaked in Brazil during its recent surge.Credit: Joao Guimaraes/AFP/Getty

More than a year after Brazil detected its first case of COVID-19, the country is facing its darkest phase of the pandemic yet. Researchers are devastated by the recent surge in cases and say that the government's failure to follow science-based guidance in responding to the pandemic has made the crisis much worse.

They add that President Jair Bolsonaro's administration has publicly undermined science while refusing to implement protective national lockdowns and spreading misinformation.

“Being a scientist in Brazil is so sad and frustrating,” says Jesem Orellana, an epidemiologist at the Oswaldo Cruz Foundation’s centre in Manaus. “Half of our deaths were preventable. It’s a total disaster.”



['Tropical Trump' victory in Brazil stuns scientists](#)

A surge in coronavirus infections has brought many of Brazil's intensive-care units to the [brink of collapse](#). And daily and monthly death tolls have reached record highs. Since the pandemic began, more than 389,000 people in Brazil have died from the illness caused by SARS-CoV-2, representing 13% of the world's COVID-19 mortalities — even though the country has less than 3% of the global population.

Bolsonaro, a polarizing figure who has been likened to former US president Donald Trump, has been contradicting scientific opinion since the beginning of the pandemic, [when he called COVID-19](#) a “little flu”. Late last year, [he also implied](#) that COVID-19 vaccines could be dangerous, saying: “If you turn into a crocodile, it’s your problem.”

Brazilian researchers were well aware of Bolsonaro's anti-science stance heading into the pandemic. After taking office in 2019, he [slashed funding for Brazil's universities](#) and for its science and education ministries. He also accused Brazil's National Space Research Institute of falsifying satellite data that showed accelerated deforestation in the Amazon. Still, his handling of the COVID-19 crisis came as a shock, says Natalia Pasternak, a microbiologist and president of the Question of Science Institute in São Paulo. “I don't think that any of us could foresee that it would be this bad.”

Bolsonaro's administration did not respond to a request for comment from *Nature*'s news team.

Tried-and-tested tools

Bolsonaro's government has gone against scientific advice a number of times during the pandemic, including in promoting unproven COVID-19 cures. But the most costly of its errors, says Orellana, has been ignoring tried-and-tested pandemic-containment strategies.



Brazilian President Jair Bolsonaro's undermining of science during the COVID-19 pandemic has made its effects worse for the country, researchers say. Credit: Ueslei Marcelino/Reuters/Alamy

Despite research showing that face masks can reduce the chances of transmitting and catching SARS-CoV-2, Bolsonaro weakened a federal mandate for the wearing of masks last July. He has [also refused to wear a face mask himself](#), even after testing positive for COVID-19. And he declined to issue national orders to close non-essential businesses during the

pandemic, saying lockdowns would be economically harmful, particularly for the poor, and [labelling state governors](#) who enforced them “tyrants”.

“Sadly, in the twenty-first century, we are failing at a national level to incorporate old, efficacious tools that could save tens of thousands of lives,” says Orellana.



[Scandal over COVID vaccine trial at Peruvian universities prompts outrage](#)

A recent study that tracked COVID-19 outbreaks across Brazil from late February to early October, found that regions implementing strict measures such as lockdowns and mask mandates had fewer deaths per capita than other comparable regions¹.

“In the absence of a coordinated action from the federal level, what we saw were different responses at local levels, that were not sufficient to avoid the heavy death toll,” says Marcia Castro, chair of the Department of Global Health and Population at the Harvard T.H. Chan School of Public Health and one of the study’s authors.

“The government has been a denialist of the pandemic,” says Gabriela Lotta, who studies public administration and government at the Getulio Vargas Foundation in Rio de Janeiro, Brazil. “It denies that it is serious, denies that it needs intervention, and denies the necessary measures defended by science to face it.”

Runaway virus

Although scientists acknowledge that the current COVID-19 surge in Brazil is partly due to the spread of coronavirus variants — in particular a highly transmissible version of the virus called P.1 — they say government inaction has allowed the spread to happen.

The P.1 variant probably emerged in Manaus, a city in the Amazon, in November 2020². In January, after Manaus was overrun with P.1 infections, Orellana pleaded at a public meeting of the Inter-American Court of Human Rights for politicians to close travel in and out of the Amazon.



Medical facilities such as this one in Santo André, Brazil, have been stretched to the limit during the country's recent COVID-19 surge.Credit: Alexandre Schneider/Getty

But patients infected with P.1 and their family members were airlifted across the country for treatment, and airports and bus terminals remained open. By

March, [scientists detected P.1](#) as the dominant variant in six out of eight Brazilian states they studied.

Neighbouring nations tried to shut themselves off from Brazil, but many are now seeing more cases of P.1 inside their borders. For instance, 40% of COVID-19 cases in Lima are now P.1 infections.



[Latin America's embrace of an unproven COVID treatment is hindering drug trials](#)

Mauricio Nogueira, a virologist at the FAMERP medical school in São José do Rio Preto, Brazil, says researchers in Brazil studying SARS-CoV-2 variants are unable to study them properly because Bolsonaro has cut funding for science so severely. “We don’t have funds to do basic research, such as to understand how the variants are more or less virulent,” he says. “We don’t have the lab equipment or reagents for that.”

As variants continue to evolve — there are currently about 90 circulating in Brazil — this inability to investigate them properly threatens the country’s pandemic response and recovery. Some studies suggest that variants can diminish the protection that COVID-19 vaccines offer.

Public messaging

Brazilian scientists say that the Bolsonaro administration's promotion of misinformation has made things worse. Some, including Orellana and Pasternak, are increasingly putting aside their research to make television appearances in which they promote practices such as social distancing.

"It's very difficult to implement preventive measures when misinformation comes directly from the federal government," says Pasternak.

Brazil's politics have left scientists feeling "helpless", says Nogueira. "We have the tools or at least the capability to help the country, but we are being ignored and not supported by the leaders of the country."



[Latin American scientists join the coronavirus vaccine race: 'No one's coming to rescue us'](#)

Efforts to counter Brazil's current surge have not been helped by the country's slow vaccine rollout, says Ricardo Gazzinelli, president of the Brazilian Society for Immunology. Bolsonaro questioned the "rush" to procure vaccines last year because he thought the pandemic was coming to an end.

Only about one in ten Brazilians have received a COVID-19 vaccine so far. If the vaccine rollout doesn't scale up and people continue to ignore mask guidance, deaths from COVID-19 in Brazil could exceed half a million by mid-June, [according to models](#) developed by the Institute for Health Metrics and Evaluation at the University of Washington in Seattle.

“All we can do right now is brace for impact,” says Nogueira.

Nature **593**, 15-16 (2021)

doi: <https://doi.org/10.1038/d41586-021-01031-w>

References

1. 1.

Castro, M. C. *et al.* *Science* <https://doi.org/10.1126/science.abh1558> (2021).

2. 2.

Faria, N. R. *et al.* *Science* <https://doi.org/10.1126/science.abh2644> (2021).

Jobs from Nature Careers

- - - [All jobs](#)
 - - **Postdoc (f/m/d) – Molecular mechanisms of translation in yeast –**
[Max Planck Institute for Biophysical Chemistry \(MPIBPC\)](#)
[Göttingen, Germany](#)
[JOB POST](#)
 - **Laboratory Research Scientist - Cancer Epigenetics Laboratory**

Francis Crick Institute

London, United Kingdom

JOB POST

- **PhD student (m/f/div) in MS-based proteomics of small proteins**

Max Planck Institute of Biophysics (MPIBP)

Frankfurt am Main, Germany

JOB POST

- **Senior/Laboratory Research Scientist**

Francis Crick Institute

London, United Kingdom

JOB POST

This article was downloaded by **calibre** from <https://www.nature.com/articles/d41586-021-01031-w>

NEWS
26 April 2021

Malaria vaccine shows promise — now come tougher trials

Preliminary results suggest the vaccine is up to 77% effective in young children, but researchers await larger studies.

- [Heidi Ledford](#)
 1. Heidi Ledford
[View author publications](#)

You can also search for this author in [PubMed](#) [Google Scholar](#)



A previous version of an experimental malaria vaccine was trialled at Ewin Polyclinic in Cape Coast, Ghana. Credit: Cristina Aldehuela/AFP/Getty

A vaccine against malaria has shown promise in early clinical trials, raising hopes that it might one day prove to be an effective weapon against one of the world's biggest killers of children.

In a trial in 450 children aged 5–17 months, the vaccine, called R21, was up to 77% effective at preventing malaria over the course of one year — which, if confirmed, would clear a 75% effectiveness target set by the World Health Organization. The results are presented in a preprint posted on the server SSRN on 20 April¹.

R21 is a modified form of a vaccine that has already been deployed in an ongoing study in hundreds of thousands of children in Malawi, Kenya and Ghana. That vaccine, called RTS,S or Mosquirix, is about 56% effective over one year, and 36% effective over four years.

R21 is designed to be both more potent and cheaper to produce than Mosquirix, says Kwadwo Koram, an epidemiologist at the University of Ghana in Accra. But it remains to be seen if the promising results from this trial, which was done in Nanoro, Burkina Faso, will hold up when the vaccine is tested in a larger study. “Now we all wait patiently to see what will come out,” says Koram. “If that shows 75% efficacy, then we would be very happy and jumping around.”

Researchers plan to test R21 in a larger trial of 4,800 children, which is slated to start next week, says Halidou Tinto, a lead author of the study and a parasitologist at the Health Sciences Research Institute in Nanoro. The team has also been working with the Serum Institute of India, a vaccine-manufacturing powerhouse in Pune that has pledged to produce at least 200 million doses of the vaccine each year if it is eventually authorized for use.

Slow progress

It took researchers less than a year to develop a roster of effective vaccines against COVID-19, but half a century of toil has still not yielded a vaccine against malaria that meets the World Health Organization’s efficacy goal. Part of the problem is low investment in preventing a disease that predominately affects low- and middle-income countries. Another issue is the malaria parasite (*Plasmodium* spp.) itself, which has a complex life cycle and the ability to mutate key proteins, generating fresh strains.

Initial hubris gave way to frustration as researchers realized that vaccines against malaria would be difficult to produce, says Nicholas White, who studies tropical medicine at Mahidol University in Bangkok. “People thought that it would be easy,” he says, “but it became increasingly clear that these parasites are clever.”

But the urgency has remained: malaria still kills about 400,000 people a year, most of them infants and children under the age of 5.

R21 and Mosquirix both target the malaria parasite in the sporozoite phase of its life cycle — the phase in which it enters the human body from its mosquito hosts. The vaccines include a protein secreted by the parasite at

that stage, in the hope of stimulating an antibody response against it. R21 includes a higher concentration of these proteins.

Each of the vaccines is administered with a chemical called an adjuvant, which boosts immune responses to the inoculation. But the adjuvant used with R21 is easier to make than that used with Mosquirix, raising hopes that it could be cheaper, as well.

Still, White urges caution until larger trials have been conducted, noting that efficacy sometimes drops when studies are scaled up. “Definitely it’s exciting because of the possibility of large-scale production at relatively low cost,” he says. “But because it’s a small study, I don’t think you can say, ‘Wow, slam dunk, we’ve got a much better vaccine.’”

Lasting effects

Researchers will also be looking to see how durable the effects of the vaccine are. The R21 trial lasted for one year, but Burkina Faso is plagued by malaria for only about six months of each year, notes Stephen Hoffman, chief executive of Sanaria, a company in Rockville, Maryland, that is also developing malaria vaccines. During the second half of the study, there was only one case of malaria in the control group that did not receive the vaccine, Hoffman notes, making it impossible to judge whether the benefits of the vaccine lasted for the full year.

Researchers will continue to administer booster shots and follow the 450 participants for at least another year, says Tinto, and are hoping to extend the study for one to two years after that. The next, larger trial will also include countries in which malaria is a year-round threat, he says.

After Mosquirix, R21 is the candidate vaccine closest to widespread deployment, but researchers around the world are looking for ways to improve on these two vaccines, including targeting proteins expressed at different stages of the parasite’s life cycle. “I think R21 has now hit a ceiling for where we can go for this single-component vaccine,” says Stefan Kappe, who studies malaria-parasite biology and immunology at the Seattle

Children's Research Institute in Washington. "From here on out, we need to build on additional components."

Kappe is collaborating with researchers at Sanaria who are looking for ways to inoculate people using a disabled version of the whole parasite, rather than individual proteins. The hope is that the approach will yield a broader and more durable immune response by exposing the immune system to the parasite's full complement of proteins. But doing so will involve a series of technical challenges — including finding ways to grow the principal component of a vaccine, which must be aseptic, in mosquitoes.

For now, the R21 results are encouraging, says Koram. When coupled with other preventive measures, such as effective mosquito control, even a vaccine with less than 75% efficacy could help to reduce deaths, he says: "Every little piece is good."

Nature **593**, 17 (2021)

doi: <https://doi.org/10.1038/d41586-021-01096-7>

References

1. 1.

Datoo, M. S. *et al.* Preprint at SSRN
<https://doi.org/10.2139/ssrn.3830681> (2021).

Jobs from Nature Careers

- - - [All jobs](#)
 - - [Postdoc \(f/m/d\) – Molecular mechanisms of translation in yeast –](#)

[Max Planck Institute for Biophysical Chemistry \(MPIBPC\)](#)

[Göttingen, Germany](#)

[JOB POST](#)

- [Laboratory Research Scientist - Cancer Epigenetics Laboratory](#)

[Francis Crick Institute](#)

[London, United Kingdom](#)

[JOB POST](#)

- [PhD student \(m/f/div\) in MS-based proteomics of small proteins](#)

[Max Planck Institute of Biophysics \(MPIBP\)](#)

[Frankfurt am Main, Germany](#)

[JOB POST](#)

- [Senior/Laboratory Research Scientist](#)

[Francis Crick Institute](#)

[London, United Kingdom](#)

[JOB POST](#)

NEWS

23 April 2021

What's next for physics' standard model? Muon results throw theories into confusion

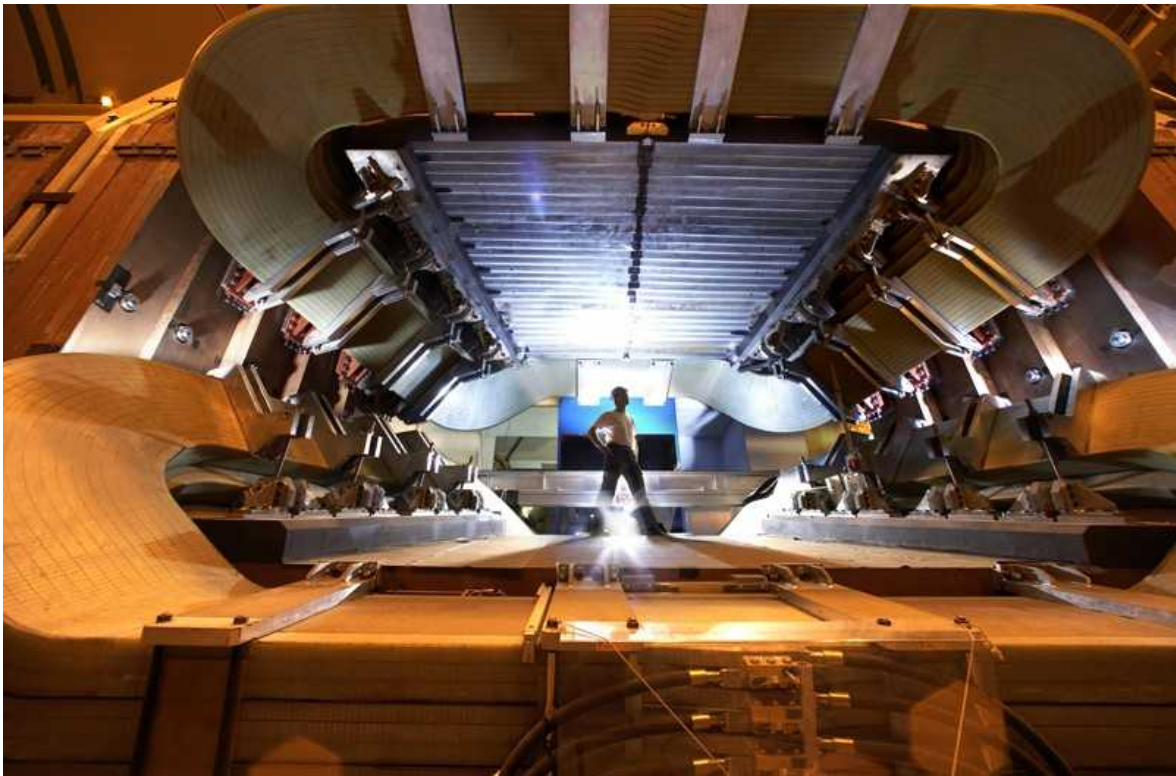
Anomalies to fundamental theory have physicists trying to concoct new explanations.

- [Davide Castelvecchi](#)

1. Davide Castelvecchi

[View author publications](#)

You can also search for this author in [PubMed](#) [Google Scholar](#)



The Large Hadron's Collider LHCb detector, pictured, reported anomalies in the behaviour of muons, two weeks before the Muon $g - 2$ experiment announced a puzzling finding about muon magnetism. Credit: Peter Ginter/CERN

Physicists should be ecstatic right now. Taken at face value, the surprisingly strong magnetism of the elementary particles called muons, [revealed by an experiment this month](#), suggests that the established theory of fundamental particles is incomplete. If the discrepancy pans out, it would be the first time that the theory has failed to account for observations since its inception five decades ago — and there is nothing physicists love more than proving a theory wrong.

But rather than pointing to a new and revolutionary theory, the result — announced on 7 April¹ by the Muon $g - 2$ experiment near Chicago, Illinois — poses a riddle. It seems maddeningly hard to explain it in a way that is compatible with everything else physicists know about elementary particles. And additional anomalies in the muon's behaviour, reported in March² by a collider experiment, only make that task harder. The result is that researchers

have to perform the theoretical-physics equivalent of a triple somersault to make an explanation work.

Zombie models

Take supersymmetry, or SUSY, a theory that many physicists once thought was the most promising for extending the current paradigm, the standard model of particle physics. Supersymmetry comes in many variants, but in general, it posits that every particle in the standard model has a yet-to-be-discovered heavier counterpart, called a superpartner. Superpartners could be among the ‘virtual particles’ that constantly pop in and out of the empty space surrounding the muon, a quantum effect that would help to explain why this particle’s magnetic field is stronger than expected.

If so, these particles could solve two mysteries at once: muon magnetism and dark matter, the unseen stuff that, through its gravitational pull, seems to keep galaxies from flying apart.

Until ten years ago, various lines of evidence had suggested that a superpartner weighing as much as a few hundred protons could constitute dark matter. Many expected that the collisions at the Large Hadron Collider (LHC) outside Geneva, Switzerland, would produce a plethora of these new particles, but so far none has materialized. The data that the LHC has produced so far suggest that typical superpartners, if they exist, cannot weigh less than 1,000 protons (the bounds can be higher depending on the type of superparticle and the flavour of supersymmetry theory).

“Many people would say supersymmetry is almost dead,” says Dominik Stöckinger, a theoretical physicist at the Dresden University of Technology in Germany, who is a member of the Muon $g - 2$ collaboration. But he still sees it as a plausible way to explain his experiment’s findings. “If you look at it in comparison to any other ideas, it’s not worse than the others,” he says.

There is one way in which Muon $g - 2$ could resurrect supersymmetry and also provide evidence for dark matter, Stöckinger says. There could be not one superpartner, but two appearing in LHC collisions, both of roughly

similar masses — say, around 550 and 500 protons. Collisions would create the more massive one, which would then rapidly decay into two particles: the lighter superpartner plus a run-of-the-mill, standard-model particle carrying away the 50 protons' worth of mass difference.

The LHC detectors are well-equipped to reveal this kind of decay as long as the ordinary particle — the one that carries away the mass difference between the two superpartners — is large enough. But a very light particle could escape unobserved. “This is well-known to be a blind spot for LHC,” says Michael Peskin, a theoretician at the SLAC National Accelerator Laboratory in Menlo Park, California.

The trouble is that models that include two superpartners with similar masses also tend to predict that the Universe should contain a much larger amount of dark matter than astronomers observe. So an additional mechanism would be needed — one that can reduce the amount of predicted dark matter, Peskin explains. This adds complexity to the theory. For it to fit the observations, all its parts would have to work “just so”.

Meanwhile, physicists have uncovered more hints that muons behave oddly. An experiment at the LHC, called LHCb, has found tentative evidence that muons occur significantly less often than electrons as the breakdown products of certain heavier particles called B mesons². According to the standard model, muons are supposed to be identical to electrons in every way except for their mass, which is 207 times larger. As a consequence, B mesons should produce electrons and muons at rates that are nearly equal.

The LHCb muon anomalies suffer from the same problem as the new muon-magnetism finding: various possible explanations exist, but they are all “ad hoc”, says physicist Adam Falkowski, at the University of Paris-Saclay. “I’m quite appalled by this procession of zombie SUSY models dragged out of their graves,” says Falkowski.

Other options

The task of explaining Muon $g - 2$'s results becomes even harder when researchers try concoct a theory that fits both those findings and the LHCb

results, physicists say. “Extremely few models could explain both simultaneously,” says Stöckinger. In particular, the supersymmetry model that explains Muon $g - 2$ and dark matter would do nothing for LHCb.

Some solutions nevertheless exist that could miraculously fit both. One is the leptoquark — a hypothetical particle that could have the ability to transform a quark into either a muon or an electron (which are both examples of a lepton). Leptoquarks could resurrect an attempt made by physicists in the 1970s to achieve a ‘grand unification’ of particle physics, showing that its three fundamental forces — strong, weak and electromagnetic — are all aspects of the same force.

Most of the grand-unification schemes of that era failed experimental tests, and the surviving leptoquark models have become more complicated — but they still have their fans. “Leptoquarks could solve another big mystery: why different families of particles have such different masses,” says Gino Isidori, a theoretician at the University of Zurich in Switzerland. One family is made of the lighter quarks — the constituents of protons and neutrons — and the electron. Another has heavier quarks and the muon, and a third family has even heavier counterparts.

Apart from the leptoquark, there is one other major contender that might reconcile both the LHCb and Muon $g - 2$ discrepancies. It is a particle called the Z' boson because of its similarity with the Z boson, which carries the ‘weak force’ responsible for nuclear decay. It, too, could help to solve the mystery of the three families, says Ben Allanach, a theorist at the University of Cambridge, UK. “We’re building models where some features come out very naturally, you can understand these hierarchies,” he says. He adds that both leptoquarks and the Z' boson have an advantage: they still have not been completely ruled out by the LHC, but the machine should ultimately see them if they exist.

The LHC is currently undergoing an upgrade, and it will start to smash protons together again in April 2022. The coming deluge of data could strengthen the muon anomalies and perhaps provide hints of the long-sought new particles (although a [proposed electron–positron collider](#), primarily designed to study the Higgs boson, might be needed to address some of the LHC’s blind spots, Peskin says). Meanwhile, beginning next year, Muon $g -$

2 will release further measurements. Once it's known more precisely, the size of the discrepancy between muon magnetism and theory could itself rule out some explanations and point to others.

Unless, that is, the discrepancies disappear and the standard model wins again. A new calculation, reported this month, of the standard model's prediction for muon magnetism³ gave a value much closer to the experimental result. So far, those who have bet against the standard model have always lost, which makes physicists cautious. "We are — maybe — at the beginning of a new era," Stöckinger says.

Nature **593**, 18-19 (2021)

doi: <https://doi.org/10.1038/d41586-021-01033-8>

References

1. 1.

Abi, B. *et al.* *Phys. Rev. Lett.* **126**, 141801 (2021).

2. 2.

LHCb Collaboration *et al.* Preprint at <https://arxiv.org/abs/2103.11769> (2021).

3. 3.

Borsanyi, Sz *et al.* *Nature* <https://doi.org/10.1038/s41586-021-03418-1> (2021).

Jobs from Nature Careers

- - - [All jobs](#)

- **Postdoc (f/m/d) – Molecular mechanisms of translation in yeast –**

Max Planck Institute for Biophysical Chemistry (MPIBPC)
Göttingen, Germany

JOB POST

- **Laboratory Research Scientist - Cancer Epigenetics Laboratory**

Francis Crick Institute
London, United Kingdom

JOB POST

- **PhD student (m/f/div) in MS-based proteomics of small proteins**

Max Planck Institute of Biophysics (MPIBP).
Frankfurt am Main, Germany

JOB POST

- **Senior/Laboratory Research Scientist**

Francis Crick Institute
London, United Kingdom

JOB POST

| [Section menu](#) | [Main menu](#) |

NEWS

23 April 2021

How a historic funding boom might transform the US National Science Foundation

Proposed budget increases for the research funding agency could bolster US innovation efforts, but some worry this will change the agency's mission.

- [Ariana Remmel](#)

1. Ariana Remmel

[View author publications](#)

You can also search for this author in [PubMed](#) [Google Scholar](#)



The US National Science Foundation is a major source of research funding in the United States. Credit: Shutterstock

US officials are discussing whether the National Science Foundation (NSF) — which funds about 25% of all basic academic research in the country — should get a historic budget boost, potentially changing the US science landscape. During congressional hearings last week, legislators evaluated proposals that would increase the agency's funding by as much as US\$100 billion over about five years. Any of these, if passed, would represent one of the largest increases for the NSF since it launched nearly 70 years ago.

A big cash influx for the NSF, which supports basic research and the development of the science, technology, engineering and mathematics (STEM) workforce, could help to fortify the country's status as a global leader in innovation — at a time when US officials are worried that it's losing ground to other nations. In particular, China [has aggressively invested](#) in research and development at a rate that may soon surpass the United States' own research and development funding levels. In 2019, China's patent office [received more than twice as many applications](#) as its US counterpart did.



China is closing gap with United States on research spending

“It is not an overstatement to say that we are already losing leadership,” says Rita Colwell, a microbiologist at the University of Maryland, College Park, who led the NSF from 1998 to 2004. “If we don’t invest significantly in basic research and technology-transfer capabilities, we will find ourselves far below leadership in the years ahead.”

The Biden administration, the US Senate and the US House of Representatives have each put forward a slightly different vision for expanding the NSF, although each of their proposals agrees that the agency should invest in emerging technologies and assist in their commercialization. That suggestion has made some researchers nervous about losing funding for basic research — a core priority for the NSF since its inception. As US legislators debate the merits of the proposals and converge on a final plan, one thing is certain: big changes are on the horizon for the NSF.

A boost for basic science

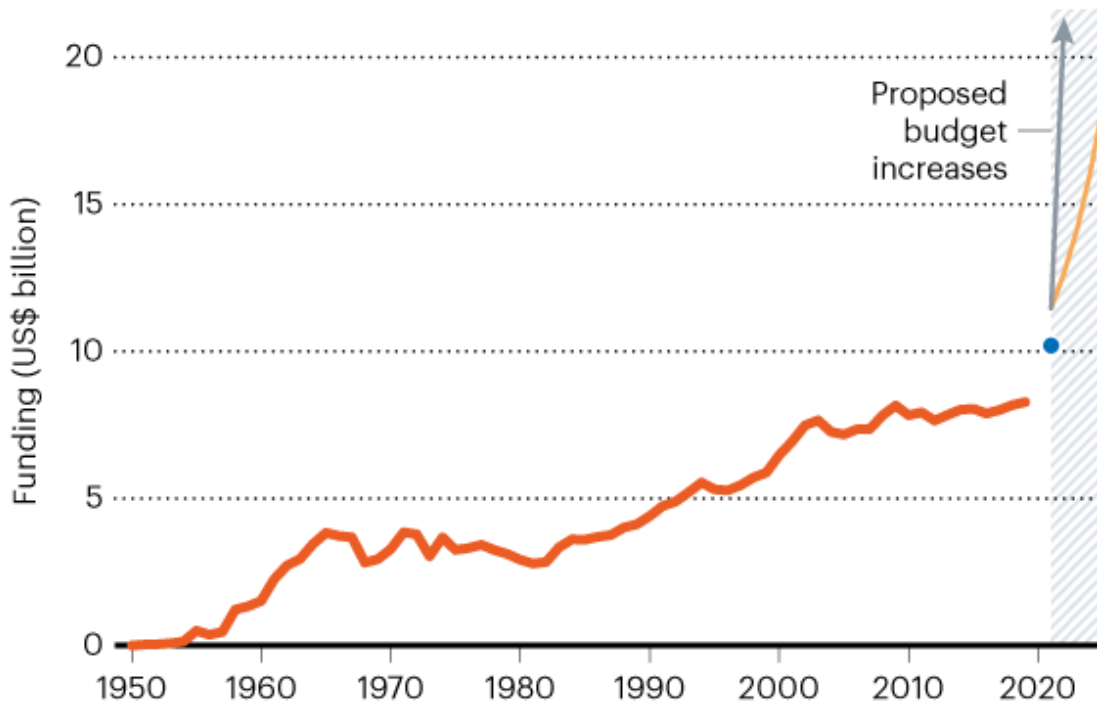
“The National Science Foundation budget should have been substantially increased long before now,” says Colwell. Since its launch in 1950, the agency has seen its budget slowly and steadily plod towards its current level of \$8.5 billion (see ‘Slow and steady’). In comparison, the National

Institutes of Health (NIH) — the country's top science funding agency for biomedical research — received \$42.9 billion this year.

SLOW AND STEADY

Since its launch in 1950, the US National Science Foundation has experienced only gradual changes in its budget. Now it stands to gain a massive funding boost if any of the proposals under consideration are adopted.

- Requested by President Joe Biden*
- NSF For the Future Act (US House of Representatives)
- Endless Frontier Act (US Senate)



Years are fiscal years, and funding is in constant 2020 dollars to adjust for inflation. Data exclude the \$3 billion given to the NSF in 2009 through the American Recovery and Reinvestment Act.

*Excludes \$50 billion requested by President Biden with no time frame specified.

©nature

The NIH's budget more than doubled between 1990 and 2003, and during this time it was able to fund roughly 30% of the grant proposals it received (that proportion has since dropped to around 20%). Members of the scientific community say that boost was responsible for significant achievements in US science. “The mRNA vaccines are a product of doubling our investment in the NIH,” said Sudip Parikh, chief executive of the American Association for the Advancement of Science, at a presentation to the National Press Club earlier this month. The NIH funded two research

projects¹ in 2002 that laid some of the foundation for [today's highly effective mRNA-based COVID-19 vaccines.](#)

US officials hope that a big budget boost for the NSF could similarly yield breakthroughs. With its current budget, the NSF funds only 20% of grant applicants each year, even though 30% of applicants' proposals are rated as highly meritorious by review panels, said NSF director Sethuraman Panchanathan during the Senate appropriations hearing on 13 April.

"My worry is that when we leave behind these ideas, somebody else picks up on [them]," namely global competitors, said Panchanathan. To properly support all the highly meritorious applications would require a doubling of the NSF budget at least, he explained.

From bench to market

What's badly needed, officials say, are more mechanisms for translating basic research into commercial technology. So all three proposals include money to create a technology directorate within the NSF.

The Biden administration's infrastructure plan proposed a \$50-billion infusion of cash for the NSF, with a focus on funding research and development for emerging technologies. The Senate's Endless Frontier Act would increase the agency's budget to \$100 billion over five years to support a new technology directorate. And members of the House proposed the National Science Foundation for the Future Act, which would increase the budget to \$18.3 billion by 2026, and create a much smaller technology initiative called the Directorate for Science and Engineering Solutions.



Biden pursues giant boost for science spending

Not everyone is in favour of building such a directorate at the NSF, however. Critics, including legislators in US states with national laboratories, worry that it would duplicate existing government efforts. At last week's Senate appropriations hearing, senator Joe Manchin pointed out that the US Department of Energy (DOE) already supports work at national laboratories involving technologies, such as quantum computing and artificial intelligence, that are highlighted in the Endless Frontier Act. Manchin, a West Virginia Democrat, chairs the Senate committee that oversees the DOE. He said that tasking the NSF with a greater responsibility for developing innovative technologies might just "reinvent the wheel".

In his testimony, Panchanathan assured legislators that the new directorate would partner with initiatives at the DOE and other federal agencies while also capitalizing on existing areas of expertise at the NSF.

Far from diminishing the importance of basic research, a technology directorate could "add a dimension" to the NSF mission, says Neal Lane, a science-policy researcher at Rice University in Houston, Texas, who served as NSF director from 1993 to 1998.



[NSF grant changes raise alarm about commitment to basic research](#)

Still, researchers worry that the rapid expansion of technology-focused initiatives at the NSF might eclipse its primary focus on basic science — a mission unique to the NSF among federal agencies. Paul Hanle, former president of the climate-science research group Climate Central, says the NSF's investments in fundamental research need to be carefully safeguarded so that the new technology focus does not “gobble up resources and push inquiry-based science into the sidelines”.

Given that the three proposals are similar, change at the NSF seems inevitable, says Christopher Hill, a science and technology-policy researcher at George Mason University in Arlington, Virginia. But, he says, a cash infusion alone won't lead to technological innovations. For this initiative to be successful in the long term, he adds, the NSF might have to undergo a cultural shift that would reflect its broader focus.

Equitable funding

During last week's hearings, some legislators expressed concern that a marked boost in NSF funding would not be distributed equitably. For instance, they pointed out that more than one-quarter of NSF funds in 2020 went to just three US states: California, Massachusetts and New York.



[Trump proposes slashing science spending at the NSF](#)

Members of the science community are also concerned that an influx of funding will draw more graduate students and postdocs to research who won't be able to find jobs if the budget later tightens. This happened after the NIH's budget stagnated following a boom in 2003.

Still, proponents of a budget boost hope that it could help to address a lack of diversity in the STEM workforce.

For now, Congress continues to iron out the details of the funding boost with the goal of arriving at a single plan. The Senate has now introduced a new draft of the Endless Frontier Act, with updated language to address the broad perspectives presented in last week's hearings.

"I've never been as optimistic that, finally, the National Science budget will be significantly increased," says Lane.

Nature **593**, 19-20 (2021)

doi: <https://doi.org/10.1038/d41586-021-01076-x>

References

1. 1.

Karikó, K., Buckstein, M., Ni, H. & Weissman, D. *et al.* *Immunity* **23**, 165–175 (2005).

Jobs from Nature Careers

- - - [All jobs](#)
 - - **Postdoc (f/m/d) – Molecular mechanisms of translation in yeast –**

[Max Planck Institute for Biophysical Chemistry \(MPIBPC\)](#)
[Göttingen, Germany](#)

[JOB POST](#)

 - **Laboratory Research Scientist - Cancer Epigenetics Laboratory**

[Francis Crick Institute](#)
[London, United Kingdom](#)

[JOB POST](#)

 - **PhD student (m/f/div) in MS-based proteomics of small proteins**

[Max Planck Institute of Biophysics \(MPIBP\)](#)
[Frankfurt am Main, Germany](#)

[JOB POST](#)

■ **Senior/Laboratory Research Scientist**

Francis Crick Institute

London, United Kingdom

JOB POST

This article was downloaded by **calibre** from <https://www.nature.com/articles/d41586-021-01076-x>

| [Section menu](#) | [Main menu](#) |

NEWS

29 April 2021

- Clarification [30 April 2021](#)

Key COVID research hit by cut to UK foreign-aid budget

UK scientists buffeted by uncertainty as the pandemic's economic fallout reduces research funds.

- [Holly Else](#)
 1. Holly Else
[View author publications](#)

You can also search for this author in [PubMed](#) [Google Scholar](#)



COVID-19 patients in Belem, Brazil: cuts to a UK research fund have affected a project tracking coronavirus variants in Brazil. Credit: Tarso Sarraf/AFP via Getty

Bitter and angry are the words that epidemiologist Oliver Pybus uses to describe his feelings when he opened an e-mail from his university's research-services department this month. The e-mail told him that funding for one of his research projects will be cut by one-quarter. It was the second such notification he had received in 2021. The first listed a 70% cut to another project.

Pybus, who is at the University of Oxford, UK, is part of one of the world's leading teams working on identifying and [tracking new variants of the SARS-CoV-2 coronavirus](#). The latest cut to his team's funding will affect a surveillance project in [Brazil, where COVID infections, some caused by fast-spreading variants, are surging](#). Both cuts are the result of reductions that the UK government made last year to its foreign-aid budget, some of which funds research.

“There can’t be many more important scientific projects today than this,” says Pybus. He and his team are tracking the genomic changes in the SARS-CoV-2 virus and have so far identified significant variants of concern. “We have been working absolutely flat out for 14 months. Everyone is drained and exhausted. It makes me feel that has been unappreciated,” he says.

The reductions to the UK aid budget, also known as official development assistance (ODA), have hit more than 800 other research projects, affecting thousands of UK and overseas researchers. Since 2014, the government has channelled a portion of ODA funding to public science agencies to help researchers address pressing problems in the developing world, such as emerging infectious diseases, by building collaborations with researchers overseas. But in November, in response to the economic fallout of the COVID-19 pandemic, politicians slashed provisions for the ODA from 0.7% of gross national income to 0.5%. Many saw the move as controversial.

The cut left UK Research and Innovation (UKRI), which oversees the main ODA research schemes and is the nation’s central research funder, with a shortfall. As a result, it has been unable to meet its existing commitments to universities that had already secured multi-year grants. More than 12,000 people have signed a petition to reverse the cut, which reduced ODA funding for 2021–22 to £125 million (US\$174 million), £120 million less than they were expecting.

Shaky ground

All this comes at an uncertain time for UK science. Earlier this year, universities questioned how the United Kingdom will pay its way into the [European Commission’s research and innovation programme, Horizon Europe](#). Because the country is no longer part of the European Union, it will need to pay £1 billion to £2 billion a year to be an ‘associate’ member of the fund, so that UK-based researchers can bid for grants. Rumours suggested that the money would come at the expense of the domestic science budget, raising hackles, until the Department of Business, Energy and Industrial Strategy (BEIS) — the ministry responsible for science — announced that it had found alternative funding. In response to the ODA cut, the BEIS says

that the United Kingdom is still a world-leading aid donor and has spent £10 billion this year tackling poverty, climate change and COVID-19.

“The biggest concern at the moment is inconsistency, in that the government seems to be sending contradictory signals on an almost weekly basis,” says James Wilsdon, a science-policy researcher at the University of Sheffield, UK. That’s leading to a lack of confidence among researchers, he adds.

It’s not only the public purse that has been stretched by the pandemic. Restrictions on movement, as a result of COVID-19 lockdowns, have left medical-research charities with a £300-million hole in their finances, according to the Association of Medical Research Charities. Many members, such as Cancer Research UK, have been unable to hold their usual fundraising activities or open their shops, leading to cuts in their funding of research.

And there will be more difficult decisions ahead, says Ottoline Leyser, the head of UKRI. In a blog in January, she said that this year “is likely to be particularly challenging” as the agency continues to fund COVID-19 projects, redistributes spending for projects delayed by COVID-19 and faces the reduction in ODA funding.

Emergency funds

In mid-March, UKRI began writing to universities that would be affected by the ODA cut to tell them about the shortfall. The letters ask institutions to reprofile, reduce or terminate the grants that had been won. Many are now scrambling to work out how to do this, and Pybus’s team is one of those affected. The University of Oxford has 18 awards affected, and administrators have applied the cut equally across grants, “with very significant impact on research and researchers, here and with our overseas partners”, according to a spokesperson for the institution. “Several of the affected grants involve COVID-19 research,” says the spokesperson, adding that previous ODA grants supported the development of the [Oxford–AstraZeneca COVID vaccine](#).

At University College London (UCL), where 36 projects are affected and the cuts total £6.6 million, administrators have created a emergency global health research fund worth up £2 million to help alleviate some of the pressure on its scientists. David Price, the institution's head of research, says that the cuts are unprecedented and that more could follow because the UK National Institute for Health Research (NIHR) — which uses the ODA to fund global health research — has yet to announce how it will handle the fall in its ODA allocation. The NIHR declined *Nature*'s request for comment for this article, but in March said that it might need to reduce its ambitions and would prioritize existing projects for funding.

At UCL, developmental neurobiologist Nick Greene has had a global-health grant cut by 25%. The grant is jointly funded by several organizations hit by the aid reduction, including the NIHR. The trial, which was about to start in northern China in collaboration with Peking University in Beijing, will look at whether inositol supplements can prevent some neural-tube defects during pregnancy. It will be the precursor to a larger clinical trial and is the culmination of 20 years' work, he says.

Greene now faces the prospect that the trial might not go ahead. If it does, it's likely that the teams involved will cut the number of participants they recruit. "There is the stress of not knowing what the next step is," he says.

Nature **593**, 20-21 (2021)

doi: <https://doi.org/10.1038/d41586-021-01134-4>

Updates & Corrections

- **Clarification 30 April 2021:** This article has been amended to clarify Oliver Pybus's views on the importance of the project.

Jobs from Nature Careers

- - - [All jobs](#)

o

- **Postdoc (f/m/d) – Molecular mechanisms of translation in yeast –**

Max Planck Institute for Biophysical Chemistry (MPIBPC)

Göttingen, Germany

JOB POST

- **Laboratory Research Scientist - Cancer Epigenetics Laboratory**

Francis Crick Institute

London, United Kingdom

JOB POST

- **PhD student (m/f/div) in MS-based proteomics of small proteins**

Max Planck Institute of Biophysics (MPIBP)

Frankfurt am Main, Germany

JOB POST

- **Senior/Laboratory Research Scientist**

Francis Crick Institute

London, United Kingdom

JOB POST

This article was downloaded by **calibre** from <https://www.nature.com/articles/d41586-021-01134-4>

| [Section menu](#) | [Main menu](#) |

NEWS

23 April 2021

One million coronavirus sequences: popular genome site hits mega milestone

GISAID's impressive effort to understand the spread of COVID-19 has seen scientists upload sequences from most nations on Earth.

- [Amy Maxmen](#)

1. Amy Maxmen

[View author publications](#)

You can also search for this author in [PubMed](#) [Google Scholar](#)



Positive COVID tests are prepared for sequencing to study variants at the University of Maryland in Baltimore.Credit: Michael Robinson Chavez/The Washington Post via Getty

More than 1.2 million coronavirus genome sequences from 172 countries and territories have now been shared on a popular online data platform, which is a testament to the hard work of researchers around the world during the pandemic.

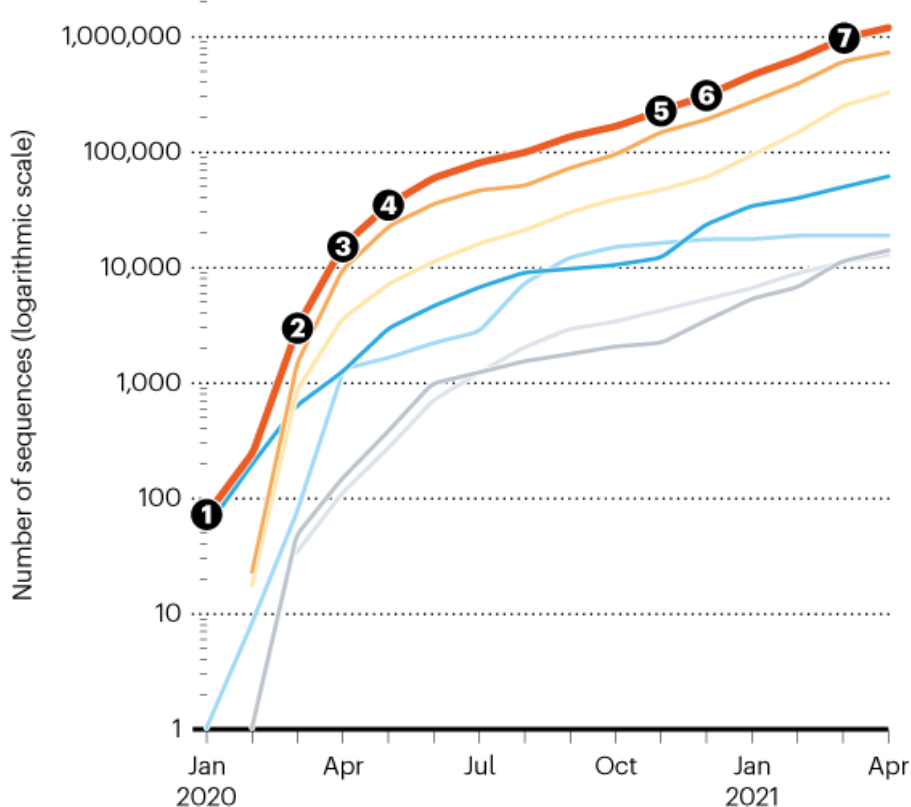
Sequence data have been crucial to scientists studying the [origins of SARS-CoV-2](#), the [epidemiology of COVID-19 outbreaks](#) and the movement of [viral variants](#) across the planet.

“Because countries are submitting data from so many parts of the world, you have a system where we can watch how the virus spreads through the world, and see if control measures and the vaccines still work,” says Sebastian Maurer-Stroh, a Singapore-based scientific adviser at the the non-profit organization hosting the repository, GISAID — the Global Initiative on Sharing Avian Influenza Data.

COLLABORATION IN THE TIME OF COVID

More than one million SARS-CoV-2 genome sequences have been shared on the GISAID data-sharing platform since January 2020, and are helping researchers to track the spread of viral variants. Most are from the United States and Europe, but contributions come from every region of the world.

— Global — Europe — North America — Asia
— Oceania — South America — Africa



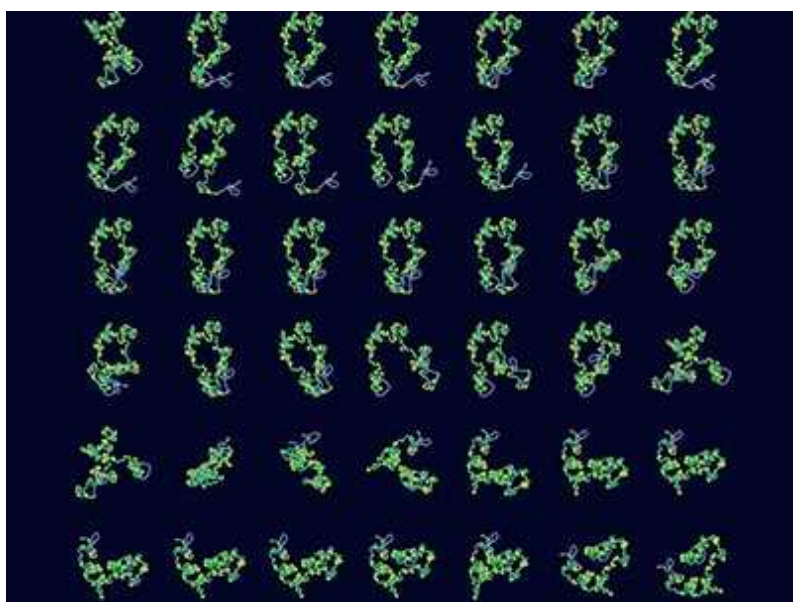
- ① **January:** First SARS-CoV-2 genome, from China.
- ② **March:** First African sequence, from Nigeria.
- ③ **April:** Victoria, Australia, has 1,300 cases; 80% are sequenced, identifying clusters from cruise ships and hospitality venues.
- ④ **May:** UK sequences 6% of cases, more than any other country.
- ⑤ **November:** South African surge prompts intensified surveillance. Researchers find a widespread new variant — B.1.351.
- ⑥ **December:** 40% of genomes sequenced in Manaus, Brazil, are of the P.1 variant, with mutations linked to increased transmissibility and immune evasion.
- ⑦ **March:** US sequencing rate doubles, owing to a government mandate for surveillance and funding from the Centers for Disease Control and Prevention.

Source: GISAID

Several databases for genome sequences exist, but GISAID is by far the most popular for SARS-CoV-2. It was conceived in 2006 as a [repository of genomic data](#) from flu viruses. At the time, many countries withheld genomic information for a range of reasons. One fear was that the countries generating the data would not get credit, or would not reap the benefits of research stemming from their original sequencing work. But after two years of negotiations between governments and scientists about data-sharing agreements, GISAID launched.

Charting the spread

When COVID-19 began spreading in China, Maurer-Stroh says, the GISAID team immediately reached out to researchers and politicians around the world, to understand what barriers might prevent them from sharing genomic data on SARS-CoV-2.



[Scientists call for fully open sharing of coronavirus genome data](#)

For example, when researchers in West Africa said that they lacked bioinformatics training, a scientist affiliated with GISAID in Senegal began to hold workshops on sequencing, analytics and how to use the tools on the

platform. Some of GISAID's features allow researchers to see how genomes they've uploaded relate to others, or to explore where new variants appear from day to day.

Although outreach has helped, Maurer-Stroh says the site's popularity is mainly due to its mechanism of sharing and the quality of its tools for sequence display and analysis.

Some wealthy countries have uploaded huge numbers of sequences and account for the lion's share in their regions (see 'Collaboration in the time of COVID'). For example, as of 20 April, the United States had shared 303,359 sequences, and the United Kingdom's tally stood at 379,510 sequences.

Not entirely comprehensive

But glaring gaps exist. Not a single SARS-CoV-2 sequence has been uploaded from Tanzania, where the late president John Magufuli denied the existence of the pandemic for many months. And several countries with significant outbreaks, including El Salvador (67,851 cases, but only 6 sequences uploaded) and Lebanon (513,006 cases, 49 sequences uploaded) are lagging far behind.

To search or download sequences from GISAID, or use the platform's genomic-analysis tools, people must register with their name, and agree to terms that include not publishing studies based on the data without acknowledging the scientists who uploaded the sequences, and even contacting them to ask about collaboration. Such gatekeeping has upset some scientists, who argue that there should be no barriers standing in the way of access.

But GISAID probably would not have hit the one-million mark without such an approach, because it would have lacked assurances against exploitation, speculates Tulio de Oliveira, the director of the KwaZulu-Natal Research Innovation and Sequencing Platform in Durban, South Africa. He says: "This is the first time I've seen people sharing so much data before publication."

doi: <https://doi.org/10.1038/d41586-021-01069-w>

Jobs from Nature Careers

- - - [All jobs](#)
 - - **Postdoc (f/m/d) – Molecular mechanisms of translation in yeast –**
 - **Postdoc (f/m/d) – Molecular mechanisms of translation in yeast –**
 - [Max Planck Institute for Biophysical Chemistry \(MPIBPC\)](#)
 - [Göttingen, Germany](#)
 - [JOB POST](#)
 - **Laboratory Research Scientist - Cancer Epigenetics Laboratory**
 - [Francis Crick Institute](#)
 - [London, United Kingdom](#)
 - [JOB POST](#)
 - **PhD student (m/f/div) in MS-based proteomics of small proteins**
 - [Max Planck Institute of Biophysics \(MPIBP\)](#)
 - [Frankfurt am Main, Germany](#)
 - [JOB POST](#)
 - **Senior/Laboratory Research Scientist**

Francis Crick Institute

London, United Kingdom

JOB POST

This article was downloaded by **calibre** from <https://www.nature.com/articles/d41586-021-01069-w>

| [Section menu](#) | [Main menu](#) |

NEWS FEATURE

04 May 2021

Microplastics are everywhere — but are they harmful?

Scientists are rushing to study the tiny plastic specks that are in marine animals — and in us.

- [XiaoZhi Lim](#) ⁰

1. XiaoZhi Lim

1. XiaoZhi Lim is a freelance writer in Medfield, Massachusetts.

[View author publications](#)

You can also search for this author in [PubMed](#) [Google Scholar](#)



Microplastics collected from the Magothy River in Maryland. Credit: Will Parson/Chesapeake Bay Program

Dunzhu Li used to microwave his lunch each day in a plastic container. But Li, an environmental engineer, stopped when he and his colleagues made a disturbing discovery: plastic food containers shed huge numbers of tiny specks — called microplastics — into hot water. “We were shocked,” Li says. Kettles and baby bottles also shed microplastics, Li and other researchers, at Trinity College Dublin, reported last October¹. If parents prepare baby formula by shaking it up in hot water inside a plastic bottle, their infant might end up swallowing more than one million microplastic particles each day, the team calculated.

What Li and other researchers don't yet know is whether this is dangerous. Everyone eats and inhales sand and dust, and it's not clear if an extra diet of plastic specks will harm us. "Most of what you ingest is going to pass straight through your gut and out the other end," says Tamara Galloway, an ecotoxicologist at the University of Exeter, UK. "I think it is fair to say the potential risk might be high," says Li, choosing his words carefully.

Researchers have been worried about the potential harms of microplastics for almost 20 years — although most studies have focused on the risks to marine life. Richard Thompson, a marine ecologist at the University of Plymouth, UK, coined the term in 2004 to describe plastic particles smaller than 5 millimetres across, after his team found them on British beaches. Scientists have since seen microplastics everywhere they have looked: in deep oceans; in Arctic snow and Antarctic ice; in shellfish, table salt, drinking water and beer; and drifting in the air or falling with rain over mountains and cities. These tiny pieces could take decades or more to degrade fully. "It's almost certain that there is a level of exposure in just about all species," says Galloway.



Clean-up workers collect plastic pellets from the Arniston beach in Western Cape, South Africa.Credit: Tom Camacho/Science Photo Library

The earliest investigations of microplastics focused on microbeads found in personal-care products, and pellets of virgin plastic that can escape before they are moulded into objects, as well as on fragments that slowly erode from discarded bottles and other large debris. All these wash into rivers and oceans: in 2015, oceanographers estimated there were between 15 trillion and 51 trillion microplastic particles floating in surface waters worldwide. Other sources of microplastic have since been identified: plastic specks shear off from car tyres on roads and synthetic microfibres shed from clothing, for instance. The particles blow around between sea and land, so people might be inhaling or eating plastic from any source.

From limited surveys of microplastics in the air, water, salt and seafood, children and adults might ingest anywhere from dozens to more than 100,000 microplastic specks each day, Albert Koelmans, an environmental scientist at Wageningen University in the Netherlands, reported this March². He and his colleagues think that in the worst cases, people might be ingesting around the mass of a credit card's worth of microplastic a year.



[Bottles, bags, ropes and toothbrushes: the struggle to track ocean plastics](#)

Regulators are taking the first step towards quantifying the risk to people's health — measuring exposure. This July, the California State Water Resources Control Board, a branch of the state's environmental protection agency, will become the world's first regulatory authority to announce standard methods for quantifying microplastic concentrations in drinking water, with the aim of monitoring water over the next four years and publicly reporting the results.

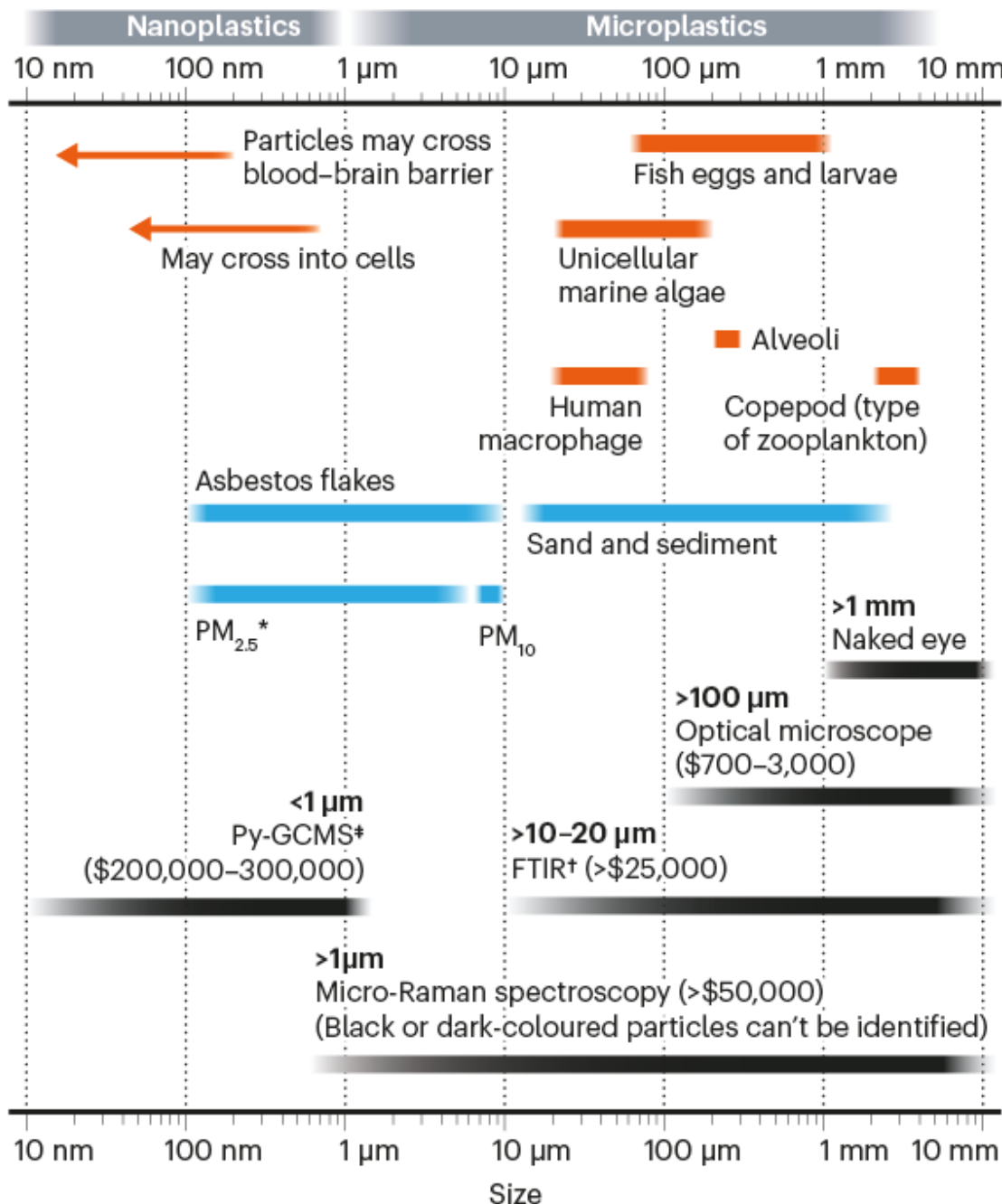
Evaluating the effects of tiny specks of plastic on people or animals is the other half of the puzzle. This is easier said than done. More than 100 laboratory studies have exposed animals, mostly aquatic organisms, to microplastics. But their findings — that exposure might lead some organisms to reproduce less effectively or suffer physical damage — are hard to interpret because microplastics span many shapes, sizes and chemical compositions, and many of the studies used materials that were quite unlike those found in the environment.

The tiniest specks, called nanoplastics — smaller than 1 micrometre — worry researchers most of all (see 'Microplastics to scale'). Some might be able to enter cells, potentially disrupting cellular activity. But most of these particles are too small for scientists even to see; they were not counted in Koelmans' diet estimates, for instance, and California will not try to monitor them.

MICROPLASTICS TO SCALE

Micro- and nanoplastics are of similar size to many biological organisms, and become harder and more expensive to analyse as they get smaller.

— Biological objects — Non-biological particles — Tools for analysis



*Particulate matter less than 2.5 micrometres (PM_{2.5}) or less than 10 µm (PM₁₀) in diameter, often from soot, vehicle exhaust or dust; †FTIR, Fourier-transform infrared spectroscopy; *Py-GCMS, pyrolysis-gas chromatography-mass spectrometry.

Source (tools and costs): S. Primpke *et al.* *Appl. Spectrosc.* **74**, 1012–1047 (2020).

One thing is clear: the problem will only grow. Almost 400 million tonnes of plastics are produced each year, a mass projected to more than double by 2050. Even if all plastic production were magically stopped tomorrow, existing plastics in landfills and the environment — a mass estimated at around 5 billion tonnes — would continue degrading into tiny fragments that are impossible to collect or clean up, constantly raising microplastic levels. Koelmans calls this a “plastic time bomb”.

“If you ask me about risks, I am not that frightened today,” he says. “But I am a bit concerned about the future if we do nothing.”

Modes of harm

Researchers have several theories about how plastic specks might be harmful. If they’re small enough to enter cells or tissues, they might irritate just by being a foreign presence — as with the long, thin fibres of asbestos, which can inflame lung tissue and lead to cancer. There’s a potential parallel with air pollution: sooty specks from power plants, vehicle exhausts and forest fires called PM₁₀ and PM_{2.5} — particulate matter measuring 10 µm and 2.5 µm across — are known to deposit in the airways and lungs, and high concentrations can damage respiratory systems. Still, PM₁₀ levels are thousands of times higher than the concentrations at which microplastics have been found in air, Koelmans notes.

The larger microplastics are more likely to exert negative effects, if any, through chemical toxicity. Manufacturers add compounds such as plasticizers, stabilizers and pigments to plastics, and many of these substances are hazardous — for example, interfering with endocrine (hormonal) systems. But whether ingesting microplastics significantly raises our exposure to these chemicals depends on how quickly they move out of the plastic specks and how fast the specks travel through our bodies — factors that researchers are only beginning to study.

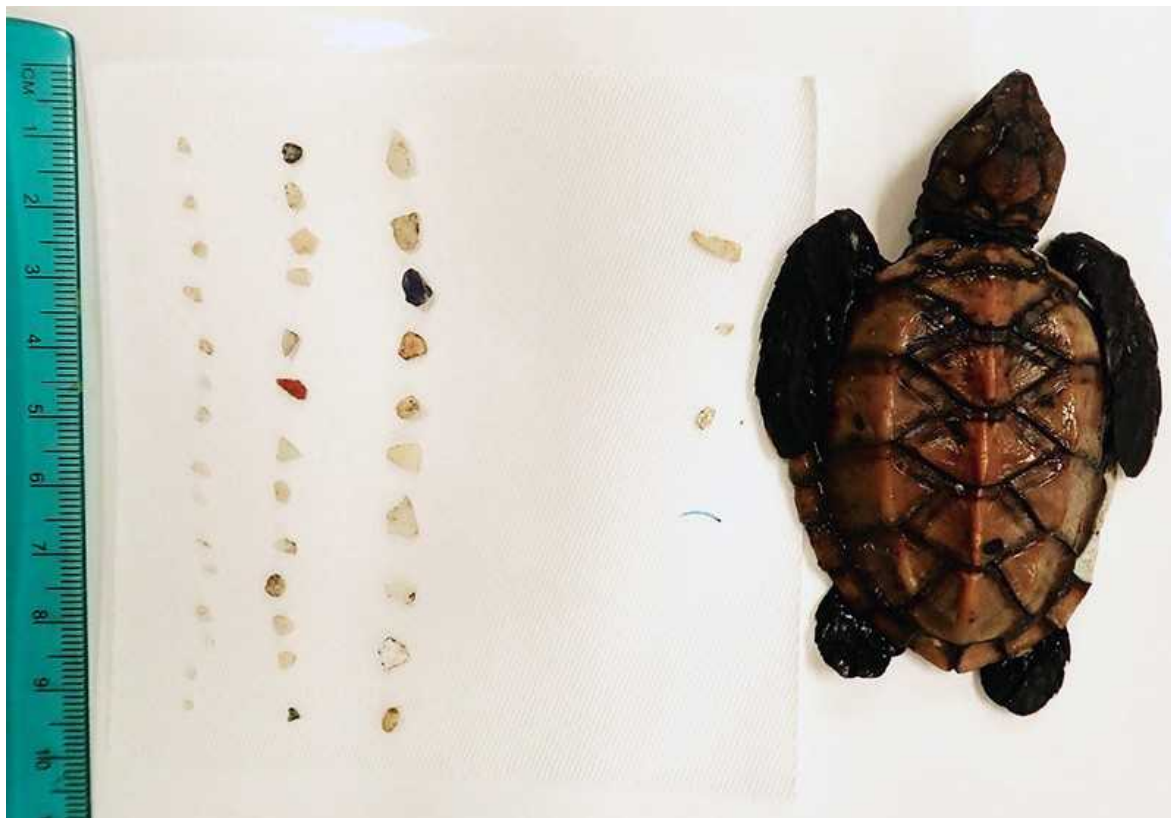


Microplastics collected in the San Francisco Bay area, labelled for study.Credit: Cole Brookson

Another idea is that microplastics in the environment might attract chemical pollutants and then deliver them into animals that eat the contaminated specks. But animals ingest pollutants from food and water anyway, and it's even possible that plastic specks, if largely uncontaminated when swallowed, could help to remove pollutants from animal guts. Researchers still can't agree on whether pollutant-carrying microplastics are a significant problem, says Jennifer Lynch, a marine biologist affiliated with the US National Institute of Standards and Technology in Gaithersburg, Maryland.

Perhaps the simplest mode of harm — when it comes to marine organisms, at least — might be that organisms swallow plastic specks of no nutritional value, and don't eat enough food to survive. Lynch, who also leads the Center for Marine Debris Research at Hawaii Pacific University in Honolulu, has autopsied sea turtles that are found dead on beaches, looking at plastics in their guts and chemicals in their tissues. In 2020, her team completed a set of analyses for 9 hawksbill turtle hatchlings, under 3 weeks

old. One hatchling, only 9 centimetres long, had 42 pieces of plastic in its gastrointestinal tract. Most were microplastics.



A Hawaiian hawksbill sea turtle post-hatchling pictured beside its microplastic stomach contents. Credit: Jennifer Lynch

“We don’t believe any of them died specifically from plastics,” Lynch says. But she wonders whether the hatchlings might have struggled to grow as fast as they need to. “It’s a very tough stage of life for those little guys.”

Marine studies

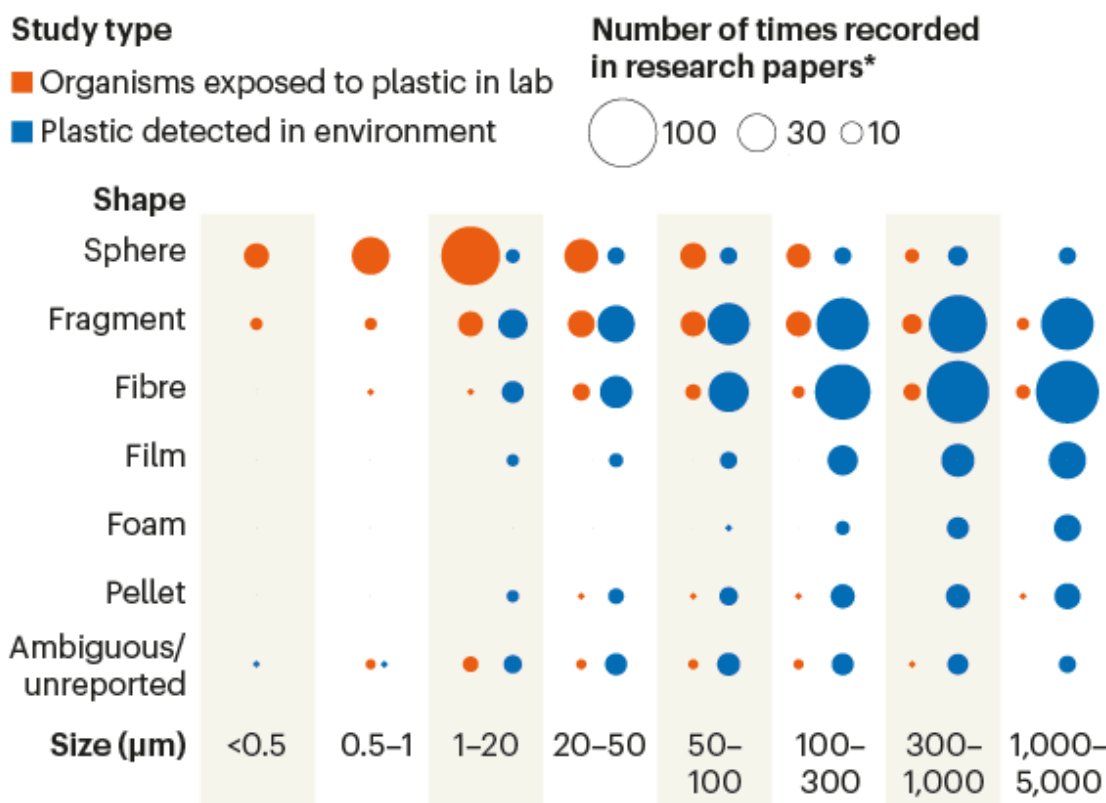
Researchers have done the most work on microplastic risks to marine organisms. Zooplankton, for instance, among the smallest marine organisms, grow more slowly and reproduce less successfully in the presence of microplastics, says Penelope Lindeque, a marine biologist at the Plymouth Marine Laboratory, UK: the animals’ eggs are smaller and less likely to

hatch. Her experiments show that the reproduction problems stem from the zooplankton not eating enough food³.

But, because ecotoxicologists started running experiments before they knew what kinds of microplastics exist in aquatic environments, they depended heavily on manufactured materials, typically using polystyrene spheres of smaller sizes and at concentrations much higher than surveys found (see ‘Sizing up microplastics’).

SIZING UP MICROPLASTICS

Laboratory scientists studying how microplastics affect organisms use shapes and sizes that are different from the microplastics detected in environmental assays. The tiniest specks, or nanoplastics, measuring less than 1 micrometre across, are rarely reported in environmental studies because they are so hard to detect.



*Nature analysis of 136 detection and 159 exposure studies.

©nature

Source: *Nature* analysis

Scientists have started shifting to more environmentally realistic conditions and using fibres or fragments of plastics, rather than spheres. Some have started coating their test materials in chemicals that mimic biofilms, which appear to make animals more likely to eat microplastics.

Fibres seem to be a particular problem. Compared with spheres, fibres take longer to pass through zooplankton, Lindeque says. In 2017, Australian researchers reported that zooplankton exposed to microplastic fibres produced half the usual number of larvae and that the resulting adults were smaller. The fibres were not ingested, but the researchers saw that they interfered with swimming, and identified deformations in the organisms' bodies⁴. Another study⁵ in 2019 found that adult Pacific mole crabs (*Emerita analoga*) exposed to fibres lived shorter lives.



Red microplastic fibres wrap around a *Temora* copepod, a species of zooplankton. Credit: Plymouth Marine Laboratory

Most laboratory studies expose organisms to one type of microplastic, of a specific size, polymer and shape. In the natural environment, organisms are exposed to a mixture, says Koelmans. In 2019, he and his doctoral student Merel Kooi plotted the abundances of microplastics reported from 11

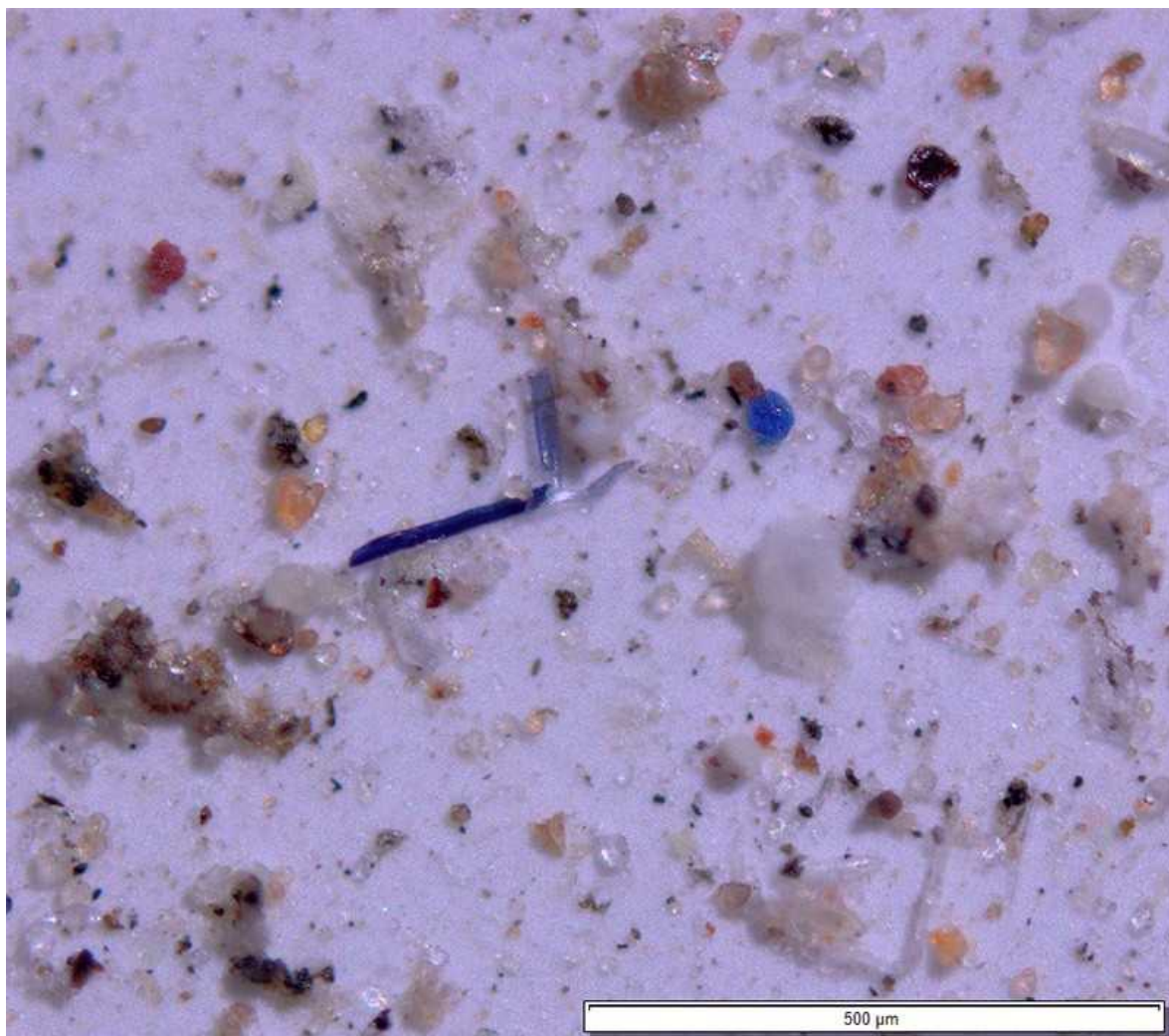
surveys of oceans, rivers and sediment, to build models of mixtures in aquatic environments.

Last year, the two teamed up with colleagues to use this model in computer simulations that predict how often fish would encounter microplastics small enough to eat, and the likelihood of eating enough specks to affect growth. The researchers found that at current microplastic pollution levels, fish run that risk at 1.5% of locations checked for microplastics⁶. But there are likely to be hotspots where the risks would be higher, says Koelmans. One possibility is the deep sea: once there, and often buried in sediment, it is unlikely the microplastics will travel elsewhere and there is no way to clean them up.

The oceans already face many stressors, which makes Lindeque more afraid that microplastics will further deplete zooplankton populations than that they will transfer up the food chain to reach people. “If we knock out something like zooplankton, the base of our marine food web, we’d be more worried about impacts on fish stocks and the ability to feed the world’s population.”

Human studies

No published study has yet directly examined the effects of plastic specks on people, leading researchers say. The only available studies rely on laboratory experiments that expose cells or human tissues to microplastics, or use animals such as mice or rats. In one study⁷, for instance, mice fed large quantities of microplastics showed inflammation in their small intestines. Mice exposed to microplastics in two studies had a lowered sperm count⁸ and fewer, smaller pups⁹, compared with control groups. Some of the *in vitro* studies on human cells or tissues also suggest toxicity. But, just as with the marine studies, it’s not clear that the concentrations used are relevant to what mice — or people — are exposed to. Most of the studies also used polystyrene spheres, which don’t represent the diversity of microplastics that people ingest. Koelmans also points out that these studies are among the first of their kind, and could end up being outliers once there’s an established body of evidence. There are more *in vitro* studies than animal studies, but researchers say they still don’t know how to extrapolate the effects of solid plastic specks on tissues to possible health problems in whole animals.



Spot the plastic? Dust, sediment, and microplastic fibres and beads are mingled in this millimetre-wide magnified image of particles sampled from national parks and wilderness areas in the western United States. Credit: Janice Brahney, Utah State University

One question surrounding risk is whether microplastics could remain in the human body, potentially accumulating in some tissues. Studies in mice have found that microplastics around $5\text{ }\mu\text{m}$ across could stay in the intestines or reach the liver. Using very limited data on how quickly mice excrete microplastics and the assumption that only a fraction of particles $1\text{--}10\text{ }\mu\text{m}$ in size would be absorbed into the body through the gut, Koelmans and colleagues estimate that a person might accumulate several thousand microplastic particles in their body over their lifetime².

Some researchers have started to explore whether microplastics can be found in human tissue. In December, a team documented this for the first time in a study that looked at six placentas¹⁰. Researchers broke down the tissue with a chemical, then examined what was left, and ended up with 12 particles of microplastic in 4 of those placentas. Yet it's not impossible that these specks were the result of contamination when the placentas were collected or analysed, says Rolf Halden, an environmental-health engineer at Arizona State University in Tempe — although he commends the researchers for their efforts to avoid contamination, which included keeping delivery wards free of plastic objects, and for showing that a control set of blank materials taken through the same sample analysis was not contaminated. “There is a continuing challenge of demonstrating conclusively that a given particle actually originated in a tissue,” he says.



[Chemistry can make plastics sustainable – but isn't the whole solution](#)

Those who are worried by their microplastic exposure can reduce it, says Li. His work on kitchenware found that the amounts of plastic shed depend highly on temperature — which is why he's stopped microwaving food in plastic containers. To reduce issues with baby bottles, his team suggests that parents could rinse sterilized bottles with cool water that has been boiled in non-plastic kettles, so as to wash away any microplastics released during sterilization. And they can prepare baby formula in glass containers, filling feeding bottles after the milk has cooled. The team is now recruiting parents

to volunteer samples of their babies' urine and stools for microplastic analysis.

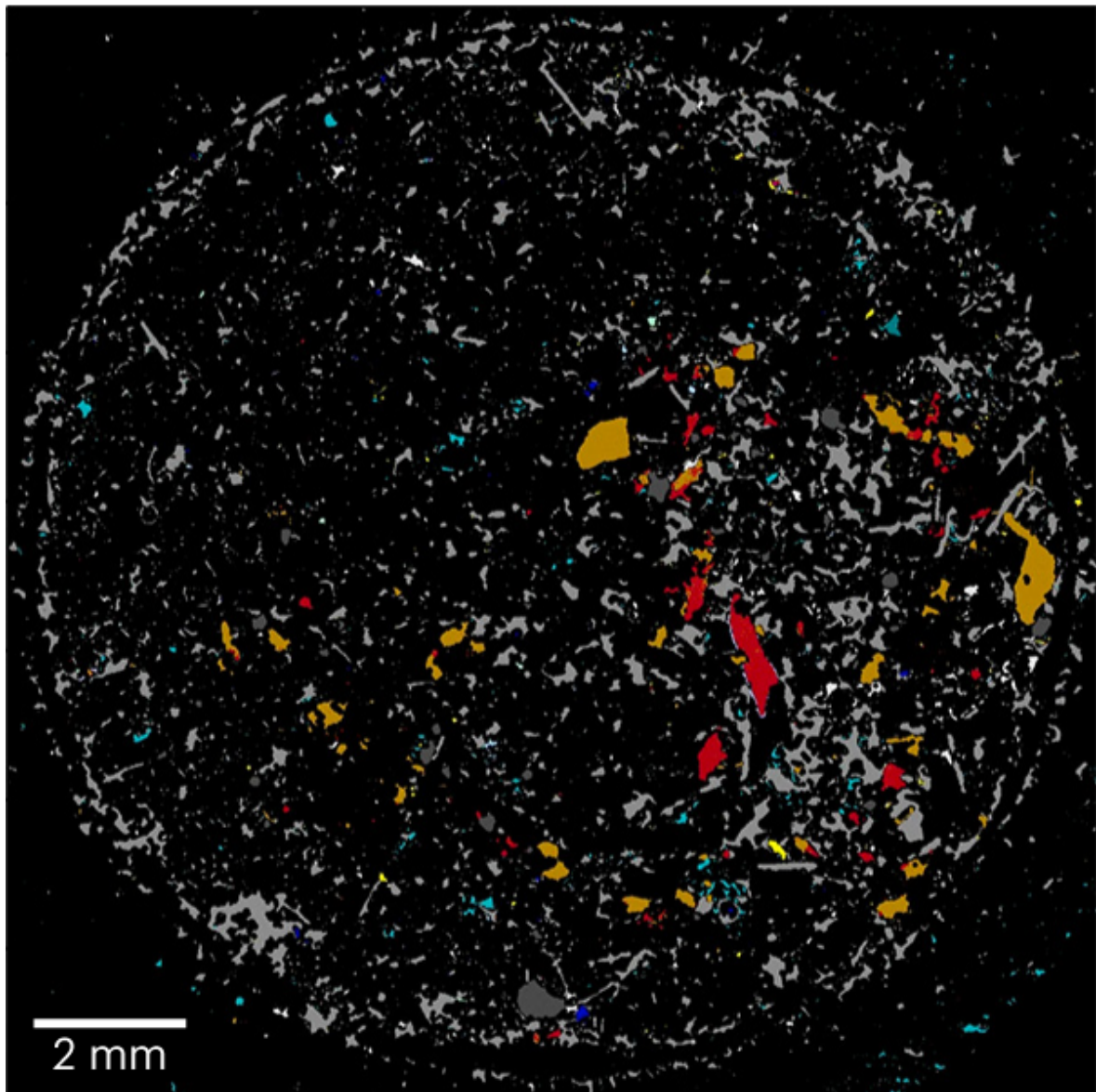
The nano fraction

Particles that are small enough to penetrate and hang around in tissues, or even cells, are the most worrying kind, and warrant more attention in environmental sampling, says Halden. One study¹¹ that deliberately let pregnant mice inhale extremely tiny particles, for instance, later found the particles in almost every organ in their fetuses. “From a risk perspective, that’s where the real concern is, and that’s where we need more data.”

To enter cells, particles generally need to be smaller than a few hundred nanometres. There was no formal definition of a nanoplastic until 2018, when French researchers proposed the upper size limit of 1 μm — tiny enough to remain dispersed through a water column where organisms can more easily consume them, instead of sinking or floating as larger microplastics do, says Alexandra ter Halle, an analytical chemist at Paul Sabatier University in Toulouse, France.

But researchers know almost nothing about nanoplastics; they are invisible and cannot simply be scooped up. Just measuring them has stumped scientists.

Researchers can use optical microscopes and spectrometers — which distinguish between particles by their differing interactions with light — to measure the length, width and chemical make-up of plastic particles down to a few micrometres. Below that scale, plastic particles become difficult to distinguish from non-plastic particles such as marine sediment or biological cells. “You’re looking for the needle in the haystack, but the needle looks like the hay,” says Roman Lehner, a nanomaterials scientist at the Sail and Explore Association, a Swiss non-profit research group.



A false-colour image, using infrared spectrometry analysis, of a sample from a waste-water treatment plant in Oldenburg, Germany. Fragments picked out in colour are plastic polymers; other fragments include rubber, soot, sand and plant fibres. Source: S. Primpke *et al.* *Anal. Bioanal. Chem.* **410**, 5131–5141 (2018).

In 2017, ter Halle and her colleagues proved for the first time that nanoplastic exists in an environmental sample: seawater collected from the Atlantic Ocean¹². She extracted colloidal solids from the water, filtered away any particles larger than 1 µm, burnt what remained, and used a mass spectrometer — which fragments molecules and sorts the fragments by

molecular weight — to confirm that plastic polymers had existed in the remnants.

That, however, gave no information on the exact sizes or shapes of the nanoplastics. Ter Halle got some idea by studying the surfaces of two degraded plastic containers she collected during the expedition. The top few hundred micrometres had become crystalline and brittle, she found; she thinks that this may also be true of the nanoplastics that probably broke off from these surfaces¹³. For now, because researchers cannot collect nanoplastics from the environment, those doing laboratory studies grind up their own plastic, expecting to get similar particles.



Tainted water: the scientists tracing thousands of fluorinated chemicals in our environment

Using home-made nanoplastics has an advantage: researchers can introduce tags to help track the particles inside test organisms. Lehner and colleagues prepared fluorescent nano-sized plastic particles and placed them under tissue built from human intestinal-lining cells¹⁴. The cells did absorb the particles, but did not show signs of cytotoxicity.

Finding plastic specks lodged in intact slices of tissue — through a biopsy, for instance — and observing any pathological effects would be the final piece of the puzzle over microplastic risks, Lehner says. This would be

“highly desirable”, says Halden. But to reach tissues, the particles would have to be very small, so both researchers think it would be very difficult to detect them conclusively.

Collecting all these data will take a lot of time. Ter Halle has collaborated with ecologists to quantify microplastic ingestion in the wild. Analysing only particles larger than 700 µm in some 800 samples of insects and fish took thousands of hours, she said. The researchers are now examining the particles in the 25–700 µm range. “This is difficult and tedious, and this is going to take a long time to get the results,” she says. To look at the smaller size range, she adds, “the effort is exponential.”



A sample of plastics collected on one of Alexandra ter Halle’s ocean expeditions. Credit: Vinci Sato@ Expedition 7th Continent

No time to lose

For the moment, levels of microplastics and nanoplastics in the environment are too low to affect human health, researchers think. But their numbers will rise. Last September, researchers projected¹⁵ that the amount of plastic added to existing waste each year — whether carefully disposed of in sealed

landfills or strewn across land and sea — could more than double from 188 million tonnes in 2016 to 380 million tonnes in 2040. By then, around 10 million tonnes of this could be in the form of microplastics, the scientists estimated — a calculation that didn't include the particles continually being eroded from existing waste.

It is possible to rein in some of our plastic waste, says Winnie Lau at the Pew Charitable Trusts in Washington DC, who is the first author on the study. The researchers found that if every proven solution to curb plastic pollution were adopted in 2020 and scaled up as quickly as possible — including switching to systems of reuse, adopting alternative materials, and recycling plastic — the amount of plastic waste added could drop to 140 million tonnes per year by 2040.

By far the biggest gains would come from cutting out plastics that are used only once and discarded. “There’s no point producing things that last for 500 years and then using them for 20 minutes,” Galloway says. “It’s a completely unsustainable way of being.”

Nature **593**, 22–25 (2021)

doi: <https://doi.org/10.1038/d41586-021-01143-3>

References

1. 1.

Li, D. *et al.* *Nature Food* **1**, 746–754 (2020).

2. 2.

Nor, N. H. M., Kooi, M., Diepens, N. J. & Koelmans, A. A. *Environ. Sci. Technol.* **55**, 5084–5096 (2021).

3. 3.

Botterell, Z. L. R. *et al.* *Environ. Pollut.* **245**, 98–110 (2018).

4. 4.

Ziajahromi, S., Kumar A., Neale, P. A. & Leusch, F. D. L. *Environ. Sci. Technol.* **51**, 13397–13406 (2017).

5. 5.

Horn, D. A., Granek, E. F & Steele, C. L. *Limnol. Oceanogr. Lett.* **5**, 74–83 (2019).

6. 6.

Koelmans, A. A., Redondo-Hasselerharm, P. E., Nor, N. H. M. & Kooi, M. *Environ. Sci. Technol.* **54**, 12307–12315 (2020).

7. 7.

Li, B. *et al.* *Chemosphere* **244**, 125492 (2020).

8. 8.

Jin, H. *et al.* *J. Hazard. Mater.* **401**, 123430 (2021).

9. 9.

Park, E.-J. *et al.* *Toxicol. Lett.* **324**, 75–85 (2020).

10. 10.

Ragusa, A. *et al.* *Environ. Int.* **146**, 106274 (2021).

11. 11.

Fournier, S. B. *et al.* *Part. Fibre Toxicol.* **17**, 55 (2020).

12. 12.

Ter Halle, A. *et al.* *Environ. Sci. Technol.* **51**, 13689–13697 (2017).

13. 13.

Rowenczyk, L. *et al.* *Environ. Sci. Technol.* **54**, 4102–4109 (2020).

14. 14.

Caldwell, J. *et al.* *Environ. Sci. Nano* **8**, 502–513 (2021).

15. 15.

Lau, W. W. Y. *et al.* *Science* **369**, 1455–1461 (2020).

Jobs from Nature Careers

- - - [All jobs](#)
 - - **Postdoc (f/m/d) – Molecular mechanisms of translation in yeast –**
- **Max Planck Institute for Biophysical Chemistry (MPIBPC)**
Göttingen, Germany
[JOB POST](#)
- **Laboratory Research Scientist - Cancer Epigenetics Laboratory**
Francis Crick Institute
London, United Kingdom
[JOB POST](#)
- **PhD student (m/f/div) in MS-based proteomics of small proteins**

Max Planck Institute of Biophysics (MPIBP).

Frankfurt am Main, Germany

JOB POST

▪ **Senior/Laboratory Research Scientist**

Francis Crick Institute

London, United Kingdom

JOB POST

This article was downloaded by **calibre** from <https://www.nature.com/articles/d41586-021-01143-3>

| [Section menu](#) | [Main menu](#) |

NEWS FEATURE

05 May 2021

Fevers are plaguing the oceans — and climate change is making them worse

Sudden marine heatwaves can devastate ecosystems, and scientists are scrambling to predict when they will strike.

- [Giuliana Viglione](#) 0

1. Giuliana Viglione

1. Giuliana Viglione is a freelance journalist in Washington DC.

[View author publications](#)

You can also search for this author in [PubMed](#) [Google Scholar](#)

Ten years ago, dead fish began washing ashore on the beaches of Western Australia. The culprit was a huge swathe of unusually warm water that ravaged kelp forests and scores of commercially important marine creatures, from abalone to scallops to lobster. Over the following weeks, some of Western Australia's most lucrative fisheries came close to being wiped out. To this day, some of them have not recovered.

After the crisis, scientists came together to assess the damage and try to understand what had caused the unusual warming. “This event really had such devastating consequences for marine ecosystems,” says Jessica Benthuysen, a physical oceanographer at the Australian Institute of Marine Science in Perth.

Since that event, researchers have seen dozens of similar hot spells in ocean regions around the world and have now given them a name — [marine heatwaves](#). Although scientists have come up with a few different ways to define the events, they generally agree that they involve warm spells in surface waters of the ocean that last at least five days and reach a temperature threshold well above the normal range¹.

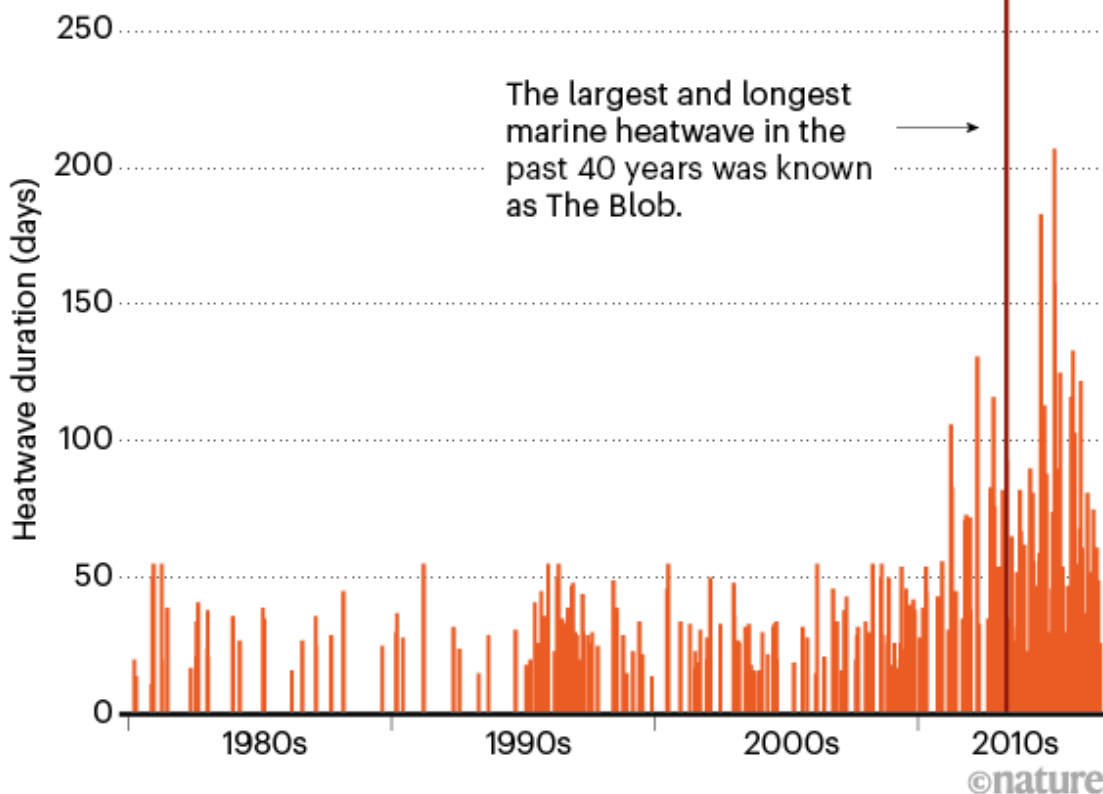
The effects of marine heatwaves can reverberate up the food chain, says Pippa Moore, a marine-community ecologist at Newcastle University, UK. Warm, low-nutrient water in the Northwest Pacific during a 2013–16 marine heatwave known as The Blob devastated phytoplankton growth. Then, Chinook salmon (*Oncorhynchus tshawytscha*) populations plunged, and as many as one million seabirds died in the Gulf of Alaska. Marine heatwaves have also caused massive amounts of coral bleaching in reefs around the world over the past several decades.

Like their counterparts in the atmosphere, marine heatwaves are getting worse: climate change is [magnifying their frequency](#) (see ‘Fevered waters’), extending their length and pushing them to higher temperatures. All that puts a premium on understanding their causes and learning how to forecast them.

Such predictions would help fisheries managers decide whether to limit harvests or even close off some areas to fishing entirely. For now, forecasting methods are still in their infancy. But with fresh observational data sets, ever-improving models and global attention turned to understanding the phenomena, scientists hope to substantially improve their predictions in the coming years.

FEVERED WATERS

A plot of the 300 largest marine heatwaves between 1981 and 2017 shows that such events are hitting more frequently and lingering for longer.



Source: Ref. 7

That could be a major win, say researchers, because the ocean provides hundreds of billions of dollars' worth of food and other resources, many of which are threatened by marine heatwaves. “We really need to get a handle on when and where these events are going to occur,” says Hillary Scannell, a physical oceanographer at Columbia University’s Lamont–Doherty Earth Observatory in Palisades, New York. That will help societies plan for what to do when marine heatwaves are heading their way, she says.

High-pressure situation

The summer of 2013–14 was a difficult one in Brazil. A severe drought devastated crops and sparked water shortages in São Paolo. At the same

time, the ocean was heating up and chlorophyll concentrations — a measure of biological productivity — were dropping sharply. When Regina Rodrigues, a physical oceanographer at the Federal University of Santa Catarina in Florianópolis, Brazil, started digging into the data, she found that the drought and ocean warming had a common cause: a high-pressure atmospheric system that had sat over the southeastern part of the country for much of the summer².

This type of long-lasting high-pressure system is associated with a phenomenon known as atmospheric blocking, and it's one of the most common drivers of marine heatwaves — and heatwaves over land, too. Atmospheric blocking leads to sparse cloud cover and relatively calm winds. The lack of clouds allows more solar radiation to reach the ocean and warm it; at the same time, the still air inhibits mixing and evaporation. All these factors can lead to a build-up of heat in the upper ocean. And that can shift the wind patterns in ways that intensify or prolong the warming.

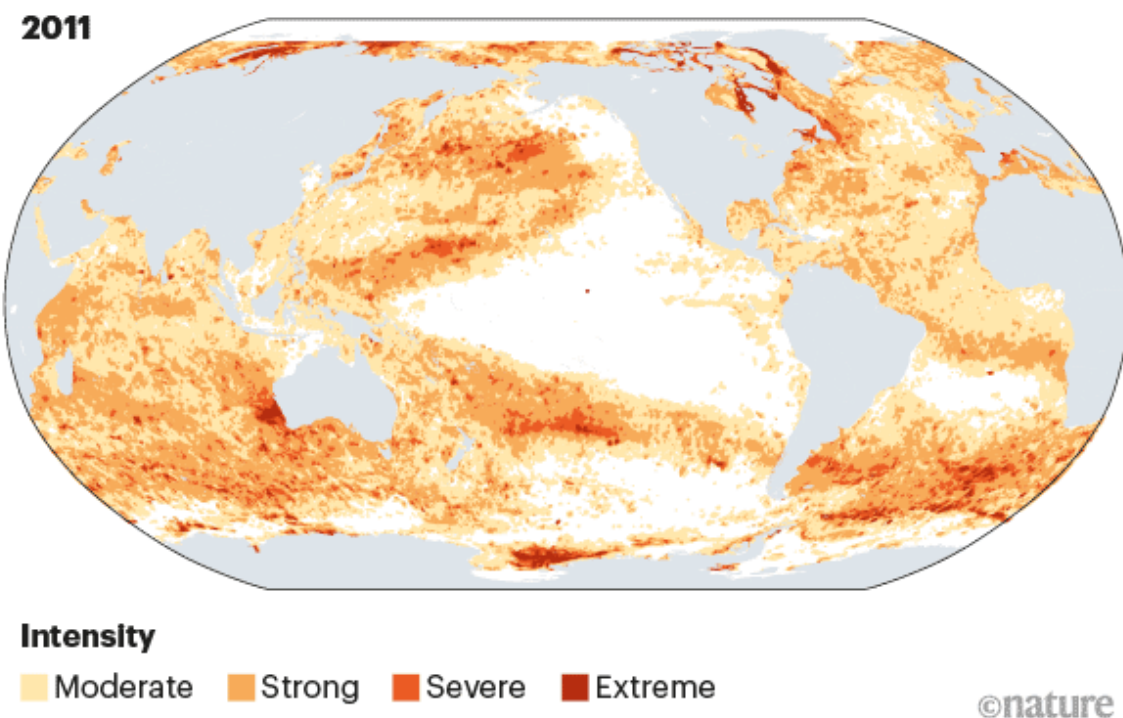
In a study² published in 2019, Rodrigues and her team found that about 60% of marine heatwave events in the southwestern part of the Atlantic Ocean — including the 2013–14 event — were the result of high-pressure systems that originated somewhere over the Indian Ocean, thousands of kilometres away. These systems then moved through the atmosphere towards South America. But because atmospheric blocking relies on so many factors, it's a complex phenomenon to recreate in a numerical model. “It depends on so many aspects of the climate system that it's really hard to get it right,” Rodrigues says.

These seemingly disconnected, far-flung regions are linked through ‘teleconnections’. Rodrigues likens them to tossing a stone in a lake and watching the ripples spread outwards. In her study, she found that the process generally starts when air near Earth's surface warms and rises. Convection above the Indian Ocean pokes the atmosphere, she says, causing atmospheric waves that reach South America and result in a marine heatwave. This interconnectedness of the climate system complicates predictions. Rather than just modelling a specific, small region of interest in the ocean, researchers have to account for processes happening around the globe.

Teasing apart the climatic conditions that lead to a marine heatwave is a painstaking process, says Robert Schlegel, a data scientist at Sorbonne University's Villefranche Sea Institute in France. Schlegel is among the researchers turning to statistical and machine-learning methods to try to understand the main causes of the ocean's heatwaves.

HOT SPOTS

An analysis of sea surface temperature data collected by satellites shows the warmest extremes for each pixel annually for the years 2011 through 2020.



Source: Schlegel, R. W. [Marine Heatwave Tracker](#) (2020)

Deep drivers

Sometimes, the drivers of a marine heatwave hide in the ocean itself. That happened with the event off Western Australia, when the southward-flowing Leeuwin Current grew stronger. As the current intensified, it carried larger-than-usual quantities of warm water from the Indian Ocean, bathing hundreds of kilometres of coastline in a months-long heatwave³.

A similar pattern caused a 2015–16 marine heatwave in the Tasman Sea between Australia and New Zealand that set records for its duration and intensity in that part of the ocean. A 2017 study⁴ traced that event back to a strengthening of the East Australian Current, which brings warm tropical waters to those countries' shores. Such ocean-driven events can penetrate much deeper into the ocean than do their atmosphere-driven counterparts, says Neil Holbrook, an ocean and climate scientist at Australia's University of Tasmania, who co-authored the paper.



[These corals could survive climate change — and help save the world's reefs](#)

These deeper events pose a unique challenge to climate scientists. Almost all of the current understanding of marine heatwaves is restricted to what happens in the surface ocean, where researchers can use satellite instruments to map the temperature and track events in near-real time. But beneath the surface is a world of complex currents. “We can see and define the heatwave on the surface,” says Sofia Darmaraki, a physical oceanographer at Dalhousie University in Halifax, Canada. “But the surface is just the tip of the iceberg of the marine heatwave.”

There are relatively few observational networks tracking conditions beneath the surface. Floats and buoys provide data in some regions, but they are completely missing in others. Understanding how subsurface heat anomalies develop, persist and evolve is one of the biggest open questions in marine-

heatwave research. And because the vast majority of the ocean's inhabitants reside below the surface, this is a critical frontier for scientists to explore, Scannell says. "We haven't really fully understood how the subsurface marine heatwaves impact the ecosystems."



Marine heatwaves often wreak havoc on ecosystems and can lead to widespread coral bleaching. Credit: The Ocean Agency/Ocean Image Bank

BenthuySEN and other researchers in Australia are trying to fill in some of those gaps, using a strategy known as event-based sampling. The country's Integrated Marine Observing System (IMOS) and its partners maintain a fleet of ocean gliders — underwater, remotely pilotable instruments — that are on standby. When a marine heatwave develops, the IMOS team can mobilize quickly to get its gliders in the water to collect key data about temperature and salinity.



[Climate change has doubled the frequency of ocean heatwaves](#)

One test came early this year when waters off Western Australia began to warm again. The researchers used a glider to track the development of what turned out to be the strongest marine heatwave in that part of the ocean since the devastating event a decade earlier. The glider swam more than 500 kilometres and captured the cooling effect of a tropical cyclone that tore through the waters in early February. In March and April, the team deployed two more gliders off the coast of Tasmania to help map the extent of a persistent heatwave in the Tasman Sea. That pair revealed that the temperature anomalies were higher in the ocean's subsurface than in its uppermost waters.

The researchers say that data collected by these gliders could help to improve predictions from dynamical forecasting models, which simulate the physics of processes in the ocean and atmosphere. “Collecting near-real-time data and ensuring that those could go into short-term models definitely has a lot of promise to help people make decisions and communicate what might be happening,” Benthuysen says.

Limited forecasts

Forecasting efforts around the world are currently unable to predict the extremes very far in advance, says Alex Sen Gupta, a climate scientist and oceanographer at the University of New South Wales in Sydney. “The science of ocean forecasting is quite a long way behind the science of weather forecasting.”

Some models might be able to predict a singular event a few days or a week ahead of time, Sen Gupta says. But beyond that, the chaotic nature of the climate system makes individual events more difficult to forecast. And for many stakeholders, the current models are not sophisticated enough or at fine-enough scales to inform the kinds of policy decision they need to make to prepare for a potential heatwave.

Jahson Alemu I, a marine ecologist at the National University of Singapore, notes that the resolution of today’s predictive models is not much smaller than the island of Tobago. That makes it hard both to make decisions and to communicate risks to the public, says Alemu I, who is also director of SpeSeas, a non-governmental organization focused on marine issues in the Caribbean.



[Save reefs to rescue all ecosystems](#)

Currently, researchers tend to rely on statistical models based on past patterns to give them a sense of whether a heatwave is likely to occur over a

given time period. But these models are a sort of stopgap measure until dynamical models are sophisticated enough to predict the events. “Statistical methods rely on patterns that you’ve seen in the past repeating themselves,” says Alistair Hobday, a marine scientist at the Commonwealth Scientific and Industrial Research Organisation (CSIRO) in Hobart, Australia. In a world with a rapidly changing climate, he says, such models will begin to fail. “The dynamical model is the way to go.”

Hobday leads a project at CSIRO to predict marine heatwaves. In December, the group released its first statistical forecast created with machine-learning techniques that examined both historical data and models of sea surface temperatures and the amount of heat stored in the upper ocean. The forecast warned of a high likelihood of a marine heatwave developing off the coast of Western Australia between January and April.

In fact, temperatures offshore did rise to abnormal highs in the beginning of the year. This year’s statistical forecast was a kind of proof-of-concept, Hobday says — the team intentionally chose a large region and a long time period over which a heatwave might be expected. But next year, his team plans to release a dynamical forecast for the region that will provide a finer-scale look at marine-heatwave risks.

Worsening future

There is one type of marine-heatwave prediction that climate scientists feel confident in making: that climate change is going to intensify and exacerbate the events. As people continue to pump greenhouse gases into the atmosphere, climate models project that rising global temperatures will exacerbate nearly every measure of marine heatwaves. “You expect that extremes will increase under climate change,” Holbrook says. “Things are just kind of going to get worse.”



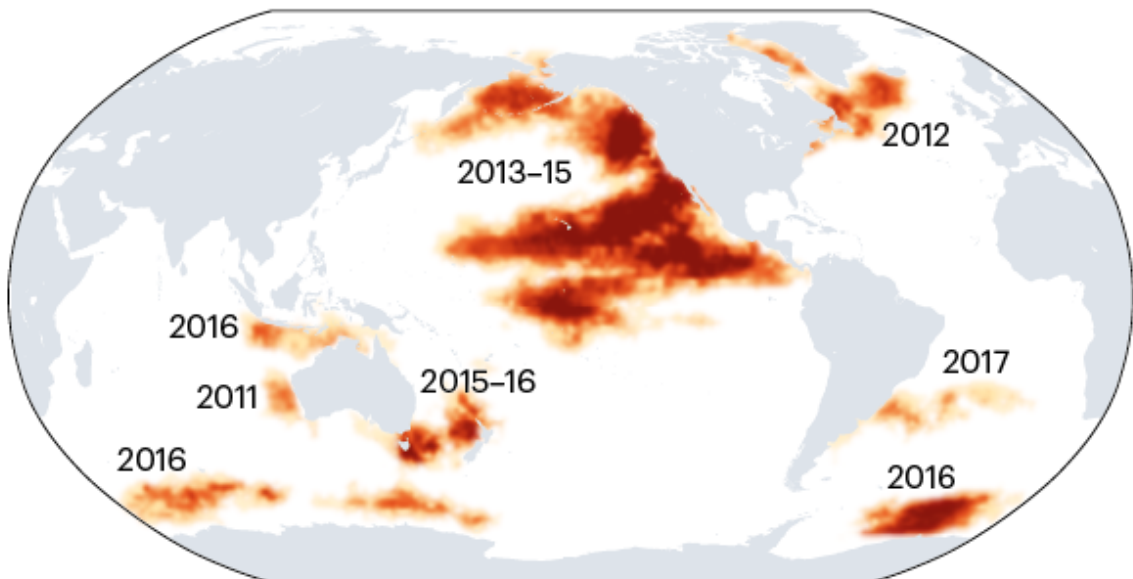
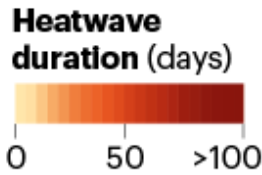
Five priorities for a sustainable ocean economy

Some of these changes are already happening. Between 1925 and 2016, the number of annual marine heatwave days around the globe increased by more than 50%. And from the beginning of the satellite record in 1982, marine heatwaves have increased in intensity across nearly two-thirds of the ocean⁵. And scientists predict that those trends will continue. Several studies have shown that even under moderate warming scenarios, almost all of the ocean will experience more-frequent and longer-lasting marine heatwaves over the coming years^{6,7}.

Many of the extreme events over the past several decades have been made worse by climate change, too. A 2020 study⁷ examining seven of the highest-impact marine heatwaves since 1981 concluded that all but one were at least partially due to human-driven warming (see ‘Four decades of marine heatwaves’). The researchers compared climate model simulations using pre-industrial concentrations of carbon dioxide in the atmosphere with model runs using present-day concentrations.

FOUR DECADES OF HEATWAVES

More than 30,000 distinct marine heatwaves occurred between September 1981 and December 2017, according to one study⁷. The map shows the most prominent over the past decade.



*Definitions and durations of marine heatwaves differ between studies.

©nature

Source: Ref. 7

The results showed that some of the events were so strong that they were fully attributable to anthropogenic climate change, says Charlotte Laufkötter, a climate scientist at the University of Bern in Switzerland who led that work. “In pre-industrial times, they couldn’t have occurred.”

And at some point in the next century, scientists project that much of the ocean will have warmed past the temperature threshold that defines these events — plunging many parts of the world into a state of permanent marine heatwave. “If we have such strong warming,” Laufkötter says, “it’s not an extreme event any more. It’s always there.”

Nature 593, 26-28 (2021)

doi: <https://doi.org/10.1038/d41586-021-01142-4>

References

1. 1.
Hobday, A. J. *et al.* *Prog. Oceanogr.* **141**, 227–238 (2016).
2. 2.
Rodrigues, R. R., Taschetto, A. S., Sen Gupta, A. & Foltz, G. R. *Nature Geosci.* **12**, 620–626 (2019).
3. 3.
Feng, M., McPhaden, M. J., Xie, S.-P. & Hafner, J. *Sci. Rep.* **3**, 1277 (2013).
4. 4.
Oliver, E. C. J. *et al.* *Nature Commun.* **8**, 16101 (2017).
5. 5.
Oliver, E. C. J. *et al.* *Nature Commun.* **9**, 1324 (2018).
6. 6.
Frölicher, T. L., Fischer, E. M. & Gruber, N. *Nature* **560**, 360–364 (2018).
7. 7.
Laufkötter, C., Zscheischler, J. & Frölicher, T. L. *Science* **369**, 1621–1625 (2020).

Jobs from Nature Careers

- -

- [All jobs](#)
 -
- [Postdoc \(f/m/d\) – Molecular mechanisms of translation in yeast –](#)

[Max Planck Institute for Biophysical Chemistry \(MPIBPC\)](#)
[Göttingen, Germany](#)

[JOB POST](#)
- [Laboratory Research Scientist - Cancer Epigenetics Laboratory](#)

[Francis Crick Institute](#)
[London, United Kingdom](#)

[JOB POST](#)
- [PhD student \(m/f/div\) in MS-based proteomics of small proteins](#)

[Max Planck Institute of Biophysics \(MPIBP\)](#)
[Frankfurt am Main, Germany](#)

[JOB POST](#)
- [Senior/Laboratory Research Scientist](#)

[Francis Crick Institute](#)
[London, United Kingdom](#)

[JOB POST](#)

This article was downloaded by **calibre** from <https://www.nature.com/articles/d41586-021-01142-4>

| [Section menu](#) | [Main menu](#) |

Books & Arts

- **[How Navy money changed the course of sea science](#)** [04 May 2021]

Book Review • A history of US oceanography reveals the ways in which military funding influenced discovery.

- **[Scientific success by numbers](#)** [03 May 2021]

Book Review • Big data bibliometrics must take into account qualitative analyses of research as a social institution, rooted in history, economics and politics.

BOOK REVIEW

04 May 2021

How Navy money changed the course of sea science

A history of US oceanography reveals the ways in which military funding influenced discovery.

- [Ann Finkbeiner](#) 0

1. [Ann Finkbeiner](#)

1. Ann Finkbeiner is a freelance science writer in Baltimore, Maryland, and author of *The Jasons*. She blogs at www.lastwordonnothing.com.

[View author publications](#)

You can also search for this author in [PubMed](#) [Google Scholar](#)



Scientists at the Scripps Institution of Oceanography take measurements in the Pacific Ocean in the 1950s. Credit: Scripps Institution of Oceanography/UC San Diego

Science on a Mission: How Military Funding Shaped What We Do and Don't Know about the Ocean Naomi Oreskes Univ. Chicago Press (2020)

These two statements are uncontroversial: the path of science is more or less determined by the educated curiosity of scientists; the funding of science is sometimes based on condition of usefulness. So, does usefulness affect science's path? Sometimes it does, especially when the funder has skin in the game. Pharmaceutical and chemical companies supported science to exonerate potentially dangerous products; the tobacco industry funded researchers to obscure the damage done by smoking.

Historian of science Naomi Oreskes has studied how the fossil-fuel industry adopted tobacco's malign tactics. Now, in *Science on a Mission*, she focuses

on the complexities of research driven by the military, as part of historians' concern with how the US government's enormous investments after the Second World War might have changed science. She offers case histories from oceanography, although many of her insights extend to multiple fields.



Inventions of war

In the years before, during and after the Second World War, US oceanography was focused at the Scripps Institution of Oceanography in La Jolla, California; the Woods Hole Oceanographic Institution in Massachusetts; and the Lamont Geological Observatory in Palisades, New York. These centres of excellent individual research were funded almost entirely by the US Navy. What difference did that make to what science they did or did not do? "The short answer," writes Oreskes, "is: a lot."

The Navy funded research into underwater acoustics, ocean temperatures and densities, and sea-floor maps, so its submarines could communicate, navigate and hide from and find the enemy. The Navy supplied the questions, but didn't care what answers the oceanographers found; they were free to follow where the science led. Nevertheless, Oreskes argues, the mere fact of having a military mission affected scientists' sense of autonomy, and resulted in them neglecting certain areas.



Discovery is always political

One strong driver was dislike of military associations. At Scripps and Woods Hole, in the 1930s and 1960s, respectively, groups of scientists strenuously objected to their institutions' directors relying on defence money. Their worries were mostly generic — whether Navy funding would open them to charges of having found what the service wanted them to find — and came down to arguments about the purity of curiosity-driven research versus the suspect nature of applied research. In neither situation did the scientists win. Scripps's director eventually left; at Woods Hole, the concerned scientists did.

In another case, the science was delayed: in 1964, the Navy began funding the deep submersible *Alvin* as a salvage and listening system. Not until 1974, when the cash began running out and the US National Science Foundation and the National Oceanic and Atmospheric Administration (both funders of curiosity-driven research) kicked in money, was *Alvin* freed to pursue the spectacular observations of deep-sea vents that led to understanding of extremophiles.

Sound and fury

Oreskes's most complex and lengthy case study began with the Navy's need to understand ocean circulation. Research at Woods Hole, particularly by Henry Stommel, led to the discovery of the thermocline, the zone between the upper, warm ocean and the cold abyss, in which temperature drops and density and salinity rise, affecting how sound travels. Navy funding enabled Stommel to develop the thermohaline circulation model, a theory that changes in temperature, density and salinity drive circulation. The money also led Maurice Ewing and Joe Worzel to discover the sound channel, a sort of underwater acoustic highway along which sound travels faster — and related shadow zones, in which it hardly travels at all. These features allow submarines to hide or communicate. The Navy's needs and oceanographers' curiosity coincided in a fundamental discovery about how oceans move.

But ocean acoustics had other implications, too. In these cases, some fields flourished while others starved. Sound travels more slowly in cold water than in warm, and in 1979, Walter Munk at Scripps and Carl Wunsch at the Massachusetts Institute of Technology in Cambridge realized that by measuring the speed of sound in the ocean, they were also measuring the ocean's temperature. Given that oceans cover more than half of Earth, measurements of ocean acoustics and temperature would be an excellent indicator of global warming.



[From blackboards to bombs](#)

In 1993, the Navy began a programme to set off undersea bangs, time their arrival at a distant point, and infer the water temperature along the way. Unfortunately, the scientists involved publicly and professionally downplayed the possibility that explosive sounds could affect marine animals such as whales. The programme became a long-running political, media and public-relations nightmare that was finally killed off a decade after it began.

Science on a Mission is what you want in a history: interesting research, stories with context and multiple points of view, clearly and compellingly written. But Oreskes's case that the Navy's mission affected the path of oceanography feels oddly incomplete. As she says, proving it would require an impossible comparison of two paths: one driven by scientific curiosity and the other by Navy funding. She also conflates military-driven science with mission-driven science. Is the reader meant to infer that the same scientific neglect or swerve applies to civilian missions, such as fighting climate change or developing a COVID-19 vaccine?

If so, is that bad? Running through the book is an issue that Oreskes flags but doesn't resolve: that many fields in many eras have assigned different values to different kinds of research. One value equates mission-driven research with applied research, and curiosity-driven with pure research — and deems applied research less noble, and pure research, more. Another is a stigma attached to working for the military. Sometimes these values might be extrapolated to the science itself, and military, applied, mission-driven science is seen as less credible. I wonder if I am meant to distrust the oceanography done with Navy funding — a qualm that is inevitable, although maybe the subject of a different book entirely.

Nature **593**, 29-30 (2021)

doi: <https://doi.org/10.1038/d41586-021-01168-8>

Jobs from Nature Careers

-
-

- [All jobs](#)
 -
- [Postdoc \(f/m/d\) – Molecular mechanisms of translation in yeast –](#)

[Max Planck Institute for Biophysical Chemistry \(MPIBPC\)](#)
[Göttingen, Germany](#)

[JOB POST](#)
- [Laboratory Research Scientist - Cancer Epigenetics Laboratory](#)

[Francis Crick Institute](#)
[London, United Kingdom](#)

[JOB POST](#)
- [PhD student \(m/f/div\) in MS-based proteomics of small proteins](#)

[Max Planck Institute of Biophysics \(MPIBP\)](#)
[Frankfurt am Main, Germany](#)

[JOB POST](#)
- [Senior/Laboratory Research Scientist](#)

[Francis Crick Institute](#)
[London, United Kingdom](#)

[JOB POST](#)

This article was downloaded by **calibre** from <https://www.nature.com/articles/d41586-021-01168-8>

| [Section menu](#) | [Main menu](#) |

BOOK REVIEW

03 May 2021

Scientific success by numbers

Big data bibliometrics must take into account qualitative analyses of research as a social institution, rooted in history, economics and politics.

- [Cassidy R. Sugimoto](#) 0

1. [Cassidy R. Sugimoto](#)

1. Cassidy R. Sugimoto is a professor of informatics at Indiana University Bloomington.

[View author publications](#)

You can also search for this author in [PubMed](#) [Google Scholar](#)



Art by Albert-László Barabási's laboratory, on display at the Ludwig Museum in Budapest.Credit: Dániel Végel/Ludwig Museum Archives

The Science of Science *Dashun Wang & Albert-László Barabási* Cambridge Univ. Press (2021)

Research institutions are under increasing pressure to make decisions faster, with fewer resources. The science of science can provide information on how to organize research effectively to meet societal needs.

The field uses quantitative tools to understand the discovery system. It complements venerable disciplines such as the history, philosophy and sociology of science, and relies on century-old bibliometric techniques that exploit the traces left by publications, grants and patents. Findings can illuminate trends, reveal disparities and inform policies for hiring, funding, training and more.

In their book *The Science of Science*, computational social scientist Dashun Wang and network scientist Albert-László Barabási present an introduction to a burgeoning part of this activity. They frame it as a big-data approach,

but it is perhaps better understood as applying the tools of network science to study science. Their primer fields interesting anecdotes, engaging call-out boxes and an accessible style. But its narrow view leads to worrying interpretations.



[Let's move beyond the rhetoric: it's time to change how we judge research](#)

They describe the science of science as emerging, without engaging with its historical or interdisciplinary foundations. In fact, the titular term was used in the 1963 book *Little Science, Big Science*, in which science historian Derek de Solla Price advocated that the community “turn the tools of science on science itself” — and has been used in major scientometric publications since the 1970s.

In the style of a management handbook, Wang and Barabási promise to help scientists to navigate their careers, arguing that the science of science aims to maximize individuals’ odds of success. They suggest that their insights will help administrators to spot the people who will bring the greatest benefit to a department, and they encourage funding agencies to identify those most likely to be high performing.

But the research community has moved from promoting indicators such as the journal impact factor and *h*-index to critiquing them. These measures often do more harm than good, creating what economists Margit Osterloh

and Bruno Frey call a “[taste for rankings](#)”, rather than a “taste for science”. They lead scholars to salami-slice — publish data in increments to glean as many papers as possible — or worse, to compete.



[The Leiden Manifesto for research metrics](#)

These concerns have been promoted through consensus statements such as the [Leiden Manifesto](#) and the [Declaration on Research Assessment](#), which has been signed by thousands of institutions and more than 17,000 individuals. The documents call on the community to end reliance on poorly constructed indicators that can reify structural biases such as racism, sexism and classism. Policymakers are implored to remember Goodhart’s law: when a measure becomes a target, it ceases to be a good measure.

Not only do Wang and Barabási ignore this conversation — they seem to advocate the gamesmanship that the community has committed to dismantle.

Matthew and Matilda

They open with a discussion of scientific careers, listing dozens of people. They name only a handful of women in the entire book: half in a paragraph about the English department at Duke University in Durham, North

Carolina, and then brief references to Marie Curie, Cleopatra and the sociologist Dorothy Swaine Thomas.

Sociologist Harriet Zuckerman is the sole woman acknowledged for her scientific work, in the section on collaboration. Her contributions to the concept of the Matthew effect — which describes the disproportionate rewards reaped by those in privileged positions — are neglected in favour of discussing her husband's research on the subject. Also unmentioned is the Matilda effect. Coined by historian of science Margaret Rossiter, this term describes “the systematic undervaluing of women’s contributions to science”. It is named after suffragist Matilda Gage, who described the phenomenon in 1870.



In Retrospect: The Social Function of Science

The invisibility of women and people from other minoritized groups is not simply a matter of equity — it challenges the bases of the arguments in the book. Decades of empirical evidence from sociology and scientometrics show the strong influence of social and demographic factors on scientific performance. To ignore this is to enjoin administrators, funders and hiring committees to look to past success as a chief indicator of future success, without considering systemic barriers.

Things improve when Wang and Barabási tackle the optimization of research teams. They contend that large teams develop science, whereas small ones disrupt it. They emphasize the productivity of “super-tie collaborators” — scholars who continuously co-author papers across time, which they suggest is a mechanism for success. They provide evidence that the best teams draw from a variety of ethnicities, institutions and nations — reinforcing (largely without citing) work from sociology and scientometrics.

They imply that research on scientific collaboration began in 2000. Yet Zuckerman’s 1964 dissertation examined collaboration among Nobel laureates in the United States, and science historians Donald Beaver and Richard Rosen developed a comprehensive theory of collaboration in the first issue of *Scientometrics* in 1978. The empirical analyses that Wang and Barabási cite are drawn from between 2000 and 2005, before the rise of China as a scientific superpower, leading to anachronistic moments.

Lifetime impact

The authors introduce several concepts of their own, including “ultimate impact”. They argue that the lifetime citations of a paper are a factor of perceptions of novelty and importance (fitness), how fast a work begins to be cited (immediacy) and for how long it is cited (longevity). They present a formula to predict the total number of citations a paper will acquire. They admit that this can lead to “the premature abortion of valuable ideas”.



A kinder research culture is possible

They then advocate the *Q*-factor, which seeks to define and predict scientific careers by quantifying an individual's ability to turn an idea into a discovery with a given citation impact. This rests on the assumption that all scientists have access to the same resources, ignoring the massive disparities across countries and institutions. Wang and Barabási imply that highly productive scientists possess an inherent talent or ability, yet they assert that randomness is a key variable in “hot streaks” of output. Actionable and equitable science policy is unlikely to be built on ideas of either innate brilliance or unpredictability.

Promisingly, they close with a research agenda for investigating failures, acknowledging that focusing on success overlooks this crucial aspect of research. Where do research functions such as synthesizing, replicating or curating sit in this binary classification, I wonder? Normal science, by definition, is the accumulation of findings from a broad labour force. The most productive and highly cited researchers stand on many shoulders. If the workforce is classified as either superstars or failures, cumulative scholarship is lost.

Science does not happen in a vacuum. It is a social and intellectual institution, rooted in historical, economic and political contexts. Underplaying these elements has grave consequences. Ultimately, Wang and

Barabási deliver a dispatch from an era that assumed that science was a meritocracy – despite ample evidence to the contrary.

Nature **593**, 30-31 (2021)

doi: <https://doi.org/10.1038/d41586-021-01169-7>

Jobs from Nature Careers

- - - [All jobs](#)
 - - [Postdoc \(f/m/d\) – Molecular mechanisms of translation in yeast –](#)
[Max Planck Institute for Biophysical Chemistry \(MPIBPC\)](#)
[Göttingen, Germany](#)
[JOB POST](#)
 - [Laboratory Research Scientist - Cancer Epigenetics Laboratory](#)
[Francis Crick Institute](#)
[London, United Kingdom](#)
[JOB POST](#)
 - [PhD student \(m/f/div\) in MS-based proteomics of small proteins](#)
[Max Planck Institute of Biophysics \(MPIBP\)](#)

Frankfurt am Main, Germany

JOB POST

▪ **Senior/Laboratory Research Scientist**

Francis Crick Institute

London, United Kingdom

JOB POST

This article was downloaded by **calibre** from <https://www.nature.com/articles/d41586-021-01169-7>

| [Section menu](#) | [Main menu](#) |

Opinion

- **[Cooperative AI: machines must learn to find common ground](#)** [04 May 2021]
Comment • To help humanity solve fundamental problems of cooperation, scientists need to reconceive artificial intelligence as deeply social.
- **[Fix databases that fail with two surnames](#)** [04 May 2021]
Correspondence •
- **[African swine fever ravaging Borneo's wild pigs](#)** [04 May 2021]
Correspondence •
- **[Brazil: video inspires young women to work in solar energy](#)** [04 May 2021]
Correspondence •
- **[Five principles for scientists on social media](#)** [14 April 2021]
Correspondence •

COMMENT

04 May 2021

Cooperative AI: machines must learn to find common ground

To help humanity solve fundamental problems of cooperation, scientists need to reconceive artificial intelligence as deeply social.

- [Allan Dafoe](#) ⁰,
- [Yoram Bachrach](#) ¹,
- [Gillian Hadfield](#) ²,
- [Eric Horvitz](#) ³,
- [Kate Larson](#) ⁴ &
- [Thore Graepel](#) ⁵

1. [Allan Dafoe](#)

1. Allan Dafoe is associate professor and director at the Centre for the Governance of AI, Future of Humanity Institute, University of Oxford, UK.

[View author publications](#)

You can also search for this author in [PubMed](#) [Google Scholar](#)

2. [Yoram Bachrach](#)

1. Yoram Bachrach is a research scientist at DeepMind, London.

[View author publications](#)

You can also search for this author in [PubMed](#) [Google Scholar](#)

3. [Gillian Hadfield](#)

1. Gillian Hadfield is director at the Schwartz Reisman Institute for Technology and Society, University of Toronto, Canada; and senior policy adviser at OpenAI, San Francisco, California, USA; and a faculty affiliate at the Vector Institute for Artificial Intelligence and at the Center for Human-Compatible AI at the University of California, Berkeley.

[View author publications](#)

You can also search for this author in [PubMed](#) [Google Scholar](#)

4. [Eric Horvitz](#)

1. Eric Horvitz is chief scientific officer at Microsoft, Redmond, Washington, USA.

[View author publications](#)

You can also search for this author in [PubMed](#) [Google Scholar](#)

5. [Kate Larson](#)

1. Kate Larson is professor of computer science at the University of Waterloo, Canada, and a research scientist at DeepMind, Montreal, Canada.

[View author publications](#)

You can also search for this author in [PubMed](#) [Google Scholar](#)

6. [Thore Graepel](#)

1. Thore Graepel is research lead at DeepMind, London; and professor of computer science at University College London.

[View author publications](#)

You can also search for this author in [PubMed](#) [Google Scholar](#)



A huddle at the 2017 United Nations Climate Change Conference, where attendees cooperated on mutually beneficial joint actions on climate. Credit: Sean Gallup/Getty

Artificial-intelligence assistants and recommendation algorithms interact with billions of people every day, influencing lives in myriad ways, yet they still have little understanding of humans. Self-driving vehicles controlled by artificial intelligence (AI) are gaining mastery of their interactions with the natural world, but they are still novices when it comes to coordinating with other cars and pedestrians or collaborating with their human operators.

The state of AI applications reflects that of the research field. It has long been steeped in a kind of methodological individualism. As is evident from introductory textbooks, the canonical AI problem is that of a solitary machine confronting a non-social environment. Historically, this was a sensible starting point. An AI agent — much like an infant — must first master a basic understanding of its environment and how to interact with it.

Even in work involving multiple AI agents, the field has not yet tackled the hard problems of cooperation. Most headline results have come from two-player zero-sum games, such as backgammon, chess¹, Go² and poker³. Gains in these competitive examples can be made only at the expense of others. Although such settings of pure conflict are vanishingly rare in the real world, they make appealing research projects. They are culturally cherished, relatively easy to benchmark (by asking whether the AI can beat the opponent), have natural curricula (because students train against peers of their own skill level) and have simpler solutions than semi-cooperative games do.

AI needs social understanding and cooperative intelligence to integrate well into society. The coming years might give rise to diverse ecologies of AI systems that interact in rapid and complex ways with each other and with humans: on pavements and roads, in consumer and financial markets, in e-mail communication and social media, in cybersecurity and physical security. Autonomous vehicles or smart cities that do not engage well with humans will fail to deliver their benefits, and might even disrupt stable human relationships.



[Don't ask if artificial intelligence is good or fair, ask how it shifts power](#)

We need to build a science of cooperative AI. As researchers in the field and its governance, we argue that it is time to prioritize the development of

cooperative intelligence that has the ability to promote mutually beneficial joint action, even when incentives are not fully aligned. Just as psychologists studying humans have found that the infant brain does not develop fully without social interaction, progress towards socially valuable AI will be stunted unless we put the problem of cooperation at the centre of our research.

Cooperative intelligence is unlikely to emerge as a by-product of research on other kinds of AI. We need more work on cooperative games and complex social spaces, on understanding norms and behaviours, and on social tools and infrastructure that promote cooperation. The AI community should learn more from, and contribute to, other fields that work on cooperation.

From autonomy to cooperation

Parents encourage their children to grow beyond their dependencies and become autonomous. But autonomy is rarely regarded as the sole goal for humans. Rather, we are generally most productive when we work cooperatively as part of broader society. Similarly, certain kinds of autonomy in AI systems are useful precisely because they enable the system to contribute effectively to broader cooperative efforts. Most of the value from self-driving vehicles will come not from driving on empty roads, but from vehicles coordinating smoothly with the flow of pedestrians, cyclists and cars driven by humans. Thus, cooperative intelligence is not an alternative to autonomous intelligence, but goes beyond it.

AI research on cooperation will need to bring together many clusters of work. A first cluster consists of AI–AI cooperation, tackling ever more difficult, rich and realistic settings (see ‘Four elements of cooperative intelligence’). A second is AI–human cooperation, for which we will need to advance natural-language understanding, enable machines to learn about people’s preferences, and make machine reasoning more accessible to humans. A third cluster is work on tools for improving (and not harming) human–human cooperation, such as ways of making the algorithms that govern social media better at promoting healthy online communities.

Four elements of cooperative intelligence

In most settings, people's incentives are not fully aligned. Nevertheless, they can often cooperate, taking joint action to achieve mutually beneficial outcomes. One example is countries agreeing and enforcing carbon cuts to tackle climate change. The cooperative intelligence needed to achieve this has four parts:

Understanding. The ability to take into account the consequences of actions, to predict another's behaviour, and the implications of another's beliefs and preferences.

Communication. The ability to explicitly and credibly share information with others relevant to understanding behaviour, intentions and preferences.

Commitment. The ability to make credible promises when needed for cooperation.

Norms and institutions. Social infrastructure — such as shared beliefs or rules — that reinforces understanding, communication and commitment.

AI–AI cooperation

Multi-agent AI research has seen most success in two-player zero-sum settings, from the superhuman performance of IBM's chess-playing computer Deep Blue to the powerful demonstration of deep reinforcement learning by the program AlphaGo. However, few interactions in the real world are characterized by pure conflict — when there is no possibility of bargains, negotiations or threats. So, improving skill at inherently rivalrous games is unlikely to be the most promising way for AI to produce social value.

Games of pure common interest are a step towards developing cooperative agents. The cooperative card game Hanabi⁴ requires players to communicate private information and intentions under strong constraints about what can be said and when. Team games such as robot soccer⁵ need players on a team to work as one, jointly planning their moves and passing the ball. In these examples, all agents on a team share the same goals. Mastering these games requires many skills essential to cooperation. Research avenues include

building AIs that can understand what teammates are thinking and planning; communicate plans; and even cooperate with different kinds of teammate who might think differently and react more slowly (known as ad hoc teamwork).

Yet because these situations are restricted to a perfect harmony of interests, they represent the easy case for cooperation. Real-world relationships almost always involve a mixture of common and conflicting interests. This tension gives rise to the rich texture of human cooperation problems, including bargaining, trust and mistrust, deception and credible communication, commitment problems and assurances, politics and coalitions, and norms and institutions. AI agents will need to learn how to manage these harder cooperation problems, as humans do.



Computer scientists in Leipzig, Germany, prepare their robot soccer team for a test game. Credit: dpa picture alliance/Alamy

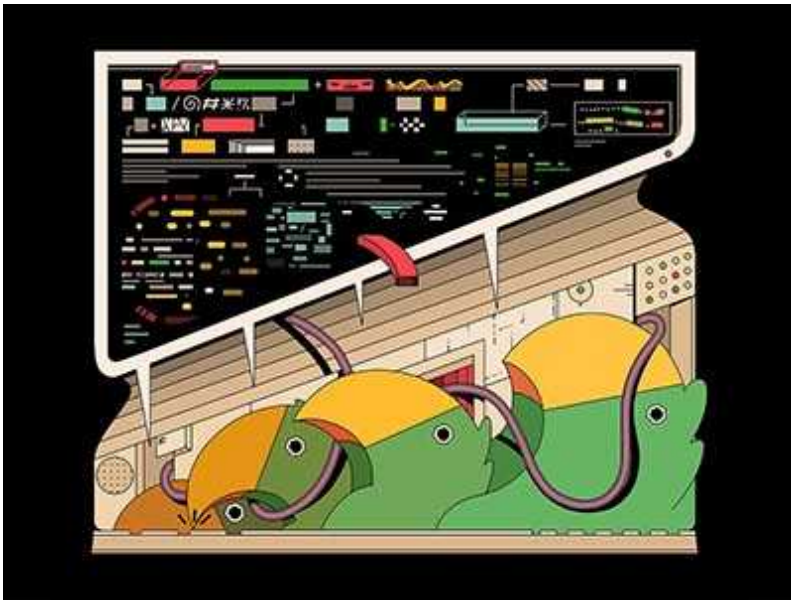
An example is the board game Diplomacy, in which players negotiate non-binding alliances with others. To succeed, AI agents will need to understand each other well enough to recognize when their interests are aligned with

those of other players. They will have to develop a common vocabulary to communicate their intentions. They will benefit from being able to communicate credibly, despite possible incentives to lie. They must overcome mutual fears of betrayal, so as to agree on and execute jointly beneficial plans. They might even learn to establish norms relating to the adherence of agreements. To enable progress in these cooperative skills, researchers have devised variants of Diplomacy that modify the difficulty of these challenges, such as introducing an agreed simple vocabulary or permitting binding commitments.

Human–AI cooperation

AI is increasingly present, underlying everything from dynamic pricing strategies to loans and prison-sentencing decisions. Collaborative industrial robots work on factory floors alongside labourers⁶, care robots help human health workers and personal AI assistants (such as Amazon’s Alexa, Apple’s Siri and Google Assistant) help us with scheduling, albeit in an elementary way.

The design of agents that will act in accordance with human intentions, preferences and values — known as AI alignment⁷ — is a crucial part of cooperative AI. But it is only a part, because the relationship between a single human (acting as the principal) and a single machine (acting as the agent) isn’t always clear. Real-world cooperation problems often involve multiple stakeholders, some conflicting interests and integration with our institutional and normative infrastructure.



Robo-writers: the rise and risks of language-generating AI

A particular challenge facing researchers working on human–AI cooperation is that it involves, well, humans. Today, many deployed machine-learning models are trained either on massive data sets or in simulated environments that can generate years of experience in seconds. For example, the program AlphaZero learnt to play chess by playing 44 million games against itself over 9 hours. By contrast, humans produce data slowly, and require researchers to consider compensation, ethics and privacy. There might be ways to use fewer human participants, such as extensively training AIs in simulation and then fine-tuning them in the real world.

Many AI practitioners have dreamt of building autonomous and human-like intelligence. They envisioned systems that could replace human labour, acting with the speed and resilience of machines, and scaling up rapidly given increases in computing power, algorithmic efficiency and capital. However, unlike systems that have tight integration with human workers, autonomous systems might pose greater safety risks. Human-like AI might be more likely to displace labour.

Instead, we could develop AI assistants that complement human intelligence and depend on us for tasks in which humans have a comparative advantage. As Stanford University radiologist Curtis Langlotz put it: “AI won’t replace

radiologists, but radiologists who use AI will replace radiologists who don't.”

Progress will require advances in understanding human language, gestures and activities, and ad hoc teamwork, in addition to preference learning by machines, safety, interpretability by humans⁸, and understanding of norms. Research will need to approach increasingly rich and realistic environments. Instead of benchmarking progress mainly by whether autonomous machines can outperform autonomous humans on a task, researchers should also assess the performance of human–machine teams.

AI for human collaboration

Humans confront ubiquitous cooperation problems as commuters, neighbours, co-workers and citizens. The global scientific community, for example, could benefit from better tools for identifying relevant work and promising collaborations. Technology is crucial, mediating our ability to find and process information, communicate and self-organize. Digital systems and AI can expand this toolkit.

Some AI tools, such as machine language translation, seem strongly disposed towards promoting cooperation. Today, 2 people who speak any of more than 100 languages can communicate with the aid of a smartphone and a translation app.



People who speak different languages can communicate using an AI-based translation device. Credit: Akio Kon/Bloomberg via Getty

Digital platforms such as Wikipedia, Reddit and Twitter provide tools to combine user-provided content. AI advances could improve this community infrastructure, for example, by routing relevant information to contributors more efficiently to enhance collaborative editing. Other advances could improve user rating and reputation systems through better modelling and by accounting for the rater's repute or relevance, as well as by enabling recommendation algorithms that more intelligently promote a community's values.

Building healthy online communities is challenging; just as social media can connect us, so too can it polarize, stress, misinform, distract and addict us⁹. Researchers and developers need to find better ways to name and measure desirable properties and build algorithms that encourage them. [Platforms for political deliberation](#) can be designed to promote empathy about different viewpoints and cultivate community consensus. Methods for achieving this include language comprehension that links to structured databases of knowledge, or clustering algorithms to identify related perspectives.

Next steps

To succeed, cooperative AI must connect with the broader science of cooperation, which spans the social, behavioural and natural sciences. AI research will need to converse with multiple fields. These include psychology, to understand human cognition; law and policy, to understand institutions; history, sociology and anthropology, to understand culture; and political science and economics, to understand problems of information, commitment and social choice. Adjacent research areas are developing AI with socially desirable properties, such as alignment, interpretability and fairness^{[10,11](#)}. Each of these addresses a distinct, but complementary, set of challenges.

The need for interdisciplinarity is exemplified by a landmark work: Robert Axelrod's *The Evolution of Cooperation*, published in 1984^{[12](#)}. Axelrod, a political scientist, brought together game theorists, mathematicians, economists, biologists and psychologists in a tournament to help devise the best algorithms for the iterated Prisoner's Dilemma, the canonical example of why two rational people might not cooperate. The winning solution that cooperated most successfully, called Tit for Tat, was devised by Anatol Rapoport, a US scholar with a background spanning mathematics, biology, network science and peace studies.



Time to regulate AI that interprets human emotions

Axelrod's tournament offered another lesson. It gave researchers a benchmark for success in the design of cooperative algorithms, just as ImageNet¹³ did for computer vision by collecting and labelling millions of photos. Cooperative AI research will similarly gain momentum if investigators can devise, agree on and adopt benchmarks that cover a diverse set of challenges: playing cooperative board games, integrating into massive multiplayer video games, navigating simplified environments that require machine–human interaction, and anticipating tasks as a personal assistant might. Similar to the state-of-the-art in language modelling, considerable effort and creativity will be needed to make sure these benchmarks remain sufficiently rich and ambitious, and do not have socially harmful blind spots.

The most important challenges of cooperation might be the most difficult to benchmark; they involve creatively stepping out of our habitual roles to change the ‘game’ itself. Indeed, if we are to take the social nature of intelligence seriously, we need to move from individual objectives to the shared, poorly defined ways humans solve social problems: creating language, norms and institutions.

Science is a social enterprise, so promoting research into cooperative AI will require social interventions. A recent milestone was a December 2020 workshop on cooperative AI at the leading machine-learning conference NeurIPS. It involved speakers from a diverse array of disciplines, and resulted in a review of Open Problems in Cooperative AI¹⁴.

We and others are establishing a Cooperative AI Foundation to support this nascent field (www.cooperativeai.org), backed by a large philanthropic commitment. The foundation’s mission will be to catalyse advances in cooperative intelligence to benefit all of humanity, including efforts to fund fellowships, organize conferences, support benchmarks and environments, and award prizes.

The crucial crises confronting humanity are challenges of cooperation: the need for collective action on climate change, on political polarization, on misinformation, on global public health or on other common goods, such as water, soil and clean air. As the potential of AI continues to scale up, a

nudge in the direction of cooperative AI today could enable us to achieve much-needed global cooperation in the future.

Nature **593**, 33-36 (2021)

doi: <https://doi.org/10.1038/d41586-021-01170-0>

References

1. 1.

Campbell, M., Hoane Jr, A. J. & Hsu, F.-H. *Artif. Intell.* **134**, 57–83 (2002).

2. 2.

Silver, D. *et al.* *Nature* **529**, 484–489 (2016).

3. 3.

Moravčík, M. *et al.* *Science* **356**, 508–513 (2017).

4. 4.

Bard, N. *et al.* *Artif. Intell.* **280**, 103216 (2020).

5. 5.

Kitano, H. *et al.* *AI Magazine* **18**, 73 (1997).

6. 6.

Villani, V., Pini, F., Leali, F. & Secchi, C. *Mechatronics* **55**, 248–266 (2018).

7. 7.

Russell, S. *Human Compatible: Artificial Intelligence and the Problem of Control* (Penguin, 2019).

8. 8.

Adadi, A. & Berrada, M. *IEEE Access* **6**, 52138–52160 (2018).

9. 9.

Allcott, H., Braghieri, L., Eichmeyer, S. & Gentzkow, M. *Am. Econ. Rev.* **110**, 629–676 (2020).

10. 10.

Barocas, S., Hardt, M. & Narayanan, A. *Fairness and Machine Learning* (Fairmlbook.org, 2019).

11. 11.

Buolamwini, J. & Gebru, T. *Proc. Mach. Learn. Res.* **81**, 77–91 (2018).

12. 12.

Axelrod, R. *The Evolution of Cooperation* (Basic, 1984).

13. 13.

Deng, J. *et al.* *IEEE Conf. Comput. Vis. Pattern Recognit.* **2009**, 248–255 (2009).

14. 14.

Dafoe, A. *et al.* Preprint at <https://arxiv.org/abs/2012.08630> (2020).

Jobs from Nature Careers

- - - [All jobs](#)
 -
 -

Postdoc (f/m/d) – Molecular mechanisms of translation in yeast –

Max Planck Institute for Biophysical Chemistry (MPIBPC)

Göttingen, Germany

JOB POST

- **Laboratory Research Scientist - Cancer Epigenetics Laboratory**

Francis Crick Institute

London, United Kingdom

JOB POST

- **PhD student (m/f/div) in MS-based proteomics of small proteins**

Max Planck Institute of Biophysics (MPIBP)

Frankfurt am Main, Germany

JOB POST

- **Senior/Laboratory Research Scientist**

Francis Crick Institute

London, United Kingdom

JOB POST

| [Section menu](#) | [Main menu](#) |

CORRESPONDENCE

04 May 2021

Fix databases that fail with two surnames

- [Jorge Mira Pérez](#) ⁰ &
- [M. Carmen Parafita Couto](#) ¹

1. [Jorge Mira Pérez](#)

1. University of Santiago de Compostela, Spain.

[View author publications](#)

You can also search for this author in [PubMed](#) [Google Scholar](#)

2. M. Carmen Parafita Couto

1. Leiden University, the Netherlands.

[View author publications](#)

You can also search for this author in [PubMed](#) [Google Scholar](#)

Scientific databases widely used in anglophone countries should cater for contributors from cultures that do not follow the format of a given name followed by one family name. Such inconsistencies cause problems for academic referencing and mask scientists' cultural diversity in the scientific record.

In Spain, for example, people have two surnames, one from each parent. One of us, who should be indexed as Mira Pérez, J., is often wrongly cited as Pérez, J. M.. Spanish scientists use hyphens or drop a name to avoid such

errors. Asian scientists can face a similar problem (see [Nature 451, 766–767; \(2008\)](#); [N. Puniamoorthy et al. Nature 452, 530; 2008](#)): in Indonesia, for example, many have only one name (see [go.nature.com/3xgf6v](#)).

The anglophone naming system can also intrude on other aspects of research, including grant applications and conference registration. EasyChair is an example of a conference-managing system that has diversified to accommodate people with two surnames or none at all (<https://easychair.org>).

Nature 593, 37 (2021)

doi: <https://doi.org/10.1038/d41586-021-01188-4>

Jobs from Nature Careers

- - - [All jobs](#)
 -
 - **Postdoc (f/m/d) – Molecular mechanisms of translation in yeast –**
[Max Planck Institute for Biophysical Chemistry \(MPIBPC\)](#)
[Göttingen, Germany](#)
[JOB POST](#)
 - **Laboratory Research Scientist - Cancer Epigenetics Laboratory**
[Francis Crick Institute](#)
[London, United Kingdom](#)

JOB POST

- **PhD student (m/f/div) in MS-based proteomics of small proteins**

Max Planck Institute of Biophysics (MPIBP)

Frankfurt am Main, Germany

JOB POST

- **Senior/Laboratory Research Scientist**

Francis Crick Institute

London, United Kingdom

JOB POST

This article was downloaded by **calibre** from <https://www.nature.com/articles/d41586-021-01188-4>

| [Section menu](#) | [Main menu](#) |

CORRESPONDENCE

04 May 2021

African swine fever ravaging Borneo's wild pigs

- [Robert M. Ewers](#) ⁰,
- [Senthilvel K. S. S. Nathan](#) ¹ &
- [Peter A. K. Lee](#) ²

1. [Robert M. Ewers](#)

1. Imperial College London, Ascot, UK.

[View author publications](#)

You can also search for this author in [PubMed](#) [Google Scholar](#)

2. Senthilvel K. S. S. Nathan

1. Sabah Wildlife Department, Kota Kinabalu, Sabah, Malaysia.

[View author publications](#)

You can also search for this author in [PubMed](#) [Google Scholar](#)

3. Peter A. K. Lee

1. Sabah Department of Veterinary Services, Kota Kinabalu, Sabah, Malaysia.

[View author publications](#)

You can also search for this author in [PubMed](#) [Google Scholar](#)

African swine fever has breached the island of Borneo, where it is wiping out populations of the wild bearded pig *Sus barbatus*. First confirmed in early February, the outbreak has driven a precipitous decline in this species in less than two months. Field sites in the east of the Sabah region are reporting a complete absence of live pigs in forests. Local extinctions across swathes of Borneo are a realistic prospect.

Bearded pigs are listed as vulnerable by the International Union for Conservation of Nature. They are seen as ‘ecosystem engineers’ in the Bornean rainforest, where they are one of the most abundant species of mammal. Bearded pigs can be legally hunted under permit, and are an important source of animal protein for many communities.

The African swine fever virus is already island-hopping across southeast Asia, threatening 11 species of endemic pig, including the Sulawesi warty pig (*Sus celebensis*). Opportunities to control the disease in wild-pig populations are limited. Vaccines for domestic pigs are still in development, so the best hope for stemming loss of the wild animals could be to protect isolated populations in geographically defensible locations.

Nature **593**, 37 (2021)

doi: <https://doi.org/10.1038/d41586-021-01189-3>

Jobs from Nature Careers

- - - [All jobs](#)
 - - [Postdoc \(f/m/d\) – Molecular mechanisms of translation in yeast –](#)
[Max Planck Institute for Biophysical Chemistry \(MPIBPC\), Göttingen, Germany](#)

JOB POST

- **Laboratory Research Scientist - Cancer Epigenetics Laboratory**

Francis Crick Institute

London, United Kingdom

JOB POST

- **PhD student (m/f/div) in MS-based proteomics of small proteins**

Max Planck Institute of Biophysics (MPIBP)

Frankfurt am Main, Germany

JOB POST

- **Senior/Laboratory Research Scientist**

Francis Crick Institute

London, United Kingdom

JOB POST

This article was downloaded by **calibre** from <https://www.nature.com/articles/d41586-021-01189-3>

CORRESPONDENCE

04 May 2021

Brazil: video inspires young women to work in solar energy

- [Aline Cristiane Pan](#)⁰,
- [Aline Kirsten Vidal de Oliveira](#)¹,
- [Kathlen Schneider](#)²,
- [Natália Chaves](#)³ &
- [Izete Zanesco](#)⁴

1. Aline Cristiane Pan

1. Brazilian Women's Network in Solar Energy, Florianópolis, Brazil.

[View author publications](#)

You can also search for this author in [PubMed](#) [Google Scholar](#)

2. [Aline Kirsten Vidal de Oliveira](#)

1. Brazilian Women's Network in Solar Energy, Florianópolis, Brazil.

[View author publications](#)

You can also search for this author in [PubMed](#) [Google Scholar](#)

3. Kathlen Schneider

1. Brazilian Women's Network in Solar Energy, Florianópolis, Brazil.

[View author publications](#)

You can also search for this author in [PubMed](#) [Google Scholar](#)

4. Natália Chaves

1. Brazilian Women's Network in Solar Energy, Florianópolis, Brazil.

[View author publications](#)

You can also search for this author in [PubMed](#) [Google Scholar](#)

5. Izete Zanesco

1. Brazilian Women's Network in Solar Energy, Florianópolis, Brazil.

[View author publications](#)

You can also search for this author in [PubMed](#) [Google Scholar](#)

The solar-energy industry in Brazil is booming. It employs 43,000 people, only 20% of whom are women. Just 12% of these women have technical and scientific roles. To encourage girls to enter these professions, the Brazilian Women's Network in Solar Energy (*Rede Brasileira de Mulheres na Energia Solar*, or MESol) has released a video called *Women of Energy*.

The video (see go.nature.com/3ucs9zj) highlights women working in renewable-energy research, teaching and industry. It aims to address the perceived lack of female role models in this sector. As one teenager who watched it said: “I didn't know so many women work in this area.”

A diverse workforce improves creativity, innovation and decision-making, and also boosts profits (see go.nature.com/39safwv and [M. W. Nielsen et al. Proc. Natl Acad. Sci. USA 114, 1740–1742; 2017](#)). Efforts to achieve gender equity require companies to make changes to management, leadership and the personal development of employees.

The video was produced with support from the German Cooperation for Sustainable Development as part of Brazil's Professionals for the Energy of the Future initiative.

Nature **593**, 37 (2021)

doi: <https://doi.org/10.1038/d41586-021-01147-z>

Jobs from Nature Careers

- - - [All jobs](#)
 - - [Postdoc \(f/m/d\) – Molecular mechanisms of translation in yeast –](#)
[Max Planck Institute for Biophysical Chemistry \(MPIBPC\), Göttingen, Germany](#)
[JOB POST](#)
 - [Laboratory Research Scientist - Cancer Epigenetics Laboratory](#)
[Francis Crick Institute, London, United Kingdom](#)
[JOB POST](#)
 - [PhD student \(m/f/div\) in MS-based proteomics of small proteins](#)

Max Planck Institute of Biophysics (MPIBP)

Frankfurt am Main, Germany

JOB POST

▪ **Senior/Laboratory Research Scientist**

Francis Crick Institute

London, United Kingdom

JOB POST

This article was downloaded by **calibre** from <https://www.nature.com/articles/d41586-021-01147-z>

| [Section menu](#) | [Main menu](#) |

CORRESPONDENCE

14 April 2021

Five principles for scientists on social media

- [Marcel Bogers](#) 0

1. [Marcel Bogers](#)

1. Eindhoven University of Technology, the Netherlands

[View author publications](#)

You can also search for this author in [PubMed](#) [Google Scholar](#)

To enable the information sharing, networking and serendipitous encounters that we would normally experience at physical conferences and seminars, many scientists are looking to improve their online engagement through social media. Based on my experiences, I offer five suggestions.

First, see and be seen: communication is two-way, so listen, too. Second, select and specialize: focus on those things that suit you; there's only so much you can do. Third, serve: think about where you can add most value. Fourth, socialize: don't forget about relationships just because they're digital. Fifth, strategize: make social media part of your overall communication strategy, even if it's just emerging.

I follow these principles by responding to posts I am tagged in. I tweet only on topics that I feel able to discuss. I stick to Facebook for more personal engagement, to Twitter for sharing interesting developments in research and practice, and to LinkedIn for the occasional announcement of new research and events. I use my accounts to showcase my own work, yes, but also to amplify others' contributions and promote our collective domain.

Challenges regarding scientists' engagement will remain post-pandemic ([Nature 589, 155–157; 2021](#)). Social media can help us to overcome these and find new routes to scholarly impact and visibility.

Nature **593**, 37 (2021)

doi: <https://doi.org/10.1038/d41586-021-01002-1>

Jobs from Nature Careers

- - - [All jobs](#)
 - - [Postdoc \(f/m/d\) – Molecular mechanisms of translation in yeast –](#)
[Max Planck Institute for Biophysical Chemistry \(MPIBPC\), Göttingen, Germany](#)
[JOB POST](#)
 - [Laboratory Research Scientist - Cancer Epigenetics Laboratory](#)
[Francis Crick Institute, London, United Kingdom](#)
[JOB POST](#)
 - [PhD student \(m/f/div\) in MS-based proteomics of small proteins](#)

Max Planck Institute of Biophysics (MPIBP)

Frankfurt am Main, Germany

JOB POST

▪ **Senior/Laboratory Research Scientist**

Francis Crick Institute

London, United Kingdom

JOB POST

This article was downloaded by **calibre** from <https://www.nature.com/articles/d41586-021-01002-1>

| [Section menu](#) | [Main menu](#) |

Work

- **Sell yourself and your science in a compelling personal statement** [23 April 2021]

Career Feature • Don't get bogged down in technical details, and balance the professional and the personal.

- **Reactive, reproducible, collaborative: computational notebooks evolve** [03 May 2021]

Technology Feature • A new breed of notebooks is taking data visualization and collaborative functionality to the next level, with spreadsheet simplicity.

- **Global virus tracker** [03 May 2021]

Where I Work • Virologist Kanta Subbarao stalks respiratory viruses around the world and in the culture dish.

CAREER FEATURE

23 April 2021

Sell yourself and your science in a compelling personal statement

Don't get bogged down in technical details, and balance the professional and the personal.

- [Andy Tay](#)

1. Andy Tay
[View author publications](#)

You can also search for this author in [PubMed](#) [Google Scholar](#)

[Find a new job](#)



Credit: Getty

Personal statements — essays highlighting personal circumstances, qualities and achievements — are used extensively in science to evaluate candidates for jobs, awards and promotions. Five researchers offer tips for making yours stand out in a crowded and competitive market.

STEVE OH: Convey personal qualities beyond academic interests

*Steve Oh is director of the Stem Cell Processing Group at the A*STAR Bioprocessing Technology Institute in Singapore.*

As a principal investigator, I have read a good number of personal statements from students applying for science scholarships and jobs. The ones that stand out recount the applicant's biography, bringing out their character as well as their professional qualities. Personal statements are often

centred on academic and research achievements. But, in my opinion, a good scientist should also demonstrate social skills, be interested in making an impact on society through, for example, entrepreneurship, and have awareness of the world outside the country they live in. Memorable personal statements tend to bring out ‘soft’ skills, such as having macro-level thinking abilities and awareness of the impact that science can have on society.



Careers Collection: Publishing

To achieve this balance of professional and personal, consider two elements. First, explain your motivations to pursue a scientific career. These might include a family illness, an inspiring talk by a scientist, or great mentorship from a colleague. Second, describe how you have gone out of your way to get experience in science, such as proactively seeking opportunities for a laboratory internship, or what you have learnt from overcoming difficulties with your experiments. This information brings out qualities, such as curiosity and perseverance, that are crucial to being a good scientist.

I vividly remember the personal statement of one of my PhD students. He described his struggle with having only one healthy kidney — and how, despite this, he continued to do sports like rock climbing. He also wrote about how he did badly in his undergraduate studies: he had to take a year

off to recharge before returning to school and excelling. His story shows resilience and honesty — traits that I love in a researcher.

SILVIA KARIUKI: Do not be afraid to defend your decisions

Silvia Kariuki is a postdoctoral fellow at the Kenya Medical Research Institute (KEMRI) Wellcome Trust Research Programme in Kilifi.

When I was planning to return to Kenya, where I grew up, to start a postdoctoral project, fellow researchers, friends and family members all asked why I was choosing to go back. They felt my career would suffer because Kenya's scientific infrastructure is not as advanced as that in the United States, where I spent 13 years working and completing my undergraduate and PhD degrees.

Two years into my return to Kenya, when writing my personal statement for the Wellcome International Training Fellowship to follow up on my postdoctoral project, I explained that the Kenya Medical Research Institute—Wellcome Trust Research Programme in Kilifi could provide a good research environment for me. I would be able to study human genetic variants that confer protective effects against severe malaria infection, and my research would have a real-world impact by informing the production of malaria therapies. In my personal statement, I wrote that I wanted to pursue my scientific career in Kenya despite the scepticism I had faced — and it convinced the fellowship committee that I had thought deeply about my career move.

I also seek advice from mentors when writing a personal statement. I usually send mine to two to three senior scientists who have had more experience writing them and who have been on review committees for fellowship applications. One suggestion I usually get is to be ‘more human’. The judges would like to hear your personal voice and read about your motivation, even if these might be unconventional.

KELLY CLANCY: Use stories to show who you are

Kelly Clancy is a postdoctoral fellow in neuroscience at University College London.

Stories can make a personal statement stand out. It's hard, of course — I've heard colleagues say it's a trope for neuroscience-related personal statements to open with something like "I got interested in neuroscience after seeing my grandmother suffer from Alzheimer's." But I think that cynicism is unfair: it's a beautiful impulse to get into science for a personal reason, and having a personal connection to science can drive important new insights.

I included the story that inspired the project I'd proposed in my application to the Branco Weiss postdoctoral fellowship. My best friend from high school had lost three limbs to an improvised explosive device while serving as a medic in Afghanistan. I described how this incident led to my interest in the field of neuroprosthetic devices that can restore motor capabilities, and the shortcomings I wanted to address with my work.

My advice for writing a personal statement is to not get bogged down in technical details. Don't just focus on what you want to study — explain why. Demonstrate how you think. What led you to do the work or research you've undertaken so far? What are the questions that drive you and your science, and why are they important? Perhaps most importantly (and this is for all of us, not just those writing personal statements): ask, "What drives my science? Is it a reflection of my ego, wanting to be right or smart and to get high-profile publications? Or is it an extension of my will to do good in the world, my curiosity and my love of understanding?" The world is full of questions and problems to solve. Using stories in personal statements can help applicants to explain what scientific questions they care about, and why they matter.



Collection: the PhD

With the support from the Branco Weiss Fellowship, my colleagues and I have since developed neuroprosthetic techniques that were just published¹ and used these methods to explore interesting basic neuroscience questions and less-invasive neuroprosthetic interfaces.

WEI GAO: Demonstrate ambition and don't exaggerate

Wei Gao is an assistant professor of mechanical engineering at the California Institute of Technology in Pasadena.



Wei Gao, an assistant professor of mechanical engineering. Credit: Wei Gao

A personal statement should highlight your aspirations and dreams. A CV can list all your publications, but they won't all be read thoroughly, and members of the selection committee might miss the significance of your work.

Think of a personal statement as a document that complements your CV. I use it to explain the big problems my research is tackling and its impact. In my application to be a World Economic Forum Young Scientist, I described my concerns about worsening mental health in our society and discussed how my research on wearable sensors can improve early diagnosis of mental illness by sensing metabolites such as cortisol, a stress-related hormone, in sweat. It would be difficult to explain my aspirations clearly in a short, typically list-based, CV. In a personal statement, I can demonstrate my ambition in greater detail.

A good personal statement should avoid exaggerating your contribution. This is especially true for a multi-author paper on which you didn't have a leading role. Focus on the work that you led and to not overstate your contributions to your field. Even if your contribution was significant, being humble in a personal statement is a good quality. Research is a culmination of the efforts of many researchers, and is never attributable to just one person.

ABHIMANYU VEERAKUMARASIVAM: Break the essay down and tailor it to your audience

Abhimanyu Veerakumarasivam is dean of the School of Medical and Life Sciences at Sunway University Subang Jaya in Malaysia.



Abhimanyu Veerakumarasivam in the lab.Credit: Sunway University

One way to simplify the writing process is to break your personal statement down into several key elements, including who you are, what you have accomplished, why you are applying for a role or award and how you will contribute to the organization.

When I was organizing the Association of Southeast Asian Nations (ASEAN) Science Leadership Programme from 2017 to 2019, my committee and I divided the application statement into a few questions focused on the ‘who, what, why and how’, which would help applicants to better structure their essays. I found this format particularly useful because, in Asia, our default culture is to not stand out, and many qualified candidates might be too shy to share their personal stories or too humble to share their achievements.

I found that creating a more defined structure around the personal statement allowed applicants to reflect on the experience they have gained from working in the region, which has many low-income countries and little investment in science. I would not always get these details in an open-ended personal essay.

One candidate discussed the huge disparities in science in the ASEAN region and his desire to bridge the gaps. By doing so, the candidate demonstrated that he had a good awareness of his environment and the unique challenges of working in that setting while highlighting his willingness to take action to bridge the gaps.

Applicants should also tailor their personal statements to their audience. For instance, students applying to graduate schools and scholarships will often send generic personal statements with their applications. If applicants want an academic institution to invest in them, then their personal statements need to reflect a genuine interest in the organization they’re applying to. The candidates with better statements usually include details of labs they are interested in working in and specifics about research topics they find fascinating.

Nature **593**, 153-155 (2021)

doi: <https://doi.org/10.1038/d41586-021-01101-z>

These interviews have been edited for length and clarity.

References

1. 1.

K. B. Clancy *et al. Neuron* **109**, 677–689 (2021).

Jobs from Nature Careers

- - - [All jobs](#)
 - - [Postdoc \(f/m/d\) – Molecular mechanisms of translation in yeast –](#)
[Max Planck Institute for Biophysical Chemistry \(MPIBPC\)](#)
[Göttingen, Germany](#)
[JOB POST](#)
 - [Laboratory Research Scientist - Cancer Epigenetics Laboratory](#)
[Francis Crick Institute](#)
[London, United Kingdom](#)
[JOB POST](#)
 - [PhD student \(m/f/div\) in MS-based proteomics of small proteins](#)

Max Planck Institute of Biophysics (MPIBP).

Frankfurt am Main, Germany

JOB POST

▪ **Senior/Laboratory Research Scientist**

Francis Crick Institute

London, United Kingdom

JOB POST

This article was downloaded by **calibre** from <https://www.nature.com/articles/d41586-021-01101-z>

| [Section menu](#) | [Main menu](#) |

TECHNOLOGY FEATURE

03 May 2021

Reactive, reproducible, collaborative: computational notebooks evolve

A new breed of notebooks is taking data visualization and collaborative functionality to the next level, with spreadsheet simplicity.

- [Jeffrey M. Perkel](#)

1. Jeffrey M. Perkel

[View author publications](#)

You can also search for this author in [PubMed](#) [Google Scholar](#)

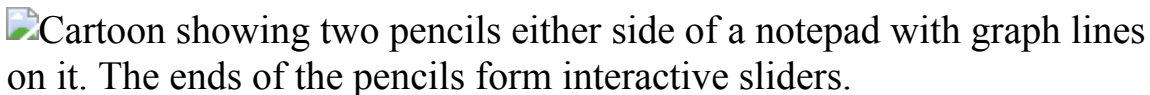


Illustration by The Project Twins

This year marks ten years since the launch of the IPython Notebook. The open-source tool, now known as the Jupyter Notebook, has become an exceedingly popular piece of data-science kit, with millions of notebooks deposited to the GitHub code-sharing site.

Computational notebooks combine code, results, text and images in a single document, yielding what Stephen Wolfram, creator of the Mathematica software package, has called a “computational essay”. And whether written using Jupyter, Mathematica, RStudio or any other platform, researchers can use them for iterative data exploration, communication, teaching and more.

But computational notebooks can also be confusing and foster poor coding practices. And they are difficult to share, collaborate on and reproduce. A 2019 study found that just 24% of 863,878 publicly available Jupyter notebooks on GitHub could be successfully re-executed, and only 4% produced the same results ([J. F. Pimentel et al. in 2019 IEEE/ACM 16th International Conference on Mining Software Repositories \(MSR\) 507–517; IEEE, 2019](#)).

“Notebooks are messy,” says Anita Sarma, a computer scientist at Oregon State University in Corvallis who studies human–computer interaction. “You write stuff, you keep old crusty code behind, and it’s hard to kind of figure out which cells to execute in which order, because you were trying different things.”

But a growing suite of platforms and tools aims to smooth these rough edges. Some make notebooks ‘reactive’, so that code re-executes whenever software variables change; others focus on collaboration and version control. But all provide researchers with innovative ways to explore, document and share their data with colleagues and the world.



[A toolkit for data transparency takes shape](#)

For Sergei Pond, notebooks have provided an outlet for documenting the genetics of the pandemic. Pond, a computational biologist at Temple

University in Philadelphia, Pennsylvania, has created some three dozen documents related to SARS-CoV-2, the virus that causes COVID-19. “My default setting”, he says, is to “write up an interactive notebook and send it to my collaborators so they can play with the data, [so] they can immediately see what’s there.”

His notebook platform of choice is called Observable. It’s based in San Francisco, California, and was founded in 2019 by two Google alumni: Mike Bostock, developer of the D3 JavaScript library that powers many of the interactive data visualizations on the web today, and Melody Meckfessel. The company’s web-based notebook system allows users to create, share and reuse sophisticated, interactive visualizations written in JavaScript, the programming language understood by web browsers. According to Meckfessel, “hundreds of thousands” of users do so every month.

Unlike Jupyter, which passes code to an external ‘kernel’ that executes it, Observable code runs in the browser itself. That makes the platform fast and responsive, Bostock says. But because JavaScript is not a typical data-science language, researchers often use Observable not for data processing but for visualization.

Pond, for instance, uses Observable to share colourful maps, graphs, protein structures and sequence alignments that represent data that he generates in other software. Observable’s modular structure means that other programmers can easily apply those visualizations to their own data. But Pond’s notebooks also take advantage of another key Observable feature: reactivity.

Jeffrey Perkel www.jeffreyperkel.com
Technology editor, Springer Nature

Publish



...

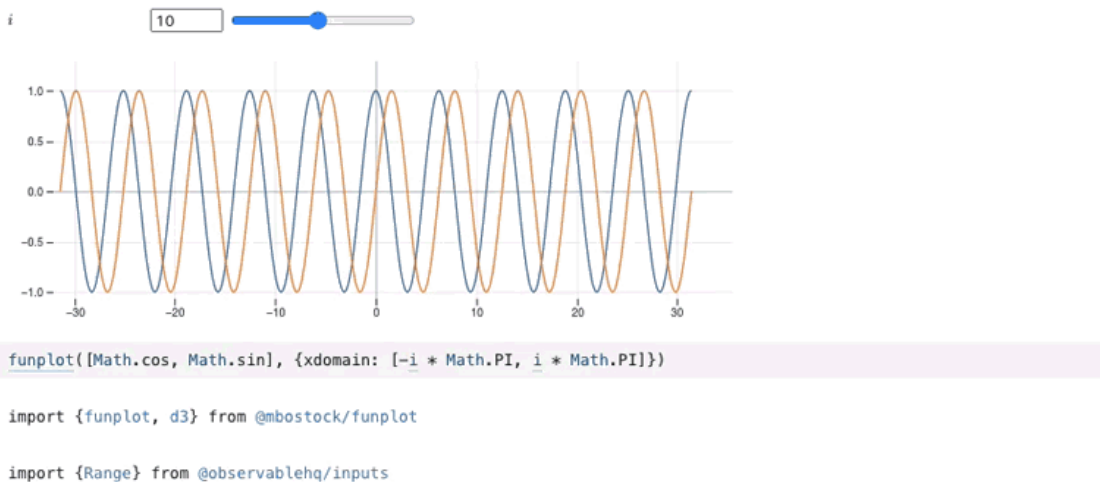
You Edited Apr 2

Reactive notebooks

This document demonstrates the **reactivity** and **modularity** of Observable notebooks.

We will plot the graph of $\sin(x)$ — and $\cos(x)$ — over the interval $-i\pi \leq x \leq +i\pi$. These graphical elements were written by others and applied here using `import` directives in the cells at the bottom.

Move the slider or type a number (1-20) in the text box below to adjust the value of `i`, and thus, the x-range of the graph. Note that as you do so, the graph refreshes automatically.



Reactive notebooks such as Observable update as their content changes.

Suppose you have a Jupyter notebook that plots a line. In one code cell, you define the slope and y-intercept; in the next, you draw the graph. The notebook structure allows coders to return to the earlier cell to change the slope after the plot has been rendered. But that change does not cause the figure to be automatically redrawn; the user must manually re-execute the cell that plots it.

This workflow can lead to ‘state problems’, in which a notebook’s output does not reflect its code — as would happen, for instance, if the user deletes the cell that defines a variable after it has been executed. In 2018, Joel Grus, then a software engineer at the Allen Institute for Artificial Intelligence in Seattle, Washington, highlighted this behaviour, and the ensuing confusion, in a widely viewed talk entitled “I don’t like notebooks”. But, “to a large

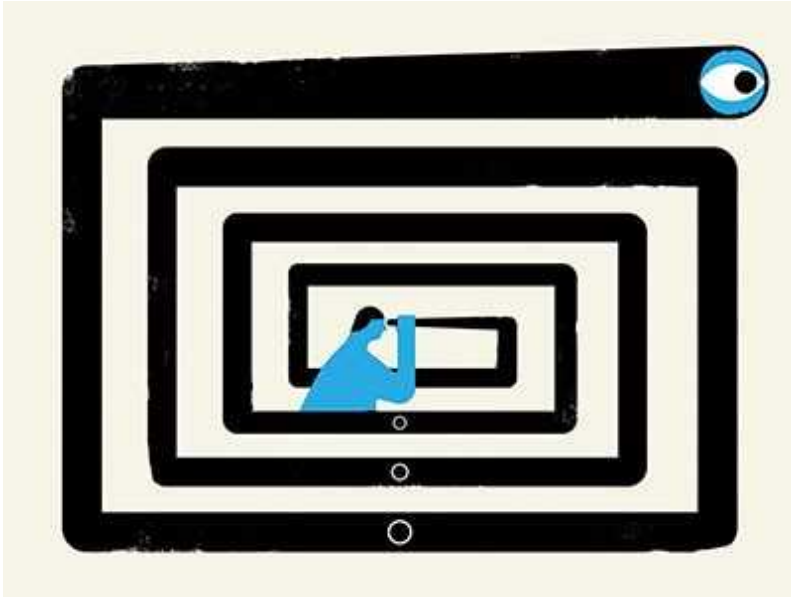
degree, having fully reactive notebooks eliminates that feature,” he says now.

Reactive notebooks are similar to spreadsheets, Bostock explains. Just as Microsoft Excel knows to recalculate a formula if the underlying cells change, reactive notebooks track how code cells relate to one another to ensure that a notebook’s output always reflects its variables.

Combined with visual widgets, such as sliders and pull-down lists, such behaviour makes notebooks interactive, allowing readers to explore how changing variables or assumptions can affect results. Herb Susmann, a biostatistics PhD student at the University of Massachusetts Amherst, for instance, uses reactive documents to explain statistical concepts. “It really helps me get more of a visceral feel for how these statistical things work,” he says. (That said, reactivity isn’t always desirable, particularly if cells take a long time to execute, or when data sets are very large.)

React and collaborate

Other reactive notebook systems exist for researchers who don’t use JavaScript. Susmann, for instance, has built a reactive notebook for R programmers, called Reactor. And Fons van der Plas, a software engineer in Berlin, created Pluto, a reactive notebook platform for the programming language Julia. Henri Drake, a graduate student of climate physics at the Massachusetts Institute of Technology in Cambridge, uses Pluto to demonstrate concepts in climate science. “Coding it up as an interactive Pluto notebook makes it a way more engaging experience for a first-time user,” Drake says, “and can really help people understand the models that I’m building.”



Why Jupyter is data scientists' computational notebook of choice

Fernando Pérez, a co-founder of Project Jupyter at the University of California, Berkeley, notes that Jupyter itself “is agnostic on the topic of reactivity”. Most kernels so far have been non-reactive, but they don’t have to be: Richa Gadgil, a former Jupyter intern at California Polytechnic State University in San Luis Obispo, for instance, spent her internship co-developing an experimental reactive kernel for Python. “It was a test of the Jupyter architecture and the Jupyter architecture passed that test,” says Brian Granger, who directed her work.

Another open-source system, called Vizier, focuses on data-driven reactivity, says Juliana Freire, a computer scientist at New York University, who co-directed the project. With built-in data validation functions and a spreadsheet interface, Vizier users can massage their data to fix inconsistencies — such as those caused by a column that contains both ‘Y/N’ and ‘yes/no’ responses. As they do so, the notebook re-executes. “You analyse, you clean, you analyse, you clean,” Freire says. “And as you do that, you save the whole provenance of the process.” As a result, users can revert to an earlier stage of clean-up and try again, all the time logging the changes that they have made. (Vizier notebooks can handle Python, SQL and Scala code.)

Some commercial reactive systems, including Observable, Deepnote and JetBrains’ Datalore (the last two of which are based in the Czech Republic),

also emphasize another notebook pain point: collaboration. Observable, for instance, allows real-time collaborative editing, much as Google Docs does, as well as commenting. There are two plan tiers: Personal (free for up to 5 members in the same interactive document) and Teams (for 6 or more members: US\$15 per editor, per month; free for viewers).

Gábor Csányi, who studies molecular modelling at the University of Cambridge, UK, uses Deepnote (free for up to 3 collaborators, then \$12 per user, per month) in his teaching. With his university's previous system, a student seeking help could share a copy of a notebook with Csányi, but it wasn't possible for both of them to view and edit the same document at the same time. "It was sort of a pain," he says. But with Deepnote, he can help students to debug their code in real time. "Just like you do with Google Docs, we see each other's cursors. We are editing the same notebook, and as they press shift-enter on a cell, I see the result. That was an incredible experience in how personalized support could be done efficiently."

Real-time collaboration is "a topic of massive activity" in the Jupyter project as well, says Pérez, and an in-development prototype is available on GitHub. "I'm pretty optimistic that this will happen soonish," he says.

Version control

Many commercial platforms also address another notebook challenge: version control.

The file format of Jupyter notebooks includes code, metadata, and computational output. As those outputs are often binary images, version control — the process that developers use to track how files change, which is optimized for plain-text files — can become difficult. Complicating matters, programmers can struggle to adapt standard version-control workflows to the fast, iterative nature of data exploration. As a result, crucial experimental details can be lost.



[NatureTech hub](#)

Commercial platforms tend to provide built-in notebook versioning. For those who prefer to stick with Jupyter, two plug-ins are available: nbdime, which provides an intelligent, structured view of file changes, including of graphical output; and Verdant, which offers a graphical interface that tracks how cells are modified, reordered and executed.

According to developer Mary Beth Kery, who studies human–computer interaction at Carnegie Mellon University in Pittsburgh, Pennsylvania, Verdant can smooth interactions with collaborators and peer reviewers. “Somebody will say, oh, did you try this in the model, or did you try this analysis?” she says. Many times, the answer is yes, but because the analysis didn’t work, the code is deleted. “What you want to do during the meeting is just pull it back up and be like, oh, yeah, I did, and here’s why it didn’t work. And our tool lets you actually do that.”

Such features can make an already user-friendly computing paradigm even friendlier — and easier to share. And that makes them even more powerful vehicles for scientific communication. “If you do really great science but no one understands it or no one gets access to it, then what’s the point?” Drake says. “These kinds of notebooks can really get people excited and expose people to concepts that are otherwise kind of impenetrable.”

Nature **593**, 156-157 (2021)

doi: <https://doi.org/10.1038/d41586-021-01174-w>

Jobs from Nature Careers

- - - [All jobs](#)
 - - [Postdoc \(f/m/d\) – Molecular mechanisms of translation in yeast –](#)

[Max Planck Institute for Biophysical Chemistry \(MPIBPC\)](#)
[Göttingen, Germany](#)
[JOB POST](#)
 - [Laboratory Research Scientist - Cancer Epigenetics Laboratory](#)

[Francis Crick Institute](#)
[London, United Kingdom](#)
[JOB POST](#)
 - [PhD student \(m/f/div\) in MS-based proteomics of small proteins](#)

[Max Planck Institute of Biophysics \(MPIBP\)](#)
[Frankfurt am Main, Germany](#)
[JOB POST](#)

▪ **Senior/Laboratory Research Scientist**

Francis Crick Institute

London, United Kingdom

JOB POST

This article was downloaded by **calibre** from <https://www.nature.com/articles/d41586-021-01174-w>

| [Section menu](#) | [Main menu](#) |

WHERE I WORK

03 May 2021

Global virus tracker

Virologist Kanta Subbarao stalks respiratory viruses around the world and in the culture dish.

- [Kendall Powell](#) 0

1. Kendall Powell

1. Kendall Powell is a freelance writer in Boulder, Colorado.

[View author publications](#)

You can also search for this author in [PubMed](#) [Google Scholar](#)

Kanta Subbarao in the lab she oversees at The Peter Doherty Institute for Infection and Immunity, Melbourne

Kanta Subbarao is the director of the World Health Organization Collaborating Centre for Reference and Research on Influenza at the Peter Doherty Institute for Infection and Immunity in Melbourne, Australia.
Credit: Daniel Mahon for *Nature*

I'm in my research laboratory here, at the Peter Doherty Institute for Infection and Immunity in Melbourne, Australia. We work on respiratory viruses, mainly influenza and SARS-CoV-2, the virus that causes COVID-19. This is the part of the lab where we try to understand the human antibody response to moderate-risk viruses.

I've done a lot of work on flu and the coronaviruses that cause Middle East respiratory syndrome and severe acute respiratory syndrome, so we were able to quickly set up our containment areas to work with the high-risk live

SARS-CoV-2 virus in February 2020. We helped to test plasma from people who had recovered from infection, as well as antibody treatments that were developed by drug companies, to see which antibodies best neutralized the virus.

We are also working with stem-cell biologists to turn human induced pluripotent stem cells — adult cells reprogrammed back to an embryonic-like state — into heart-muscle, placental, kidney and lung cells in culture. This helps us to see what happens in specific human tissues during coronavirus infection. We can test antiviral drugs on these culture systems, too.

I also oversee a team that does global influenza surveillance. From July to October 2020, Australia had a severe lockdown, with permits required to leave home for anything other than an hour of exercise. Because we worked on the coronavirus, our institute was allowed 25% occupancy. We worked in shifts, and people handed off their experiments or samples to other team members.

It was a stressful time. But we have a great team, which has doubled in size because of all the work. During lockdown, I volunteered to read cell-culture plates to ease pressure on my team. I still offer to do it now: it keeps me connected with the demands of high-risk lab work, and I prefer it to sitting at my desk.

Nature **593**, 160 (2021)

doi: <https://doi.org/10.1038/d41586-021-01175-9>

Jobs from Nature Careers

- - - [All jobs](#)
 -
 -

Postdoc (f/m/d) – Molecular mechanisms of translation in yeast –

Max Planck Institute for Biophysical Chemistry (MPIBPC).

Göttingen, Germany

JOB POST

- **Laboratory Research Scientist - Cancer Epigenetics Laboratory**

Francis Crick Institute

London, United Kingdom

JOB POST

- **PhD student (m/f/div) in MS-based proteomics of small proteins**

Max Planck Institute of Biophysics (MPIBP).

Frankfurt am Main, Germany

JOB POST

- **Senior/Laboratory Research Scientist**

Francis Crick Institute

London, United Kingdom

JOB POST

| [Section menu](#) | [Main menu](#) |

Research

- **[A child's grave is the earliest known burial site in Africa](#)**

[05 May 2021]

News & Views • The discovery of the burial of a young child in a cave in Kenya around 78,000 years ago sheds new light on the role of symbolism in the treatment of the dead during the Middle Stone Age.

- **[Black hole jets bent by magnetic fields](#)** [05 May 2021]

News & Views • The large-scale impact of magnetic fields on galaxy clusters has been unclear. Images from the MeerKAT radio telescope suggest that such fields can bend jets of particles ejected from massive black holes in galaxy clusters.

- **[African forest maps reveal areas vulnerable to the effects of climate change](#)** [21 April 2021]

News & Views • An analysis of six million trees reveals spatial patterns in the vulnerability of Central African rainforests to climate change and human activities. The maps generated could be used to guide targeted actions across national boundaries.

- **[Prediction for magnetic moment of the muon informs a test of the standard model of particle physics](#)** [05 May 2021]

News & Views • A new first-principles computation of the effect that creates most uncertainty in calculations of the magnetic moment of the muon particle has been reported. The results might resolve a long-standing puzzle, but pose another conundrum.

- **[Jets from MRC 0600-399 bent by magnetic fields in the cluster Abell 3376](#)** [05 May 2021]

Article • Radio observations of the cluster Abell 3376, combined with numerical modelling, attribute the bent jets associated with the second-brightest galaxy in the cluster to an ordered magnetic field at the discontinuity.

- **[Leading hadronic contribution to the muon magnetic moment from lattice QCD](#)** [07 April 2021]

Article • A precise theoretical computation of the anomalous magnetic moment of the muon based on ab initio quantum chromodynamics and quantum electrodynamics calculations is presented, which favours the existing experimental values.

- **[Rashba valleys and quantum Hall states in few-layer black arsenic](#)** [05 May 2021]

Article • Two-dimensional electronic systems in few-layer black arsenic show gate-tunable Rashba bands with unique spin-valley flavours and unconventional quantum Hall states due to

synergetic spin–orbit coupling and the Stark effect.

- **Polypeptide organic radical batteries** [05 May 2021]

Article • An environmentally friendly, all-organic radical battery is demonstrated, in which redox-active polypeptides perform as both cathode and anode materials, with a metal-free organic electrolyte.

- **Correlative operando microscopy of oxygen evolution electrocatalysts** [05 May 2021]

Article • Mapping the operational chemical, physical and electronic structure of an oxygen evolution electrocatalyst at the nanoscale links the properties of the material with the observed oxygen evolution activity.

- **Projected land ice contributions to twenty-first-century sea level rise** [05 May 2021]

Article • Efficient statistical emulation of melting land ice under various climate scenarios to 2100 indicates a contribution from melting land ice to sea level increase of at least 13 centimetres sea level equivalent.

- **The Paris Climate Agreement and future sea-level rise from Antarctica** [05 May 2021]

Article • An observationally calibrated ice sheet–shelf model suggests that global warming of 3 °C will trigger rapid Antarctic ice loss, contributing about 0.5 cm per year of sea-level rise by 2100.

- **Unveiling African rainforest composition and vulnerability to global change** [21 April 2021]

Article • A large dataset of 6 million trees from 193 taxa is used to map the floristic and functional composition of central African forests and predict their vulnerability to climate change.

- **Earliest known human burial in Africa** [05 May 2021]

Article • The earliest known human burial in Africa, that of a young child, is dated to around 78,000 years ago.

- **The structure, function and evolution of a complete human chromosome 8** [07 April 2021]

Article • The complete assembly of human chromosome 8 resolves previous gaps and reveals hidden complex forms of genetic variation, enabling functional and evolutionary characterization of primate centromeres.

- **Flexible scaling and persistence of social vocal communication** [31 March 2021]

Article • A population of neurons is identified in the lateral preoptic area that can drive the full range of social communication sounds with affective scaling during mating in mice.

- [**An amygdala circuit that suppresses social engagement**](#) [31 March 2021]
Article • A circuit in the amygdala uses thyrotropin-releasing hormone to suppress male mating when a female mouse is unhealthy.
- [**Ex utero mouse embryogenesis from pre-gastrulation to late organogenesis**](#) [17 March 2021]
Article • A new culture system makes it possible to grow mouse embryos and study their development outside the uterus up to the point of late organogenesis.
- [**The antibiotic darobactin mimics a \$\beta\$ -strand to inhibit outer membrane insertase**](#) [14 April 2021]
Article • Structural studies resolve how the antibiotic darobactin inhibits the bacterial BAM insertase.
- [**Antibody resistance of SARS-CoV-2 variants B.1.351 and B.1.1.7**](#) [08 March 2021]
Article • The SARS-CoV-2 variant B.1.1.7 can be neutralized by convalescent sera or sera from vaccinated individuals, whereas the B.1.351 variant is resistant to neutralization by these sera and by several monoclonal antibodies that are in clinical use.
- [**Sensitivity of SARS-CoV-2 B.1.1.7 to mRNA vaccine-elicited antibodies**](#) [11 March 2021]
Article • Sera from vaccinated individuals and some monoclonal antibodies show a modest reduction in neutralizing activity against the B.1.1.7 variant of SARS-CoV-2; but the E484K substitution leads to a considerable loss of neutralizing activity.
- [**Escape of SARS-CoV-2 501Y.V2 from neutralization by convalescent plasma**](#) [29 March 2021]
Article • Cross-neutralization assays of early variants and the 501Y.V2 variant of SARS-CoV-2 show that plasma from individuals infected with 501Y.V2 effectively neutralizes all variants, indicating that a vaccine that targets 501Y.V2 may also be effective against other SARS-CoV-2 variants.
- [**CAR directs T cell adaptation to bile acids in the small intestine**](#) [07 April 2021]
Article • Activation of the nuclear hormone receptor CAR in T cells protects the small intestine against bile acid-driven inflammation.

NEWS AND VIEWS

05 May 2021

A child's grave is the earliest known burial site in Africa

The discovery of the burial of a young child in a cave in Kenya around 78,000 years ago sheds new light on the role of symbolism in the treatment of the dead during the Middle Stone Age.

- [Louise Humphrey](#) 0

1. [Louise Humphrey](#)

1. Louise Humphrey is at the Centre for Human Evolution Research, Department of Earth Sciences, Natural History Museum, London SW7 5BD, UK.

[View author publications](#)

You can also search for this author in [PubMed](#) [Google Scholar](#)

Much of the current debate surrounding the location and timing of the emergence of modern human behaviour focuses on Africa during the Middle Stone Age (MSA), which lasted from about 320,000 to 30,000 years ago. The first known appearances of a suite of modern human innovations relating to technology, social organization, symbolism and exploitation of the landscape and resources occurred in Africa during this period¹. This time frame is also associated with the earliest known hominin fossils placed in the modern human lineage^{2,3}. The emergence of more-complex behaviours surrounding the treatment of the dead is often framed in the broader context of an increase in symbolic capabilities⁴. [Writing in Nature](#), Martinón-Torres *et al.*⁵ present a convincing case for the intentional burial of a young child in eastern Africa, at Panga ya Saidi, a cave in Kenya (Fig. 1). The authors'

meticulous recording of this archaeological evidence has revealed the earliest known human burial in Africa.

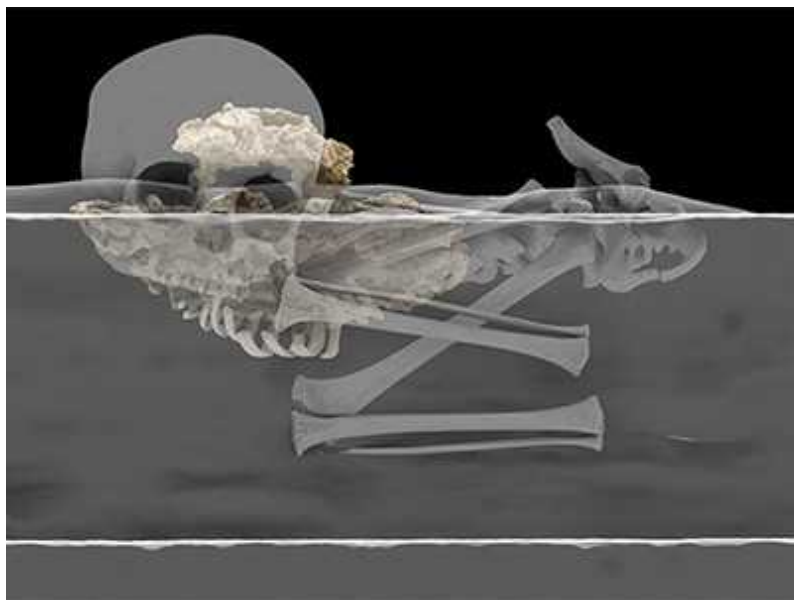


Figure 1 | Archaeological sites where treatments of the dead have been found. A range of behaviours are associated with ancient handling of the dead, which include body processing (sometimes associated with cannibalism), placement of a body in a relatively inaccessible location (such as a deep cave) or signs of a deliberate burial. Some sites at which such behaviours have been identified are linked to *Homo sapiens*^{5,10–14} and to other closely related species^{7–9,15–18} (other hominins belonging to the genus *Homo*). Martinón-Torres *et al.*⁵ report the excavation of a child's grave at Panga ya Saidi in Kenya dated to around 78,000 years ago (78 ka), which is the earliest known human burial in Africa. The fossils at El Sidrón, Sima de los Huesos, Tabun C1 and Shanidar Cave are those of Neanderthals (*Homo*

neanderthalensis); those at Gran Dolina are *Homo antecessor*, the cranium at Bodo is *Homo heidelbergensis* or *Homo rhodesiensis*; and the fossils at Rising Star Cave are *Homo naledi*.

The child, estimated to have been around three years old, seems to have been carefully arranged in a deliberately excavated pit and then covered by sediment scooped up from the cave floor. Microscopic features of the bone structure and the chemical composition of the sediment surrounding the bones reveal that the body was fresh when it was buried, and decomposed in the grave. The arrangement of the surviving bone fragments reveals that the child was placed lying gently inclined on their right side, with their legs folded and drawn up towards their chest.

Several anatomical connections between adjacent bones have survived, which suggests that the body was covered quickly after burial. A gradual trickle of sediment from above the corpse presumably prevented the bones from collapsing into the empty spaces that would have otherwise formed during the putrefaction of the soft tissues. An exception to this was the cranium and three neck bones, which collapsed into a void thought to have been created by the decay of a perishable head support. The right clavicle (one of the bones of the shoulder girdle) and two ribs had rotated in the grave, which might imply that part of the upper body was originally tightly wrapped in a perishable material.



[Read the paper: Earliest known human burial in Africa](#)

The burial pit and the archaeological layers surrounding it and directly above it are associated with MSA stone tools, securely anchoring the burial in the MSA. Martinón-Torres *et al.* date the burial itself to $78,300 \pm 4,100$ years ago. The date was obtained using probabilistic modelling and a technique called optically stimulated luminescence to determine the age of the entire sequence of the assessed archaeological layers. This finding demonstrates that humans in East Africa were deliberately burying their dead at least 78,000 years ago.

Archaeological and fossil records reveal a wide spectrum of mortuary treatments carried out by early humans (species in the genus *Homo*) spanning at least 800,000 years or so (Fig. 1). The first step towards understanding the nature of these mortuary behaviours — the actions and beliefs surrounding the treatment of the dead — is to reconstruct the series of human actions associated with the deposition of a body.

Not all mortuary behaviours leave traces that are archaeologically visible. The importance of a burial is that it documents a sequence of planned and deliberate actions involving: the creation of an artificial space to contain the body; the placement of a body or body parts into that space; and the covering of the body, often using the sediment that was removed during preparation of the grave⁶. Each of these stages can, but might not always, leave visible archaeological traces, so not all burials will be recognized as such. Other actions that leave enduring traces in the archaeological record relate to processing of the corpse, and might involve the removal of soft tissues, separation of body parts, or signs of cooking or chewing indicative of cannibalism. Examples have been found in the archaeological record of human bones that have been shaped into tools and used as decorative objects.

The second step towards understanding these mortuary behaviours is to infer whether there was any meaning associated with the treatment of the dead beyond the practical measures required to avoid attracting animal scavengers to spaces used by the living and to prevent contamination of those spaces during decay of the body. Strictly functional interventions might also include disarticulation of the body to facilitate transportation, nutritional

cannibalism, or the opportunistic use of bones or teeth as tools or as a raw material for manufacturing an object. Inferring signs of symbolic behaviour in burials is one of the more contentious areas of archaeology.



Incest uncovered at the elite prehistoric Newgrange monument in Ireland

Behaviours that might point towards a departure from purely practical motivations and towards a more meaningful treatment of the dead are those that involve an investment of time and resources beyond what is strictly required to dispose of or make use of the corpse. Such actions include careful placement of the corpse in the grave to achieve a desired body position or orientation, the wrapping or binding of the body for reasons other than to aid transportation, or the deliberate incorporation of items of value in the grave. Such items include objects that could reasonably be considered to have a personal or decorative significance, and those linked to the social role of the deceased. The interred objects might also encompass articles thought to be needed by the deceased in another existence, such as food or medicine. Repeated depositions of corpses over a prolonged period at a single location might signify the recognition of a place for the dead⁶, particularly if that location is difficult to access and other causes for the accumulation of the remains can be ruled out. The fossil assemblages at Sima de los Huesos in Spain⁷ and Rising Star Cave in South Africa⁸ can be interpreted as early examples of placement of the dead in a designated space (Fig. 1).

The presence of symbolic aspects elevates treatment of the dead from mortuary behaviour to funerary behaviour⁹. The burial reported by Martinón-Torres and colleagues reveals the care and effort taken to achieve a desired body position by supporting the child's head and wrapping the upper body. This burial, together with a previous report of the burial of a child around 74,000 years ago, associated with a shell ornament in South Africa at Border Cave¹⁰, suggests that a tradition of symbolically significant burials, at least for the very young, might have been culturally embedded in parts of Africa in the later part of the MSA.

Understanding the treatment of the dead intersects with our understanding of social organization, symbolic behaviours and the use of landscape, resources and technology. The act of burial restricts dispersal of the body and the other contents of the grave, increasing the likelihood of archaeological recovery, and provides an unambiguous association between the deceased — and hence the species they represent — and a certain set of behaviours at a specific time and place. Future discoveries in Africa and beyond could shed even more light on the evolution of modern traits and behaviour during the emergence of our species.

Nature **593**, 39-40 (2021)

doi: <https://doi.org/10.1038/d41586-021-00805-6>

References

1. 1.

McBrearty, S. & Brooks, A. S. *J. Hum. Evol.* **39**, 453–563 (2000).

2. 2.

Hublin, J.-J. *et al. Nature* **546**, 289–292 (2017).

3. 3.

Bergström, A., Stringer, C., Hajdinjak, M., Scerri, E. M. L. & Skoglund, P. *Nature* **590**, 229–237 (2021).

4. 4.

Balzeau, A. *et al. Sci. Rep.* **10**, 21230 (2020).

5. 5.

Martinón-Torres, M. *et al. Nature* **593**, 95–100 (2021).

6. 6.

Pettitt, P. *The Palaeolithic Origins of Human Burial* (Routledge, 2011).

7. 7.

Arsuaga, J. L. *et al. J. Hum. Evol.* **33**, 109–127 (1997).

8. 8.

Dirks, P. H. G. M. *et al. eLife* **4**, e09561 (2015).

9. 9.

Pomeroy, E. *et al. Evol. Anthropol.* **29**, 263–279 (2020).

10. 10.

d'Errico, F. & Backwell, L. *J. Hum. Evol.* **93**, 91–108 (2016).

11. 11.

McCown, T. D. & Keith, A. *The Stone Age of Mount Carmel* Vol. 2 (Clarendon, 1939).

12. 12.

Vandermeersch, B. *Les Hommes Fossiles de Qafzeh (Israel)* (CNRS, 1981).

13. 13.

Vermeersch, P. M. *et al.* *Antiquity* **72**, 475–484 (1998).

14. 14.

Clark, J. D. *et al.* *Nature* **423**, 747–752 (2003).

15. 15.

Rosas, A. *et al.* *L' Anthropologie* **116**, 57–76 (2012).

16. 16.

Grün, R. & Stringer, C. *J. Hum. Evol.* **39**, 601–612 (2000).

17. 17.

Fernández-Jalvo, Y., Carlos Díez, J., Cáceres, I. & Rosell, J. *J. Hum. Evol.* **37**, 591–622 (1999).

18. 18.

White, T. D. *Am. J. Phys. Anthropol.* **69**, 503–509 (1986).

Jobs from Nature Careers

- - - [All jobs](#)
 - - [Postdoc \(f/m/d\) – Molecular mechanisms of translation in yeast –](#)
[Max Planck Institute for Biophysical Chemistry \(MPIBPC\)](#)
[Göttingen, Germany](#)
[JOB POST](#)

- **Laboratory Research Scientist - Cancer Epigenetics Laboratory**

Francis Crick Institute

London, United Kingdom

JOB POST

- **PhD student (m/f/div) in MS-based proteomics of small proteins**

Max Planck Institute of Biophysics (MPIBP)

Frankfurt am Main, Germany

JOB POST

- **Senior/Laboratory Research Scientist**

Francis Crick Institute

London, United Kingdom

JOB POST

This article was downloaded by **calibre** from <https://www.nature.com/articles/d41586-021-00805-6>

NEWS AND VIEWS

05 May 2021

Black hole jets bent by magnetic fields

The large-scale impact of magnetic fields on galaxy clusters has been unclear. Images from the MeerKAT radio telescope suggest that such fields can bend jets of particles ejected from massive black holes in galaxy clusters.

- [Joydeep Bagchi](#) 0

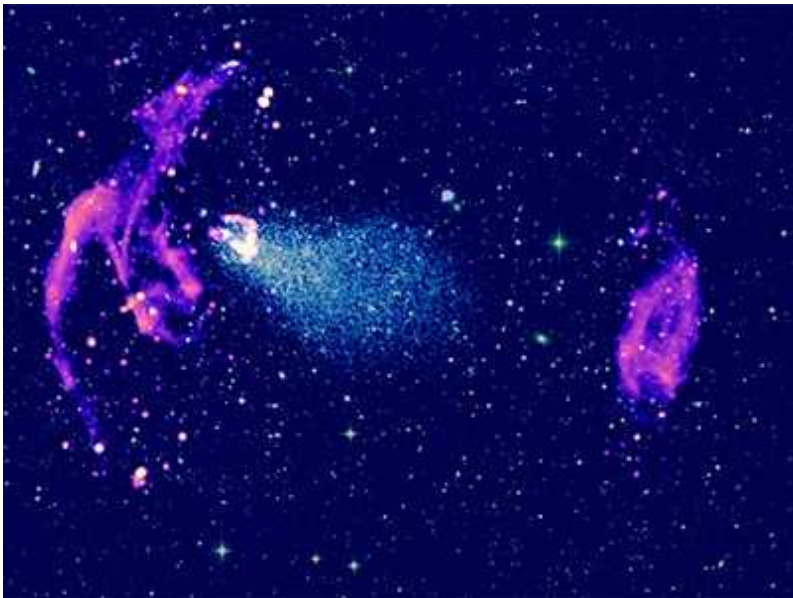
1. [Joydeep Bagchi](#)

1. Joydeep Bagchi is in the Department of Physics and Electronics, CHRIST (Deemed to be University), Bengaluru 560029, India.

[View author publications](#)

You can also search for this author in [PubMed](#) [Google Scholar](#)

Supermassive black holes (SMBHs) are millions to billions of times heavier than the Sun and lurk in the centres of almost all massive galaxies. In our cosmic neighbourhood, most of these galactic SMBHs are inactive. However, some are extremely active, releasing enormous amounts of energy across the electromagnetic spectrum as matter falls into them under gravity^{1–3}. Some spectacular manifestations of active SMBHs are radio galaxies — galaxies that eject two powerful, highly collimated jets of matter that emit radio waves. These radio jets are thought to be launched, focused and shaped by magnetic fields^{4–6}, but direct evidence of this process is limited (see go.nature.com/3xvingm). Now, in [a paper in *Nature*](#), Chibueze *et al.*⁷ report the observation of an interaction between such radio jets and magnetic fields in a galaxy cluster.



[Read the paper: Jets from MRC 0600-399 bent by magnetic fields in the cluster Abell 3376](#)

In a radio galaxy, much of the observed radiation is produced by electrons that are ejected in the vicinity of the galaxy's SMBH at speeds close to that of light. Magnetic fields in the surrounding gas cause these particles to follow circular paths and, in doing so, to emit radio waves. Such fields also hold the particles together and focus them into two narrow jets. If left undisturbed (for example, when located outside galaxy clusters), these radio jets typically extend up to hundreds of thousands of parsecs before dissipating (1 parsec is about 3 light years). In some rare cases, they can even stretch across millions of parsecs⁸ — roughly 100 times the size of the Milky Way. Consequently, these jets are extremely sensitive probes of the environment near their host galaxies.

Chibueze and colleagues obtained high-resolution images of the radio galaxy MRC 0600-399 (and a nearby radio galaxy) in the galaxy cluster Abell 3376 using the MeerKAT radio telescope in South Africa. MeerKAT consists of 64 antennas working collectively, and is one of the most sensitive radio telescopes in the world. The images show that the radio jets of MRC 0600-399 bend sharply by almost 90° (Fig. 1), as seen previously⁹. They also reveal diffuse regions of radio emission on both sides of the jet-deflection points, referred to as double-scythe structures. The authors used state-of-the-art computer simulations to demonstrate that the bent jets and

double-scythe structures can be explained if the jets travel at supersonic speed and strike a curved layer of strong, ordered magnetic fields that they cannot penetrate.

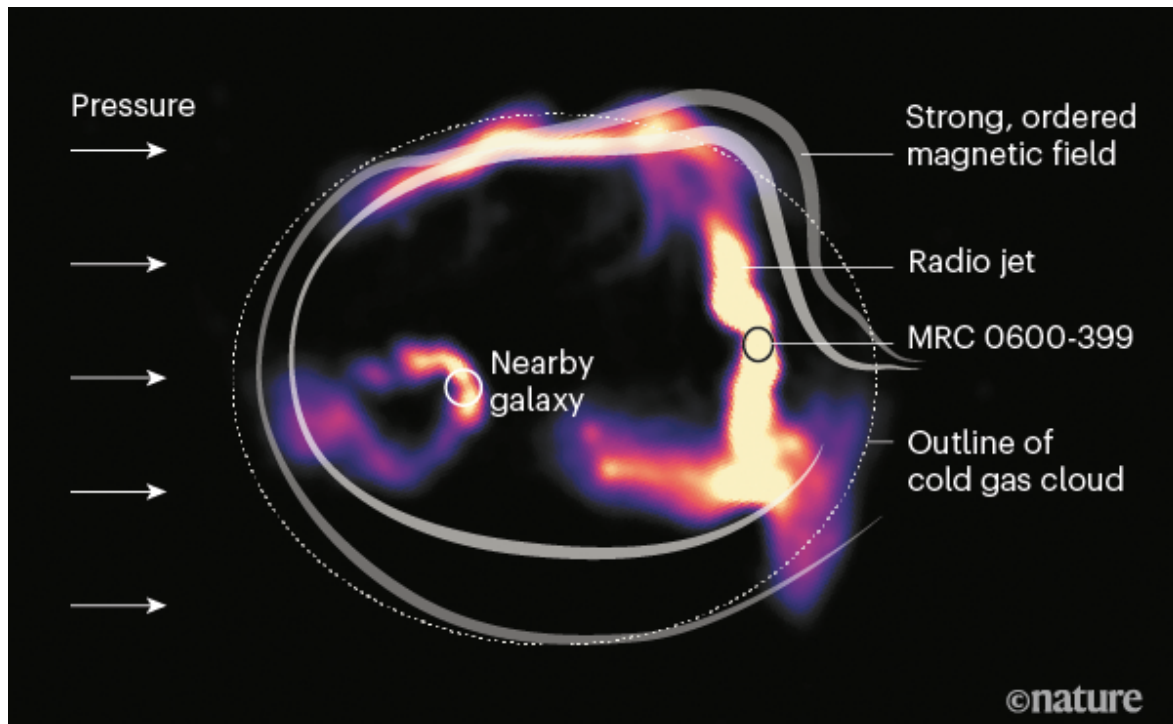
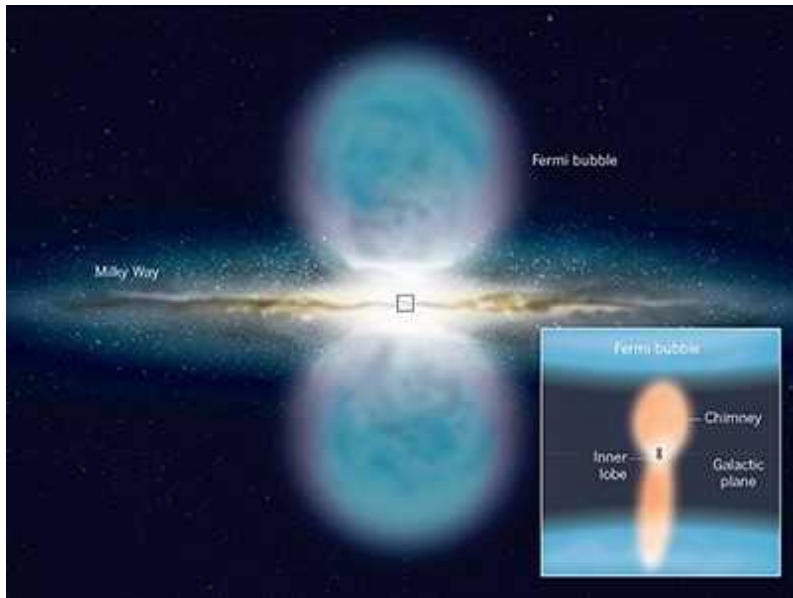


Figure 1 | Interaction between radio jets and magnetic fields. Chibueze *et al.*¹ observed the galaxy MRC 0600-399 (and the nearby galaxy) in the galaxy cluster Abell 3376 using the MeerKAT radio telescope. These two galaxies produce radio jets — powerful jets of matter that emit radio waves. The MeerKAT images show that the jets of MRC 0600-399 bend by almost 90° and reveal diffuse regions of radio emission (shown in purple) on the left and right sides of the jet-deflection points, referred to as double-scythe structures. MRC 0600-399 and the nearby galaxy are contained in a cloud of cold gas. The authors propose that this cloud is moving at high speed, and that the pressure of hot gas in the cluster causes strong, ordered magnetic fields to drape around the cloud. They suggest that the bent radio jets and double-scythe structures result from the jets interacting with this strong magnetic layer. (Concept by Mami Machida, National Astronomical Observatory of Japan.)

The origin of this strong magnetic layer is connected to ongoing cluster-building processes. Radio and X-ray observations of the cluster Abell 3376

have revealed a pair of giant arcs that trace radio emission from charged particles energized in powerful shock waves at the cluster's outskirts⁹ (see Fig. 1a of the paper⁷). These shock waves are caused by matter (comprising galaxies and cold gas) falling into the cluster under gravity and releasing energy through violent collisions and mergers.

X-ray images of Abell 3376 show an odd, comet-like structure consisting of a cold gas cloud, which encompasses both MRC 0600-399 and its nearby radio galaxy, and a long gas tail⁹ (see Fig. 1a of the paper⁷). Chibueze *et al.* propose that the gas cloud was ejected from the centre of Abell 3376 at supersonic speed, and that the pressure of the hot gas in the cluster on this fast-moving cloud produces the gas tail. They also suggest that this pressure causes the previously mentioned strong magnetic layer to drape around the boundary of the gas cloud, known as the cold front¹⁰ (Fig. 1). Without this protective magnetic layer, the cloud would evaporate rapidly, and the cold front would not form^{11,12}.



X-ray chimneys in the Galactic Centre

If the authors' interpretation is correct, it is a remarkable finding, because it implies that relatively strong, ordered magnetic fields (of a few tens of microgauss in strength) exist in the highly disrupted environments of galaxy clusters such as Abell 3376. For comparison, relatively weak magnetic fields

(of a few microgauss) have been detected¹³ in the gas at the centres of clusters less disrupted than Abell 3376. So far, it has proved extremely challenging to detect and measure magnetic fields in clusters and in the space between galaxies, and the origin of cosmic magnetic fields is still mysterious. Consequently, any observational evidence for such fields in cluster environments is valuable.

However, there is another plausible explanation for the bent jets, referred to as the slingshot model. In this scenario, MRC 0600-399 and the nearby radio galaxy are falling back towards the centre of Abell 3376 after being ejected from the centre at supersonic speed. The radio jets of MRC 0600-399 are bent simply by the pressure of gaseous wind acting in the opposite direction to the galaxy's motion. Although this alternative model can explain the bent jets, it cannot account for the peculiar double-scythe structures, which suggest that the jets are interacting with a layer of strong, ordered magnetic fields. One limitation of the current work is that the magnetic-field strength in the jet-interaction region was not measured directly but was obtained from numerical simulations.

The most exciting aspect of Chibueze and colleagues' finding is that the observations of radio jets from SMBHs in galactic centres might help to explain poorly understood processes involving gas dynamics in galaxy-cluster formation. Sensitive measurements of the polarization of radio waves could confirm the strength and ordering of the magnetic fields in the magnetic boundary layer. Moreover, the discovery of other examples of strongly distorted radio jets might enable scientists to, for example, measure the total energy injected into jets by SMBHs, understand the role of magnetic fields in jet stabilization and determine the magnetic-field strength of the gas inside clusters. In the upcoming years, the most sensitive radio telescopes ever built will reveal many spectacular processes in the Universe that cannot be seen using optical instruments.

Nature **593**, 40-41 (2021)

doi: <https://doi.org/10.1038/d41586-021-01171-z>

References

1. 1.
Lynden-Bell, D. *Nature* **223**, 690–694 (1969).
2. 2.
Sołtan, A. *Mon. Not. R. Astron. Soc.* **200**, 115–122 (1982).
3. 3.
Begelman, M. C., Blandford, R. D. & Rees, M. J. *Rev. Mod. Phys.* **56**, 255–351 (1984).
4. 4.
Blandford, R. D. & Znajek, R. L. *Mon. Not. R. Astron. Soc.* **179**, 433–456 (1977).
5. 5.
Gabuzda, D. *Galaxies* **7**, 5 (2018).
6. 6.
Meier, D. L., Koide, S. & Uchida, Y. *Science* **291**, 84–92 (2001).
7. 7.
Chibueze, J. O. *et al.* *Nature* **593**, 47–50 (2021).
8. 8.
Dabhade, P. *et al.* *Astron. Astrophys.* **635**, A5 (2020).
9. 9.
Bagchi, J., Durret, F., Lima Neto, G. B. & Paul, S. *Science* **314**, 791–794 (2006).
10. 10.

Markevitch, M. & Vikhlinin, A. *Phys. Rep.* **443**, 1–53 (2007).

11. 11.

Dursi, L. J. & Pfrommer, C. *Astrophys. J.* **677**, 993–1018 (2008).

12. 12.

Lyutikov, M. *Mon. Not. R. Astron. Soc.* **373**, 73–78 (2006).

13. 13.

Carilli, C. L. & Taylor, G. B. *Annu. Rev. Astron. Astrophys.* **40**, 319–348 (2002).

Jobs from Nature Careers

- - - [All jobs](#)
 - - [Postdoc \(f/m/d\) – Molecular mechanisms of translation in yeast –](#)
[Max Planck Institute for Biophysical Chemistry \(MPIBPC\)](#)
[Göttingen, Germany](#)
[JOB POST](#)
 - [Laboratory Research Scientist - Cancer Epigenetics Laboratory](#)
[Francis Crick Institute](#)
[London, United Kingdom](#)

JOB POST

- **PhD student (m/f/div) in MS-based proteomics of small proteins**

Max Planck Institute of Biophysics (MPIBP)

Frankfurt am Main, Germany

JOB POST

- **Senior/Laboratory Research Scientist**

Francis Crick Institute

London, United Kingdom

JOB POST

This article was downloaded by **calibre** from <https://www.nature.com/articles/d41586-021-01171-z>

| [Section menu](#) | [Main menu](#) |

NEWS AND VIEWS

21 April 2021

African forest maps reveal areas vulnerable to the effects of climate change

An analysis of six million trees reveals spatial patterns in the vulnerability of Central African rainforests to climate change and human activities. The maps generated could be used to guide targeted actions across national boundaries.

- [Marion Pfeifer](#) ⁰ &
- [Deo D. Shirima](#) ¹

1. [Marion Pfeifer](#)

1. Marion Pfeifer is at the School of Natural and Environmental Sciences, Newcastle University, Newcastle NE1 7RU, UK.

[View author publications](#)

You can also search for this author in [PubMed](#) [Google Scholar](#)

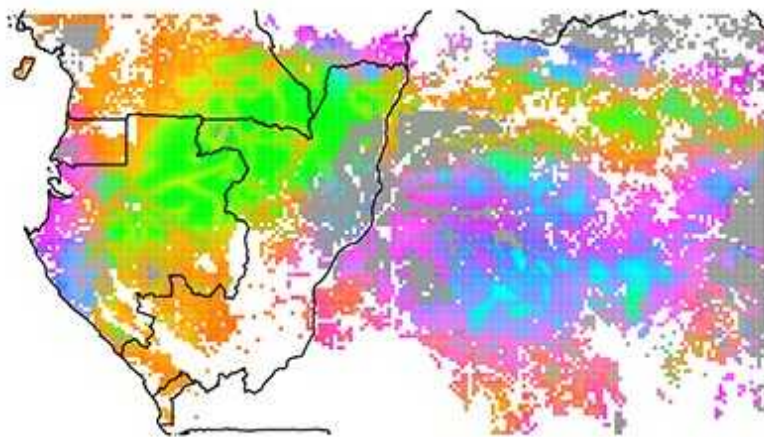
2. [Deo D. Shirima](#)

1. Deo D. Shirima is in the Department of Ecosystem and Conservation and at the National Carbon Monitoring Centre, Sokoine University of Agriculture, Morogoro, PO Box 3010, Tanzania.

[View author publications](#)

You can also search for this author in [PubMed](#) [Google Scholar](#)

Preserving the biodiversity of rainforests, and limiting the effects of climate change on them, are global challenges that are recognized in international policy agreements and commitments¹. The Central African rainforests are the second largest area of continuous rainforest in the world, after the Amazon rainforest. They store more carbon per hectare than does the Amazon and, on average, have a higher density of large trees² than does any other continent — a feature attributed to the effects of big herbivores, particularly elephants, on the competition between trees for light, water and space³. Human activities, notably logging and over-hunting, facilitated by an expanding road network⁴, pose a serious threat to Central African rainforests and their value for society⁵.



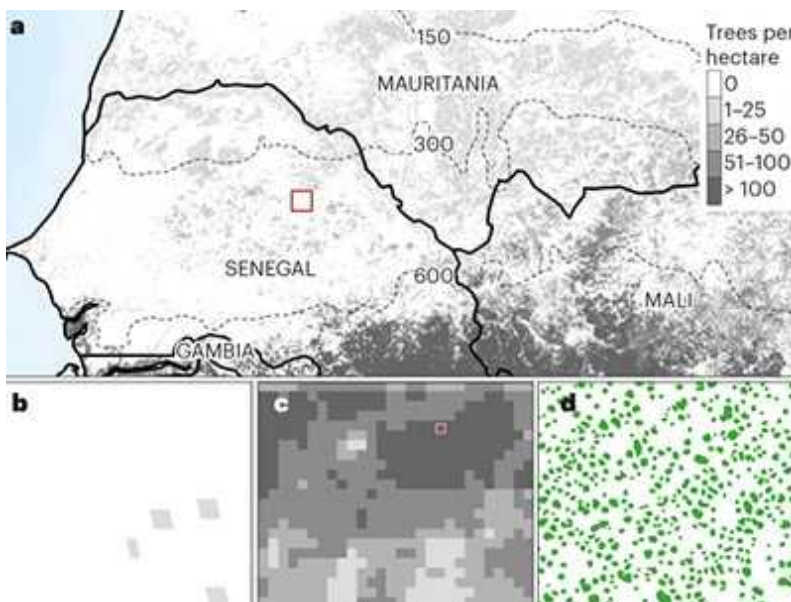
[Read the paper: Unveiling African rainforest composition and vulnerability to global change](#)

How important is climate change, when acting on top of these existing human-generated pressures, for the future of these rainforests? [Writing in Nature](#), Réjou-Méchain *et al.*⁶ provide an answer, and show that expected changes in climate in the region pose serious risks to the rainforests. Some forests in locations that have so far been relatively undisturbed by humans are more vulnerable to climate change than are those in areas already affected. For those areas already affected, the lower tree diversity as a

consequence of human intervention reduces the capacity of forests to respond to climate change.

The authors had access to an impressive commercial forest-inventory data set from 105 logging concessions (designated areas in which commercial operators are allowed to harvest timber), across five Central African countries. Analysing the abundance distribution of 6.1 million trees across 185,665 plots, the authors generate maps of floristically unique forest types — forests characterized by distinct sets of tree species. The spatial extent of these forest types is predominantly shaped by climate gradients, with further effects arising from human-induced pressures and variation in soil type.

Previous research into links between species distribution and environmental variation used approaches such as ecological niche models, which are mechanistic or correlative models that relate field observations of species with environmental variables to predict habitat suitability. But the resulting predictions of how various species will be affected by climate change have been highly uncertain. This is mainly because of sampling bias, challenges such as spatial autocorrelation (locations closer together in space tend to be more similar to each other than do locations farther apart)⁷, and high variation in the responses of individual species to environmental drivers of distribution, including human-induced factors.



[Satellites could soon map every tree on Earth](#)

Réjou-Méchain *et al.* instead applied a modelling approach called supervised component generalized linear regression, which can identify the main predictive factors from an array of possibilities. This enabled them to detect distribution patterns at the scale of species assemblages (the set of species in a community), rather than focusing on individual species, and to model species and assemblage distribution in response to predictive variables, such as those of climate and human pressures, that potentially show linear dependencies on each other (collinearity). Collinearity is a challenge in niche models, and commonly occurs between climate variables, producing results that are unreliable and difficult to interpret.

By combining their approach with a method called cluster analysis, Réjou-Méchain and colleagues show that the Central African rainforests are not a single bloc of forests, but instead encompass at least ten distinct forest types. This includes climate-driven types of forest such as the Atlantic coastal evergreen forest in Gabon, which harbours tree species that prefer cool, dark areas for the dry season. Another grouping, semi-deciduous forest, is found along the northern margin of the Central African region studied, and is characterized by species that can tolerate higher rates of water loss to the atmosphere (evapotranspiration).

Such spatial variability in the species composition of Central African rainforests has many implications. For example, it will affect forest vulnerability to climate change, how warming might interact with human pressures to change biodiversity, and how it might affect the potential of these forests to mitigate the rise in atmospheric carbon. Global warming is projected to result in a drier, hotter environment in Central Africa, and previous research has suggested potentially dangerous implications for the fate of the rainforests there⁸. They might respond to limited water availability by opening canopies and becoming more prone to fires and less carbon dense. Using climate-model projections for the year 2085, Réjou-Méchain and colleagues conclude that the current climate niches associated with the ten forest types they have identified might disappear, or move to locations that would be difficult for the forests to reach through dispersal of tree seeds (by means such as wind and animals), and would hence become inaccessible.



Prioritizing where to restore Earth's ecosystems

What do these findings mean for the future, and how can we manage the forests to minimize the threat from climate change? To provide an answer, Réjou-Méchain *et al.* looked at three components that characterize the vulnerability of forest communities to warming: their sensitivity, exposure and adaptive capacity. The authors conclude that some areas are more sensitive than others, which means that the dominant tree species in some forest types will be less able to tolerate environmental change than will those in other areas — for example, species in the northern and southwestern edge of the rainforest. Some areas, particularly those in the east, are expected to be more exposed to climate change than others. And some, especially areas under pressure from human activities, have lower local biodiversity, and might thus have less capacity to adapt compared with areas of greater biodiversity.

Réjou-Méchain *et al.* report that the areas most vulnerable to climate change and predicted to be highly vulnerable to future human-induced pressures include forests in coastal Gabon, the Democratic Republic of the Congo (Fig. 1) and the northern margin of the domain studied. This finding suggests priority regions for targeted actions to protect forests from environmental changes. One such region under human pressure is in Cameroon and contains a forest group called degraded semi-deciduous forest. Protecting this type of forest offers a fast way of generating a carbon

sink that will operate over a long time frame⁹. This is because it features long-lived ‘pioneer’ taxa, which colonize areas after a disturbance — whether natural or human induced. Such species frequently have a high requirement for light, and in this region have the potential to reach great heights in the absence of further disturbance.



Figure 1 | Kahuzi-Biéga National Park, Democratic Republic of the Congo. The road marks the boundary of this forest, which is one of the few remaining forest habitats for the eastern lowland gorilla (*Gorilla beringei graueri*). Rainforests are under threat from human-induced pressures, such as the deforestation visible outside this park. Réjou-Méchain *et al.*⁶ present maps of Central African rainforests that could aid conservation work. Credit: Adam Amir

As for elsewhere in sub-Saharan Africa, climate-change predictions for 2085 are uncertain for Central Africa. Réjou-Méchain and colleagues’ projections for the effects of human pressures for that year are probably underestimates,

especially considering that road expansions are likely to continue to push the frontier of wilderness deeper into remote forest areas. Nevertheless, the research offers convincing evidence enabling land users and managers to take decisive actions. This could include efforts to protect the areas most vulnerable to climate change from human pressures, for example by setting up protection schemes, and actions that could include boosting forest connectivity in areas that have already experienced high levels of human pressure. To ensure the effectiveness of any interventions, it will be imperative to engage with local people in developing management solutions. Conservation and the sustainable management of rainforest carbon stocks have key roles in the reduction of carbon emissions.

Perhaps most crucially, rainforests in Central Africa and the ecosystem services they provide are intertwined with people's livelihoods and food security. Developing sustainable management plans that recognize the diversity of the ways in which people interact with and depend on these forests will be a huge challenge. It will require concerted cross-disciplinary and cross-sectoral efforts that move beyond national boundaries.

Nature **593**, 42-43 (2021)

doi: <https://doi.org/10.1038/d41586-021-00978-0>

References

1. 1.

Hansen, A. J. *et al. Nature Ecol. Evol.* **4**, 1377–1384 (2020).

2. 2.

Lewis, S. L. *et al. Phil. Trans. R. Soc. B* **368**, 20120295 (2013).

3. 3.

Berzaghi, F. *et al. Nature Geosci.* **12**, 725–729 (2019).

4. 4.

Laurance, W. F., Goosem, M. & Laurance, S. G. W. *Trends Ecol. Evol.* **24**, 659–669 (2009).

5. 5.

França, F. M. *et al. Phil. Trans. R. Soc. B* **375**, 20190116 (2020).

6. 6.

Réjou-Méchain, M. *et al. Nature* **593**, 90–94 (2021).

7. 7.

Boakes, E. H. *et al. PLoS Biol.* **8**, e1000385 (2010).

8. 8.

James, R., Washington, R. & Rowell, D. P. *Phil. Trans. R. Soc. B* **368**, 20120298 (2013).

9. 9.

Giresse, P., Maley, J. & Chepstow-Lusty, A. *Glob. Planet. Change* **192**, 103257 (2020).

Jobs from Nature Careers

- - - [All jobs](#)
 - - [Postdoc \(f/m/d\) – Molecular mechanisms of translation in yeast –](#)
[Max Planck Institute for Biophysical Chemistry \(MPIBPC\)](#)
[Göttingen, Germany](#)

JOB POST

- Laboratory Research Scientist - Cancer Epigenetics Laboratory

Francis Crick Institute

London, United Kingdom

JOB POST

- PhD student (m/f/div) in MS-based proteomics of small proteins

Max Planck Institute of Biophysics (MPIBP)

Frankfurt am Main, Germany

JOB POST

- Senior/Laboratory Research Scientist

Francis Crick Institute

London, United Kingdom

JOB POST

This article was downloaded by **calibre** from <https://www.nature.com/articles/d41586-021-00978-0>

NEWS AND VIEWS

05 May 2021

Prediction for magnetic moment of the muon informs a test of the standard model of particle physics

A new first-principles computation of the effect that creates most uncertainty in calculations of the magnetic moment of the muon particle has been reported. The results might resolve a long-standing puzzle, but pose another conundrum.

- [Harvey B. Meyer](#) 

1. [Harvey B. Meyer](#)

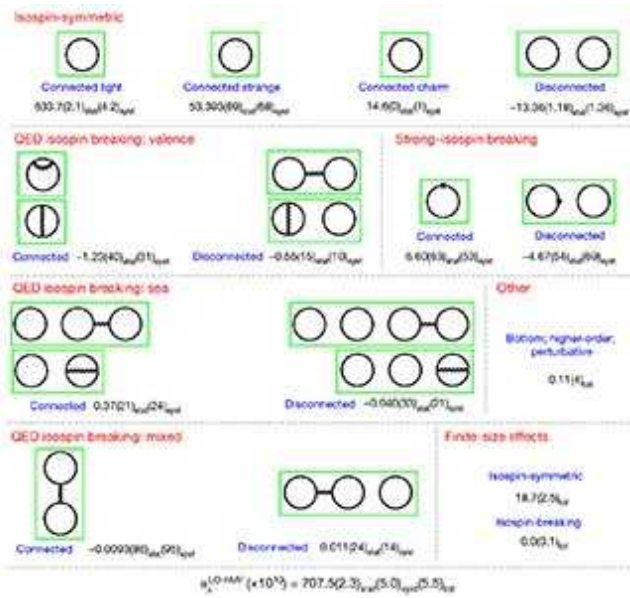
1. Harvey B. Meyer is at the Institute for Nuclear Physics, Johannes Gutenberg University Mainz, D-55099 Mainz, Germany.

[View author publications](#)

You can also search for this author in [PubMed](#) [Google Scholar](#)

The established theory of particle physics is called the standard model, and has passed a vast number of experimental tests with flying colours. But one such test — the determination of the magnetic moment of an elementary particle known as the muon — has resulted in a long-standing discrepancy between theory and experiment. The uncertainty in the theoretical determination is dominated entirely by the effects of the strong interaction, the fundamental force that binds the constituents of atomic nuclei. [Writing in Nature](#), Borsanyi *et al.*¹ report a calculation of the value of the largest of these effects to a precision commensurate with that of the experimental measurement of the magnetic moment. Using this value, they show that the

magnetic moment predicted by the standard model is compatible with experimental measurements. At the same time, they find a moderate inconsistency between their result and previous determinations of the strong-interaction effect. The previous determinations are based on a different methodology from that used by Borsanyi and colleagues, and are widely viewed as being on firm ground.

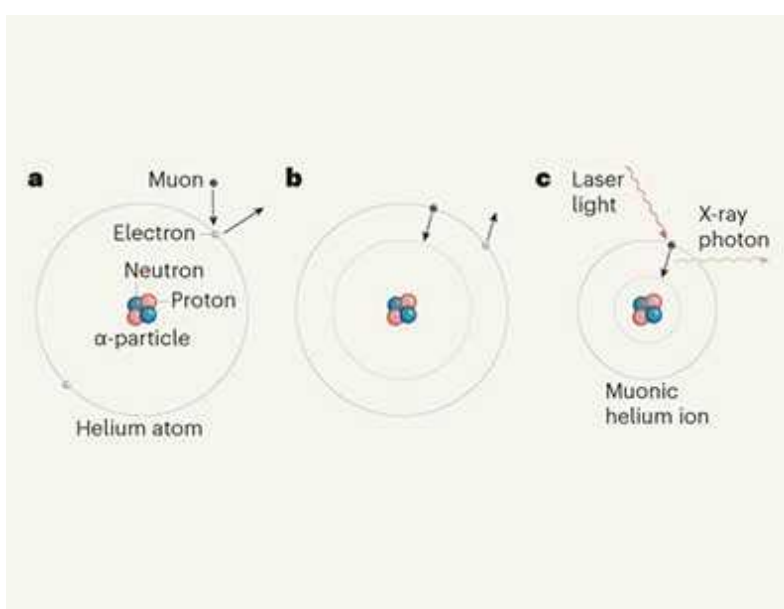


[Read the paper: Leading hadronic contribution to the muon magnetic moment from lattice QCD](#)

Despite the many successes of the standard model of particle physics, it has patent shortcomings: it neither describes gravity nor contains a candidate particle that could account for the Universe's vast amount of dark matter, which can be observed only indirectly. Physicists are exploring several avenues of research to discover what particles and forces might lie beyond the standard model. These include direct searches for new particles by the Large Hadron Collider at CERN, Europe's particle-physics laboratory near Geneva, Switzerland, and experiments dedicated to detecting dark matter. Another well-established strategy is to precisely measure quantities that can be calculated, using the standard model, to a degree of precision similar to that of the measurements; any differences in the measured and computed values would indicate the existence of physics not accounted for in the standard model.

The magnetic moments of elementary particles are prime examples of such quantities. They are proportional to the spin (intrinsic angular momentum) of the particle, and to the particle's gyromagnetic factor (g , a proportionality constant that is characteristic of each particle type). In 1928, Paul Dirac showed from his quantum relativistic theory of the electron² that g is 2 for that particle, an excellent approximation at that time. However, the actual value of g differs from 2 by a tiny amount called the anomalous magnetic moment, which is quantified as $(g - 2)/2$. This difference arises because the magnetic moment is affected by 'virtual' versions of elementary particles, which continually appear and disappear from the vacuum. In 1947, the theoretical physicist Julian Schwinger calculated³ the main contribution to the anomalous magnetic moment of the electron to be $\alpha/(2\pi)$, where α is a fundamental constant known as the fine-structure constant.

The electron has a cousin called the muon, which is 207 times heavier. The muon's greater mass means that measurements of its $g - 2$ value are much more sensitive to the fleeting presence of any heavy virtual particles not described by the standard model than are measurements of $g - 2$ for the electron. After decades of improvements, the E821 experiment at Brookhaven National Laboratory in Upton, New York, provided measurements⁴ of $g - 2$ for the muon reaching an astounding precision of 0.54 parts per million (p.p.m.).



Helium nucleus measured with record precision

An equally impressive, decades-long effort in theoretical physics aims to match the exquisite precision of the experiments in computations of the value of the muon $g - 2$ predicted on the basis of the standard model. A white paper⁵ published in 2020 summarized the status of these efforts: a precision of 0.37 p.p.m. had been achieved, but the value of $g - 2$ obtained was slightly smaller than the experimentally derived value, corresponding to a difference of 3.7 standard deviations.

The uncertainty of the theoretical predictions for the muon $g - 2$ is dominated by the effects of hadron particles. Hadrons are composite particles bound by the strong interaction, examples of which are the proton and neutron. In the white paper⁵, the leading hadronic contribution was obtained from a mathematical formula known as a dispersion relation, using as input the rates of hadron formation measured in experiments in which electrons collide with positrons, the antiparticles of electrons.

A different approach to calculating the leading hadronic contribution, first proposed⁶ in 2003, is to use lattice quantum chromodynamics (QCD) — a first-principles method to handle the strong interaction that relies on high-performance computing. The pace of improvement of lattice QCD calculations has accelerated tremendously in the past few years as a result of dedicated efforts and several methodological advances (reviewed in ref. 7). Borsanyi and colleagues' study is the latest stride towards reducing the uncertainty of lattice QCD-based calculations in this field to a level that competes with the uncertainty of determinations based on dispersion relations.

Intriguingly, when Borsanyi *et al.* use their calculations to predict the value of $g - 2$, the result obtained is compatible with the value found by the E821 experiment (Fig. 1). The authors' result also differs by a moderate 2.2 standard deviations from the value of $g - 2$ reported in the white paper⁵, which was determined using dispersion relations — a finding that certainly deserves further scrutiny.

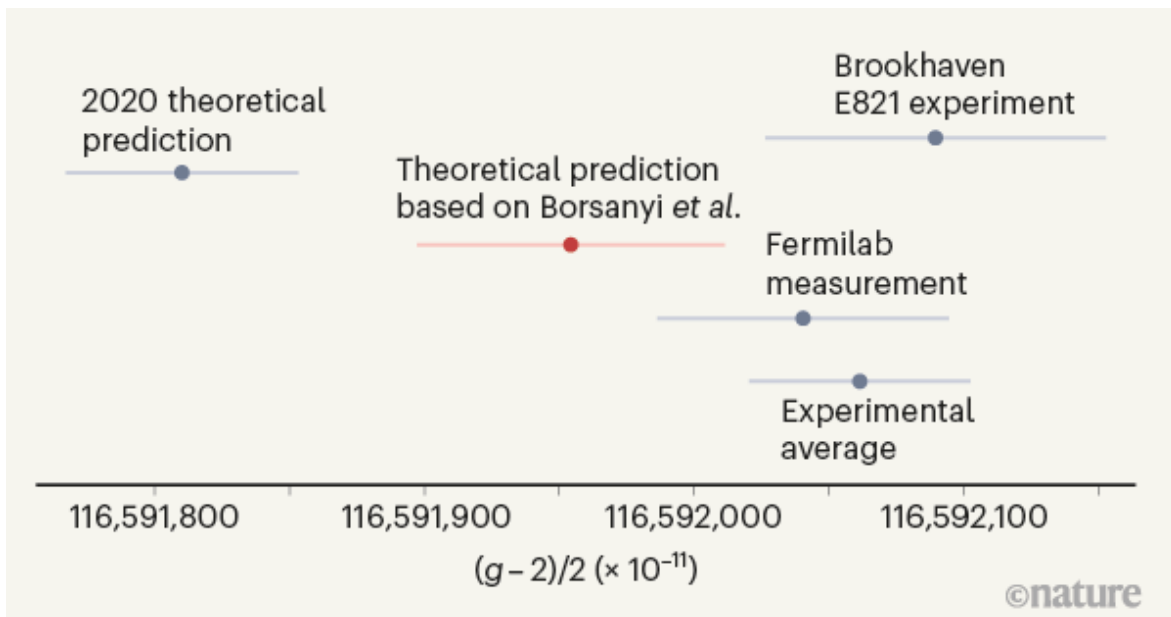
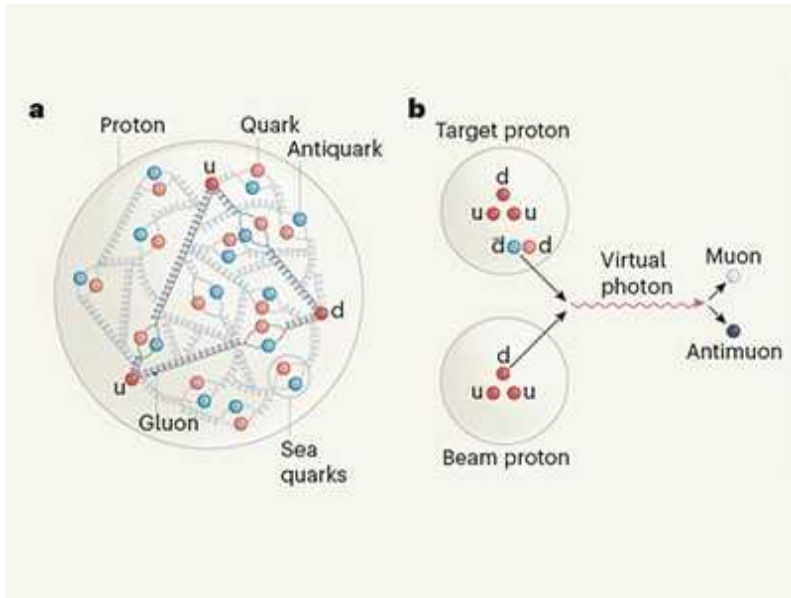


Figure 1 | Determinations of the magnetic moment of the muon particle. The magnetic moment of the muon is close, but not equal, to 2; the difference is quantified as a number known as $(g - 2)/2$. A measurement⁴ of $(g - 2)/2$ carried out in the E821 experiment at Brookhaven National Laboratory in Upton, New York, was published in 2006, and a consensus theoretical prediction was published⁵ in 2020. Borsanyi *et al.*¹ now report calculations that bring the theoretical prediction much closer to the E821 measurement. A measurement⁸ of $(g - 2)/2$ at the Fermi National Accelerator Laboratory (Fermilab) near Chicago, Illinois, was published earlier this year, and is consistent with the E821 value. The average of all of the experimental measurements differs by 4.2 standard deviations from the 2020 consensus prediction. A difference of 5.0 standard deviations between theoretical and experimental values would establish the existence of physics not accounted for by the standard model of particle physics.

Borsanyi and colleagues' comprehensive treatment of the many effects that become relevant to $g - 2$ at the quoted precision is an impressive achievement. As is standard in the lattice-QCD framework, the quantity of interest is computed by dividing space-time into a lattice of points, calculating the quantity for several values of the lattice spacing and then extrapolating to determine the value when the spacing is zero (this value is known as the continuum limit). The systematics of obtaining the continuum limit turn out to be the dominant source of uncertainty in the authors' results.

Ongoing calculations by other groups using different variants of lattice QCD will provide an important consistency check of the current findings.



Antimatter in the proton is more down than up

Since 2018, the Muon $g - 2$ Collaboration has been running an experiment at the Fermi National Accelerator Laboratory (Fermilab) near Chicago, Illinois, to check and improve on the findings of the E821 experiment. The first result was announced⁸ on 7 April 2021: the reported value of $g - 2$ agrees well with that obtained by E821. Moreover, when all the experimental measurements are combined, the discrepancy with the theoretical prediction reported in the white paper⁵ rises to the level of 4.2 standard deviations. The announcement was a truly thrilling moment for particle physicists, because a discrepancy of 5.0 standard deviations between experiment and theory is conventionally regarded as conclusive evidence of the discovery of physics not accounted for by the theory.

However, the value of the muon $g - 2$ inferred from Borsanyi and colleagues' calculation agrees with the new experimental average. The top priority for the future is therefore to clarify the discrepancy between Borsanyi and co-workers' result and the dispersion-theory result reported in the white paper. In the next few years, the precision of the Muon $g - 2$ experiment is expected⁹ to increase to about four times that of the E821 experiment, and similarly precise measurements will be made¹⁰ at the Japan

Proton Accelerator Research Complex (J-PARC) near Tokai, using a completely different technique for determining $g - 2$. More thrills are bound to come.

Nature **593**, 44-45 (2021)

doi: <https://doi.org/10.1038/d41586-021-01172-y>

References

1. 1.

Borsanyi, Sz. *et al.* Nature **593**, 51–55 (2021).

2. 2.

Dirac, P. A. M. *Proc. R. Soc. Lond. A* **117**, 610–624 (1928).

3. 3.

Schwinger, J. *Phys. Rev.* **73**, 416–417 (1948).

4. 4.

Bennett, G. W. *et al.* *Phys. Rev. D* **73**, 072003 (2006).

5. 5.

Aoyama, T. *et al.* *Phys. Rep.* **887**, 1–166 (2020).

6. 6.

Blum, T. *Phys. Rev. Lett.* **91**, 052001 (2003).

7. 7.

Meyer, H. B. & Wittig, H. *Prog. Part. Nucl. Phys.* **104**, 46–96 (2019).

8. 8.

Abi, B. *et al.* *Phys. Rev. Lett.* **126**, 141801 (2021).

9. 9.

Grange, J. *et al.* Preprint at <https://arxiv.org/abs/1501.06858> (2015).

10. 10.

Abe, M. *et al.* *Prog. Theor. Exp. Phys.* **2019**, 053C02 (2019).

Jobs from Nature Careers

- - - [All jobs](#)
 - - **[Postdoc \(f/m/d\) – Molecular mechanisms of translation in yeast –](#)**
[Max Planck Institute for Biophysical Chemistry \(MPIBPC\)](#)
[Göttingen, Germany](#)
[JOB POST](#)
 - **[Laboratory Research Scientist - Cancer Epigenetics Laboratory](#)**
[Francis Crick Institute](#)
[London, United Kingdom](#)
[JOB POST](#)
 - **[PhD student \(m/f/div\) in MS-based proteomics of small proteins](#)**

Max Planck Institute of Biophysics (MPIBP).

Frankfurt am Main, Germany

JOB POST

▪ **Senior/Laboratory Research Scientist**

Francis Crick Institute

London, United Kingdom

JOB POST

This article was downloaded by **calibre** from <https://www.nature.com/articles/d41586-021-01172-y>

| [Section menu](#) | [Main menu](#) |

- Article
- [Published: 05 May 2021](#)

Jets from MRC 0600-399 bent by magnetic fields in the cluster Abell 3376

- [James O. Chibueze](#) ORCID: [orcid.org/0000-0002-9875-7436^{1,2 na1}](https://orcid.org/0000-0002-9875-7436),
- [Haruka Sakemi](#) ^{3 na1},
- [Takumi Ohmura](#) ^{3,12 na1},
- [Mami Machida](#)⁴,
- [Hiroki Akamatsu](#)⁵,
- [Takuya Akahori](#)^{6,13},
- [Hiroyuki Nakanishi](#)⁷,
- [Viral Parekh](#)^{8,9},
- [Ruby van Rooyen](#)⁸ &
- [Tsutomu T. Takeuchi](#)^{10,11}

[Nature](#) volume 593, pages47–50(2021) [Cite this article](#)

- 808 Accesses
- 86 Altmetric
- [Metrics details](#)

Subjects

- [Astrophysical magnetic fields](#)
- [Galaxies and clusters](#)

Abstract

Galaxy clusters are known to harbour magnetic fields, the nature of which remains unresolved. Intra-cluster magnetic fields can be observed at the density contact discontinuity formed by cool and dense plasma running into hot ambient plasma^{1,2}, and the discontinuity exists³ near the second-brightest galaxy⁴, MRC 0600-399, in the merging galaxy cluster Abell 3376 (redshift 0.0461). Elongated X-ray emission in the east–west direction shows a comet-like structure that reaches the megaparsec scale⁵. Previous radio observations^{6,7} detected the bent jets from MRC 0600-399, moving in same direction as the sub-cluster, against ram pressure. Here we report radio^{8,9} observations of MRC 0600-399 that have 3.4 and 11 times higher resolution and sensitivity, respectively, than the previous results⁶. In contrast to typical jets^{10,11}, MRC 0600-399 shows a 90-degree bend at the contact discontinuity, and the collimated jets extend over 100 kiloparsecs from the point of the bend. We see diffuse, elongated emission that we name ‘double-scythe’ structures. The spectral index flattens downstream of the bend point, indicating cosmic-ray reacceleration. High-resolution numerical simulations reveal that the ordered magnetic field along the discontinuity has an important role in the change of jet direction. The morphology of the double-scythe jets is consistent with the simulations. Our results provide insights into the effect of magnetic fields on the evolution of the member galaxies and intra-cluster medium of galaxy clusters.

[Access through your institution](#)

[Change institution](#)

[Buy or subscribe](#)

Access options

Subscribe to Journal

Get full journal access for 1 year

\$199.00

only \$3.90 per issue

[Subscribe](#)

All prices are NET prices.

VAT will be added later in the checkout.

Tax calculation will be finalised during checkout.

Rent or Buy article

Get time limited or full article access on ReadCube.

from \$8.99

[Rent or Buy](#)

All prices are NET prices.

Additional access options:

- [Log in](#)
- [Access through your institution](#)
- [Learn about institutional subscriptions](#)

Fig. 1: Multi-wavelength view of A3376 and MRC 0600-399.

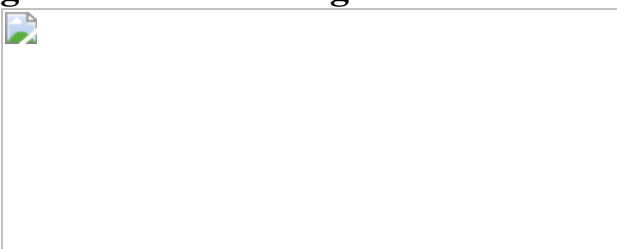


Fig. 2: Radio properties derived from MeerKAT observation.

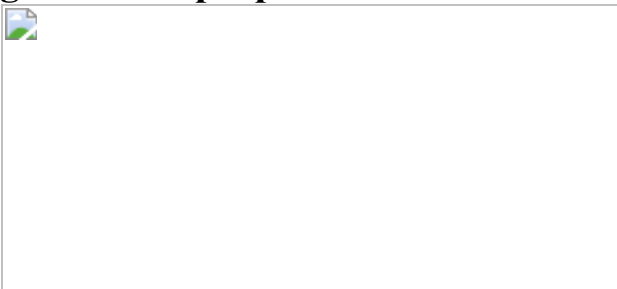


Fig. 3: Numerical simulations of the interaction between jets and intra-cluster magnetic fields.



Fig. 4: Schematic drawing of the proposed scenario.



Data availability

The raw MeerKAT data used in this work can be accessed at <https://archive.sarao.ac.za> (project ID: SCI-20190418-JC-01). The calibrated MeerKAT data and images that support the findings of this study are available from the corresponding authors upon reasonable request.

References

1. 1.

Markevitch, M. et al. Chandra observation of Abell 2142: survival of dense subcluster cores in a merger. *Astrophys. J.* **541**, 542–549 (2000).

[ADS](#) [Article](#) [Google Scholar](#)

2. 2.

Vikhlinin, A., Markevitch, M. & Murray, S. S. A moving cold front in the intergalactic medium of A3667. *Astrophys. J.* **551**, 160–171 (2001).

[ADS](#) [Article](#) [Google Scholar](#)

3. 3.

Urdampilleta, I. et al. X-ray study of the double radio relic Abell 3376 with Suzaku. *Astron. Astrophys.* **618**, A74 (2018).

[Article](#) [Google Scholar](#)

4. 4.

Durret, F. et al. The merging cluster of galaxies Abell 3376: an optical view. *Astron. Astrophys.* **560**, A78 (2013).

[Article](#) [Google Scholar](#)

5. 5.

Machado, R. E. G. & Lima Neto, G. B. Simulations of the merging galaxy cluster Abell 3376. *Mon. Not. R. Astron. Soc.* **430**, 3249–3260 (2013).

[ADS](#) [Article](#) [Google Scholar](#)

6. 6.

Bagchi, J., Durret, F., Neto, G. B. L. & Paul, S. Giant ringlike radio structures around galaxy cluster Abell 3376. *Science* **314**, 791–794

(2006).

[ADS](#) [CAS](#) [PubMed](#) [PubMed Central](#) [Article](#) [Google Scholar](#)

7. 7.

Kale, R. et al. Spectral and polarization study of the double relics in Abell 3376 using the Giant Metrewave Radio Telescope and the Very Large Array. *Mon. Not. R. Astron. Soc.* **426**, 1204–1211 (2012).

[ADS](#) [Article](#) [Google Scholar](#)

8. 8.

Jonas, J. & MeerKAT Team. The MeerKAT radio telescope. In *MeerKAT Science: On the Pathway to the SKA, I* (PoS, 2016).

9. 9.

Mauch, T. et al. The 1.28 GHz MeerKAT DEEP2 image. *Astrophys. J.* **888**, 61 (2020).

[ADS](#) [CAS](#) [Article](#) [Google Scholar](#)

10. 10.

Owen, F. N. & Rudnick, L. Radio sources with wide-angle tails in Abell clusters of galaxies. *Astrophys. J. Lett.* **205**, 1–4 (1976).

[ADS](#) [Article](#) [Google Scholar](#)

11. 11.

Jones, T. W. & Owen, F. N. Hot gas in elliptical galaxies and the formation of head-tail radio sources. *Astrophys. J.* **234**, 818–824 (1979).

[ADS](#) [CAS](#) [Article](#) [Google Scholar](#)

12. 12.

Markevitch, M. & Vikhlinin, A. Shocks and cold fronts in galaxy clusters. *Phys. Rep.* **443**, 1–53 (2007).

[ADS](#) [Article](#) [Google Scholar](#)

13. 13.

Gunn, J. E., Gott, I. & Richard, J. On the infall of matter into clusters of galaxies and some effects on their evolution. *Astrophys. J.* **176**, 1 (1972).

[ADS](#) [Article](#) [Google Scholar](#)

14. 14.

Donnert, J., Vazza, F., Brüggen, M. & ZuHone, J. magnetic field amplification in galaxy clusters and its simulation. *Space Sci. Rev.* **214**, 122 (2018).

[ADS](#) [Article](#) [Google Scholar](#)

15. 15.

ZuHone, J. A. & Roediger, E. Cold fronts: probes of plasma astrophysics in galaxy clusters. *J. Plasma Phys.* **82**, 535820301 (2016).

[Article](#) [Google Scholar](#)

16. 16.

Werner, N. et al. Deep Chandra observation and numerical studies of the nearest cluster cold front in the sky. *Mon. Not. R. Astron. Soc.* **455**, 846–858 (2016).

[ADS](#) [Article](#) [Google Scholar](#)

17. 17.

Walker, S. A., ZuHone, J., Fabian, A. & Sanders, J. The split in the ancient cold front in the Perseus cluster. *Nat. Astron.* **2**, 292–296 (2018).

[ADS](#) [Article](#) [Google Scholar](#)

18. 18.

Nolting, C., Jones, T. W., O'Neill, B. J. & Mendygral, P. J. Interactions between radio galaxies and cluster shocks. I. Jet axes aligned with shock normals. *Astrophys. J.* **876**, 154 (2019).

[ADS](#) [Article](#) [Google Scholar](#)

19. 19.

Lal, D. V. NGC 4869 in the Coma cluster: twist, wrap, overlap and bend. *Astron. J.* **160**, 161 (2020).

[ADS](#) [CAS](#) [Article](#) [Google Scholar](#)

20. 20.

Takizawa, M. Hydrodynamic simulations of a moving substructure in a cluster of galaxies: cold fronts and turbulence generation. *Astrophys. J.* **629**, 791–796 (2005).

[ADS](#) [CAS](#) [Article](#) [Google Scholar](#)

21. 21.

Asai, N., Fukuda, N. & Matsumoto, R. Three-dimensional magnetohydrodynamic simulations of cold fronts in magnetically turbulent ICM. *Astrophys. J.* **663**, 816–823 (2007).

[ADS](#) [CAS](#) [Article](#) [Google Scholar](#)

22. 22.

ZuHone, J. A., Markevitch, M. & Lee, D. Sloshing of the magnetized cool gas in the cores of galaxy clusters. *Astrophys. J.* **743**, 16 (2011).

[ADS](#) [Article](#) [Google Scholar](#)

23. 23.

Chen, H., Jones, C., Andrade-Santos, F., ZuHone, J. A. & Li, Z. Gas sloshing in Abell 2204: constraining the properties of the magnetized intracluster medium. *Astrophys. J.* **838**, 38 (2017).

[ADS](#) [Article](#) [Google Scholar](#)

24. 24.

Matsumoto, Y. et al. Magnetohydrodynamic simulation code CANS+: assessments and applications. *Publ. Astron. Soc. Jpn* **71**, 83 (2019).

[ADS](#) [Article](#) [Google Scholar](#)

25. 25.

Hallman, E. J. & Markevitch, M. Chandra observation of the merging cluster A168: a late stage in the evolution of a cold front. *Astrophys. J.* **610**, L81–L84 (2004).

[ADS](#) [CAS](#) [Article](#) [Google Scholar](#)

26. 26.

Sheardown, A. et al. A new class of X-ray tails of early-type galaxies and subclusters in galaxy clusters: slingshot tails versus ram pressure stripped tails. *Astrophys. J.* **874**, 112 (2019).

[ADS](#) [CAS](#) [Article](#) [Google Scholar](#)

27. 27.

Hickish, J. et al. A Decade of Developing Radio-Astronomy Instrumentation using CASPER Open-Source Technology. *J. Astron. Instrum.* **5**, 1641001–1641012 (2016).

[Article](#) [Google Scholar](#)

28. 28.

Offringa, A. R., van de Gronde, J. J. & Roerdink, J. B. T. M. A morphological algorithm for improving radio-frequency interference detection. *Astron. Astrophys.* **539**, A95 (2012).

[Article](#) [Google Scholar](#)

29. 29.

McMullin, J. P., Waters, B., Schiebel, D., Young, W. & Golap, K. CASA architecture and applications. *ASP Conf. Ser.* **376**, 127 (2007).

[ADS](#) [Article](#) [Google Scholar](#)

30. 30.

Offringa, A. R. et al. WSCLEAN: an implementation of a fast, generic wide-field imager for radio astronomy. *Mon. Not. R. Astron. Soc.* **444**, 606–619 (2014).

[ADS](#) [Article](#) [Google Scholar](#)

31. 31.

Kenyon, J. S., Smirnov, O. M., Grobler, T. L. & Perkins, S. J. CUBICAL – fast radio interferometric calibration suite exploiting complex optimization. *Mon. Not. R. Astron. Soc.* **478**, 2399–2415 (2018).

[ADS](#) [Article](#) [Google Scholar](#)

32. 32.

Eckert, D. et al. The gas distribution in the outer regions of galaxy clusters. *Astron. Astrophys.* **541**, A57 (2012).

[Article](#) [Google Scholar](#)

33. 33.

Wang, Q. H. S., Markevitch, M. & Giacintucci, S. The merging galaxy cluster A520—a broken-up cool core, a dark subcluster, and an X-ray channel. *Astrophys. J.* **833**, 99 (2016).

[ADS](#) [Article](#) [Google Scholar](#)

34. 34.

Koide, S., Sakai, J.-I., Nishikawa, K.-I. & Mutel, R. L. Numerical simulation of bent jets: propagation into an oblique magnetic field. *Astrophys. J.* **464**, 724 (1996).

[ADS](#) [Article](#) [Google Scholar](#)

35. 35.

Rybicki, G. B. and Lightman, A. P. *Radiative Processes in Astrophysics* (Wiley-VCH, 1985).

36. 36.

Bicknell, G. V., Mukherjee, D., Wagner, A. Y., Sutherland, R. S. & Nesvadba, N. P. H. Relativistic jet feedback – II. Relationship to gigahertz peak spectrum and compact steep spectrum radio galaxies. *Mon. Not. R. Astron. Soc.* **475**, 3493–3501 (2018).

[ADS](#) [CAS](#) [Article](#) [Google Scholar](#)

37. 37.

Komarov, S., Reynolds, C. & Churazov, E. Propagation of weak shocks in cool-core galaxy clusters in two-temperature

magnetohydrodynamics with anisotropic thermal conduction. *Mon. Not. R. Astron. Soc.* **497**, 1434–1442 (2020).

[ADS](#) [Article](#) [Google Scholar](#)

38. 38.

Cavagnolo, K. W., Donahue, M., Voit, G. M. & Sun, M. Intracluster medium entropy profiles for a Chandra archival sample of galaxy clusters. *Astrophys. J. Suppl. Ser.* **182**, 12–32 (2009).

[ADS](#) [CAS](#) [Article](#) [Google Scholar](#)

39. 39.

Tajima, T. & Shibata, K. *Plasma Astrophysics* (Basic Books, 1997).

[Download references](#)

Acknowledgements

J.O.C. acknowledges support from the Italian Ministry of Foreign Affairs and International Cooperation (MAECI grant number ZA18GR02) and the South African Department of Science and Technology’s National Research Foundation (DST-NRF grant number 113121) as part of the ISARP RADIOSKY2020 Joint Research Scheme. V.P. acknowledges financial assistance from the South African Radio Astronomy Observatory (SARAO) and the South African Research Chairs Initiative of the Department of Science and Technology and National Research Foundation. This study makes use of MeerKAT data (project ID: SCI-20190418-JC-01). The MeerKAT telescope is operated by the South African Radio Astronomy Observatory, which is a facility of the National Research Foundation, an agency of the Department of Science and Innovation (DSI). SRON is supported financially by NWO, the Netherlands Organization for Scientific Research. Numerical computations and analyses were partially carried out on Cray XC50 and analysis servers, respectively, at the Center for Computational Astrophysics, National Astronomical Observatory of Japan.

The computation was carried out using the computer resources at the Research Institute for Information Technology, Kyushu University. This work was supported by JSPS KAKENHI grant numbers 20J13339 (H.S.), 20J12591 (T.O.), 19K03916, 20H01941 (M.M.) and 17H01110 and 19H05076 (T.T.T.). T.T.T. was also supported in part by the Sumitomo Foundation Fiscal 2018 Grant for Basic Science Research Projects (180923) and Collaboration Funding of the Institute of Statistical Mathematics “New Development of the Studies on Galaxy Evolution with a Method of Data Science”. The development of SAOImageDS9 software (<https://sites.google.com/cfa.harvard.edu/saoimageds9/about?authuser=0>) was made possible by funding from the Chandra X-ray Science Center (CXC), the High Energy Astrophysics Science Archive Center (HEASARC) and the JWST Mission office at the Space Telescope Science Institute. This research used Astropy, a community-developed core Python package for Astronomy.

Author information

Author notes

1. These authors contributed equally: James O. Chibueze, Haruka Sakemi, Takumi Ohmura

Affiliations

1. Centre for Space Research, Potchefstroom campus, North-West University, Potchefstroom, South Africa
James O. Chibueze
2. Department of Physics and Astronomy, Faculty of Physical Sciences, University of Nigeria, Nsukka, Nigeria
James O. Chibueze
3. Graduate School of Science, Kyushu University, Fukuoka, Japan

Haruka Sakemi & Takumi Ohmura

4. Division of Science, National Astronomical Observatory of Japan,
Tokyo, Japan

Mami Machida

5. SRON Netherlands Institute for Space Research, Utrecht, The
Netherlands

Hiroki Akamatsu

6. Mizusawa VLBI Observatory, National Astronomical Observatory of
Japan, Tokyo, Japan

Takuya Akahori

7. Graduate School of Science and Engineering, Kagoshima University,
Kagoshima, Japan

Hiroyuki Nakanishi

8. South African Radio Astronomy Observatory, Cape Town, South
Africa

Viral Parekh & Ruby van Rooyen

9. Department of Physics and Electronics, Rhodes University, Makhanda,
South Africa

Viral Parekh

10. Division of Particle and Astrophysical Science, Nagoya University,
Nagoya, Japan

Tsutomu T. Takeuchi

11. The Research Center for Statistical Machine Learning, the Institute of
Statistical Mathematics, Tokyo, Japan

Tsutomu T. Takeuchi

12. Institute for Cosmic Ray Research, The University of Tokyo, Chiba, Japan

Takumi Ohmura

13. Operation Division, Square Kilometre Array Organization, Jodrel Bank Observatory, Macclesfield, UK

Takuya Akahori

Authors

1. James O. Chibueze

[View author publications](#)

You can also search for this author in [PubMed](#) [Google Scholar](#)

2. Haruka Sakemi

[View author publications](#)

You can also search for this author in [PubMed](#) [Google Scholar](#)

3. Takumi Ohmura

[View author publications](#)

You can also search for this author in [PubMed](#) [Google Scholar](#)

4. Mami Machida

[View author publications](#)

You can also search for this author in [PubMed](#) [Google Scholar](#)

5. Hiroki Akamatsu

[View author publications](#)

You can also search for this author in [PubMed](#) [Google Scholar](#)

6. Takuya Akahori

[View author publications](#)

You can also search for this author in [PubMed](#) [Google Scholar](#)

7. Hiroyuki Nakanishi

[View author publications](#)

You can also search for this author in [PubMed](#) [Google Scholar](#)

8. Viral Parekh

[View author publications](#)

You can also search for this author in [PubMed](#) [Google Scholar](#)

9. Ruby van Rooyen

[View author publications](#)

You can also search for this author in [PubMed](#) [Google Scholar](#)

10. Tsutomu T. Takeuchi

[View author publications](#)

You can also search for this author in [PubMed](#) [Google Scholar](#)

Contributions

J.O.C. conducted the observations and data reduction. V.P. participated in the MeerKAT data reduction, and H.S. analysed the results and processed their implementations. T.O. and M.M. constructed the theory and model and conducted the numerical simulations. H.A. performed X-ray data analysis and wrote the scientific discussion. T.A. contributed to the writing of the MeerKAT proposal and the scientific discussion. T.T.T., R.v.R. and H.N. contributed to the scientific discussions. All authors reviewed the manuscript.

Corresponding authors

Correspondence to [James O. Chibueze](#) or [Haruka Sakemi](#) or [Takumi Ohmura](#).

Ethics declarations

Competing interests

The authors declare no competing interests.

Additional information

Peer review information *Nature* thanks Joydeep Bagchi and Maxim Markevitch for their contribution to the peer review of this work. Peer reviewer reports are available.

Publisher's note Springer Nature remains neutral with regard to jurisdictional claims in published maps and institutional affiliations.

Supplementary information

[Peer Review File](#)

Rights and permissions

[Reprints and Permissions](#)

About this article



Check for
updates

Cite this article

Chibueze, J.O., Sakemi, H., Ohmura, T. *et al.* Jets from MRC 0600-399 bent by magnetic fields in the cluster Abell 3376. *Nature* **593**, 47–50 (2021). <https://doi.org/10.1038/s41586-021-03434-1>

[Download citation](#)

- Received: 21 September 2020
- Accepted: 08 March 2021
- Published: 05 May 2021
- Issue Date: 06 May 2021
- DOI: <https://doi.org/10.1038/s41586-021-03434-1>

Comments

By submitting a comment you agree to abide by our [Terms](#) and [Community Guidelines](#). If you find something abusive or that does not comply with our terms or guidelines please flag it as inappropriate.

[Access through your institution](#)

[Change institution](#)

[Buy or subscribe](#)

Associated Content

[Black hole jets bent by magnetic fields](#)

- Joydeep Bagchi

Nature News & Views 05 May 2021

| [Section menu](#) | [Main menu](#) |

- Article
- [Published: 07 April 2021](#)

Leading hadronic contribution to the muon magnetic moment from lattice QCD

- [Sz. Borsanyi](#) ORCID: orcid.org/0000-0001-8071-8546¹,
- [Z. Fodor](#) ORCID: orcid.org/0000-0003-2519-5687^{1,2,3,4,5},
- [J. N. Guenther](#)^{6 nAff10},
- [C. Hoelbling](#) ORCID: orcid.org/0000-0001-5715-1086¹,
- [S. D. Katz](#)⁴,
- [L. Lellouch](#) ORCID: orcid.org/0000-0002-0032-6073⁷,
- [T. Lippert](#)^{1,2},
- [K. Miura](#)^{7,8,9},
- [L. Parato](#)⁷,
- [K. K. Szabo](#)^{1,2},
- [F. Stokes](#)²,
- [B. C. Toth](#)¹,
- [Cs. Torok](#)² &
- [L. Varnhorst](#)^{1 nAff10}

[Nature](#) volume **593**, pages 51–55(2021) [Cite this article](#)

- 13k Accesses
- 2 Citations
- 834 Altmetric
- [Metrics details](#)

Subjects

- [Phenomenology](#)
- [Theoretical particle physics](#)

Abstract

The standard model of particle physics describes the vast majority of experiments and observations involving elementary particles. Any deviation from its predictions would be a sign of new, fundamental physics. One long-standing discrepancy concerns the anomalous magnetic moment of the muon, a measure of the magnetic field surrounding that particle. Standard-model predictions¹ exhibit disagreement with measurements² that is tightly scattered around 3.7 standard deviations. Today, theoretical and measurement errors are comparable; however, ongoing and planned experiments aim to reduce the measurement error by a factor of four. Theoretically, the dominant source of error is the leading-order hadronic vacuum polarization (LO-HVP) contribution. For the upcoming measurements, it is essential to evaluate the prediction for this contribution with independent methods and to reduce its uncertainties. The most precise, model-independent determinations so far rely on dispersive techniques, combined with measurements of the cross-section of electron–positron annihilation into hadrons^{3,4,5,6}. To eliminate our reliance on these experiments, here we use ab initio quantum chromodynamics (QCD) and quantum electrodynamics simulations to compute the LO-HVP contribution. We reach sufficient precision to discriminate between the measurement of the anomalous magnetic moment of the muon and the predictions of dispersive methods. Our result favours the experimentally measured value over those obtained using the dispersion relation. Moreover, the methods used and developed in this work will enable further increased precision as more powerful computers become available.

[Access through your institution](#)

[Change institution](#)

[Buy or subscribe](#)

Access options

Subscribe to Journal

Get full journal access for 1 year

\$199.00

only \$3.90 per issue

[Subscribe](#)

All prices are NET prices.

VAT will be added later in the checkout.

Tax calculation will be finalised during checkout.

Rent or Buy article

Get time limited or full article access on ReadCube.

from \$8.99

[Rent or Buy](#)

All prices are NET prices.

Additional access options:

- [Log in](#)
- [Access through your institution](#)
- [Learn about institutional subscriptions](#)

Fig. 1: Contributions to a_μ , including examples of the corresponding Feynman diagrams.

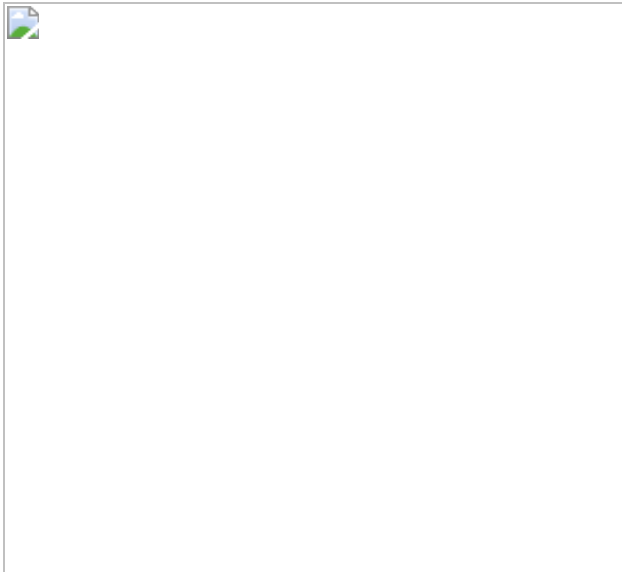


Fig. 2: Continuum extrapolation of the light connected component of a_μ , $\langle\langle \boldsymbol{a} \rangle\rangle_{-\langle\langle \boldsymbol{\mu} \rangle\rangle}^{\langle\langle \bf{light} \rangle\rangle}$.

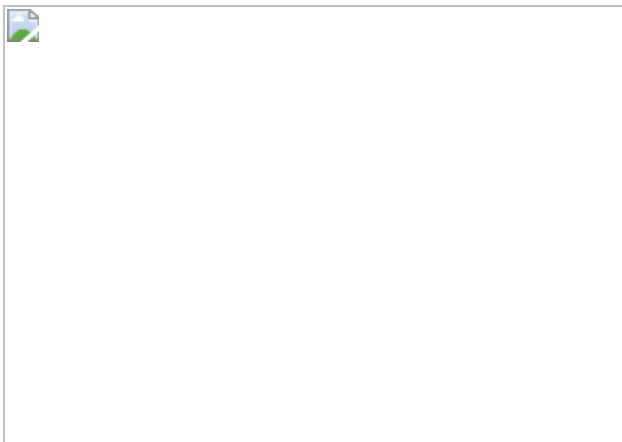


Fig. 3: Comparison of recent results for the LO-HPV contribution to the anomalous magnetic moment of the muon.

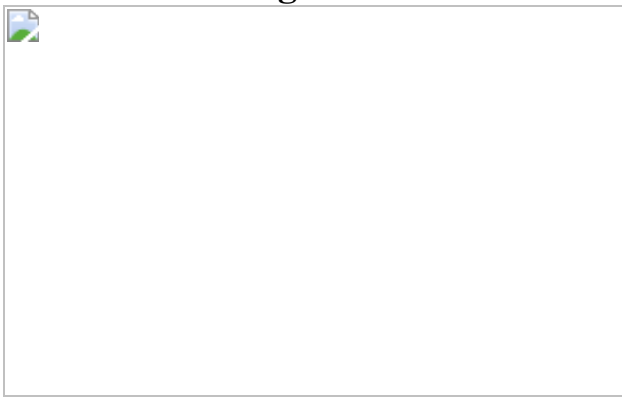
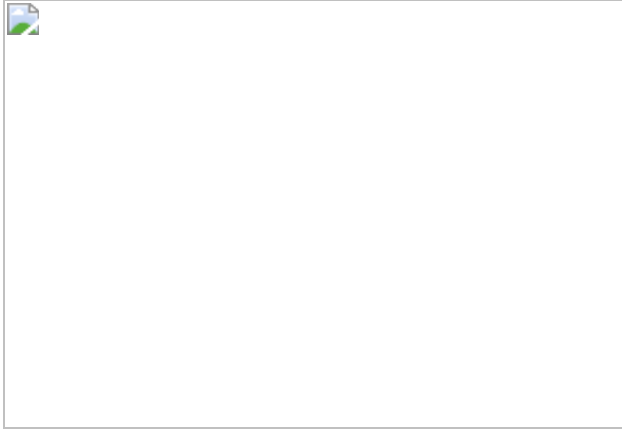


Fig. 4: Continuum extrapolation of the isospin-symmetric, light, connected component of the window observable $a_{\mu,\text{win}}$,

$\{\{\{\boldsymbol{a}\}\}\}_{\{\{\boldsymbol{\mu }\}\{\bf ,win\}\}}^{\{\{\rm l\}\}}\{\bf ight\}\}\}_{\{\bf iso\}\}\}.$



Data availability

The datasets used for the figures and tables are available from the corresponding author on request.

Code availability

A CPU code for configuration production and measurements can be obtained from the corresponding author upon request. The Wilson flow evolution code, which was used to determine w_0 , can be downloaded from <https://arxiv.org/abs/1203.4469>.

References

1. 1.

Tanabashi, M. et al. Review of particle physics. *Phys. Rev. D* **98**, 030001 (2018).

[ADS](#) [Article](#) [Google Scholar](#)

2. 2.

Bennett, G. W. et al. Final report of the muon E821 anomalous magnetic moment measurement at BNL. *Phys. Rev. D* **73**, 072003 (2006).

[ADS](#) [Article](#) [Google Scholar](#)

3. 3.

Davier, M., Hoecker, A., Malaescu, B. & Zhang, Z. A new evaluation of the hadronic vacuum polarisation contributions to the muon anomalous magnetic moment and to $\langle\alpha(m_Z^2)\rangle$. *Eur. Phys. J. C* **80**, 241 (2020); erratum **80**, 410 (2020).

[ADS](#) [CAS](#) [Article](#) [Google Scholar](#)

4. 4.

Keshavarzi, A., Nomura, D. & Teubner, T. $g - 2$ of charged leptons, $\langle\alpha(M_Z^2)\rangle$, and the hyperfine splitting of muonium. *Phys. Rev. D* **101**, 014029 (2020).

[ADS](#) [CAS](#) [Article](#) [Google Scholar](#)

5. 5.

Colangelo, G., Hoferichter, M. & Stoffer, P. Two-pion contribution to hadronic vacuum polarization. *J. High Energy Phys.* **2019**, 006 (2019).

[Article](#) [Google Scholar](#)

6. 6.

Hoferichter, M., Hoid, B. L. & Kubis, B. Three-pion contribution to hadronic vacuum polarization. *J. High Energy Phys.* **2019**, 137 (2019).

[Article](#) [Google Scholar](#)

7. 7.

Aoyama, T. et al. The anomalous magnetic moment of the muon in the Standard Model. *Phys. Rep.* **887**, 1–166 (2020).

[ADS](#) [CAS](#) [Article](#) [Google Scholar](#)

8. 8.

Bernecker, D. & Meyer, H. B. Vector correlators in lattice QCD: methods and applications. *Eur. Phys. J. A* **47**, 148 (2011).

[ADS](#) [Article](#) [Google Scholar](#)

9. 9.

Lautrup, B. E., Peterman, A. & de Rafael, E. Recent developments in the comparison between theory and experiments in quantum electrodynamics. *Phys. Rep.* **3**, 193–259 (1972).

[ADS](#) [Article](#) [Google Scholar](#)

10. 10.

de Rafael, E. Hadronic contributions to the muon $g-2$ and low-energy QCD. *Phys. Lett. B* **322**, 239–246 (1994).

[ADS](#) [Article](#) [Google Scholar](#)

11. 11.

Blum, T. Lattice calculation of the lowest order hadronic contribution to the muon anomalous magnetic moment. *Phys. Rev. Lett.* **91**, 052001 (2003).

[ADS](#) [CAS](#) [Article](#) [Google Scholar](#)

12. 12.

Borsanyi, S. et al. High-precision scale setting in lattice QCD. *J. High Energy Phys.* **2012**, 010 (2012).

[Article](#) [Google Scholar](#)

13. 13.

Dowdall, R. J., Davies, C. T. H., Lepage, G. P. & McNeile, C. V_{us} from π and K decay constants in full lattice QCD with physical u , d , s and c quarks. *Phys. Rev. D* **88**, 074504 (2013).

[ADS](#) [Article](#) [Google Scholar](#)

14. 14.

Borsanyi, S. et al. Hadronic vacuum polarization contribution to the anomalous magnetic moments of leptons from first principles. *Phys. Rev. Lett.* **121**, 022002 (2018).

[ADS](#) [CAS](#) [Article](#) [Google Scholar](#)

15. 15.

Neff, H., Eicker, N., Lippert, T., Negele, J. W. & Schilling, K. On the low fermionic eigenmode dominance in QCD on the lattice. *Phys. Rev. D* **64**, 114509 (2001).

[ADS](#) [Article](#) [Google Scholar](#)

16. 16.

Giusti, L., Hernandez, P., Laine, M., Weisz, P. & Wittig, H. Low-energy couplings of QCD from current correlators near the chiral limit. *J. High Energy Phys.* **2004**, 013 (2004).

[ADS](#) [Article](#) [Google Scholar](#)

17. 17.

DeGrand, T. A. & Schaefer, S. Improving meson two point functions in lattice QCD. *Comput. Phys. Commun.* **159**, 185–191 (2004).

[ADS](#) [CAS](#) [Article](#) [Google Scholar](#)

18. 18.

Shintani, E. et al. Covariant approximation averaging. *Phys. Rev. D* **91**, 114511 (2015).

[ADS](#) [Article](#) [Google Scholar](#)

19. 19.

Blum, T. et al. Calculation of the hadronic vacuum polarization contribution to the muon anomalous magnetic moment. *Phys. Rev. Lett.* **121**, 022003 (2018).

[ADS](#) [CAS](#) [Article](#) [Google Scholar](#)

20. 20.

Aubin, C. et al. Light quark vacuum polarization at the physical point and contribution to the muon $g - 2$. *Phys. Rev. D* **101**, 014503 (2020).

[ADS](#) [CAS](#) [Article](#) [Google Scholar](#)

21. 21.

de Divitiis, G. M. et al. Isospin breaking effects due to the up-down mass difference in Lattice QCD. *J. High Energy Phys.* **2012**, 124 (2012).

[Article](#) [Google Scholar](#)

22. 22.

de Divitiis, G. M. et al. Leading isospin breaking effects on the lattice. *Phys. Rev. D* **87**, 114505 (2013).

[ADS](#) [Article](#) [Google Scholar](#)

23. 23.

Colangelo, G., Durr, S. & Haefeli, C. Finite volume effects for meson masses and decay constants. *Nucl. Phys. B* **721**, 136–174 (2005).

[ADS](#) [Article](#) [Google Scholar](#)

24. 24.

Davoudi, Z. & Savage, M. J. Finite-volume electromagnetic corrections to the masses of mesons, baryons and nuclei. *Phys. Rev. D* **90**, 054503 (2014).

[ADS](#) [Article](#) [Google Scholar](#)

25. 25.

Borsanyi, S. et al. Ab initio calculation of the neutron-proton mass difference. *Science* **347**, 1452–1455 (2015).

[ADS](#) [CAS](#) [Article](#) [Google Scholar](#)

26. 26.

Fodor, Z. et al. Quantum electrodynamics in finite volume and nonrelativistic effective field theories. *Phys. Lett. B* **755**, 245–248 (2016).

[ADS](#) [CAS](#) [Article](#) [Google Scholar](#)

27. 27.

Aubin, C. et al. Finite-volume effects in the muon anomalous magnetic moment on the lattice. *Phys. Rev. D* **93**, 054508 (2016).

[ADS](#) [Article](#) [Google Scholar](#)

28. 28.

Bijnens, J. & Relefors, J. Vector two-point functions in finite volume using partially quenched chiral perturbation theory at two loops. *J. High Energy Phys.* **2017**, 114 (2017).

[ADS](#) [Article](#) [Google Scholar](#)

29. 29.

Hansen, M. T. & Patella, A. Finite-volume effects in $\langle\langle g-2 \rangle\rangle_\mu$. *Phys. Rev. Lett.* **123**, 172001 (2019).

[ADS](#) [CAS](#) [Article](#) [Google Scholar](#)

30. 30.

Jegerlehner, F. & Szafron, R. $\langle\langle \rho^0 - \gamma \rangle\rangle$ mixing in the neutral channel pion form factor $\langle\langle F_\pi \rangle\rangle$ and its role in comparing e^+e^- with τ spectral functions. *Eur. Phys. J. C* **71**, 1632 (2011).

31. 31.

Chakraborty, B. et al. The hadronic vacuum polarization contribution to a_μ from full lattice QCD. *Phys. Rev. D* **96**, 034516 (2017).

[ADS](#) [Article](#) [Google Scholar](#)

32. 32.

Gérardin, A. et al. The leading hadronic contribution to $(g-2)_\mu$ from lattice QCD with $N_f = 2 + 1$ flavours of $O(a)$ improved Wilson quarks. *Phys. Rev. D* **100**, 014510 (2019).

[ADS](#) [MathSciNet](#) [Article](#) [Google Scholar](#)

33. 33.

Davies, C. T. H. et al. Hadronic-vacuum-polarization contribution to the muon's anomalous magnetic moment from four-flavor lattice QCD. *Phys. Rev. D* **101**, 034512 (2020).

[ADS](#) [CAS](#) [Article](#) [Google Scholar](#)

34. 34.

Giusti, D., Lubicz, V., Martinelli, G., Sanfilippo, F. & Simula, S. Electromagnetic and strong isospin-breaking corrections to the muon $g - 2$ from Lattice QCD+QED. *Phys. Rev. D* **99**, 114502 (2019).

[ADS](#) [CAS](#) [Article](#) [Google Scholar](#)

35. 35.

Giusti, D., Sanfilippo, F. & Simula, S. Light-quark contribution to the leading hadronic vacuum polarization term of the muon $g - 2$ from twisted-mass fermions. *Phys. Rev. D* **98**, 114504 (2018).

[ADS](#) [CAS](#) [Article](#) [Google Scholar](#)

36. 36.

Shintani, E. et al. Hadronic vacuum polarization contribution to the muon $g - 2$ with 2+1 flavor lattice QCD on a larger than $(10 \text{ fm})^4$ lattice at the physical point. *Phys. Rev. D* **100**, 034517 (2019).

[ADS](#) [CAS](#) [Article](#) [Google Scholar](#)

37. 37.

Bazavov, A. et al. Gradient flow and scale setting on MILC HISQ ensembles. *Phys. Rev. D* **93**, 094510 (2016).

[ADS](#) [Article](#) [Google Scholar](#)

[Download references](#)

Acknowledgements

We thank J. Charles, A. El-Khadra, M. Hoferichter, F. Jegerlehner, C. Lehner, M. Knecht, A. Kronfeld, E. de Rafael and participants of the online workshop ‘The hadronic vacuum polarization from lattice QCD at high precision’ (16–20 November 2020) for discussions. We thank J. Bailey, W. Lee and S. Sharpe for correspondence on staggered XPT. Special thanks to A. Keshavarzi for cross-section data and discussions, and to G. Colangelo and H. Meyer for constructive criticism. The computations were performed on JUQUEEN, JURECA, JUWELS and QPACE at Forschungszentrum Jülich, on SuperMUC and SuperMUC-NG at Leibniz Supercomputing Centre in Munich, on Hazel Hen and HAWK at the High Performance Computing Center in Stuttgart, on Turing and Jean Zay at CNRS IDRIS, on Joliot-Curie at CEA TGCC, on Marconi in Rome and on GPU clusters in Wuppertal and Budapest. We thank the Gauss Centre for Supercomputing, PRACE and GENCI (grant 52275) for awarding us computer time on these machines. This project was partially funded by DFG grant SFB/TR55, by BMBF grant 05P18PXFCA, by the Hungarian National Research, Development and Innovation Office grant KKP126769 and by the Excellence Initiative of Aix-Marseille University - A*MIDEX, a French “Investissements d’Avenir” programme, through grants AMX-18-ACE-005, AMX-19-IET-008 - IPhU and ANR-11-LABX-0060.

Author information

Author notes

1. J. N. Guenther & L. Varnhorst

Present address: Aix Marseille Université, Université de Toulon,
CNRS, CPT, IPhU, Marseille, France

Affiliations

1. Department of Physics, University of Wuppertal, Wuppertal, Germany

Sz. Borsanyi, Z. Fodor, C. Hoelbling, T. Lippert, K. K. Szabo, B. C. Toth & L. Varnhorst

2. Jülich Supercomputing Centre, Forschungszentrum Jülich, Jülich, Germany

Z. Fodor, T. Lippert, K. K. Szabo, F. Stokes & Cs. Torok

3. Department of Physics, Pennsylvania State University, University Park, PA, USA

Z. Fodor

4. Institute for Theoretical Physics, Eötvös University, Budapest, Hungary

Z. Fodor & S. D. Katz

5. Department of Physics, University of California, San Diego, La Jolla, CA, USA

Z. Fodor

6. Department of Physics, University of Regensburg, Regensburg, Germany

J. N. Guenther

7. Aix Marseille Université, Université de Toulon, CNRS, CPT, IPhU, Marseille, France

L. Lellouch, K. Miura & L. Parato

8. Helmholtz Institute Mainz, Mainz, Germany

K. Miura

9. Kobayashi-Maskawa Institute for the Origin of Particles and the Universe, Nagoya University, Nagoya, Japan

K. Miura

Authors

1. Sz. Borsanyi

[View author publications](#)

You can also search for this author in [PubMed](#) [Google Scholar](#)

2. Z. Fodor

[View author publications](#)

You can also search for this author in [PubMed](#) [Google Scholar](#)

3. J. N. Guenther

[View author publications](#)

You can also search for this author in [PubMed](#) [Google Scholar](#)

4. C. Hoelbling

[View author publications](#)

You can also search for this author in [PubMed](#) [Google Scholar](#)

5. S. D. Katz

[View author publications](#)

You can also search for this author in [PubMed](#) [Google Scholar](#)

6. L. Lellouch

[View author publications](#)

You can also search for this author in [PubMed](#) [Google Scholar](#)

7. T. Lippert

[View author publications](#)

You can also search for this author in [PubMed](#) [Google Scholar](#)

8. K. Miura

[View author publications](#)

You can also search for this author in [PubMed](#) [Google Scholar](#)

9. L. Parato

[View author publications](#)

You can also search for this author in [PubMed](#) [Google Scholar](#)

10. K. K. Szabo

[View author publications](#)

You can also search for this author in [PubMed](#) [Google Scholar](#)

11. F. Stokes

[View author publications](#)

You can also search for this author in [PubMed](#) [Google Scholar](#)

12. B. C. Toth

[View author publications](#)

You can also search for this author in [PubMed](#) [Google Scholar](#)

13. Cs. Torok

[View author publications](#)

You can also search for this author in [PubMed](#) [Google Scholar](#)

14. L. Varnhorst

[View author publications](#)

You can also search for this author in [PubMed](#) [Google Scholar](#)

Contributions

S.B., K.K.S. and B.C.T. wrote the codes and carried out the runs for configuration generation and measurements. S.B., Z.F., K.K.S., B.C.T. and

L.V. were the main developers of the scale setting; L.L., K.K.S. and B.C.T. of the isospin breaking; F.S., K.K.S. and B.C.T. of the XPT; L.L., F.S. and C.T. of the MLLGS model; L.L., K.K.S. and B.C.T. of the RHO model; S.B., Z.F. and K.K.S. of the lattice finite-size study; K.K.S. and C.T. of the finite-size effects of isospin breaking; C.H., K.K.S. and B.C.T. of the overlap simulations. The global analysis strategy was developed by S.B., Z.F., S.D.K., L.L., F.S., K.K.S. and B.C.T. The global fits were carried out by S.B., J.N.G., S.D.K. and B.C.T. R-ratio and perturbative computations were done by Z.F., L.L., K.K.S. and C.T. Various crosschecks were performed by K.M., L.P., B.C.T. and C.T. S.B., Z.F., L.L., T.L. and K.K.S. were involved in acquisition of computer resources. Z.F., L.L. and K.K.S. wrote the main paper. Z.F. and K.K.S. coordinated the project.

Corresponding author

Correspondence to [Z. Fodor](#).

Ethics declarations

Competing interests

The authors declare no competing interests.

Additional information

Peer review information *Nature* thanks Gilberto Colangelo, Harvey Meyer and the other, anonymous, reviewer(s) for their contribution to the peer review of this work.

Publisher's note Springer Nature remains neutral with regard to jurisdictional claims in published maps and institutional affiliations.

Extended data figures and tables

Extended Data Fig. 1 Upper and lower bounds on the light isospin-symmetric component of a_μ ,

$\langle [\{ \{ \boldsymbol{a} \} \} - \{ \{ \boldsymbol{\mu} \} \}]^{\rm l} \rangle_{\bf light} \rangle_0$.

The bounds are computed using the lattice correlator below a time separation of t_c and an analytical formula describing the large-time behaviour above t_c . The results shown are obtained with the 4HEX action on two different lattice sizes, 56×84 and 96×96 , both at $a = 0.112$ fm lattice spacing and $M_\pi = 121$ MeV Goldstone pion mass. We also carried out another simulation with $M_\pi = 104$ MeV. From these two, we interpolate to $M_\pi = 110$ MeV. This value ensures that a particular average of pion tastes is fixed to the physical value of the pion mass (see text). Error bars are statistical errors (s.e.m.).

Extended Data Fig. 2 Isospin-symmetric component of $\langle [\{ \{ \boldsymbol{a} \} \} - \{ \{ \boldsymbol{\mu} \} \}]^{\rm l} \rangle_{\bf light}$, computed with a sliding window.

The window starts at t_1 and ends 0.5 fm later. The plot shows the difference between a fine and a coarse lattice with spacing $a = 0.064$ fm and $a = 0.119$ fm. The black squares with error bars are obtained from the simulation, and errors are statistical (s.e.m.). The coloured curves are the predictions of NLO, NNLO SXPT, and the SRHO and SMLGS models. They are computed at the parameters (pion mass, taste violation, volume) of the simulations.

Extended Data Fig. 3 Example continuum limits of $\langle [\{ \{ \boldsymbol{a} \} \} - \{ \{ \boldsymbol{\mu} \} \}]^{\rm l} \rangle_{\bf light}$.

The light-green triangles labelled ‘none’ correspond to our lattice results with no taste improvement. The blue squares represent data that have undergone no taste improvement for $t < 1.3$ fm and SRHO improvement

above. The blue curves correspond to example continuum extrapolations of improved data to polynomials in a^2 , up to and including a^4 . We note that extrapolations in $a^2\alpha_s(1/a)^3$, with $\alpha_s(1/a)$ the strong coupling at the lattice scale, are also considered in our final result. The red circles and curves are the same as the blue points, but correspond to SRHO taste improvement for $t \geq 0.4$ fm and no improvement for smaller t . The purple histogram results from fits using the SRHO improvement, and the corresponding central value and error is the purple band. The darker grey circles correspond to results corrected with SRHO in the range 0.4–1.3 fm and with NNLO SXPT for larger t . These latter fits serve to estimate the systematic uncertainty of the SRHO improvement. The grey band includes this uncertainty, and the corresponding histogram is shown with grey. Errors are s.e.m.

[Extended Data Fig. 4 Comparison of the continuum extrapolation of \$\langle\langle a \rangle\rangle_{\mu}^{\(B\)}\$ to those of \$\langle\langle a \rangle\rangle_{\mu}^{\(B\)}\$ and \$\langle\langle a \rangle\rangle_{\mu}^{\(disc\)}\$.](#)

Top, grey points correspond to our uncorrected results for $\langle\langle a \rangle\rangle_{\mu}^{(light)}$. The red symbols show the same results with our standard SRHO taste improvement. They have a much milder continuum limit that exhibits none of the nonlinear behaviour of the grey points. The red curves show typical examples of illustrative continuum extrapolations of those points. Bottom, grey and red points and curves are the same quantities, but for $\langle\langle a \rangle\rangle_{\mu}^{(disc)}$. Combining the results from the two individual continuum extrapolations of $\langle\langle a \rangle\rangle_{\mu}^{(light)}$ and $\langle\langle a \rangle\rangle_{\mu}^{(disc)}$, according to equation (6), gives the result with statistical errors illustrated by the red band, with combined statistical and systematic errors indicated by the broader pink band. The blue points correspond to our results for $\langle\langle a \rangle\rangle_{\mu}^{(I=0)}$ for each of our simulations, and are obtained by combining the two sets of grey points, according to equation (6). As these blue points show, the resulting continuum-limit behaviour of $\langle\langle a \rangle\rangle_{\mu}$

$\}^{\wedge}\{\{\rm{light}}\}\})$) is much milder than that of either the uncorrected $\langle a \rangle_{\mu}^{\wedge}\{\{\rm{light}}\}\rangle$ or $\langle a \rangle_{\mu}^{\wedge}\{\{\rm{disc}}\}\rangle$, and shows none of their curvature. This behaviour resembles much more that of the taste-improved red points. Moreover, all of the blue points, including typical continuum extrapolations drawn as blue lines, lie within the bands. This suggests that our taste improvements neither bias the central values of our continuum-extrapolated $\langle a \rangle_{\mu}^{\wedge}\{\{\rm{light}}\}\rangle$ and $\langle a \rangle_{\mu}^{\wedge}\{\{\rm{disc}}\}\rangle$, nor do they lead to an underestimate of uncertainties. Errors are s.e.m.

Extended Data Fig. 5 Continuum extrapolations of the contributions to $w_0 M_Q$.

From top to bottom: isospin-symmetric, electromagnetic valence–valence, sea–valence and sea–sea components. The results are multiplied by $\langle 10 \rangle^4 / M \langle \varOmega \rangle^{\wedge}\{\ast\}$) and the electric derivatives are multiplied by $\langle e \rangle^{\ast}\{\wedge\{2\}}$), where the asterisk denotes physical value. Error bars show statistical errors (s.e.m.). Dashed lines are continuum extrapolations, showing illustrative examples from our several thousand fits. Only the lattice spacing dependence is shown: the data points are moved to the physical light- and strange-quark mass point. This adjustment varies from fit to fit, and the red data points are obtained in an a^2 -linear fit to all ensembles. If in a fit the adjusted points differ considerably from the red points, we show them with grey colour. The final result is obtained from a weighted histogram of the several thousand fits.

Extended Data Table 1 Isospin-symmetric component of $\langle \boldsymbol{a} \rangle_{\mu}^{\wedge}\{\{\bf{light}\}\}$
[Full size table](#)

Extended Data Table 2 Finite-size effect in the reference box of the isospin-symmetric component of a_μ

[Full size table](#)

Supplementary information

Supplementary Information

This file contains Supplementary Information, including Supplementary Figures 1–30 and Supplementary Tables 1–20, and Supplementary References.

Rights and permissions

[Reprints and Permissions](#)

About this article



Check for
updates

Cite this article

Borsanyi, S., Fodor, Z., Guenther, J.N. *et al.* Leading hadronic contribution to the muon magnetic moment from lattice QCD. *Nature* **593**, 51–55 (2021). <https://doi.org/10.1038/s41586-021-03418-1>

[Download citation](#)

- Received: 02 August 2020
- Accepted: 04 March 2021
- Published: 07 April 2021
- Issue Date: 06 May 2021
- DOI: <https://doi.org/10.1038/s41586-021-03418-1>

Further reading

- [Is the standard model broken? Physicists cheer major muon result](#)
 - Davide Castelvecchi

Nature (2021)
- [What's next for physics' standard model? Muon results throw theories into confusion](#)
 - Davide Castelvecchi

Nature (2021)

Comments

By submitting a comment you agree to abide by our [Terms](#) and [Community Guidelines](#). If you find something abusive or that does not comply with our terms or guidelines please flag it as inappropriate.

[Access through your institution](#)

[Change institution](#)

[Buy or subscribe](#)

Associated Content

[Prediction for magnetic moment of the muon informs a test of the standard model of particle physics](#)

- Harvey B. Meyer

Nature News & Views 05 May 2021

| [Section menu](#) | [Main menu](#) |

- Article
- [Published: 05 May 2021](#)

Rashba valleys and quantum Hall states in few-layer black arsenic

- [Feng Sheng](#) [ORCID: orcid.org/0000-0003-0846-6238](#)¹_{nal},
- [Chenqiang Hua](#)¹_{hal},
- [Man Cheng](#)¹_{nal},
- [Jie Hu](#)¹,
- [Xikang Sun](#)¹,
- [Qian Tao](#)¹,
- [Hengzhe Lu](#)¹,
- [Yunhao Lu](#) [ORCID: orcid.org/0000-0001-6825-7206](#)¹,
- [Mianzeng Zhong](#) [ORCID: orcid.org/0000-0003-0343-5248](#)²,
- [Kenji Watanabe](#) [ORCID: orcid.org/0000-0003-3701-8119](#)³,
- [Takashi Taniguchi](#) [ORCID: orcid.org/0000-0002-1467-3105](#)³,
- [Qinglin Xia](#) [ORCID: orcid.org/0000-0002-9599-7864](#)²,
- [Zhu-An Xu](#) [ORCID: orcid.org/0000-0001-9290-2762](#)^{1,4} &
- [Yi Zheng](#) [ORCID: orcid.org/0000-0002-9487-1151](#)^{1,4}

[Nature](#) volume 593, pages56–60(2021) [Cite this article](#)

- 2463 Accesses
- 28 Altmetric
- [Metrics details](#)

Subjects

- [Electronic properties and materials](#)

- [Quantum Hall](#)

Abstract

Exciting phenomena may emerge in non-centrosymmetric two-dimensional electronic systems when spin–orbit coupling (SOC)¹ interplays dynamically with Coulomb interactions^{2,3}, band topology^{4,5} and external modulating forces^{6,7,8}. Here we report synergetic effects between SOC and the Stark effect in centrosymmetric few-layer black arsenic, which manifest as particle–hole asymmetric Rashba valley formation and exotic quantum Hall states that are reversibly controlled by electrostatic gating. The unusual findings are rooted in the puckering square lattice of black arsenic, in which heavy $4p$ orbitals form a Brillouin zone-centred Γ valley with p_z symmetry, coexisting with doubly degenerate D valleys of p_x origin near the time-reversal-invariant momenta of the X points. When a perpendicular electric field breaks the structure inversion symmetry, strong Rashba SOC is activated for the p_x bands, which produces spin–valley-flavoured D^\pm valleys paired by time-reversal symmetry, whereas Rashba splitting of the Γ valley is constrained by the p_z symmetry. Intriguingly, the giant Stark effect shows the same p_x -orbital selectiveness, collectively shifting the valence band maximum of the D^\pm Rashba valleys to exceed the Γ Rashba top. Such an orchestrating effect allows us to realize gate-tunable Rashba valley manipulations for two-dimensional hole gases, hallmarked by unconventional even-to-odd transitions in quantum Hall states due to the formation of a flavour-dependent Landau level spectrum. For two-dimensional electron gases, the quantization of the Γ Rashba valley is characterized by peculiar density-dependent transitions in the band topology from trivial parabolic pockets to helical Dirac fermions.

[Access through your institution](#)

[Change institution](#)

[Buy or subscribe](#)

Access options

[Subscribe to Journal](#)

Get full journal access for 1 year

\$199.00

only \$3.90 per issue

[Subscribe](#)

All prices are NET prices.

VAT will be added later in the checkout.

Tax calculation will be finalised during checkout.

Rent or Buy article

Get time limited or full article access on ReadCube.

from \$8.99

[Rent or Buy](#)

All prices are NET prices.

Additional access options:

- [Log in](#)
- [Access through your institution](#)
- [Learn about institutional subscriptions](#)

Fig. 1: Flavour-dependent Rashba valley formation in BAs by synergetic Rashba and Stark effects.

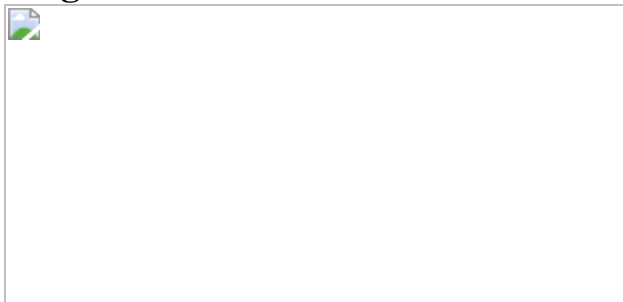


Fig. 2: SdHOs and exotic QHS transitions in BAs 2DHG and 2DEG.



Fig. 3: Quantum Hall signatures of gate-tunable Rashba valley formation in BAs 2DHG and 2DEG with particle-hole asymmetry.

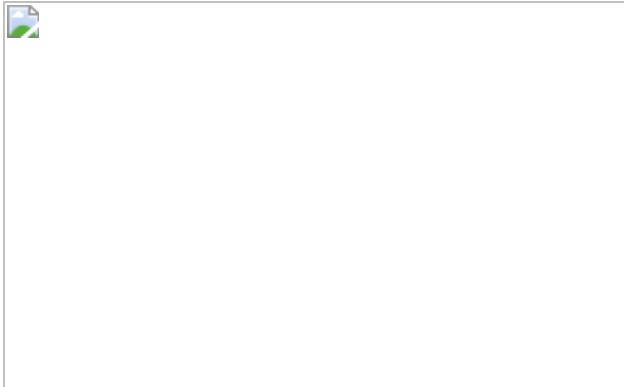


Fig. 4: Rashba band topology of BAs 2DHG and 2DEG.



Data availability

The authors declare that the main data supporting the findings of this study are available within the paper and the [Supplementary Information file](#). Extra data are available from the corresponding authors upon reasonable request. [Source data](#) are provided with this paper.

References

1. 1.

Manchon, A., Koo, H. C., Nitta, J., Frolov, S. M. & Duine, R. A. New perspectives for Rashba spin–orbit coupling. *Nat. Mater.* **14**, 871–882 (2015).

[ADS](#) [CAS](#) [PubMed](#) [Article](#) [Google Scholar](#)

2. 2.

Seki, S., Yu, X. Z., Ishiwata, S. & Tokura, Y. Observation of skyrmions in a multiferroic material. *Science* **336**, 198–201 (2012).

[ADS](#) [CAS](#) [PubMed](#) [Article](#) [Google Scholar](#)

3. 3.

Kimura, T. et al. Magnetic control of ferroelectric polarization. *Nature* **426**, 55–58 (2003).

[ADS](#) [CAS](#) [PubMed](#) [Article](#) [Google Scholar](#)

4. 4.

Bernevig, B. A., Hughes, T. L. & Zhang, S. C. Quantum spin Hall effect and topological phase transition in HgTe quantum wells. *Science* **314**, 1757–1761 (2006).

[ADS](#) [CAS](#) [PubMed](#) [Article](#) [Google Scholar](#)

5. 5.

Hasan, M. Z. & Kane, C. L. Colloquium: Topological insulators. *Rev. Mod. Phys.* **82**, 3045–3067 (2010).

[ADS](#) [CAS](#) [Article](#) [Google Scholar](#)

6. 6.

Li, X., Zhang, F. & Niu, Q. Unconventional quantum Hall effect and tunable spin Hall effect in Dirac materials: application to an isolated MoS₂ trilayer. *Phys. Rev. Lett.* **110**, 066803 (2013).

[ADS](#) [PubMed](#) [Article](#) [Google Scholar](#)

7. 7.

Movva, H. C. P. et al. Density-dependent quantum Hall states and Zeeman splitting in monolayer and bilayer WSe₂. *Phys. Rev. Lett.* **118**, 247701 (2017).

[ADS](#) [PubMed](#) [Article](#) [Google Scholar](#)

8. 8.

Pisoni, R. et al. Interactions and magnetotransport through spin–valley coupled Landau levels in monolayer MoS₂. *Phys. Rev. Lett.* **121**, 247701 (2018).

[ADS](#) [CAS](#) [PubMed](#) [Article](#) [Google Scholar](#)

9. 9.

Winkler, R. *Spin–Orbit Coupling Effects in Two-Dimensional Electron and Hole Systems* (Springer-Verlag, 2003).

10. 10.

Wang, Z. et al. Origin and magnitude of ‘designer’ spin-orbit interaction in graphene on semiconducting transition metal dichalcogenides. *Phys. Rev. X* **6**, 041020 (2016).

[Google Scholar](#)

11. 11.

Li, L. K. et al. Black phosphorus field-effect transistors. *Nat. Nanotechnol.* **9**, 372–377 (2014).

[ADS](#) [CAS](#) [PubMed](#) [Article](#) [Google Scholar](#)

12. 12.

Carvalho, A. et al. Phosphorene: from theory to applications. *Nat. Rev. Mater.* **1**, 16061 (2016).

[ADS](#) [CAS](#) [Article](#) [Google Scholar](#)

13. 13.

Xia, F., Wang, H., Hwang, J. C., Castro Neto, A. H. & Yang, L. Black phosphorus and its isoelectronic materials. *Nat. Rev. Phys.* **1**, 306–317 (2019).

[CAS](#) [Article](#) [Google Scholar](#)

14. 14.

Shportko, K. et al. Resonant bonding in crystalline phase-change materials. *Nat. Mater.* **7**, 653–658 (2008).

[ADS](#) [CAS](#) [PubMed](#) [Article](#) [Google Scholar](#)

15. 15.

Kooi, B. J. & Wuttig, M. Chalcogenides by design: functionality through metavalent bonding and confinement. *Adv. Mater.* **32**, 1908302 (2020).

[CAS](#) [Article](#) [Google Scholar](#)

16. 16.

Chen, Y. et al. Black arsenic: a layered semiconductor with extreme in-plane anisotropy. *Adv. Mater.* **30**, 1800754 (2018).

[Article](#) [Google Scholar](#)

17. 17.

Wang, Z. et al. Defects controlled hole doping and multivalley transport in SnSe single crystals. *Nat. Commun.* **9**, 47 (2018).

[ADS](#) [PubMed](#) [PubMed Central](#) [Article](#) [Google Scholar](#)

18. 18.

Li, L. K. et al. Quantum Hall effect in black phosphorus two-dimensional electron system. *Nat. Nanotechnol.* **11**, 593–597 (2016).

[ADS](#) [CAS](#) [PubMed](#) [Article](#) [Google Scholar](#)

19. 19.

Murakawa, H. et al. Detection of Berry's phase in a bulk Rashba semiconductor. *Science* **342**, 1490–1493 (2013).

[ADS](#) [CAS](#) [PubMed](#) [Article](#) [Google Scholar](#)

20. 20.

Ishizaka, K. et al. Giant Rashba-type spin splitting in bulk BiTeI. *Nat. Mater.* **10**, 521–526 (2011).

[ADS](#) [CAS](#) [PubMed](#) [Article](#) [Google Scholar](#)

21. 21.

Khoo, K., Mazzoni, M. & Louie, S. Tuning the electronic properties of boron nitride nanotubes with transverse electric fields: a giant dc Stark effect. *Phys. Rev. B* **69**, 201401 (2004).

[ADS](#) [Article](#) [Google Scholar](#)

22. 22.

Kim, J. et al. Observation of tunable band gap and anisotropic Dirac semimetal state in black phosphorus. *Science* **349**, 723–726 (2015).

[CAS](#) [PubMed](#) [Article](#) [Google Scholar](#)

23. 23.

Liu, Y. et al. Gate-tunable giant Stark effect in few-layer black phosphorus. *Nano Lett.* **17**, 1970–1977 (2017).

[ADS](#) [CAS](#) [PubMed](#) [Article](#) [Google Scholar](#)

24. 24.

Ramasubramaniam, A., Naveh, D. & Towe, E. Tunable band gaps in bilayer transition-metal dichalcogenides. *Phys. Rev. B* **84**, 205325 (2011).

[ADS](#) [Article](#) [Google Scholar](#)

25. 25.

Yang, F. Y. et al. Quantum Hall effect in electron-doped black phosphorus field-effect transistors. *Nano Lett.* **18**, 6611–6616 (2018).

[ADS](#) [CAS](#) [PubMed](#) [Article](#) [Google Scholar](#)

26. 26.

Xu, S. et al. Odd-integer quantum Hall states and giant spin susceptibility in p-type few-layer WSe₂. *Phys. Rev. Lett.* **118**, 067702 (2017).

[ADS](#) [PubMed](#) [Article](#) [Google Scholar](#)

27. 27.

Feng, Y. et al. Rashba-like spin splitting along three momentum directions in trigonal layered PtBi₂. *Nat. Commun.* **10**, 4765 (2019).

[ADS](#) [PubMed](#) [PubMed Central](#) [Article](#) [Google Scholar](#)

28. 28.

Geim, A. K. & Novoselov, K. S. The rise of graphene. *Nat. Mater.* **6**, 183–191 (2007).

[ADS](#) [CAS](#) [PubMed](#) [Article](#) [Google Scholar](#)

29. 29.

Xu, Y. et al. Observation of topological surface state quantum Hall effect in an intrinsic three-dimensional topological insulator. *Nat. Phys.* **10**, 956–963 (2014).

[CAS](#) [Article](#) [Google Scholar](#)

30. 30.

Shoenberg, D. *Magnetic Oscillations in Metals* (Cambridge Univ. Press, 1984).

31. 31.

Kammhuber, J. et al. Conductance through a helical state in an indium antimonide nanowire. *Nat. Commun.* **8**, 478 (2017).

[ADS](#) [CAS](#) [PubMed](#) [PubMed Central](#) [Article](#) [Google Scholar](#)

32. 32.

Sun, J. et al. Helical hole state in multiple conduction modes in Ge/Si core/shell nanowire. *Nano Lett.* **18**, 6144–6149 (2018).

[ADS](#) [CAS](#) [PubMed](#) [Article](#) [Google Scholar](#)

33. 33.

Wang, L. et al. One-dimensional electrical contact to a two-dimensional material. *Science* **342**, 614–617 (2013).

[ADS](#) [CAS](#) [PubMed](#) [Article](#) [Google Scholar](#)

34. 34.

Zomer, P. J., Guimarães, M. H. D., Brant, J. C., Tombros, N. & van Wees, B. J. Fast pick up technique for high quality heterostructures of bilayer graphene and hexagonal boron nitride. *Appl. Phys. Lett.* **105**, 013101 (2014).

[ADS](#) [Article](#) [Google Scholar](#)

35. 35.

Long, G. et al. Achieving ultrahigh carrier mobility in two-dimensional hole gas of black phosphorus. *Nano Lett.* **16**, 7768–7773 (2016).

[ADS](#) [CAS](#) [PubMed](#) [Article](#) [Google Scholar](#)

36. 36.

Kresse, G. & Furthmüller, J. Efficiency of ab-initio total energy calculations for metals and semiconductors using a plane-wave basis set. *Comput. Mater. Sci.* **6**, 15–50 (1996).

[CAS](#) [Article](#) [Google Scholar](#)

37. 37.

Kresse, G. & Joubert, D. From ultrasoft pseudopotentials to the projector augmented-wave method. *Phys. Rev. B* **59**, 1758–1775 (1999).

[ADS](#) [CAS](#) [Article](#) [Google Scholar](#)

38. 38.

Klimeš, J., Bowler, D. R. & Michaelides, A. Chemical accuracy for the van der Waals density functional. *J. Phys. Condens. Matter* **22**, 022201 (2010).

[ADS](#) [PubMed](#) [Article](#) [Google Scholar](#)

39. 39.

Koelling, D. D. & Harmon, B. N. A technique for relativistic spin-polarised calculations. *J. Phys. C* **10**, 3107–3114 (1977).

[ADS](#) [CAS](#) [Article](#) [Google Scholar](#)

40. 40.

Bawden, L. et al. Hierarchical spin-orbital polarization of a giant Rashba system. *Sci. Adv.* **1**, e1500495 (2015).

[ADS](#) [PubMed](#) [PubMed Central](#) [Article](#) [Google Scholar](#)

[Download references](#)

Acknowledgements

This work is supported by the National Key R&D Program of the MOST of China (grant numbers 2017YFA0303002, 2016YFA0300204 and 2019YFA0308602), the National Science Foundation of China (grant numbers 11790313, 11574264, 11774305 and 61904205), Zhejiang Provincial Natural Science Foundation (grant numbers D19A040001 and R21A040006) and the Natural Science Foundation of Hunan Province (grant number 2020JJ4677). Y.Z. acknowledges the funding support from the Fundamental Research Funds for the Central Universities. A portion of this work was performed on the Steady High Magnetic Field Facilities, High Magnetic Field Laboratory, CAS. We thank Z. H. Liu of Longde Group Ltd for providing natural BAs crystals.

Author information

Author notes

1. These authors contributed equally: Feng Sheng, Chenqiang Hua, Man Cheng

Affiliations

1. Zhejiang Province Key Laboratory of Quantum Technology and Device, Department of Physics, Zhejiang University, Hangzhou, People's Republic of China

Feng Sheng, Chenqiang Hua, Man Cheng, Jie Hu, Xikang Sun, Qian Tao, Hengzhe Lu, Yunhao Lu, Zhu-An Xu & Yi Zheng

2. School of Physics and Electronics, Hunan Key Laboratory of Nanophotonics and Devices, Central South University, Changsha, People's Republic of China

Mianzeng Zhong & Qinglin Xia

3. National Institute for Materials Science, Tsukuba, Japan

Kenji Watanabe & Takashi Taniguchi

4. State Key Laboratory of Silicon Materials, Zhejiang University, Hangzhou, People's Republic of China

Zhu-An Xu & Yi Zheng

Authors

1. Feng Sheng

[View author publications](#)

You can also search for this author in [PubMed](#) [Google Scholar](#)

2. Chenqiang Hua

[View author publications](#)

You can also search for this author in [PubMed](#) [Google Scholar](#)

3. Man Cheng

[View author publications](#)

You can also search for this author in [PubMed](#) [Google Scholar](#)

4. Jie Hu

[View author publications](#)

You can also search for this author in [PubMed](#) [Google Scholar](#)

5. Xikang Sun

[View author publications](#)

You can also search for this author in [PubMed](#) [Google Scholar](#)

6. Qian Tao

[View author publications](#)

You can also search for this author in [PubMed](#) [Google Scholar](#)

7. Hengzhe Lu

[View author publications](#)

You can also search for this author in [PubMed](#) [Google Scholar](#)

8. Yunhao Lu

[View author publications](#)

You can also search for this author in [PubMed](#) [Google Scholar](#)

9. Mianzeng Zhong

[View author publications](#)

You can also search for this author in [PubMed](#) [Google Scholar](#)

10. Kenji Watanabe

[View author publications](#)

You can also search for this author in [PubMed](#) [Google Scholar](#)

11. Takashi Taniguchi

[View author publications](#)

You can also search for this author in [PubMed](#) [Google Scholar](#)

12. Qinglin Xia

[View author publications](#)

You can also search for this author in [PubMed](#) [Google Scholar](#)

13. Zhu-An Xu

[View author publications](#)

You can also search for this author in [PubMed](#) [Google Scholar](#)

14. Yi Zheng

[View author publications](#)

You can also search for this author in [PubMed](#) [Google Scholar](#)

Contributions

Q.X. and Y.Z. initiated and supervised the project. F.S. fabricated BAs devices and carried out all the measurements, assisted by M.C., J.H. and X.S. C.H. and Y.L. did the DFT calculations. K.W. and T.T. prepared high-quality boron nitride single crystals. F.S., C.H., M.C., Q.X. and Y.Z. analysed the data and wrote the paper with inputs from all authors.

Corresponding authors

Correspondence to [Qinglin Xia](#) or [Zhu-An Xu](#) or [Yi Zheng](#).

Ethics declarations

Competing interests

The authors declare no competing interests.

Additional information

Peer review information *Nature* thanks Aleksandr Rodin and the other, anonymous, reviewer(s) for their contribution to the peer review of this work. Peer reviewer reports are available.

Publisher's note Springer Nature remains neutral with regard to jurisdictional claims in published maps and institutional affiliations.

Extended data figures and tables

Extended Data Fig. 1 Projected band structures of BP, BAs and SnSe.

a–c, Energy bands of ML BP (**a**), BAs (**b**) and SnSe (**c**). According to orbital analysis, the Γ valley consists of p_z electrons, whereas along Γ –X, p_x orbitals dominate the TRS-paired D valleys. **d–f**, Projected band structures of bulk BP (**d**), BAs (**e**) and SnSe (**f**), which are consistent with the ML results. Note that SnSe has an extra set of p_y -symmetry valleys along the armchair direction¹⁷, which become merged with Γ valleys in BP and BAs^{11,16}.

Extended Data Fig. 2 Electric-field-dependent valley energy gaps and GSE coefficients of bilayer, trilayer and quadruple-layer BAs.

a, Energy gaps versus E_z for the Γ and D valleys in bilayer (BL) BAs. The GSE coefficients are the linear slopes of the gap curves. **b**, **c**, Energy gap evolutions of the Γ and D valleys in trilayer (TL) (**b**) and quadruple-layer (QL) (**c**) BAs. For different layer numbers, the D-valley GSE coefficient S_D is consistently larger than the Γ -valley GSE coefficient S_Γ . This is mainly due to E_z -dependent s – p hybridization, which contributes negatively to the

GSE due to the antibonding VBM of the Γ valley (see Supplementary Note 5).

Extended Data Fig. 3 Energy bands of QL BAs under an electric field.

a, Pristine band structure of QL BAs without an electric field. All bands are spin doubly degenerate. **b**, Electronic band structure of QL BAs under $E_z = 0.3 \text{ V nm}^{-1}$, which activates the synergetic Rashba and Stark effects, and thus creates the spin–valley-flavoured D^\pm valleys in the VB and the conventional Γ Rashba valleys in the CB. Near the D^\pm VBM, the energy splitting is about 6.85 meV. Layer-dependent Rashba splitting is summarized in Supplementary Note 6. Note that under the realistic experimental conditions ($E_z > 0.1 \text{ V nm}^{-1}$), gate-induced charge carriers in BAs are quantum confined within four interfacial MLs to form the 2DEG or the 2DHG for positive and negative V_g , respectively. Therefore, our DFT calculations mainly focus on QL BAs, compared with ML, BL and TL BAs.

Extended Data Fig. 4 E_z -dependent Rashba splitting energy E_{SO} of the D^\pm and Γ valleys in QL BAs.

The DFT-calculated E_{SO} of the D^\pm valleys is larger than that of the Γ Rashba valleys within the whole E_z range. Using the LK formula fitting (Supplementary Note 9), we can also deduce experimental E_{SO} from V_g -dependent SdHOs, as shown by the black curve. Although DFT overestimates E_{SO} by a factor of two, it is clear that both DFT and experimental results show the same trend in the linear growth of E_{SO} as a function of E_z . Equally important, both results prove that E_{SO} is substantial enough to be probed by quantum transport below liquid helium temperature. Note that E_z is calculated by interfacial Gauss's law (Supplementary Note 6).

Extended Data Fig. 5 FET transfer curves and V_g -dependent current–voltage (I – V) characteristics of high-mobility BAs-S9.

a, Transfer curves of BAs-S9 at 0.27 K (black line) and 300 K (red line), respectively. At 0.27 K, the device shows ambipolar FET characteristics with a well defined bandgap for V_g between 1.4 V and –1.1 V. **b**, Ambipolar I – V characteristics of BAs-S9 for varying V_g at 0.27 K, proving ohmic contacts achieved by Pd/Au electrodes for both the 2DHG and the 2DEG when $|V_g| \geq 2$ V. The data were measured in a two-terminal configuration using a Keithley 2400 source-measure unit.

Extended Data Fig. 6 Angle-dependent SdHOs of the 2DHG and the 2DEG in BAs devices.

a, Angle-dependent R_{xx} versus B_\perp in the 2DHG with $p = 7.14 \times 10^{12} \text{ cm}^{-2}$ (BAs-S2, $V_g = -7$ V), which barely shows any changes in the positions of the SdHO extrema. **b**, Angle-dependent R_{xx} versus B_\perp in the 2DEG with $n = 3.95 \times 10^{12} \text{ cm}^{-2}$ (BAs-S9, $V_g = 5$ V), which also shows high agreement in SdHO peak positions. These results confirm that no Zeeman-splitting-induced LL crossing occurs within the experimental maximum B of 14 T. Note that R_{xx} data for different θ are offset for clarity. The measurement T is 1.6 K. See Supplementary Note 2 for detailed discussions.

Extended Data Fig. 7 Three-dimensional illustration of particle–hole asymmetric Rashba bands in BAs with $B = 15$ T.

a, The spin–valley-flavoured Rashba bands in the VB of QL BAs. **b**, The Γ Rashba bands in the CB of QL BAs. The three-dimensional band structures of QL BAs are based on the calculation results in Extended Data Fig. 3 ($E_z = 0.3 \text{ V nm}^{-1}$). For the 2DHG, low, negative V_g creates two single-flavoured FSs with $\tau_z s_z = 1$, whereas high, negative V_g leads to the formation of inner–outer-nested FSs when E_F intersects oppositely flavoured spin channels. For the 2DEG, the FS topology is dependent on the relative position of E_F to the Zeeman energy gap E_S . Note that the high

in-plane band anisotropy in BAs has profound effects on the D^\pm Rashba formation, by pushing p_y orbitals to much higher energy. Without the unique puckering square lattice, the D^\pm valley would split into helical inner–outer Rashba bands centring on X. For the 2DEG, we can also see the square lattice warping of the Γ Rashba bands.

Extended Data Fig. 8 LL spectrum of the spin–valley-flavoured D^\pm valleys in QL BAs.

a, Spin–valley-flavoured D^\pm valleys in QL BAs under $E_z = 0.3 \text{ V nm}^{-1}$. Here, the D^- valley is placed on the left side of D^+ to highlight the fact that the D^\pm Rashba splitting is centred on the TRIM points of X. **b**, Flavour-dependent LL spectrum of the D^\pm Rashba valleys, in which LLs are divided into two groups (n_I and n_{II}) with opposite $\tau_z s_z$ signs. Note that the $n_I = 0$ and $n_{II} = 0$ LLs are spin non-degenerate, whereas all $n_i \neq 0$ LLs are doubly degenerate as required by TRS (see Supplementary Note 3).

Extended Data Fig. 9 DFT-calculated evolution of E_F versus V_g for the 2DHG and the 2DEG.

a, E_F positions of the 2DHG for $V_g = -2 \text{ V}$ and $V_g = -8 \text{ V}$, represented by blue and red lines, respectively, in the D^\pm Rashba valleys of QL BAs under $E_z = 0.2 \text{ V nm}^{-1}$. **b**, E_F positions of the 2DEG for $V_g = 2 \text{ V}$ and $V_g = 8.5 \text{ V}$, represented by blue and red lines, respectively, in the Γ Rashba valley of QL BAs under $E_z = 0.2 \text{ V nm}^{-1}$. As discussed in Supplementary Note 5, the V_g -induced charge carriers are mainly confined within four interfacial MLs with $E_z = 0.2 \text{ V nm}^{-1}$. By calculating the QL BAs band structure, the FS size and effective Fermi wavevector $\langle\langle k \rangle\rangle_{\langle\langle \rm F \rangle\rangle}^{\langle\langle \prime \rangle\rangle}$ can be determined for different chemical potentials measured from the VBM/CBM. It is also standard to extract the experimental k_F at different V_g for both the 2DHG and the 2DEG, by the LK formula fitting to the beating patterns of SdHOs. By matching the effective $\langle\langle k \rangle\rangle_{\langle\langle \rm F \rangle\rangle}^{\langle\langle \prime \rangle\rangle}$ to the experimental k_F , we can quantitatively get the positions of V_g -

dependent E_F in the electronic bands of BAs. It is clear that the DFT calculation results are highly consistent with the SdHO results.

Extended Data Fig. 10 Berry phase analysis by the LK formula fitting.

a, The black curve is a representative SdHO curve for the $V_g = +9$ V 2DEG measured at 0.27 K, compared with the red curve representing the LK fitting result. The fitting processes reveal a π phase change in high- V_g SdHOs at around 5 T, when cyclotron orbiting electrons of the inner FS are allowed to acquire a helical geometric phase without adverse inter LL scattering (the inset of **a**). **b**, The phase offsets versus V_g curve of the 2DEG obtained from the LK fitting. The reference line corresponds to the π Berry phase. For the 2DEG, at low V_g (< 5 V), both inner and outer pockets are trivial, consistent with the quantum Hall measurements in Fig. 3. As V_g increases above 7 V, the inner pocket acquires a Berry phase of π , whereas the outer FS remains trivial. The different band topology between the inner and outer FSs of the Γ Rashba valleys may be induced by square lattice warping or suggest the existence of hierarchical Rashba band splitting⁴⁰. **c**, The black curve is the SdHOs for the $V_g = -7$ V 2DHG, which is compared with the red curve from the LK fitting. **d**, V_g -dependent phase offsets of the 2DHG obtained from the LK fitting. For the 2DHG, the LK formula fitting confirms that both FSs, either two single flavoured pockets (low, positive V_g) or inner–outer-nested FSs, have trivial geometric phase offsets.

Supplementary information

Supplementary Information

This file contains Supplementary Notes 1-9, Supplementary References, and Supplementary Figures 1-13.

Peer Review File

Source data

[Source Data Fig. 2](#)

[Source Data Fig. 3](#)

[Source Data Fig. 4](#)

Rights and permissions

[Reprints and Permissions](#)

About this article



Check for
updates

Cite this article

Sheng, F., Hua, C., Cheng, M. *et al.* Rashba valleys and quantum Hall states in few-layer black arsenic. *Nature* **593**, 56–60 (2021).
<https://doi.org/10.1038/s41586-021-03449-8>

[Download citation](#)

- Received: 26 October 2020
- Accepted: 11 March 2021
- Published: 05 May 2021
- Issue Date: 06 May 2021
- DOI: <https://doi.org/10.1038/s41586-021-03449-8>

Comments

By submitting a comment you agree to abide by our [Terms](#) and [Community Guidelines](#). If you find something abusive or that does not comply with our terms or guidelines please flag it as inappropriate.

[Access through your institution](#)

[Change institution](#)

[Buy or subscribe](#)

This article was downloaded by **calibre** from <https://www.nature.com/articles/s41586-021-03449-8>

| [Section menu](#) | [Main menu](#) |

- Article
- [Published: 05 May 2021](#)

Polypeptide organic radical batteries

- [Tan P. Nguyen¹](#), [nal](#),
- [Alexandra D. Easley²](#), [nal](#),
- [Nari Kang²](#),
- [Sarosh Khan¹](#),
- [Soon-Mi Lim](#) [ORCID: orcid.org/0000-0002-7186-4629¹](#),
- [Yohannes H. Rezenom¹](#),
- [Shaoyang Wang³](#),
- [David K. Tran¹](#),
- [Jingwei Fan¹](#),
- [Rachel A. Letteri¹](#),
- [Xun He¹](#),
- [Lu Su¹](#),
- [Cheng-Han Yu¹](#),
- [Jodie L. Lutkenhaus](#) [ORCID: orcid.org/0000-0002-2613-6016^{1,3}](#) &
- [Karen L. Wooley](#) [ORCID: orcid.org/0000-0003-4086-384X^{1,2,3}](#)

[Nature](#) volume 593, pages61–66(2021)[Cite this article](#)

- 4236 Accesses
- 150 Altmetric
- [Metrics details](#)

Subjects

- [Batteries](#)
- [Electronic materials](#)
- [Polymer synthesis](#)

Abstract

In only a few decades, lithium-ion batteries have revolutionized technologies, enabling the proliferation of portable devices and electric vehicles¹, with substantial benefits for society. However, the rapid growth in technology has highlighted the ethical and environmental challenges of mining lithium, cobalt and other mineral ore resources, and the issues associated with the safe usage and non-hazardous disposal of batteries². Only a small fraction of lithium-ion batteries are recycled, further exacerbating global material supply of strategic elements^{3,4,5}. A potential alternative is to use organic-based redox-active materials^{6,7,8} to develop rechargeable batteries that originate from ethically sourced, sustainable materials and enable on-demand deconstruction and reconstruction. Making such batteries is challenging because the active materials must be stable during operation but degradable at end of life. Further, the degradation products should be either environmentally benign or recyclable for reconstruction into a new battery. Here we demonstrate a metal-free, polypeptide-based battery, in which viologens and nitroxide radicals are incorporated as redox-active groups along polypeptide backbones to function as anode and cathode materials, respectively. These redox-active polypeptides perform as active materials that are stable during battery operation and subsequently degrade on demand in acidic conditions to generate amino acids, other building blocks and degradation products. Such a polypeptide-based battery is a first step to addressing the need for alternative chemistries for green and sustainable batteries in a future circular economy.

[Access through your institution](#)

[Change institution](#)

[Buy or subscribe](#)

Access options

[Subscribe to Journal](#)

Get full journal access for 1 year

\$199.00

only \$3.90 per issue

[Subscribe](#)

All prices are NET prices.

VAT will be added later in the checkout.

Tax calculation will be finalised during checkout.

Rent or Buy article

Get time limited or full article access on ReadCube.

from \$8.99

[Rent or Buy](#)

All prices are NET prices.

Additional access options:

- [Log in](#)
- [Access through your institution](#)
- [Learn about institutional subscriptions](#)

Fig. 1: A polypeptide-based organic radical battery.

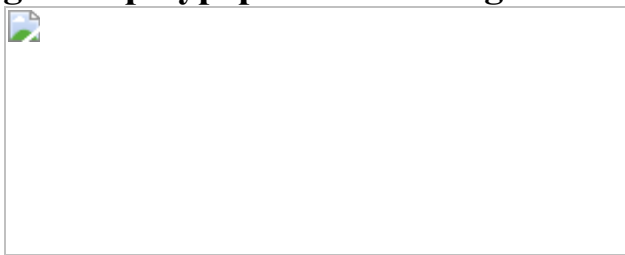


Fig. 2: Syntheses of redox-active polypeptides.

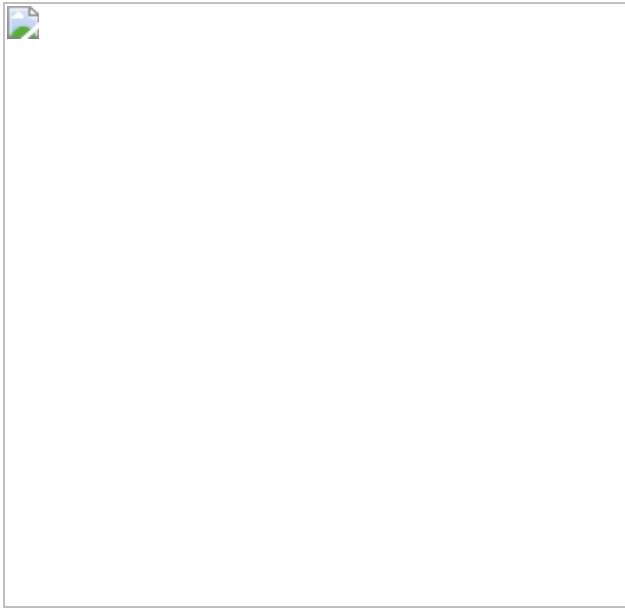


Fig. 3: Cyclic voltammograms of redox-active polypeptides.



Fig. 4: Electrochemical response of polypeptide composite half-cells and full cell.

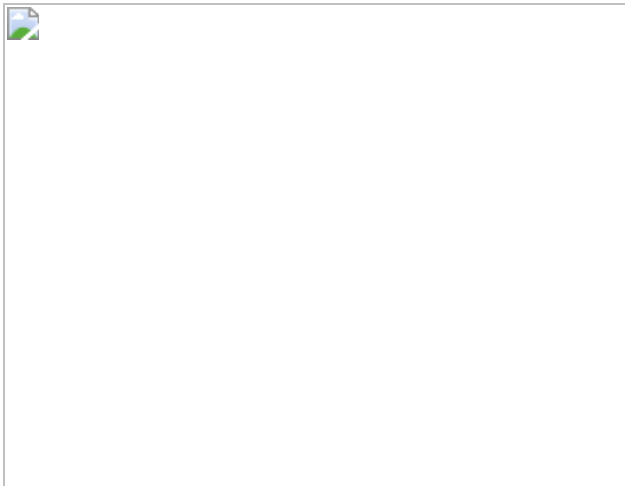


Fig. 5: Degradation of viologen and biTEMPO polypeptides.



Data availability

All data generated or analysed during this study are included in paper and its [Supplementary Information](#). [Source data](#) are provided with this paper.

References

1. 1.

Lopez, J., Mackanic, D. G., Cui, Y. & Bao, Z. Designing polymers for advanced battery chemistries. *Nat. Rev. Mater.* **4**, 312–330 (2019).

[CAS](#) [Article](#) [ADS](#) [Google Scholar](#)

2. 2.

Turcheniuk, K., Bondarev, D., Singhal, V. & Yushin, G. Ten years left to redesign lithium-ion batteries. *Nature* **559**, 467–470 (2018).

[CAS](#) [PubMed](#) [Article](#) [ADS](#) [PubMed Central](#) [Google Scholar](#)

3. 3.

Zeng, X., Li, J. & Singh, N. Recycling of spent lithium-ion battery: a critical review. *Crit. Rev. Environ. Sci. Technol.* **44**, 1129–1165 (2014).

[CAS](#) [Article](#) [Google Scholar](#)

4. 4.

Olivetti, E. A., Ceder, G., Gaustad, G. G. & Fu, X. Lithium-ion battery supply chain considerations: analysis of potential bottlenecks in critical metals. *Joule* **1**, 229–243 (2017).

[Article](#) [Google Scholar](#)

5. 5.

Wild, A., Strumpf, M., Häupler, B., Hager, M. D. & Schubert, U. S. All-organic battery composed of thianthrene- and TCAQ-based polymers. *Adv. Energy Mater.* **7**, 1601415 (2017).

[Article](#) [CAS](#) [Google Scholar](#)

6. 6.

Banza Lubaba Nkulu, C. et al. Sustainability of artisanal mining of cobalt in DR Congo. *Nat. Sustain.* **1**, 495–504 (2018).

[PubMed](#) [PubMed Central](#) [Article](#) [Google Scholar](#)

7. 7.

Koshika, K., Chikushi, N., Sano, N., Oyaizu, K. & Nishide, H. A TEMPO-substituted polyacrylamide as a new cathode material: an organic rechargeable device composed of polymer electrodes and aqueous electrolyte. *Green Chem.* **12**, 1573–1575 (2010).

[CAS](#) [Article](#) [Google Scholar](#)

8. 8.

Esquivel, J. P. et al. A metal-free and biotically degradable battery for portable single-use applications. *Adv. Energy Mater.* **7**, 1700275 (2017).

[Article](#) [CAS](#) [Google Scholar](#)

9. 9.

Friebe, C., Lex-Balducci, A. & Schubert, U. S. Sustainable energy storage: recent trends and developments toward fully organic batteries. *ChemSusChem* **12**, 4093 (2019).

[CAS](#) [PubMed](#) [PubMed Central](#) [Article](#) [Google Scholar](#)

10. 10.

Janoschka, T., Hager, M. D. & Schubert, U. S. Powering up the future: radical polymers for battery applications. *Adv. Mater.* **24**, 6397–6409 (2012).

[CAS](#) [PubMed](#) [Article](#) [PubMed Central](#) [Google Scholar](#)

11. 11.

Kim, J., Kim, J. H. & Ariga, K. Redox-active polymers for energy storage nanoarchitectonics. *Joule* **1**, 739–768 (2017).

[CAS](#) [Article](#) [Google Scholar](#)

12. 12.

Tomlinson, E. P., Hay, M. E. & Boudouris, B. W. Radical polymers and their application to organic electronic devices. *Macromolecules* **47**, 6145–6158 (2014).

[CAS](#) [Article](#) [ADS](#) [Google Scholar](#)

13. 13.

Lutkenhaus, J. A radical advance for conducting polymers. *Science* **359**, 1334–1335 (2018).

[CAS](#) [PubMed](#) [Article](#) [ADS](#) [PubMed Central](#) [Google Scholar](#)

14. 14.

Joo, Y., Agarkar, V., Sung, S. H., Savoie, B. M. & Boudouris, B. W. A nonconjugated radical polymer glass with high electrical conductivity. *Science* **359**, 1391–1395 (2018).

[CAS](#) [PubMed](#) [Article](#) [ADS](#) [PubMed Central](#) [Google Scholar](#)

15. 15.

Coates, G. W. & Getzler, Y. D. Y. L. Chemical recycling to monomer for an ideal, circular polymer economy. *Nat. Rev. Mater.* **5**, 501–516 (2020).

[CAS](#) [Article](#) [ADS](#) [Google Scholar](#)

16. 16.

Muench, S. et al. Polymer-based organic batteries. *Chem. Rev.* **116**, 9438–9484 (2016).

[CAS](#) [PubMed](#) [Article](#) [PubMed Central](#) [Google Scholar](#)

17. 17.

Zhang, K., Monteiro, M. J. & Jia, Z. Stable organic radical polymers: synthesis and applications. *Polym. Chem.* **7**, 5589–5614 (2016).

[CAS](#) [Article](#) [Google Scholar](#)

18. 18.

Janoschka, T. et al. An aqueous, polymer-based redox-flow battery using non-corrosive, safe, and low-cost materials. *Nature* **527**, 78–81 (2015).

[CAS](#) [PubMed](#) [Article](#) [ADS](#) [PubMed Central](#) [Google Scholar](#)

19. 19.

Koshika, K., Sano, N., Oyaizu, K. & Nishide, H. An aqueous, electrolyte-type, rechargeable device utilizing a hydrophilic radical polymer-cathode. *Macromol. Chem. Phys.* **210**, 1989–1995 (2009).

[CAS](#) [Article](#) [Google Scholar](#)

20. 20.

Sano, N. et al. Polyviologen hydrogel with high-rate capability for anodes toward an aqueous electrolyte-type and organic-based rechargeable device. *ACS Appl. Mater. Interfaces* **5**, 1355–1361 (2013).

[CAS](#) [PubMed](#) [Article](#) [PubMed Central](#) [Google Scholar](#)

21. 21.

Suga, T., Ohshiro, H., Sugita, S., Oyaizu, K. & Nishide, H. Emerging n-type redox-active radical polymer for a totally organic polymer-based rechargeable Battery. *Adv. Mater.* **21**, 1627–1630 (2009).

[CAS](#) [Article](#) [Google Scholar](#)

22. 22.

Suga, T., Sugita, S., Ohshiro, H., Oyaizu, K. & Nishide, H. p- and n-type bipolar redox-active radical polymer: toward totally organic polymer-based rechargeable devices with variable configuration. *Adv. Mater.* **23**, 751–754 (2011).

[CAS](#) [PubMed](#) [Article](#) [PubMed Central](#) [Google Scholar](#)

23. 23.

Oka, K., Kato, R., Oyaizu, K. & Nishide, H. Poly(vinyldibenzothiophenesulfone): its redox capability at very negative potential toward an all-organic rechargeable device with high-energy density. *Adv. Funct. Mater.* **28**, 1805858 (2018).

[Article](#) [CAS](#) [Google Scholar](#)

24. 24.

Qu, J. et al. Synthesis and properties of DNA complexes containing 2,2,6,6-tetramethyl-1-piperidinoxy (TEMPO) moieties as organic radical battery materials. *Chemistry* **14**, 3250–3259 (2008).

[CAS](#) [PubMed](#) [Article](#) [PubMed Central](#) [Google Scholar](#)

25. 25.

Ibe, T., Frings, R. B., Lachowicz, A., Kyo, S. & Nishide, H. Nitroxide polymer networks formed by Michael addition: on site-cured electrode-active organic coating. *Chem. Commun.* **46**, 3475–3477 (2010).

[CAS](#) [Article](#) [Google Scholar](#)

26. 26.

Qu, J. et al. Helical polyacetylenes carrying 2,2,6,6-tetramethyl-1-piperidinyloxy and 2,2,5,5-tetramethyl-1-pyrrolidinyloxy moieties: their synthesis, properties, and function. *J. Polym. Sci. A* **45**, 5431–5445 (2007).

[CAS](#) [Article](#) [Google Scholar](#)

27. 27.

Otaki, M. & Goto, H. Helical spin polymer with magneto-electro-optical activity. *Macromolecules* **52**, 3199–3209 (2019).

[CAS](#) [Article](#) [ADS](#) [Google Scholar](#)

28. 28.

Hatakeyama-Sato, K., Wakamatsu, H., Katagiri, R., Oyaizu, K. & Nishide, H. An ultrahigh output rechargeable electrode of a

hydrophilic radical polymer/nanocarbon hybrid with an exceptionally large current density beyond 1 A cm⁻². *Adv. Mater.* **30**, 1800900 (2018).

[Article](#) [CAS](#) [Google Scholar](#)

29. 29.

Hiejima, T. & Kaneko, J. Spiral configuration of nitroxide radicals along the polypeptide helix and their magnetic properties. *Macromolecules* **46**, 1713–1722 (2013).

[CAS](#) [Article](#) [ADS](#) [Google Scholar](#)

30. 30.

Belshaw, P. J., Mzengeza, S. & Lajoie, G. A. Chlorotrimethylsilane mediated formation of ω -allyl esters of aspartic and glutamic acids. *Synth. Commun.* **20**, 3157–3160 (1990).

[CAS](#) [Article](#) [Google Scholar](#)

31. 31.

Deming, T. J. Synthesis of side-chain modified polypeptides. *Chem. Rev.* **116**, 786–808 (2016).

[CAS](#) [PubMed](#) [Article](#) [PubMed Central](#) [Google Scholar](#)

32. 32.

Fan, J. et al. Construction of a versatile and functional nanoparticle platform derived from a helical diblock copolypeptide-based biomimetic polymer. *Polym. Chem.* **5**, 3977–3981 (2014).

[CAS](#) [PubMed](#) [PubMed Central](#) [Article](#) [Google Scholar](#)

33. 33.

Engler, A. C., Lee, H.-i. & Hammond, P. T. Highly efficient “grafting onto” a polypeptide backbone using click chemistry. *Angew. Chem. Int. Ed.* **48**, 9334–9338 (2009).

[CAS](#) [Article](#) [Google Scholar](#)

34. 34.

Hoyle, C. E. & Bowman, C. N. Thiol–ene click chemistry. *Angew. Chem. Int. Ed.* **49**, 1540–1573 (2010).

[CAS](#) [Article](#) [Google Scholar](#)

35. 35.

Hansen, K.-A. et al. A methoxyamine-protecting group for organic radical battery materials—an alternative approach. *ChemSusChem* **13**, 2386 (2020).

[CAS](#) [PubMed](#) [Article](#) [PubMed Central](#) [Google Scholar](#)

36. 36.

Galbo, J. P. Process for preparing N-methoxy derivatives of 4-hydroxy-2,2,6,6-tetramethylpiperidine and 2,2,6,6-tetramethyl-4-piperidone. US patent 5374729A (1994).

37. 37.

Deming, T. J. Noodle gels for cells. *Nat. Mater.* **9**, 535–536 (2010).

[CAS](#) [PubMed](#) [Article](#) [ADS](#) [PubMed Central](#) [Google Scholar](#)

38. 38.

Lalatsa, A., Schätzlein, A. G., Mazza, M., Le, T. B. H. & Uchegbu, I. F. Amphiphilic poly(l-amino acids) — new materials for drug delivery. *J. Control. Release* **161**, 523–536 (2012).

[CAS](#) [PubMed](#) [Article](#) [PubMed Central](#) [Google Scholar](#)

39. 39.

Matson, J. B. & Stupp, S. I. Self-assembling peptide scaffolds for regenerative medicine. *Chem. Commun.* **48**, 26–33 (2012).

[CAS](#) [Article](#) [Google Scholar](#)

40. 40.

Shpilevaya, I. & Foord, J. S. Electrochemistry of methyl viologen and anthraquinonedisulfonate at diamond and diamond powder electrodes: the influence of surface chemistry. *Electroanalysis* **26**, 2088–2099 (2014).

[CAS](#) [Article](#) [Google Scholar](#)

41. 41.

Bard, A. J. & Faulkner, L. R. *Electrochemical Methods: Fundamentals and Applications* 2nd edn, Ch. 6 (Wiley, 2000).

42. 42.

Bugnon, L., Morton, C. J. H., Novak, P., Vetter, J. & Nesvadba, P. Synthesis of poly(4-methacryloyloxy-TEMPO) via group-transfer polymerization and its evaluation in organic radical battery. *Chem. Mater.* **19**, 2910–2914 (2007).

[CAS](#) [Article](#) [Google Scholar](#)

43. 43.

Janoschka, T. et al. Reactive inkjet printing of cathodes for organic radical batteries. *Adv. Energy Mater.* **3**, 1025–1028 (2013).

[CAS](#) [Article](#) [Google Scholar](#)

44. 44.

Vlad, A., Rolland, J., Hauffman, G., Ernould, B. & Gohy, J.-F. Melt-polymerization of TEMPO methacrylates with nano carbons enables superior battery materials. *ChemSusChem* **8**, 1692–1696 (2015).

[CAS](#) [PubMed](#) [Article](#) [PubMed Central](#) [Google Scholar](#)

45. 45.

Lutkenhaus, J. et al. Solution-processable thermally crosslinked organic radical polymer battery cathodes. *ChemSusChem* **13**, 2371 (2020).

[PubMed](#) [Article](#) [CAS](#) [PubMed Central](#) [Google Scholar](#)

46. 46.

Elsabahy, M., Samarajeewa, S., Raymond, J. E., Clark, C. & Wooley, K. L. Shell-crosslinked knedel-like nanoparticles induce lower immunotoxicity than their non-crosslinked analogs. *J. Mater. Chem. B* **1**, 5241–5255 (2013).

[CAS](#) [Article](#) [Google Scholar](#)

[Download references](#)

Acknowledgements

This work was financially supported by the National Science Foundation (DMR-1507429, DMR-1905818, CHE-2003771 and DMREF-1629094; K.L.W. and T.P.N.; synthesis and structural characterization), the Welch Foundation (A-0001, K.L.W.; A-1717, C.-H.Y.) and the US Department of Energy Office of Science (DE-SC0014006; J.L.L. and A.D.E.; electrochemical measurements). A.D.E. acknowledges support by a National Science Foundation Graduate Research Fellowship.

Author information

Author notes

1. These authors contributed equally: Tan P. Nguyen, Alexandra D. Easley

Affiliations

1. Department of Chemistry, Texas A&M University, College Station, TX, USA

Tan P. Nguyen, Sarosh Khan, Soon-Mi Lim, Yohannes H. Rezenom, David K. Tran, Jingwei Fan, Rachel A. Letteri, Xun He, Lu Su, Cheng-Han Yu, Jodie L. Lutkenhaus & Karen L. Wooley

2. Department of Materials Science and Engineering, Texas A&M University, College Station, TX, USA

Alexandra D. Easley, Nari Kang & Karen L. Wooley

3. Artie McFerrin Department of Chemical Engineering, Texas A&M University, College Station, TX, USA

Shaoyang Wang, Jodie L. Lutkenhaus & Karen L. Wooley

Authors

1. Tan P. Nguyen

[View author publications](#)

You can also search for this author in [PubMed](#) [Google Scholar](#)

2. Alexandra D. Easley

[View author publications](#)

You can also search for this author in [PubMed](#) [Google Scholar](#)

3. Nari Kang

[View author publications](#)

You can also search for this author in [PubMed](#) [Google Scholar](#)

4. Sarosh Khan

[View author publications](#)

You can also search for this author in [PubMed](#) [Google Scholar](#)

5. Soon-Mi Lim

[View author publications](#)

You can also search for this author in [PubMed](#) [Google Scholar](#)

6. Yohannes H. Rezenom

[View author publications](#)

You can also search for this author in [PubMed](#) [Google Scholar](#)

7. Shaoyang Wang

[View author publications](#)

You can also search for this author in [PubMed](#) [Google Scholar](#)

8. David K. Tran

[View author publications](#)

You can also search for this author in [PubMed](#) [Google Scholar](#)

9. Jingwei Fan

[View author publications](#)

You can also search for this author in [PubMed](#) [Google Scholar](#)

10. Rachel A. Letteri

[View author publications](#)

You can also search for this author in [PubMed](#) [Google Scholar](#)

11. Xun He

[View author publications](#)

You can also search for this author in [PubMed](#) [Google Scholar](#)

12. Lu Su

[View author publications](#)

You can also search for this author in [PubMed](#) [Google Scholar](#)

13. Cheng-Han Yu

[View author publications](#)

You can also search for this author in [PubMed](#) [Google Scholar](#)

14. Jodie L. Lutkenhaus

[View author publications](#)

You can also search for this author in [PubMed](#) [Google Scholar](#)

15. Karen L. Wooley

[View author publications](#)

You can also search for this author in [PubMed](#) [Google Scholar](#)

Contributions

T.P.N. and A.D.E. contributed equally to this work. T.P.N., A.D.E., J.L.L. and K.L.W. developed the study. T.P.N. synthesized and structurally characterized the viologen and biTEMPO polypeptides. A.D.E. performed the electrochemical characterization of the materials. XPS and scanning electron microscopy data were obtained by N.K., electron paramagnetic resonance by S.W. and thermal characterization by A.D.E. and D.K.T. The degradation study was done by T.P.N., with help from Y.H.R. for mass spectrometry. The cytotoxicity study was done by S.K. and S.-M.L. The manuscript was written by T.P.N. and A.D.E., with help from J.F., R.A.L., X.H., L.S., C.-H.Y., J.L.L. and K.L.W.

Corresponding authors

Correspondence to [Jodie L. Lutkenhaus](#) or [Karen L. Wooley](#).

Ethics declarations

Competing interests

The authors declare no competing interests.

Additional information

Peer review information *Nature* thanks Jung Ho Kim, David Mercerreyes and Ulrich Schubert for their contribution to the peer review of this work.

Publisher's note Springer Nature remains neutral with regard to jurisdictional claims in published maps and institutional affiliations.

Extended data figures and tables

[**Extended Data Fig. 1 Molecular structures of viologen and biTEMPO analogues**](#)

[**Extended Data Fig. 2 Electrochemistry assemblies.**](#)

a, The half sandwich cell: viol-Cl or biTEMPO polypeptide composite working electrode and lithium metal reference electrode, with a filter-paper separator. **b**, The full sandwich cell: viol-Cl polypeptide composite working electrode and biTEMPO polypeptide composite reference electrode, with a filter-paper separator.

[**Extended Data Fig. 3 Electrochemical performance of full cell without polypeptide active material as a control.**](#)

Electrochemical characterization of a PVDF + CB symmetric full cell is shown, including cyclic voltammograms (i), charge–discharge curves (ii) and cycling response at 1C (iii) (PVDF + CB composite electrode, 0.5 M TBACF₃SO₃ in PC and filter paper, PVDF + CB composite electrode). The composite electrodes were cast in an identical manner to the polypeptide composite electrodes, with a composition of 86 wt% CB and 14 wt% PVDF on ITO-coated glass substrates. After 250 cycles, the capacity was 1.7 mA h g⁻¹, whereas the capacity of the polypeptide-based full cell was 7.5 mA h g⁻¹ (Fig. 4g–i).

[Extended Data Fig. 4 Electrode morphology before and after testing the full cell.](#)

a, b, Scanning electron micrographs of the viol-Cl polypeptide composite electrode (**a**) and the biTEMPO polypeptide composite electrode (**b**), before (i) and after (ii) 50 charge–discharge cycles in the full sandwich cell configuration (viol-Cl polypeptide composite electrode, 0.5 M TBACF₃SO₃ in PC and filter paper, biTEMPO polypeptide composite electrode). [Source data](#)

[Extended Data Fig. 5 Cell viability study.](#)

Dose–response curves for redox-active polypeptides. Data are expressed as mean ± s.d. of three determinations. The statistical analysis was performed using GraphPad Prism, with the black lines representing four-parameter fits. [Source data](#)

[Extended Data Fig. 6 Cell viability study.](#)

Dose–response curves for redox-active polypeptides after acid degradation. Data are expressed as mean ± s.d. of three determinations. The statistical analysis was performed using GraphPad Prism, with the black lines representing four-parameter fits. [Source data](#)

[Extended Data Fig. 7 Cell viability study.](#)

Comparison of IC₅₀ values of viologen polypeptide, biTEMPO polypeptide, viologen analogue, biTEMPO analogue and their degraded products.

[Source data](#)

Extended Data Table 1 Performance of selected polymer-based batteries

[Full size table](#)

Extended Data Table 2 Elemental analysis of the synthesized polymers

[Full size table](#)

Extended Data Table 3 Degradation conditions used for the viologen and biTEMPO polypeptides

[Full size table](#)

Supplementary information

[Supplementary Information](#)

This file contains supplementary experimental procedures for additional electrochemistry characterizations and the synthetic details for the viologen and BiTEMPO polypeptides and their analogs. Spectral data (NMR and FTIR) is provided for all the synthesized species. Supplementary Figures are provided for electrochemical, degradation, and cell viability studies.

Source data

[Source Data Fig. 3](#)

[Source Data Fig. 4](#)

[Source Data Extended Data Fig. 4](#)

[Source Data Extended Data Fig. 5](#)

[Source Data Extended Data Fig. 6](#)

[Source Data Extended Data Fig. 7](#)

Rights and permissions

[Reprints and Permissions](#)

About this article



Check for
updates

Cite this article

Nguyen, T.P., Easley, A.D., Kang, N. *et al.* Polypeptide organic radical batteries. *Nature* **593**, 61–66 (2021). <https://doi.org/10.1038/s41586-021-03399-1>

[Download citation](#)

- Received: 13 May 2020
- Accepted: 26 February 2021
- Published: 05 May 2021
- Issue Date: 06 May 2021
- DOI: <https://doi.org/10.1038/s41586-021-03399-1>

Comments

By submitting a comment you agree to abide by our [Terms](#) and [Community Guidelines](#). If you find something abusive or that does not comply with our terms or guidelines please flag it as inappropriate.

[Access through your institution](#)

[Change institution](#)

[Buy or subscribe](#)

This article was downloaded by **calibre** from <https://www.nature.com/articles/s41586-021-03399-1>

| [Section menu](#) | [Main menu](#) |

- Article
- [Published: 05 May 2021](#)

Correlative operando microscopy of oxygen evolution electrocatalysts

- [J. Tyler Mefford](#) [ORCID: orcid.org/0000-0003-4965-4147^{1,2}](#),
- [Andrew R. Akbashev](#) [ORCID: orcid.org/0000-0003-1573-1773^{1,2}](#),
- [Minkyung Kang](#) [ORCID: orcid.org/0000-0003-3248-8496³](#),
- [Cameron L. Bentley](#) [ORCID: orcid.org/0000-0001-7867-6068³](#),
- [William E. Gent](#) [ORCID: orcid.org/0000-0001-7663-3988¹](#),
- [Haitao D. Deng¹](#),
- [Daan Hein Alsem⁴](#),
- [Young-Sang Yu](#) [ORCID: orcid.org/0000-0002-0545-9019⁵](#),
- [Norman J. Salmon⁴](#),
- [David A. Shapiro](#) [ORCID: orcid.org/0000-0002-4186-6017⁵](#),
- [Patrick R. Unwin](#) [ORCID: orcid.org/0000-0003-3106-2178³](#) &
- [William C. Chueh](#) [ORCID: orcid.org/0000-0002-7066-3470^{1,2}](#)

[Nature](#) volume 593, pages67–73(2021)[Cite this article](#)

- 3074 Accesses
- 62 Altmetric
- [Metrics details](#)

Subjects

- [Electrocatalysis](#)
- [Energy](#)
- [Microscopy](#)

Abstract

Transition metal (oxy)hydroxides are promising electrocatalysts for the oxygen evolution reaction^{1,2,3}. The properties of these materials evolve dynamically and heterogeneously⁴ with applied voltage through ion insertion redox reactions, converting materials that are inactive under open circuit conditions into active electrocatalysts during operation⁵. The catalytic state is thus inherently far from equilibrium, which complicates its direct observation. Here, using a suite of correlative operando scanning probe and X-ray microscopy techniques, we establish a link between the oxygen evolution activity and the local operational chemical, physical and electronic nanoscale structure of single-crystalline $\beta\text{-Co(OH)}_2$ platelet particles. At pre-catalytic voltages, the particles swell to form an $\alpha\text{-CoO}_2\text{H}_{1.5}\cdot0.5\text{H}_2\text{O}$ -like structure—produced through hydroxide intercalation—in which the oxidation state of cobalt is +2.5. Upon increasing the voltage to drive oxygen evolution, interlayer water and protons de-intercalate to form contracted $\beta\text{-CoOOH}$ particles that contain Co^{3+} species. Although these transformations manifest heterogeneously through the bulk of the particles, the electrochemical current is primarily restricted to their edge facets. The observed Tafel behaviour is correlated with the local concentration of Co^{3+} at these reactive edge sites, demonstrating the link between bulk ion-insertion and surface catalytic activity.

[Access through your institution](#)

[Change institution](#)

[Buy or subscribe](#)

Access options

Subscribe to Journal

Get full journal access for 1 year

\$199.00

only \$3.90 per issue

Subscribe

All prices are NET prices.
VAT will be added later in the checkout.
Tax calculation will be finalised during checkout.

Rent or Buy article

Get time limited or full article access on ReadCube.

from \$8.99

Rent or Buy

All prices are NET prices.

Additional access options:

- [Log in](#)
- [Access through your institution](#)
- [Learn about institutional subscriptions](#)

Fig. 1: Mass loading and scan-rate-dependent electrochemistry of β -Co(OH)₂.

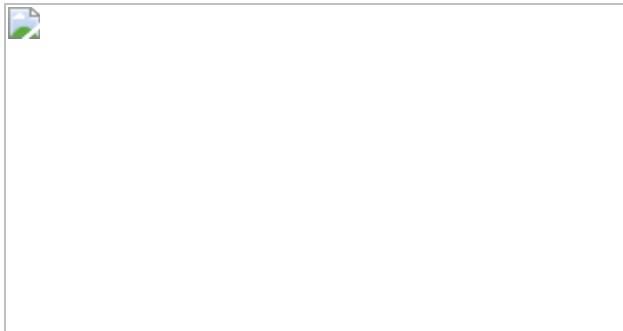


Fig. 2: SECCM of bulk redox transformations and OER activity of β -Co(OH)₂ particles.

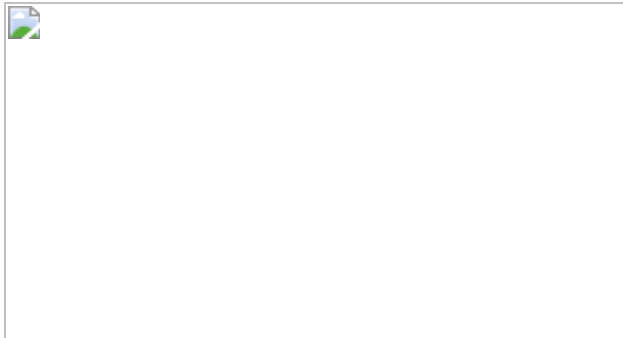


Fig. 3: Operando EC-AFM of a β -Co(OH)₂ particle.

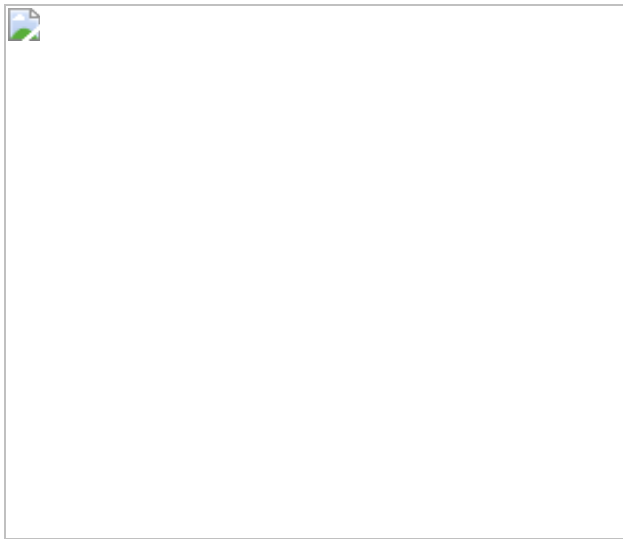


Fig. 4: Operando STXM of β -Co(OH)₂ particles.

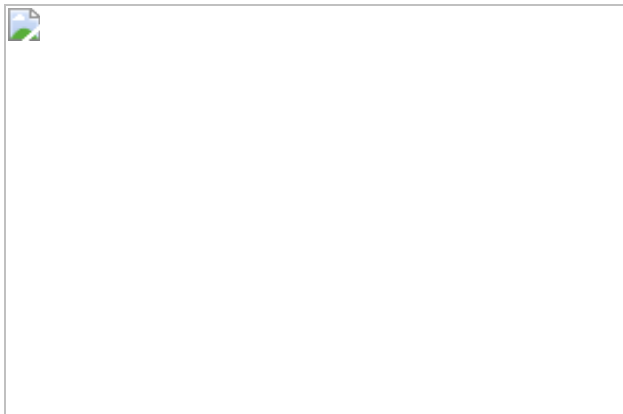
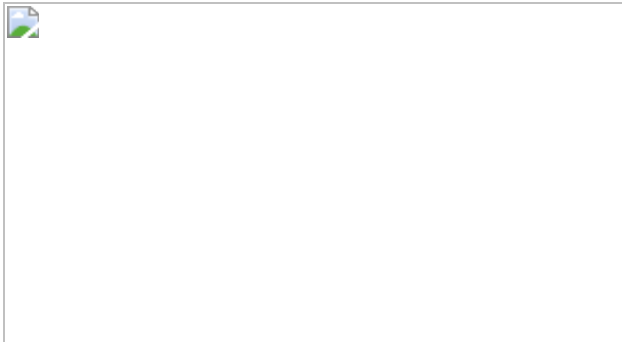


Fig. 5: Correlations between Co oxidation state at the edge of the particles and OER activity.



Data availability

The experimental data that support the findings of this study are available in ref. [31](#).

References

1. 1.

Burke, M. S., Enman, L. J., Batchellor, A. S., Zou, S. & Boettcher, S. W. Oxygen evolution reaction electrocatalysis on transition metal oxides and (oxy)hydroxides: activity trends and design principles. *Chem. Mater.* **27**, 7549–7558 (2015).

[CAS Article](#) [Google Scholar](#)

2. 2.

Hong, W. T. et al. Toward the rational design of non-precious transition metal oxides for oxygen electrocatalysis. *Energy Environ. Sci.* **8**, 1404–1427 (2015).

[CAS Article](#) [Google Scholar](#)

3. 3.

Dau, H. et al. The mechanism of water oxidation: from electrolysis via homogeneous to biological catalysis. *ChemCatChem* **2**, 724–761

(2010).

[CAS](#) [Article](#) [Google Scholar](#)

4. 4.

Kuai, C. et al. Phase segregation reversibility in mixed-metal hydroxide water oxidation catalysts. *Nat. Catal.* **3**, 743–753 (2020).

[CAS](#) [Article](#) [Google Scholar](#)

5. 5.

Mefford, J. T., Zhao, Z., Bajdich, M. & Chueh, W. C. Interpreting Tafel behavior of consecutive electrochemical reactions through combined thermodynamic and steady state microkinetic approaches. *Energy Environ. Sci.* **13**, 622–634 (2020).

[CAS](#) [Article](#) [Google Scholar](#)

6. 6.

Mefford, J. T., Akbashev, A. R., Zhang, L. & Chueh, W. C. Electrochemical reactivity of faceted β -Co(OH)₂ single crystal platelet particles in alkaline electrolytes. *J. Phys. Chem. C* **123**, 18783–18794 (2019).

[CAS](#) [Article](#) [Google Scholar](#)

7. 7.

Doyle, A. D., Bajdich, M. & Vojvodic, A. Theoretical insights to bulk activity towards oxygen evolution in oxyhydroxides. *Catal. Lett.* **147**, 1533–1539 (2017).

[Article](#) [Google Scholar](#)

8. 8.

Burke, M. S., Kast, M. G., Trotochaud, L., Smith, A. M. & Boettcher, S. W. Cobalt–iron (oxy)hydroxide oxygen evolution electrocatalysts: the role of structure and composition on activity, stability, and mechanism. *J. Am. Chem. Soc.* **137**, 3638–3648 (2015).

[CAS](#) [PubMed](#) [Article](#) [Google Scholar](#)

9. 9.

Wahab, O. J., Kang, M. & Unwin, P. R. Scanning electrochemical cell microscopy: A natural technique for single entity electrochemistry. *Curr. Opin. Electrochem.* **22**, 120–128 (2020).

[CAS](#) [Article](#) [Google Scholar](#)

10. 10.

Bentley, C. L. et al. Nanoscale electrochemical mapping. *Anal. Chem.* **91**, 84–108 (2019).

[CAS](#) [PubMed](#) [Article](#) [Google Scholar](#)

11. 11.

Bentley, C. L., Kang, M. & Unwin, P. R. Nanoscale structure dynamics within electrocatalytic materials. *J. Am. Chem. Soc.* **139**, 16813–16821 (2017).

[CAS](#) [PubMed](#) [Article](#) [Google Scholar](#)

12. 12.

Bajdich, M., García-Mota, M., Vojvodic, A., Nørskov, J. K. & Bell, A. T. Theoretical investigation of the activity of cobalt oxides for the electrochemical oxidation of water. *J. Am. Chem. Soc.* **135**, 13521–13530 (2013).

[CAS](#) [PubMed](#) [Article](#) [Google Scholar](#)

13. 13.

Stevens, M. B. et al. Ternary Ni-Co-Fe oxyhydroxide oxygen evolution catalysts: Intrinsic activity trends, electrical conductivity, and electronic band structure. *Nano Res.* **12**, 2288–2295 (2019).

[CAS](#) [Article](#) [Google Scholar](#)

14. 14.

Dette, C., Hurst, M. R., Deng, J., Nellist, M. R. & Boettcher, S. W. Structural evolution of metal (oxy)hydroxide nanosheets during the oxygen evolution reaction. *ACS Appl. Mater. Interfaces* **11**, 5590–5594 (2019).

[CAS](#) [PubMed](#) [Article](#) [Google Scholar](#)

15. 15.

Toma, F. M. et al. Mechanistic insights into chemical and photochemical transformations of bismuth vanadate photoanodes. *Nat. Commun.* **7**, 12012 (2016).

[ADS](#) [PubMed](#) [PubMed Central](#) [Article](#) [Google Scholar](#)

16. 16.

Kamachi, M. U. & Padhy, N. Electrochemical scanning probe microscope (EC-SPM) for the in situ corrosion study of materials: an overview with examples. *Corros. Rev.* **29**, 73–103 (2011).

[Google Scholar](#)

17. 17.

Deng, J. et al. Morphology dynamics of single-layered $\text{Ni(OH)}_2/\text{NiOOH}$ nanosheets and subsequent Fe incorporation studied by in situ electrochemical atomic force microscopy. *Nano Lett.* **17**, 6922–6926 (2017).

[ADS](#) [CAS](#) [PubMed](#) [Article](#) [Google Scholar](#)

18. 18.

Bernard, P. et al. AC quartz crystal microbalance applied to the studies of the nickel hydroxide behaviour in alkaline solutions. *Electrochim. Acta* **36**, 743–746 (1991).

[CAS](#) [Article](#) [Google Scholar](#)

19. 19.

Young, M. J., Kiryutina, T., Bedford, N. M., Woehl, T. J. & Segre, C. U. Discovery of anion insertion electrochemistry in layered hydroxide nanomaterials. *Sci. Rep.* **9**, 2462 (2019).

[ADS](#) [PubMed](#) [PubMed Central](#) [Article](#) [Google Scholar](#)

20. 20.

Li, F., Hillman, A. R., Lubetkin, S. D. & Roberts, D. J. Electrochemical quartz crystal microbalance studies of potentiodynamic electrolysis of aqueous chloride solution: surface processes and evolution of H₂ and Cl₂ gas bubbles. *J. Electroanal. Chem. (Lausanne)* **335**, 345–362 (1992).

[CAS](#) [Article](#) [Google Scholar](#)

21. 21.

Cherepanova, S., Leont'eva, N., Drozdov, V. & Doronin, V. Thermal evolution of Mg-Al and Ni-Al layered double hydroxides: the structure of the dehydrated phase. *Acta Crystallogr. A* **72**, 651–659 (2016).

[CAS](#) [Article](#) [Google Scholar](#)

22. 22.

Ma, R. et al. Tetrahedral Co(II) coordination in α -type cobalt hydroxide: Rietveld refinement and X-ray absorption spectroscopy. *Inorg. Chem.* **45**, 3964–3969 (2006).

[CAS](#) [PubMed](#) [Article](#) [Google Scholar](#)

23. 23.

Hall, D. S., Lockwood, D. J., Bock, C. & MacDougall, B. R. Nickel hydroxides and related materials: a review of their structures, synthesis and properties. *Proc. R. Soc. A* **471**, 20140792 (2015).

[ADS](#) [PubMed](#) [Article](#) [Google Scholar](#)

24. 24.

Liu, S., Li, L., Patterson, N. A. & Manthiram, A. Morphological transformations during in situ electrochemical generation of 2-dimensional Co_3O_4 hexagonal nanoplates. *J. Electrochem. Soc.* **163**, A150–A155 (2016).

[CAS](#) [Article](#) [Google Scholar](#)

25. 25.

Lim, J. et al. Origin and hysteresis of lithium compositional spatiodynamics within battery primary particles. *Science* **353**, 566–571 (2016).

[ADS](#) [CAS](#) [PubMed](#) [Article](#) [Google Scholar](#)

26. 26.

Gerken, J. B. et al. Electrochemical water oxidation with cobalt-based electrocatalysts from pH 0–14: the thermodynamic basis for catalyst structure, stability, and activity. *J. Am. Chem. Soc.* **133**, 14431–14442 (2011).

[CAS](#) [PubMed](#) [Article](#) [Google Scholar](#)

27. 27.

McAlpin, J. G. et al. EPR evidence for Co(IV) species produced during water oxidation at neutral pH. *J. Am. Chem. Soc.* **132**, 6882–6883 (2010).

[CAS](#) [PubMed](#) [Article](#) [Google Scholar](#)

28. 28.

Risch, M. et al. Water oxidation by amorphous cobalt-based oxides: in situ tracking of redox transitions and mode of catalysis. *Energy Environ. Sci.* **8**, 661–674 (2015).

[CAS](#) [Article](#) [Google Scholar](#)

29. 29.

Kanan, M. W. et al. Structure and valency of a cobalt-phosphate water oxidation catalyst determined by in situ X-ray spectroscopy. *J. Am. Chem. Soc.* **132**, 13692–13701 (2010).

[CAS](#) [PubMed](#) [Article](#) [Google Scholar](#)

30. 30.

Bergmann, A. et al. Unified structural motifs of the catalytically active state of Co(oxyhydr)oxides during the electrochemical oxygen evolution reaction. *Nat. Catal.* **1**, 711–719 (2018).

[CAS](#) [Article](#) [Google Scholar](#)

31. 31.

Mefford, J. T. Replication data for "Correlative operando microscopy of oxygen evolution electrocatalysts".
<https://doi.org/10.7910/DVN/TNTHXS> (2021).

[Download references](#)

Acknowledgements

J.T.M., A.R.A., W.E.G. and W.C.C. acknowledge funding provided by the US Department of Energy (DOE), Office of Basic Energy Sciences, Division of Materials Sciences and Engineering (contract no. DE-AC0276SF00515). C.L.B. acknowledges financial support from the Ramsay Memorial Fellowship Trust. Both M.K. and P.R.U. acknowledge support from Warwick-Monash Alliance Accelerator funding. Separately, P.R.U. acknowledges support from a Royal Society Wolfson Research Merit Award. Part of this work was performed at the Stanford Nano Shared Facilities (SNSF)/Stanford Nano-fabrication Facility (SNF), supported by the National Science Foundation under award ECCS-1542152. D.H.A. and N.J.S. acknowledge support from the DOE Office of Basic Energy Sciences SBIR program under awards DE-SC-0007691 and DE-SC-0009573. This research used resources of the Advanced Light Source, which is a DOE Office of Science User Facility under contract no. DE-AC02-05CH11231. We thank J. Lim, S. B. Kalirai, C. Baeumer, L. Zhang, Y.-L. Liang and C. E. D. Chidsey for discussions and assistance with the experiments.

Author information

Affiliations

1. Department of Materials Science and Engineering, Stanford University, Stanford, CA, USA

J. Tyler Mefford, Andrew R. Akbashev, William E. Gent, Haitao D. Deng & William C. Chueh

2. Stanford Institute for Materials and Energy Sciences, SLAC National Accelerator Laboratory, Menlo Park, CA, USA

J. Tyler Mefford, Andrew R. Akbashev & William C. Chueh

3. Department of Chemistry, University of Warwick, Coventry, UK

Minkyung Kang, Cameron L. Bentley & Patrick R. Unwin

4. Hummingbird Scientific, Lacey, WA, USA

Daan Hein Alsem & Norman J. Salmon

5. Advanced Light Source, Lawrence Berkeley National Laboratory, Berkeley, CA, USA

Young-Sang Yu & David A. Shapiro

Authors

1. J. Tyler Mefford

[View author publications](#)

You can also search for this author in [PubMed](#) [Google Scholar](#)

2. Andrew R. Akbashev

[View author publications](#)

You can also search for this author in [PubMed](#) [Google Scholar](#)

3. Minkyung Kang

[View author publications](#)

You can also search for this author in [PubMed](#) [Google Scholar](#)

4. Cameron L. Bentley

[View author publications](#)

You can also search for this author in [PubMed](#) [Google Scholar](#)

5. William E. Gent

[View author publications](#)

You can also search for this author in [PubMed](#) [Google Scholar](#)

6. Haitao D. Deng

[View author publications](#)

You can also search for this author in [PubMed](#) [Google Scholar](#)

7. Daan Hein Alsem

[View author publications](#)

You can also search for this author in [PubMed](#) [Google Scholar](#)

8. Young-Sang Yu

[View author publications](#)

You can also search for this author in [PubMed](#) [Google Scholar](#)

9. Norman J. Salmon

[View author publications](#)

You can also search for this author in [PubMed](#) [Google Scholar](#)

10. David A. Shapiro

[View author publications](#)

You can also search for this author in [PubMed](#) [Google Scholar](#)

11. Patrick R. Unwin

[View author publications](#)

You can also search for this author in [PubMed](#) [Google Scholar](#)

12. William C. Chueh

[View author publications](#)

You can also search for this author in [PubMed](#) [Google Scholar](#)

Contributions

J.T.M. and W.C.C. developed the concept of the experiments, J.T.M. performed the synthesis, STXM, UV-vis, EQCM, RDE, SEM and XRD experiments. A.R.A. performed the EC-AFM and TEM experiments. P.R.U., M.K. and C.L.B. designed and performed the SECCM experiments. W.E.G. wrote the principal components analysis and non-negative matrix

factorization code for the STXM data analysis. H.D.D. performed the EC-AFM image alignment. D.H.A. and N.J.S. designed and fabricated the STXM cell. Y.-S.Y. and D.A.S. assisted with the STXM experiments. All authors contributed to the discussion of the results and writing of the manuscript.

Corresponding authors

Correspondence to [J. Tyler Mefford](#) or [William C. Chueh](#).

Ethics declarations

Competing interests

D.H.A. and N.J.S. are employed by Hummingbird Scientific, which designed and manufactured the STXM microfluidic liquid cell used in these experiments.

Additional information

Peer review information *Nature* thanks Shannon Boettcher, Marcel Risch and the other, anonymous, reviewer(s) for their contribution to the peer review of this work. Peer reviewer reports are available.

Publisher's note Springer Nature remains neutral with regard to jurisdictional claims in published maps and institutional affiliations.

Supplementary information

[Supplementary Information](#)

This file contains supplementary text, supplementary figures 1 – 12, supplementary equations and supplementary references.

[Peer Review File](#)

Supplementary Video 1

Supplementary Video 2

Rights and permissions

Reprints and Permissions

About this article



Check for
updates

Cite this article

Mefford, J.T., Akbashev, A.R., Kang, M. *et al.* Correlative operando microscopy of oxygen evolution electrocatalysts. *Nature* **593**, 67–73 (2021). <https://doi.org/10.1038/s41586-021-03454-x>

Download citation

- Received: 19 February 2020
- Accepted: 15 March 2021
- Published: 05 May 2021
- Issue Date: 06 May 2021
- DOI: <https://doi.org/10.1038/s41586-021-03454-x>

Comments

By submitting a comment you agree to abide by our [Terms](#) and [Community Guidelines](#). If you find something abusive or that does not comply with our terms or guidelines please flag it as inappropriate.

[Access through your institution](#)

[Change institution](#)

[Buy or subscribe](#)

This article was downloaded by **calibre** from <https://www.nature.com/articles/s41586-021-03454-x>

| [Section menu](#) | [Main menu](#) |

- Article
- [Published: 05 May 2021](#)

Projected land ice contributions to twenty-first-century sea level rise

- [Tamsin L. Edwards](#) ORCID: [orcid.org/0000-0002-4760-4704¹](https://orcid.org/0000-0002-4760-4704),
- [Sophie Nowicki](#)^{2,3},
- [Ben Marzeion](#) ORCID: [orcid.org/0000-0002-6185-3539^{4,5}](https://orcid.org/0000-0002-6185-3539),
- [Regine Hock](#) ORCID: [orcid.org/0000-0001-8336-9441^{6,7}](https://orcid.org/0000-0001-8336-9441),
- [Heiko Goelzer](#) ORCID: [orcid.org/0000-0002-5878-9599^{8,9,10}](https://orcid.org/0000-0002-5878-9599),
- [Hélène Seroussi](#) ORCID: [orcid.org/0000-0001-9201-1644¹¹](https://orcid.org/0000-0001-9201-1644),
- [Nicolas C. Jourdain](#) ORCID: [orcid.org/0000-0002-1372-2235¹²](https://orcid.org/0000-0002-1372-2235),
- [Donald A. Slater](#) ORCID: [orcid.org/0000-0001-8394-6149^{13,14,15}](https://orcid.org/0000-0001-8394-6149),
- [Fiona E. Turner](#)¹,
- [Christopher J. Smith](#) ORCID: [orcid.org/0000-0003-0599-4633^{16,17}](https://orcid.org/0000-0003-0599-4633),
- [Christine M. McKenna](#) ORCID: [orcid.org/0000-0002-9677-4582¹⁶](https://orcid.org/0000-0002-9677-4582),
- [Erika Simon](#)²,
- [Ayako Abe-Ouchi](#) ORCID: [orcid.org/0000-0003-1745-5952¹⁸](https://orcid.org/0000-0003-1745-5952),
- [Jonathan M. Gregory](#)^{19,20},
- [Eric Larour](#)¹¹,
- [William H. Lipscomb](#) ORCID: [orcid.org/0000-0002-7100-3730²¹](https://orcid.org/0000-0002-7100-3730),
- [Antony J. Payne](#)²²,
- [Andrew Shepherd](#)²³,
- [Cécile Agosta](#) ORCID: [orcid.org/0000-0003-4091-1653²⁴](https://orcid.org/0000-0003-4091-1653),
- [Patrick Alexander](#)^{25,26},
- [Torsten Albrecht](#) ORCID: [orcid.org/0000-0001-7459-2860²⁷](https://orcid.org/0000-0001-7459-2860),
- [Brian Anderson](#)²⁸,
- [Xylar Asay-Davis](#) ORCID: [orcid.org/0000-0002-1990-892X²⁹](https://orcid.org/0000-0002-1990-892X),
- [Andy Aschwanden](#)⁶,

- [Alice Barthel](#) ORCID: orcid.org/0000-0002-2481-8646²⁹,
- [Andrew Bliss](#) ORCID: orcid.org/0000-0002-8637-1923³⁰,
- [Reinhard Calov](#)²⁷,
- [Christopher Chambers](#) ORCID: orcid.org/0000-0001-8847-6123³¹,
- [Nicolas Champollion](#)^{4,12},
- [Youngmin Choi](#) ORCID: orcid.org/0000-0002-2656-5371^{11,32},
- [Richard Cullather](#)²,
- [Joshua Cuzzzone](#)¹¹,
- [Christophe Dumas](#)²⁴,
- [Denis Felikson](#) ORCID: orcid.org/0000-0002-3785-5112^{2,33},
- [Xavier Fettweis](#) ORCID: orcid.org/0000-0002-4140-3813³⁴,
- [Koji Fujita](#) ORCID: orcid.org/0000-0003-3753-4981³⁵,
- [Benjamin K. Galton-Fenzi](#)^{36,37},
- [Rupert Gladstone](#) ORCID: orcid.org/0000-0002-1582-3857³⁸,
- [Nicholas R. Golledge](#)²⁸,
- [Ralf Greve](#) ORCID: orcid.org/0000-0002-1341-4777^{31,39},
- [Tore Hattermann](#)^{40,41},
- [Matthew J. Hoffman](#) ORCID: orcid.org/0000-0001-5076-0540²⁹,
- [Angelika Humbert](#) ORCID: orcid.org/0000-0002-0244-8760^{42,43},
- [Matthias Huss](#)^{44,45,46},
- [Philippe Huybrechts](#) ORCID: orcid.org/0000-0003-1406-0525⁴⁷,
- [Walter Immerzeel](#) ORCID: orcid.org/0000-0002-2010-9543⁴⁸,
- [Thomas Kleiner](#)⁴²,
- [Philip Kraaijenbrink](#) ORCID: orcid.org/0000-0002-0126-8602⁴⁸,
- [Sébastien Le clec'h](#) ORCID: orcid.org/0000-0003-1203-8682⁴⁷,
- [Victoria Lee](#)⁴⁹,
- [Gunter R. Leguy](#)²¹,
- [Christopher M. Little](#) ORCID: orcid.org/0000-0002-9228-5861⁵⁰,
- [Daniel P. Lowry](#)⁵¹,
- [Jan-Hendrik Malles](#)^{4,5},
- [Daniel F. Martin](#)⁵²,
- [Fabien Maussion](#) ORCID: orcid.org/0000-0002-3211-506X⁵³,
- [Mathieu Morlighem](#) ORCID: orcid.org/0000-0001-5219-1310³²,
- [James F. O'Neill](#)¹,

- [Isabel Nias](#) ORCID: [orcid.org/0000-0002-5657-8691^{2,54}](https://orcid.org/0000-0002-5657-8691),
- [Frank Pattyn](#) ORCID: [orcid.org/0000-0003-4805-5636⁹](https://orcid.org/0000-0003-4805-5636),
- [Tyler Pelle](#) ORCID: [orcid.org/0000-0002-9772-1730³²](https://orcid.org/0000-0002-9772-1730),
- [Stephen F. Price](#) ORCID: [orcid.org/0000-0001-6878-2553²⁹](https://orcid.org/0000-0001-6878-2553),
- [Aurélien Quiquet](#) ORCID: [orcid.org/0000-0001-6207-3043²⁴](https://orcid.org/0000-0001-6207-3043),
- [Valentina Radic](#)⁵⁵,
- [Ronja Reese](#) ORCID: [orcid.org/0000-0001-7625-040X²⁷](https://orcid.org/0000-0001-7625-040X),
- [David R. Rounce](#) ORCID: [orcid.org/0000-0002-4481-4191^{6,56}](https://orcid.org/0000-0002-4481-4191),
- [Martin Rückamp](#) ORCID: [orcid.org/0000-0003-2512-7238⁴²](https://orcid.org/0000-0003-2512-7238),
- [Akiko Sakai](#) ORCID: [orcid.org/0000-0002-6320-6212³⁵](https://orcid.org/0000-0002-6320-6212),
- [Courtney Shafer](#)⁵²,
- [Nicole-Jeanne Schlegel](#) ORCID: [orcid.org/0000-0001-8035-448X¹¹](https://orcid.org/0000-0001-8035-448X),
- [Sarah Shannon](#) ORCID: [orcid.org/0000-0002-7644-2724²²](https://orcid.org/0000-0002-7644-2724),
- [Robin S. Smith](#)¹⁹,
- [Fiammetta Straneo](#) ORCID: [orcid.org/0000-0002-1735-2366¹³](https://orcid.org/0000-0002-1735-2366),
- [Sainan Sun](#)⁹,
- [Lev Tarasov](#)⁵⁷,
- [Luke D. Trusel](#) ORCID: [orcid.org/0000-0002-7792-6173⁵⁸](https://orcid.org/0000-0002-7792-6173),
- [Jonas Van Breedam](#) ORCID: [orcid.org/0000-0003-1504-9520⁴⁷](https://orcid.org/0000-0003-1504-9520),
- [Roderik van de Wal](#) ORCID: [orcid.org/0000-0003-2543-3892^{8,48}](https://orcid.org/0000-0003-2543-3892),
- [Michiel van den Broeke](#) ORCID: [orcid.org/0000-0003-4662-7565⁸](https://orcid.org/0000-0003-4662-7565),
- [Ricarda Winkelmann](#)^{27,59},
- [Harry Zekollari](#) ORCID: [orcid.org/0000-0002-7443-4034^{9,44,45,60}](https://orcid.org/0000-0002-7443-4034),
- [Chen Zhao](#) ORCID: [orcid.org/0000-0003-0368-1334³⁷](https://orcid.org/0000-0003-0368-1334),
- [Tong Zhang](#)^{29,61} &
- [Thomas Zwinger](#) ORCID: [orcid.org/0000-0003-3360-4401⁶²](https://orcid.org/0000-0003-3360-4401)

[Nature](#) volume **593**, pages 74–82(2021) [Cite this article](#)

- 2259 Accesses
- 590 Altmetric
- [Metrics details](#)

Subjects

- [Climate and Earth system modelling](#)
- [Cryospheric science](#)
- [Projection and prediction](#)

Abstract

The land ice contribution to global mean sea level rise has not yet been predicted¹ using ice sheet and glacier models for the latest set of socio-economic scenarios, nor using coordinated exploration of uncertainties arising from the various computer models involved. Two recent international projects generated a large suite of projections using multiple models^{2,3,4,5,6,7,8}, but primarily used previous-generation scenarios⁹ and climate models¹⁰, and could not fully explore known uncertainties. Here we estimate probability distributions for these projections under the new scenarios^{11,12} using statistical emulation of the ice sheet and glacier models. We find that limiting global warming to 1.5 degrees Celsius would halve the land ice contribution to twenty-first-century sea level rise, relative to current emissions pledges. The median decreases from 25 to 13 centimetres sea level equivalent (SLE) by 2100, with glaciers responsible for half the sea level contribution. The projected Antarctic contribution does not show a clear response to the emissions scenario, owing to uncertainties in the competing processes of increasing ice loss and snowfall accumulation in a warming climate. However, under risk-averse (pessimistic) assumptions, Antarctic ice loss could be five times higher, increasing the median land ice contribution to 42 centimetres SLE under current policies and pledges, with the 95th percentile projection exceeding half a metre even under 1.5 degrees Celsius warming. This would severely limit the possibility of mitigating future coastal flooding. Given this large range (between 13 centimetres SLE using the main projections under 1.5 degrees Celsius warming and 42 centimetres SLE using risk-averse projections under current pledges), adaptation planning for twenty-first-century sea level rise must account for a factor-of-three uncertainty in the land ice contribution until climate policies and the Antarctic response are further constrained.

[Access through your institution](#)
[Change institution](#)
[Buy or subscribe](#)

Access options

Subscribe to Journal

Get full journal access for 1 year

\$199.00

only \$3.90 per issue

[Subscribe](#)

All prices are NET prices.

VAT will be added later in the checkout.

Tax calculation will be finalised during checkout.

Rent or Buy article

Get time limited or full article access on ReadCube.

from \$8.99

[Rent or Buy](#)

All prices are NET prices.

Additional access options:

- [Log in](#)
- [Access through your institution](#)
- [Learn about institutional subscriptions](#)

Fig. 1: Ice sheet and glacier mass loss generally increases linearly with global mean temperature.

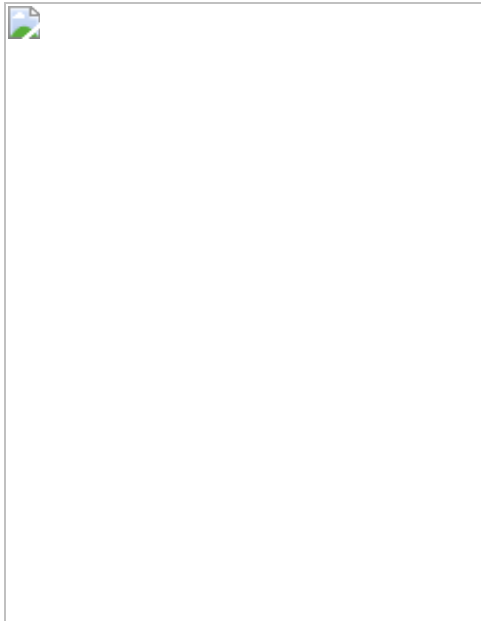


Fig. 2: Ice sheet mass loss strongly depends on ice–ocean parameters.

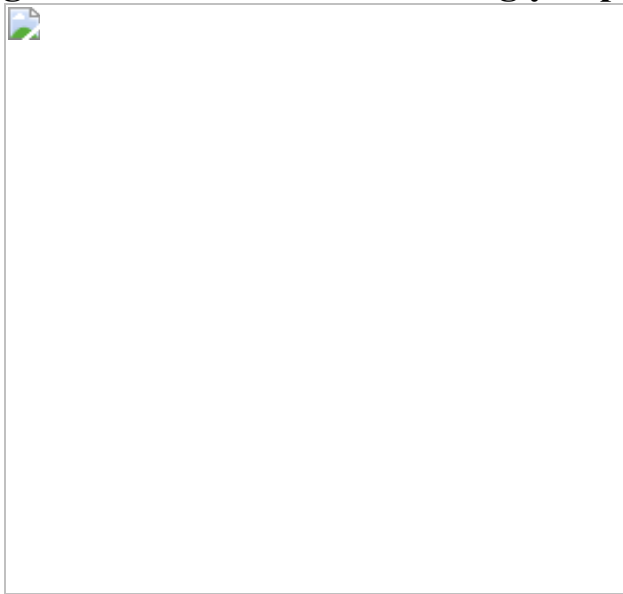


Fig. 3: Projected land ice contribution to 21st-century sea level rise and for selected regions at 2100.

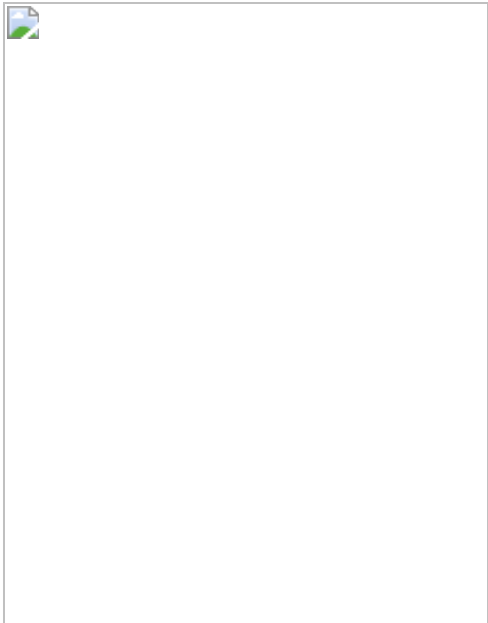


Fig. 4: Climate and ice sheet projections show a wide range of responses to greenhouse gas emissions scenario.



Data availability

All global climate, simple climate, ice sheet and glacier model data used as inputs to this study are provided with the code as described above. Main and risk-averse projections at 2100 from the analysis are provided in Supplementary Information for each of the 23 regions, and the Antarctic, glacier and land ice sums.

Code availability

R code and input data are available at <https://github.com/tamsinedwards/emulandice>. Each simulation in the sea level projections file has a label in the ‘publication’ column for the reference (Goelzer2020⁶, Seroussi2020⁷, Payne2021⁸ or Marzeion2020⁵), or ‘New’ if previously unpublished.

References

1. 1.

Oppenheimer, M. et al. Sea Level Rise and Implications for Low-Lying Islands, Coasts and Communities. In *IPCC Special Report on the Ocean and Cryosphere in a Changing Climate* (eds Pörtner, H.-O. et al.) (IPCC, 2019).

2. 2.

Nowicki, S. M. J. et al. Ice Sheet Model Intercomparison Project (ISMIP6) contribution to CMIP6. *Geosci. Model Dev.* **9**, 4521–4545 (2016).

[PubMed](#) [PubMed Central](#) [Article](#) [ADS](#) [Google Scholar](#)

3. 3.

Nowicki, S. et al. Experimental protocol for sea level projections from ISMIP6 stand-alone ice sheet models. *Cryosphere* **14**, 2331–2368 (2020).

[Article](#) [ADS](#) [Google Scholar](#)

4. 4.

Hock, R. et al. GlacierMIP – a model intercomparison of global-scale glacier mass-balance models and projections. *J. Glaciol.* **65**, 453–467 (2019).

[Article](#) [ADS](#) [Google Scholar](#)

5. 5.

Marzeion, B. et al. Partitioning the uncertainty of ensemble projections of global glacier mass change. *Earth's Future* **8**, e2019EF001470

(2020).

[Article](#) [ADS](#) [Google Scholar](#)

6. 6.

Goelzer, H. et al. The future sea-level contribution of the Greenland ice sheet: a multi-model ensemble study of ISMIP6. *Cryosphere* **14**, 3071–3096 (2020).

[Article](#) [ADS](#) [Google Scholar](#)

7. 7.

Seroussi, H. et al. ISMIP6 Antarctica: a multi-model ensemble of the Antarctic ice sheet evolution over the 21st century. *Cryosphere* **14**, 3033–3070 (2020).

[Article](#) [ADS](#) [Google Scholar](#)

8. 8.

Payne, A. et al. Future sea level change under CMIP5 and CMIP6 scenarios from the Greenland and Antarctic ice sheets. *Geophys. Res. Lett.* (in the press).

9. 9.

van Vuuren, D. P. et al. The representative concentration pathways: an overview. *Clim. Change* **109**, 5–31 (2011).

[Article](#) [ADS](#) [Google Scholar](#)

10. 10.

Taylor, K. E., Stouffer, R. J. & Meehl, G. A. An overview of CMIP5 and the experiment design. *Bull. Am. Meteorol. Soc.* **93**, 485–498 (2012).

[Article](#) [ADS](#) [Google Scholar](#)

11. 11.

Riahi, K. et al. The Shared Socioeconomic Pathways and their energy, land use, and greenhouse gas emissions implications: an overview. *Glob. Environ. Change* **42**, 153–168 (2017).

[Article](#) [Google Scholar](#)

12. 12.

McKenna, C. M. et al. Stringent mitigation substantially reduces risk of unprecedented near-term warming rates. *Nat. Clim. Change* **11**, 126–131 (2021).

[Article](#) [ADS](#) [Google Scholar](#)

13. 13.

Eyring, V. et al. Overview of the Coupled Model Intercomparison Project Phase 6 (CMIP6) experimental design and organization. *Geosci. Model Dev.* **9**, 1937–1958 (2016).

[Article](#) [ADS](#) [Google Scholar](#)

14. 14.

Goelzer, H. et al. Design and results of the ice sheet model initialisation experiments initMIP-Greenland: an ISMIP6 intercomparison. *Cryosphere* **12**, 1433–1460 (2018).

[Article](#) [ADS](#) [Google Scholar](#)

15. 15.

Seroussi, H. et al. initMIP-Antarctica: an ice sheet model initialization experiment of ISMIP6. *Cryosphere* **13**, 1441–1471 (2019).

[Article](#) [ADS](#) [Google Scholar](#)

16. 16.

Slater, D. A. et al. Estimating Greenland tidewater glacier retreat driven by submarine melting. *Cryosphere* **13**, 2489–2509 (2019).

[Article](#) [ADS](#) [Google Scholar](#)

17. 17.

Slater, D. A. et al. Twenty-first-century ocean forcing of the Greenland ice sheet for modelling of sea level contribution. *Cryosphere* **14**, 985–1008 (2020).

[Article](#) [ADS](#) [Google Scholar](#)

18. 18.

Favier, L. et al. Assessment of sub-shelf melting parameterisations using the ocean–ice-sheet coupled model NEMO(v3.6)–Elmer/Ice(v8.3). *Geosci. Model Dev.* **12**, 2255–2283 (2019).

[Article](#) [ADS](#) [Google Scholar](#)

19. 19.

Jourdain, N. C. et al. A protocol for calculating basal melt rates in the ISMIP6 Antarctic ice sheet projections. *Cryosphere* **14**, 3111–3134 (2020).

[Article](#) [ADS](#) [Google Scholar](#)

20. 20.

Goelzer, H. et al. Remapping of Greenland ice sheet surface mass balance anomalies for large ensemble sea-level change projections. *Cryosphere* **14**, 1747–1762 (2020).

[Article](#) [ADS](#) [Google Scholar](#)

21. 21.

Barthel, A. et al. CMIP5 model selection for ISMIP6 ice sheet model forcing: Greenland and Antarctica. *Cryosphere* **14**, 855–879 (2020).

[Article](#) [ADS](#) [Google Scholar](#)

22. 22.

O'Neill, B. C. et al. The Scenario Model Intercomparison Project (ScenarioMIP) for CMIP6. *Geosci. Model Dev.* **9**, 3461–3482 (2016).

[Article](#) [ADS](#) [Google Scholar](#)

23. 23.

Andrianakis, I. & Challenor, P. G. The effect of the nugget on Gaussian process emulators of computer models. *Comput. Stat. Data Anal.* **56**, 4215–4228 (2012).

[MathSciNet](#) [MATH](#) [Article](#) [Google Scholar](#)

24. 24.

Gramacy, R. B. & Lee, H. K. H. Cases for the nugget in modeling computer experiments. *Stat. Comput.* **22**, 713–722 (2012).

[MathSciNet](#) [MATH](#) [Article](#) [Google Scholar](#)

25. 25.

Edwards, T. L. et al. Revisiting Antarctic ice loss due to marine ice cliff instability. *Nature* **566**, 58–64 (2019).

[CAS](#) [PubMed](#) [Article](#) [ADS](#) [Google Scholar](#)

26. 26.

Church, J. A. et al. Sea level change. In *Climate Change 2013: The Physical Science Basis. Contribution of Working Group I to the Fifth Assessment Report of the Intergovernmental Panel on Climate Change* (eds Stocker, T. F. et al.) Ch. 13 (Cambridge Univ. Press, 2013).

27. 27.

Levermann, A. et al. Projecting Antarctica's contribution to future sea level rise from basal ice shelf melt using linear response functions of 16 ice sheet models (LARMIP-2). *Earth Syst. Dynam.* **11**, 35–76 (2020).

[Article](#) [ADS](#) [Google Scholar](#)

28. 28.

Bulthuis, K. et al. Uncertainty quantification of the multi-centennial response of the Antarctic ice sheet to climate change. *Cryosphere* **13**, 1349–1380 (2019).

[Article](#) [ADS](#) [Google Scholar](#)

29. 29.

Nauels, A. et al. Synthesizing long-term sea level rise projections – the MAGICC sea level model v2.0. *Geosci. Model Dev.* **10**, 2495–2524 (2017).

[Article](#) [ADS](#) [Google Scholar](#)

30. 30.

Palmer, M. D. et al. Exploring the drivers of global and local sea-level change over the 21st century and beyond. *Earth's Future* **8**, e2019EF001413 (2020).

[Article](#) [ADS](#) [Google Scholar](#)

31. 31.

Biemans, H. et al. Importance of snow and glacier meltwater for agriculture on the Indo-Gangetic Plain. *Nature Sustain.* **2**, 594–601 (2019).

[Article](#) [Google Scholar](#)

32. 32.

Forster, P. M., Maycock, A. C., McKenna, C. M. & Smith, C. J. Latest climate models confirm need for urgent mitigation. *Nat. Clim. Change* **10**, 7–10 (2019).

[Article](#) [ADS](#) [Google Scholar](#)

33. 33.

Meehl, G. et al. Context for interpreting equilibrium climate sensitivity and transient climate response from the CMIP6 Earth system models. *Sci. Adv.* **6**, eaba1981 (2020).

[PubMed](#) [PubMed Central](#) [Article](#) [ADS](#) [Google Scholar](#)

34. 34.

Meredith, M. et al. Polar Regions. In *IPCC Special Report on the Ocean and Cryosphere in a Changing Climate* (eds Pörtner, H.-O. et al.) Ch. 3 (2019).

35. 35.

Naughten, K. A. et al. Future projections of Antarctic ice shelf melting based on CMIP5 scenarios. *J. Clim.* **31**, 5243–5261 (2018).

[Article](#) [ADS](#) [Google Scholar](#)

36. 36.

Mottram, R. et al. What is the surface mass balance of Antarctica? An intercomparison of regional climate model estimates. Preprint at

<https://doi.org/10.5194/tc-2019-333> (2020).

37. 37.

Roussel, M.-L., Lemonnier, F., Genthon, C. & Krinner, G. Evaluating Antarctic precipitation in ERA5 and CMIP6 against CloudSat observations. *Cryosphere* **14**, 2715–2727 (2020).

[Article](#) [ADS](#) [Google Scholar](#)

38. 38.

Reese, R. et al. The role of history and strength of the oceanic forcing in sea level projections from Antarctica with the Parallel Ice Sheet Model. *Cryosphere* **14**, 3097–3110 (2020).

[Article](#) [ADS](#) [Google Scholar](#)

39. 39.

Golledge, N. R. et al. The multi-millennial Antarctic commitment to future sea-level rise. *Nature* **526**, 421–425 (2015).

[CAS](#) [PubMed](#) [Article](#) [ADS](#) [Google Scholar](#)

40. 40.

Golledge, N. R. et al. Global environmental consequences of twenty-first-century ice-sheet melt. *Nature* **566**, 65–72 (2019).

[CAS](#) [Article](#) [PubMed](#) [ADS](#) [Google Scholar](#)

41. 41.

DeConto, R. M. & Pollard, D. Contribution of Antarctica to past and future sea-level rise. *Nature* **531**, 591–597 (2016).

[CAS](#) [PubMed](#) [Article](#) [ADS](#) [Google Scholar](#)

42. 42.

Clerc, F., Minchew, B. M. & Behn, M. D. Marine ice cliff instability mitigated by slow removal of ice shelves. *Geophys. Res. Lett.* **46**, 12108–12116 (2019).

[Article](#) [ADS](#) [Google Scholar](#)

43. 43.

Williamson, D. B. & Sansom, P. G. How are emergent constraints quantifying uncertainty and what do they leave behind? *Bull. Am. Meterol. Soc.* **100**, 2571–2588 (2019).

[Article](#) [ADS](#) [Google Scholar](#)

44. 44.

Farinotti, D. et al. A consensus estimate for the ice thickness distribution of all glaciers on Earth. *Nat. Geosci.* **12**, 168–173 (2019).

[CAS](#) [Article](#) [ADS](#) [Google Scholar](#)

45. 45.

Trusel, L. D. et al. Divergent trajectories of Antarctic surface melt under two twenty-first-century climate scenarios. *Nat. Geosci.* **8**, 927–932 (2015).

[CAS](#) [Article](#) [ADS](#) [Google Scholar](#)

46. 46.

Bell, R. E. et al. Antarctic ice shelf potentially stabilized by export of meltwater in surface river. *Nature* **544**, 344–348 (2017).

[CAS](#) [PubMed](#) [Article](#) [ADS](#) [Google Scholar](#)

47. 47.

O'Hagan, A. Bayesian analysis of computer code outputs: a tutorial. *Reliab. Eng. Syst. Saf.* **91**, 1290–1300 (2006).

[Article](#) [Google Scholar](#)

48. 48.

Gu, M. et al. RobustGaSP: robust Gaussian stochastic process emulation in R. *R J.* **11**, 112–136 (2019).

[Article](#) [Google Scholar](#)

49. 49.

Gu, M., Wang, X. & Berger, J. O. Robust Gaussian stochastic process emulation. *Ann. Stat.* **46**, 3038–3066 (2018).

[MathSciNet](#) [MATH](#) [Article](#) [Google Scholar](#)

50. 50.

van Beers, W. C. M. & Kleijnen, J. P. C. Kriging for interpolation in random simulation. *J. Oper. Res. Soc.* **54**, 255–262 (2003).

[MATH](#) [Article](#) [Google Scholar](#)

51. 51.

Salter, J. M. & Williamson, D. A comparison of statistical emulation methodologies for multi-wave calibration of environmental models. *Environmetrics* **27**, 507–523 (2016).

[MathSciNet](#) [PubMed](#) [PubMed Central](#) [Article](#) [Google Scholar](#)

52. 52.

Williamson, D. & Blaker, A. T. Evolving Bayesian emulators for structured chaotic time series, with application to large climate models. *SIAM/ASA J. Uncertain. Quant.* **2**, 1–28 (2014).

[MathSciNet](#) [MATH](#) [Article](#) [Google Scholar](#)

53. 53.

Williamson, D., Blaker, A., Hampton, C. & Salter, J. Identifying and removing structural biases in climate models with history matching. *Clim. Dyn.* **45**, 1299–1324 (2015).

[Article](#) [Google Scholar](#)

54. 54.

Araya-Melo, P. A., Crucifix, M. & Bounceur, N. Global sensitivity analysis of the Indian monsoon during the Pleistocene. *Clim. Past* **11**, 45–61 (2015).

[Article](#) [Google Scholar](#)

55. 55.

Bounceur, N., Crucifix, M. & Wilkinson, R. D. Global sensitivity analysis of the climate–vegetation system to astronomical forcing: an emulator-based approach. *Earth Syst. Dynam.* **6**, 205–224 (2015).

[Article](#) [ADS](#) [Google Scholar](#)

56. 56.

Lord, N. S. et al. Emulation of long-term changes in global climate: application to the late Pliocene and future. *Clim. Past* **13**, 1539–1571 (2017).

[Article](#) [Google Scholar](#)

57. 57.

Bowman, K. W. et al. A hierarchical statistical framework for emergent constraints: application to snow–albedo feedback. *Geophys. Res. Lett.* **45**, 13050–13059 (2018).

[ADS](#) [Google Scholar](#)

58. 58.

Nowicki, S. et al. Insights into spatial sensitivities of ice mass response to environmental change from the SeaRISE ice sheet modeling project. I: Antarctica. *J. Geophys. Res. Earth* **118**, 1002–1024 (2013).

[Article](#) [ADS](#) [Google Scholar](#)

59. 59.

Nowicki, S. et al. Insights into spatial sensitivities of ice mass response to environmental change from the SeaRISE ice sheet modeling project. II: Greenland. *J. Geophys. Res. Earth* **118**, 1025–1044 (2013).

[Article](#) [ADS](#) [Google Scholar](#)

60. 60.

Saito, F., Abe-Ouchi, A., Takahashi, K. & Blatter, H. SeaRISE experiments revisited: potential sources of spread in multi-model projections of the Greenland ice sheet. *Cryosphere* **10**, 43–63 (2016).

[Article](#) [ADS](#) [Google Scholar](#)

61. 61.

Rougier, J., Sexton, D. M. H., Murphy, J. M. & Stainforth, D. A. Analyzing the climate sensitivity of the HadSM3 climate model using ensembles from different but related experiments. *J. Clim.* **22**, 3540–3557 (2009).

[Article](#) [ADS](#) [Google Scholar](#)

62. 62.

Bastos, L. S. & O'Hagan, A. Diagnostics for Gaussian process emulators. *Technometrics* **51**, 425–438 (2009).

[MathSciNet](#) [Article](#) [Google Scholar](#)

63. 63.

Silverman, B. W. *Density Estimation* (Chapman and Hall, 1986).

64. 64.

The IMBIE Team. Mass balance of the Greenland Ice Sheet from 1992 to 2018. *Nature* **579**, 233–239 (2020).

65. 65.

The IMBIE Team. Mass balance of the Antarctic Ice Sheet from 1992 to 2017. *Nature* **558**, 219–222 (2018).

[Article](#) [ADS](#) [CAS](#) [Google Scholar](#)

66. 66.

Price, S. F., Payne, A. J., Howat, I. M. & Smith, B. E. Committed sea-level rise for the next century from Greenland ice sheet dynamics during the past decade. *Proc. Natl Acad. Sci. USA* **108**, 8978–8983 (2011).

[CAS](#) [PubMed](#) [Article](#) [ADS](#) [Google Scholar](#)

67. 67.

Alevropoulos-Borrill, A. V., Nias, I. J., Payne, A. J., Golledge, N. R. & Bingham, R. J. Ocean-forced evolution of the Amundsen Sea catchment, West Antarctica, by 2100. *Cryosphere* **14**, 1245–1258 (2020).

[Article](#) [ADS](#) [Google Scholar](#)

[Download references](#)

Acknowledgements

We thank J. Rougier for providing advice and support throughout, and writing the original random effects model. We also thank B. Fox-Kemper, H. Hewitt, R. Kopp, S. Drijfhout and J. Rohmer for discussions, suggestions and support. We thank N. Barrand, W. Chang, V. Volodina and D. Williamson for their thorough and constructive comments, which greatly improved the manuscript. We thank the Climate and Cryosphere (CliC) Project, which provided support for ISMIP6 and GlacierMIP through sponsoring of workshops, hosting the websites and ISMIP6 wiki, and promotion. We acknowledge the World Climate Research Programme, which, through its Working Group on Coupled Modelling, coordinated and promoted CMIP5 and CMIP6. We thank the climate modelling groups for producing and making available their model output, the Earth System Grid Federation (ESGF) for archiving the CMIP data and providing access, the University at Buffalo for ISMIP6 data distribution and upload, and the multiple funding agencies who support CMIP5 and CMIP6 and ESGF. We thank the ISMIP6 steering committee, the ISMIP6 model selection group and the ISMIP6 dataset preparation group for their continuous engagement in defining ISMIP6. This is ISMIP6 contribution no. 13. This publication was supported by PROTECT, which has received funding from the European Union's Horizon 2020 research and innovation programme under grant agreement no. 869304. This is PROTECT contribution number 12. T.L.E. was supported by PROTECT and the UK Natural Environment Research Council grant NE/T007443/1. F.T. was supported by PROTECT. J.F.O'N. was supported by the UK Natural Environment Research Council London Doctoral Training Partnership. R. Gladstone's contribution was supported by Academy of Finland grants 286587 and 322430, and T. Zwinger's by grant 322430. W.H.L. and G.R.L. were supported by the National Center for Atmospheric Research, which is a major facility sponsored by the National Science Foundation under Cooperative Agreement no. 1852977. Computing and data storage resources for CISM simulations, including the Cheyenne supercomputer (<https://doi.org/10.5065/D6RX99HX>), were provided by the Computational and Information Systems Laboratory (CISL) at NCAR. Support for X.A.-D., M.J.H., S.F.P. and T. Zhang was provided through the Scientific Discovery through Advanced Computing (SciDAC) programme funded by

the US Department of Energy (DOE), Office of Science, Advanced Scientific Computing Research and Biological and Environmental Research programmes. N.R.G., D.P.L. and B.A. were supported by New Zealand Ministry for Business, Innovation and Employment contracts RTUV1705 ('NZSeaRise') and ANTA1801 ('Antarctic Science Platform'). J.M.G. and R.S.S. were supported by the National Centre for Atmospheric Science, funded by the UK National Environment Research Council. R. Calov was funded by the PalMod project of the Bundesministerium für Bildung und Forschung (BMBF) with the grants FKZ 01LP1502C and 01LP1504D. D.F.M. and C.S. were supported by the Director, Office of Science, Offices of Advanced Scientific Computing Research (ASCR) and Biological and Environmental Research (BER), of the US Department of Energy under contract no. DE-AC02-05CH11231, as a part of the ProSPect SciDAC Partnership. BISICLES simulations used resources of the National Energy Research Scientific Computing Center (NERSC), a US Department of Energy Office of Science User Facility operated under contract no. DE-AC02-05CH11231. C.Z. and B.K.G.-F. were supported under the Australian Research Council's Special Research Initiative for Antarctic Gateway Partnership (project ID SR140300001) and received grant funding from the Australian Government for the Australian Antarctic Program Partnership (project ID ASCI000002). Work was performed by E.L., N.-J.S. and H.S. at the California Institute of Technology's Jet Propulsion Laboratory under a contract with the National Aeronautics and Space Administration; support was provided by grants from NASA's Cryospheric Science, Sea Level Change Team, and Modeling, Analysis and Prediction (MAP) programmes. They acknowledge computational resources and support from the NASA Advanced Supercomputing Division. The CMIP5 and CMIP6 projection data were processed by C.M.M. with funding from the European Union's CONSTRAIN project as part of the Horizon 2020 Research and Innovation Programme under grant agreement number 820829. A. Barthel was supported by the DOE Office of Science HiLAT-RASM project and Early Career Research programme. T.A. and R.W. are supported by the Deutsche Forschungsgemeinschaft (DFG) in the framework of the priority programme 'Antarctic research with comparative investigations in Arctic ice areas' by grants WI4556/2-1 and WI4556/4-1, and within the framework of the PalMod project (FKZ: 01LP1925D) supported by the German Federal Ministry of Education and Research (BMBF) as a

Research for Sustainability initiative (FONA). R.R. is supported by the Deutsche Forschungsgemeinschaft (DFG) by grant WI4556/3-1 and through the TiPACCs project that receives funding from the European Union's Horizon 2020 Research and Innovation programme under grant agreement no. 820575. Development of PISM is supported by NASA grant NNX17AG65G and NSF grants PLR-1603799 and PLR-1644277. The authors gratefully acknowledge the European Regional Development Fund (ERDF), the German Federal Ministry of Education and Research and the Land Brandenburg for supporting this project by providing resources for the high-performance computer system at the Potsdam Institute for Climate Impact Research. Computer resources for this project have also been provided by the Gauss Centre for Supercomputing, Leibniz Supercomputing Centre (<http://www.lrz.de>, last access: 16 July 2020) under project IDs pr94ga and pn69ru. R. Greve and C.C. were supported by Japan Society for the Promotion of Science (JSPS) KAKENHI grant nos JP16H02224 and JP17H06323. R. Greve was supported by JSPS KAKENHI grant no. JP17H06104, by a Leadership Research Grant of Hokkaido University's Institute of Low Temperature Science (ILTS), and by the Arctic Challenge for Sustainability (ArCS, ArCS II) project of the Japanese Ministry of Education, Culture, Sports, Science and Technology (MEXT) (programme grant nos JPMXD1300000000, JPMXD1420318865). F.P. and S. Sun were supported by the MIMO project within the STEREO III programme of the Belgian Science Policy Office, contract SR/00/336 and the Fonds de la Recherche Scientifique (FNRS) and the Fonds Wetenschappelijk Onderzoek-Vlaanderen (FWO) under the EOS project no. O0100718F. A. Shepherd was supported by the UK Natural Environment Research Council in partnership with the Centre for Polar Observation and Modelling and the British Antarctic Survey and by the European Space Agency Climate Change Initiative. D.F. was supported by an appointment to the NASA Postdoctoral Program at the NASA Goddard Space Flight Center, administered by Universities Space Research Association under contract with NASA. R.v.d.W. acknowledges the support of the Future Deltas programme of Utrecht University. C.J.S. was supported by a NERC/IIASA Collaborative Research Fellowship (NE/T009381/1). H.G. has received funding from the programme of the Netherlands Earth System Science Centre (NESSC), financially supported by the Dutch Ministry of Education, Culture and Science (OCW) under

grant no. 024.002.001 and from the Research Council of Norway under projects INES (270061) and KeyClim (295046). F.S. acknowledges support from DOE Office of Science grant no. DE-SC0020073. High-performance computing and storage resources were provided by the Norwegian Infrastructure for Computational Science through projects NN9560K, NN9252K, NS9560K, NS9252K and NS5011K.

Author information

Affiliations

1. Department of Geography, King's College London, London, UK
Tamsin L. Edwards, Fiona E. Turner & James F. O'Neill
2. NASA Goddard Space Flight Center, Greenbelt, MD, USA
Sophie Nowicki, Erika Simon, Richard Cullather, Denis Felikson & Isabel Nias
3. Geology Department and RENEW Institute, University at Buffalo, Buffalo, NY, USA
Sophie Nowicki
4. Institute of Geography, University of Bremen, Bremen, Germany
Ben Marzeion, Nicolas Champollion & Jan-Hendrik Malles
5. MARUM – Center for Marine Environmental Sciences, University of Bremen, Bremen, Germany
Ben Marzeion & Jan-Hendrik Malles
6. Geophysical Institute, University of Alaska Fairbanks, Fairbanks, USA
Regine Hock, Andy Aschwanden & David R. Rounce

7. Department of Geosciences, University of Oslo, Oslo, Norway
Regine Hock
8. Institute for Marine and Atmospheric Research Utrecht, Utrecht University, Utrecht, The Netherlands
Heiko Goelzer, Roderik van de Wal & Michiel van den Broeke
9. Laboratoire de Glaciologie, Université Libre de Bruxelles, Brussels, Belgium
Heiko Goelzer, Frank Pattyn, Sainan Sun & Harry Zekollari
10. NORCE Norwegian Research Centre, Bjerknes Centre for Climate Research, Bergen, Norway
Heiko Goelzer
11. Jet Propulsion Laboratory, California Institute of Technology, Pasadena, CA, USA
Hélène Seroussi, Eric Larour, Youngmin Choi, Joshua Cuzzone & Nicole-Jeanne Schlegel
12. Institut des géosciences de l'environnement, Université Grenoble Alpes, CNRS, IRD, G-INP, Grenoble, France
Nicolas C. Jourdain & Nicolas Champollion
13. Scripps Institution of Oceanography, University of California San Diego, La Jolla, CA, USA
Donald A. Slater & Fiammetta Straneo
14. School of Geography and Sustainable Development, University of St Andrews, St Andrews, UK
Donald A. Slater

15. School of Geosciences, University of Edinburgh, Edinburgh, UK
Donald A. Slater
16. Priestley International Centre for Climate, University of Leeds, Leeds, UK
Christopher J. Smith & Christine M. McKenna
17. International Institute for Applied Systems Analysis, (IIASA), Laxenburg, Austria
Christopher J. Smith
18. Atmosphere and Ocean Research Institute, The University of Tokyo, Tokyo, Japan
Ayako Abe-Ouchi
19. National Centre for Atmospheric Science, University of Reading, Reading, UK
Jonathan M. Gregory & Robin S. Smith
20. Met Office, Hadley Centre, Exeter, UK
Jonathan M. Gregory
21. Climate and Global Dynamics Laboratory, National Center for Atmospheric Research, Boulder, CO, USA
William H. Lipscomb & Gunter R. Leguy
22. School of Geographical Sciences, University of Bristol, Bristol, UK
Antony J. Payne & Sarah Shannon
23. Centre for Polar Observation and Modelling, School of Earth and Environment, University of Leeds, Leeds, UK

Andrew Shepherd

24. Laboratoire des Sciences du Climat et de l'Environnement, LSCE-IPSL, CEA-CNRS-UVSQ, Université Paris-Saclay, Gif-sur-Yvette, France

Cécile Agosta, Christophe Dumas & Aurélien Quiquet

25. Lamont–Doherty Earth Observatory, Columbia University, Palisades, NY, USA

Patrick Alexander

26. NASA Goddard Institute for Space Studies, New York, NY, USA

Patrick Alexander

27. Potsdam Institute for Climate Impact Research (PIK), Member of the Leibniz Association, Potsdam, Germany

Torsten Albrecht, Reinhard Calov, Ronja Reese & Ricarda Winkelmann

28. Antarctic Research Centre, Victoria University of Wellington, Wellington, New Zealand

Brian Anderson & Nicholas R. Golledge

29. Theoretical Division, Los Alamos National Laboratory, Los Alamos, NM, USA

Xylar Asay-Davis, Alice Barthel, Matthew J. Hoffman, Stephen F. Price & Tong Zhang

30. Department of Anthropology and Geography, Colorado State University, Fort Collins, CO, USA

Andrew Bliss

31. Institute of Low Temperature Science, Hokkaido University, Sapporo, Japan

Christopher Chambers & Ralf Greve

32. Department of Earth System Science, University of California Irvine, Irvine, CA, USA

Youngmin Choi, Mathieu Morlighem & Tyler Pelle

33. Universities Space Research Association, Goddard Earth Sciences Technology and Research Studies and Investigations, Columbia, MD, USA

Denis Felikson

34. Laboratory of Climatology, Department of Geography, University of Liège, Liège, Belgium

Xavier Fettweis

35. Graduate School of Environmental Studies, Nagoya University, Nagoya, Japan

Koji Fujita & Akiko Sakai

36. Australian Antarctic Division, Kingston, Tasmania, Australia

Benjamin K. Galton-Fenzi

37. Australian Antarctic Program Partnership, Institute for Marine and Antarctic Studies, University of Tasmania, Hobart, Tasmania, Australia

Benjamin K. Galton-Fenzi & Chen Zhao

38. Arctic Centre, University of Lapland, Rovaniemi, Finland

Rupert Gladstone

39. Arctic Research Center, Hokkaido University, Sapporo, Japan

Ralf Greve

40. Norwegian Polar Institute, Tromsø, Norway

Tore Hattermann

41. Energy and Climate Group, Department of Physics and Technology,
The Arctic University – University of Tromsø, Tromsø, Norway

Tore Hattermann

42. Alfred-Wegener-Institut Helmholtz-Zentrum für Polar- und
Meeresforschung, Bremerhaven, Germany

Angelika Humbert, Thomas Kleiner & Martin Rückamp

43. Department of Geoscience, University of Bremen, Bremen, Germany

Angelika Humbert

44. Laboratory of Hydraulics, Hydrology and Glaciology (VAW), ETH
Zurich, Zurich, Switzerland

Matthias Huss & Harry Zekollari

45. Swiss Federal Institute for Forest, Snow and Landscape Research
(WSL), Birmensdorf, Switzerland

Matthias Huss & Harry Zekollari

46. Department of Geosciences, University of Fribourg, Fribourg,
Switzerland

Matthias Huss

47. Earth System Science and Departement Geografie, Vrije Universiteit
Brussel, Brussels, Belgium

Philippe Huybrechts, Sébastien Le clec'h & Jonas Van Breedam

48. Department of Physical Geography, Utrecht University, Utrecht, The Netherlands

Walter Immerzeel, Philip Kraaijenbrink & Roderik van de Wal

49. Centre for Polar Observation and Modelling, School of Geographical Sciences, University of Bristol, Bristol, UK

Victoria Lee

50. Atmospheric and Environmental Research, Lexington, MA, USA

Christopher M. Little

51. GNS Science, Lower Hutt, New Zealand

Daniel P. Lowry

52. Computational Research Division, Lawrence Berkeley National Laboratory, Berkeley, CA, USA

Daniel F. Martin & Courtney Shafer

53. Department of Atmospheric and Cryospheric Sciences, University of Innsbruck, Innsbruck, Austria

Fabien Maussion

54. School of Environmental Sciences, University of Liverpool, Liverpool, UK

Isabel Nias

55. Department of Earth, Ocean and Atmospheric Sciences, University of British Columbia, Vancouver, British Columbia, Canada

Valentina Radić

56. Department of Civil and Environmental Engineering, Carnegie Mellon University, Pittsburgh, PA, USA

David R. Rounce

57. Department of Physics and Physical Oceanography, Memorial University of Newfoundland, St John's, Newfoundland, Canada

Lev Tarasov

58. Department of Geography, Pennsylvania State University, University Park, PA, USA

Luke D. Trusel

59. Department of Physics and Astronomy, University of Potsdam, Potsdam, Germany

Ricarda Winkelmann

60. Department of Geoscience and Remote Sensing, Delft University of Technology, Delft, The Netherlands

Harry Zekollari

61. State Key Laboratory of Earth Surface Processes and Resource Ecology, Beijing Normal University, Beijing, China

Tong Zhang

62. CSC-IT Center for Science, Espoo, Finland

Thomas Zwinger

Authors

1. Tamsin L. Edwards

[View author publications](#)

You can also search for this author in [PubMed](#) [Google Scholar](#)

2. Sophie Nowicki

[View author publications](#)

You can also search for this author in [PubMed](#) [Google Scholar](#)

3. Ben Marzeion

[View author publications](#)

You can also search for this author in [PubMed](#) [Google Scholar](#)

4. Regine Hock

[View author publications](#)

You can also search for this author in [PubMed](#) [Google Scholar](#)

5. Heiko Goelzer

[View author publications](#)

You can also search for this author in [PubMed](#) [Google Scholar](#)

6. Hélène Seroussi

[View author publications](#)

You can also search for this author in [PubMed](#) [Google Scholar](#)

7. Nicolas C. Jourdain

[View author publications](#)

You can also search for this author in [PubMed](#) [Google Scholar](#)

8. Donald A. Slater

[View author publications](#)

You can also search for this author in [PubMed](#) [Google Scholar](#)

9. Fiona E. Turner

[View author publications](#)

You can also search for this author in [PubMed](#) [Google Scholar](#)

10. Christopher J. Smith

[View author publications](#)

You can also search for this author in [PubMed](#) [Google Scholar](#)

11. Christine M. McKenna

[View author publications](#)

You can also search for this author in [PubMed](#) [Google Scholar](#)

12. Erika Simon

[View author publications](#)

You can also search for this author in [PubMed](#) [Google Scholar](#)

13. Ayako Abe-Ouchi

[View author publications](#)

You can also search for this author in [PubMed](#) [Google Scholar](#)

14. Jonathan M. Gregory

[View author publications](#)

You can also search for this author in [PubMed](#) [Google Scholar](#)

15. Eric Larour

[View author publications](#)

You can also search for this author in [PubMed](#) [Google Scholar](#)

16. William H. Lipscomb

[View author publications](#)

You can also search for this author in [PubMed](#) [Google Scholar](#)

17. Antony J. Payne

[View author publications](#)

You can also search for this author in [PubMed](#) [Google Scholar](#)

18. Andrew Shepherd

[View author publications](#)

You can also search for this author in [PubMed](#) [Google Scholar](#)

19. Cécile Agosta

[View author publications](#)

You can also search for this author in [PubMed](#) [Google Scholar](#)

20. Patrick Alexander

[View author publications](#)

You can also search for this author in [PubMed](#) [Google Scholar](#)

21. Torsten Albrecht

[View author publications](#)

You can also search for this author in [PubMed](#) [Google Scholar](#)

22. Brian Anderson

[View author publications](#)

You can also search for this author in [PubMed](#) [Google Scholar](#)

23. Xylar Asay-Davis

[View author publications](#)

You can also search for this author in [PubMed](#) [Google Scholar](#)

24. Andy Aschwanden

[View author publications](#)

You can also search for this author in [PubMed](#) [Google Scholar](#)

25. Alice Barthel

[View author publications](#)

You can also search for this author in [PubMed](#) [Google Scholar](#)

26. Andrew Bliss

[View author publications](#)

You can also search for this author in [PubMed](#) [Google Scholar](#)

27. Reinhard Calov

[View author publications](#)

You can also search for this author in [PubMed](#) [Google Scholar](#)

28. Christopher Chambers

[View author publications](#)

You can also search for this author in [PubMed](#) [Google Scholar](#)

29. Nicolas Champollion

[View author publications](#)

You can also search for this author in [PubMed](#) [Google Scholar](#)

30. Youngmin Choi

[View author publications](#)

You can also search for this author in [PubMed](#) [Google Scholar](#)

31. Richard Cullather

[View author publications](#)

You can also search for this author in [PubMed](#) [Google Scholar](#)

32. Joshua Cuzzzone

[View author publications](#)

You can also search for this author in [PubMed](#) [Google Scholar](#)

33. Christophe Dumas

[View author publications](#)

You can also search for this author in [PubMed](#) [Google Scholar](#)

34. Denis Felikson

[View author publications](#)

You can also search for this author in [PubMed](#) [Google Scholar](#)

35. Xavier Fettweis

[View author publications](#)

You can also search for this author in [PubMed](#) [Google Scholar](#)

36. Koji Fujita

[View author publications](#)

You can also search for this author in [PubMed](#) [Google Scholar](#)

37. Benjamin K. Galton-Fenzi

[View author publications](#)

You can also search for this author in [PubMed](#) [Google Scholar](#)

38. Rupert Gladstone

[View author publications](#)

You can also search for this author in [PubMed](#) [Google Scholar](#)

39. Nicholas R. Golledge

[View author publications](#)

You can also search for this author in [PubMed](#) [Google Scholar](#)

40. Ralf Greve

[View author publications](#)

You can also search for this author in [PubMed](#) [Google Scholar](#)

41. Tore Hattermann

[View author publications](#)

You can also search for this author in [PubMed](#) [Google Scholar](#)

42. Matthew J. Hoffman

[View author publications](#)

You can also search for this author in [PubMed](#) [Google Scholar](#)

43. Angelika Humbert

[View author publications](#)

You can also search for this author in [PubMed](#) [Google Scholar](#)

44. Matthias Huss

[View author publications](#)

You can also search for this author in [PubMed](#) [Google Scholar](#)

45. Philippe Huybrechts

[View author publications](#)

You can also search for this author in [PubMed](#) [Google Scholar](#)

46. Walter Immerzeel

[View author publications](#)

You can also search for this author in [PubMed](#) [Google Scholar](#)

47. Thomas Kleiner

[View author publications](#)

You can also search for this author in [PubMed](#) [Google Scholar](#)

48. Philip Kraaijenbrink

[View author publications](#)

You can also search for this author in [PubMed](#) [Google Scholar](#)

49. Sébastien Le clec'h

[View author publications](#)

You can also search for this author in [PubMed](#) [Google Scholar](#)

50. Victoria Lee

[View author publications](#)

You can also search for this author in [PubMed](#) [Google Scholar](#)

51. Gunter R. Leguy

[View author publications](#)

You can also search for this author in [PubMed](#) [Google Scholar](#)

52. Christopher M. Little

[View author publications](#)

You can also search for this author in [PubMed](#) [Google Scholar](#)

53. Daniel P. Lowry

[View author publications](#)

You can also search for this author in [PubMed](#) [Google Scholar](#)

54. Jan-Hendrik Malles

[View author publications](#)

You can also search for this author in [PubMed](#) [Google Scholar](#)

55. Daniel F. Martin

[View author publications](#)

You can also search for this author in [PubMed](#) [Google Scholar](#)

56. Fabien Maussion

[View author publications](#)

You can also search for this author in [PubMed](#) [Google Scholar](#)

57. Mathieu Morlighem

[View author publications](#)

You can also search for this author in [PubMed](#) [Google Scholar](#)

58. James F. O'Neill

[View author publications](#)

You can also search for this author in [PubMed](#) [Google Scholar](#)

59. Isabel Nias

[View author publications](#)

You can also search for this author in [PubMed](#) [Google Scholar](#)

60. Frank Pattyn

[View author publications](#)

You can also search for this author in [PubMed](#) [Google Scholar](#)

61. Tyler Pelle

[View author publications](#)

You can also search for this author in [PubMed](#) [Google Scholar](#)

62. Stephen F. Price

[View author publications](#)

You can also search for this author in [PubMed](#) [Google Scholar](#)

63. Aurélien Quiquet

[View author publications](#)

You can also search for this author in [PubMed](#) [Google Scholar](#)

64. Valentina Radić

[View author publications](#)

You can also search for this author in [PubMed](#) [Google Scholar](#)

65. Ronja Reese

[View author publications](#)

You can also search for this author in [PubMed](#) [Google Scholar](#)

66. David R. Rounce

[View author publications](#)

You can also search for this author in [PubMed](#) [Google Scholar](#)

67. Martin Rückamp

[View author publications](#)

You can also search for this author in [PubMed](#) [Google Scholar](#)

68. Akiko Sakai

[View author publications](#)

You can also search for this author in [PubMed](#) [Google Scholar](#)

69. Courtney Shafer

[View author publications](#)

You can also search for this author in [PubMed](#) [Google Scholar](#)

70. Nicole-Jeanne Schlegel

[View author publications](#)

You can also search for this author in [PubMed](#) [Google Scholar](#)

71. Sarah Shannon

[View author publications](#)

You can also search for this author in [PubMed](#) [Google Scholar](#)

72. Robin S. Smith

[View author publications](#)

You can also search for this author in [PubMed](#) [Google Scholar](#)

73. Fiammetta Straneo

[View author publications](#)

You can also search for this author in [PubMed](#) [Google Scholar](#)

74. Sainan Sun

[View author publications](#)

You can also search for this author in [PubMed](#) [Google Scholar](#)

75. Lev Tarasov

[View author publications](#)

You can also search for this author in [PubMed](#) [Google Scholar](#)

76. Luke D. Trusel

[View author publications](#)

You can also search for this author in [PubMed](#) [Google Scholar](#)

77. Jonas Van Breedam

[View author publications](#)

You can also search for this author in [PubMed](#) [Google Scholar](#)

78. Roderik van de Wal

[View author publications](#)

You can also search for this author in [PubMed](#) [Google Scholar](#)

79. Michiel van den Broeke

[View author publications](#)

You can also search for this author in [PubMed](#) [Google Scholar](#)

80. Ricarda Winkelmann

[View author publications](#)

You can also search for this author in [PubMed](#) [Google Scholar](#)

81. Harry Zekollari

[View author publications](#)

You can also search for this author in [PubMed](#) [Google Scholar](#)

82. Chen Zhao

[View author publications](#)

You can also search for this author in [PubMed](#) [Google Scholar](#)

83. Tong Zhang

[View author publications](#)

You can also search for this author in [PubMed](#) [Google Scholar](#)

84. Thomas Zwinger

[View author publications](#)

You can also search for this author in [PubMed](#) [Google Scholar](#)

Contributions

T.L.E. conceived the idea, carried out all statistical analysis except the random effects model, produced the figures, and wrote the manuscript. S.N. led ISMIP6, including experimental design, organization and analysis, and provided scientific interpretation. B.M. and R.H. co-led GlacierMIP and contributed simulations (below), and provided data and interpretation. H.G. and H.S. led the processing and analysis in ISMIP6 for the Greenland and Antarctic ice sheets, respectively, contributed simulations (below), and provided scientific interpretation and advice. N.C.J. and D.A.S. co-derived with T.L.E. the ice sheet continuous parameter distributions for the emulator, and also derived the corresponding ocean forcing parameterization studies with X.A.-D., F.S. and T.H. for Antarctica and with F.S., D.F. and M.M. for Greenland. F.T. performed the random effects model cross-check for Antarctica. C.J.S. provided the FaIR projections and C.M.M. provided the CMIP5 and CMIP6 projection data for the emulator. E.S. led the ISMIP6 data processing. A.A.-O., J.M.G., E.L., W.H.L., A.J.P., A. Shepherd contributed to the ISMIP6 experimental design, organization and analysis as members of its steering committee, and R.S.S. and W.H.L. led the ISMIP6 atmosphere focus group. C.M.L., A. Barthel and C.A. selected the CMIP5 models for ISMIP6, X.F. and P.A. ran the surface mass

balance model for the Greenland and R. Cullather prepared the Antarctic surface mass balance, and L.D.T. and M.v.d.B. provided the ice shelf collapse forcing. For Antarctica: T.K. and A.H. contributed the AWI/PISM simulations; M.J.H., T. Zhang and S.F.P. contributed the DOE/MALI simulations; R. Greve and R. Calov contributed the ILTS_PIK/SICOPOLIS simulations; H.G. and R.v.d.W. contributed the IMAU/IMAUICE simulations; N.-J.S. and H.S. contributed the JPL/ISSM simulations; C.D. and A.Q. contributed the LSCE/GRISLI simulations; G.R.L. and W.H.L. contributed the NCAR/CISM simulations; R.R., T.A. and R.W. contributed the PIK/PISM simulations; T.P., M.M. and H.S. contributed the UCIJPL/ISSM simulations; F.P. and S. Sun contributed the ULB/fETISH simulations; C.Z., R. Gladstone, B.K.G.-F. and T. Zwinger contributed the UTAS/Elmer/Ice simulations; J.V.B. and P.H. contributed the VUB/AISMPALEO simulations; N.R.G. and D.P.L. contributed the VUW/PISM simulations; and D.F.M., C. Shafer and J.F.O’N. contributed the CPOM/BISICLES simulations. For Greenland: M.R. and A.H. contributed the AWI/ISSM simulations; V.L. and A.J.P. contributed the BGC/BISICLES simulations; I.N., D.F. and S.N. contributed the GSFC/ISSM simulations; R. Greve, R. Calov and C.C. contributed the ILTS_PIK/SICOPOLIS simulations; H.G., R.v.d.W. and M.v.d.B. contributed the IMAU/IMAUICE simulations; N.-J.S. and H.S. contributed the JPL/ISSM simulations; J.C. and N.-J.S. contributed the JPL/ISSMPALEO simulations; A.Q. and C.D. contributed the LSCE/GRISLI simulations; L.T. contributed the MUN/GSM simulations; W.H.L. and G.R.L. contributed the NCAR/CISM simulations; A.A. contributed the UAF/PISM simulations; Y.C., H.S. and M.M. contributed the UCIJPL/ISSM simulations; S.L.c. and P.H. contributed the VUB/GISM simulations; and D.P.L. and N.R.G. contributed the VUW/PISM simulations. For global glaciers: B.A. contributed the AND2012 simulations; K.F. and A. Sakai contributed the GLIMB simulations; M. Huss contributed the GloGEM simulations; H.Z. contributed the GloGEMflow simulations; S. Shannon contributed the JULES simulations; P.K. and W.I. contributed the KRA2017 simulations; B.M. and J.-H.M. contributed the MAR2012 simulations; F.M. and N.C. contributed the OGGM simulations; D.R.R. and R.H. contributed the PyGEM simulations; A. Bliss and V.R. contributed the RAD2014 simulations; R.v.d.W.

contributed the WAL2001 simulations; and A. Bliss and J.-H.M. assisted with data handling. All authors contributed to the manuscript.

Corresponding author

Correspondence to [Tamsin L. Edwards](#).

Ethics declarations

Competing interests

The authors declare no competing interests.

Additional information

Peer review information *Nature* thanks Nicholas Barrand, Won Chang, Victoria Volodina, Daniel Williamson and the other, anonymous, reviewer(s) for their contribution to the peer review of this work.

Publisher's note Springer Nature remains neutral with regard to jurisdictional claims in published maps and institutional affiliations.

Extended data figures and tables

[Extended Data Fig. 1 Emulator leave-one-out validation for ice sheets and eight glacier regions.](#)

a–l, Left: emulator predictions versus simulations for each regional sea level contribution in the year 2100, with percentage of predictions falling outside ± 2 emulator standard deviations and mean absolute error in cm SLE. Right: standardized residuals (emulated minus simulated, divided by emulator standard deviation). Predictions falling outside ± 2 emulator standard deviations are shown in orange.

[Extended Data Fig. 2 Emulator leave-one-out validation for 11 glacier regions.](#)

As for Extended Data Fig. 1, but for the remaining glacier emulators.

[Extended Data Fig. 3 Temperature projections for 2015–2100 from FaIR and CMIP6 ensembles.](#)

a, b, Global surface air temperature projections under different greenhouse gas scenarios (see text) from the FaIR simple climate model ensemble (**a**; $N = 5,000$; same as Fig. 3a), and CMIP6 global climate model ensemble (**b**; $N \approx 30$ models per scenario; see [Methods](#)) sampled with a kernel density estimate ($N = 1,000$).

Extended Data Fig. 4 Sensitivity of ice sheet projections at 2100 under SSP5-85 to uncertain inputs.

a, Greenland. **b**, West Antarctica. **c**, East Antarctica. **d**, Antarctic Peninsula. Box and whiskers show [5, 25, 50, 75, 95]th percentiles. Indices refer to test (see Extended Data Table 3). Sensitivity test 1, default; 2, CMIP6 global climate model ensemble projections of global mean surface air temperature, instead of FaIR simple climate model; 3, fixed global mean surface air temperature; 4, fixed glacier retreat (Greenland) or basal melt (Antarctica) parameter. Antarctic regions only: basal melt parameter has sensitivity test 5: ‘mean Antarctic’ distribution; 6, ‘Pine Island Glacier’ distribution; 7, uniform, high distribution; 8, uniform, very high distribution. Ice shelf collapse scenario: sensitivity test 9, off; 10, on. 11, Risk-averse projections using the high ‘Pine Island Glacier’ distribution for basal melt (test 6), ice shelf collapse on (test 10), and the ice sheet and climate models that give the highest sea level contributions (Extended Data Fig. 5; test 6, 7).

Extended Data Fig. 5 Robustness of ice sheet projections under NDCs to ice sheet/climate model simulation selection and treatment.

a, Greenland. **b**, West Antarctica. **c**, East Antarctica. **d**, Antarctic Peninsula. Box and whiskers show [5, 25, 50, 75, 95]th percentiles. Indices refer to test (see Extended Data Table 4). Robustness test 1, default; 2, higher-resolution ice sheet models; 3, ice sheet models with the most complete sampling of uncertainties (10 models for Greenland, four for Antarctica); 4, single ice sheet model with the most complete sampling of uncertainties and (coincidentally) high sensitivity to retreat or basal melting parameter. Antarctic regions only: robustness test 5, alternative single ice sheet model with nearly as complete sampling but low sensitivity to basal melt parameter; 6, ice sheet models with the highest sensitivity to basal melt parameter; 7, climate models that lead to highest sea level contributions. 8, ice sheet models with 2015–2020 mass change in the range 0–0.6 cm SLE; 9, only ice sheet models that use the standard ISMIP melt parameterizations; 10, higher basal melt value assigned to ice sheet models that do not use the standard ISMIP6 melt parameterizations.

Extended Data Fig. 6 Sensitivity to basal melting by Antarctic ice sheet and climate model.

Vertical lines show ice sheet models that do not use the ISMIP6 basal melt parameterization, and the basal melt value they are assigned. Ice sheet models include the high and low sensitivity models in Extended Data Fig. 5: test 4 (ILTS_PIK/SICOPOLIS) and test 5 (LSCE/GRISLI).

Extended Data Fig. 7 Effect of Antarctic ice shelf collapse by climate model.

Additional sea level contribution at 2100 when using ice shelf collapse for six climate models, ordered by maximum impact on the Peninsula contribution. **a**, West Antarctica, **b**, East Antarctica and **c**, Antarctic Peninsula.

Extended Data Table 1 The additional 22 Greenland and 37 Antarctic ice sheet model experiments not previously described elsewhere

[Full size table](#)

Extended Data Table 2 Emulator structure and validation

[Full size table](#)

Extended Data Table 3 Sensitivity tests

[Full size table](#)

Extended Data Table 4 Robustness checks

[Full size table](#)

Supplementary information

Supplementary Information

Timeseries of projections provided as Comma Separated Value (CSV) files, and screen-readable versions of Extended Data Tables 3 and 4.

Rights and permissions

[Reprints and Permissions](#)

About this article



Check for
updates

Cite this article

Edwards, T.L., Nowicki, S., Marzeion, B. *et al.* Projected land ice contributions to twenty-first-century sea level rise. *Nature* **593**, 74–82 (2021). <https://doi.org/10.1038/s41586-021-03302-y>

[Download citation](#)

- Received: 30 December 2019
- Accepted: 27 January 2021
- Published: 05 May 2021
- Issue Date: 06 May 2021
- DOI: <https://doi.org/10.1038/s41586-021-03302-y>

Comments

By submitting a comment you agree to abide by our [Terms](#) and [Community Guidelines](#). If you find something abusive or that does not comply with our terms or guidelines please flag it as inappropriate.

[Access through your institution](#)

[Change institution](#)

[Buy or subscribe](#)

This article was downloaded by **calibre** from <https://www.nature.com/articles/s41586-021-03302-y>.

| [Section menu](#) | [Main menu](#) |

- Article
- [Published: 05 May 2021](#)

The Paris Climate Agreement and future sea-level rise from Antarctica

- [Robert M. DeConto](#) ORCID: [orcid.org/0000-0003-2800-6466¹](https://orcid.org/0000-0003-2800-6466),
- [David Pollard²](#),
- [Richard B. Alley^{2,3}](#),
- [Isabella Velicogna⁴](#),
- [Edward Gasson⁵](#),
- [Natalya Gomez](#) ORCID: [orcid.org/0000-0002-2463-7917⁶](https://orcid.org/0000-0002-2463-7917),
- [Shaina Sadai¹](#),
- [Alan Condron](#) ORCID: [orcid.org/0000-0002-7337-1713⁷](https://orcid.org/0000-0002-7337-1713),
- [Daniel M. Gilford](#) ORCID: [orcid.org/0000-0003-2422-0887⁸](https://orcid.org/0000-0003-2422-0887),
- [Erica L. Ashe](#) ORCID: [orcid.org/0000-0002-7445-6321⁸](https://orcid.org/0000-0002-7445-6321),
- [Robert E. Kopp](#) ORCID: [orcid.org/0000-0003-4016-9428⁸](https://orcid.org/0000-0003-4016-9428),
- [Dawei Li^{1,9}](#) &
- [Andrea Dutton](#) ORCID: [orcid.org/0000-0002-3836-119X¹⁰](https://orcid.org/0000-0002-3836-119X)

[Nature](#) volume 593, pages83–89(2021) [Cite this article](#)

- 2475 Accesses
- 1027 Altmetric
- [Metrics details](#)

Subjects

- [Climate and Earth system modelling](#)
- [Climate-change impacts](#)
- [Cryospheric science](#)

Abstract

The Paris Agreement aims to limit global mean warming in the twenty-first century to less than 2 degrees Celsius above preindustrial levels, and to promote further efforts to limit warming to 1.5 degrees Celsius¹. The amount of greenhouse gas emissions in coming decades will be consequential for global mean sea level (GMSL) on century and longer timescales through a combination of ocean thermal expansion and loss of land ice². The Antarctic Ice Sheet (AIS) is Earth's largest land ice reservoir (equivalent to 57.9 metres of GMSL)³, and its ice loss is accelerating⁴. Extensive regions of the AIS are grounded below sea level and susceptible to dynamical instabilities^{5,6,7,8} that are capable of producing very rapid retreat⁸. Yet the potential for the implementation of the Paris Agreement temperature targets to slow or stop the onset of these instabilities has not been directly tested with physics-based models. Here we use an observationally calibrated ice sheet–shelf model to show that with global warming limited to 2 degrees Celsius or less, Antarctic ice loss will continue at a pace similar to today's throughout the twenty-first century. However, scenarios more consistent with current policies (allowing 3 degrees Celsius of warming) give an abrupt jump in the pace of Antarctic ice loss after around 2060, contributing about 0.5 centimetres GMSL rise per year by 2100—an order of magnitude faster than today⁴. More fossil-fuel-intensive scenarios⁹ result in even greater acceleration. Ice-sheet retreat initiated by the thinning and loss of buttressing ice shelves continues for centuries, regardless of bedrock and sea-level feedback mechanisms^{10,11,12} or geoengineered carbon dioxide reduction. These results demonstrate the possibility that rapid and unstoppable sea-level rise from Antarctica will be triggered if Paris Agreement targets are exceeded.

[Access through your institution](#)

[Change institution](#)

[Buy or subscribe](#)

Access options

Subscribe to Journal

Get full journal access for 1 year

\$199.00

only \$3.90 per issue

[Subscribe](#)

All prices are NET prices.

VAT will be added later in the checkout.

Tax calculation will be finalised during checkout.

Rent or Buy article

Get time limited or full article access on ReadCube.

from \$8.99

[Rent or Buy](#)

All prices are NET prices.

Additional access options:

- [Log in](#)
- [Access through your institution](#)
- [Learn about institutional subscriptions](#)

Fig. 1: Antarctic contribution to future GMSL rise.

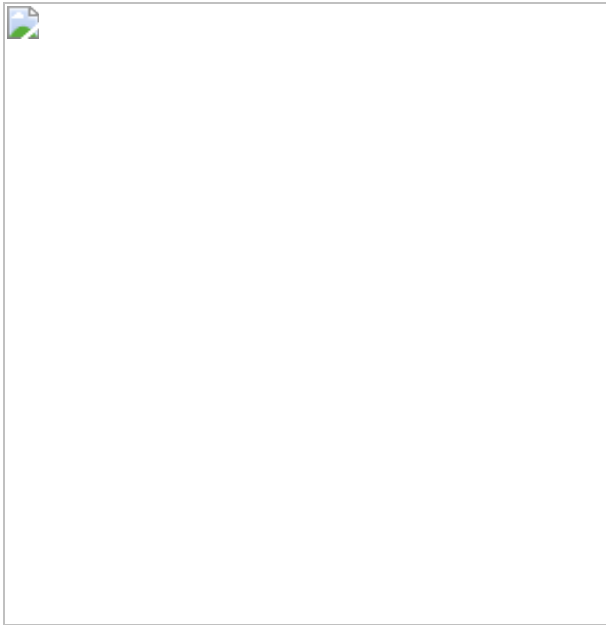


Fig. 2: Ice-sheet evolution following the +3 °C global warming emissions trajectory.

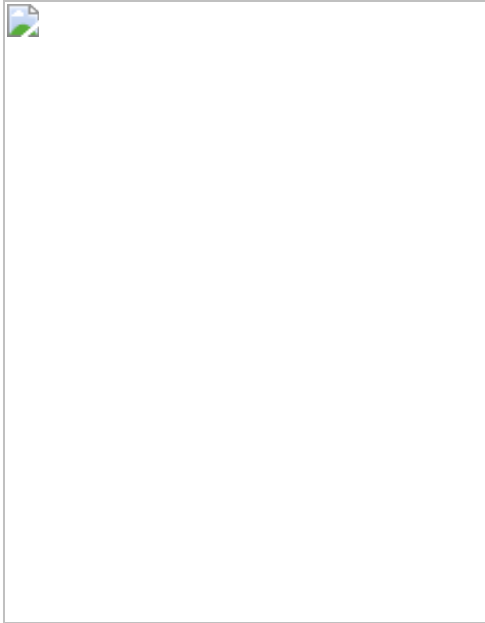
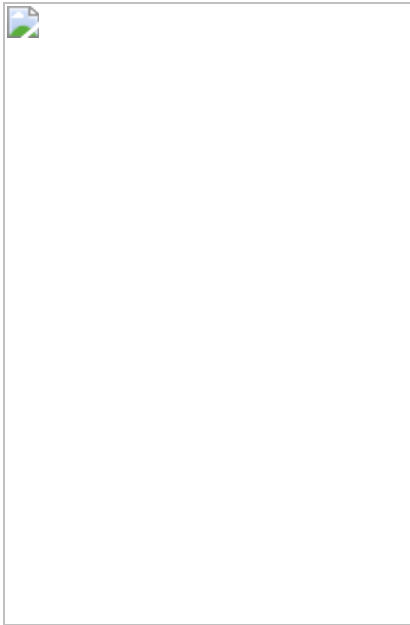


Fig. 3: AIS thresholds and commitments to GMSL rise with delayed mitigation.



Data availability

Model-generated data associated with this work are available with this paper. Three-dimensional ice-sheet model output associated with Fig. 2 and Extended Data Figs. 3, 5 are available at the ScholarWorks@UMASS Amherst repository (<https://doi.org/10.7275/j005-r778>). Climate model forcing used in our main ensembles and meltwater-feedback simulations (Fig. 1) are reported in refs. 46,80. [Source data](#) are provided with this paper.

Code availability

The modified ice-sheet model codes based on ref. 51 are available from the corresponding author. CESM1.2.2 GCM⁸⁷ is available from NCAR (<https://www.cesm.ucar.edu/models/cesm1.2/>) and the RCM is reported in ref. 79. The Earth–sea level model is described in refs. 12,49.

References

1. 1.

UNFCCC. *Adoption of the Paris Agreement* FCCC/CP/2015/L.9/Rev.1 (United Nations Framework Convention on Climate Change, 2015); <https://unfccc.int/resource/docs/2015/cop21/eng/109r01.pdf>.

2. 2.

Mengel, M., Nauels, A., Rogelj, J. & Schleussner, C.-F. Committed sea-level rise under the Paris Agreement and the legacy of delayed mitigation action. *Nat. Commun.* **9**, 601 (2018).

[PubMed](#) [PubMed Central](#) [Article](#) [ADS](#) [CAS](#) [Google Scholar](#)

3. 3.

Morlighem, M. et al. Deep glacial troughs and stabilizing ridges unveiled beneath the margins of the Antarctic ice sheet. *Nat. Geosci.* **13**, 132–137 (2020).

[CAS](#) [Article](#) [ADS](#) [Google Scholar](#)

4. 4.

Shepherd, A. et al. Mass balance of the Antarctic Ice Sheet from 1992 to 2017. *Nature* **558**, 219–222 (2018).

[Article](#) [ADS](#) [CAS](#) [Google Scholar](#)

5. 5.

Weertman, J. Stability of the junction of an ice sheet and an ice shelf. *J. Glaciol.* **13**, 3–11 (1974).

[Article](#) [ADS](#) [Google Scholar](#)

6. 6.

Schoof, C. Ice sheet grounding line dynamics: steady states, stability, and hysteresis. *J. Geophys. Res. Earth Surf.* **112**, F03S28 (2007).

[Article](#) [ADS](#) [Google Scholar](#)

7. 7.

Pollard, D., DeConto, R. M. & Alley, R. B. Potential Antarctic Ice Sheet retreat driven by hydrofracturing and ice cliff failure. *Earth Planet. Sci. Lett.* **412**, 112–121 (2015).

[CAS](#) [Article](#) [ADS](#) [Google Scholar](#)

8. 8.

DeConto, R. M. & Pollard, D. Contribution of Antarctica to past and future sea-level rise. *Nature* **531**, 591–597 (2016).

[CAS](#) [PubMed](#) [Article](#) [ADS](#) [Google Scholar](#)

9. 9.

Meinshausen, N. et al. The RCP greenhouse gas concentrations and their extensions from 1765 to 2300. *Clim. Change* **109**, 213–241 (2011).

[CAS](#) [Article](#) [ADS](#) [Google Scholar](#)

10. 10.

Barletta, V. R. et al. Observed rapid bedrock uplift in Amundsen Sea Embayment promotes ice-sheet stability. *Science* **360**, 1335–1339 (2018).

[CAS](#) [PubMed](#) [Article](#) [ADS](#) [Google Scholar](#)

11. 11.

Larour, E. et al. Slowdown in Antarctic mass loss from solid Earth and sea-level feedbacks. *Science* **364**, eaav7908 (2019).

[CAS](#) [PubMed](#) [Article](#) [ADS](#) [Google Scholar](#)

12. 12.

Gomez, N., Pollard, D. & Holland, D. Sea level feedback lowers projections of future Antarctic Ice Sheet mass loss. *Nat. Commun.* **6**, 8798 (2015).

[CAS](#) [PubMed](#) [PubMed Central](#) [Article](#) [ADS](#) [Google Scholar](#)

13. 13.

Fürst, J. J. et al. The safety band of Antarctic ice shelves. *Nat. Clim. Chang.* **6**, 479 (2016).

[Article](#) [ADS](#) [Google Scholar](#)

14. 14.

Paolo, F. S., Fricker, H. & Padman, L. Volume loss from Antarctic ice shelves is accelerating. *Science* **348**, 327–331 (2015).

[CAS](#) [PubMed](#) [Article](#) [ADS](#) [Google Scholar](#)

15. 15.

Gudmundsson, G. H. Ice-shelf buttressing and the stability of marine ice sheets. *Cryosphere* **7**, 647–655 (2013).

[Article](#) [ADS](#) [Google Scholar](#)

16. 16.

Bassis, J. N. & Walker, C. C. Upper and lower limits on the stability of calving glaciers from the yield strength envelope of ice. *Proc. R. Soc. Lond. A* **468**, 913–931 (2012).

[ADS](#) [Google Scholar](#)

17. 17.

Parizek, B. R. et al. Ice-cliff failure via retrogressive slumping. *Geology* **47**, 1–4 (2019).

[Article](#) [ADS](#) [Google Scholar](#)

18. 18.

Clerc, F., Minchew, B. M. & Behn, M. D. Marine ice cliff instability mitigated by slow removal of ice shelves. *Geophys. Res. Lett.* **46**, 12108–12116 (2019).

[Article](#) [ADS](#) [Google Scholar](#)

19. 19.

Vaughan, D. G. Relating the occurrence of crevasses to surface strain rates. *J. Glaciol.* **39**, 255–266 (1993).

[Article](#) [ADS](#) [Google Scholar](#)

20. 20.

Schlemm, T. & Levermann, A. A simple stress-based cliff-calving law. *Cryosphere* **13**, 2475–2488 (2019).

[Article](#) [ADS](#) [Google Scholar](#)

21. 21.

An, L. et al. Bed elevation of Jakobshavn Isbræ, West Greenland, from high-resolution airborne gravity and other data. *Geophys. Res. Lett.* **44**, 3728–3736 (2017).

[Article](#) [ADS](#) [Google Scholar](#)

22. 22.

Khazendar, A. et al. Interruption of two decades of Jakobshavn Isbræ acceleration and thinning as regional ocean cools. *Nat. Geosci.* **12**,

277–283 (2019).

[CAS](#) [Article](#) [ADS](#) [Google Scholar](#)

23. 23.

Joughin, I. et al. Seasonal to decadal scale variations in the surface velocity of Jakobshavn Isbræ, Greenland: observation and model-based analysis. *J. Geophys. Res. Earth Surf.* **117**, F02030 (2012).

[Article](#) [ADS](#) [Google Scholar](#)

24. 24.

Rignot, E. et al. Accelerated ice discharge from the Antarctic Peninsula following the collapse of Larsen B ice shelf. *Geophys. Res. Lett.* **31**, L18401 (2004).

[Article](#) [ADS](#) [CAS](#) [Google Scholar](#)

25. 25.

Scambos, T. A., Berthier, E. & Shuman, C. A. The triggering of subglacial lake drainage during rapid glacier drawdown: Crane Glacier, Antarctic Peninsula. *Ann. Glaciol.* **52**, 74–82 (2011).

[Article](#) [ADS](#) [Google Scholar](#)

26. 26.

Milillo, P. et al. Heterogeneous retreat and ice melt of Thwaites Glacier, West Antarctica. *Sci. Adv.* **5**, eaau3433 (2019).

[CAS](#) [PubMed](#) [PubMed Central](#) [Article](#) [ADS](#) [Google Scholar](#)

27. 27.

Atkinson, B. K. Subcritical crack growth in geological materials. *J. Geophys. Res. Solid Earth* **89**, 4077–4114 (1984).

[CAS](#) [Article](#) [Google Scholar](#)

28. 28.

Kuipers Munneke, P., Ligtenberg, S. R. M., van den Broeke, M. R. & Vaughan, D. G. Firn air depletion as a precursor of Antarctic ice-shelf collapse. *J. Glaciol.* **60**, 205–214 (2014).

[Article](#) [ADS](#) [Google Scholar](#)

29. 29.

Banwell, A. F., Willis, I. C., Macdonald, G. J., Goodsell, B. & MacAyeal, D. R. Direct measurements of ice-shelf flexure caused by surface meltwater ponding and drainage. *Nat. Commun.* **10**, 730 (2019).

[CAS](#) [PubMed](#) [PubMed Central](#) [Article](#) [ADS](#) [Google Scholar](#)

30. 30.

Trusel, L. D. et al. Divergent trajectories of Antarctic surface melt under two twenty-first-century climate scenarios. *Nat. Geosci.* **8**, 927–932 (2015).

[CAS](#) [Article](#) [ADS](#) [Google Scholar](#)

31. 31.

Robel, A. A. & Banwell, A. F. A speed limit on ice shelf collapse through hydrofracture. *Geophys. Res. Lett.* **46**, 12092–12100 (2019).

[Article](#) [ADS](#) [Google Scholar](#)

32. 32.

Fawcett, A. A. et al. Can Paris pledges avert severe climate change? *Science* **350**, 1168–1169 (2015).

[CAS](#) [PubMed](#) [Article](#) [ADS](#) [PubMed Central](#) [Google Scholar](#)

33. 33.

Edwards, T. L. et al. Revisiting Antarctic ice loss due to marine ice-cliff instability. *Nature* **566**, 58–64 (2019).

[CAS](#) [PubMed](#) [Article](#) [ADS](#) [Google Scholar](#)

34. 34.

Dutton, A., Webster, J. M., Zwart, D. & Lambeck, K. Tropical tales of polar ice: evidence of Last Interglacial polar ice sheet retreat recorded by fossil reefs of the granitic Seychelles islands. *Quat. Sci. Rev.* **107**, 182–196 (2015).

[Article](#) [ADS](#) [Google Scholar](#)

35. 35.

Grant, G. R. et al. The amplitude and origin of sea-level variability during the Pliocene epoch. *Nature* **574**, 237–241 (2019).

[CAS](#) [PubMed](#) [Article](#) [ADS](#) [PubMed Central](#) [Google Scholar](#)

36. 36.

Dumitru, O. A. et al. Constraints on global mean sea level during Pliocene warmth. *Nature* **574**, 233–236 (2019).

[CAS](#) [PubMed](#) [Article](#) [ADS](#) [PubMed Central](#) [Google Scholar](#)

37. 37.

Gilford, D. M. et al. Could the Last Interglacial constrain projections of future Antarctic ice mass loss and sea-level rise? *J. Geophys. Res. Earth Surf.* **125**, e2019JF005418 (2020).

[Article](#) [ADS](#) [Google Scholar](#)

38. 38.

Velicogna, I., Sutterley, T. C. & van den Broeke, M. Regional acceleration in ice mass loss from Greenland and Antarctica using GRACE time-variable gravity data. *Geophys. Res. Lett.* **41**, 8130–8137 (2014).

[Article](#) [ADS](#) [Google Scholar](#)

39. 39.

Rohling, E. J. et al. Asynchronous Antarctic and Greenland ice-volume contributions to the last interglacial sea-level highstand. *Nat. Commun.* **10**, 5040 (2019).

[PubMed](#) [PubMed Central](#) [Article](#) [ADS](#) [CAS](#) [Google Scholar](#)

40. 40.

Cook, C. P. et al. Dynamic behaviour of the East Antarctic Ice Sheet during Pliocene warmth. *Nat. Geosci.* **6**, 765–769 (2013).

[CAS](#) [Article](#) [ADS](#) [Google Scholar](#)

41. 41.

Golledge, N. R. et al. Global environmental consequences of twenty-first-century ice-sheet melt. *Nature* **566**, 65–72 (2019).

[CAS](#) [PubMed](#) [Article](#) [ADS](#) [Google Scholar](#)

42. 42.

Seroussi, H. & Morlighem, M. Representation of basal melting at the grounding line in ice flow models. *Cryosphere* **12**, 3085–3096 (2018).

[Article](#) [ADS](#) [Google Scholar](#)

43. 43.

Tsai, V. C., Stewart, A. L. & Thompson, A. F. Marine ice-sheet profiles and stability under coulomb basal conditions. *J. Glaciol.* **61**, 205–215 (2017).

[Article](#) [Google Scholar](#)

44. 44.

Pattyn, F. Sea-level response to melting of Antarctic ice shelves on multi-centennial time scales with the fast Elementary Thermomechanical Ice Sheet model (f.ETISh v1.0). *Cryosphere* **11**, 1851–1878 (2017).

[Article](#) [ADS](#) [Google Scholar](#)

45. 45.

Seroussi, H. et al. ISMIP6 Antarctica: a multi-model ensemble of the Antarctic ice sheet evolution over the 21st century. *Cryosphere* **14**, 3033–3070 (2020).

[Article](#) [ADS](#) [Google Scholar](#)

46. 46.

Sadai, S., Condron, A., DeConto, R. & Pollard, D. Future climate response to Antarctic Ice Sheet melt caused by anthropogenic warming. *Sci. Adv.* **6**, eaaz1169 (2020).

[PubMed](#) [PubMed Central](#) [Article](#) [ADS](#) [Google Scholar](#)

47. 47.

Bell, R. E. et al. Antarctic ice shelf potentially stabilized by export of meltwater in surface river. *Nature* **544**, 344–348 (2017).

[CAS](#) [PubMed](#) [Article](#) [ADS](#) [Google Scholar](#)

48. 48.

Lai, C.-Y. et al. Vulnerability of Antarctica's ice shelves to meltwater-driven fracture. *Nature* **584**, 574–578 (2020).

[CAS](#) [PubMed](#) [Article](#) [ADS](#) [PubMed Central](#) [Google Scholar](#)

49. 49.

Pollard, D., Gomez, N. & DeConto, R. Variations of the Antarctic Ice Sheet in a coupled ice sheet-Earth-sea level model: sensitivity to viscoelastic earth properties. *J. Geophys. Res. Earth Surf.* **122**, 2169–9011 (2017).

[Article](#) [Google Scholar](#)

50. 50.

Powell, E., Gomez, N., Hay, C., Latychev, K. & Mitrovica, J. X. Viscous effects in the solid earth response to modern Antarctic ice mass flux: implications for geodetic studies of WAIS stability in a warming world. *J. Clim.* **33**, 443–459 (2020).

[Article](#) [ADS](#) [Google Scholar](#)

51. 51.

Pollard, D. & DeConto, R. Description of a hybrid ice sheet-shelf model, and application to Antarctica. *Geosci. Model Dev.* **5**, 1273–1295 (2012).

[Article](#) [ADS](#) [Google Scholar](#)

52. 52.

Pollard, D. & DeConto, R. M. A simple inverse method for the distribution of basal sliding coefficients under ice sheets, applied to Antarctica. *Cryosphere* **6**, 953–971 (2012).

[Article](#) [ADS](#) [Google Scholar](#)

53. 53.

Fretwell, P. et al. Bedmap2: improved ice bed, surface and thickness datasets for Antarctica. *Cryosphere* **7**, 375–393 (2013).

[Article](#) [ADS](#) [Google Scholar](#)

54. 54.

Holland, P. R., Jenkins, A. & Holland, D. The response of ice shelf basal melting to variations in ocean temperature. *J. Clim.* **21**, 2558–2572 (2008).

[Article](#) [ADS](#) [Google Scholar](#)

55. 55.

Pollard, D., Chang, W., Haran, M., Applegate, P. & DeConto, R. Large ensemble modeling of last deglacial retreat of the West Antarctic Ice Sheet: comparison of simple and advanced statistical techniques. *Geosci. Model Dev.* **9**, 1697–1723 (2016).

[Article](#) [ADS](#) [Google Scholar](#)

56. 56.

Rignot, E., Jacobs, S., Mouginot, J. & Scheuchl, B. Ice shelf melting around Antarctica. *Science* **314**, 266–270 (2013).

[Article](#) [ADS](#) [CAS](#) [Google Scholar](#)

57. 57.

Schmidtko, S., Heywood, K. J., Thompson, A. F. & Aoki, S. Multidecadal warming of Antarctic waters. *Science* **346**, 1227–1231 (2014).

[CAS](#) [PubMed](#) [Article](#) [ADS](#) [Google Scholar](#)

58. 58.

Nick, F. M., Van der Veen, C. J., Vieli, A. & Benn, D. I. A physically based calving model applied to marine outlet glaciers and implications for the glacier dynamics. *J. Glaciol.* **56**, 781–794 (2010).

[Article](#) [ADS](#) [Google Scholar](#)

59. 59.

Tsai, C.-Y., Forest, C. E. & Pollard, D. The role of internal climate variability in projecting Antarctica's contribution to future sea-level rise. *Clim. Dyn.* **55**, 1875–1892 (2020).

[Article](#) [Google Scholar](#)

60. 60.

Benn, D. I., Warren, C. R. & Mottram, R. H. Calving processes and the dynamics of calving glaciers. *Earth Sci. Rev.* **82**, 143–179 (2007).

[Article](#) [ADS](#) [Google Scholar](#)

61. 61.

Ma, Y., Tripathy, C. S. & Bassis, J. N. Bounds on the calving cliff height of marine terminating glaciers. *Geophys. Res. Lett.* **44**, 1369–1375 (2017).

[Article](#) [ADS](#) [Google Scholar](#)

62. 62.

Robel, A. A. Thinning sea ice weakens buttressing force of iceberg mélange and promotes calving. *Nat. Commun.* **8**, 14596 (2017).

[PubMed](#) [PubMed Central](#) [Article](#) [ADS](#) [Google Scholar](#)

63. 63.

Joughin, I., Shean, D. E., Smith, B. E. & Floricioiu, D. A decade of variability on Jakobshavn Isbræ: ocean temperatures pace speed through influence on mélange rigidity. *Cryosphere* **14**, 211–227 (2020).

[PubMed](#) [PubMed Central](#) [Article](#) [ADS](#) [Google Scholar](#)

64. 64.

Pollard, D., DeConto, R. M. & Alley, R. B. A continuum model (PSUMEL1) of ice mélange and its role during retreat of the Antarctic Ice Sheet. *Geosci. Model Dev.* **11**, 5149–5172 (2018).

[Article](#) [ADS](#) [Google Scholar](#)

65. 65.

Locarnini, R. A. et al. *World Ocean Atlas 2013, Volume 1: Temperature* (National Oceanographic Data Center, 2013).

66. 66.

Bindschadler, R. A. et al. Ice-sheet model sensitivities to environmental forcing and their use in projecting future sea level (the SeaRISE project). *J. Glaciol.* **59**, 195–224 (2013).

[Article](#) [ADS](#) [Google Scholar](#)

67. 67.

Le Brocq, A., Payne, A. J. & Vieli, A. An improved Antarctic dataset for high resolution numerical ice sheet models (ALBMAP v1). *Earth Syst. Sci. Data* **2**, 247–260 (2010).

[Article](#) [ADS](#) [Google Scholar](#)

68. 68.

Jenkins, A. et al. West Antarctic Ice Sheet retreat in the Amundsen Sea driven by decadal oceanic variability. *Nat. Geosci.* **11**, 733–738 (2018).

[CAS](#) [Article](#) [ADS](#) [Google Scholar](#)

69. 69.

Whitehouse, P. L., Bentley, M. J., Milne, G. A., King, M. A. & Thomas, I. D. A new glacial isostatic adjustment model for Antarctica: calibrated and tested using observations of relative sea-level change and present-day uplift rates. *Geophys. J. Int.* **190**, 1464–1482 (2012).

[Article](#) [ADS](#) [Google Scholar](#)

70. 70.

Ivins, E. R. et al. Antarctic contribution to sea level rise observed by GRACE with improved GIA correction. *J. Geophys. Res. Solid Earth* **118**, 3126–3141 (2013).

[Article](#) [ADS](#) [Google Scholar](#)

71. 71.

Geruo, A., Wahr, J. & Zhong, S. Computations of the viscoelastic response of a 3-D compressible Earth to surface loading: an application to Glacial Isostatic Adjustment in Antarctica and Canada. *Geophys. J. Int.* **192**, 557–572 (2013).

[Article](#) [ADS](#) [Google Scholar](#)

72. 72.

Capron, E. et al. Temporal and spatial structure of multi-millennial temperature changes at high latitudes during the last interglacial. *Quat. Sci. Rev.* **103**, 116–133 (2014).

[Article](#) [ADS](#) [Google Scholar](#)

73. 73.

Clark, P. U. et al. Oceanic forcing of penultimate deglacial and last interglacial sea-level rise. *Nature* **577**, 660–664 (2020).

[CAS](#) [PubMed](#) [Article](#) [ADS](#) [PubMed Central](#) [Google Scholar](#)

74. 74.

Austermann, J., Mitrovica, J. X., Huybers, P. & Rovere, A. Detection of a dynamic topography signal in last interglacial sea-level records. *Sci. Adv.* **3**, e1700457 (2017).

[PubMed](#) [PubMed Central](#) [Article](#) [ADS](#) [Google Scholar](#)

75. 75.

Goelzer, H., Huybrechts, P., Loutre, M.-F. & Fichefet, T. Last Interglacial climate and sea-level evolution from a coupled ice sheet–climate model. *Clim. Past* **12**, 2195–2213 (2016).

[Article](#) [Google Scholar](#)

76. 76.

Helsen, M. M., van de Berg, W. J., van de Wal, R. S. W., van den Broeke, M. R. & Oerlemans, J. Coupled regional climate-ice-sheet simulation shows limited Greenland ice loss during the Eemian. *Clim. Past* **9**, 1773–1788 (2013).

[Article](#) [Google Scholar](#)

77. 77.

NEEM community members. Eemian interglacial reconstructed from a Greenland folded ice core. *Nature* **493**, 489–494 (2013).

[Article](#) [ADS](#) [CAS](#) [Google Scholar](#)

78. 78.

Nicholl, J. A. L. et al. A Laurentide outburst flooding event during the last interglacial period. *Nat. Geosci.* **5**, 901–904 (2012).

[CAS](#) [Article](#) [ADS](#) [Google Scholar](#)

79. 79.

Pal, J. S. et al. Regional climate modeling for the developing world – the ITCP RegCM3 and RegCNET. *Bull. Am. Meteorol. Soc.* **88**, 1395–1409 (2007).

[Article](#) [ADS](#) [Google Scholar](#)

80. 80.

Shields, C. A. & Kiehl, J. T. Simulating the Pineapple Express in the half degree Community Climate System Model, CCSM4. *Geophys. Res. Lett.* **43**, 7767–7773 (2016).

[Article](#) [ADS](#) [Google Scholar](#)

81. 81.

van Wessem, J. M. et al. Updated cloud physics in a regional atmospheric climate model improves the modelled surface energy balance of Antarctica. *Cryosphere* **8**, 125–135 (2014).

[Article](#) [ADS](#) [Google Scholar](#)

82. 82.

Lenaerts, J. T. M., Vizcaino, M., Fyke, J., van Kampenhout, L. & van den Broeke, M. R. Present-day and future Antarctic ice sheet climate and surface mass balance in the Community Earth System Model. *Clim. Dyn.* **47**, 1367–1381 (2016).

[Article](#) [Google Scholar](#)

83. 83.

Morelli, A. & Danesi, S. Seismological imaging of the Antarctic continental lithosphere: a review. *Global Planet. Change* **42**, 155–165 (2004).

[Article](#) [ADS](#) [Google Scholar](#)

84. 84.

Heeszel, D. S. et al. Upper mantle structure of central and West Antarctica from array analysis of Rayleigh wave phase velocities. *J. Geophys. Res. Solid Earth* **121**, 1758–1775 (2016).

[Article](#) [ADS](#) [Google Scholar](#)

85. 85.

Nield, G. A. et al. Rapid bedrock uplift in the Antarctic Peninsula explained by viscoelastic response to recent ice unloading. *Earth Planet. Sci. Lett.* **397**, 32–41 (2014).

[CAS](#) [Article](#) [ADS](#) [Google Scholar](#)

86. 86.

Zhao, C. et al. Rapid ice unloading in the Fleming glacier region, southern Antarctic Peninsula, and its effect on bedrock uplift rates. *Earth Planet. Sci. Lett.* **473**, 164–176 (2017).

[CAS](#) [Article](#) [ADS](#) [Google Scholar](#)

87. 87.

Hurrell, J. W. et al. The Community Earth System Model: a framework for collaborative research. *Bull. Am. Meteorol. Soc.* **94**, 1339–1360 (2013).

[Article](#) [ADS](#) [Google Scholar](#)

[Download references](#)

Acknowledgements

We thank T. Naish for guidance on Pliocene sea-level targets. This research was supported by the NSF under awards 1664013, 2035080, 1443347 and 1559040, and by a grant to the NASA Sea Level Change Team 80NSSC17K0698.

Author information

Affiliations

1. Department of Geosciences, University of Massachusetts Amherst, Amherst, MA, USA

Robert M. DeConto, Shaina Sadai & Dawei Li

2. Earth and Environmental Systems Institute, Pennsylvania State University, University Park, PA, USA

David Pollard & Richard B. Alley

3. Department of Geosciences, Pennsylvania State University, University Park, PA, USA

Richard B. Alley

4. Earth System Science, University of California, Irvine, CA, USA

Isabella Velicogna

5. School of Geographical Sciences, University of Bristol, Bristol, UK

Edward Gasson

6. Department of Earth and Planetary Sciences, McGill University,
Montreal, Quebec, Canada

Natalya Gomez

7. Department of Geology and Geophysics, Woods Hole Oceanographic
Institution, Woods Hole, MA, USA

Alan Condron

8. Department of Earth and Planetary Sciences, Rutgers University,
Piscataway, NJ, USA

Daniel M. Gilford, Erica L. Ashe & Robert E. Kopp

9. School of Oceanography, Shanghai Jiao Tong University, Shanghai,
China

Dawei Li

10. Department of Geoscience, University of Wisconsin-Madison,
Madison, WI, USA

Andrea Dutton

Authors

1. Robert M. DeConto

[View author publications](#)

You can also search for this author in [PubMed](#) [Google Scholar](#)

2. David Pollard

[View author publications](#)

You can also search for this author in [PubMed](#) [Google Scholar](#)

3. Richard B. Alley

[View author publications](#)

You can also search for this author in [PubMed](#) [Google Scholar](#)

4. Isabella Velicogna

[View author publications](#)

You can also search for this author in [PubMed](#) [Google Scholar](#)

5. Edward Gasson

[View author publications](#)

You can also search for this author in [PubMed](#) [Google Scholar](#)

6. Natalya Gomez

[View author publications](#)

You can also search for this author in [PubMed](#) [Google Scholar](#)

7. Shaina Sadai

[View author publications](#)

You can also search for this author in [PubMed](#) [Google Scholar](#)

8. Alan Condron

[View author publications](#)

You can also search for this author in [PubMed](#) [Google Scholar](#)

9. Daniel M. Gilford

[View author publications](#)

You can also search for this author in [PubMed](#) [Google Scholar](#)

10. Erica L. Ashe

[View author publications](#)

You can also search for this author in [PubMed](#) [Google Scholar](#)

11. Robert E. Kopp

[View author publications](#)

You can also search for this author in [PubMed](#) [Google Scholar](#)

12. Dawei Li

[View author publications](#)

You can also search for this author in [PubMed](#) [Google Scholar](#)

13. Andrea Dutton

[View author publications](#)

You can also search for this author in [PubMed](#) [Google Scholar](#)

Contributions

R.M.D. and D.P. conceived the model experiments and developed the main model codes with conceptual input from R.B.A.; R.M.D. and D.P. wrote the manuscript with input from R.B.A., I.V., E.G., N.G., and S.S.; I.V. provided GRACE mass change estimates; E.G. contributed to climate forcing scenarios; S.S. and A.C. provided CESM1.2.2 climatologies; N.G. collaborated on coupled ice–Earth simulations; A.D. provided palaeo sea-level target ranges; D.L. compiled CMIP5 and CMIP6 GCM results; and D.M.G., E.L.A. and R.E.K. developed the statistical model described in Supplementary Information.

Corresponding author

Correspondence to [Robert M. DeConto](#).

Ethics declarations

Competing interests

The authors declare no competing interests.

Additional information

Peer review information *Nature* thanks Jacqueline Austermann and the other, anonymous, reviewer(s) for their contribution to the peer review of this work.

Publisher's note Springer Nature remains neutral with regard to jurisdictional claims in published maps and institutional affiliations.

Extended data figures and tables

Extended Data Fig. 1 Ensemble observational targets.

196 simulations (grey lines), each using a unique combination of hydrofracturing and ice-cliff calving parameters (Extended Data Table 1) compared with observations (blue dashed boxes). Solid blue lines show simulations without hydrofracturing and ice-cliff calving. Red lines show simulations with maximum parameter values in our main ensemble. Additional simulations (black lines) allow ice-cliff calving rates of up to 26 km yr^{-1} , twice the maximum value used in our main ensembles. The vertical heights of the blue boxes represent the likely range of observations. Changes in ice mass above floatation are shown in equivalent GMSL. **a**, Simulated annual contributions to GMSL in the RCP8.5 ensemble compared with the 1992–2017 IMBIE⁴ observational average (0.15–0.46 mm yr⁻¹; dashed blue box). **b**, LIG ensemble simulations from 130 to 125 kyr ago. The height of the dashed blue box shows the LIG target range (3.1–6.1 m), the width represents ~1,000-yr age uncertainty³⁴. **c**, The same LIG simulations as in **b**, showing the rate of GMSL change contributed by Antarctica, smoothed over a 25-yr window. The peak in the early LIG is mainly caused by marine-based ice loss in West Antarctica. **d**, The same as **b**, except for warmer mid-Pliocene conditions. Maximum ice loss is compared with observational estimates of 11–21 m (refs. ^{35,36}; blue dashed lines). Note the saturation of the simulated GMSL values near the top of the LIG and Pliocene ensemble range, and the failure of the model to produce realistic LIG or Pliocene sea levels without hydrofracturing and ice-cliff calving enabled (blue lines). [Source data](#)

Extended Data Fig. 2 RCP8.5 ensembles calibrated with alternative GRACE estimates.

a, b, The fan charts show the time-evolving uncertainty and range around the median ensemble value (black line) in 10% increments. RCP8.5 ice-sheet model ensembles calibrated with GRACE estimates of annual mass change averaged from 2002–2017 using alternative GIA corrections (Methods). Use of GIA corrections produces estimates of mass loss between 2002 and 2017 of 0.2–0.54 mm yr⁻¹ (**a**) and 0.39–0.53 mm yr⁻¹ (**b**). The more restrictive and higher range of GRACE estimates in **b** skews the distribution and shifts the ensemble median values of GMSL upwards from 27 cm to 30 cm in 2100 and from 4.44 m to 4.94 m in 2200.

Extended Data Fig. 3 Last Interglacial and Pliocene ice-sheet simulations.

a–e, Ice-sheet simulations with the updated model physics used in our future ensembles and driven with the same LIG and Pliocene climate forcing used in ref. ⁸. Simulations without hydrofracturing and ice-cliff calving (**a, b, d**) correspond to blue lines in Extended Data Fig. [1](#). Simulations using maximum hydrofracturing and ice-cliff calving parameters (**c, e**) correspond to red lines in Extended Data Fig. [1](#). **a**, Modern (1950) ice-sheet simulation. **b, c**, LIG simulations run from 130 to 125 kyr ago are shown at 125 kyr ago. Values at the top of each panel are the maximum GMSL contribution between 129 and 128 kyr ago. Values in parentheses are the GMSL contribution at 125 kyr ago. **d, e**, Warm Pliocene simulations. Values shown are the maximum GMSL achieved during the simulations. Smaller values in parentheses show GMSL contributions after 5,000 model years (Extended Data Fig. [2d](#)). Ice mass gain after peak retreat is caused by post-retreat bedrock rebound and enhanced precipitation in the warm Pliocene atmosphere.

Extended Data Fig. 4 RCP8.5 ensembles calibrated with modern and palaeo observations.

The fan charts show the time-evolving uncertainty and range around the median ensemble value (black line) in 10% increments. Mean and median ensemble values are shown at 2100. **a**, Raw ensemble with a range of plausible model parameters based on glaciological observations (Extended Data Table 1). **b**, The ensemble trimmed with IMBIE⁴ (1992–2017) estimates of ice mass change. **c**, The ensemble trimmed with IMBIE rates of ice mass change plus LIG sea-level constraints between 129 and 128 kyr ago³⁴. **d**, The same as **c**, except with the addition of maximum mid-Pliocene sea-level constraints^{35,36} (Extended Data Fig. 1). Future ensembles in the main text (Fig. 1, Table 1) use the combined IMBIE + LIG + Pliocene history matching constraints as shown in **d**. [Source data](#)

Extended Data Fig. 5 Future retreat of Thwaites Glacier (TG) and Pine Island Glacier (PIG) with +3 °C global warming.

The Amundsen Sea sector of the ice sheet in a nested, high-resolution (1 km) simulation using average calibrated values of hydrofracturing and ice-cliff calving parameters ($CALVLIQ = 107 \text{ m}^{-1} \text{ yr}^2$; $VCLIF = 7.7 \text{ km yr}^{-1}$), consistent with those used in CESM1.2.2-forced simulations (Fig. 1h) and CDR simulations (Fig. 3, Table 1). **a–c**, The ice sheet in 2050. **d–f**, The ice sheet in 2100. **a, d**, Ice-sheet geometry and annually averaged ice-cliff calving rates at thick, weakly buttressed grounding lines. The solid line in all panels is the grounding line and the dashed line is its initial position. Note that simulated ice-cliff calving rates are generally much slower than the maximum allowable value of 7.7 km yr^{-1} . Ice shelves downstream of calving ice cliffs are the equivalent of weak mélange, incapable of stopping calving⁶⁴. **b, e**, Ice surface speed showing streaming and fast flow just upstream of calving ice cliffs where driving stresses are greatest. **c, f**, Change in ice thickness relative to the initial state. **g**, GMSL contributions within the nested domain at model spatial resolutions spanning 1–10 km.

Extended Data Fig. 6 Antarctic contribution to sea level under standard RCP forcing.

a–c, The fan charts show the time-evolving uncertainty and range around the median ensemble value (thick black line) in 10% increments. The RCP ensembles use the same IMBIE, LIG and Pliocene observational constraints applied to the simulations in Fig. 1. GMSL contributions in simulations without hydrofracturing or ice-cliff calving (excluded from the validated ensembles) are shown for East Antarctica (thin blue line), West Antarctica (thin red line) and the total Antarctic contribution (thin black line). **a**, RCP2.6; **b**, RCP4.5; and **c**, RCP8.5. [Source data](#)

Extended Data Fig. 7 Long-term magnitudes and rates of GMSL rise contributed by Antarctica.

a, Ensemble median (50th percentile) projections of GMSL rise contributed by Antarctica with emissions forcing consistent with the +1.5 °C and +2.0 °C Paris Agreement ambitions, versus a +3.0 °C scenario closer to current NDCs. **b**, Median (50th percentile) rates of GMSL rise in the same emissions scenarios as in **a**, illustrating a sharp jump in ice loss in the warmer +3.0 °C scenario after 2060 (also see Fig. 1), and reduced net ice loss before 2060 (black line) caused by increased snowfall. **c**, Ensemble median (50th percentile) projections of GMSL rise contributed by Antarctica with emissions forcing consistent with standard RCP scenarios, highlighting the potential for extreme GMSL rise under high (RCP8.5) emissions. **d**, Ensemble median (50th percentile) rates of GMSL rise in the same RCP scenarios as shown in **c**. Note the much larger vertical-axis scales in **c** and **d** relative to **a** and **b**.

Extended Data Fig. 8 Coupled ice–Earth–sea level model simulations.

a–c, Simulations without hydrofracturing and ice-cliff calving processes. **d–f**, Simulations with hydrofracturing and ice-cliff calving enabled (Methods). GMSL contributions are from the WAIS only. Various Earth viscosity profiles (coloured lines) are compared with the ice-sheet model’s standard ELRA formulation (black line). The most extreme viscosity profile (blue line) assumes a thin lithosphere and very weak underlying mantle, like that observed in the Amundsen sea¹⁰, but extended continent-wide. **a**, RCP2.6

without hydrofracturing or ice-cliff calving. **b**, RCP2.6 with hydrofracturing and ice-cliff calving. **c**, RCP4.5 without hydrofracturing or ice-cliff calving. **d**, RCP4.5 with hydrofracturing and ice-cliff calving. **e**, RCP8.5 without hydrofracturing or ice-cliff calving. **f**, RCP8.5 with hydrofracturing and ice-cliff calving.

Extended Data Table 1 Model ensemble parameter values

[Full size table](#)

Extended Data Table 2 Antarctic sea-level contributions with alternative maximum ice-cliff calving rates

[Full size table](#)

Supplementary information

[Supplementary Information](#)

This file contains Supplementary Methods, Supplementary Notes, Supplementary Figures 1–6, and Supplementary Tables 1–2. The Supplementary Information shows 1) uncertainty in future Antarctic climate forcing, 2) an alternative ice shelf hydrofracturing scheme, an improved formulation of buttressing at grounding lines, and 4) statistical emulation of our physical model ensembles.

Source data

[Source Data Fig. 1](#)

[Source Data Fig. 3](#)

[Source Data Extended Data Fig. 1](#)

[Source Data Extended Data Fig. 4](#)

[Source Data Extended Data Fig. 6](#)

Rights and permissions

[Reprints and Permissions](#)

About this article



Cite this article

DeConto, R.M., Pollard, D., Alley, R.B. *et al.* The Paris Climate Agreement and future sea-level rise from Antarctica. *Nature* **593**, 83–89 (2021).
<https://doi.org/10.1038/s41586-021-03427-0>

[Download citation](#)

- Received: 15 October 2018
- Accepted: 08 March 2021
- Published: 05 May 2021
- Issue Date: 06 May 2021
- DOI: <https://doi.org/10.1038/s41586-021-03427-0>

Comments

By submitting a comment you agree to abide by our [Terms](#) and [Community Guidelines](#). If you find something abusive or that does not comply with our terms or guidelines please flag it as inappropriate.

[Access through your institution](#)

[Change institution](#)

Buy or subscribe

This article was downloaded by **calibre** from <https://www.nature.com/articles/s41586-021-03427-0>

| [Section menu](#) | [Main menu](#) |

- Article
- [Published: 21 April 2021](#)

Unveiling African rainforest composition and vulnerability to global change

- [Maxime Réjou-Méchain](#) [ORCID: orcid.org/0000-0003-2824-267X¹](#),
- [Frédéric Mortier](#) [ORCID: orcid.org/0000-0001-5473-709X^{2,3}](#),
- [Jean-François Bastin^{1,2,3,4}](#),
- [Guillaume Cornu](#) [ORCID: orcid.org/0000-0002-7523-5176^{2,3}](#),
- [Nicolas Barbier](#) [ORCID: orcid.org/0000-0002-5323-3866¹](#),
- [Nicolas Bayol⁵](#),
- [Fabrice Bénédet](#) [ORCID: orcid.org/0000-0001-9281-5677^{2,3}](#),
- [Xavier Bry⁶](#),
- [Gilles Dauby](#) [ORCID: orcid.org/0000-0002-9498-413X¹](#),
- [Vincent Deblauwe](#) [ORCID: orcid.org/0000-0001-9881-1052^{7,8}](#),
- [Jean-Louis Doucet⁴](#),
- [Charles Doumenge^{2,3}](#),
- [Adeline Fayolle](#) [ORCID: orcid.org/0000-0002-6770-0031⁴](#),
- [Claude Garcia](#) [ORCID: orcid.org/0000-0002-7351-0226^{2,3,9}](#),
- [Jean-Paul Kibambe Lubamba^{10,11}](#),
- [Jean-Joël Loumeto¹²](#),
- [Alfred Ngomanda¹³](#),
- [Pierre Ploton](#) [ORCID: orcid.org/0000-0002-8800-3593¹](#),
- [Bonaventure Sonké¹⁴](#),
- [Catherine Trottier^{6,15}](#),
- [Ruppert Vimal¹⁶](#),
- [Olga Yongo¹⁷](#),
- [Raphaël Pélassier](#) [ORCID: orcid.org/0000-0003-4845-5090¹](#) &

- [Sylvie Gourlet-Fleury](#). ORCID: [orcid.org/0000-0002-1136-4307^{2,3}](https://orcid.org/0000-0002-1136-4307)

[Nature](#) volume **593**, pages90–94(2021)[Cite this article](#)

- 3220 Accesses
- 1 Citations
- 172 Altmetric
- [Metrics details](#)

Subjects

- [Climate-change impacts](#)
- [Community ecology](#)
- [Forest ecology](#)
- [Tropical ecology](#)

Abstract

Africa is forecasted to experience large and rapid climate change¹ and population growth² during the twenty-first century, which threatens the world's second largest rainforest. Protecting and sustainably managing these African forests requires an increased understanding of their compositional heterogeneity, the environmental drivers of forest composition and their vulnerability to ongoing changes. Here, using a very large dataset of 6 million trees in more than 180,000 field plots, we jointly model the distribution in abundance of the most dominant tree taxa in central Africa, and produce continuous maps of the floristic and functional composition of central African forests. Our results show that the uncertainty in taxon-specific distributions averages out at the community level, and reveal highly deterministic assemblages. We uncover contrasting floristic and functional compositions across climates, soil types and anthropogenic gradients, with functional convergence among types of forest that are floristically dissimilar. Combining these spatial predictions with scenarios of climatic and anthropogenic global change suggests a high vulnerability

of the northern and southern forest margins, the Atlantic forests and most forests in the Democratic Republic of the Congo, where both climate and anthropogenic threats are expected to increase sharply by 2085. These results constitute key quantitative benchmarks for scientists and policymakers to shape transnational conservation and management strategies that aim to provide a sustainable future for central African forests.

[Access through your institution](#)

[Change institution](#)

[Buy or subscribe](#)

Access options

Subscribe to Journal

Get full journal access for 1 year

\$199.00

only \$3.90 per issue

[Subscribe](#)

All prices are NET prices.

VAT will be added later in the checkout.

Tax calculation will be finalised during checkout.

Rent or Buy article

Get time limited or full article access on ReadCube.

from \$8.99

[Rent or Buy](#)

All prices are NET prices.

Additional access options:

- [Log in](#)
- [Access through your institution](#)
- [Learn about institutional subscriptions](#)

Fig. 1: Floristic composition of central African forests.



Fig. 2: Predicted functional composition of central African forests.



Fig. 3: Main forest types across central Africa and their functional composition.

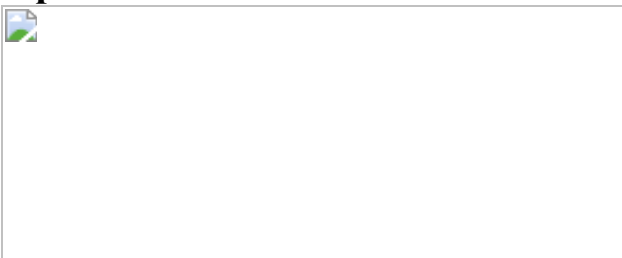
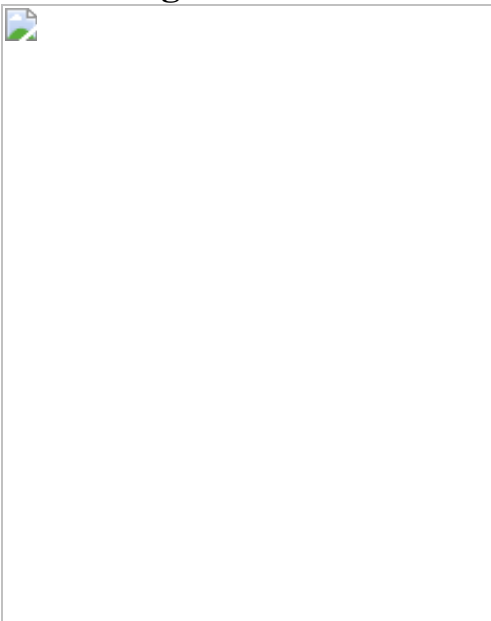


Fig. 4: Predicted vulnerability of central African tree communities to global changes.



Data availability

All maps and data used for this article are accessible online in a public repository at <https://doi.org/10.18167/DVN1/UCNCA7>. Raw floristic data are, however, archived in a private data repository, owing to the highly sensitive nature of commercial inventory data, and access may be granted for research purposes using the form provided in the public repository.

Code availability

R scripts are available at <https://github.com/MaximeRM/ScriptNature>.

References

1. 1.

Diffenbaugh, N. S. & Giorgi, F. Climate change hotspots in the CMIP5 global climate model ensemble. *Clim. Change* **114**, 813–822 (2012).

[ADS](#) [PubMed](#) [PubMed Central](#) [Google Scholar](#)

2. 2.

United Nations, Department of Economic and Social Affairs, Population Division. *World Population Prospects: The 2017 Revision, Key Findings and Advance Tables*. Working Paper No. ESA/P/WP/248 (2017).

3. 3.

Malhi, Y., Adu-Bredou, S., Asare, R. A., Lewis, S. L. & Mayaux, P. African rainforests: past, present and future. *Phil. Trans. R. Soc. B* **368**, 20120312 (2013).

[Google Scholar](#)

4. 4.

James, R., Washington, R. & Rowell, D. P. Implications of global warming for the climate of African rainforests. *Phil. Trans. R. Soc. B* **368**, 20120298 (2013).

[Google Scholar](#)

5. 5.

Abernethy, K., Maisels, F. & White, L. J. Environmental issues in Central Africa. *Annu. Rev. Environ. Resour.* **41**, 1–33 (2016).

[Google Scholar](#)

6. 6.

Hubau, W. et al. Asynchronous carbon sink saturation in African and Amazonian tropical forests. *Nature* **579**, 80–87 (2020).

[ADS](#) [CAS](#) [Google Scholar](#)

7. 7.

De Wasseige, C., Tadoum, M., Atyi, E. & Doumenge, C. *The Forests of the Congo Basin: Forests and Climate Change* (Weyrich, 2015).

8. 8.

Stévert, T. et al. A third of the tropical African flora is potentially threatened with extinction. *Sci. Adv.* **5**, eaax9444 (2019).

[ADS](#) [PubMed](#) [PubMed Central](#) [Google Scholar](#)

9. 9.

Parmentier, I. et al. The odd man out? Might climate explain the lower tree α -diversity of African rain forests relative to Amazonian rain forests? *J. Ecol.* **95**, 1058–1071 (2007).

[Google Scholar](#)

10. 10.

Réjou-Méchain, M. et al. Regional variation in tropical forest tree species composition in the Central African Republic: an assessment based on inventories by forest companies. *J. Trop. Ecol.* **24**, 663–674 (2008).

[Google Scholar](#)

11. 11.

Réjou-Méchain, M. et al. Tropical tree assembly depends on the interactions between successional and soil filtering processes. *Glob. Ecol. Biogeogr.* **23**, 1440–1449 (2014).

[Google Scholar](#)

12. 12.

Fayolle, A. et al. Geological substrates shape tree species and trait distributions in African moist forests. *PLoS One* **7**, e42381 (2012).

[ADS](#) [CAS](#) [PubMed](#) [PubMed Central](#) [Google Scholar](#)

13. 13.

Fayolle, A. et al. Patterns of tree species composition across tropical African forests. *J. Biogeogr.* **41**, 2320–2331 (2014).

[Google Scholar](#)

14. 14.

Droissart, V. et al. Beyond trees: biogeographical regionalization of tropical Africa. *J. Biogeogr.* **45**, 1153–1167 (2018).

[Google Scholar](#)

15. 15.

Sosef, M. S. et al. Exploring the floristic diversity of tropical Africa. *BMC Biol.* **15**, 15 (2017).

[PubMed](#) [PubMed Central](#) [Google Scholar](#)

16. 16.

Parmentier, I. et al. Predicting alpha diversity of African rain forests: models based on climate and satellite-derived data do not perform better than a purely spatial model. *J. Biogeogr.* **38**, 1164–1176 (2011).

[Google Scholar](#)

17. 17.

Bry, X., Trottier, C., Verron, T. & Mortier, F. Supervised component generalized linear regression using a PLS-extension of the fisher scoring algorithm. *J. Multivariate Anal.* **119**, 47–60 (2013).

[MathSciNet](#) [MATH](#) [Google Scholar](#)

18. 18.

ter Steege, H. et al. Continental-scale patterns of canopy tree composition and function across Amazonia. *Nature* **443**, 444–447 (2006).

[ADS](#) [Google Scholar](#)

19. 19.

Slik, J. W. et al. Soils on exposed Sunda shelf shaped biogeographic patterns in the equatorial forests of Southeast Asia. *Proc. Natl Acad. Sci. USA* **108**, 12343–12347 (2011).

[ADS](#) [CAS](#) [Google Scholar](#)

20. 20.

Philippon, N. et al. The light-deficient climates of western Central African evergreen forests. *Environ. Res. Lett.* **14**, 034007 (2019).

[ADS](#) [CAS](#) [Google Scholar](#)

21. 21.

Sullivan, M. J. P. et al. Long-term thermal sensitivity of Earth's tropical forests. *Science* **368**, 869–874 (2020).

[ADS](#) [CAS](#) [Google Scholar](#)

22. 22.

Beale, C. M., Lennon, J. J. & Gimona, A. Opening the climate envelope reveals no macroscale associations with climate in European birds. *Proc. Natl Acad. Sci. USA* **105**, 14908–14912 (2008).

[ADS](#) [CAS](#) [Google Scholar](#)

23. 23.

Deblauwe, V. et al. Remotely sensed temperature and precipitation data improve species distribution modelling in the tropics. *Glob. Ecol. Biogeogr.* **25**, 443–454 (2016).

[Google Scholar](#)

24. 24.

Maguire, K. C. et al. Controlled comparison of species- and community-level models across novel climates and communities. *Proc. R. Soc. B* **283**, 20152817 (2016).

[Google Scholar](#)

25. 25.

Morin-Rivat, J. et al. Present-day central African forest is a legacy of the 19th century human history. *eLife* **6**, e20343 (2017).

[PubMed](#) [PubMed Central](#) [Google Scholar](#)

26. 26.

Ricklefs, R. E. Intrinsic dynamics of the regional community. *Ecol. Lett.* **18**, 497–503 (2015).

[Google Scholar](#)

27. 27.

Violle, C. et al. Let the concept of trait be functional! *Oikos* **116**, 882–892 (2007).

[Google Scholar](#)

28. 28.

Díaz, S. et al. The global spectrum of plant form and function. *Nature* **529**, 167–171 (2016).

[ADS](#) [Google Scholar](#)

29. 29.

Rüger, N. et al. Demographic trade-offs predict tropical forest dynamics. *Science* **368**, 165–168 (2020).

[ADS](#) [Google Scholar](#)

30. 30.

Ouédraogo, D.-Y. et al. The determinants of tropical forest deciduousness: disentangling the effects of rainfall and geology in central Africa. *J. Ecol.* **104**, 924–935 (2016).

[Google Scholar](#)

31. 31.

Shipley, B. *From Plant Traits to Vegetation Structure: Chance and Selection in the Assembly of Ecological Communities* (Cambridge University Press, 2010).

32. 32.

Feeley, K. J. & Silman, M. R. Biotic attrition from tropical forests correcting for truncated temperature niches. *Glob. Change Biol.* **16**, 1830–1836 (2010).

[ADS](#) [Google Scholar](#)

33. 33.

Parry, M. et al. *Climate Change 2007 – Impacts, Adaptation, and Vulnerability: Contribution of Working Group II to the Fourth Assessment Report of the IPCC* (Cambridge University Press, 2007).

34. 34.

Foden, W. B. et al. Identifying the world's most climate change vulnerable species: a systematic trait-based assessment of all birds, amphibians and corals. *PLoS One* **8**, e65427 (2013).

[ADS](#) [CAS](#) [PubMed](#) [PubMed Central](#) [Google Scholar](#)

35. 35.

Lachenaud, O., Stévert, T., Ikabanga, D., Ndjabounda, E. C. N. & Walters, G. The littoral forests of the Libreville area (Gabon) and their importance for conservation: description of a new endemic species (Rubiaceae). *Plant Ecol. Evol.* **146**, 68–74 (2013).

[Google Scholar](#)

36. 36.

Aguirre-Gutiérrez, J. et al. Drier tropical forests are susceptible to functional changes in response to a long-term drought. *Ecol. Lett.* **22**, 855–865 (2019).

[Google Scholar](#)

37. 37.

Claeys, F. et al. Climate change would lead to a sharp acceleration of Central African forests dynamics by the end of the century. *Environ. Res. Lett.* **14**, 044002 (2019).

[ADS](#) [CAS](#) [Google Scholar](#)

38. 38.

McDowell, N. G. et al. Pervasive shifts in forest dynamics in a changing world. *Science* **368**, eaaz9463 (2020).

[CAS](#) [Google Scholar](#)

39. 39.

Zhou, L. et al. Widespread decline of Congo rainforest greenness in the past decade. *Nature* **509**, 86–90 (2014).

[ADS](#) [CAS](#) [Google Scholar](#)

40. 40.

Purvis, A. Phylogenetic approaches to the study of extinction. *Annu. Rev. Ecol. Evol. Syst.* **39**, 301–319 (2008).

[Google Scholar](#)

41. 41.

Yachi, S. & Loreau, M. Biodiversity and ecosystem productivity in a fluctuating environment: the insurance hypothesis. *Proc. Natl Acad. Sci. USA* **96**, 1463–1468 (1999).

[ADS](#) [CAS](#) [Google Scholar](#)

42. 42.

Neves, D. M. et al. Evolutionary diversity in tropical tree communities peaks at intermediate precipitation. *Sci. Rep.* **10**, 1188 (2020).

[ADS](#) [CAS](#) [PubMed](#) [PubMed Central](#) [Google Scholar](#)

43. 43.

Letcher, S. G. Phylogenetic structure of angiosperm communities during tropical forest succession. *Proc. R. Soc. B* **277**, 97–104 (2010).

[Google Scholar](#)

44. 44.

Letouzey, R. Notice de la carte phytogéographique du Cameroun au 1:500000 (Institut de la Carte Internationale de la végétation Toulouse-France et Institut de la recherche agronomique (Herbier National) Yaoundé-Cameroun, 1985).

45. 45.

Boulvert, Y. Carte phytogéographique de la République Centrafricaine (feuille ouest–feuille est) à 1 000 000 (Editions de l'ORSTOM, 1986).

46. 46.

Fyllas, N. M., Quesada, C. A. & Lloyd, J. Deriving plant functional types for Amazonian forests for use in vegetation dynamics models. *Perspect. Plant Ecol. Evol. Syst.* **14**, 97–110 (2012).

[Google Scholar](#)

47. 47.

Mitchard, E. T. A. et al. Markedly divergent estimates of Amazon forest carbon density from ground plots and satellites. *Glob. Ecol. Biogeogr.* **23**, 935–946 (2014).

[PubMed](#) [PubMed Central](#) [Google Scholar](#)

48. 48.

Visconti, P., Pressey, R. L., Bode, M. & Segan, D. B. Habitat vulnerability in conservation planning—when it matters and how much. *Conserv. Lett.* **3**, 404–414 (2010).

[Google Scholar](#)

49. 49.

Putz, F. E. et al. Sustaining conservation values in selectively logged tropical forests: the attained and the attainable. *Conserv. Lett.* **5**, 296–303 (2012).

[Google Scholar](#)

50. 50.

Gourlet-Fleury, S. et al. Tropical forest recovery from logging: a 24 year silvicultural experiment from Central Africa. *Phil. Trans. R. Soc. B* **368**, 20120302 (2013).

[Google Scholar](#)

51. 51.

Clark, C. J., Poulsen, J. R., Malonga, R. & Elkan, P. W. Jr. Logging concessions can extend the conservation estate for Central African tropical forests. *Conserv. Biol.* **23**, 1281–1293 (2009).

[CAS](#) [Google Scholar](#)

52. 52.

Curtis, P. G., Slay, C. M., Harris, N. L., Tyukavina, A. & Hansen, M. C. Classifying drivers of global forest loss. *Science* **361**, 1108–1111 (2018).

[ADS](#) [CAS](#) [Google Scholar](#)

53. 53.

Réjou-Méchain, M. et al. Detecting large-scale diversity patterns in tropical trees: can we trust commercial forest inventories? *For. Ecol. Manage.* **261**, 187–194 (2011).

[Google Scholar](#)

54. 54.

African Plant Database v.3.4.0 (Conservatoire et Jardin Botaniques de la Ville de Genève and South African National Biodiversity Institute, Pretoria, accessed 10 February 2017).

55. 55.

The Angiosperm Phylogeny Group. An update of the Angiosperm Phylogeny Group classification for the orders and families of flowering plants: APG III. *Bot. J. Linn. Soc.* **161**, 105–121 (2009).

[Google Scholar](#)

56. 56.

Dauby, G. et al. RAINBIO: a mega-database of tropical African vascular plants distributions. *PhytoKeys* **74**, 1–18 (2016).

[Google Scholar](#)

57. 57.

Chave, J. et al. Towards a worldwide wood economics spectrum. *Ecol. Lett.* **12**, 351–366 (2009).

[Google Scholar](#)

58. 58.

Zanne, A. E. et al. Data from: towards a worldwide wood economic spectrum. *Dryad* <https://doi.org/10.5061/dryad.234> (2009).

59. 59.

Gourlet-Fleury, S. et al. Environmental filtering of dense-wooded species controls above-ground biomass stored in African moist forests. *J. Ecol.* **99**, 981–990 (2011).

[Google Scholar](#)

60. 60.

Westoby, M. & Wright, I. J. Land-plant ecology on the basis of functional traits. *Trends Ecol. Evol.* **21**, 261–268 (2006).

[Google Scholar](#)

61. 61.

Chave, J. et al. Improved allometric models to estimate the aboveground biomass of tropical trees. *Glob. Change Biol.* **20**, 3177–3190 (2014).

[ADS](#) [Google Scholar](#)

62. 62.

Bénédict, F. et al. CoForTraits, African plant traits information database v.1.0, <https://doi.org/10.18167/DVN1/Y2BIZK> (2013).

63. 63.

Davies, T. J. et al. Phylogenetic conservatism in plant phenology. *J. Ecol.* **101**, 1520–1530 (2013).

[Google Scholar](#)

64. 64.

Cramer, W. et al. Global response of terrestrial ecosystem structure and function to CO₂ and climate change: Results from six dynamic global vegetation models. *Glob. Change Biol.* **7**, 357–373 (2001).

[ADS](#) [Google Scholar](#)

65. 65.

Menzel, A. Phenology: its importance to the global change community. *Clim. Change* **54**, 379 (2002).

[Google Scholar](#)

66. 66.

Borchert, R., Rivera, G. & Hagnauer, W. Modification of vegetative phenology in a tropical semi-deciduous forest by abnormal drought and rain. *Biotropica* **34**, 27–39 (2002).

[Google Scholar](#)

67. 67.

Kraft, N. J. B., Valencia, R. & Ackerly, D. D. Functional traits and niche-based tree community assembly in an Amazonian forest. *Science* **322**, 580–582 (2008).

[ADS](#) [CAS](#) [Google Scholar](#)

68. 68.

Schamp, B. S. & Aarssen, L. W. The assembly of forest communities according to maximum species height along resource and disturbance gradients. *Oikos* **118**, 564–572 (2009).

[Google Scholar](#)

69. 69.

New, M., Lister, D., Hulme, M. & Makin, I. A high-resolution data set of surface climate over global land areas. *Clim. Res.* **21**, 1–25 (2002).

[Google Scholar](#)

70. 70.

Hijmans, R. J., Cameron, S. E., Parra, J. L., Jones, P. G. & Jarvis, A. Very high resolution interpolated climate surface for global land areas. *Int. J. Climatol.* **25**, 1965–1978 (2005).

[Google Scholar](#)

71. 71.

Funk, C. et al. The climate hazards infrared precipitation with stations —a new environmental record for monitoring extremes. *Sci. Data* **2**, 150066 (2015).

[PubMed](#) [PubMed Central](#) [Google Scholar](#)

72. 72.

Nachtergaele, F. et al. The harmonized world soil database. In *Proc. 19th World Congress of Soil Science, Soil Solutions for a Changing World* (eds Gilkes, R. & Prakongkep, N.) 34–37 (International Union of Soil Sciences, 2010).

73. 73.

Woolmer, G. et al. Rescaling the human footprint: a tool for conservation planning at an ecoregional scale. *Landsc. Urban Plan.* **87**, 42–53 (2008).

[Google Scholar](#)

74. 74.

Venter, O. et al. Sixteen years of change in the global terrestrial human footprint and implications for biodiversity conservation. *Nat. Commun.* **7**, 12558 (2016).

[ADS](#) [CAS](#) [PubMed](#) [PubMed Central](#) [Google Scholar](#)

75. 75.

Geldmann, J., Joppa, L. N. & Burgess, N. D. Mapping change in human pressure globally on land and within protected areas. *Conserv. Biol.* **28**, 1604–1616 (2014).

[Google Scholar](#)

76. 76.

Linard, C., Gilbert, M., Snow, R. W., Noor, A. M. & Tatem, A. J. Population distribution, settlement patterns and accessibility across Africa in 2010. *PLoS One* **7**, e31743 (2012).

[ADS](#) [CAS](#) [PubMed](#) [PubMed Central](#) [Google Scholar](#)

77. 77.

Lloyd, C. T. et al. Global spatio-temporally harmonised datasets for producing high-resolution gridded population distribution datasets. *Big Earth Data* **3**, 108–139 (2019).

[Google Scholar](#)

78. 78.

Boulesteix, A.-L. & Strimmer, K. Partial least squares: a versatile tool for the analysis of high-dimensional genomic data. *Brief. Bioinform.* **8**, 32–44 (2007).

[CAS](#) [Google Scholar](#)

79. 79.

Carrascal, L. M., Galván, I. & Gordo, O. Partial least squares regression as an alternative to current regression methods used in ecology. *Oikos* **118**, 681–690 (2009).

[Google Scholar](#)

80. 80.

Tenenhaus, M. *La Régression PLS: Théorie et Pratique* (Editions Technip, 1998).

81. 81.

Sabatier, R., Lebreton, J. D. & Chessel, D. in *Multiway Data Analysis* (eds Coppi, R. & Bolasco, S.) 341–352 (1989).

82. 82.

Ter Braak, C. J. F. in *Theory and Models In Vegetation Science* (eds Prentice, I. C. & van der Maarel, E.) 69–77 (Springer, 1987).

83. 83.

Bry, X. & Verron, T. THEME: THEmatic model exploration through multiple co-structure maximization. *J. Chemometr.* **29**, 637–647 (2015).

[CAS](#) [Google Scholar](#)

84. 84.

Cornu, G., Mortier, F., Trottier, C. & Bry, X. SCGLR: supervised component generalized linear regression. R version 3.0 <https://cran.r-project.org/web/packages/SCGLR/index.html> (2016).

85. 85.

Ward, J. H. Jr. Hierarchical grouping to optimize an objective function. *J. Am. Stat. Assoc.* **58**, 236–244 (1963).

[MathSciNet](#) [Google Scholar](#)

86. 86.

Ploton, P. et al. Spatial validation reveals poor predictive performance of large-scale ecological mapping models. *Nat. Commun.* **11**, 4540 (2020).

[ADS](#) [CAS](#) [PubMed](#) [PubMed Central](#) [Google Scholar](#)

87. 87.

Scrucca, L., Fop, M., Murphy, T. B. & Raftery, A. E. mclust 5: clustering, classification and density estimation using gGaussian finite mixture models. *R J.* **8**, 289–317 (2016).

[PubMed](#) [PubMed Central](#) [Google Scholar](#)

88. 88.

Dormann, C. F. et al. Methods to account for spatial autocorrelation in the analysis of species distributional data: A review. *Ecography* **30**, 609–628 (2007).

[Google Scholar](#)

89. 89.

Renard, D. et al. RGeostats: the geostatistical package v.11.0. 1 <http://rgeostats.free.fr/> (MINES ParisTech, 2014).

90. 90.

Platts, P. J., Omeny, P. A. & Marchant, R. AFRICLIM: high-resolution climate projections for ecological applications in Africa. *Afr. J. Ecol.* **53**, 103–108 (2015).

[Google Scholar](#)

91. 91.

Janssens, S. B. et al. A large-scale species level dated angiosperm phylogeny for evolutionary and ecological analyses. *Biodivers. Data J.* **8**, e39677 (2020).

[PubMed](#) [PubMed Central](#) [Google Scholar](#)

92. 92.

Abouheif, E. A method for testing the assumption of phylogenetic independence in comparative data. *Evol. Ecol. Res.* **1**, 895–909 (1999).

[Google Scholar](#)

93. 93.

Chao, A., Chiu, C.-H. & Jost, L. Phylogenetic diversity measures based on Hill numbers. *Phil. Trans. R. Soc. B* **365**, 3599–3609 (2010).

[Google Scholar](#)

94. 94.

R Core Team. *R: a language and environment for statistical computing*. (R Foundation for Statistical Computing, 2017).

95. 95.

Chessel, D., Dufour, A. B. & Thioulouse, J. The ade4 package – I: one-table methods. *R News* **4**, 5–10 (2004).

[Google Scholar](#)

96. 96.

Lafarge, T. & Pateiro-Lopez, B. alphashape3d: implementation of the 3D alpha-shape for the reconstruction of 3D sets from a point cloud. R version 1.3.1 <https://cran.r-project.org/web/packages/alphashape3d/index.html> (2017).

97. 97.

Wickham, H. *ggplot2: Elegant Graphics for Data Analysis* (Springer-Verlag, 2016).

98. 98.

Hijmans, R. J. raster: geographic data analysis and modelling. R version 3.4-5 <https://cran.r-project.org/web/packages/raster/index.html> (2017).

99. 99.

Marcon, E. & Héault, B. entropart: An R package to measure and partition diversity. *J. Stat. Softw.* **67**, 1–26 (2015).

[Google Scholar](#)

100. 100.

Dufrêne, M. & Legendre, P. Species assemblages and indicator species: the need for a flexible asymmetrical approach. *Ecol. Monogr.* **67**, 345–366 (1997).

[Google Scholar](#)

[Download references](#)

Acknowledgements

We thank the 105 forest companies that provided access, albeit restricted, to their inventory data for research purposes and members of the central African plot network (<https://central-african-plot-network.netlify.app/>), Y. Yalibanda, F. Allah-Barem, F. Baya, F. Boyemba, M. Mbasi Mbula, P. Berenger, M. Mazengue, V. Istace, I. Zombo, E. Forni, Nature+ and the CEB-Precious Woods company for giving access to the scientific inventories described in Supplementary Fig. 4, some of which were funded by the AFD and the FFEM (for example, DynAfFor and P3FAC projects). We thank J. Chave, P. Couteron, S. Lewis and M. Tadesse for their comments and discussions on previous versions, B. Sultan for useful discussions on climate projections, O. J. Hardy for advice on phylogenetical analyses, B. Locatelli for advice on vulnerability analyses, G. Vieilledent for discussions on the human-induced forest-disturbance intensity index and A. Stokes for English editing. This work was supported by the CoForTips project (ANR-12-EBID-0002) funded by the ERA-NET BiodivERsA, with the national funders ANR, BELSPO and FWF, as part of the 2012 BiodivERsA call for research proposals, the GAMBAS project funded by the French National Research Agency (ANR-18-CE02-0025) and the project 3DForMod funded by the UE FACCE ERA-GAS consortium (ANR-17-EGAS-0002-01). This study is a contribution to the research program of LMI DYCOFAC (Dynamique des écosystèmes continentaux d'Afrique Centrale en contexte de changements globaux).

Author information

Affiliations

1. AMAP, Univ. Montpellier, IRD, CNRS, CIRAD, INRAE, Montpellier, France

Maxime Réjou-Méchain, Jean-François Bastin, Nicolas Barbier, Gilles Dauby, Pierre Ploton & Raphaël Pélissier

2. CIRAD, Forêts et Sociétés, Montpellier, France

Frédéric Mortier, Jean-François Bastin, Guillaume Cornu, Fabrice Bénédet, Charles Doumenge, Claude Garcia & Sylvie Gourlet-Fleurys

3. Forêts et Sociétés, Univ. Montpellier, CIRAD, Montpellier, France

Frédéric Mortier, Jean-François Bastin, Guillaume Cornu, Fabrice Bénédet, Charles Doumenge, Claude Garcia & Sylvie Gourlet-Fleury

4. TERRA Teaching and Research Centre, Gembloux Agro-Bio Tech, University of Liège, Gembloux, Belgium

Jean-François Bastin, Jean-Louis Doucet & Adeline Fayolle

5. FRM Ingénierie, Mauguio, France

Nicolas Bayol

6. IMAG, CNRS, Univ. Montpellier, Montpellier, France

Xavier Bry & Catherine Trottier

7. Center for Tropical Research, Institute of the Environment and Sustainability, University of California, Los Angeles, Los Angeles, CA, USA

Vincent Deblauwe

8. International Institute of Tropical Agriculture, Yaoundé, Cameroon

Vincent Deblauwe

9. Forest Management and Development Team, Department of Environmental System Science, Institute of Integrative Biology, ETH Zürich, Zürich, Switzerland

Claude Garcia

10. Faculté des Sciences Agronomiques, Département de Gestion des Ressources Naturelles, Université de Kinshasa, Kinshasa, Democratic Republic of the Congo

Jean-Paul Kibambe Lubamba

11. Wildlife Conservation Society, Kinshasa, Democratic Republic of the Congo

Jean-Paul Kibambe Lubamba

12. Faculté des Sciences et Techniques, Université Marien Ngouabi, Brazzaville, Congo

Jean-Joël Loumeto

13. Institut de Recherche en Écologie Tropicale (IRET/CENAREST), Libreville, Gabon

Alfred Ngomanda

14. Plant Systematic and Ecology Laboratory, Higher Teacher's Training College, University of Yaoundé I, Yaoundé, Cameroon

Bonaventure Sonké

15. AMIS, Univ. Paul Valéry Montpellier 3, Montpellier, France

Catherine Trottier

16. GEODE UMR 5602, CNRS, Université Jean-Jaurès, Toulouse, France

Ruppert Vimal

17. Laboratoire de Biodiversité Végétale et Fongique, Faculté des Sciences, Université de Bangui, Bangui, Central African Republic

Olga Yongo

Authors

1. Maxime Réjou-Méchain
[View author publications](#)

You can also search for this author in [PubMed](#) [Google Scholar](#)

2. Frédéric Mortier

[View author publications](#)

You can also search for this author in [PubMed](#) [Google Scholar](#)

3. Jean-François Bastin

[View author publications](#)

You can also search for this author in [PubMed](#) [Google Scholar](#)

4. Guillaume Cornu

[View author publications](#)

You can also search for this author in [PubMed](#) [Google Scholar](#)

5. Nicolas Barbier

[View author publications](#)

You can also search for this author in [PubMed](#) [Google Scholar](#)

6. Nicolas Bayol

[View author publications](#)

You can also search for this author in [PubMed](#) [Google Scholar](#)

7. Fabrice Bénédet

[View author publications](#)

You can also search for this author in [PubMed](#) [Google Scholar](#)

8. Xavier Bry

[View author publications](#)

You can also search for this author in [PubMed](#) [Google Scholar](#)

9. Gilles Dauby

[View author publications](#)

You can also search for this author in [PubMed](#) [Google Scholar](#)

10. Vincent Deblauwe

[View author publications](#)

You can also search for this author in [PubMed](#) [Google Scholar](#)

11. Jean-Louis Doucet

[View author publications](#)

You can also search for this author in [PubMed](#) [Google Scholar](#)

12. Charles Doumenge

[View author publications](#)

You can also search for this author in [PubMed](#) [Google Scholar](#)

13. Adeline Fayolle

[View author publications](#)

You can also search for this author in [PubMed](#) [Google Scholar](#)

14. Claude Garcia

[View author publications](#)

You can also search for this author in [PubMed](#) [Google Scholar](#)

15. Jean-Paul Kibambe Lubamba

[View author publications](#)

You can also search for this author in [PubMed](#) [Google Scholar](#)

16. Jean-Joël Loumeto

[View author publications](#)

You can also search for this author in [PubMed](#) [Google Scholar](#)

17. Alfred Ngomanda

[View author publications](#)

You can also search for this author in [PubMed](#) [Google Scholar](#)

18. Pierre Ploton

[View author publications](#)

You can also search for this author in [PubMed](#) [Google Scholar](#)

19. Bonaventure Sonké

[View author publications](#)

You can also search for this author in [PubMed](#) [Google Scholar](#)

20. Catherine Trottier

[View author publications](#)

You can also search for this author in [PubMed](#) [Google Scholar](#)

21. Ruppert Vimal

[View author publications](#)

You can also search for this author in [PubMed](#) [Google Scholar](#)

22. Olga Yongo

[View author publications](#)

You can also search for this author in [PubMed](#) [Google Scholar](#)

23. Raphaël Pélissier

[View author publications](#)

You can also search for this author in [PubMed](#) [Google Scholar](#)

24. Sylvie Gourlet-Fleury

[View author publications](#)

You can also search for this author in [PubMed](#) [Google Scholar](#)

Contributions

Conceptualization: M.R.-M., F.M., R.P. and S.G.-F.; data curation: G.C. and F.B.; formal analysis: M.R.-M. and F.M.; project administration: C.G.;

writing (original draft): M.R.-M., F.M., R.P. and S.G.-F.; writing (review and editing): all authors.

Corresponding author

Correspondence to [Maxime Réjou-Méchain](#).

Ethics declarations

Competing interests

The authors declare no competing interests.

Additional information

Peer review information *Nature* thanks Jonas Geldmann, Marion Pfeifer, Philip Platts and the other, anonymous, reviewer(s) for their contribution to the peer review of this work.

Publisher's note Springer Nature remains neutral with regard to jurisdictional claims in published maps and institutional affiliations.

Extended data figures and tables

[Extended Data Fig. 1 Study area and sampling plots.](#)

In green, the current distribution of tropical forests following the ESA-CCI landcover product (v.1.6), with a dark-green-to-white gradient representing anthropogenic pressure (see [Methods](#)) and non-forested areas represented in beige. The sampling grid cells ($n = 1,571$ $10 \times 10\text{-km}^2$ grid cells) are in black and the flooding forests, as proposed by the ESA-CCI landcover, are in blue.

[Extended Data Fig. 2 Taxon CA planes 1–2 and 1–3 with labels for the 12 most representative taxa on each axis.](#)

a, Planes 1–2. **b**, Planes 1–3. Colour code corresponds to that reported in Fig. 1. The first eigenvalues are reported in **b**, highlighting in black the first three axes. Taxon codes and scores of the 193 taxa are provided in Supplementary Table 2.

Extended Data Fig. 3 Individual predicted floristic gradients illustrated by the three first axes of the correspondence analysis performed on predicted taxon abundances.

a–c, CA axis 1 (**a**), CA axis 2 (**b**) and CA axis 3 (**c**). A composite map of these three axes is given in Fig. 1 and the corresponding taxon CA planes are provided in Extended Data Fig. 2.

Extended Data Fig. 4 Plans 1–2, 1–3 and 2–3 of the SCGLR CCs.

a, CC1 and CC2. **b**, CC1 and CC3. **c**, CC2 and CC3. All climatic variables with a correlation of less than 0.75 with the two components (dashed circle) were excluded for the sake of clarity. For abbreviations, see Extended Data Table 2.

Extended Data Fig. 5 Spatial cross-validation results of the predictions of functional assemblages.

a–c, The observed and predicted community weighted mean trait values within the 1,571 10x10-km² grid cells are given for wood density (**a**), deciduousness (**b**) and maximum diameter (**c**). The 1:1 line is displayed in red.

Extended Data Fig. 6 Projected changes under the RCP 4.5 scenario in 2085 of the climatic conditions of the 10 forest types.

Areas for which climate models predict similar climatic components (CCs) values to those currently found within forest types (in black) are illustrated

with a colour gradient indicating the level of agreement amongst the 18 climate models (as a percentage; no colour indicates that none of the original 18 climate models predicted similar conditions). More specifically, we used 3D concave hull (alpha shape) models to assess where the combinations of current CCs corresponding to each forest type are predicted to be represented in 2085.

Extended Data Fig. 7 The vulnerability map under two different RCP scenarios and for two different years.

a–d, Vulnerability maps under RCP 4.5 in 2055 (**a**), RCP 8.5 in 2055 (**b**), RCP 4.5 in 2085 (**c**) and RCP 8.5 in 2085 (**d**). As can be seen, the predicted vulnerability is little affected by the IPCC scenario chosen because it expresses a relative vulnerability over the study area and, if different scenarios predict different amplitudes of climate change, spatial patterns of climate exposure remains similar (see [Methods](#)).

Extended Data Fig. 8 Current and projected anthropogenic pressure over central Africa.

a, b, Current (**a**) and projected (**b**) anthropogenic pressure predicted from our index of human-induced forest-disturbance intensity.

Extended Data Fig. 9 Protected area network and areas dedicated to logging activities in central Africa.

The protected area network is shown in blue; areas dedicated to logging are shown in orange and red. Data on protected areas were obtained from the World Database on Protected Areas (<https://www.iucn.org/theme/protected-areas/our-work/world-database-protected-areas>, last accessed 14 August 2018), excluding marine, hunting and game-oriented areas, except for the Democratic Republic of the Congo, for which data from the World Resource Institute were used and downloaded from ArcGIS hub (<https://hub.arcgis.com/datasets/1bcd463ccb6549c9a0676edb9f751f9b>, last accessed 1 June 2019). Logging activity data were provided by the Observatoire des Forêts d'Afrique Centrale based on an unpublished work

completed in June 2018, except for the Democratic Republic of the Congo, for which more updated data (June 2019) were provided by the AGEDUFOR national project. Areas in orange illustrate forest concessions that are known to have, or to be in the process of having, an officially validated sustainable forest management plan. Red areas illustrate forest areas that are currently dedicated to logging but that either do not have an official management plan or have an uncertain status.

Extended Data Table 1 Characteristics of the floristic groups

[Full size table](#)

Extended Data Table 2 Climatic predictors

[Full size table](#)

Supplementary information

[Supplementary Information](#)

This file contains Supplementary Figs 1-9 and Supplementary Tables 1-2.

[Reporting Summary](#)

Rights and permissions

[Reprints and Permissions](#)

About this article



Check for
updates

Cite this article

Réjou-Méchain, M., Mortier, F., Bastin, JF. *et al.* Unveiling African rainforest composition and vulnerability to global change. *Nature* **593**, 90–

94 (2021). <https://doi.org/10.1038/s41586-021-03483-6>

[Download citation](#)

- Received: 29 October 2019
- Accepted: 22 March 2021
- Published: 21 April 2021
- Issue Date: 06 May 2021
- DOI: <https://doi.org/10.1038/s41586-021-03483-6>

Further reading

- [African forest maps reveal areas vulnerable to the effects of climate change](#)
 - Marion Pfeifer
 - & Deo D. Shirima

Nature (2021)

Comments

By submitting a comment you agree to abide by our [Terms](#) and [Community Guidelines](#). If you find something abusive or that does not comply with our terms or guidelines please flag it as inappropriate.

[Access through your institution](#)

[Change institution](#)

[Buy or subscribe](#)

Associated Content

African forest maps reveal areas vulnerable to the effects of climate change

- Marion Pfeifer
- Deo D. Shirima

Nature News & Views 21 Apr 2021

This article was downloaded by **calibre** from <https://www.nature.com/articles/s41586-021-03483-6>

| [Section menu](#) | [Main menu](#) |

- Article
- [Published: 05 May 2021](#)

Earliest known human burial in Africa

- [María Martinón-Torres](#) ORCID: [orcid.org/0000-0002-2750-4554^{1,2}](https://orcid.org/0000-0002-2750-4554),
- [Francesco d'Errico^{3,4}](#),
- [Elena Santos^{5,6}](#),
- [Ana Álvaro Gallo¹](#),
- [Noel Amano](#) ORCID: [orcid.org/0000-0002-7871-2230⁷](https://orcid.org/0000-0002-7871-2230),
- [William Archer^{8,9,10}](#),
- [Simon J. Armitage](#) ORCID: [orcid.org/0000-0003-1480-9188^{11,4}](https://orcid.org/0000-0003-1480-9188),
- [Juan Luis Arsuaga^{5,12}](#),
- [José María Bermúdez de Castro^{1,2}](#),
- [James Blinkhorn^{7,11,13}](#),
- [Alison Crowther^{7,14}](#),
- [Katerina Douka](#) ORCID: [orcid.org/0000-0002-0558-0011^{7,15}](https://orcid.org/0000-0002-0558-0011),
- [Stéphan Dubernet](#) ORCID: [orcid.org/0000-0003-4278-3501¹⁶](https://orcid.org/0000-0003-4278-3501),
- [Patrick Faulkner^{7,17}](#),
- [Pilar Fernández-Colón¹](#),
- [Nikos Kourampas^{18,19}](#),
- [Jorge González García²⁰](#),
- [David Larréina¹](#),
- [François-Xavier Le Bourdonnec](#) ORCID: [orcid.org/0000-0002-1051-5337¹⁶](https://orcid.org/0000-0002-1051-5337),
- [George MacLeod¹⁹](#),
- [Laura Martín-Francés^{1,2}](#),
- [Diyendo Massilani²¹](#),
- [Julio Mercader](#) ORCID: [orcid.org/0000-0002-5637-7937^{7,22}](https://orcid.org/0000-0002-5637-7937),
- [Jennifer M. Miller⁷](#),

- [Emmanuel Ndiema](#)^{7,23},
- [Belén Notario](#)¹,
- [Africa Pitarch Martí](#)^{3,24},
- [Mary E. Prendergast](#)²⁵,
- [Alain Queffelec](#) [ORCID: orcid.org/0000-0002-9763-7600](#)³,
- [Solange Rigaud](#) [ORCID: orcid.org/0000-0002-9108-200X](#)³,
- [Patrick Roberts](#) [ORCID: orcid.org/0000-0002-4403-7548](#)^{7,14},
- [Mohammad Javad Shoaei](#)⁷,
- [Ceri Shipton](#)^{26,27},
- [Ian Simpson](#) [ORCID: orcid.org/0000-0003-2447-7877](#)¹⁸,
- [Nicole Boivin](#) [ORCID: orcid.org/0000-0002-7783-4199](#)^{7,14,22,28} &
- [Michael D. Petraglia](#) [ORCID: orcid.org/0000-0003-2522-5727](#)^{7,14,29,30}

[Nature](#) volume **593**, pages95–100(2021)[Cite this article](#)

- 3850 Accesses
- 1479 Altmetric
- [Metrics details](#)

Subjects

- [Archaeology](#)
- [Biological anthropology](#)
- [Palaeontology](#)

Abstract

The origin and evolution of hominin mortuary practices are topics of intense interest and debate^{1,2,3}. Human burials dated to the Middle Stone Age (MSA) are exceedingly rare in Africa and unknown in East Africa^{1,2,3,4,5,6}. Here we describe the partial skeleton of a roughly 2.5- to 3.0-year-old child dating to 78.3 ± 4.1 thousand years ago, which was recovered in the MSA layers of Panga ya Saidi (PYS), a cave site in the

tropical upland coast of Kenya^{7,8}. Recent excavations have revealed a pit feature containing a child in a flexed position. Geochemical, granulometric and micromorphological analyses of the burial pit content and encasing archaeological layers indicate that the pit was deliberately excavated. Taphonomical evidence, such as the strict articulation or good anatomical association of the skeletal elements and histological evidence of putrefaction, support the in-place decomposition of the fresh body. The presence of little or no displacement of the unstable joints during decomposition points to an interment in a filled space (grave earth), making the PYS finding the oldest known human burial in Africa. The morphological assessment of the partial skeleton is consistent with its assignment to *Homo sapiens*, although the preservation of some primitive features in the dentition supports increasing evidence for non-gradual assembly of modern traits during the emergence of our species. The PYS burial sheds light on how MSA populations interacted with the dead.

[Access through your institution](#)

[Change institution](#)

[Buy or subscribe](#)

Access options

Subscribe to Journal

Get full journal access for 1 year

\$199.00

only \$3.90 per issue

[Subscribe](#)

All prices are NET prices.

VAT will be added later in the checkout.

Tax calculation will be finalised during checkout.

Rent or Buy article

Get time limited or full article access on ReadCube.

from \$8.99

[Rent or Buy](#)

All prices are NET prices.

Additional access options:

- [Log in](#)
- [Access through your institution](#)
- [Learn about institutional subscriptions](#)

Fig. 1: Location of PYS and stratigraphic context of burial.

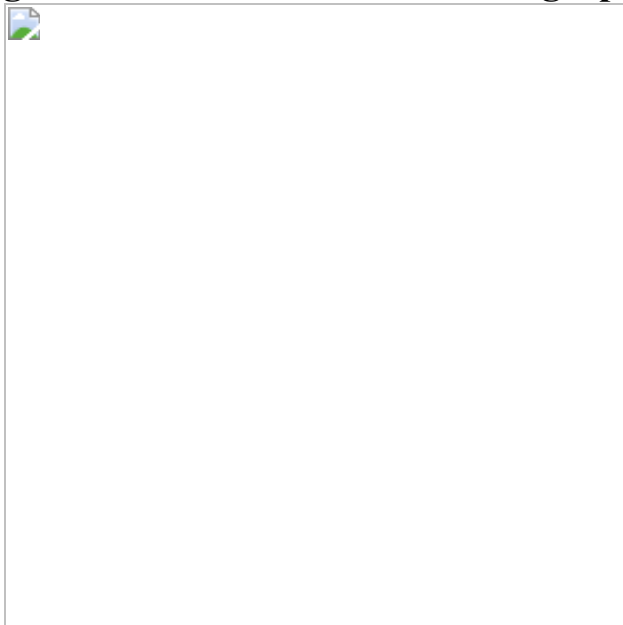


Fig. 2: PYS human fossil.

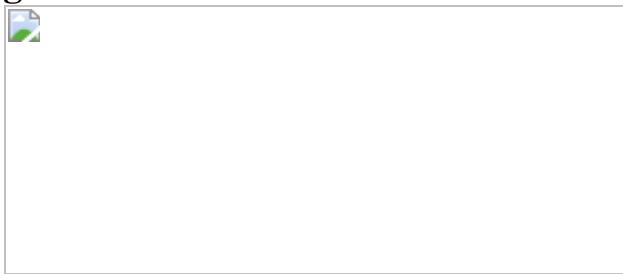
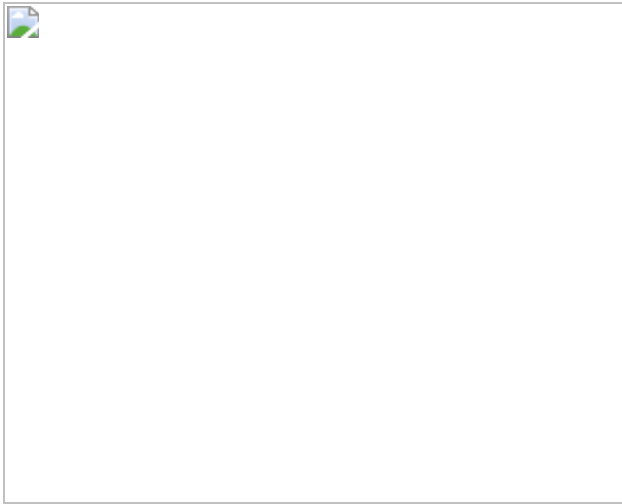


Fig. 3: Mtoto's preservation and position in the pit.



Data availability

The data that support the findings of this study are available from the corresponding authors upon reasonable request.

References

1. 1.

Mcbrearty, S. & Brooks, A. S. The revolution that wasn't: a new interpretation of the origin of modern human behavior. *J. Hum. Evol.* **39**, 453–563 (2000).

[CAS](#) [PubMed](#) [PubMed Central](#) [Google Scholar](#)

2. 2.

Mounier, A. & Mirazón Lahr, M. Deciphering African late middle Pleistocene hominin diversity and the origin of our species. *Nat. Commun.* **10**, 3406 (2019).

[ADS](#) [PubMed](#) [PubMed Central](#) [Google Scholar](#)

3. 3.

Scerri, E. M. L. et al. Did our species evolve in subdivided populations across Africa, and why does it matter? *Trends Ecol. Evol.* **33**, 582–594 (2018).

[PubMed](#) [PubMed Central](#) [Google Scholar](#)

4. 4.

Carbonell, E. & Mosquera, M. The emergence of a symbolic behaviour: the sepulchral pit of Sima de los Huesos, Sierra de Atapuerca, Burgos, Spain. *C. R. Palevol* **5**, 155–160 (2006).

[Google Scholar](#)

5. 5.

Pettitt, P. *The Palaeolithic Origins of Human Burial* (Routledge, 2011).

6. 6.

Zilhão, J. in *Death Rituals and Social Order in the Ancient World: Death Shall Have No Dominion* (eds Renfrew, C. et al.) 27–44 (Cambridge Univ. Press, 2016).

7. 7.

Roberts, P. et al. Late Pleistocene to Holocene human palaeoecology in the tropical environments of coastal eastern Africa. *Palaeogeogr. Palaeoclimatol. Palaeoecol.* **537**, 109438 (2020).

[Google Scholar](#)

8. 8.

Shipton, C. et al. 78,000-year-old record of Middle and Later stone age innovation in an East African tropical forest. *Nat. Commun.* **9**, 1832 (2018).

[ADS](#) [PubMed](#) [PubMed Central](#) [Google Scholar](#)

9. 9.

d'Errico, F. et al. Trajectories of cultural innovation from the Middle to Later Stone Age in Eastern Africa: personal ornaments, bone artifacts, and ochre from Panga ya Saidi, Kenya. *J. Hum. Evol.* **141**, 102737 (2020).

[PubMed](#) [PubMed Central](#) [Google Scholar](#)

10. 10.

Prendergast, M. E. et al. Reconstructing Asian faunal introductions to eastern Africa from multi-proxy biomolecular and archaeological datasets. *PLoS ONE* **12**, e0182565 (2017).

[PubMed](#) [PubMed Central](#) [Google Scholar](#)

11. 11.

Skoglund, P. et al. Reconstructing prehistoric African population structure. *Cell* **171**, 59–71.e21 (2017).

[CAS](#) [PubMed](#) [PubMed Central](#) [Google Scholar](#)

12. 12.

Grove, M. & Blinkhorn, J. Neural networks differentiate between Middle and Later Stone Age lithic assemblages in eastern Africa. *PLoS ONE* **15**, e0237528 (2020).

[CAS](#) [PubMed](#) [PubMed Central](#) [Google Scholar](#)

13. 13.

Duday, A. in *Social Archaeology of Funerary Remains* (eds Gowland, R. L. & Knüsel, C. J.) 30–56 (Oxbow Books, 2006).

14. 14.

Knüsel, C. J. Crouching in fear: terms of engagement for funerary remains. *J. Soc. Archaeol.* **14**, 26–58 (2014).

[Google Scholar](#)

15. 15.

Blaizot, F. *Les Espaces Funéraires de l'Habitat Groupé des Ruelles à Serris du VIIe au XIe Siècles Seine et Marne, Île-de-France: Taphonomie du Squelette, Modes d'Inhumation, Organisation et Dynamique* (Univ. Bordeaux, 2011).

16. 16.

Kapandii, I. A. *Physiologie Articulaire: Schémas Comment Mécanique Humaine* Vol. 3 (Maloine, 1972).

17. 17.

Defleur, A. *Les Sépultures Moustériennes* (Editions de CNRS, 1993).

18. 18.

Backwell, L., Huchet, J.-B., Jashashvili, T., Dirks, P. H. G. M. & Berger, L. R. Termites and necrophagous insects associated with early Pleistocene (Gelasian) *Australopithecus sediba* at Malapa, South Africa. *Palaeogeogr. Palaeoclimatol. Palaeoecol.* **560**, 109989 (2020).

[Google Scholar](#)

19. 19.

Ghiorse, W. C. in *Manganese in Soils and Plants* (eds Graham, R. D. et al.) 75–85 (Springer, 1988).

20. 20.

Thompson, I. A., Huber, D. M., Guest, C. A. & Schulze, D. G. Fungal manganese oxidation in a reduced soil. *Environ. Microbiol.* **7**, 1480–1487 (2005).

[CAS](#) [PubMed](#) [PubMed Central](#) [Google Scholar](#)

21. 21.

Gargett, R. H. Middle Palaeolithic burial is not a dead issue: the view from Qafzeh, Saint-Césaire, Kebara, Amud, and Dederiyeh. *J. Hum. Evol.* **37**, 27–90 (1999).

[CAS](#) [PubMed](#) [PubMed Central](#) [Google Scholar](#)

22. 22.

Bailey, S. E. & Hublin, J.-J. in *Neanderthals Revisited: New Approaches and Perspectives* (eds Hublin, J.-J. et al.) 191–209 (Springer, 2006).

23. 23.

Grine, F. E. Middle Stone Age human fossils from Die Kelders Cave 1, Western Cape Province, South Africa. *J. Hum. Evol.* **38**, 129–145 (2000).

[CAS](#) [PubMed](#) [PubMed Central](#) [Google Scholar](#)

24. 24.

Liu, W. et al. The earliest unequivocally modern humans in southern China. *Nature* **526**, 696–699 (2015).

[ADS](#) [CAS](#) [PubMed](#) [PubMed Central](#) [Google Scholar](#)

25. 25.

Martín-Albaladejo, M., Martín-Torres, M., García-González, R., Arsuaga, J. L. & Bermúdez de Castro, J. M. Morphometric analysis of

Atapuerca-Sima de los Huesos lower first molars. *Quat. Int.* **433**, 156–162 (2017).

[Google Scholar](#)

26. 26.

Henshilwood, C. S. & Marean, C. W. The origin of modern human behavior: critique of the models and their test implications. *Curr. Anthropol.* **44**, 627–651 (2003).

[Google Scholar](#)

27. 27.

Vermeersch, P. M., Paulissen, E., Gijselings, G. & Janssen, J. Middle Palaeolithic chert exploitation pits near Qena (Upper Egypt). *Paéorient* **12**, 61–65 (1986).

[Google Scholar](#)

28. 28.

Van Peer, P., Vermeersch, P. M. & Paulissen, E. *Chert Quarrying, Lithic Technology and Human Burial at the Palaeolithic Site of Taramsa I, Upper Egypt* Vol. 5 (Leuven Univ. Press, 2010).

29. 29.

Vermeersch, P. M. et al. A Middle Palaeolithic burial of a modern human at Taramsa Hill, Egypt. *Antiquity* **72**, 475–484 (1998).

[Google Scholar](#)

30. 30.

d'Errico, F. & Backwell, L. Earliest evidence of personal ornaments associated with burial: the Conus shells from Border Cave. *J. Hum. Evol.* **93**, 91–108 (2016).

[Google Scholar](#)

31. 31.

Beaumont, P. B., de Villiers, H. & Vogel, J. C. Modern man in sub-Saharan Africa prior to 49000 years BP: a review and evaluation with particular reference to Border Cave. *S. Afr. J. Sci.* **74**, 409–419 (1978).

[Google Scholar](#)

32. 32.

Cooke, H. B. S., Malan, B. D. & Wells, L. H. Fossil man in the Lebombo Mountains, South Africa: the ‘Border Cave,’ Ingwavuma District, Zululand. *Man* **45**, 6–13 (1945).

[Google Scholar](#)

33. 33.

d’Errico, F. et al. Additional evidence on the use of personal ornaments in the Middle Paleolithic of North Africa. *Proc. Natl Acad. Sci. USA* **106**, 16051–16056 (2009).

[ADS](#) [Google Scholar](#)

34. 34.

Henshilwood, C. S., d’Errico, F. & Watts, I. Engraved ochres from the Middle Stone Age levels at Blombos Cave, South Africa. *J. Hum. Evol.* **57**, 27–47 (2009).

[Google Scholar](#)

35. 35.

Henshilwood, C. S. et al. An abstract drawing from the 73,000-year-old levels at Blombos Cave, South Africa. *Nature* **562**, 115–118 (2018).

[ADS](#) [CAS](#) [Google Scholar](#)

36. 36.

Steele, T. E., Alvarez-Fernandez, E. & Hallet-Desguez, E. A review of shells as personal ornamentation during the African Middle Stone Age. *Paleoanthropology* **24**, 24–51 (2019).

[Google Scholar](#)

37. 37.

White, T. D. Cut marks on the Bodo cranium: a case of prehistoric defleshing. *Am. J. Phys. Anthropol.* **69**, 503–509 (1986).

[CAS](#) [Google Scholar](#)

38. 38.

Clark, J. D. et al. Stratigraphic, chronological and behavioural contexts of Pleistocene *Homo sapiens* from Middle Awash, Ethiopia. *Nature* **423**, 747–752 (2003).

[ADS](#) [CAS](#) [Google Scholar](#)

39. 39.

Dirks, P. H. G. M. et al. Geological and taphonomic evidence for deliberate body disposal by the primitive hominin species *Homo naledi* from the Dinaledi Chamber. *eLife* **4**, e09561 (2015).

[PubMed](#) [PubMed Central](#) [Google Scholar](#)

40. 40.

Stiner, M. C. Love and death in the Stone Age: what constitutes first evidence of mortuary treatment of the human body? *Biol. Theory* **12**, 248–261 (2017).

[Google Scholar](#)

41. 41.

Scerri, E. M. L., Chikhi, L. & Thomas, M. G. Beyond multiregional and simple out-of-Africa models of human evolution. *Nat. Ecol. Evol.* **3**, 1370–1372 (2019).

[PubMed](#) [PubMed Central](#) [Google Scholar](#)

42. 42.

Brooks, A. S. et al. Long-distance stone transport and pigment use in the earliest Middle Stone Age. *Science* **360**, 90–94 (2018).

[ADS](#) [CAS](#) [PubMed](#) [PubMed Central](#) [Google Scholar](#)

43. 43.

Henshilwood, C. S. et al. A 100,000-year-old ochre-processing workshop at Blombos Cave, South Africa. *Science* **334**, 219–222 (2011).

[ADS](#) [CAS](#) [PubMed](#) [PubMed Central](#) [Google Scholar](#)

44. 44.

Wadley, L. in *The Oxford Handbook of African Archaeology* (eds Mitchell, P. & Lane, P.) 15 (Oxford Univ. Press, 2020).

45. 45.

Richter, D. et al. The age of the hominin fossils from Jebel Irhoud, Morocco, and the origins of the Middle Stone Age. *Nature* **546**, 293–296 (2017).

[ADS](#) [CAS](#) [Google Scholar](#)

46. 46.

Guo, Y.-J. et al. New ages for the Upper Palaeolithic site of Xibaimaying in the Nihewan Basin, northern China: implications for small-tool and microblade industries in north-east Asia during Marine Isotope Stages 2 and 3. *J. Quat. Sci.* **32**, 540–552 (2017).

[Google Scholar](#)

47. 47.

Li, B., Jacobs, Z. & Roberts, R. G. Validation of the $L_n T_n$ method for D_e determination in optical dating of K-feldspar and quartz. *Quat. Geochronol.* **58**, 101066 (2020).

[Google Scholar](#)

48. 48.

Blegen, N. et al. Distal tephras of the eastern Lake Victoria basin, equatorial East Africa: correlations, chronology and a context for early modern humans. *Quat. Sci. Rev.* **122**, 89–111 (2015).

[ADS](#) [Google Scholar](#)

49. 49.

Bronk Ramsey, C. Bayesian analysis of radiocarbon dates. *Radiocarbon* **51**, 337–360 (2009).

[Google Scholar](#)

50. 50.

Dabney, J. et al. Complete mitochondrial genome sequence of a Middle Pleistocene cave bear reconstructed from ultrashort DNA fragments. *Proc. Natl Acad. Sci. USA* **110**, 15758–15763 (2013).

[ADS](#) [CAS](#) [PubMed](#) [PubMed Central](#) [Google Scholar](#)

51. 51.

Rohland, N., Glocke, I., Aximu-Petri, A. & Meyer, M. Extraction of highly degraded DNA from ancient bones, teeth and sediments for high-throughput sequencing. *Nat. Protocols* **13**, 2447–2461 (2018).

[CAS](#) [PubMed](#) [PubMed Central](#) [Google Scholar](#)

52. 52.

Gansauge, M.-T. et al. Single-stranded DNA library preparation from highly degraded DNA using T4 DNA ligase. *Nucleic Acids Res.* **45**, e79 (2017).

[CAS](#) [PubMed](#) [PubMed Central](#) [Google Scholar](#)

53. 53.

Kircher, M., Sawyer, S. & Meyer, M. Double indexing overcomes inaccuracies in multiplex sequencing on the Illumina platform. *Nucleic Acids Res.* **40**, e3 (2012).

[CAS](#) [PubMed](#) [PubMed Central](#) [Google Scholar](#)

54. 54.

Korlević, P. et al. Reducing microbial and human contamination in DNA extractions from ancient bones and teeth. *Biotechniques* **59**, 87–93 (2015).

[PubMed](#) [PubMed Central](#) [Google Scholar](#)

55. 55.

Glocke, I. & Meyer, M. Extending the spectrum of DNA sequences retrieved from ancient bones and teeth. *Genome Res.* **27**, 1230–1237 (2017).

[CAS](#) [PubMed](#) [PubMed Central](#) [Google Scholar](#)

56. 56.

Slon, V. et al. Mammalian mitochondrial capture, a tool for rapid screening of DNA preservation in faunal and undiagnostic remains, and its application to Middle Pleistocene specimens from Qesem Cave (Israel). *Quat. Int.* **398**, 210–218 (2016).

[Google Scholar](#)

57. 57.

Fu, Q. et al. DNA analysis of an early modern human from Tianyuan Cave, China. *Proc. Natl Acad. Sci. USA* **110**, 2223–2227 (2013).

[ADS](#) [CAS](#) [PubMed](#) [PubMed Central](#) [Google Scholar](#)

58. 58.

Maricic, T., Whitten, M. & Pääbo, S. Multiplexed DNA sequence capture of mitochondrial genomes using PCR products. *PLoS ONE* **5**, e14004 (2010).

[ADS](#) [PubMed](#) [PubMed Central](#) [Google Scholar](#)

59. 59.

Renaud, G., Stenzel, U. & Kelso, J. leeHom: adaptor trimming and merging for Illumina sequencing reads. *Nucleic Acids Res.* **42**, e141 (2014).

[PubMed](#) [PubMed Central](#) [Google Scholar](#)

60. 60.

Altschul, S. F., Gish, W., Miller, W., Myers, E. W. & Lipman, D. J. Basic local alignment search tool. *J. Mol. Biol.* **215**, 403–410 (1990).

[CAS](#) [PubMed](#) [PubMed Central](#) [Google Scholar](#)

61. 61.

Huson, D. H., Auch, A. F., Qi, J. & Schuster, S. C. MEGAN analysis of metagenomic data. *Genome Res.* **17**, 377–386 (2007).

[CAS](#) [PubMed](#) [PubMed Central](#) [Google Scholar](#)

62. 62.

Slon, V. et al. Neandertal and Denisovan DNA from Pleistocene sediments. *Science* **356**, 605–608 (2017).

[ADS](#) [CAS](#) [PubMed](#) [PubMed Central](#) [Google Scholar](#)

63. 63.

Li, H. & Durbin, R. Fast and accurate short read alignment with Burrows-Wheeler transform. *Bioinformatics* **25**, 1754–1760 (2009).

[CAS](#) [PubMed](#) [PubMed Central](#) [Google Scholar](#)

64. 64.

Meyer, M. et al. A high-coverage genome sequence from an archaic Denisovan individual. *Science* **338**, 222–226 (2012).

[ADS](#) [CAS](#) [PubMed](#) [PubMed Central](#) [Google Scholar](#)

65. 65.

Scheuer, L. & Black, S. in *Human Osteology: In Archeology and Forensic Science* (eds. Cox, M. & Mays, S.) 9–22 (Cambridge Univ. Press, 2000).

66. 66.

Bullock, P. et al. *Handbook for Soil Thin Section Description* (Waine Research, 1985).

67. 67.

Stoops, G. *Guidelines for Analysis and Description of Soil and Regolith Thin Sections*. (Soil Science Soc. Am., 2003).

68. 68.

Stoops, G., Marcelino, V. & Mees, F. (eds.) *Interpretation of Micromorphological Features of Soils and Regoliths* (Elsevier, 2018).

69. 69.

Hollund, H. I. et al. What happened here? Bone histology as a tool in decoding the postmortem histories of archaeological bone from Castricum, the Netherlands. *Int. J. Osteoarchaeol.* **22**, 537–548 (2012).

[Google Scholar](#)

70. 70.

Hedges, R. E. M., Millard, A. R. & Pike, A. W. G. Measurements and relationships of diagenetic alteration of bone from three archaeological sites. *J. Archaeol. Sci.* **22**, 201–209 (1995).

[Google Scholar](#)

71. 71.

Millard, A. R. in *Handbook of Archaeological Sciences* (eds. Brothwell, D. R. & Pollard, A. M.) 637–674 (Wiley, 2001).

72. 72.

Hackett, C. J. Microscopical focal destruction (tunnels) in exhumed human bones. *Med. Sci. Law* **21**, 243–265 (1981).

[CAS](#) [PubMed](#) [PubMed Central](#) [Google Scholar](#)

73. 73.

Jans, M. M. E. in *Current Developments in Bioerosion* (eds. Wissak, M. & Tapanila, L.) 397–404 (Springer, 2008).

74. 74.

Carlsen, O. *Dental Morphology* (Munksgaard, 1987).

75. 75.

Tobias, P. V. *The Skulls, Endocasts and Teeth of Homo habilis* Vol. 4 (Cambridge Univ. Press, 1991).

76. 76.

Turner, C. G., Nichol, C. R. & Scott, G. R. in *Advances in Dental Anthropology* (eds. Kelley, M. & Larsen, C.) 13–31 (Wiley-Liss, 1991).

77. 77.

Scott, G. R. & Turner, C. G. *The Anthropology of Modern Human Teeth: Dental Morphology and Its Variation in Recent Human Populations*. (Cambridge Univ. Press, 1997).

78. 78.

Martinón-Torres, M. et al. Dental evidence on the hominin dispersals during the Pleistocene. *Proc. Natl Acad. Sci. USA* **104**, 13279–13282 (2007).

[ADS](#) [Google Scholar](#)

79. 79.

Martinón-Torres, M. et al. Dental remains from Dmanisi (Republic of Georgia): morphological analysis and comparative study. *J. Hum. Evol.* **55**, 249–273 (2008).

[Google Scholar](#)

80. 80.

Martínez de Pinillos, M., Martinón-Torres, M., Martín-Francés, L., Arsuaga, J. L. & Bermúdez de Castro, J. M. Comparative analysis of the trigonid crests patterns in *Homo* antecessor molars at the enamel and dentine surfaces. *Quat. Int.* **433**, 189–198 (2017).

[Google Scholar](#)

81. 81.

Martinón-Torres, M., Bermúdez de Castro, J. M., Gómez-Robles, A., Prado-Simón, L. & Arsuaga, J. L. Morphological description and comparison of the dental remains from Atapuerca-Sima de los Huesos site (Spain). *J. Hum. Evol.* **62**, 7–58 (2012).

[PubMed](#) [PubMed Central](#) [Google Scholar](#)

82. 82.

Molnar, S. Human tooth wear, tooth function and cultural variability. *Am. J. Phys. Anthropol.* **34**, 175–189 (1971).

[CAS](#) [PubMed](#) [PubMed Central](#) [Google Scholar](#)

83. 83.

Lefèvre, J. Etude odontologique des hommes de Muge. *Bull. Mem. Soc. Anthropol. Paris* **10**, 301–333 (1973).

[Google Scholar](#)

84. 84.

Bermúdez de Castro, J. M., Sarmiento, S., Cunha, E., Rosas, A. & Bastir, M. Dental size variation in the Atapuerca-SH Middle Pleistocene hominids. *J. Hum. Evol.* **41**, 195–209 (2001).

[PubMed](#) [PubMed Central](#) [Google Scholar](#)

85. 85.

Bailey, S. E. A morphometric analysis of maxillary molar crowns of Middle-Late Pleistocene hominins. *J. Hum. Evol.* **47**, 183–198 (2004).

[PubMed](#) [PubMed Central](#) [Google Scholar](#)

86. 86.

Olejniczak, A. J. et al. Dental tissue proportions and enamel thickness in Neandertal and modern human molars. *J. Hum. Evol.* **55**, 12–23 (2008).

[PubMed](#) [PubMed Central](#) [Google Scholar](#)

87. 87.

Martin, L. Significance of enamel thickness in hominoid evolution. *Nature* **314**, 260–263 (1985).

[ADS](#) [CAS](#) [PubMed](#) [PubMed Central](#) [Google Scholar](#)

88. 88.

Kono, R. T. Molar enamel thickness and distribution patterns in extant great apes and humans: new insights based on a 3-dimensional whole crown perspective. *Anthropol. Sci.* **112**, 121–146 (2004).

[Google Scholar](#)

89. 89.

Toussaint, M. et al. The Neandertal lower right deciduous second molar from Trou de l'Abîme at Couvin, Belgium. *J. Hum. Evol.* **58**, 56–67 (2010).

[PubMed](#) [PubMed Central](#) [Google Scholar](#)

90. 90.

Zanolli, C. et al. Is the deciduous/permanent molar enamel thickness ratio a taxon-specific indicator in extant and extinct hominids? *C. R. Palevol* **16**, 702–714 (2017).

[Google Scholar](#)

91. 91.

Olejniczak, A. J. & Grine, F. E. High-resolution measurement of Neandertal tooth enamel thickness by microfocal computed-tomography. *S. Afr. J. Sci.* **101**, 219–220 (2005).

[Google Scholar](#)

92. 92.

Maureille, B., Rougier, H., Houët, F. & Vandermeersch, B. Les dents inférieures du Néandertalien Regourdou 1 (site de Regourdou, commune de Montignac, Dordogne): analyses métriques et comparatives. *Paleo* **13**, 183–200 (2001).

[Google Scholar](#)

93. 93.

Scolan, H., Santos, F., Tillier, A.-M., Maureille, B. & Quintard, A. Des nouveaux vestiges Néanderthaliens à Las Pélénos (Monsempron-Libos, Lot-et-Garonne, France). *Bull. Mem. Soc. Anthropol. Paris* **24**, 69–95 (2012).

[Google Scholar](#)

94. 94.

Bayle, P. et al. in *Pleistocene Databases: Acquisition, Storing, Sharing* (eds. Macchiarelli, R. & Weniger, G. C.) 29–46 (Mettmann: Wissenschaftliche Schriften des Neanderthal Museums 4, 2011).

95. 95.

Macchiarelli, R., Bondioli, L., Mazurier, A. & Zanolli, C. in *Technique and Application in Dental Anthropology* (eds. Irish, J. D. & Nelson, G. C.) 425–448 (Cambridge Univ. Press, 2008).

96. 96.

Mitteroecker, P. & Bookstein, F. Linear discrimination, ordination, and the visualization of selection gradients in modern morphometrics. *Evol. Biol.* **38**, 100–114 (2011).

[Google Scholar](#)

97. 97.

Bookstein, F. *Morphometric Tools for Landmark Data Geometric and Biology* (Cambridge Univ. Press, 1991).

98. 98.

Mitteroecker, P., Gunz, P., Windhager, S. & Schaefer, K. A brief review of shape, form, and allometry in geometric morphometrics, with applications to human facial morphology. *Hystrix* **24**, 59–66 (2013).

[Google Scholar](#)

99. 99.

ISO. *Particle Size Analysis — Laser Diffraction Methods* <https://www.iso.org/obp/ui/#iso:std:iso:13320:ed-1:v2:en> (ISO, 2009).

100. 100.

Jones, R. M. Particle size analysis by laser diffraction: ISO 13320, standard operating procedures, and mie theory. *Am. Lab.* **35**, 44–47 (2003).

[CAS](#) [Google Scholar](#)

101. 101.

Macdonald, P. & Du, J. *Mixdist: Finite Mixture Distribution Models* <https://cran.r-project.org/package=mixdist> (2012).

102. 102.

Konert, M. & Vandenberghe, J. Comparison of laser grain size analysis with pipette and sieve analysis: A solution for the underestimation of the clay fraction. *Sedimentology* **44**, 523–535 (1997).

[ADS](#) [CAS](#) [Google Scholar](#)

103. 103.

Sitzia, L., Gayo, E. M. & de Pol-Holz, R. A perched, high-elevation wetland complex in the Atacama Desert (northern Chile) and its implications for past human settlement. *Quat. Res.* **92**, 33–52 (2019).

[Google Scholar](#)

104. 104.

Aitchison, J. *The Statistical Analysis of Compositional Data* (Chapman and Hall, 1986).

105. 105.

Martín-Fernández, J. A., Barcelo-Vidal, C. & Pawlowsky-Glahn, V. Dealing with zeros and missing values in compositional data sets using nonparametric imputation. *Math. Geol.* **35**, 253–278 (2003).

[MATH](#) [Google Scholar](#)

106. 106.

Dray, S. & Dufour, A.-B. The ade4 package: implementing the duality diagram for ecologists. *J. Stat. Soft.* **22**, 4 (2007).

[Google Scholar](#)

107. 107.

Pitarch Martí, A., Wei, Y., Gao, X., Chen, F. & d'Errico, F. The earliest evidence of coloured ornaments in China: the ochred ostrich eggshell beads from Shuidonggou Locality 2. *J. Anthropol. Archaeol.* **48**, 102–113 (2017).

[Google Scholar](#)

108. 108.

Downs, R. T. The RRUFF project: An integrated study of the chemistry, crystallography, raman and infrared spectroscopy of minerals. *Prog. Abstr. 19th Gen. Meeting Intl Mineralog. Assoc.* O03-13 (2006).

109. 109.

Julien, C. M., Massot, M. & Poinsignon, C. Lattice vibrations of manganese oxides. Part I. Periodic structures. *Spectrochim. Acta A Mol. Biomol. Spectrosc.* **60**, 689–700 (2004).

[ADS](#) [CAS](#) [PubMed](#) [PubMed Central](#) [Google Scholar](#)

110. 110.

Bellot-Gurlet, L. et al. Raman studies of corrosion layers formed on archaeological irons in various media. *J. Nano Res.* **8**, 147–156 (2009).

[CAS](#) [Google Scholar](#)

111. 111.

Hanesch, M. Raman spectroscopy of iron oxides and (oxy) hydroxides at low laser power and possible applications in environmental magnetic studies. *Geophys.* **177**, 941–948 (2009).

[CAS](#) [Google Scholar](#)

112. 112.

Babay, S., Mhiri, T. & Toumi, M. Synthesis, structural and spectroscopic characterizations of maghemite γ -Fe₂O₃ prepared by one-step coprecipitation route. *J. Mol. Struct.* **1085**, 286–293 (2015).

[ADS](#) [CAS](#) [Google Scholar](#)

[Download references](#)

Acknowledgements

Funding for this project was provided by the SEALINKS project under a European Research Council (ERC) grant (no. 206148) and the Max Planck Society (to N.B.). Funding for the hominin analyses was from the Dirección General de Investigación of the Ministerio de Ciencia, Innovación y Universidades, grant numbers PGC2018-093925-B-C31 and C33 (MCI/AEI/FEDER, UE) and The Leakey Foundation, through the personal support of G. Getty (2013) and D. Crook (2014–2020) to M.M.-T.; analyses were also carried out at the laboratories of the CENIEH-ICTS with the support of the CENIEH staff. E.S. has a Ramón Areces/Atapuerca Foundation postdoctoral grant. L.M.-F. is a beneficiary of an Atapuerca Foundation postdoctoral grant. S.J.A. and F.d'E. acknowledge support from the Research Council of Norway, through its Centres of Excellence funding scheme, SFF Centre for Early Sapiens Behaviour (SapienCE) (no. 262618). F.d'E. was funded by the ERC grant TRACSYMBOLS (no. 249587), the Agence Nationale de la Recherche (ANR-10-LABX-52), LaScArBx Cluster of Excellence, and the Talents programme of the University of Bordeaux, Initiative d'Excellence. A.P.M. was funded by the Beatriu de Pinós postdoctoral programme (2017 BP-A 00046) of the Government of Catalonia's Secretariat for Universities & Research of the Ministry of Economy and Knowledge. We thank B. Kimeu for the extraction of Mtoto in the field, N. Blegen for conducting the digital work in the field, R. Blasco for insights about taphonomy, R. García and P. Saladié for assisting in anatomical identification, S. Sarmiento for the tooth photographs and M.

O'Reilly for assisting with graphic design. We thank G. Musuko and family for permission to excavate the site. Permission to conduct the research was granted by the National Commission for Science, Technology and Innovation Office of the President of the Republic of Kenya through affiliation with the National Museums of Kenya (NMK). We are grateful for the support of the NMK administration, staff from the preparation and archaeology section, and the British Institute in Eastern Africa.

Author information

Affiliations

1. CENIEH (National Research Center on Human Evolution), Burgos, Spain

María Martinón-Torres, Ana Álvaro Gallo, José María Bermúdez de Castro, Pilar Fernández-Colón, David Larréina, Laura Martín-Francés & Belén Notario

2. Anthropology Department, University College London, London, UK

María Martinón-Torres, José María Bermúdez de Castro & Laura Martín-Francés

3. UMR 5199 CNRS De la Préhistoire à l'Actuel: Culture, Environnement, et Anthropologie (PACEA), Université Bordeaux, Talence, France

Francesco d'Errico, Africa Pitarch Martí, Alain Queffelec & Solange Rigaud

4. SFF Centre for Early Sapiens Behaviour (SapienCE), University of Bergen, Bergen, Norway

Francesco d'Errico & Simon J. Armitage

5. Centro Mixto UCM-ISCIII de Evolución y Comportamiento Humanos,
Instituto de Salud Carlos III, Madrid, Spain

Elena Santos & Juan Luis Arsuaga

6. Cátedra de Otoacústica Evolutiva y Paleoantropología (HM Hospitales
- Universidad de Alcalá), Departamento de Ciencias de la Vida,
Universidad de Alcalá, Alcalá de Henares, Spain

Elena Santos

7. Department of Archaeology, Max Planck Institute for the Science of
Human History, Jena, Germany

Noel Amano, James Blinkhorn, Alison Crowther, Katerina
Douka, Patrick Faulkner, Julio Mercader, Jennifer M.
Miller, Emmanuel Ndiema, Patrick Roberts, Mohammad Javad
Shoaee, Nicole Boivin & Michael D. Petraglia

8. Department of Archaeology and Anthropology, National Museum,
Bloemfontein, South Africa

William Archer

9. Department of Archaeology, University of Cape Town, Cape Town,
South Africa

William Archer

10. Department of Human Evolution, Max Planck Institute for
Evolutionary Anthropology, Leipzig, Germany

William Archer

11. Department of Geography, Royal Holloway, University of London,
Egham, UK

Simon J. Armitage & James Blinkhorn

12. Departamento de Paleontología, Facultad de Ciencias Geológicas,
Universidad Complutense de Madrid, Madrid, Spain

Juan Luis Arsuaga

13. Pan-African Evolution Research Group, Max Planck Institute for the
Science of Human History, Jena, Germany

James Blinkhorn

14. School of Social Science, The University of Queensland, Brisbane,
Queensland, Australia

Alison Crowther, Patrick Roberts, Nicole Boivin & Michael D.
Petraglia

15. Research Laboratory for Archaeology and the History of Art,
University of Oxford, Oxford, UK

Katerina Douka

16. UMR 5060 CNRS-Université Bordeaux Montaigne IRAMAT-CRP2A:
Institut de recherche sur les Archéomatériaux – Centre de recherche en
physique appliquée à l’archéologie, Maison de l’archéologie, Pessac,
France

Stéphan Dubernet & François-Xavier Le Bourdonnec

17. Faculty of Arts and Social Sciences, Department of Archaeology, The
University of Sydney, Sydney, New South Wales, Australia

Patrick Faulkner

18. Centre for Open Learning, University of Edinburgh, Edinburgh, UK

Nikos Kourampas & Ian Simpson

19. Biological and Environmental Sciences, University of Stirling,
Stirling, UK

Nikos Kourampas & George MacLeod

20. 3D Applications Engineer and Heritage Specialist Digital Heritage and Humanities Collections, University of South Florida, Tampa, FL, USA

Jorge González García

21. Department of Evolutionary Genetics, Max Planck Institute for Evolutionary Anthropology, Leipzig, Germany

Diyendo Massilani

22. Department of Anthropology and Archaeology, University of Calgary, Calgary, Alberta, Canada

Julio Mercader & Nicole Boivin

23. National Museums of Kenya, Department of Earth Sciences, Nairobi, Kenya

Emmanuel Ndiema

24. Seminari d'Estudis i Recerques Prehistòriques (SERP), Facultat de Geografia i Història, Departament d'Història i Arqueologia, Universitat de Barcelona, Barcelona, Spain

Africa Pitarch Martí

25. Department of Anthropology, Rice University, Houston, TX, USA

Mary E. Prendergast

26. Institute of Archaeology, University College London, London, UK

Ceri Shipton

27. Centre of Excellence for Australian Biodiversity and Heritage, The Australian National University, Canberra, Australian Capital Territory, Australia

Ceri Shipton

28. Department of Anthropology, National Museum of Natural History,
Smithsonian Institution, Washington, DC, USA

Nicole Boivin

29. Human Origins Program, National Museum of Natural History,
Smithsonian Institution, Washington, DC, USA

Michael D. Petraglia

30. Australian Research Centre for Human Evolution (ARCHE), Griffith
University, Brisbane, Queensland, Australia

Michael D. Petraglia

Authors

1. María Martinón-Torres

[View author publications](#)

You can also search for this author in [PubMed](#) [Google Scholar](#)

2. Francesco d'Errico

[View author publications](#)

You can also search for this author in [PubMed](#) [Google Scholar](#)

3. Elena Santos

[View author publications](#)

You can also search for this author in [PubMed](#) [Google Scholar](#)

4. Ana Álvaro Gallo

[View author publications](#)

You can also search for this author in [PubMed](#) [Google Scholar](#)

5. Noel Amano

[View author publications](#)

You can also search for this author in [PubMed](#) [Google Scholar](#)

6. William Archer

[View author publications](#)

You can also search for this author in [PubMed](#) [Google Scholar](#)

7. Simon J. Armitage

[View author publications](#)

You can also search for this author in [PubMed](#) [Google Scholar](#)

8. Juan Luis Arsuaga

[View author publications](#)

You can also search for this author in [PubMed](#) [Google Scholar](#)

9. José María Bermúdez de Castro

[View author publications](#)

You can also search for this author in [PubMed](#) [Google Scholar](#)

10. James Blinkhorn

[View author publications](#)

You can also search for this author in [PubMed](#) [Google Scholar](#)

11. Alison Crowther

[View author publications](#)

You can also search for this author in [PubMed](#) [Google Scholar](#)

12. Katerina Douka

[View author publications](#)

You can also search for this author in [PubMed](#) [Google Scholar](#)

13. Stéphan Dubernet

[View author publications](#)

You can also search for this author in [PubMed](#) [Google Scholar](#)

14. Patrick Faulkner

[View author publications](#)

You can also search for this author in [PubMed](#) [Google Scholar](#)

15. Pilar Fernández-Colón

[View author publications](#)

You can also search for this author in [PubMed](#) [Google Scholar](#)

16. Nikos Kourampas

[View author publications](#)

You can also search for this author in [PubMed](#) [Google Scholar](#)

17. Jorge González García

[View author publications](#)

You can also search for this author in [PubMed](#) [Google Scholar](#)

18. David Larreina

[View author publications](#)

You can also search for this author in [PubMed](#) [Google Scholar](#)

19. François-Xavier Le Bourdonnec

[View author publications](#)

You can also search for this author in [PubMed](#) [Google Scholar](#)

20. George MacLeod

[View author publications](#)

You can also search for this author in [PubMed](#) [Google Scholar](#)

21. Laura Martín-Francés

[View author publications](#)

You can also search for this author in [PubMed](#) [Google Scholar](#)

22. Diyendo Massilani

[View author publications](#)

You can also search for this author in [PubMed](#) [Google Scholar](#)

23. Julio Mercader

[View author publications](#)

You can also search for this author in [PubMed](#) [Google Scholar](#)

24. Jennifer M. Miller

[View author publications](#)

You can also search for this author in [PubMed](#) [Google Scholar](#)

25. Emmanuel Ndiema

[View author publications](#)

You can also search for this author in [PubMed](#) [Google Scholar](#)

26. Belén Notario

[View author publications](#)

You can also search for this author in [PubMed](#) [Google Scholar](#)

27. Africa Pitarch Martí

[View author publications](#)

You can also search for this author in [PubMed](#) [Google Scholar](#)

28. Mary E. Prendergast

[View author publications](#)

You can also search for this author in [PubMed](#) [Google Scholar](#)

29. Alain Queffelec

[View author publications](#)

You can also search for this author in [PubMed](#) [Google Scholar](#)

30. Solange Rigaud

[View author publications](#)

You can also search for this author in [PubMed](#) [Google Scholar](#)

31. Patrick Roberts

[View author publications](#)

You can also search for this author in [PubMed](#) [Google Scholar](#)

32. Mohammad Javad Shoaei

[View author publications](#)

You can also search for this author in [PubMed](#) [Google Scholar](#)

33. Ceri Shipton

[View author publications](#)

You can also search for this author in [PubMed](#) [Google Scholar](#)

34. Ian Simpson

[View author publications](#)

You can also search for this author in [PubMed](#) [Google Scholar](#)

35. Nicole Boivin

[View author publications](#)

You can also search for this author in [PubMed](#) [Google Scholar](#)

36. Michael D. Petraglia

[View author publications](#)

You can also search for this author in [PubMed](#) [Google Scholar](#)

Contributions

N.B., M.D.P. and E.N. designed and directed the PYS research; C.S. and J.B. directed the field excavations; M.M.-T., J.M.B.d.C., J.L.A., E.S. and L.M.-F. analysed the hominin fossil; P.F.-C. conducted the mechanical restoration and conservation of the hominin; E.S. and J.G.G. conducted the virtual restoration and reconstruction of the hominin; F.d'E., N.A., W.A., S.J.A., J.B., A.C., S.D., K.D., F.-X.L.B., A.A.G., B.N., D.L., N.K., G.M., D.M., J.M., J.M.M., A.P.M., M.E.P., A.Q., S.R., P.R., M.J.S., C.S. and I.S. conducted analytical studies; M.M.-T., M.D.P., F.d'E. and N.B. wrote the paper with contributions of all authors.

Corresponding authors

Correspondence to [María Martinón-Torres](#) or [Nicole Boivin](#) or [Michael D. Petraglia](#).

Ethics declarations

Competing interests

The authors declare no competing interests.

Additional information

Peer review information *Nature* thanks Louise Humphrey, Richard Klein, Wu Liu and the other, anonymous, reviewer(s) for their contribution to the peer review of this work. Peer reviewer reports are available.

Publisher's note Springer Nature remains neutral with regard to jurisdictional claims in published maps and institutional affiliations.

Extended data figures and tables

[**Extended Data Fig. 1 PYS MSA lithics.**](#)

Top, the relative sizes of flakes through layers 18–17 (MSA) and layer 16 (early LSA) visualized with a violin plot, illustrating the density of values by layer as a continuous distribution. Note the decrease across layers 17–16. The flakes recovered from the burial ($n = 14$), shown here with a box plot, fall within the variation in product weight for the MSA. The box plot shows the median value for burial lithics at the centre, with two neighbouring hinges marking the 25th and 75th percentiles. The whiskers plot the distance from the hinge values to the largest and smallest values in the burial dataset, to a maximum distance of 1.5 times the interquartile range (data beyond this range, if present, would have been plotted as individual outlier points). Below, faceted limestone flakes from MSA layers of PYS. A, limestone flake from burial context (809) with faceted dihedral platform; B, retouched limestone flake with large faceted platform from layer 17.

Extended Data Fig. 2 Bayesian model for the age estimation of PYS.

Left, Bayesian model of all available age determinations from PYS, produced using OxCal 4.4.2 and IntCal20. Right, age estimate of the burial determined using Bayesian model. A full description (OxCal code) of the age model is provided in Supplementary Information [C](#).

Extended Data Fig. 3 Reconstruction of key taphonomic events of Mtoto's burial.

a–c, The 3D sequence illustrates the reconstruction of the key taphonomic events that affected the shape and relationship of the head and the spine. **a**, Original right lateral decubitus position of the child in the burial pit. **b**, Lateral compression of the thorax because of the sediment weight; the ribs are flattened but the rib cage does not collapse, as is common in decomposition in filled space (earth grave). **c**, The head dislocates, as is typical in the case of burials with perishable head support. **d**, Ideal reconstruction of Mtoto's original position at the moment of its discovery at the site.

Extended Data Fig. 4 Analysis of sediment from the stratigraphic sequence and the burial pit.

a, Particle size ternary diagram indicating the higher content of sand and silt in the burial pit in comparison to the encasing archaeological layers, and in particular layer 19. **b**, Examples of particle size distribution and multimodal decomposition showing the similarities of sand and silt modes between the burial samples and samples 137 (base of layer 17) and 138 (top of layer 18). **c**, Elemental profiles of sediment from layers 17, 18, 19 and the burial pit. Element concentrations are expressed in percentages. Data are presented as mean values. Sediment samples from the burial pit display an elemental composition notably similar to the three samples identified as an anomaly at the top of layer 18 and the base of layer 17. **d**, Results of PCA of the centre log ratio data (selected elements: SiO_2 , K_2O , TiO_2 , MnO , Fe_2O_3 , Zn, Ga,

As, Rb, Y, Zr and Ba). Confidence ellipses at 95%. The burial pit samples markedly differ from layer 19.

Extended Data Fig. 5 Micromorphological and histological analysis.

a–h, Polarizing microscopy (**a, c–f**) and SEM (**g, h**) images of bone and sediment from Mtoto's burial and from surrounding contexts (**b**). **a**, Ferruginous microfacies (MF-fer: here a coarser-grained variant) adhering on cancellous bone (PPL). **b**, Small vertebrate bone fragment from ferruginous sediment at the top of layer 18, about 20 cm above Mtoto's skeleton. Note the good histological preservation and longitudinal and transverse fracturing (PPL). **c**, Mtoto's bone fragment. A Fe-oxide-stained calcite crust (Ca) covers the bone surface. A thin zone of non-clouded bone (HAP—conventionally ‘hydroxyapatite’) immediately beneath the bone surface is underlain with clouded, Ca-enriched bone of the mesosteum (CLb). Note the sharp boundary between HAP and CLb (especially on the left side), and the dense non-Wedl bioerosion foci within CLb (linear longitudinal tunnels at about 45°; budding tunnels (dark spots), attributed to bacteria) and enlarged osteocyte lacunae (smaller dark spots). Double arrow shows two possible Wedl tunnels (PPL). **d**, As in **c**, but in XPL. The calcitic crust (Ca) comprises two layers: an Fe-oxide-stained, microcrystalline layer, and a latter layer of clear, coarser-crystalline calcite (grey arrow). Birefringent areas within CLb mark osteons. Note the loss of birefringence in bioerosion foci (for example, lower right corner). **e**, Enlarged osteocyte canaliculi and lacunae, possibly due to fungal or fungal and bacterial action, in clouded, Ca-enriched bone (PPL). **f**, Advanced alteration of putative human bone (general histological index: 2), with small areas of preserved histology, pervasive clouding, fissuring (for example, blue arrow), dissolution pores (for example, green arrow) and Fe and Mn impregnation (black spots). Note the spatial patterning of bioerosion, with domains of larger, circular, coalescent non-Wedl (bacterial) MFD (for example, red arrow) and smaller, more typical tunnels (budding and linear longitudinal: for example, white arrow). A crust of calcite speleothem (grey arrows) encrusts a transverse fracture across the bone (PPL). **g**, Budding and linear longitudinal tunnels in highly altered bone (area marked with white arrow in **f**). Some smaller-scale, spongiform bioerosion is also shown, surrounded

with permineralized rims (white) of redeposited ‘hydroxyapatite’ (light blue arrows) (SEM image). **h**, Periosteum of clouded bone (Cb), encrusted with carbonate deposits (MF-carb). Larger circular-elliptical pores (blue/turquoise) are Haversian canals. Dashed circles show foci of fine-scale (0.1–1 µm) bacterial bioerosion within clouded bone (SEM image, with colour temperature filter to enhance resolution).

Extended Data Fig. 6 Histological analysis of Mtoto’s bone.

Elemental composition of clouded bone (Cb) and encrusting calcium carbonate precipitate (Cc) (SEM–EDS image and spectra). The pictured area corresponds to that of Fig. [3c, d](#). Diffuse lighter grey areas within the clouded bone may be permineralized rims around fine-scale (0.1–1 µm) bioerosion foci. Note the variable enrichment in Ca (especially in spectrum 21) and the low concentrations of Fe, Al, and Mg in the authigenic Ca-P phase that makes up the clouded bone. The pervasive recrystallization of the bone hydroxyapatite into a Ca-enriched, amorphous or cryptocrystalline calcium phosphate appears to be associated with fine-scale bacterial microtunnelling.

Extended Data Fig. 7 PYS shell analysis.

a, Fragments of *Achatina cf. fulica* found in close association with the child’s skeleton. Observation of anatomical features allows precise identification of the provenance of the fragments on the shell. Fragments PYS-2017-200407 and PYS-2017-200404 come from the area of the body whorl adjacent to the middle portion of the parietal callus. Fragment PYS-2017-200405 must come from a portion of the shell close to that of the previous fragment and may derive from the same individual. Fragment PYS-2017-200406 comes from the middle of the body whorl, on its dorsal aspect. Although anatomically it is compatible with provenance from the same individual, its very dark colour, suggestive of a higher Mn intake, and different texture of the concretion coating its outer surface indicate that it had a different taphonomic history and may derive from a different shell. Fragment PYS-2017-200086.D comes from the middle of the body whorl, on its ventral aspect. **b**, Refitting of fragments PYS-2017-200407 and PYS-2017-200404. The two large fragments refit along an ancient fracture

perpendicularly intercepting the shell growth lines. **c**, Modern striations on the inner surface of specimen PYS-2017-200406, probably produced during excavation or cleaning of the fragments. The modern origin of the striations is shown by their random orientation and absence of the thin manganese patina adhering to the inner surface of this specimen. **d**, Micrographs and 3D reconstruction of an area of the outer surface of fragment PYS-2017-200404 showing two grooves obliquely crossing the decussated sculpture of the outer shell surface. The internal morphology and outlines of the grooves indicate that they were made by a pointed agent, possibly a stone tool, following the irregular morphology of the shell natural surface and slightly changing direction when falling into concave areas. The antiquity of the lines is demonstrated by the red sediment coating the specimen, which fills in the striations and almost completely buries them when they run into natural grooves of the shell. **e**, Fragments of *Achatina* cf. *fulica* found in feature 809 (bottom) and their anatomical origin (top). The twelve fragments mostly come from body whorls and last whorls of the spire of *Achatina* snails, with only two from the parietal wall and the apex. They present a similar state of preservation, colour, taphonomic modifications and type of concretions to the five fragments found in direct association with the skeleton. None of them bears incisions similar to those recorded on specimen PYS-2017-200404. Fragments comprising the control sample from layer 18 are, in general, more free from concretions than those from the skeleton and feature 809. **f**, Biplot and linear regression correlating the length and width of *Achatina* cf. *fulica* fragments from the grave pit ($n = 12$) and the skeleton ($n = 5$) with those from layer 18 ($n = 581$) (top), and box plots of length and width distributions of *Achatina* cf. *fulica* fragments from these two contexts (bottom). Rectangles in the box plots show the second and third quartiles, central bar indicates the median, and whiskers the extreme values. The fragments from the burial pit are significantly larger in size ($P = 0.001$) while displaying the same length/width ratio. Incorporation in the grave infilling have preserved *Achatina* fragments from the higher levels of fragmentation that have affected fragments exposed to trampling on the occupation surface in layer 18.

Extended Data Fig. 8 PYS human dental remains.

a, PYS dental remains: isolated teeth (left) and mCT 3D reconstruction of the two molars included in the maxillary and mandibular bones (right). All molars are positioned with the mesial surface towards the top and the distal surface towards the bottom. L (left); R (right); dm2 (second deciduous molar), M¹ (permanent upper first molar), M₁ (permanent lower first molar). **b**, bgPCA of the Procrustes shape coordinates of the PYS Ldm2 EDJ compared with those of Neanderthals ($n = 6$), fossil *H. sapiens* ($n = 3$) and modern humans ($n = 5$). **c**, bgPCA of the Procrustes shape coordinates of the PYS RM1 EDJ compared with those of Neanderthals ($n = 6$), fossil *H. sapiens* ($n = 2$) and modern humans ($n = 12$). **d**, bgPCA of the Procrustes shape coordinates of the PYS RM1 EDJ compared with those of Neanderthals ($n = 12$), fossil *H. sapiens* ($n = 3$) and modern humans ($n = 12$).

Extended Data Table 1 PYS faunal remains

[Full size table](#)

Extended Data Table 2 Diagenesis of identifiable and putative human bone in Mtoto's section

[Full size table](#)

Supplementary information

[Supplementary Information](#)

This file contains Supplementary Sections A-J, including Supplementary Figures and Supplementary Tables 1-11 – see contents page for details.

[Reporting Summary](#)

[Peer Review File](#)

Rights and permissions

[Reprints and Permissions](#)

About this article



Cite this article

Martinón-Torres, M., d'Errico, F., Santos, E. *et al.* Earliest known human burial in Africa. *Nature* **593**, 95–100 (2021).
<https://doi.org/10.1038/s41586-021-03457-8>

[Download citation](#)

- Received: 12 May 2020
- Accepted: 16 March 2021
- Published: 05 May 2021
- Issue Date: 06 May 2021
- DOI: <https://doi.org/10.1038/s41586-021-03457-8>

Comments

By submitting a comment you agree to abide by our [Terms](#) and [Community Guidelines](#). If you find something abusive or that does not comply with our terms or guidelines please flag it as inappropriate.

[Access through your institution](#)

[Change institution](#)

[Buy or subscribe](#)

Associated Content

A child's grave is the earliest known burial site in Africa

- Louise Humphrey

Nature News & Views 05 May 2021

This article was downloaded by **calibre** from <https://www.nature.com/articles/s41586-021-03457-8>

| [Section menu](#) | [Main menu](#) |

The structure, function and evolution of a complete human chromosome 8
[Download PDF](#)

- Article
- Open Access
- [Published: 07 April 2021](#)

The structure, function and evolution of a complete human chromosome 8

- [Glennis A. Logsdon](#) ORCID: orcid.org/0000-0003-2396-0656¹,
- [Mitchell R. Vollger](#) ORCID: orcid.org/0000-0002-8651-1615¹,
- [PingHsun Hsieh](#)¹,
- [Yafei Mao](#) ORCID: orcid.org/0000-0002-9648-4278¹,
- [Mikhail A. Liskovskykh](#)²,
- [Sergey Koren](#) ORCID: orcid.org/0000-0002-1472-8962³,
- [Sergey Nurk](#)³,
- [Ludovica Mercuri](#) ORCID: orcid.org/0000-0002-3688-4501⁴,
- [Philip C. Dishuck](#) ORCID: orcid.org/0000-0003-2223-9787¹,
- [Arang Rhee](#) ORCID: orcid.org/0000-0002-9809-8127³,
- [Leonardo G. de Lima](#) ORCID: orcid.org/0000-0001-6340-6065⁵,
- [Tatiana Dvorkina](#)⁶,
- [David Porubsky](#) ORCID: orcid.org/0000-0001-8414-8966¹,
- [William T. Harvey](#)¹,
- [Alla Mikheenko](#)⁶,
- [Andrey V. Bzikadze](#)⁷,
- [Milinn Kremitzki](#)⁸,
- [Tina A. Graves-Lindsay](#)⁸,
- [Chirag Jain](#)³,
- [Kendra Hoekzema](#)¹,
- [Shwetha C. Murali](#)^{1,9},
- [Katherine M. Munson](#) ORCID: orcid.org/0000-0001-8413-6498¹,
- [Carl Baker](#)¹,
- [Melanie Sorensen](#)¹,
- [Alexandra M. Lewis](#)¹,
- [Urvashi Surti](#)¹⁰,

- [Jennifer L. Gerton](#) [ORCID: orcid.org/0000-0003-0743-3637⁵](#),
- [Vladimir Larionov²](#),
- [Mario Ventura](#) [ORCID: orcid.org/0000-0001-7762-8777⁴](#),
- [Karen H. Miga](#) [ORCID: orcid.org/0000-0002-3670-4507¹¹](#),
- [Adam M. Phillippy](#) [ORCID: orcid.org/0000-0003-2983-8934³](#) &
- [Evan E. Eichler](#) [ORCID: orcid.org/0000-0002-8246-4014^{1,9}](#)

[Nature](#) volume **593**, pages101–107(2021)[Cite this article](#)

- 23k Accesses
- 3 Citations
- 346 Altmetric
- [Metrics details](#)

Subjects

- [Centromeres](#)
- [Evolutionary genetics](#)
- [Genome evolution](#)
- [Genomics](#)

Abstract

The complete assembly of each human chromosome is essential for understanding human biology and evolution^{1,2}. Here we use complementary long-read sequencing technologies to complete the linear assembly of human chromosome 8. Our assembly resolves the sequence of five previously long-standing gaps, including a 2.08-Mb centromeric α -satellite array, a 644-kb copy number polymorphism in the β -defensin gene cluster that is important for disease risk, and an 863-kb variable number tandem repeat at chromosome 8q21.2 that can function as a neocentromere. We show that the centromeric α -satellite array is generally methylated except for a 73-kb hypomethylated region of diverse higher-order α -satellites enriched with CENP-A nucleosomes, consistent with the location of the kinetochore. In addition, we confirm the overall organization and methylation pattern of the centromere in a diploid human genome. Using a dual long-read sequencing approach, we complete high-quality draft assemblies of the orthologous centromere from chromosome 8 in chimpanzee, orangutan and macaque to reconstruct its evolutionary history. Comparative and phylogenetic analyses show that the higher-order α -satellite structure evolved in the great ape ancestor with a layered symmetry, in which more ancient higher-order

repeats locate peripherally to monomeric α -satellites. We estimate that the mutation rate of centromeric satellite DNA is accelerated by more than 2.2-fold compared to the unique portions of the genome, and this acceleration extends into the flanking sequence.

[Download PDF](#)

Main

Since the announcement of the sequencing of the human genome 20 years ago^{1,2}, human chromosomes have remained unfinished owing to large regions of highly identical repeats clustered within centromeres, regions of segmental duplication, and the acrocentric short arms of chromosomes. The presence of large swaths (more than 100 kb) of highly identical repeats that are themselves copy number polymorphic has meant that such regions have persisted as gaps, which limits our understanding of human genetic variation and evolution^{3,4}. The advent of long-read sequencing technologies and the use of DNA from complete hydatidiform moles, however, have now made it possible to assemble these regions from native DNA for the first time^{5,6,7}. Here we present the first, to our knowledge, complete linear assembly of human chromosome 8. We chose to assemble chromosome 8 because it carries a modestly sized centromere (approximately 1.5–2.2 Mb)^{8,9}, in which AT-rich, 171-base-pair (bp) α -satellite repeats are organized into a well-defined higher-order repeat (HOR) array. The chromosome, however, also contains one of the most structurally dynamic regions in the human genome—the β -defensin gene cluster at 8p23.1 (refs. ^{10,11,12})—as well as a recurrent polymorphic neocentromere at 8q21.2, which have been largely unresolved for the past 20 years.

Telomere-to-telomere assembly of chromosome 8

Unlike the assembly of the human X chromosome¹³, we took advantage of both ultra-long Oxford Nanopore Technologies (ONT) and Pacific Biosciences (PacBio) high-fidelity (HiFi) data to resolve the gaps in human chromosome 8 (Fig. [1a, b](#), Methods). We first generated 20-fold sequence coverage of ultra-long ONT data and 32.4-fold coverage of PacBio HiFi data from a complete hydatidiform mole (CHM13hTERT, hereafter referred to as CHM13) (Supplementary Fig. [1](#)). Then, we assembled complex regions in chromosome 8 by creating a library of singly unique nucleotide k -mers (SUNKs)¹⁴, or sequences of length k that occur approximately once per haploid genome (here, $k = 20$), from CHM13 PacBio HiFi data. We validated the SUNKs with Illumina data from the same genome and used them to barcode ultra-long ONT reads (Fig. [1b](#)). Ultra-long ONT reads that share highly similar barcodes were assembled into an initial sequence scaffold that traverses each chromosome 8 gap (Fig. [1b](#)). We

improved the base-pair accuracy of the sequence scaffolds by replacing the raw ONT sequence with concordant PacBio HiFi contigs and integrating them into a previously generated⁵ linear assembly of human chromosome 8 (Fig. 1b, Methods).

Fig. 1: Telomere-to-telomere assembly of human chromosome 8.

 figure1



a, Gaps in the GRCh38 chromosome 8 reference sequence. **b**, Targeted assembly method to resolve complex repeat regions in the human genome. Ultra-long ONT reads (grey) are barcoded with SUNKs (coloured bars) and assembled into a sequence scaffold. Regions within the scaffold sharing high sequence identity with PacBio HiFi contigs (dark grey) are replaced, improving the base accuracy to greater than 99.99%. The PacBio HiFi assembly is integrated into an assembly of CHM13 chromosome 8

(ref. [5](#)) and validated. **c**, Sequence, structure, methylation status and genetic composition of the CHM13 β-defensin locus. The locus contains three segmental duplications (dups) at chr8:7098892–7643091, chr8:11528114–12220905 and chr8:12233870–12878079. A 4,110,038-bp inversion (chr8:7500325–11610363) separates the first and second duplications. Iso-Seq data reveal that the third duplication (light blue) contains 12 new protein-coding genes, five of which are *DEFB* genes (Extended Data Fig. [3g](#)). **d**, Copy number of the *DEFB* genes (chr8:7783837–7929198 in GRCh38) throughout the human population, determined from a collection of 1,105 high-coverage genomes (Methods). Data are median ± s.d.

[Full size image](#)

The complete telomere-to-telomere sequence of human chromosome 8 is 146,259,671 bases long and includes 3,334,256 bases that are missing from the current reference genome (GRCh38). Most of the additions reside within distinct chromosomal regions: a 644-kb copy number polymorphic β-defensin gene cluster that maps to chromosome 8p23.1 (Fig. [1c, d](#)); the complete centromere corresponding to 2.08 Mb of α-satellite HORs (Fig. [2](#)); an 863-kb 8q21.2 variable number tandem repeat (VNTR) (Extended Data Fig. [1](#)); and both telomeric regions that end with the canonical TTAGGG repeat sequence (Extended Data Fig. [2](#)). We validated the assembly with optical maps (Bionano Genomics), single-cell DNA template strand sequencing (Strand-seq)[15,16](#), and comparisons to finished bacterial artificial chromosome (BAC) sequences as well as Illumina whole-genome sequencing data derived from the same source genome (Supplementary Fig. [2](#), Methods). We estimate the overall base accuracy of our chromosome 8 assembly to be between 99.9915% and 99.9999% (quality value score between 40.70 and 63.19, as determined from sequenced BACs and mapped *k*-mers[17](#), respectively). An analysis of 24 million human full-length transcripts generated from isoform sequencing (Iso-Seq) data identifies 61 protein-coding and 33 noncoding loci that map to this finished chromosome 8 sequence better than to GRCh38 (Extended Data Fig. [3a–f](#), Supplementary Table [1](#)), including the discovery of new genes mapping to copy number polymorphic regions (Fig. [1c, d](#), Extended Data Fig. [3g](#)).

Fig. 2: Sequence, structure and epigenetic map of the chromosome 8 centromeric region.

 **figure2**

a, Schematic showing the composition of the CHM13 chromosome 8 centromere. The centromeric region consists of a 2.08-Mb D8Z2 α -satellite HOR array flanked by regions of monomeric and/or divergent α -satellite interspersed with retrotransposons, β -satellite and γ -satellite. The predicted restriction digest pattern is shown. The D8Z2

α -satellite HOR array is heavily methylated except for a 73-kb hypomethylated region, which is contained within a 632-kb CENP-A chromatin domain (Extended Data Fig. 9, Supplementary Fig. 8). A pairwise sequence identity heat map indicates that the centromere is composed of five distinct evolutionary layers (dashed arrows). **b**, Pulsed-field gel Southern blot of CHM13 DNA confirms the structure and organization of the chromosome 8 centromeric HOR array. Left, ethidium bromide (EtBr) staining; right, ^{32}P -labelled chromosome 8 α -satellite-specific probe. $n = 2$. See Supplementary Fig. 9a,b for gel source data. **c**, Representative images of a CHM13 chromatin fibre showing CENP-A enrichment in an unmethylated region. $n = 3$. Scale bar, 1 μm .

[Full size image](#)

Our targeted assembly method successfully resolved the β -defensin gene cluster¹⁰ into a single 7.06-Mb locus, eliminating two 50-kb gaps in GRCh38 (Fig. 1c, Extended Data Fig. 4). We estimate the base accuracy of this locus to be 99.9911% (quality value score 40.48; based on mapped BACs) (Extended Data Fig. 5a). Our analysis reveals CHM13 has a more structurally complex haplotype than GRCh38 (Fig. 1d, Extended Data Fig. 4), consistent with previously published reports^{10,12}. We resolve the breakpoints of one of the largest common inversion polymorphisms in the human genome (4.11 Mb) and show that the breakpoints map within large, highly identical duplications that are copy number polymorphic (Fig. 1c,d, Extended Data Fig. 5b). In contrast to the human reference, which carries two such segmental duplications, there are three segmental duplications in CHM13: a 544-kb segmental duplication on the distal end and two 693- and 644-kb segmental duplications on the proximal end (Fig. 1c). Each segmental duplication cassette carries at least five β -defensin genes and, as a result, we identify five additional β -defensin genes that are almost identical at the amino acid level to the reference (Fig. 1c, Supplementary Table 2). Because ONT data allow methylation signals to be assessed¹⁸, we determined the methylation status of cytosine residues across the entire β -defensin locus. All three segmental duplications contain a 151–163-kb methylated region that resides in the long-terminal repeat (LTR)-rich region of the duplication, whereas the remainder of the duplication, including the β -defensin gene cluster, is largely unmethylated (Fig. 1c). Complete sequence resolution of this alternative haplotype is important because the inverted haplotype preferentially predisposes to recurrent microdeletions associated with developmental delay, microcephaly and congenital heart defects^{19,20}. Copy number polymorphism of the five β -defensin genes has been associated with immune-related phenotypes, such as psoriasis and Crohn's disease^{11,21}.

Sequence resolution of the chromosome 8 centromere

Previous studies estimate the length of the chromosome 8 centromere to be between 1.5 and 2.2 Mb, on the basis of analysis of the HOR α -satellite array^{8,9}. Although α -satellite HORs of different lengths are thought to comprise the centromere, the predominant species has a unit length of 11 monomers (1,881 bp)^{8,9}. During assembly, we spanned the chromosome 8 centromere with 11 ultra-long ONT reads (mean length 389.4 kb), which were replaced with PacBio HiFi contigs based on SUNK barcoding. Our chromosome 8 centromere assembly consists of a 2.08-Mb D8Z2 α -satellite HOR array flanked by blocks of monomeric α -satellite on the p-arm (392 kb) and q-arm (588 kb) (Fig. 2a). Both monomeric α -satellite blocks are interspersed with long and short interspersed nuclear elements (LINEs and SINEs, respectively), LTRs and β -satellites, with tracts of γ -satellite specific to the q-arm. Several methods were used to validate its organization. First, long-read sequence read-depth analysis from two orthogonal native DNA sequencing platforms shows uniform coverage, which suggests that the assembly is free from large structural errors (Extended Data Fig. 6a). Fluorescent in situ hybridization (FISH) on metaphase chromosomes confirms the long-range organization of the centromere (Extended Data Fig. 6a–c). Droplet digital PCR shows that there are $1,344 \pm 142$ (mean \pm s.d.) D8Z2 HORs within the α -satellite array, consistent with our estimates (Extended Data Fig. 6d, Methods). Pulsed-field gel electrophoresis Southern blots on CHM13 DNA digested with two different restriction enzymes supports the banding pattern predicted from the assembly (Fig. 2a, b). Finally, applying our assembly approach to ONT and HiFi data available for a diploid human genome (HG00733) (Supplementary Table 3, Methods) generates two additional chromosome 8 centromere haplotypes, replicating the overall organization with only subtle differences in the overall length of HOR arrays (Extended Data Fig. 7, Supplementary Table 4).

We find that the chromosome 8 centromeric HOR array is primarily composed of four distinct HOR types represented by 4, 7, 8 or 11 α -satellite monomer cassettes (Fig. 2a, Extended Data Fig. 8). Although the 11-monomer HOR predominates (36%), the other HORs are also abundant (19–23%) and are all derivatives of the 11-monomer HOR (Extended Data Fig. 8b, c). Notably, we find that the HORs are differentially distributed regionally across the centromere. Although most regions show a mixture of different HOR types, we also identify regions of homogeneity, such as clusters of 11-monomer HORs mapping to the periphery of the HOR array (92 and 158 kb in length) and a 177-kb region in the centre composed solely of 7-monomer HORs. To investigate the epigenetic organization, we inferred methylated cytosine residues along the centromeric region and find that most of the α -satellite HOR array is methylated, except for a small, 73-kb hypomethylated region (Fig. 2a). To determine whether this hypomethylated region is the site of the epigenetic centromere (marked by the presence of nucleosomes that contain the histone H3 variant CENP-A), we performed CENP-A chromatin immunoprecipitation with high-throughput sequencing (ChIP-seq) on CHM13 cells and found that CENP-A is primarily located within a 632-kb

stretch that encompasses the hypomethylated region (Fig. 2a, Extended Data Fig. 9). Subsequent chromatin fibre FISH revealed that CENP-A maps to the hypomethylated region within the α -satellite HOR array (Fig. 2c). Notably, the hypomethylated region shows some of the greatest HOR admixture, which suggests a potential optimization of HOR subtypes associated with the active kinetochore (mean entropy over the 73-kb region = 1.91) (Extended Data Fig. 8a, Methods).

To understand the long-range organization and evolution of the centromere, we generated a pairwise sequence identity heat map, which compares the sequence identity of 5-kb fragments along the length of the centromere (Fig. 2a, Supplementary Fig. 3). We find that the centromere consists of five major evolutionary layers that show mirror symmetry. The outermost layer resides in the monomeric α -satellite, where sequences are highly divergent from the rest of the centromere but are more similar to each other (Fig. 2a, arrow 1). The second layer defines the monomeric-to-HOR transition and is a short (57–60 kb) region. The p and q regions are 87–92% identical with each other but only 78% or less with other centromeric satellites (Fig. 2a, arrow 2). The third layer is completely composed of HORs. The p and q regions are 92 and 149 kb in length, respectively, and share more than 96% sequence identity with each other (Fig. 2a, arrow 3) but less than that with the rest of the centromere. This layer consists largely of homogenous 11-monomer HORs and defines the transition from unmethylated to methylated DNA. The fourth layer is the largest and defines the bulk of the α -satellite HORs (1.42 Mb in total). It shows the greatest variety of HOR subtypes and, once again, the p and q blocks share identity with each other but are more divergent from the remaining layers (Fig. 2a, arrow 4). Finally, the fifth layer encompasses the centre-most 416 kb of the HOR array—a region of near-perfect sequence identity that is divergent from the rest of the centromere (Fig. 2a, arrow 5).

Sequence resolution of the chromosome 8q21.2 VNTR

The layered and mirrored nature of the chromosome 8 centromere is reminiscent of another GRCh38 gap region located at chromosome 8q21.2 (Extended Data Fig. 1). This region is a cytogenetically recognizable euchromatic variant²² that contains one of the largest VNTRs in the human genome²². The 12.192-kb repeating unit carries the *REXO1L1* (also known as *GOR*) pseudogene and is highly copy number polymorphic among humans^{22,23}. This VNTR is of biological interest because it is the site of a recurrent neocentromere, in which a functional centromere devoid of α -satellite has been observed in several unrelated individuals^{24,25}. Using our approach, we successfully assembled the VNTR into an 863.5-kb sequence composed of approximately 71 repeating units (67 complete and 7 partial units) (Extended Data Fig. 1a). A pulsed-field gel Southern blot confirms the VNTR length and structure (Extended Data Fig. 1a, b), and chromatin fibre FISH estimates 67 ± 5.2 (mean \pm

s.d.) repeat units, consistent with the assembly (Extended Data Fig. 10, Methods). Among humans, the repeat unit varies from 53 to 326 copies, creating tandem repeat arrays ranging from 652 kb to 3.97 Mb (Extended Data Fig. 1c). The higher-order structure of the VNTR consists of five distinct domains that alternate in orientation (Extended Data Fig. 1a), in which each domain contains 5 to 23 complete repeat units that are more than 98.5% identical to each other (Extended Data Fig. 1a). Detection of methylated cytosine residues¹⁸ shows that each 12.192-kb repeat is primarily methylated in the 3-kb region that corresponds to *REXO1L1* (also known as *GOR1*), whereas the rest of the repeat unit is hypomethylated (Extended Data Fig. 1a). Mapping of centromeric chromatin from a cell line that contains an 8q21.2 neocentromere²⁵ shows that approximately 98% of CENP-A nucleosomes map to the hypomethylated region of the repeat unit in the CHM13 assembly (Extended Data Fig. 1a). Although this is consistent with the VNTR being the potential site of the functional kinetochore of the neocentromere, sequence and assembly of this and other neocentromere-containing cell lines is vitally important.

Centromere evolutionary reconstruction

In an effort to fully reconstruct the evolutionary history of the chromosome 8 centromere over the past 25 million years, we applied the same approach to reconstruct the orthologous centromeres in chimpanzee, orangutan and macaque. We first generated 40- to 56-fold ONT data and 25- to 40-fold PacBio HiFi data of each nonhuman primate (NHP) genome (Supplementary Table 5). Using this data, we generated two contiguous draft assemblies of the chimpanzee chromosome 8 centromere (one for each haplotype) and one haplotype assembly from the orangutan and macaque chromosome 8 centromeres (Fig. 3). Mapping of long-read data to each assembly shows uniform coverage, indicating a lack of large structural errors (Supplementary Figs. 4, 5). Assessment of base accuracy indicates that the assemblies are 99.9988–100% accurate (quality value score > 49.3) (Methods). Analysis of each NHP chromosome 8 centromere reveals distinct HOR arrays ranging in size from 1.69 Mb in chimpanzee to 10.92 Mb in macaque, consistent with estimates from short-read sequence data and cytogenetic analyses^{26,27} (Fig. 3). Our data, once again, reveal a mirrored and layered organization, with the chimpanzee organization being most similar to human (Figs. 2a, 3). Each NHP chromosome 8 centromere is composed of four or five distinct layers, with the outermost layer showing the lowest degree of sequence identity (73–78% in chimpanzee and orangutan; 90–92% in macaque) and the innermost layer showing the highest sequence identity (90–100% in chimpanzee and orangutan; 94–100% in macaque). The orangutan structure is notable in that there appears to be very little admixture of HOR units between the layers, in contrast to other apes in which the different HOR cassettes are derived from a major HOR structure. The blocks of orangutan HORs (with the exception of layer 3) show reduced

sequence identity. This suggests that the orangutan centromere evolved as a mosaic of independent HOR units. In contrast to all apes, the macaque lacks HORs and, instead, contains a basic dimeric repeat structure²⁶, which is much more homogenous and highly identical (>90%) across the nearly 11 Mb of assembled centromeric array.

Fig. 3: Sequence and structure of the chimpanzee, orangutan, and macaque chromosome 8 centromeres.

 **figure3**

a–d, Structure and sequence identity of the chimpanzee (H1) (**a**), chimpanzee (H2) (**b**), orangutan (**c**) and macaque (**d**) chromosome 8 centromeres. Each centromere has a mirrored organization consisting of four or five distinct evolutionary layers. The size of each centromeric region is consistent with microscopic analyses, showing

increasingly bright DAPI staining with increasing centromere size. See Supplementary Figs. 10 and 11 for sequence identity heat maps plotted on the same colour scale. H1, haplotype 1; H2, haplotype 2. Scale bar, 1 μm.

[Full size image](#)

Phylogenetically, we find that all great ape higher-order α -satellite sequences (corresponding to layers 2–5) cluster into a single clade, and the monomeric α -satellite (layer 1) split into two clades separated by tens of millions of years (Fig. 4a). The proximal clade contains monomeric α -satellite from both the p- and q-arms, whereas the more divergent clade shares monomeric α -satellite solely from the q-arm, and specifically, the α -satellite nestled between clusters of γ -satellite (Supplementary Fig. 6a,b). Unlike great apes, both monomeric and dimeric repeat structures from the macaque group together and are sister clades to the monomeric ape clades, which suggests a common ancient origin restricted to these flanking pericentromeric regions. We used the orthology of flanking primate sequences to understand how rapidly sequences decay over the course of evolution. We assessed divergence based on 10-kb windows of pairwise alignments in the approximately 2-Mb flanking the α -satellite HOR array (Fig. 4b). We find that the mean allelic divergence increases more than threefold as the sequence transitions from unique to monomeric α -satellite. Such increases are rare in the human genome, in which only 1.27–1.99% of nearly 20,000 random loci show comparable levels of divergence (Supplementary Fig. 6c). Using evolutionary models (Methods), we estimate a minimal mutation rate of the chromosome 8 centromeric region to be approximately 4.8×10^{-8} and 8.4×10^{-8} mutations per base pair per generation on the p- and q-arms, respectively, which is 2.2- to 3.8-fold higher than the basal mean mutation rate (approximately 2.2×10^{-8}) (Supplementary Table 6). These analyses provide a complete comparative sequence analysis of a primate centromere for an orthologous chromosome and a framework for future studies of genetic variation and evolution of these regions across the genome.

Fig. 4: Evolution of the chromosome 8 centromere.

 **figure4**

a, Phylogenetic tree of human, chimpanzee, orangutan and macaque α -satellites from the chromosome 8 centromeric regions (Supplementary Fig. [6a, b](#)). **b**, Plot showing the sequence divergence between CHM13 and nonhuman primates in the regions flanking the chromosome 8 α -satellite HOR array. See Supplementary Fig. [6d](#) for a model of centromere evolution.

[Full size image](#)

Discussion

Chromosome 8 is the first human autosome to be sequenced and assembled from telomere to telomere and contains only the third completed human centromere^{13,28}, to our knowledge. Both chromosome 8 and X centromeres (Supplementary Fig. 7) contain a pocket of hypomethylation (approximately 61–73 kb in length), and we show that this region is enriched for the centromeric histone CENP-A, consistent with the functional kinetochore-binding site^{29,30}. Notably, enrichment of CENP-A extends over a broader swath of sequence (632 kb), with its peak centred over the hypomethylated region composed of diverse HORs. The layered and mirrored organization of the chromosome 8 centromere supports a model of evolution^{31,32,33}, in which highly identical repeats expand, pushing older, more divergent repeats to the edges in an assembly-line fashion (Supplementary Fig. 6d). The chromosome 8 centromere reveals five such layers, and this organization is generally identified in other NHP centromeres. We confirm that HOR structures evolved after apes diverged from Old World monkeys (less than 25 million years ago)^{26,34,35} but also distinguish different classes of monomeric repeats that share an ancient origin with the Old World monkeys. One ape monomeric clade (present only in the q-arm) groups with the clade of the macaques (Supplementary Fig. 6a,b). We hypothesize that this approximately 70-kb segment present in chimpanzee and human, but absent in orangutan, represents the remnants of the ancestral centromere. Sequence comparisons show that mutation rates increase by at least two to fourfold in proximity to the HOR array, probably owing to the action of concerted evolution, unequal crossing-over, and saltatory amplification^{33,36,37}. Among three human centromere 8 haplotypes, we identify regions of excess allelic variation and structural divergence (Extended Data Fig. 7), and these locations differ among haplotypes. Nevertheless, the first sequence of a complete human genome is imminent, and the next challenge will be applying the methods to fully phase and assemble diploid genomes^{38,39,40}.

Methods

Data reporting

No statistical methods were used to predetermine sample size. The experiments were not randomized, and investigators were not blinded to allocation during experiments and outcome assessment.

Cell line sources

CHM13hTERT (CHM13) cells were originally isolated from a hydatidiform mole at Magee-Womens Hospital as part of a research study (IRB MWH-20-054). Cryogenically frozen cells from this culture were grown and transformed with the human telomerase reverse transcriptase (TERT) gene to immortalize the cell line. This cell line has been authenticated by STR analysis, tested negative for mycoplasma contamination, and karyotyped to show a 46,XX karyotype¹³. Human HG00733 lymphoblastoid cells were originally obtained from a female Puerto Rican child, immortalized with the Epstein-Barr virus (EBV), and stored at the Coriell Institute for Medical Research. Chimpanzee (*Pan troglodytes*; Clint; S006007) fibroblast cells were originally obtained from a male western chimpanzee named Clint (now deceased) at the Yerkes National Primate Research Center and immortalized with EBV. Orangutan (*Pongo abelii*; Susie; PR01109) fibroblast cells were originally obtained from a female Sumatran orangutan named Susie (now deceased) at the Gladys Porter Zoo, immortalized with EBV, and stored at the Coriell Institute for Medical Research. Macaque (*Macaca mulatta*; AG07107) fibroblast cells were originally obtained from a female rhesus macaque of Indian origin and stored at the Coriell Institute for Medical Research. The HG00733, chimpanzee, orangutan and macaque cell lines have not yet been authenticated or assessed for mycoplasma contamination, to our knowledge.

Cell culture

CHM13 cells were cultured in complete AmnioMax C-100 Basal Medium (Thermo Fisher Scientific, 17001082) supplemented with 15% AmnioMax C-100 Supplement (Thermo Fisher Scientific, 12556015) and 1% penicillin-streptomycin (Thermo Fisher Scientific, 15140122). HG00733 cells were cultured in RPMI 1640 with l-glutamine (Thermo Fisher Scientific, 11875093) supplemented with 15% FBS (Thermo Fisher Scientific, 16000-044) and 1% penicillin-streptomycin (Thermo Fisher Scientific, 15140122). Chimpanzee (*P. troglodytes*; S006007) and macaque (*M. mulatta*; AG07107) cells were cultured in MEMα containing ribonucleosides, deoxyribonucleosides and l-glutamine (Thermo Fisher Scientific, 12571063) supplemented with 12% FBS (Thermo Fisher Scientific, 16000-044) and 1% penicillin-streptomycin (Thermo Fisher Scientific, 15140122). Orangutan (*P. abelii*; PR01109) cells were cultured in MEMα containing ribonucleosides, deoxyribonucleosides and l-glutamine (Thermo Fisher Scientific, 12571063) supplemented with 15% FBS (Thermo Fisher Scientific, 16000-044) and 1% penicillin-streptomycin (Thermo Fisher Scientific, 15140122). All cells were cultured in a humidity-controlled environment at 37 °C with 5% CO₂.

DNA extraction, library preparation and sequencing

PacBio HiFi data were generated from the HG00733, chimpanzee, orangutan and macaque genomes as previously described³⁶ with modifications. In brief, high-molecular-weight (HMW) DNA was extracted from cells using a modified Qiagen Gentra Puregene Cell Kit protocol³⁷. HMW DNA was used to generate HiFi libraries via the SMRTbell Express Template Prep Kit v2 and SMRTbell Enzyme Clean Up kits (PacBio). Size selection was performed with SageELF (Sage Science), and fractions sized 11, 14, 18, 22, or 25 kb (as determined by FEMTO Pulse (Agilent)) were chosen for sequencing. Libraries were sequenced on the Sequel II platform (Instrument Control SW v7.1 or v8.0) with three to seven SMRT Cells 8M (PacBio) using either Sequel II Sequencing Chemistry 1.0 and 12-h pre-extension or Sequel II Sequencing Chemistry 2.0 and 3- or 4-h pre-extension, both with 30-h movies, aiming for a minimum estimated coverage of 25× in HiFi reads (assuming a genome size of 3.2 Gb). Raw data were processed using the CCS algorithm (v.3.4.1 or v.4.0.0) with the following parameters: –minPasses 3 –minPredictedAccuracy 0.99 –maxLength 21000 or 50000.

Ultra-long ONT data were generated from the CHM13, HG00733, chimpanzee and orangutan genomes according to a previously published protocol⁴¹. In brief, 5×10^7 cells were lysed in a buffer containing 10 mM Tris-Cl (pH 8.0), 0.1 M EDTA (pH 8.0), 0.5% (w/v) SDS, and 20 $\mu\text{g ml}^{-1}$ RNase A for 1 h at 37 °C. Proteinase K (200 $\mu\text{g ml}^{-1}$) was added, and the solution was incubated at 50 °C for 2 h. DNA was purified via two rounds of 25:24:1 phenol-chloroform-isoamyl alcohol extraction followed by ethanol precipitation. Precipitated DNA was solubilized in 10 mM Tris (pH 8) containing 0.02% Triton X-100 at 4 °C for two days. Libraries were constructed using the Rapid Sequencing Kit (SQK-RAD004) from ONT with modifications to the manufacturer's protocol. Specifically, 2–3 μg of DNA was resuspended in a total volume of 18 μl with 16.6% FRA buffer. FRA enzyme was diluted 2- to 12-fold into FRA buffer, and 1.5 μl of diluted FRA was added to the DNA solution. The DNA solution was incubated at 30 °C for 1.5 min, followed by 8 °C for 1 min to inactivate the enzyme. RAP enzyme was diluted 2- to 12-fold into RAP buffer, and 0.5 μl of diluted RAP was added to the DNA solution. The DNA solution was incubated at room temperature for 2 h before loading onto a primed FLO-MIN106 R9.4.1 flow cell for sequencing on a GridION using MinKNOW (v.2.0 - v1.9.12).

Additional ONT data were generated from the CHM13, HG00733, chimpanzee, orangutan, and macaque genomes. In brief, HMW DNA was extracted from cells using a modified Qiagen Gentra Puregene Cell Kit protocol³⁷. HMW DNA was prepared into libraries with the Ligation Sequencing kit (SQK-LSK109) from ONT and loaded onto primed FLO-MIN106 or FLO-PRO002 R9.4.1 flow cells for sequencing on a GridION or PromethION, respectively, using MinKNOW (v.2.0 –

v.19.12). All ONT data were base called with Guppy 3.6.0 or 4.0.11 with the HAC model.

PacBio HiFi whole-genome assembly

The CHM13 genome was assembled from PacBio HiFi data using HiCanu⁵ as previously described⁵. The HG00733 genome was assembled from PacBio HiFi data (Supplementary Table 3) using hifiasm⁶ (v.0.7). The chimpanzee, orangutan and macaque genomes were assembled from PacBio HiFi data (Supplementary Table 5) using HiCanu⁵ (v.2.0). Contigs from each assembly were used to replace the ONT-based sequence scaffolds in targeted regions (described below).

Targeted sequence assembly

Gapped regions within human chromosome 8 were targeted for assembly via a SUNK-based method that combines both PacBio HiFi and ONT data. Specifically, CHM13 PacBio HiFi data were used to generate a library of SUNKs ($k = 20$; total = 2,062,629,432) via Jellyfish (v.2.2.4) on the basis of the sequencing coverage of the HiFi dataset. In total, 99.88% (2,060,229,331) of the CHM13 PacBio HiFi SUNKs were validated with CHM13 Illumina data (SRR3189741). A subset of CHM13 ultra-long ONT reads aligning to the CHM1 β -defensin patch (GenBank: KZ208915.1) or select regions within the GRCh38 chromosome 8 reference sequence (chr8:42,881,543–47,029,467 for the centromere and chr8:85,562,829–85,848,463 for the 8q21.2 locus) were barcoded with Illumina-validated SUNKs. Reads sharing at least 50 SUNKs were selected for inspection to determine whether their SUNK barcodes overlapped. SUNK barcodes can be composed of ‘valid’ and ‘invalid’ SUNKs. Valid SUNKs are those that occur once in the genome and are located at the exact position on the read. By contrast, invalid SUNKs are those that occur once in the genome but are falsely located at the position on the read, and this may be due to a sequencing or base-calling error, for example. Valid SUNKs were identified within the barcode as those that share pairwise distances with at least ten other SUNKs on the same read. Reads that shared a SUNK barcode containing at least three valid SUNKs and their corresponding pairwise distances ($\pm 1\%$ of the read length) were assembled into a tile. The process was repeated using the tile and subsetted ultra-long ONT reads several times until a sequence scaffold spanning the gapped region was generated. Validation of the scaffold organization was carried out via three independent methods. First, the sequence scaffold and underlying ONT reads were subjected to RepeatMasker (v.3.3.0) to ensure that read overlaps were concordant in repeat structure. Second, the centromeric scaffold and underlying ONT reads were subjected to StringComposer⁴² to validate the HOR organization in overlapping reads. Finally, the sequence scaffold for each target region was incorporated into the CHM13

chromosome 8 assembly previously generated⁵, thereby filling the gaps in the chromosome 8 assembly. CHM13 PacBio HiFi and ONT data were aligned to the entire chromosome 8 assembly via pbmm2 (v.1.1.0) (for PacBio data; <https://github.com/PacificBiosciences/pbmm2>) or Winnowmap⁴³ (v.1.0) (for ONT data) to identify large collapses or misassemblies. Although the ONT-based scaffolds are structurally accurate, they are only 87–98% accurate at the base level owing to base-calling errors in the raw ONT reads⁷. Therefore, we sought to improve the base accuracy of the sequence scaffolds by replacing the ONT sequences with PacBio HiFi contigs assembled from the CHM13 genome⁵, which have a consensus accuracy greater than 99.99%⁵. Therefore, we aligned CHM13 PacBio HiFi contigs generated via HiCanu⁵ to the chromosome 8 assembly via minimap2⁴⁴ (v2.17-r941; parameters: minimap2 -t 8 -I 8G -a --eqx -x asm20 -s 5000) to identify contigs that share high sequence identity with the ONT-based sequence scaffolds. A typical scaffold had multiple PacBio HiFi contigs that aligned to regions within it. Therefore, the scaffold was used to order and orient the PacBio HiFi contigs and bridge gaps between them when necessary. PacBio HiFi contigs with high sequence identity replaced almost all regions of the ONT-based scaffolds: ultimately, the chromosome 8 assembly consists of 146,254,195 bp of PacBio HiFi contigs and only 5,490 bp of ONT sequence scaffolds (99.9963% PacBio HiFi contigs and 0.0037% ONT scaffold). The chromosome 8 assembly was incorporated into a whole-genome assembly of CHM13 previously generated⁵ for validation via orthogonal methods (detailed below). The HG00733, chimpanzee, orangutan and macaque chromosome 8 centromeres were assembled via the same SUNK-based method.

Accuracy estimation

The accuracy of the CHM13 chromosome 8 assembly was estimated from mapped k -mers using Merqury¹⁷. In brief, Merqury (v.1.1) was run on the chromosome 8 assembly with the following command: eval/qv.sh CHM13.k21.meryl chr8.fasta chr8_v9.

CHM13 Illumina data (SRR1997411, SRR3189741, SRR3189742 and SRR3189743) were used to identify k -mers with $k = 21$. In Merqury, every k -mer in the assembly is evaluated for its presence in the Illumina k -mer database, with any k -mer missing in the Illumina set counted as base-level ‘error’. We detected 1,474 k -mers found only in the assembly out of 146,259,650, resulting in a quality value score of 63.19, estimated as follows: $-10 \times \log(1 - (1 - 1,474/146,259,650)^{(1/21)}) = 63.19$.

The accuracy percentage for chromosome 8 was estimated from this quality value score as: $100 - (10^{(63.19/-10)}) \times 100 = 99.999952$.

The accuracy of the CHM13 chromosome 8 assembly and β -defensin locus were also estimated from sequenced BACs. In brief, 66 BACs from the CHM13 chromosome 8 (BAC library VMRC59) were aligned to the chromosome 8 assembly via minimap2⁴⁴ (v2.17-r941) with the following parameters: -I 8G -2K 1500m --secondary = no -a --eqx -Y -x asm20 -s 200000 -z 10000,1000 -r 50000 -O 5,56 -E 4,1 -B 5. The quality value was then estimated using the CIGAR string in the resulting BAM, counting alignment differences as errors according to the following formula:

$$\$ \$ \begin{array}{c} \backslash \text{begin}\{\text{array}\} \{c\}, \backslash \text{rm}\{\text{Quality}\} \}, \backslash \text{rm}\{\text{value}\} \} = -10 \times \log_{10} [1 - (\backslash \text{rm}\{\text{matches}\} / (\backslash \text{rm}\{\text{mismatches}\} + \backslash \text{rm}\{\text{matches}\} + \backslash \text{rm}\{\text{insertions}\} + \backslash \text{rm}\{\text{deletions}\}))] \end{array} \$ \$$$

The median quality value was 40.6988 for the entire chromosome 8 assembly and 40.4769 for the β -defensin locus (chr8:6300000–13300000; estimated from 47 individual BACs) (see Extended Data Fig. 5 for more details), which falls within the 95% confidence interval for the whole chromosome. This quality value score was used to estimate the base accuracy³⁶ as follows:

$$\$ \$ 100 - (10^{(40.6988/-10)}) \times 100 = 99.9915 \$ \$$$

$$\$ \$ 100 - (10^{(40.4769/-10)}) \times 100 = 99.9910 \$ \$$$

The BAC quality value estimation should be considered a lower bound, because differences between the BACs and the assembly may originate from errors in the BAC sequences themselves. BACs were previously shown to occasionally contain sequencing errors that are not supported by the underlying PacBio HiFi reads³⁶. In addition, the upper bound for the estimated BAC quality value is limited to approximately 53, because BACs are typically 200 kb and, as a result, the maximum calculable quality value is 1 error in 200 kb (quality value 53). We also note that the quality value of the centromeric region could not be estimated from BACs owing to biases in BAC library preparation, which preclude centromeric sequences in BAC clones.

The accuracy of the HG00733, chimpanzee, orangutan and macaque chromosome 8 centromere assemblies was estimated with Merqury¹⁷. In brief, Merqury (v.1.1) was run on the centromere assemblies as described above for the CHM13 chromosome 8 assembly. Ultimately, we detected 248 k -mers found only in the HG00733 maternal assembly out of 3,877,376 bp (estimated quality value score of 55.16; base accuracy of 99.9997%); 10,562 k -mers found only in the HG00733 paternal assembly out of 3,597,645 bp (estimated quality value score of 38.54; base accuracy of 99.986%); 0 k -mers found only in the chimpanzee H1 assembly out of 2,803,083 bp (estimated quality value score of infinity; base accuracy of 100%); 20 k -mers found only in the chimpanzee H2 assembly out of 3,603,864 bp (estimated quality value score of 65.7796; base accuracy of 99.9999%); 1,302 k -mers found only in the orangutan

assembly out of 5,372,621 bp (estimated quality value score of 49.3774; accuracy of 99.9988%); and 104 k -mers found only in the macaque assembly out of 14,999,980 bp (estimated quality value score of 64.8128; accuracy of 99.9999%). We note that Merqury detects the presence of erroneous k -mers in the assembly that have no support within the raw reads, but it cannot detect the absence of true k -mers (variants) within the assembled repeat copies. Thus, within these highly repetitive arrays, Merqury is useful for comparative analyses but may overestimate the overall accuracy of the consensus.

Strand-seq analysis

We evaluated the directional and structural contiguity of CHM13 chromosome 8 assembly, including the centromere, using Strand-seq data. First, all Strand-seq libraries produced from the CHM13 genome³⁶ were aligned to the CHM13 assembly, including chromosome 8 using BWA-MEM⁴⁵ (v.0.7.17-r1188) with default parameters for paired-end mapping. Next, duplicate reads were marked by sambamba⁴⁶ (v.0.6.8) and removed before subsequent analyses. We used SAMtools⁴⁷ (v.1.9) to sort and index the final BAM file for each Strand-seq library. To detect putative misassembly breakpoints in the chromosome 8 assembly, we ran breakpointR⁴⁸ on all BAM files to detect strand-state breakpoints. Misassemblies are visible as recurrent changes in strand state across multiple Strand-seq libraries³⁹. To increase our sensitivity of misassembly detection, we created a ‘composite file’ that groups directional reads across all available Strand-seq libraries^{49,50}. Next, we ran breakpointR on the ‘composite reads file’ using the function ‘runBreakpointr’ to detect regions that are homozygous (‘ww’; ‘HOM’ - all reads mapped in minus orientation) or heterozygous inverted (‘wc’, ‘HET’ - approximately equal number of reads mapped in minus and plus orientation). To further detect any putative chimaerism in the chromosome 8 assembly, we applied Strand-seq to assign 200-kb long chunks of the chromosome 8 assembly to unique groups corresponding to individual chromosomal homologues using SaaRclust^{39,51}. For this, we used the SaaRclust function ‘scaffoldDenovoAssembly’ on all BAM files.

Bionano analysis

Bionano Genomics data were generated from the CHM13 genome¹³. Long DNA molecules labelled with Bionano’s Direct Labelling Enzyme were collected on a Bionano Saphyr Instrument to a coverage of 130×. The molecules were assembled with the Bionano assembly pipeline Solve (v.3.4), using the nonhaplotype-aware parameters and GRCh38 as the reference. The resulting data produced 261 genome maps with a total length of 2.921.6 Mb and a genome map N50 of 69.02 Mb.

The molecule set and the nonhaplotype-aware map were aligned to the CHM13 draft assembly and the GRCh38 assembly, and discrepancies were identified between the Bionano maps and the sequence references using scripts in the Bionano Solve software package—runCharacterize.py, runSV.py, and align_bnx_to_cmap.py.

A second version of the map was assembled using the haplotype-aware parameters. This map was also aligned to GRCh38 and the final CHM13 assembly to verify heterozygous locations. These regions were then examined further.

Analysis of Bionano alignments revealed three heterozygous sites within chromosome 8 located at approximately chr8:21,025,201, chr8:80,044,843 and chr8:121,388,618 (Supplementary Table 2). The structure with the greatest ONT read support was selected for inclusion in the chromosome 8 assembly (Supplementary Table 2).

TandemMapper and TandemQUAST analysis of the centromeric HOR array

We assessed the structure of the CHM13 and NHP centromeric HOR arrays by applying TandemMapper and TandemQUAST⁵² (<https://github.com/ablab/TandemTools>; version from 20 March 2020), which can detect large structural assembly errors in repeat arrays. For the CHM13 centromere, we first aligned ONT reads longer than 50 kb to the CHM13 assembly containing the contiguous chromosome 8 with

Winnowmap⁴³ (v.1.0) and extracted reads aligning to the centromeric HOR array (chr8:44243868–46323885). We then inputted these reads in the following TandemQUAST command: tandemquast.py -t 24 --nano {ont_reads.fa} -o {out_dir} chr8.fa. For the NHP centromeres, we aligned ONT reads to the whole-genome assemblies containing the contiguous chromosome 8 centromeres with Winnowmap⁴³ (v.1.0) and extracted reads aligning to the centromeric HOR arrays. We then inputted these reads in the following TandemQUAST command: tandemquast.py-t 24 --nano {ont_reads.fa} -o {out_dir} chr8.fa.

Methylation analysis

Nanopolish¹⁸ (v.0.12.5) was used to measure the frequency of CpG methylation from raw ONT reads (>50 kb in length for CHM13) aligned to whole-genome assemblies via Winnowmap⁴³ (v.1.0). Nanopolish distinguishes 5-methylcytosine from unmethylated cytosine via a Hidden Markov model (HMM) on the raw nanopore current signal. The methylation caller generates a log-likelihood value for the ratio of probability of methylated to unmethylated CpGs at a specific *k*-mer. We filtered methylation calls using the nanopore_methylation_utilities tool (<https://github.com/isaclee/nanopore-methylation-utilities>)⁵³, which uses a log-likelihood ratio of 2.5 as a threshold for calling methylation. CpG sites with log-likelihood ratios greater than 2.5 (methylated) or less than -2.5 (unmethylated) are considered high quality and included in the analysis. Reads that do not have any high-quality CpG sites are filtered from the BAM for subsequent methylation analysis. Nanopore_methylation_utilities integrates methylation information into the BAM file for viewing in IGV⁵⁴ bisulfite mode, which was used to visualize CpG methylation.

Iso-Seq data generation and sequence analyses

RNA was purified from approximately 1×10^7 CHM13 cells using an RNeasy kit (Qiagen; 74104) and prepared into Iso-Seq libraries following a standard protocol⁵⁵. Libraries were loaded on two SMRT Cells 8M and sequenced on the Sequel II. The data were processed via isoseq3 (v.8.0), ultimately generating 3,576,198 full-length non-chimeric reads. Poly-A

trimmed transcripts were aligned to this CHM13 chr8 assembly and to GRCh38 with minimap2⁴⁴ (v.2.17-r941) with the following parameters: -ax splice -f 1000 --sam-hit-only --secondary = no --eqx. Transcripts were assigned to genes using featureCounts⁵⁶ with GENCODE⁵⁷ (v.34) annotations, supplemented with CHESS v.2.2⁵⁸ for any transcripts unannotated in GENCODE. Each transcript was scored for the percentage identity of its alignment to each assembly, requiring 90% of the length of each transcript to align to the assembly for it to count as aligned. For each gene, the percentage identity of non-CHM13 transcripts to GRCh38 was compared to the CHM13 chromosome 8 assembly. Genes with an improved representation in the CHM13 assembly were identified with a cut-off value of 20 improved reads per gene, with at least 0.2% average improvement in percentage identity. GENCODE (v.34) transcripts were lifted over to the CHM13 chr8 assembly using Liftoff⁵⁹ to compare the GRCh38 annotations to this assembly and Iso-Seq transcripts.

We combined the 3.6 million full-length transcript data (above) with 20,937,742 full-length non-chimeric publicly available human Iso-Seq data (Supplementary Table 8). In total, we compared the alignment of 24,513,940 full-length non-chimeric reads from 13 tissue and cell line sources to both the completed CHM13 chromosome 8 assemblies and the current human reference genome, GRCh38. Of the 848,048 non-CHM13 cell line transcripts that align to chromosome 8, 93,495 (11.02%) align with at least 0.1% greater percentage identity to the CHM13 assembly, and 52,821 (6.23%) to GRCh38. This metric suggests that the chromosome 8 reference improves human gene annotation by approximately 4.79% even though most of those changes are subtle in nature. Overall, 61 protein-coding and 33 noncoding loci have improved alignments to the CHM13 assembly compared to GRCh38, with >0.2% average percentage identity improvement, and at least 20 supporting transcripts (Extended Data Fig. 3a–c, Supplementary Table 1). As an example, *WDYHV1* (also known as *NTAQ1*) has four amino acid replacements, with 13 transcripts sharing the identical open reading frame to CHM13 (Extended Data Fig. 3d).

Pairwise sequence identity heat maps

To generate pairwise sequence identity heat maps, we fragmented the centromere assemblies into 5-kb fragments (for example, 1–5,000, 5,001–10,000, and so on) and made all possible pairwise alignments between the fragments using the following minimap2⁴⁴ (v.2.17-r941) command: minimap2 -f 0.0001 -t 32 -X --eqx -ax ava-ont. The sequence identity was determined from the CIGAR string of the alignments and then visualized using ggplot2 (geom_raster) in R (v.1.1.383)⁶⁰. The colour of each segment was determined by sorting the data by identity and then creating 10 equally sized bins, each of which received a distinct colour from the spectral pallet. The choice of a 5-kb window came after testing a variety of window sizes. Ultimately, we found 5 kb to be a good balance between resolution of the figure (because each 5 kb fragment is plotted as a pixel) and sensitivity of minimap2 (fragments less than 5 kb often missed alignments with the ava-ont preset). A schematic illustrating this process is shown in Supplementary Fig. 3.

Miropeats analysis

To compare the organization and orientation of the CHM13 and GRCh38 β -defensin loci, we aligned the two β -defensin regions (CHM13 chr8:6300000–13300000; GRCh38 chr8:6545299–13033398) to each other using the following minimap2⁴⁴ parameters: minimap2 -x asm20 -s 200000 -p 0.01 -N 1000 --cs {GRCh38_defensin.fasta} {CHM13_defensin.fasta}. Then, we applied a version of Miropeats⁶¹ that is modified to use minimap2⁴⁴ alignments (<https://github.com/mrvollger/minimiro>) to produce the figure showing homology between the two sequences.

Analysis of α -satellite organization

To determine the organization of the CHM13 chromosome 8 centromeric region, we used two independent approaches. First, we subjected the CHM13 centromere assembly to an in silico restriction enzyme digestion in which a set of restriction enzyme recognition sites were identified within the assembly. In agreement with previous findings that XbaI digestion can generate a pattern of HORs within the chromosome 8 HOR array⁹, we found that each α -satellite HOR could be extracted via XbaI digestion. The

in silico digestion analysis indicates that the chromosome 8 centromeric HOR array consists of 1,462 HOR units: 283 4-monomer HORs, 4 5-monomer HORs, 13 6-monomer HORs, 356 7-monomer HORs, 295 8-monomer HORs, and 511 11-monomer HORs. As an alternative approach, we subjected the centromere assembly to StringComposer⁴² (<https://github.com/ablab/stringdecomposer>, version from 28 February 2020) using a set of 11 α -satellite monomers derived from a chromosome 8 11-mer HOR unit. The sequence of the α -satellite monomers used are as follows: A:

AGCATTCTCAGAACACCTCGTATGTTGCAATCAAGTCACAG
AGTTGAACCTTCCGTTCATAGAGCAGGTTGGAAACA
CTCTTATTGTAGTATCTGGAAGTGGACATTGGAGCGCTTCAGGC
CTATGGTAAAAAGGAAATATCTTCCCATAAAAACGACATAGA; B:
AGCTATCTCAGGAACCTGTTATGATGCATCTAACACTAACAGT
GTTGAACCTTGTACTGACAG
AGCACTTGAAACACTCTTTTGGAAATCTGCAAGTGGATATTGG
ATCGCTTGAGGATTCGTTGGAAACGGGATGCAATATAAACGT
ACACAGC; C:

AGCATACTCAGAAAATACCTTGCCATATTCCATTCAAGTCACAGA
GTGGAACATTCCCATTCATAGAGCAGGTTGGAAACACTCTTTG
GAGTATCTGGAAGTGGACATTGGAGCGCTTCTGAACTATGGTG
AAAAAGGAAATATCTTCCAATGAAAACAAGACAGA; D:
AGCATTCTGAGAAACTTATTGTGATGTGTGTCCTCAACAAACGG
ACTTGAACCTTCGTTCATGCAGTACTTCTGGAACACTCTTTT
GAAGATTCTGCATCGGGATATTGGATAGCTTGAGGATTCGTTG
GAAACGGGCTTACATGTAAAAATTAGACAGC; E:

AGCATTCTCAGAAACTTCTTGTGGTG
TCTGCATTCAAGTCACAGAAATTGAACCTCTCCTCACATAGAGCAG
TTGTGCAGCACTCTATTGTAGTATCTGGAAGTGGACATTGGAGG
GCTTGAGCCTATCTGGAAAAAGGAAATATCTTCCCATGAATGCG
AGATAGA; F:

AGTAATCTCAGAACATGTTATGCTGTATCTACTCAACTAAGTGT
GCTGAACATTCTATTGATAGAGCAGTTTGAGACCCTCTTCTT
GGAATCTGCAAGTGGATATTGGATAGATTGAGGATTCGTTGGA
AACGGGATTATATAAAAAGTAGACAGC; G:

AGCATTCTCAGAAACTTCTTGTGATGTTGCATCCAGCTCTCAGA
GTTGAACATTCCCTTCATAGAGTAGGTTGAAACCCCTTTTAT

AGTGTCTGGAAGCGGGCATTGGAGCGCTTCAGGCCTATGCTGA
 AAAAGGAAATATCTACATATAGAAACTAGACAGA; H:
 AGCATTCTGAGAACATCAAGTTGTGATGTGGGTACTCAACTAACAG
 TGTTGATCCATTCTTGATACAGCAGTTGAACCACACTTTG
 TAGAATCTGCAAGTGGATATTGGATAGCTGTGAGGATTCTGG
 AAACGGGAATGTCTCATAGAAAAATTAGACAGA; I:
 AGCATTCTCAGAACCTTGATTGTGATGTGTTCTCCACTAACAG
 AGTTGAACCTTCTTGACAGAACTGTTCTGAAACATTCTTTA
 TAGAATCTGGAAGTGGATATTGGAAAGCTTGAGGATTCTGG
 GAAACGGGAATATCTCAAATAAAATCTAGCCAGA; J:
 AGCATTCTAAGAACATCTAGGGATGTTACATTCAAGTCACAG
 AGTTGAACATTCC
 CTTCACAGAGCAGGTTGAAACAATCTCTCGTACTATCTGGCA
 GTGGACATTGAGCTCTTGGGGCCTATGCTGAAAAAGGAAATA
 TCTTCCGACAAAAACTAGTCAGA; K:
 AGCATTCGCAGAACATCCCCTTGATGTGCACTCAACTGTCAG
 AATTGAACCTTGGTTGGAGAGAGCACTTTGAAACACACT
 TTTGTAGAATCTGCAGGTGGATATTGGCT
 AGCTTGAGGATTCTGTTGGAACCGTAATGTCTCAAAGAAAAT
 CTAGACAGA.

This analysis indicated that the CHM13 chromosome 8 centromeric HOR array consists of 1,515 HOR units: 286 4-monomer HORs, 12 6-monomer HORs, 366 7-monomer HORs, 303 8-monomer HORs, 3 10-monomer HORs, 539 11-monomer HORs, 2 12-monomer HORs, 2 13-monomer HORs, 1 17-monomer HOR, and 1 18-monomer HOR, which is concordant with the *in silico* restriction enzyme digestion results. The predominant HOR types from StringComposer⁴² are presented in Extended Data Fig. 8.

Copy number estimation

To estimate the copy number for the 8q21.2 VNTR and *DEFB* loci in human lineages, we applied a read-depth based copy number genotyper¹⁴ to a collection of 1,105 published high-coverage genomes^{62,63,64,65,66,67}. In brief, sequencing reads were divided into multiples of 36-monomer HORs, which were then mapped to a repeat-masked human reference genome

(GRCh38) using mrsFAST⁶⁸ (v.3.4.1). To increase the mapping sensitivity, we allowed up to two mismatches per 36-monomer HOR. The read depth of mappable sequences across the genome was corrected for underlying GC content, and copy number estimate for the locus of interest was computed by summarizing over all mappable bases for each sample.

Entropy calculation

To define regions of increased admixture within the centromeric HOR array, we calculated the entropy using the frequencies of the different HOR units in 10-unit windows (1 unit slide) over the entire array. The following formula was used to determine entropy:

$$\$ \$ \{ \text{rm}\{\text{Entropy}\} \} = -\Sigma (\{ \{ \text{rm}\{\text{frequency}\} \} \}_i \{ \text{rm}\{i\} \}) \times \log_2 (\{ \{ \text{rm}\{\text{frequency}\} \} \}_i \{ \text{rm}\{i\} \})) \$ \$$$

in which frequency is: (no. of HORs)/(total no. of HORs) in a 10-unit window. The analysis is analogous to that previously performed⁶⁹.

Droplet digital PCR

Droplet digital PCR was performed on CHM13 genomic DNA to estimate the number of D8Z2 α -satellite HORs, as was previously done for the DXZ1 α -satellite HORs¹³. In brief, genomic DNA was isolated from CHM13 cells using the DNeasy Blood & Tissue Kit (Qiagen). DNA was quantified using a Qubit Fluorometer and the Qubit dsDNA HS Assay (Invitrogen). Reactions (20 μ l) were prepared with 0.1 ng of gDNA for the D8Z2 assay or 1 ng of gDNA for the *MTUS1* single-copy gene (as a control). EvaGreen droplet digital PCR (Bio-Rad) master mixes were simultaneously prepared for the D8Z2 and *MTUS1* reactions, which were then incubated for 15 min to allow for restriction digest, according to the manufacturer's protocol.

Pulsed-field gel electrophoresis and Southern blot

CHM13 genomic DNA was prepared in agarose plugs and digested with either BamHI or MfeI (to characterize the chromosome 8 centromeric

region) or BmgBI (to characterize the chromosome 8q21.2 region) in the buffer recommended by the manufacturer. The digested DNA was separated with the CHEF Mapper system (Bio-Rad; autoprogram, 5–850-kb range, 16 h run), transferred to a membrane (Amersham Hybond-N+) and blot-hybridized with a 156 bp probe specific to the chromosome 8 centromeric α-satellite or 8q21.2 region. The probe was labelled with ^{32}P by PCR-amplifying a synthetic DNA template 233: 5'-

TTTGTGGAAGTGGACATTGCGCTTGTAGCCTATCTGGAAAAAAGG
AAATATCTCCCATGAATGCGAGATAGAAGTAATCTCAGAA
ACATGTTATGCTGTATCTACTCAACTAACTGTGCTGAACATTCTA
TTGTAAAAAATAGACAGAACGCATT-3' (for the centromere of chromosome 8); 264: 5'-TTTGTGGAAGTGGACATTGCG
CCCGAGGGGCCGCGCAGGGATTCCGGGGACCGGGAGTGGGG
GGTTGGGGTTACTCTTGGCTTTGCCCTCTCCTGCCGCCGGCTGC
TCCAGTTCTTCGCTTGCGCGAGGTGGTAAAAATAGACAGAA
GCATT-3' (for the organization of the chromosome 8q21.2 locus) with PCR primers 129: 5'-TTTGTGGAAGTGGACATTTC-3' and 130: 5'-
AATGCTTCTGTCTATTTA-3'. The blot was incubated for 2 h at 65 °C for pre-hybridization in Church's buffer (0.5 M Na-phosphate buffer containing 7% SDS and 100 µg ml⁻¹ of unlabelled salmon sperm carrier DNA). The labelled probe was heat denatured in a boiling water bath for 5 min and snap-cooled on ice. The probe was added to the hybridization Church's buffer and allowed to hybridize for 48 h at 65 °C. The blot was washed twice in 2× SSC (300 mM NaCl, 30 mM sodium citrate, pH 7.0), 0.05% SDS for 10 min at room temperature, twice in 2× SSC, 0.05% SDS for 5 min at 60 °C, twice in 0.5× SSC, 0.05% SDS for 5 min at 60 °C, and twice in 0.25× SSC, 0.05% SDS for 5 min at 60 °C. The blot was exposed to X-ray film for 16 h at -80 °C. Uncropped, unprocessed images of all gels and blots are shown in Supplementary Fig. 9.

FISH and immunofluorescence

To validate the organization of the chromosome 8 centromere, we performed FISH on metaphase chromosome spreads as previously described⁷⁰ with slight modifications. In brief, CHM13 cells were treated with colcemid and resuspended in HCM buffer (10 mM HEPES pH7.3, 30 mM glycerol, 1 mM CaCl₂, 0.8 mM MgCl₂). After 10 min, cells were fixed

with methanol:acetic acid (3:1), dropped onto previously clean slides, and soaked in 1× PBS. Slides were incubated overnight in cold methanol, hybridized with labelled FISH probes at 68 °C for 2 min, and incubated overnight at 37 °C. Slides were washed three times in 0.1× SSC at 65 °C for 5 min each before mounting in Vectashield containing 5 µg ml⁻¹ DAPI. Slides were imaged on a fluorescence microscope (Leica DM RXA2) equipped with a charge-coupled device camera (CoolSNAP HQ2) and a 100× 1.6–0.6 NA objective lens. Images were collected using Leica Application Suite X (v.3.7).

The probes used to validate the organization of the chromosome 8 centromere were picked from the human large-insert clone fosmid library ABC10. ABC10 end sequences were mapped using MEGABLAST (similarity = 0.99, parameters: -D 2 -v 7 -b 7 -e 1e-40 -p 80 -s 90 -W 12 -t 21 -F F) to a repeat-masked CHM13 genome assembly containing the complete chromosome 8 (parameters: -e wublast -xsmall -no_is -s -species Homo sapiens). Expected insert size for fosmids was set to (min) 32 kb and (max) 48 kb. Resulting clone alignments were grouped into the following categories based on uniqueness of the alignment for a given pair of clones, alignment orientation and the inferred insert size from the assembly. (1) Concordant best: unique alignment for clone pair, insert size within expected fosmid range, expected orientation. (2) Concordant tied: non-unique alignment for clone pair, insert size within expected fosmid range, expected orientation. (3) Discordant best: unique alignment of clone pair, insert size too small, too large or in opposite expected orientation of expected fosmid clone. (4) Discordant tied: non unique alignment for clone pair, insert size too small, too large or in opposite expected orientation of expected fosmid clone. (5) Discordant trans: clone pair has ends mapping to different contigs.

Clones aligning to regions within the chromosome 8 centromeric region were selected for FISH validation. The fosmid clones used for validation of the chromosome 8 centromeric region are:

174552_ABC10_2_1_000046302400_C7 for the p-arm monomeric α -satellite region (Cy5; blue), 174222_ABC10_2_1_000044375100_H13 for the p-arm portion of the D8Z2 HOR array (FluorX; green), 171417_ABC10_2_1_000045531400_M19 for the central portion of the

D8Z2 HOR array (Cy3; red), 173650_ABC10_2_1_000044508400_J14 for the q-arm portion of the D8Z2 HOR array (FluorX; green), and 173650_ABC10_2_1_000044091500_K11 for the q-arm monomeric α -satellite region (Cy5; blue).

To determine the location of CENP-A relative to methylated DNA (specifically, 5-methylcytosines), we performed immunofluorescence on stretched CHM13 chromatin fibres as previously described^{71,72} with modifications. In brief, CHM13 cells were swollen in a hypotonic buffer consisting of a 1:1:1 ratio of 75 mM KCl, 0.8% sodium citrate, and dH₂O for 5 min. Then, 3.5×10^4 cells were cytospon onto an ethanol-washed glass slide with a Shandon Cytospin 4 at 55g for 4 min with high acceleration and allowed to adhere for 1 min before immersing in a salt-detergent-urea lysis buffer (25 mM Tris pH 7.5, 0.5 M NaCl, 1% Triton X-100 and 0.3 M urea) for 15 min at room temperature. The slide was slowly removed from the lysis buffer over a time period of 38 s and subsequently washed in PBS, incubated in 4% formaldehyde in PBS for 10 min, and washed with PBS and 0.1% Triton X-100. The slide was rinsed in PBS and 0.05% Tween-20 (PBST) for 3 min, blocked for 30 min with immunofluorescence block (2% FBS, 2% BSA, 0.1% Tween-20 and 0.02% NaN₂), and then incubated with a mouse monoclonal anti-CENP-A antibody (1:200, Enzo, ADI-KAM-CC006-E) and rabbit monoclonal anti-5-methylcytosine antibody (1:200, RevMAb, RM231) for 3 h at room temperature. Cells were washed three times for 5 min each in PBST and then incubated with Alexa Fluor 488 goat anti-rabbit (1:200, Thermo Fisher Scientific, A-11034) and Alexa Fluor 594 conjugated to goat anti-mouse (1:200, Thermo Fisher Scientific, A-11005) for 1.5 h. Cells were washed three times for 5 min each in PBST, fixed for 10 min in 4% formaldehyde, and washed three times for 1 min each in dH₂O before mounting in Vectashield containing 5 μ g ml⁻¹ DAPI. Slides were imaged on an inverted fluorescence microscope (Leica DMI6000) equipped with a charge-coupled device camera (Leica DFC365 FX) and a 40 \times 1.4 NA objective lens.

To assess the repeat organization of the 8q21 neocentromere, we performed FISH⁷³ on CHM13 chromatin fibres. DNA fibres were obtained following Henry H. Q. Heng's protocol with minor modifications⁷⁴. In brief, chromosomes were fixed with methanol:acetic acid (3:1), dropped onto

previously clean slides, and soaked in 1× PBS. Manual elongation was performed by coverslip in NaOH:ethanol (5:2) solution. Slides were mounted in Vectashield containing 5 µg ml⁻¹ DAPI and imaged on a fluorescence microscope (Leica DM RXA2) equipped with a charge-coupled device camera (CoolSNAP HQ2) and a 100× 1.6–0.6 NA objective lens. The probes used for validation of the 8q21.2 locus were picked from the same ABC10 fosmid library described above and include 174552_ABC10_2_1_000044787700_O7 for Probe 1 (Cy3; red) and 173650_ABC10_2_1_000044086000_F24 for Probe 2 (FluorX; green). Several CHM13 8q21.2 chromatin fibres were imaged. We quantified the number and intensity of the probe signals on a set of CHM13 chromatin fibres using ImageJ's Gel Analysis tool (v.1.51) and found that there were 63 ± 7.55 green signals and 67 ± 5.20 red signals ($n = 3$ independent experiments), consistent with the 67 full and 7 partial repeats in the CHM13 8q21.2 VNTR.

Native CENP-A ChIP-seq and analysis

We performed two independent replicates of native CENP-A ChIP-seq on CHM13 cells as previously described^{25,72} with some modifications. In brief, 3×10^7 – 4×10^7 cells were collected and resuspended in 2 ml of ice-cold buffer I (0.32 M sucrose, 15 mM Tris, pH 7.5, 15 mM NaCl, 5 mM MgCl₂, 0.1 mM EGTA, and 2× Halt Protease Inhibitor Cocktail (Thermo Fisher 78429)). Ice-cold buffer II (2 ml; 0.32 M sucrose, 15 mM Tris, pH 7.5, 15 mM NaCl, 5 mM MgCl₂, 0.1 mM EGTA, 0.1% IGEPAL, and 2× Halt Protease Inhibitor Cocktail) was added, and samples were placed on ice for 10 min. The resulting 4 ml of nuclei were gently layered on top of 8 ml of ice-cold buffer III (1.2 M sucrose, 60 mM KCl, 15 mM Tris pH 7.5, 15 mM NaCl, 5 mM MgCl₂, 0.1 mM EGTA, and 2× Halt Protease Inhibitor Cocktail (Thermo Fisher 78429)) and centrifuged at 10,000g for 20 min at 4 °C. Pelleted nuclei were resuspended in buffer A (0.34 M sucrose, 15 mM HEPES, pH 7.4, 15 mM NaCl, 60 mM KCl, 4 mM MgCl₂ and 2× Halt Protease Inhibitor Cocktail) to 400 ng ml⁻¹. Nuclei were frozen on dry ice and stored at 80 °C. MNase digestion reactions were carried out on 200–300 µg chromatin, using 0.2–0.3 U µg⁻¹ MNase (Thermo Fisher 88216) in buffer A supplemented with 3 mM CaCl₂ for 10 min at 37 °C. The reaction

was quenched with 10 mM EGTA on ice and centrifuged at 500g for 7 min at 4 °C. The chromatin was resuspended in 10 mM EDTA and rotated at 4 °C for 2 h. The mixture was adjusted to 500 mM NaCl, rotated for another 45 min at 4 °C and then centrifuged at maximum speed (21,100g) for 5 min at 4 °C, yielding digested chromatin in the supernatant. Chromatin was diluted to 100 ng ml⁻¹ with buffer B (20 mM Tris, pH 8.0, 5 mM EDTA, 500 mM NaCl and 0.2% Tween 20) and precleared with 100 µl 50% protein G Sepharose bead (GE Healthcare) slurry for 20 min at 4 °C, rotating. Precleared supernatant (10–20 µg bulk nucleosomes) was saved for further processing. To the remaining supernatant, 20 µg mouse monoclonal anti-CENP-A antibody (Enzo ADI-KAM-CC006-E) was added and rotated overnight at 4 °C. Immunocomplexes were recovered by the addition of 200 ml 50% protein G Sepharose bead slurry followed by rotation at 4 °C for 3 h. The beads were washed three times with buffer B and once with buffer B without Tween. For the input fraction, an equal volume of input recovery buffer (0.6 M NaCl, 20 mM EDTA, 20 mM Tris, pH 7.5 and 1% SDS) and 1 ml of RNase A (10 mg ml⁻¹) was added, followed by incubation for 1 h at 37 °C. Proteinase K (100 mg ml⁻¹, Roche) was then added, and samples were incubated for another 3 h at 37 °C. For the ChIP fraction, 300 µl of ChIP recovery buffer (20 mM Tris, pH 7.5, 20 mM EDTA, 0.5% SDS and 500 mg ml⁻¹ proteinase K) was added directly to the beads and incubated for 3–4 h at 56 °C. The resulting proteinase K-treated samples were subjected to a phenol–chloroform extraction followed by purification with a QIAGEN MinElute PCR purification column. Unamplified bulk nucleosomal and ChIP DNA were analysed using an Agilent Bioanalyzer instrument and a 2100 High Sensitivity Kit.

Sequencing libraries were generated using the TruSeq ChIP Library Preparation Kit Set A (Illumina IP-202-1012) according to the manufacturer's instructions, with some modifications. In brief, 5–10 ng bulk nucleosomal or ChIP DNA was end-repaired and A-tailed. Illumina TruSeq adaptors were ligated, libraries were size-selected to exclude polynucleosomes using an E-Gel SizeSelect II agarose gel, and the libraries were PCR-amplified using the PCR polymerase and primer cocktail provided in the kit. The resulting libraries were submitted for 150 bp, paired-end Illumina sequencing using a NextSeq 500/550 High Output Kit v2.5 (300 cycles). The resulting reads were assessed for quality using

FastQC (<https://github.com/s-andrews/FastQC>), trimmed with Sickle (<https://github.com/najoshi/sickle>; v1.33) to remove low-quality 5' and 3' end bases, and trimmed with Cutadapt⁷⁵ (v.1.18) to remove adapters.

Processed CENP-A ChIP and bulk nucleosomal reads were aligned to the CHM13 whole-genome assembly⁵ using two different approaches: (1) BWA-MEM⁷⁶ (v.0.7.17) and (2) a *k*-mer-based mapping approach we developed (described below).

For BWA-MEM mapping, data were aligned with the following parameters: bwa mem -k 50 -c 1000000 {index} {read1.fastq.gz} for single-end data, and bwa mem -k 50 -c 1000000 {index} {read1.fastq.gz} {read2.fastq.gz} for paired-end data. The resulting SAM files were filtered using SAMtools⁴⁷ with FLAG score 2308 to prevent multi-mapping of reads. With this filter, reads mapping to more than one location are randomly assigned a single mapping location, thereby preventing mapping biases in highly identical regions. Alignments to the chromosome 8 centromere were downsampled to the same coverage and normalized with deepTools⁷⁷ (v.3.4.3) bamCompare with the following parameters: bamCompare -b1 {ChIP.bam} -b2 {Bulk_nucleosomal.bam} --operation ratio --binSize 1000 -o {out.bw}. The resulting bigWig file was visualized on the UCSC Genome Browser using the CHM13 chromosome 8 assembly as an assembly hub.

For the *k*-mer-based mapping, the initial BWA-MEM alignment was used to identify reads specific to the chromosome 8 centromeric region (chr8:43600000–47200000). The *k*-mers (*k* = 50) were identified from each chromosome 8 centromere-specific data set using Jellyfish (v.2.3.0) and mapped back onto reads and chromosome 8 centromere assembly allowing for no mismatches. Approximately 93–98% of all *k*-mers identified in the reads were also found within the D8Z2 HOR array. Each *k*-mer from the read data was then placed once at random between all sites in the HOR array that had a perfect match to that *k*-mer. These data were then visualized using a histogram with 1-kb bins in R (R core team, 2020).

Mappability of short reads within the chromosome 8 centromeric region

To determine the mappability of short reads within the chromosome 8 centromeric HOR array, we performed a simulation where we generated 300,000 random 150-bp fragments from five equally sized (416 kb) regions across the CHM13 D8Z2 HOR array. We mapped these fragments back to the CHM13 chromosome 8 centromeric region using BWA-MEM (v0.7.17) or the *k*-mer-based approach, as described above. For BWA-MEM mapping, the 150-bp fragments were aligned with the following parameters: bwa mem -k 50 -c 1000000 {index} {fragments.fasta}. The resulting SAM files were filtered using SAMtools⁴⁷ with FLAG score 2308 to prevent multi-mapping of reads and then converted to a BAM file. BAM files were visualized in IGV⁵⁴. For the *k*-mer-based mapping, *k*-mers (*k* = 50) were identified from each set of 150-bp fragments using Jellyfish (v.2.3.0) and mapped back onto the fragments and the chromosome 8 centromere assembly allowing for no mismatches. *k*-mers with perfect matches to multiple sites within the centromeric region were assigned to one of the sites at random. These data were visualized using a histogram with 1-kb bins in R (R core team, 2020).

Phylogenetic analysis

To assess the phylogenetic relationship between α -satellite repeats, we first masked every non- α -satellite repeat in the human and NHP centromere assemblies using RepeatMasker⁷⁸ (v.4.1.0). Then, we subjected the masked assemblies to StringComposer⁴² (version available 28 February 2020) using a set of 11 α -satellite monomers derived from a chromosome 8 11-monomer HOR unit (described in the ‘Analysis of α -satellite organization’ section above). This tool identifies the location of α -satellite monomers in the assemblies, and we used this to extract the α -satellite monomers from the HOR/dimeric array and monomeric regions into multi-FASTA files. We ultimately extracted 12,989, 8,132, 12,224, 25,334 and 63,527 α -satellite monomers from the HOR/dimeric array in human, chimpanzee (H1), chimpanzee (H2), orangutan and macaque, respectively, and 2,879, 3,781, 3,351, 1,573 and 8,127 monomers from the monomeric regions in human, chimpanzee (H1), chimpanzee (H2), orangutan and macaque, respectively. We randomly selected 100 and 50 α -satellite monomers from the HOR/dimeric array and monomeric regions and aligned them with MAFFT^{79,80} (v.7.453). We used IQ-TREE⁸¹ to reconstruct the maximum-

likelihood phylogeny with model selection and 1000 bootstraps. The resulting tree file was visualized in iTOL^{[82](#)}.

To estimate sequence divergence along the pericentromeric regions, we first mapped each NHP centromere assembly to the CHM13 centromere assembly using minimap2^{[44](#)} (v.2.17-r941) with the following parameters: -ax asm20 --eqx -Y -t 8 -r 500000. Then, we generated a BED file of 10 kb windows located within the CHM13 centromere assembly. We used the BED file to subset the BAM file, which was subsequently converted into a set of FASTA files. FASTA files contained at least 5 kb of orthologous sequences from one or more NHP centromere assemblies. Pairs of human and NHP orthologous sequences were realigned using MAFFT (v.7.453) and the following command: mafft --maxiterate 1000 --localpair. Sequence divergence was estimated using the Tamura-Nei substitution model^{[83](#)}, which accounts for recurrent mutations and differences between transversions and transitions as well as within transitions. Mutation rate per segment was estimated using Kimura's model of neutral evolution^{[84](#)}. In brief, we modelled the estimated divergence (D) is a result of between-species substitutions and within-species polymorphisms; that is, $D = 2\mu t + 4N_e\mu$, in which N_e is the ancestral human effective population size, t is the divergence time for a given human–NHP pair, and μ is the mutation rate. We assumed a generation time of [20, 29] years and the following divergence times: human–macaque = $[23 \times 10^6, 25 \times 10^6]$ years, human–orangutan = $[12 \times 10^6, 14 \times 10^6]$ years, human–chimpanzee = $[4 \times 10^6, 6 \times 10^6]$ years. To convert the genetic unit to a physical unit, our computation also assumes $N_e = 10,000$ and uniformly drawn values for the generation and divergence times.

Reporting summary

Further information on research design is available in the [Nature Research Reporting Summary](#) linked to this paper.

Data availability

The complete CHM13 chromosome 8 sequence and all data generated and/or used in this study are publicly available and listed in Supplementary Table 9 with their BioProject, accession numbers and/or URL. For convenience, we also list their BioProjects and/or URLs here: complete CHM13 chromosome 8 sequence ([PRJNA686384](#)); CHM13 ONT, Iso-Seq, and CENP-A ChIP-seq data ([PRJNA559484](#)); CHM13 Strand-Seq alignments (<https://zenodo.org/record/3998125>); HG00733 ONT data ([PRJNA686388](#)); HG00733 PacBio HiFi data ([PRJEB36100](#)); testis and fetal brain Iso-Seq data ([PRJNA659539](#)); and NHPs (chimpanzee (Clint; S006007), orangutan (Susie; PR01109), and macaque (AG07107)) ONT and PacBio HiFi data ([PRJNA659034](#)). All CHM13 BACs used in this study are listed in Supplementary Table 10 with their accession numbers.

Code availability

Custom code for the SUNK-based assembly method is available at https://github.com/glogsdon1/sunk-based_assembly. All other code is publicly available.

References

1. 1.

International Human Genome Project Consortium. Initial sequencing and analysis of the human genome. *Nature* **409**, 860–921 (2001).

[ADS](#) [Article](#) [Google Scholar](#)

2. 2.

Venter, J. C. et al. The sequence of the human genome. *Science* **291**, 1304–1351 (2001).

[ADS](#) [CAS](#) [PubMed](#) [PubMed Central](#) [Article](#) [Google Scholar](#)

3. 3.

Alkan, C. et al. Genome-wide characterization of centromeric satellites from multiple mammalian genomes. *Genome Res.* **21**, 137–145 (2011).

[CAS](#) [PubMed](#) [PubMed Central](#) [Article](#) [Google Scholar](#)

4. 4.

International Human Genome Sequencing Consortium. Finishing the euchromatic sequence of the human genome. *Nature* **431**, 931–945 (2004).

[ADS](#) [Article](#) [CAS](#) [Google Scholar](#)

5. 5.

Nurk, S. et al. HiCanu: accurate assembly of segmental duplications, satellites, and allelic variants from high-fidelity long reads. *Genome Res.* gr.263566.120 (2020).

6. 6.

Cheng, H., Concepcion, G. T., Feng, X., Zhang, H. & Li, H. Haplotype-resolved de novo assembly with phased assembly graphs. *Nat. Methods* **18**, 170–175 (2021).

[CAS](#) [PubMed](#) [Article](#) [Google Scholar](#)

7. 7.

Logsdon, G. A., Vollger, M. R. & Eichler, E. E. Long-read human genome sequencing and its applications. *Nat. Rev. Genet.* **21**, 597–614 (2020).

[CAS](#) [PubMed](#) [PubMed Central](#) [Article](#) [Google Scholar](#)

8. 8.

McNulty, S. M. & Sullivan, B. A. Alpha satellite DNA biology: finding function in the recesses of the genome. *Chromosome Res.* **26**,

115–138 (2018).

[CAS](#) [PubMed](#) [PubMed Central](#) [Article](#) [Google Scholar](#)

9. 9.

Ge, Y., Wagner, M. J., Siciliano, M. & Wells, D. E. Sequence, higher order repeat structure, and long-range organization of alpha satellite DNA specific to human chromosome 8. *Genomics* **13**, 585–593 (1992).

[CAS](#) [PubMed](#) [Article](#) [Google Scholar](#)

10. 10.

Hollox, E. J., Armour, J. A. & Barber, J. C. K. Extensive normal copy number variation of a β -defensin antimicrobial-gene cluster. *Am. J. Hum. Genet.* **73**, 591–600 (2003).

[CAS](#) [PubMed](#) [PubMed Central](#) [Article](#) [Google Scholar](#)

11. 11.

Hollox, E. J. et al. Psoriasis is associated with increased beta-defensin genomic copy number. *Nat. Genet.* **40**, 23–25 (2008).

[CAS](#) [PubMed](#) [Article](#) [Google Scholar](#)

12. 12.

Mohajeri, K. et al. Interchromosomal core duplicons drive both evolutionary instability and disease susceptibility of the chromosome 8p23.1 region. *Genome Res.* **26**, 1453–1467 (2016).

[CAS](#) [PubMed](#) [PubMed Central](#) [Article](#) [Google Scholar](#)

13. 13.

Miga, K. H. et al. Telomere-to-telomere assembly of a complete human X chromosome. *Nature* **585**, 79–84 (2020).

[ADS](#) [CAS](#) [PubMed](#) [PubMed Central](#) [Article](#) [Google Scholar](#)

14. 14.

Sudmant, P. H. et al. Diversity of human copy number variation and multicopy genes. *Science* **330**, 641–646 (2010).

[ADS](#) [CAS](#) [PubMed](#) [PubMed Central](#) [Article](#) [Google Scholar](#)

15. 15.

Falconer, E. & Lansdorp, P. M. Strand-seq: a unifying tool for studies of chromosome segregation. *Semin. Cell Dev. Biol.* **24**, 643–652 (2013).

[CAS](#) [PubMed](#) [Article](#) [Google Scholar](#)

16. 16.

Sanders, A. D., Falconer, E., Hills, M., Spierings, D. C. J. & Lansdorp, P. M. Single-cell template strand sequencing by Strand-seq enables the characterization of individual homologs. *Nat. Protocols* **12**, 1151–1176 (2017).

[CAS](#) [PubMed](#) [Article](#) [Google Scholar](#)

17. 17.

Rhie, A., Walenz, B. P., Koren, S. & Phillippy, A. M. Merqury: reference-free quality, completeness, and phasing assessment for genome assemblies. *Genome Biol.* **21**, 245 (2020).

[CAS](#) [PubMed](#) [PubMed Central](#) [Article](#) [Google Scholar](#)

18. 18.

Simpson, J. T. et al. Detecting DNA cytosine methylation using nanopore sequencing. *Nat. Methods* **14**, 407–410 (2017).

[CAS](#) [PubMed](#) [Article](#) [Google Scholar](#)

19. 19.

Devriendt, K. et al. Delineation of the critical deletion region for congenital heart defects, on chromosome 8p23.1. *Am. J. Hum. Genet.* **64**, 1119–1126 (1999).

[CAS](#) [PubMed](#) [PubMed Central](#) [Article](#) [Google Scholar](#)

20. 20.

Giglio, S. et al. Heterozygous submicroscopic inversions involving olfactory receptor-gene clusters mediate the recurrent t(4;8)(p16;p23) translocation. *Am. J. Hum. Genet.* **71**, 276–285 (2002).

[CAS](#) [PubMed](#) [PubMed Central](#) [Article](#) [Google Scholar](#)

21. 21.

Cantsilieris, S. & White, S. J. Correlating multiallelic copy number polymorphisms with disease susceptibility. *Hum. Mutat.* **34**, 1–13 (2013).

[CAS](#) [PubMed](#) [Article](#) [Google Scholar](#)

22. 22.

Tyson, C. et al. Expansion of a 12-kb VNTR containing the REXO1L1 gene cluster underlies the microscopically visible euchromatic variant of 8q21.2. *Eur. J. Hum. Genet.* **22**, 458–463 (2014).

[CAS](#) [PubMed](#) [Article](#) [Google Scholar](#)

23. 23.

Warburton, P. E. et al. Analysis of the largest tandemly repeated DNA families in the human genome. *BMC Genomics* **9**, 533 (2008).

[PubMed](#) [PubMed Central](#) [Article](#) [CAS](#) [Google Scholar](#)

24. 24.

Hasson, D. et al. Formation of novel CENP-A domains on tandem repetitive DNA and across chromosome breakpoints on human chromosome 8q21 neocentromeres. *Chromosoma* **120**, 621–632 (2011).

[PubMed](#) [Article](#) [Google Scholar](#)

25. 25.

Hasson, D. et al. The octamer is the major form of CENP-A nucleosomes at human centromeres. *Nat. Struct. Mol. Biol.* **20**, 687–695 (2013).

[CAS](#) [PubMed](#) [PubMed Central](#) [Article](#) [Google Scholar](#)

26. 26.

Alkan, C. et al. Organization and evolution of primate centromeric DNA from whole-genome shotgun sequence data. *PLOS Comput. Biol.* **3**, 1807–1818 (2007).

[CAS](#) [PubMed](#) [Article](#) [Google Scholar](#)

27. 27.

Cacheux, L., Ponger, L., Gerbault-Seureau, M., Richard, F. A. & Escudé, C. Diversity and distribution of alpha satellite DNA in the genome of an Old World monkey: *Cercopithecus solatus*. *BMC Genomics* **17**, 916 (2016).

[PubMed](#) [PubMed Central](#) [Article](#) [CAS](#) [Google Scholar](#)

28. 28.

Jain, M. et al. Linear assembly of a human centromere on the Y chromosome. *Nat. Biotechnol.* **36**, 321–323 (2018).

[CAS](#) [PubMed](#) [PubMed Central](#) [Article](#) [Google Scholar](#)

29. 29.

Warburton, P. E. et al. Immunolocalization of CENP-A suggests a distinct nucleosome structure at the inner kinetochore plate of active centromeres. *Curr. Biol.* **7**, 901–904 (1997).

[CAS](#) [PubMed](#) [Article](#) [Google Scholar](#)

30. 30.

Vafa, O. & Sullivan, K. F. Chromatin containing CENP-A and α -satellite DNA is a major component of the inner kinetochore plate. *Curr. Biol.* **7**, 897–900 (1997).

[CAS](#) [PubMed](#) [Article](#) [Google Scholar](#)

31. 31.

Smith, G. P. Evolution of repeated DNA sequences by unequal crossover. *Science* **191**, 528–535 (1976).

[ADS](#) [CAS](#) [PubMed](#) [Article](#) [Google Scholar](#)

32. 32.

Shepelev, V. A., Alexandrov, A. A., Yurov, Y. B. & Alexandrov, I. A. The evolutionary origin of man can be traced in the layers of defunct ancestral alpha satellites flanking the active centromeres of human chromosomes. *PLoS Genet.* **5**, e1000641 (2009).

[PubMed](#) [PubMed Central](#) [Article](#) [CAS](#) [Google Scholar](#)

33. 33.

Alexandrov, I., Kazakov, A., Tumeneva, I., Shepelev, V. & Yurov, Y. Alpha-satellite DNA of primates: old and new families. *Chromosoma* **110**, 253–266 (2001).

[CAS](#) [PubMed](#) [Article](#) [Google Scholar](#)

34. 34.

Koga, A. et al. Evolutionary origin of higher-order repeat structure in alpha-satellite DNA of primate centromeres. *DNA Res.* **21**, 407–415 (2014).

[CAS](#) [PubMed](#) [PubMed Central](#) [Article](#) [Google Scholar](#)

35. 35.

Alexandrov, I. A., Mitkevich, S. P. & Yurov, Y. B. The phylogeny of human chromosome specific alpha satellites. *Chromosoma* **96**, 443–453 (1988).

[CAS](#) [PubMed](#) [Article](#) [PubMed Central](#) [Google Scholar](#)

36. 36.

Vollger, M. R. et al. Improved assembly and variant detection of a haploid human genome using single-molecule, high-fidelity long reads. *Ann. Hum. Genet.* **84**, 125–140 (2019).

[PubMed](#) [PubMed Central](#) [Article](#) [CAS](#) [Google Scholar](#)

37. 37.

Huddleston, J. et al. Reconstructing complex regions of genomes using long-read sequencing technology. *Genome Res.* **24**, 688–696 (2014).

[CAS](#) [PubMed](#) [PubMed Central](#) [Article](#) [Google Scholar](#)

38. 38.

Garg, S. et al. Chromosome-scale, haplotype-resolved assembly of human genomes. *Nat. Biotechnol.* **39**, 309–312 (2021).

39. 39.

Porubsky, D. et al. Fully phased human genome assembly without parental data using single-cell strand sequencing and long reads. *Nat. Biotechnol.* **39**, 302–308 (2021).

40. 40.

Ebert, P. et al. Haplotype-resolved diverse human genomes and integrated analysis of structural variation. *Science* <https://doi.org/10.1126/science.abf7117> (2021).

41. 41.

Logsdon, G. A. HMW gDNA purification and ONT ultra-long-read data generation. *protocols.io* <https://doi.org/10.17504/protocols.io.bchhit36> (2020).

42. 42.

Dvorkina, T., Bzikadze, A. V. & Pevzner, P. A. The string decomposition problem and its applications to centromere analysis and assembly. *Bioinformatics* **36** (Suppl. 1), i93–i101 (2020).

[CAS](#) [PubMed](#) [PubMed Central](#) [Article](#) [Google Scholar](#)

43. 43.

Jain, C. et al. Weighted minimizer sampling improves long read mapping. *Bioinformatics* **36** (Suppl. 1), i111–i118 (2020).

[CAS](#) [PubMed](#) [Article](#) [Google Scholar](#)

44. 44.

Li, H. Minimap2: pairwise alignment for nucleotide sequences. *Bioinformatics* **34**, 3094–3100 (2018).

[CAS](#) [PubMed](#) [PubMed Central](#) [Article](#) [Google Scholar](#)

45. 45.

Li, H. & Durbin, R. Fast and accurate long-read alignment with Burrows-Wheeler transform. *Bioinformatics* **26**, 589–595 (2010).

[PubMed](#) [PubMed Central](#) [Article](#) [CAS](#) [Google Scholar](#)

46. 46.

Tarasov, A., Vilella, A. J., Cuppen, E., Nijman, I. J. & Prins, P. Sambamba: fast processing of NGS alignment formats. *Bioinformatics* **31**, 2032–2034 (2015).

[CAS](#) [PubMed](#) [PubMed Central](#) [Article](#) [Google Scholar](#)

47. 47.

Li, H. et al. The sequence alignment/map format and SAMtools. *Bioinformatics* **25**, 2078–2079 (2009).

[PubMed](#) [PubMed Central](#) [Article](#) [CAS](#) [Google Scholar](#)

48. 48.

Porubsky, D. et al. breakpointR: an R/Bioconductor package to localize strand state changes in Strand-seq data. *Bioinformatics* **36**, 1260–1261 (2020).

[CAS](#) [PubMed](#) [Google Scholar](#)

49. 49.

Chaisson, M. J. P. et al. Multi-platform discovery of haplotype-resolved structural variation in human genomes. *Nat. Commun.* **10**,

1784 (2019).

[ADS](#) [PubMed](#) [PubMed Central](#) [Article](#) [CAS](#) [Google Scholar](#)

50. 50.

Sanders, A. D. et al. Characterizing polymorphic inversions in human genomes by single-cell sequencing. *Genome Res.* **26**, 1575–1587 (2016).

[CAS](#) [PubMed](#) [PubMed Central](#) [Article](#) [Google Scholar](#)

51. 51.

Ghareghani, M. et al. Strand-seq enables reliable separation of long reads by chromosome via expectation maximization. *Bioinformatics* **34**, i115–i123 (2018).

[CAS](#) [PubMed](#) [PubMed Central](#) [Article](#) [Google Scholar](#)

52. 52.

Mikheenko, A., Bzikadze, A. V., Gurevich, A., Miga, K. H. & Pevzner, P. A. TandemTools: mapping long reads and assessing/improving assembly quality in extra-long tandem repeats. *Bioinformatics* **36** (Suppl. 1), i75–i83 (2020).

[CAS](#) [PubMed](#) [PubMed Central](#) [Article](#) [Google Scholar](#)

53. 53.

Lee, I. et al. Simultaneous profiling of chromatin accessibility and methylation on human cell lines with nanopore sequencing. *Nat. Methods* **17**, 1191–1199 (2020).

[CAS](#) [PubMed](#) [Article](#) [Google Scholar](#)

54. 54.

Robinson, J. T. et al. Integrative genomics viewer. *Nat. Biotechnol.* **29**, 24–26 (2011).

[CAS](#) [PubMed](#) [PubMed Central](#) [Article](#) [Google Scholar](#)

55. 55.

Dougherty, M. L. et al. Transcriptional fates of human-specific segmental duplications in brain. *Genome Res.* **28**, 1566–1576 (2018).

[CAS](#) [PubMed](#) [PubMed Central](#) [Article](#) [Google Scholar](#)

56. 56.

Liao, Y., Smyth, G. K. & Shi, W. featureCounts: an efficient general purpose program for assigning sequence reads to genomic features. *Bioinformatics* **30**, 923–930 (2014).

[CAS](#) [PubMed](#) [PubMed Central](#) [Article](#) [Google Scholar](#)

57. 57.

Harrow, J. et al. GENCODE: the reference human genome annotation for The ENCODE Project. *Genome Res.* **22**, 1760–1774 (2012).

[CAS](#) [PubMed](#) [PubMed Central](#) [Article](#) [Google Scholar](#)

58. 58.

Pertea, M. et al. CHESS: a new human gene catalog curated from thousands of large-scale RNA sequencing experiments reveals extensive transcriptional noise. *Genome Biol.* **19**, 208 (2018).

[CAS](#) [PubMed](#) [PubMed Central](#) [Article](#) [Google Scholar](#)

59. 59.

Shumate, A. & Salzberg, S. L. Liftoff: an accurate gene annotation mapping tool. *Bioinformatics*

<https://doi.org/10.1093/bioinformatics/btaa1016> (2020).

[Article](#) [PubMed](#) [Google Scholar](#)

60. 60.

R Core Team. *R: A Language and Environment for Statistical Computing* (R Foundation for Statistical Computing, 2020).

61. 61.

Parsons, J. D. Miropeats: graphical DNA sequence comparisons. *Bioinformatics* **11**, 615–619 (1995).

[CAS](#) [Article](#) [Google Scholar](#)

62. 62.

Bergström, A. et al. Insights into human genetic variation and population history from 929 diverse genomes. *Science* **367**, eaay5012 (2020).

[PubMed](#) [PubMed Central](#) [Article](#) [CAS](#) [Google Scholar](#)

63. 63.

Mafessoni, F. et al. A high-coverage Neandertal genome from Chagyrskaya Cave. *Proc. Natl Acad. Sci. USA* **117**, 15132–15136 (2020).

[CAS](#) [PubMed](#) [Article](#) [Google Scholar](#)

64. 64.

Mallick, S. et al. The Simons Genome Diversity Project: 300 genomes from 142 diverse populations. *Nature* **538**, 201–206 (2016).

[ADS](#) [CAS](#) [PubMed](#) [PubMed Central](#) [Article](#) [Google Scholar](#)

65. 65.

Meyer, M. et al. A high-coverage genome sequence from an archaic Denisovan individual. *Science* **338**, 222–226 (2012).

[ADS](#) [CAS](#) [PubMed](#) [PubMed Central](#) [Article](#) [Google Scholar](#)

66. 66.

Prado-Martinez, J. et al. Great ape genetic diversity and population history. *Nature* **499**, 471–475 (2013).

[ADS](#) [CAS](#) [PubMed](#) [PubMed Central](#) [Article](#) [Google Scholar](#)

67. 67.

Prüfer, K. et al. A high-coverage Neandertal genome from Vindija Cave in Croatia. *Science* **358**, 655–658 (2017).

[ADS](#) [PubMed](#) [PubMed Central](#) [Article](#) [CAS](#) [Google Scholar](#)

68. 68.

Hach, F. et al. mrsFAST: a cache-oblivious algorithm for short-read mapping. *Nat. Methods* **7**, 576–577 (2010).

[CAS](#) [PubMed](#) [PubMed Central](#) [Article](#) [Google Scholar](#)

69. 69.

Gymrek, M., Golan, D., Rosset, S. & Erlich, Y. lobSTR: A short tandem repeat profiler for personal genomes. *Genome Res.* **22**, 1154–1162 (2012).

[CAS](#) [PubMed](#) [PubMed Central](#) [Article](#) [Google Scholar](#)

70. 70.

Haaf, T. & Willard, H. F. Chromosome-specific alpha-satellite DNA from the centromere of chimpanzee chromosome 4. *Chromosoma* **106**, 226–232 (1997).

[CAS](#) [PubMed](#) [Article](#) [Google Scholar](#)

71. 71.

Iwata-Otsubo, A. et al. Expanded satellite repeats amplify a discrete CENP-A nucleosome assembly site on chromosomes that drive in female meiosis. *Curr. Biol.* **27**, 2365–2373.e8 (2017).

[CAS](#) [PubMed](#) [PubMed Central](#) [Article](#) [Google Scholar](#)

72. 72.

Logsdon, G. A. et al. Human artificial chromosomes that bypass centromeric DNA. *Cell* **178**, 624–639.e19 (2019).

[CAS](#) [PubMed](#) [PubMed Central](#) [Article](#) [Google Scholar](#)

73. 73.

Ventura, M. et al. Gorilla genome structural variation reveals evolutionary parallelisms with chimpanzee. *Genome Res.* **21**, 1640–1649 (2011).

[CAS](#) [PubMed](#) [PubMed Central](#) [Article](#) [Google Scholar](#)

74. 74.

Darby, I. A. *In Situ Hybridization Protocols* (Humana Press, 2000).

75. 75.

Martin, M. Cutadapt removes adapter sequences from high-throughput sequencing reads. *EMBnet.journal* **17**, 10–12 (2011).

[Article](#) [Google Scholar](#)

76. 76.

Li, H. Aligning sequence reads, clone sequences and assembly contigs with BWA-MEM. Preprint at <https://arxiv.org/abs/1303.3997> (2013).

77. 77.

Ramírez, F., Dündar, F., Diehl, S., Grüning, B. A. & Manke, T. deepTools: a flexible platform for exploring deep-sequencing data. *Nucleic Acids Res.* **42**, W187-91 (2014).

[PubMed](#) [PubMed Central](#) [Article](#) [CAS](#) [Google Scholar](#)

78. 78.

Smit, A. F. A., Hubley, R. & Green, P. *RepeatMasker Open-4.0* (2013).

79. 79.

Katoh, K. & Standley, D. M. MAFFT multiple sequence alignment software version 7: improvements in performance and usability. *Mol. Biol. Evol.* **30**, 772–780 (2013).

[CAS](#) [PubMed](#) [PubMed Central](#) [Article](#) [Google Scholar](#)

80. 80.

Nakamura, T., Yamada, K. D., Tomii, K. & Katoh, K. Parallelization of MAFFT for large-scale multiple sequence alignments. *Bioinformatics* **34**, 2490–2492 (2018).

[CAS](#) [PubMed](#) [PubMed Central](#) [Article](#) [Google Scholar](#)

81. 81.

Nguyen, L.-T., Schmidt, H. A., von Haeseler, A. & Minh, B. Q. IQ-TREE: a fast and effective stochastic algorithm for estimating maximum-likelihood phylogenies. *Mol. Biol. Evol.* **32**, 268–274 (2015).

[CAS](#) [PubMed](#) [PubMed Central](#) [Article](#) [Google Scholar](#)

82. 82.

Letunic, I. & Bork, P. Interactive Tree Of Life (iTOL): an online tool for phylogenetic tree display and annotation. *Bioinformatics* **23**, 127–128 (2007).

[CAS](#) [PubMed](#) [Article](#) [Google Scholar](#)

83. 83.

Tamura, K. & Nei, M. Estimation of the number of nucleotide substitutions in the control region of mitochondrial DNA in humans and chimpanzees. *Mol. Biol. Evol.* **10**, 512–526 (1993).

[CAS](#) [PubMed](#) [Google Scholar](#)

84. 84.

Kimura, M. *The Neutral Theory of Molecular Evolution* (Cambridge Univ. Press, 1983).

85. 85.

Numanagić, I. et al. Fast characterization of segmental duplications in genome assemblies. *Bioinformatics* **34**, i706–i714 (2018).

[PubMed](#) [PubMed Central](#) [Article](#) [CAS](#) [Google Scholar](#)

86. 86.

Landry, J. J. M. et al. The genomic and transcriptomic landscape of a HeLa cell line. *G3 (Bethesda)* **3**, 1213–1224 (2013).

[Article](#) [CAS](#) [Google Scholar](#)

[Download references](#)

Acknowledgements

We thank S. Goodwin for sequence data generation; M. Jain and D. Miller for re-base-calling sequence data; R. Tindell, H. Visse, A. Tornabene, and G. Ellis for technical assistance; Z. Zhao for computational assistance; F. F. Dastvan for instrumentation; D. Gordon for accessioning BACs; G. Bouffard for accessioning ONT FAST5 data; J. G. Underwood for discussions; and T. Brown for assistance in editing this manuscript. We acknowledge experimental support from the W. M. Keck Microscopy Center (UW) and the computational resources of the NIH HPC Biowulf cluster (<https://hpc.nih.gov>). This research was supported, in part, by funding from the National Institutes of Health (NIH), HG002385 and HG010169 (E.E.E.); National Institute of General Medical Sciences (NIGMS), F32 GM134558 (G.A.L.); Intramural Research Program of the National Human Genome Research Institute at NIH (S.K., A.M.P., A.R.); National Library of Medicine Big Data Training Grant for Genomics and Neuroscience 5T32LM012419-04 (M.R.V.); NIH/NHGRI Pathway to Independence Award K99 HG011041 (P.H.); NIH/NHGRI R21 1R21HG010548-01 and NIH/NHGRI U01 1U01HG010971 (K.H.M.); and the Intramural Research Program of the NIH, National Cancer Institute, Center for Cancer Research, USA (V.L.). E.E.E. is an investigator of the Howard Hughes Medical Institute.

Author information

Affiliations

1. Department of Genome Sciences, University of Washington School of Medicine, Seattle, WA, USA

Glennis A. Logsdon, Mitchell R. Vollger, PingHsun Hsieh, Yafei Mao, Philip C. Dishuck, David Porubsky, William T. Harvey, Kendra Hoekzema, Shwetha C. Murali, Katherine M. Munson, Carl Baker, Melanie Sorensen, Alexandra M. Lewis & Evan E. Eichler

2. Developmental Therapeutics Branch, National Cancer Institute, Bethesda, MD, USA
Mikhail A. Liskovskykh & Vladimir Larionov
3. Genome Informatics Section, Computational and Statistical Genomics Branch, National Human Genome Research Institute, National Institutes of Health, Bethesda, MD, USA
Sergey Koren, Sergey Nurk, Arang Rhie, Chirag Jain & Adam M. Phillippy
4. Department of Biology, University of Bari, Aldo Moro, Bari, Italy
Ludovica Mercuri & Mario Ventura
5. Stowers Institute for Medical Research, Kansas City, MO, USA
Leonardo G. de Lima & Jennifer L. Gerton
6. Center for Algorithmic Biotechnology, Institute of Translational Biomedicine, Saint Petersburg State University, Saint Petersburg, Russia
Tatiana Dvorkina & Alla Mikheenko
7. Graduate Program in Bioinformatics and Systems Biology, University of California, San Diego, San Diego, CA, USA
Andrey V. Bzikadze
8. McDonnell Genome Institute, Department of Genetics, Washington University School of Medicine, St Louis, MO, USA
Milinn Kremitzki & Tina A. Graves-Lindsay
9. Howard Hughes Medical Institute, University of Washington, Seattle, WA, USA

Shwetha C. Murali & Evan E. Eichler

10. Department of Pathology, University of Pittsburgh, Pittsburgh, PA,
USA

Urvashi Surti

11. Center for Biomolecular Science and Engineering, University of
California, Santa Cruz, Santa Cruz, CA, USA

Karen H. Miga

Authors

1. Glennis A. Logsdon

[View author publications](#)

You can also search for this author in [PubMed](#) [Google Scholar](#)

2. Mitchell R. Vollger

[View author publications](#)

You can also search for this author in [PubMed](#) [Google Scholar](#)

3. PingHsun Hsieh

[View author publications](#)

You can also search for this author in [PubMed](#) [Google Scholar](#)

4. Yafei Mao

[View author publications](#)

You can also search for this author in [PubMed](#) [Google Scholar](#)

5. Mikhail A. Liskovskykh

[View author publications](#)

You can also search for this author in [PubMed](#) [Google Scholar](#)

6. Sergey Koren

[View author publications](#)

You can also search for this author in [PubMed](#) [Google Scholar](#)

7. Sergey Nurk

[View author publications](#)

You can also search for this author in [PubMed](#) [Google Scholar](#)

8. Ludovica Mercuri

[View author publications](#)

You can also search for this author in [PubMed](#) [Google Scholar](#)

9. Philip C. Dishuck

[View author publications](#)

You can also search for this author in [PubMed](#) [Google Scholar](#)

10. Arang Rhie

[View author publications](#)

You can also search for this author in [PubMed](#) [Google Scholar](#)

11. Leonardo G. de Lima

[View author publications](#)

You can also search for this author in [PubMed](#) [Google Scholar](#)

12. Tatiana Dvorkina

[View author publications](#)

You can also search for this author in [PubMed](#) [Google Scholar](#)

13. David Porubsky

[View author publications](#)

You can also search for this author in [PubMed](#) [Google Scholar](#)

14. William T. Harvey

[View author publications](#)

You can also search for this author in [PubMed](#) [Google Scholar](#)

15. Alla Mikheenko

[View author publications](#)

You can also search for this author in [PubMed](#) [Google Scholar](#)

16. Andrey V. Bzikadze

[View author publications](#)

You can also search for this author in [PubMed](#) [Google Scholar](#)

17. Milinn Kremitzki

[View author publications](#)

You can also search for this author in [PubMed](#) [Google Scholar](#)

18. Tina A. Graves-Lindsay

[View author publications](#)

You can also search for this author in [PubMed](#) [Google Scholar](#)

19. Chirag Jain

[View author publications](#)

You can also search for this author in [PubMed](#) [Google Scholar](#)

20. Kendra Hoekzema

[View author publications](#)

You can also search for this author in [PubMed](#) [Google Scholar](#)

21. Shwetha C. Murali

[View author publications](#)

You can also search for this author in [PubMed](#) [Google Scholar](#)

22. Katherine M. Munson

[View author publications](#)

You can also search for this author in [PubMed](#) [Google Scholar](#)

23. Carl Baker

[View author publications](#)

You can also search for this author in [PubMed](#) [Google Scholar](#)

24. Melanie Sorensen

[View author publications](#)

You can also search for this author in [PubMed](#) [Google Scholar](#)

25. Alexandra M. Lewis

[View author publications](#)

You can also search for this author in [PubMed](#) [Google Scholar](#)

26. Urvashi Surti

[View author publications](#)

You can also search for this author in [PubMed](#) [Google Scholar](#)

27. Jennifer L. Gerton

[View author publications](#)

You can also search for this author in [PubMed](#) [Google Scholar](#)

28. Vladimir Larionov

[View author publications](#)

You can also search for this author in [PubMed](#) [Google Scholar](#)

29. Mario Ventura

[View author publications](#)

You can also search for this author in [PubMed](#) [Google Scholar](#)

30. Karen H. Miga

[View author publications](#)

You can also search for this author in [PubMed](#) [Google Scholar](#)

31. Adam M. Phillippy

[View author publications](#)

You can also search for this author in [PubMed](#) [Google Scholar](#)

32. Evan E. Eichler

[View author publications](#)

You can also search for this author in [PubMed](#) [Google Scholar](#)

Contributions

G.A.L. and E.E.E. conceived the project; G.A.L., K.H., K.M.M., A.M.L., C.B. and M.S. generated long-read sequencing data; G.A.L., M.R.V., P.H., Y.M., S.K., S.N., P.C.D., A.R., T.D., D.P., W.T.H., A.M., A.V.B., M.K., T.A.G.-L., C.J., S.C.M., K.H.M. and A.M.P. analysed sequencing data, created genome assemblies, and performed quality control analyses; G.A.L., M.R.V., S.K., A.M.P. and S.N. finalized the chromosome 8 assembly; G.A.L., S.K., S.N., A.M., A.V.B. and K.H.M. assessed the assembly of the centromere; M.A.L. generated pulsed-field gel Southern blots; G.A.L., L.M. and M.V. generated microscopy data; L.G.D. generated and analysed droplet digital PCR data; U.S. provided the CHM13 cell line; J.L.G. and V.L. supervised experimental analyses; G.A.L., M.R.V., D.P. and E.E.E. developed the figures; and G.A.L. and E.E.E. drafted the manuscript.

Corresponding author

Correspondence to [Evan E. Eichler](#).

Ethics declarations

Competing interests

The authors declare no competing interests.

Additional information

Peer review information *Nature* thanks Amanda Larracuente, Jeremiah Smith, Nils Stein and the other, anonymous, reviewer(s) for their contribution to the peer review of this work. Peer review reports are available.

Publisher's note Springer Nature remains neutral with regard to jurisdictional claims in published maps and institutional affiliations.

Extended data figures and tables

[Extended Data Fig. 1 Sequence, structure and epigenetic map of the neocentromeric chromosome 8q21.2 VNTR.](#)

a, Schematic showing the composition of the CHM13 8q21.2 VNTR. This VNTR consists of 67 full and 7 partial 12.192-kb repeats that span 863 kb in total. The predicted restriction digest pattern is indicated. Each repeat is methylated within a 3-kb region and hypomethylated within the rest of the sequence. Mapping of CENP-A ChIP-seq data from the chromosome 8 neodicentric cell line known as MS4221^{24,25} (Methods) reveals that approximately 98% of CENP-A chromatin is located within the hypomethylated portion of the repeat. A pairwise sequence identity heat map across the region indicates a mirrored symmetry within a single layer, consistent with the evolutionarily young status of the tandem repeat. **b**, Pulsed-field gel Southern blot of CHM13 DNA digested with BmgBI confirms the size and organization of the chromosome 8q21.2 VNTR. Left, ethidium bromide staining; right, ³²P-labelled chromosome 8q21.2-specific probe. For gel source data, see Supplementary Fig. [1c](#). **c**, Copy number of the 8q21 repeat (chr8:85792897–85805090 in GRCh38) throughout the human population. CHM13 is estimated to have 144 total copies of the 8q21 repeat, or 72 copies per haplotype, whereas GRCh38 only has 26 copies (red data points). Median ± s.d. is shown.

Extended Data Fig. 2 CHM13 chromosome 8 telomeres.

a, Schematic showing the first and last megabase of the CHM13 chromosome 8 assembly. A dot plot of the terminal 5 kb shows high sequence identity among the last approximately 2.5 kb of the chromosome, consistent with the presence of a high-identity telomeric repeating unit. **b, c**, Number of TTAGGG telomeric repeats in the last 5 kb of the p-arm (**b**) and q-arm (**c**) in chromosome 8. The p-arm has a gradual transition to pure TTAGGG repeats over nearly 1 kb, whereas the q-arm has a very sharp transition to pure TTAGGG repeats that occurs over nearly 300 bp.

Extended Data Fig. 3 Genes with improved alignment to the CHM13 chromosome 8 assembly relative to GRCh38.

a, Ideogram of chromosome 8 showing protein-coding genes with improved transcript alignments to the CHM13 chromosome 8 assembly relative to GRCh38 (hg38). Each gene is labelled with its name, count of improved transcripts from the CHM13 cell line, count of improved transcripts from other tissues, the average percent improvement of non-CHM13 cell line alignments, and the number of tissue sources with improved transcript mappings. **b, c**, Differential percentage sequence identity of transcripts aligning to CHM13 or GRCh38 for CHM13 cell line transcripts (**b**) and non-CHM13 cell line transcripts (**c**). **d–f**, Multiple-sequence alignments for *WDYHV1* (**d**), *MCPH1* (**e**) and *PCMTD1* (**f**), all of which have at least 0.1% greater sequence identity of >20 full-length Iso-Seq transcripts to the CHM13 chromosome 8 assembly than to GRCh38 (Methods). For each gene, the GRCh38 annotation is compared to the same annotation lifted over to the CHM13 chromosome 8 assembly, and the substitutions are confirmed by translated predicted open reading frames from Iso-Seq transcripts. Matching amino acids are shaded in grey, those matching only the Iso-Seq data are in red, and those different from the Iso-Seq data are in blue. Each substitution in CHM13 relative to GRCh38 has an allele frequency of 0.36 in gnomAD (v3). **g**, Location of *DEFA* and *DEFB* genes in the CHM13 chromosome 8 β-defensin locus. Segmental duplication regions were identified by SEDEF⁸⁵, and new paralogues are shown in red. Duplication cassettes are marked with arrows indicating orientation for each copy.

Extended Data Fig. 4 Comparison of the CHM13 and GRCh38 β-defensin loci.

Miropeats comparison of the CHM13 and GRCh38 β-defensin loci identifies a 4.11-Mb inverted region (dashed grey line) bracketed by proximal and distal segmental duplications (dup; black and blue arrows) in CHM13. CHM13 also has an additional segmental duplication (blue arrow) relative to the GRCh38. In total, the CHM13 haplotype adds 611.9 kb of new sequence, of which 602.6 kb is located within segmental duplications and 9.3 kb is located at the distal edge of the inverted region. Coloured segments track blocks of homology between CHM13 and GRCh38.

Extended Data Fig. 5 Validation of the CHM13 β-defensin locus, and copy number of the *DEFA* gene family.

a, Coverage of CHM13 ONT and PacBio HiFi data along the CHM13 β-defensin locus (top two panels). The ONT and PacBio data have largely uniform coverage, indicating it is free of large structural errors. The dip in HiFi coverage near position 10.46 Mb is due to a G/A bias in HiFi chemistry⁵. The alignment of 47 CHM13 BACs (bottom) reveals that those regions have an estimated quality value score >25 (>99.7% accurate). **b**, Copy number of *DEFA* (chr8:6976264–6995380 in GRCh38 (hg38)) throughout the human population. Median ± s.d. is shown.

Extended Data Fig. 6 Validation of the CHM13 chromosome 8 centromeric region.

a, Coverage of CHM13 ONT and PacBio HiFi data along the CHM13 chromosome 8 centromeric region (top two panels) is largely uniform, indicating a lack of large structural errors. Analysis with TandemMapper and TandemQUAST⁵², which are tools that assess repeat structure via mapped reads (third panel) and misassembly breakpoints (fourth panel; red), indicates that the chromosome 8 D8Z2 α-satellite HOR array lacks large-scale assembly errors. Five different FISH probes targeting regions in the chromosome 8 centromeric region (bottom) are used to confirm the organization of the α-satellite DNA (**b, c**). **b, c**, Representative images of

metaphase chromosome spreads hybridized with FISH probes targeting regions within the chromosome 8 centromere (**a**). Insets show both chromosome 8s with the predicted organization of the centromeric region. **d**, Droplet digital PCR of the chromosome 8 D8Z2 α -satellite array indicates that there are $1,344 \pm 142$ D8Z2 HORs present on chromosome 8, consistent with the predictions from an *in silico* restriction digest and StringDecomposer⁴² analysis (Methods). Mean \pm s.d. is shown. Scale bar, 5 μm . Insets, 2.5 \times magnification.

Extended Data Fig. 7 Sequence, structure and epigenetic map of human diploid HG00733 chromosome 8 centromeres.

a, b, Repeat structure, α -satellite organization, methylation status and sequence identity heat map of the maternal (**a**) and paternal (**b**) chromosome 8 centromeric regions from a diploid human genome (HG00733; Supplementary Table 2) shows structural and epigenetic similarity to the CHM13 chromosome 8 centromeric region (Fig. 2a). **c–e**, Dot plot comparisons between the CHM13 and maternal (**c**), CHM13 and paternal (**d**), and maternal and paternal (**e**) chromosome 8 centromeric regions in the HG00733 genome show more than 99% sequence identity overall, with high concordance in the unique and monomeric α -satellite regions of the centromeres (dark red line) that devolves into lower sequence identity in the α -satellite HOR array, consistent with rapid evolution of this region.

Extended Data Fig. 8 Composition, organization and entropy of the CHM13 D8Z2 α -satellite HOR array.

a, HOR composition and organization of the chromosome 8 α -satellite array as determined via StringDecomposer⁴². The predominant HOR subtypes (4-, 7-, 8- and 11-monomer HORs) are shown, whereas those occurring less than 15 times are not (see [Methods](#) for absolute quantification). The entropy of the D8Z2 HOR array is plotted in the bottom panel and reveals that the hypomethylated and CENP-A-enriched regions have the highest consistent entropy in the entire array. **b**, Organization of α -satellite monomers within each HOR. The initial monomer of the 4- and 7-monomer HORs is a hybrid

of the A and E monomers, with the first 87 bp the A monomer and the subsequent 84 bp the E monomer. **c**, Abundance of the predominant HOR types within the D8Z2 HOR array as determined via StringDecomposer⁴².

Extended Data Fig. 9 Location of CENP-A chromatin within the CHM13 D8Z2 α -satellite HOR array.

a, b, Plot of the ratio of CENP-A ChIP to bulk nucleosome reads mapped via BWA-MEM (**a**), or the number of k -mer-mapped CENP-A ChIPs (black) or bulk nucleosome (dark grey) reads (**b**) (Methods). Shown are two independent replicates of CENP-A ChIP-seq performed on CHM13 cells (top two panels), as well as single replicates of CENP-A ChIP-seq performed on human diploid neocentromeric cell lines (bottom two panels; Methods). Although the neocentromeric cell lines have a neocentromere located on either chromosome 13 (IMS13q) or 8 (MS4221)^{24,25}, they both have at least one karyotypically normal chromosome 8 from which centromeric chromatin can be mapped. We limited our analysis to diploid cell lines rather than aneuploid ones to avoid potentially confounding results stemming from multiple chromosome 8 copies that vary in structure, such as those observed in HeLa cells⁸⁶.

Extended Data Fig. 10 Validation of the CHM13 8q21.2 VNTR.

a, Coverage of CHM13 ONT and PacBio HiFi data along the 8q21.2 VNTR (top two panels) is largely uniform, indicating a lack of large structural errors. Two FISH probes targeting the 12.192-kb repeat in the 8q21.2 VNTR are used to estimate the number of repeats in the CHM13 genome (**b, c**). **b**, Representative FISH images of a CHM13 stretched chromatin fibre. Although the FISH probes were designed against the entire VNTR array, stringent washing during FISH produces a punctate probe signal pattern, which may be due to stronger hybridization of the probe to a specific region in the 12.192-kb repeat (perhaps based on GC content or a lack of secondary structures). This punctate pattern can be used to estimate the repeat copy number in the VNTR, thereby serving as a source of validation. **c**, Plot of the signal intensity on the CHM13 chromatin fibre shown in **b**. Quantification of peaks across three independent experiments

reveals an average of 63 ± 7.55 peaks and 67 ± 5.20 peaks (mean \pm s.d.) from the green and red probes, respectively, which is consistent with the number of repeat units in the 8q21.2 assembly (67 full and 7 partial repeats). Scale bar, 5 μm .

Supplementary information

Supplementary Information

This file contains Supplementary Figures 1-11, Supplementary Tables 3-5, 7 and Supplementary References.

Reporting Summary

Peer Review File

Supplementary Table 1

Genes with greater sequence identity to CHM13 chromosome 8 than GRCh38.

Supplementary Table 2

Differences in CHM13 and GRCh38 (hg38) chromosome 8 DEFA and DEFB genes.

Supplementary Table 6

CHM13 chromosome 8 centromeric mutation rate.

Supplementary Table 8

PacBio Iso-Seq datasets.

Supplementary Table 9

Datasets generated and/or used in this study.

Supplementary Table 10

CHM13 BACs used in this study.

Rights and permissions

Open Access This article is licensed under a Creative Commons Attribution 4.0 International License, which permits use, sharing, adaptation, distribution and reproduction in any medium or format, as long as you give appropriate credit to the original author(s) and the source, provide a link to the Creative Commons license, and indicate if changes were made. The images or other third party material in this article are included in the article's Creative Commons license, unless indicated otherwise in a credit line to the material. If material is not included in the article's Creative Commons license and your intended use is not permitted by statutory regulation or exceeds the permitted use, you will need to obtain permission directly from the copyright holder. To view a copy of this license, visit <http://creativecommons.org/licenses/by/4.0/>.

Reprints and Permissions

About this article



Check for
updates

Cite this article

Logsdon, G.A., Vollger, M.R., Hsieh, P. *et al.* The structure, function and evolution of a complete human chromosome 8. *Nature* **593**, 101–107 (2021). <https://doi.org/10.1038/s41586-021-03420-7>

Download citation

- Received: 04 September 2020
- Accepted: 04 March 2021
- Published: 07 April 2021
- Issue Date: 06 May 2021
- DOI: <https://doi.org/10.1038/s41586-021-03420-7>

Further reading

- **Sequence, Chromatin and Evolution of Satellite DNA**
 - Jitendra Thakur
 - , Jenika Packiaraj
 - & Steven Henikoff
- **Genomic Tackling of Human Satellite DNA: Breaking Barriers through Time**
 - Mariana Lopes
 - , Sandra Louzada
 - , Margarida Gama-Carvalho
 - & Raquel Chaves
- **Towards complete and error-free genome assemblies of all vertebrate species**
 - Arang Rhie
 - , Shane A. McCarthy
 - , Olivier Fedrigo
 - , Joana Damas

- , Giulio Formenti
- , Sergey Koren
- , Marcela Uliano-Silva
- , William Chow
- , Arkarachai Fungtammasan
- , Juwan Kim
- , Chul Lee
- , Byung June Ko
- , Mark Chaisson
- , Gregory L. Gedman
- , Lindsey J. Cantin
- , Francoise Thibaud-Nissen
- , Leanne Haggerty
- , Iliana Bista
- , Michelle Smith
- , Bettina Haase
- , Jacquelyn Mountcastle
- , Sylke Winkler
- , Sadye Paez
- , Jason Howard
- , Sonja C. Vernes
- , Tanya M. Lama
- , Frank Grutzner
- , Wesley C. Warren
- , Christopher N. Balakrishnan
- , Dave Burt
- , Julia M. George
- , Matthew T. Biegler
- , David Iorns
- , Andrew Digby
- , Daryl Eason
- , Bruce Robertson
- , Taylor Edwards
- , Mark Wilkinson
- , George Turner
- , Axel Meyer
- , Andreas F. Kautt

- , Paolo Franchini
- , H. William Detrich
- , Hannes Svardal
- , Maximilian Wagner
- , Gavin J. P. Naylor
- , Martin Pippel
- , Milan Malinsky
- , Mark Mooney
- , Maria Simbirsky
- , Brett T. Hannigan
- , Trevor Pesout
- , Marlys Houck
- , Ann Misuraca
- , Sarah B. Kingan
- , Richard Hall
- , Zev Kronenberg
- , Ivan Sović
- , Christopher Dunn
- , Zemin Ning
- , Alex Hastie
- , Joyce Lee
- , Siddarth Selvaraj
- , Richard E. Green
- , Nicholas H. Putnam
- , Ivo Gut
- , Jay Ghurye
- , Erik Garrison
- , Ying Sims
- , Joanna Collins
- , Sarah Pelan
- , James Torrance
- , Alan Tracey
- , Jonathan Wood
- , Robel E. Dagnew
- , Dengfeng Guan
- , Sarah E. London
- , David F. Clayton

- , Claudio V. Mello
- , Samantha R. Friedrich
- , Peter V. Lovell
- , Ekaterina Osipova
- , Farooq O. Al-Ajli
- , Simona Secomandi
- , Heebal Kim
- , Constantina Theofanopoulou
- , Michael Hiller
- , Yang Zhou
- , Robert S. Harris
- , Kateryna D. Makova
- , Paul Medvedev
- , Jinna Hoffman
- , Patrick Masterson
- , Karen Clark
- , Fergal Martin
- , Kevin Howe
- , Paul Fllicek
- , Brian P. Walenz
- , Woori Kwak
- , Hiram Clawson
- , Mark Diekhans
- , Luis Nassar
- , Benedict Paten
- , Robert H. S. Kraus
- , Andrew J. Crawford
- , M. Thomas P. Gilbert
- , Guojie Zhang
- , Byrappa Venkatesh
- , Robert W. Murphy
- , Klaus-Peter Koepfli
- , Beth Shapiro
- , Warren E. Johnson
- , Federica Di Palma
- , Tomas Marques-Bonet
- , Emma C. Teeling

- , Tandy Warnow
- , Jennifer Marshall Graves
- , Oliver A. Ryder
- , David Haussler
- , Stephen J. O'Brien
- , Jonas Korlach
- , Harris A. Lewin
- , Kerstin Howe
- , Eugene W. Myers
- , Richard Durbin
- , Adam M. Phillippy
- & Erich D. Jarvis

Nature (2021)

Comments

By submitting a comment you agree to abide by our [Terms](#) and [Community Guidelines](#). If you find something abusive or that does not comply with our terms or guidelines please flag it as inappropriate.

[Download PDF](#)

This article was downloaded by **calibre** from <https://www.nature.com/articles/s41586-021-03420-7>

- Article
- [Published: 31 March 2021](#)

Flexible scaling and persistence of social vocal communication

- [Jingyi Chen^{1,2}](#),
- [Jeffrey E. Markowitz³](#),
- [Varoth Lilascharoen](#) [ORCID: orcid.org/0000-0002-9732-9966⁴](#),
- [Sandra Taylor¹](#),
- [Pete Sheurpukdi¹](#),
- [Jason A. Keller](#) [ORCID: orcid.org/0000-0001-9839-7293⁵](#),
- [Jennifer R. Jensen](#) [ORCID: orcid.org/0000-0002-3347-8911¹](#),
- [Byung Kook Lim](#) [ORCID: orcid.org/0000-0002-3766-5415⁶](#),
- [Sandeep Robert Datta](#) [ORCID: orcid.org/0000-0002-8068-3862³](#) &
- [Lisa Stowers](#) [ORCID: orcid.org/0000-0002-4403-1269¹](#)

[Nature](#) volume 593, pages108–113(2021)[Cite this article](#)

- 4031 Accesses
- 79 Altmetric
- [Metrics details](#)

Subjects

- [Limbic system](#)
- [Neural circuits](#)
- [Social behaviour](#)

Abstract

Innate vocal sounds such as laughing, screaming or crying convey one's feelings to others. In many species, including humans, scaling the amplitude and duration of vocalizations is essential for effective social communication^{1,2,3}. In mice, female scent triggers male mice to emit innate courtship ultrasonic vocalizations (USVs)^{4,5}. However, whether mice flexibly scale their vocalizations and how neural circuits are structured to generate flexibility remain largely unknown. Here we identify mouse neurons from the lateral preoptic area (LPOA) that express oestrogen receptor 1 (LPOA^{ESR1} neurons) and, when activated, elicit the complete repertoire of USV syllables emitted during natural courtship. Neural anatomy and functional data reveal a two-step, di-synaptic circuit motif in which primary long-range inhibitory LPOA^{ESR1} neurons relieve a clamp of local periaqueductal grey (PAG) inhibition, enabling excitatory PAG USV-gating neurons to trigger vocalizations. We find that social context shapes a wide range of USV amplitudes and bout durations. This variability is absent when PAG neurons are stimulated directly; PAG-evoked vocalizations are time-locked to neural activity and stereotypically loud. By contrast, increasing the activity of LPOA^{ESR1} neurons scales the amplitude of vocalizations, and delaying the recovery of the inhibition clamp prolongs USV bouts. Thus, the LPOA disinhibition motif contributes to flexible loudness and the duration and persistence of bouts, which are key aspects of effective vocal social communication.

[Access through your institution](#)

[Change institution](#)

[Buy or subscribe](#)

Access options

Subscribe to Journal

Get full journal access for 1 year

\$199.00

only \$3.90 per issue

Subscribe

All prices are NET prices.

VAT will be added later in the checkout.

Tax calculation will be finalised during checkout.

Rent or Buy article

Get time limited or full article access on ReadCube.

from \$8.99

Rent or Buy

All prices are NET prices.

Additional access options:

- [Log in](#)
- [Access through your institution](#)
- [Learn about institutional subscriptions](#)

Fig. 1: Hypothalamic LPOA^{ESR1} neurons underlie USV social calling.



Fig. 2: LPOA^{VGAT}–PAG^{VGAT}–PAG^{VGLUT2} di-synaptic disinhibition circuit triggers USVs.

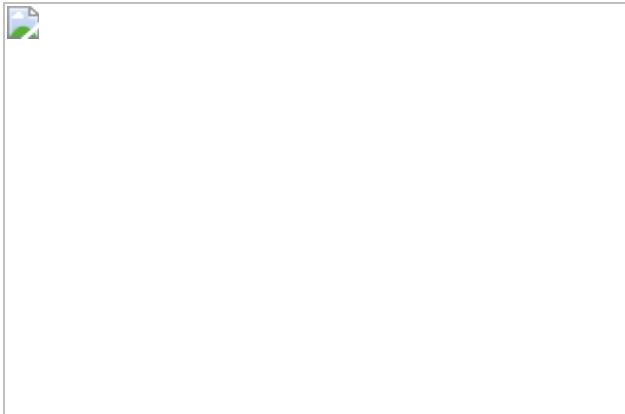
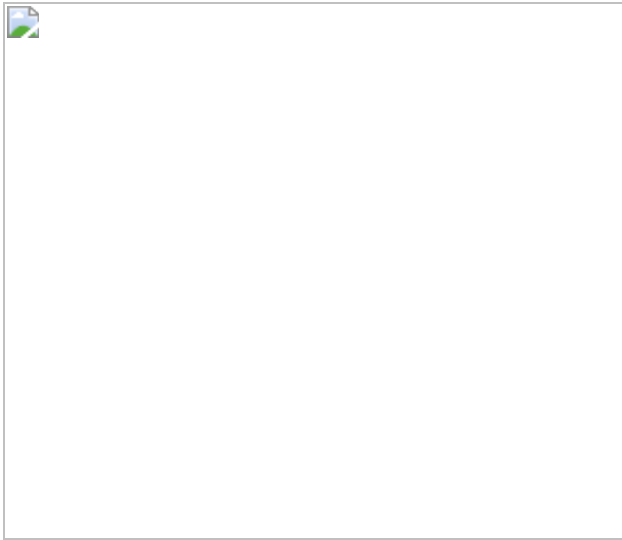


Fig. 3: LPOA^{ESR1} neuron activity scales USV amplitude and bout duration.



Fig. 4: Vocal persistence is generated through activity of local PAG^{VGAT} neurons.



Data availability

The data in this study are available from the corresponding author upon request. [Source data](#) are provided with this paper.

Code availability

All analysis code are available on GitHub:

https://github.com/stowerslab/USV_Analysis_Code.git.

References

1. 1.

Bachorowski, J. A. & Owren, M. J. Not all laughs are alike: voiced but not unvoiced laughter readily elicits positive affect. *Psychol. Sci.* **12**, 252–257 (2001).

[CAS](#) [PubMed](#) [Article](#) [PubMed Central](#) [Google Scholar](#)

2. 2.

Darwin, C. & Progger, P. *The Expression of the Emotions in Man and Animals* 3rd edn (Harper Collins, 1998).

3. 3.

Esposito, G., Nakazawa, J., Venuti, P. & Bornstein, M. H. Judgment of infant cry: the roles of acoustic characteristics and sociodemographic characteristics. *Jpn. Psychol. Res.* **57**, 126–134 (2015).

[PubMed](#) [Article](#) [PubMed Central](#) [Google Scholar](#)

4. 4.

Holy, T. E. & Guo, Z. Ultrasonic songs of male mice. *PLoS Biol.* **3**, e386 (2005).

[PubMed](#) [PubMed Central](#) [Article](#) [CAS](#) [Google Scholar](#)

5. 5.

Whitney, G., Alpern, M., Dizinno, G. & Horowitz, G. Female odors evoke ultrasounds from male mice. *Anim. Learn. Behav.* **2**, 13–18 (1974).

[CAS](#) [PubMed](#) [Article](#) [PubMed Central](#) [Google Scholar](#)

6. 6.

Keller, J. A. et al. Voluntary urination control by brainstem neurons that relax the urethral sphincter. *Nat. Neurosci.* **21**, 1229–1238 (2018).

[CAS](#) [PubMed](#) [PubMed Central](#) [Article](#) [Google Scholar](#)

7. 7.

Brainard, M. S. & Doupe, A. J. Translating birdsong: songbirds as a model for basic and applied medical research. *Annu. Rev. Neurosci.* **36**, 489–517 (2013).

[CAS](#) [PubMed](#) [PubMed Central](#) [Article](#) [Google Scholar](#)

8. 8.

Jarvis, E. D. Evolution of vocal learning and spoken language. *Science* **366**, 50–54 (2019).

[ADS](#) [CAS](#) [PubMed](#) [Article](#) [PubMed Central](#) [Google Scholar](#)

9. 9.

Gao, S. C., Wei, Y. C., Wang, S. R. & Xu, X. H. Medial Preoptic Area Modulates Courtship Ultrasonic Vocalization in Adult Male Mice. *Neurosci. Bull.* **35**, 697–708 (2019).

[PubMed](#) [PubMed Central](#) [Article](#) [Google Scholar](#)

10. 10.

Karigo, T. et al. Distinct hypothalamic control of same- and opposite-sex mounting behaviour in mice. *Nature* **589**, 258–263 (2020).

11. 11.

Michael, V. et al. Circuit and synaptic organization of forebrain-to-midbrain pathways that promote and suppress vocalization. *eLife* **9**, e63493 (2020).

[CAS](#) [PubMed](#) [PubMed Central](#) [Article](#) [Google Scholar](#)

12. 12.

Fang, Y. Y., Yamaguchi, T., Song, S. C., Tritsch, N. X. & Lin, D. A hypothalamic midbrain pathway essential for driving maternal behaviors. *Neuron* **98**, 192–207.e110 (2018).

[CAS](#) [PubMed](#) [PubMed Central](#) [Article](#) [Google Scholar](#)

13. 13.

Moffitt, J. R. et al. Molecular, spatial, and functional single-cell profiling of the hypothalamic preoptic region. *Science* **362**, eaau5324 (2018).

[ADS](#) [PubMed](#) [PubMed Central](#) [Article](#) [CAS](#) [Google Scholar](#)

14. 14.

Maggio, J. C. & Whitney, G. Ultrasonic vocalizing by adult female mice (*Mus musculus*). *J. Comp. Psychol.* **99**, 420–436 (1985).

[CAS](#) [PubMed](#) [Article](#) [Google Scholar](#)

15. 15.

Van Segbroeck, M., Knoll, A. T., Levitt, P. & Narayanan, S. MUPET-Mouse Ultrasonic Profile ExTraktion: A signal processing tool for rapid and unsupervised analysis of ultrasonic vocalizations. *Neuron* **94**, 465–485.e465, (2017).

[PubMed](#) [PubMed Central](#) [Article](#) [CAS](#) [Google Scholar](#)

16. 16.

Arriaga, G., Zhou, E. P. & Jarvis, E. D. Of mice, birds, and men: the mouse ultrasonic song system has some features similar to humans and song-learning birds. *PLoS ONE* **7**, e46610 (2012).

[ADS](#) [CAS](#) [PubMed](#) [PubMed Central](#) [Article](#) [Google Scholar](#)

17. 17.

Tschida, K. et al. A specialized neural circuit gates social vocalizations in the mouse. *Neuron* **103**, 459–472.e454 (2019).

[CAS](#) [PubMed](#) [PubMed Central](#) [Article](#) [Google Scholar](#)

18. 18.

Kohl, J. et al. Functional circuit architecture underlying parental behaviour. *Nature* **556**, 326–331 (2018).

[ADS](#) [CAS](#) [PubMed](#) [PubMed Central](#) [Article](#) [Google Scholar](#)

19. 19.

Tovote, P. et al. Midbrain circuits for defensive behaviour. *Nature* **534**, 206–212 (2016).

[ADS](#) [CAS](#) [PubMed](#) [Article](#) [Google Scholar](#)

20. 20.

Doupe, A. J. & Kuhl, P. K. Birdsong and human speech: common themes and mechanisms. *Annu. Rev. Neurosci.* **22**, 567–631 (1999).

[CAS](#) [PubMed](#) [Article](#) [PubMed Central](#) [Google Scholar](#)

21. 21.

Sainburg, T., Theilman, B., Thiels, M. & Gentner, T. Q. Parallels in the sequential organization of birdsong and human speech. *Nat. Commun.* **10**, 3636 (2019).

[ADS](#) [PubMed](#) [PubMed Central](#) [Article](#) [CAS](#) [Google Scholar](#)

22. 22.

Chabout, J., Sarkar, A., Dunson, D. B. & Jarvis, E. D. Male mice song syntax depends on social contexts and influences female preferences. *Front. Behav. Neurosci.* **9**, 76 (2015).

[PubMed](#) [PubMed Central](#) [Article](#) [Google Scholar](#)

23. 23.

Castellucci, G. A., Calbick, D. & McCormick, D. The temporal organization of mouse ultrasonic vocalizations. *PLoS ONE* **13**,

e0199929 (2018).

[PubMed](#) [PubMed Central](#) [Article](#) [CAS](#) [Google Scholar](#)

24. 24.

Guo, Z. & Holy, T. E. Sex selectivity of mouse ultrasonic songs. *Chem. Senses* **32**, 463–473 (2007).

[PubMed](#) [Article](#) [PubMed Central](#) [Google Scholar](#)

25. 25.

Nyby, J., Wysocki, C. J., Whitney, G., Dizinno, G. & Schneider, J. Elicitation of male mouse ultrasonic vocalizations: I. Urinary cues. *J. Comp. Physiol. Psychol.* **93**, 957–975 (1979).

[Article](#) [Google Scholar](#)

26. 26.

Sirotin, Y. B., Costa, M. E. & Laplagne, D. A. Rodent ultrasonic vocalizations are bound to active sniffing behavior. *Front. Behav. Neurosci.* **8**, 399 (2014).

[PubMed](#) [PubMed Central](#) [Article](#) [Google Scholar](#)

27. 27.

Hefft, S. & Jonas, P. Asynchronous GABA release generates long-lasting inhibition at a hippocampal interneuron-principal neuron synapse. *Nat. Neurosci.* **8**, 1319–1328 (2005).

[CAS](#) [PubMed](#) [Article](#) [PubMed Central](#) [Google Scholar](#)

28. 28.

Atasoy, D., Betley, J. N., Su, H. H. & Sternson, S. M. Deconstruction of a neural circuit for hunger. *Nature* **488**, 172–177 (2012).

[ADS](#) [CAS](#) [PubMed](#) [PubMed Central](#) [Article](#) [Google Scholar](#)

29. 29.

Letzkus, J. J., Wolff, S. B. & Lüthi, A. Disinhibition, a circuit mechanism for associative learning and memory. *Neuron* **88**, 264–276 (2015).

[CAS](#) [PubMed](#) [Article](#) [PubMed Central](#) [Google Scholar](#)

30. 30.

Chabout, J., Jones-Macopson, J. & Jarvis, E. D. Eliciting and analyzing male mouse ultrasonic vocalization (USV) songs. *J. Vis. Exp.* <https://doi.org/10.3791/54137> (2017).

31. 31.

Yin, X. et al. Maternal deprivation influences pup ultrasonic vocalizations of C57BL/6J mice. *PLoS ONE* **11**, e0160409 (2016).

[PubMed](#) [PubMed Central](#) [Article](#) [CAS](#) [Google Scholar](#)

32. 32.

Cetin, A. & Callaway, E. M. Optical control of retrogradely infected neurons using drug-regulated “TLoop” lentiviral vectors. *J. Neurophysiol.* **111**, 2150–2159 (2014).

[CAS](#) [PubMed](#) [PubMed Central](#) [Article](#) [Google Scholar](#)

33. 33.

Knowland, D. et al. Distinct ventral pallidal neural populations mediate separate symptoms of depression. *Cell* **170**, 284–297 (2017).

[CAS](#) [PubMed](#) [PubMed Central](#) [Article](#) [Google Scholar](#)

34. 34.

Kim, C. K. et al. Simultaneous fast measurement of circuit dynamics at multiple sites across the mammalian brain. *Nat. Methods* **13**, 325–328 (2016).

[PubMed](#) [PubMed Central](#) [Article](#) [CAS](#) [Google Scholar](#)

35. 35.

Xue, M., Atallah, B. V. & Scanziani, M. Equalizing excitation-inhibition ratios across visual cortical neurons. *Nature* **511**, 596–600 (2014).

[ADS](#) [CAS](#) [PubMed](#) [PubMed Central](#) [Article](#) [Google Scholar](#)

36. 36.

Hurst, J. L. & Beynon, R. J. Scent wars: the chemobiology of competitive signalling in mice. *BioEssays* **26**, 1288–1298 (2004).

[CAS](#) [PubMed](#) [Article](#) [PubMed Central](#) [Google Scholar](#)

37. 37.

Nyby, J. et al. Stimuli for male mouse (*Mus musculus*) ultrasonic courtship vocalizations: presence of female chemosignals and/or absence of male chemosignals. *J. Comp. Physiol. Psychol.* **95**, 623–629 (1981).

[CAS](#) [PubMed](#) [Article](#) [PubMed Central](#) [Google Scholar](#)

38. 38.

Reynolds, E. Urination as a social response in mice. *Nature* **234**, 481–483 (1971).

[ADS](#) [CAS](#) [PubMed](#) [Article](#) [PubMed Central](#) [Google Scholar](#)

39. 39.

Gordon-Fennell, A. G. et al. The lateral preoptic area: a novel regulator of reward seeking and neuronal activity in the ventral tegmental area. *Front. Neurosci.* **13**, 1433 (2020).

[PubMed](#) [PubMed Central](#) [Article](#) [Google Scholar](#)

40. 40.

Hileman, S. M., McManus, C. J., Goodman, R. L. & Jansen, H. T. Neurons of the lateral preoptic area/rostral anterior hypothalamic area are required for photoperiodic inhibition of estrous cyclicity in sheep. *Biol. Reprod.* **85**, 1057–1065 (2011).

[CAS](#) [PubMed](#) [PubMed Central](#) [Article](#) [Google Scholar](#)

41. 41.

Ono, T., Nakamura, K., Nishijo, H. & Fukuda, M. Hypothalamic neuron involvement in integration of reward, aversion, and cue signals. *J. Neurophysiol.* **56**, 63–79 (1986).

[CAS](#) [PubMed](#) [Article](#) [Google Scholar](#)

42. 42.

Osaka, T. et al. Lateral preoptic neurons inhibit thirst in the rat. *Brain Res. Bull.* **31**, 135–144 (1993).

[CAS](#) [PubMed](#) [Article](#) [PubMed Central](#) [Google Scholar](#)

43. 43.

Szymusiak, R., Gvilia, I. & McGinty, D. Hypothalamic control of sleep. *Sleep Med.* **8**, 291–301 (2007).

[PubMed](#) [Article](#) [PubMed Central](#) [Google Scholar](#)

44. 44.

Pomerantz, S. M., Nunez, A. A. & Bean, N. J. Female behavior is affected by male ultrasonic vocalizations in house mice. *Physiol. Behav.* **31**, 91–96 (1983).

[CAS](#) [PubMed](#) [Article](#) [PubMed Central](#) [Google Scholar](#)

45. 45.

Sangiamo, D. T., Warren, M. R. & Neunuebel, J. P. Ultrasonic signals associated with different types of social behavior of mice. *Nat. Neurosci.* **23**, 411–422 (2020).

[CAS](#) [PubMed](#) [PubMed Central](#) [Article](#) [Google Scholar](#)

46. 46.

Neunuebel, J. P., Taylor, A. L., Arthur, B. J. & Egnor, S. E. Female mice ultrasonically interact with males during courtship displays. *eLife* **4**, (2015).

47. 47.

Kohl, J. & Dulac, C. Neural control of parental behaviors. *Curr. Opin. Neurobiol.* **49**, 116–122 (2018).

[CAS](#) [PubMed](#) [PubMed Central](#) [Article](#) [Google Scholar](#)

48. 48.

Tan, C. L. & Knight, Z. A. Regulation of body temperature by the nervous system. *Neuron* **98**, 31–48 (2018).

[CAS](#) [PubMed](#) [PubMed Central](#) [Article](#) [Google Scholar](#)

49. 49.

Yu, S., François, M., Huesing, C. & Münzberg, H. The hypothalamic preoptic area and body weight control. *Neuroendocrinology* **106**, 187–194 (2018).

[CAS](#) [PubMed](#) [Article](#) [PubMed Central](#) [Google Scholar](#)

50. 50.

Jürgens, U. The role of the periaqueductal grey in vocal behaviour. *Behav. Brain Res.* **62**, 107–117 (1994).

[PubMed](#) [Article](#) [PubMed Central](#) [Google Scholar](#)

51. 51.

Jürgens, U. The neural control of vocalization in mammals: a review. *J. Voice* **23**, 1–10 (2009).

[PubMed](#) [Article](#) [PubMed Central](#) [Google Scholar](#)

52. 52.

Bandler, R. & Shipley, M. T. Columnar organization in the midbrain periaqueductal gray: modules for emotional expression? *Trends Neurosci.* **17**, 379–389 (1994).

[CAS](#) [PubMed](#) [Article](#) [PubMed Central](#) [Google Scholar](#)

53. 53.

Inagaki, H. K. et al. Optogenetic control of *Drosophila* using a red-shifted channelrhodopsin reveals experience-dependent influences on courtship. *Nat. Methods* **11**, 325–332 (2014).

[CAS](#) [PubMed](#) [Article](#) [PubMed Central](#) [Google Scholar](#)

[Download references](#)

Acknowledgements

We thank the Stowers laboratory for support and advice; T. Holy and T. Barnes for early constructive comments and discussions; S. Tan, N.

Koblesky and S. Simpson for exploratory behavioural tests; and L. Ye for aid with the fibre photometry experiments. The work was supported by the Dorris Neuroscience and Skaggs Scholarships (J.C.) the Anandamahidol Foundation Fellowship (V.L.), Career Award at the Scientific Interface from BWF (J.E.M.), and grants from NIH (R01NS097772 and R01DA049787 (B.K.L.); and R01NS108439 (L.S.)).

Author information

Affiliations

1. Department of Neuroscience, Scripps Research, La Jolla, CA, USA

Jingyi Chen, Sandra Taylor, Pete Sheurpukdi, Jennifer R. Jensen & Lisa Stowers

2. Biomedical Sciences Graduate Program, Scripps Research, La Jolla, CA, USA

Jingyi Chen

3. Department of Neurobiology, Harvard Medical School, Boston, MA, USA

Jeffrey E. Markowitz & Sandeep Robert Datta

4. Biological Sciences Graduate Program, University of California San Diego, La Jolla, CA, USA

Varoth Lilascharoen

5. Janelia Research Campus, Howard Hughes Medical Institute, Ashburn, VA, USA

Jason A. Keller

6. Neurobiology Section, Division of Biological Sciences, University of California San Diego, La Jolla, CA, USA

Byung Kook Lim

Authors

1. Jingyi Chen

[View author publications](#)

You can also search for this author in [PubMed](#) [Google Scholar](#)

2. Jeffrey E. Markowitz

[View author publications](#)

You can also search for this author in [PubMed](#) [Google Scholar](#)

3. Varoth Lilascharoen

[View author publications](#)

You can also search for this author in [PubMed](#) [Google Scholar](#)

4. Sandra Taylor

[View author publications](#)

You can also search for this author in [PubMed](#) [Google Scholar](#)

5. Pete Sheurpukdi

[View author publications](#)

You can also search for this author in [PubMed](#) [Google Scholar](#)

6. Jason A. Keller

[View author publications](#)

You can also search for this author in [PubMed](#) [Google Scholar](#)

7. Jennifer R. Jensen

[View author publications](#)

You can also search for this author in [PubMed](#) [Google Scholar](#)

8. Byung Kook Lim

[View author publications](#)

You can also search for this author in [PubMed](#) [Google Scholar](#)

9. Sandeep Robert Datta

[View author publications](#)

You can also search for this author in [PubMed](#) [Google Scholar](#)

10. Lissa Stowers

[View author publications](#)

You can also search for this author in [PubMed](#) [Google Scholar](#)

Contributions

J.C. and L.S. designed the study and wrote the manuscript. J.E.M. and S.R.D. developed Voseq analysis; V.L. performed slice physiology; S.T. aided in histology, behavioural testing and cell counting; B.K.L., P.S. and J.A.K. aided in data analysis and MATLAB code. J.R.J. performed behavioural analysis. All other experiments were performed by J.C.

Corresponding author

Correspondence to [Lisa Stowers](#).

Ethics declarations

Competing interests

The authors declare no competing interests.

Additional information

Peer review information *Nature* thanks Erich Jarvis and the other, anonymous, reviewer(s) for their contribution to the peer review of this work. Peer review reports are available.

Publisher's note Springer Nature remains neutral with regard to jurisdictional claims in published maps and institutional affiliations.

Extended data figures and tables

[Extended Data Fig. 1 ESR1-expressing subset of LPOA neurons express c-FOS during odour-evoked USV calling.](#)

a, Example of c-FOS expression in the preoptic area after exposure to tonic water as a control odour (no USVs) or with female odour (USVs)^{25,36,37,38}. Scale bar, 200 µm. Quantification of this experiment is shown in **c** and **d**. **b**, Immunostaining after exposure to female mouse odour shows that c-FOS⁺ in the LPOA largely overlaps with ESR1-ZsGreen cells. White squares delineate enlarged single z-stack sections shown in Fig. **1b**. Scale bar, 100 µm. **c**, **d**, Expression of c-FOS and ESR1 in the LPOA following awake behaviour with control odour (black) or female odour (yellow). **c**, Rstrocaudal distribution of c-FOS⁺ cells in the LPOA. **d**, Rstrocaudal percentage of cells co-expressing c-FOS and ESR1 in the LPOA. Data are mean ± s.e.m. $n = 4$ mice. [Source data](#)

[Extended Data Fig. 2 LPOA^{ESR1} neural activity correlates with USV calling, and chemogenetic inhibition of LPOA^{ESR1} neurons reduce USV calling.](#)

LPOA^{ESR1+} GCaMP6s activity during natural social behaviour. **a**, Top, experimental design for LPOA^{ESR1} fibre photometry recordings. Bottom, sample image showing fibre optic track and viral expression of GCaMP6s. Scale bar, 200 µm. $n = 9$ mice, >3 sections per mouse collected. In addition to evoking USV calling, the presence of a female mouse also markedly alters the behaviour of the male mouse (arousal, social sniffing, locomotion and sexual mounting), potentially confounding interpretation of the

observed neural activity. We observed that after the removal of the female mice, male mice often generated intermittent USV calls, perhaps to lure the female mice back, without the behavioural noise of mounting or social sniffing. We leveraged this post-female period to observe increases in LPOA^{ESR1/GCaMP6s} activity with a rise shortly before the onset of post-female USVs, clearly suggesting that endogenous LPOA^{ESR1} neural activity correlates with emission of USVs. **b**, Representative USV production and GCaMP6s fibre photometry of male LPOA^{ESR1} neurons as he behaves alone (pre-female), with a behaving female mouse, and after the female mouse is removed (post-female). Dashed line indicates when the female was added and removed. Top, mean USV power. Blue dots indicate USV syllable detection. Bottom, $\Delta F/F$ of LPOA^{ESR1} GCaMP6s signals was calculated by MATLAB GUI as previously described³⁴. **c**, Dark green line denotes mean *z*-score of GCaMP6s signals before and after initiation of USV with behaving female phase, light green shading indicates 95% confidence interval. Grey shading denotes 95% confidence interval of the mean of the scrambled data ($n = 9$ mice). **d**, Mean average *z*-score of GCaMP6s signals during all USV syllables evoked with a behaving female compared to scrambled data points during pre-female behaviour. Data are mean \pm s.e.m. $n = 9$ mice. *** $P = 0.0003$, unpaired *t*-test, two sided. **e**, Dark green line denotes mean *z*-score of GCaMP6s signals before and after initiation of USV during post-female stage, light green shading indicates 95% confidence interval. Grey shading denotes 95% confidence interval of the mean of the scrambled data. $n = 9$ mice. **f**, Mean average *z*-score of GCaMP6s signal of all USV syllables during post-female stage compared to scrambled data points during pre-female stages. Data are mean \pm s.e.m. $n = 9$ mice. *** $P = 2.2 \times 10^{-4}$, unpaired *t*-test, two sided. **g-i**, To determine whether the increased hypothalamic activity is involved in odour-evoked USV calling, we targeted chemogenetic inhibition to the LPOA, which is a largely unstudied heterogeneous region that has been implicated in sleep, thirst and reward behaviour^{39,40,41,42,43}, and quantified USV production during natural interactions with an awake female. **g**, Non-specific chemogenetics. Left, hM₄D_i viral injection in the LPOA of wild-type mice. Right, experimental assay; after expression of the hM₄D_i virus, male mice were injected intraperitoneally with CNO–saline–CNO–saline (every other day for 4 days in total) and allowed to interact with a freely moving female

mouse to evoke USV calling. **h**, Number of USV syllables emitted after injection with CNO (purple) or saline (black). Data are mean \pm s.e.m. $n = 10$ mice. N.S., $P = 0.11$, paired two-tailed Wilcoxon test. **i**, Number of USVs emitted across four sequential test days. Overall, the manipulation did not produce a significant effect on behaviour; however, half of this group (solid lines, $n = 5$ mice) did show a constant reduction in USVs, whereas the other half (dashed lines, $n = 5$ mice) continued to emit USVs in the presence of CNO. This experiment suggests the potential for a functional role of the hypothalamic neurons in social vocal communication and a need for a more specific viral labelling method. **j**, Average number of USVs between all saline and CNO injection days as shown in Fig. 1d. $n = 6$ mice. * $P = 0.03$, two-sided Wilcoxon test. **k**, Sample image of hM₄D_i expression in ESR1-ZsGreen mice. Scale bar, 500 μ m. $n = 6$ mice, >3 sections per mouse collected. **l**, Quantification of total time performing social behaviours observed by LPOA^{ESR1/hM₄D_i} neurons from male mice during a 4-min interaction with live female mice on CNO and saline injection days. $n = 6$ mice. * $P = 0.02$, *** $P < 0.001$, paired two-sided *t*-test. Note that we observed an unexpected increase in the anti-social defensive behaviour of the female mouse (kicking, running away), which reduced the ability of the male mouse to direct sniffing to the anogenital region. This observation is consistent with male USVs serving to enhance female courtship behaviour^{44,45}. **m**, Experiment design to express control AAV-tdTomato virus in LPOA^{ESR1} cells. **n**, Number of USVs emitted with behaving female mice over five test days, with alternating injections of either CNO or saline. **o**, Average number of USVs between saline and CNO injection days. $n = 5$ mice. $P > 0.05$, two-sided Wilcoxon test. [Source data](#)

[Extended Data Fig. 3 Optogenetic stimulation of LPOA_{ESR1/ChR2} neurons triggers USV calling in both male and female mice.](#)

a, Left, ChR2 virus injection in the LPOA region of ESR1-Cre mice. Right, sample image of co-expression of ChR2 and FOS after photostimulation. Scale bar, 50 μ m. **b**, Viral expression in the LPOA region. Composite overlay of total sections at left: bregma 0.2 mm, and right: bregma 0.3 mm. Colour intensity scales with increasing expression. $n = 12$ mice. **c**, Example

electrophysiology recording during photostimulation of LPOA^{ESR1/ChR2} neurons in ex vivo slice. Blue bar denotes 10-Hz light stimulation. Neural response is time-locked to light pulses. **d**, Number of USVs detected during 10-Hz photostimulation of LPOA^{ESR1/ChR2} cells from male mice ($n = 23$ mice) (left) and female mice ($n = 11$ mice) (right). Data are mean \pm s.e.m. **e**, **f**, Average USV power across the 40–90kHz band evoked by 10-Hz photostimulation. Solid line indicates mean of all trials; shaded region indicates 95% confidence interval. The blue (**e**) and red (**f**) traces denote male and female trials, respectively^{14,46}. Blue shaded bar denotes light stimulation at 5–10 s. **g**, Raster plot of complete dataset showing USV power evoked by photostimulation at 10 Hz (5-s duration, 15-ms pulses; between the blue lines) of LPOA^{ESR1/ChR2} neurons from female mice ($n = 11$ mice, red) and male mice ($n = 23$ mice, blue). $n = 242$ trials, each row is a single trial. Colour intensity represents average USV power across the ultrasonic band (40–90 kHz). Note that the POA has been implicated in a variety of functions including homeostatic control of internal states such as thermoregulation and thirst, sexually dimorphic social behaviours including parenting and mating behaviour, as well as motivated behaviours^{39,47,48,49}. It is likely that features of these neurons that enable them to generate USVs in the absence of social stimuli in the laboratory also enable them to participate in other neural computations that are currently unknown. [Source data](#)

[Extended Data Fig. 4 Activating LPOA^{ESR1} neurons elicit a variety of USV syllables similar to natural USVs.](#)

a, Evaluation of USV syllable types emitted by a wild-type male mouse naturally interacting with a behaving female mouse, compared to wild-type P7–P8 pup calls ($n = 18$ mice) (orange) evoked by individually isolating mice from the home cage; wild-type adult male calls ($n = 20$ mice) evoked by interaction with female or male urine, anaesthetized male or female mice on successive days (grey); or calls from experimental male mice expressing ChR2 (LPOA^{ESR1/ChR2}, $n = 23$ mice) evoked by interaction with either female urine or a live female mouse with no ChR2 light stimulation to determine the natural USV repertoire (blue, left); or male mice expressing ChR2 (LPOA^{ESR1/ChR2}, $n = 23$ mice) stimulated with light (10 Hz, 25 Hz

and 50 Hz) in the absence of a female mouse (blue, right; blue shading ‘light stimulation’); the same male mice were used in the no-light and light stimulation experiments. Dot denotes the Pearson correlations for the top 5% of the most frequently used syllables, in which the box plot shows the mean and interquartile range of these correlations, and the plus symbol (‘+’) shows the correlation of the top 95% of the most frequency used syllables. $P = 6.12 \times 10^{-115}$ ($F > 83.4$), * $P < 0.05$, *** $P < 0.001$, one-way ANOVA test. MATLAB ‘mulcompare’ function was used for group statistical analysis comparing all other groups to wild-type male USV triggered by interaction with a live female mouse. **b**, Heat map showing Pearson’s correlation score among all 40 types of syllable detected across each condition compared to wild-type male USVs during interaction with live female mouse. Results are grouped by types of sensory stimulation: female context (red); ChR2 stimulation (blue); male context (green) and pup (orange). Warmer colours indicate higher similarity, which is quantified in **a**. These data show that the repertoire of USV syllables evoked by photostimulation are rich and varied. When compared to natural USVs, they are similar to those produced by wild-type male mice as they interact with live female mice; and less similar to USVs evoked by male cues and pup USVs. [Source data](#)

Extended Data Fig. 5 LPOA^{ESR1} projections to USV motor centre (ambiguous) are sparse and unable to be functionally validated, whereas LPOA^{ESR1} projections to PAG produces robust USV production.

a, Strategy to test whether LPOA^{ESR1} neurons are anatomically or functionally connected to either the PAG or the nucleus ambiguus, which are known to evoke USV calling in the mouse^{16,17,50,51}. **b–f**, Retrograde tracing experiment from either PAG or nucleus ambiguus to label LPOA^{ESR1} cell projections by injecting a Cre-dependent FLP-expressing pseudotyped equine infectious anaemia virus (RG-EIAV-FLEX-Flp) in either the PAG or nucleus ambiguus, and a FLP-dependent AAV expressing eGFP in the LPOA of ESR1-Cre mice^{32,33}. We confirmed the specificity of viral expression by multiplex fluorescent in situ hybridization

(Extended Data Fig. [6a](#),[b](#)). We observed sparse labelling of LPOA cells that directly project to the nucleus ambiguous, and a larger population centred in the LPOA region (previously showed to be co-labelled by c-FOS and ESR1) that directly project to the region of the PAG USV-gate neurons. **b**, Example image of PAG-projecting (top) or nucleus ambiguously-projecting (bottom) eGFP⁺ cells in the LPOA as described and quantified in **c–f**. Scale bar, 200 µm. $n = 5$ mice; 5 sections per mouse. **c**, **d**, Anatomical tracing from the PAG to the LPOA resulted in robust labelling. **c**, Experimental design to express the FLEX-FLP virus in the PAG and fFLEX-eGFP in the LPOA of ESR1-Cre mice. **d**, Restrocaudal distribution of the total number of PAG-projecting eGFP⁺ cells in the LPOA. Data are mean ± s.e.m. $n = 5$ mice. **e**, **f**, Anatomical tracing from the nucleus ambiguous to the LPOA resulted in sparse labelling. **e**, Experimental design to express FLEX-FLP virus in the nucleus ambiguous and fFLEX-eGFP in the LPOA of ESR1-Cre mice. **f**, Restrocaudal distribution of the total number of nucleus ambiguously-projecting eGFP⁺ cells in the LPOA. Data are mean ± s.e.m. $n = 5$ mice. To test whether either of these projections function to evoke USV calling, we expressed ChR2 in the LPOA of ESR1-Cre mice and photostimulated from axon terminals in either the PAG or the nucleus ambiguous. **g**, Sample image of optical fibre position for stimulation of LPOA^{ESR1/ChR2} terminals in the PAG show in **j**. **h**, Experimental design for stimulation of LPOA^{ESR1/ChR2} terminals in the nucleus ambiguous. **i**, Sample image of optical fibre position for terminal stimulation in the nucleus ambiguous. Scale bar, 200 µm. $n = 5$ mice, 4 sections per mouse. **j**, Average USV power across the 40–90-kHz band of recording during PAG terminal stimulation. Solid line indicates the mean and shaded region indicate 95% confident interval (blue shading, $n = 13$ male mice; red shading, $n = 4$ female mice; 4 trials per mouse). **k**, Average USV power across 40–90-kHz band of recording during terminal stimulation of the nucleus ambiguous. Solid line indicates the mean and shaded region indicate 95% confident interval (blue shading, $n = 5$ male mice, 4 trials per mouse). **l**, **m**, Average USV power during single trials of the same male stimulated with 25 Hz for 5 s from either LPOA^{ESR1/ChR2} cell somas (**l**) or LPOA^{ESR1/ChR2} axon terminals in the PAG (**m**). [Source data](#)

Extended Data Fig. 6 LPOA-PAG projecting cells are largely inhibitory and stimulation of LPOA^{VGAT} cells elicits USVs.

a–c, RNAScope multiplex in situ hybridization histology of LPOA sections after injection of retro travelling Cre-dependent FLP-expressing virus in the PAG and a FLP-dependent eGFP (AAV-fFLEX-dGFP) in the LPOA of ESR1-Cre mice (see Extended Data Fig. 4c, d) reveals overlap of eGFP (green) (a), ESR1 (red) (b) and VGAT (magenta) (c) probes. Yellow traces are eGFP⁺ cells used as regions of interest and applied to ESR1 and VGAT channels for analysis. Scale bar, 50 μm. n = 3 mice, >3 sections per mouse with RNAScope staining. **d–g**, Electrophysiology recording of PAG neurons in ex vivo slice shows functional inhibition. **d**, Sample trace showing cell-attached recording of a PAG cell. **e**, IPSC and EPSC recordings while photostimulating (blue bars) LPOA^{ESR1/ChR2} terminals. **f**, IPSC and EPSC recordings during single light pulse. **g**, Peak conductance (calculated by amplitude or driving force) of EPSC (red) and IPSC (blue) recordings. Data are mean ± s.e.m. Bottom, percentage of observed cells with monosynaptic IPSCs (blue), EPSCs (red), or both (grey). n = 5 mice, 29 cells. **h, i**, Strategy to test whether LPOA excitatory neurons elicit USVs. **h**, Top, experimental design to express ChR2 in the LPOA of VGLUT2-Cre knock-in mice. Bottom, percentage of ChR2 overlap with either the VGLUT2-ZsGreen marker or c-FOS staining. **i**, Sample images showing overlap between ChR2 with VGLUT2-ZsGreen or c-FOS staining. Scale bars, 50 μm. n = 4 mice, 7 images per mouse used for cell quantification. **j**, Number of USVs emitted during light stimulation of LPOA^{VGLUT2/ChR2} neurons. n = 4, 16 trials per condition. **k**, Sample image indicating fibre position (white square) and ChR2 expression in the LPOA of VGAT-ZsGreen mice. Scale bars, 200 μm. n = 9 mice, 4 sections per mouse collected. **l**, Experimental design to express ChR2 in LPOA of VGAT-Cre mice and the number of USV syllables emitted during light stimulation of LPOA^{VGAT/ChR2} neurons. Data are mean ± s.e.m. n = 9 mice, 91 trials per condition. **m**, Composition of c-FOS expression (after odour-evoked USVs) in the PAG of VGAT-Cre mice. c-FOS⁺ cells (red) are largely VGAT[−] (consistent with PAG USV gate neurons being excitatory), whereas VGAT neurons are largely clustered in the ventrolateral PAG⁵².

$n = 3$ mice, overlay of 100- μm thick sections roughly at bregma -4.4 mm.

[Source data](#)

Extended Data Fig. 7 Local PAG^{VGAT} neurons inhibit PAG USV-gate cells, and photostimulation inhibits natural USVs.

Most immediate neurons ‘upstream’ of the PAG USV-gate cells are VGLUT2⁻ neurons in the PAG, ipsilateral to the PAG^{VGLUT2} neurons. **a**, Experimental design for rabies viral tracing from the PAG of VGLUT2-Cre knock-in mice. **b**, Sample PAG image from rabies tracing. Red cells on the left are cells infected with the TVA+G helper virus that overlaps with VGLUT2-ZsGreen (starter cells). The white box on the right is enlarged and showed in **c**. Scale bars, 250 μm . **c**, In total, 76 out of 87 cells labelled with rabies-tdTomato (87%) observed in ventrolateral PAG do not overlap with VGLUT2-ZsGreen cells, which suggests that they probably express VGAT. Scale bar, 100 μm . $n = 5$ mice, total 32 sections counted. To functionally test whether the PAG USV-gate neurons are subjected to local inhibition, we engineered male mice to express ChR2 in the local PAG inhibitory cells (PAG^{VGAT/ChR2}) and injected retroAAV-eGFP in the nucleus ambiguus to specifically identify PAG USV-gate neurons. **d**, Experimental design for retrograde labelling from the nucleus ambiguus to PAG USV-gate neurons, and optical manipulation of PAG^{VGAT/ChR2} cells for behaviour and physiology. **e**, Sample image of PAG section showing nucleus ambiguus-projecting cells in lateral PAG (green) and VGAT/ChR2-expressing cells (red) in ventrolateral PAG. Scale bar, 100 μm . Aq, aqueduct, fourth ventricle. Ex vivo whole-cell recordings and cell-attached recordings showed that all tested PAG^{GFP} neurons (USV-gating neurons) were inhibited within 5 ms after photostimulation of PAG^{VGAT/ChR2} neurons, consistent with monosynaptic inhibitory inputs. $n = 2$ mice, 2 sections per mouse collected. **f-h**, Ex vivo slice electrophysiology recordings of PAG USV-gate cells while photostimulating PAG^{VGAT/ChR2} neurons. **f**, IPSC and EPSC recordings during a single light pulse. **g**, Photostimulation of PAG^{VGAT/ChR2} neurons generate monosynaptic iPSCs in all cells investigated. $n = 2$ mice, 14 cells recorded. **h**, Cell-attached physiology of USV-gate neurons (PAG^{GFP}). Blue shading indicates photostimulation period. Each line showed as individual

cell recorded. **i, j**, Stimulating local PAG^{VGAT} neurons inhibit socially evoked USVs. **i**, Increasing the frequency or duration of photostimulation (5 s of 1 Hz, 5 Hz, 10 Hz, 50 Hz and 10 s of 25 Hz) of PAG^{VGAT/ChR2} neurons from male mice during interaction with awake behaving female mice to evoke natural USVs. Blue bar/shading denotes light stimulation. Number of USVs are calculated in 10-s time bins. Data are mean ± s.e.m. $n = 3$ mice, 5–6 trials per mouse per condition. **j**, Raster plot of USVs emitted before, during and after photostimulation at 25 Hz for 5 s, as showed in Fig. 2e. Blue light indicates light stimulation period. Each row is a single trial. Data are mean ± s.e.m. $n = 3$ mice, 19 trials. [Source data](#)

Extended Data Fig. 8 LPOA^{VGAT} cell population connect to PAG^{VGAT} cell population both anatomically and functionally, and the number of USV syllables and latency flexibly varies with social context.

a, Example image of PAG section for experiment described in Fig. 2f,g. Starter cells (magenta) overlap with VGAT-ZsGreen. Scale bar, 100 μ m. **b**, Sample image of LPOA section for experiment described in Fig. 2f,g showing overlap of rabies-tdTomato⁺ cells (red) with VGAT-ZsGreen (272 out of 320 cells counted, $n = 3$ mice, total of 17 sections). Scale bar, 200 μ m. **c**, Example image of RNAScope multiplex in situ hybridization in LPOA to complement Fig. 2f. Sections are stained with eGFP (green), VGAT (blue) and ESR1(red) probes. Scale bars, 25 μ m. Most LPOA neurons that projected to PAG^{VGAT} neurons co-express ESR1. $n = 2$ mice, 16 sections (20- μ m thick) collected. Top right, quantification of rabies-positive cells overlapping with VGAT⁺ or ESR1⁺ using RNAScope multiplex in situ hybridization ($n = 2$ mice, total 24 rabies-positive cells quantified). **d**, PAG^{VGAT} cells receive monosynaptic IPSC from LPOA^{VGAT/ChR2} neurons. IPSCs and EPSCs evoked by single light pulse ($n = 5$ mice, 16 cells recorded). **e–h**, To study the in vivo effects of LPOA^{ESR1} neuron activity, we expressed ChR2 in the LPOA and GCaMP6s in the PAG of VGAT-Cre mice (LPOA^{VGAT/ChR2}, PAG^{VGAT/GCaMP6s}). Photostimulation in the LPOA of awake behaving mice resulted in a decrease in fibre photometry as measured GCaMP6s fluorescence in the

local PAG inhibitory neurons and an accompanying initiation of USV production. **e**, Representative image of fibre track and viral expression of GCaMP6s in the PAG. Scale bar, 200 μ m. $n = 4$ mice, 3 sections per mouse. **f**, Number of USV syllables emitted following light stimulation of LPOA^{VGAT/ChR2} neurons while recording of PAG^{VGAT/GCaMP6s} signals. Data are mean \pm s.e.m. $n = 4$, 16 trials per condition. **g**, Mean z-score of fibre photometry signal from PAG^{VGAT/GCaMPs} with photostimulation at 25 Hz for 10 s of LPOA^{VGAT/ChR2} cells. **h**, Mean z-score of fibre photometry signal from PAG^{VGAT/GCaMPs} neurons with photostimulation at 1 Hz for 5 s of LPOA^{VGAT/ChR2} cells, in which the photostimulation is below the threshold to produce USVs. Solid line indicates mean of signals and shaded region indicates 95% confident intervals. $n = 4$ mice, 3 trials per mouse. **i–k**, To study the extent of USV syllable flexibility during natural social behaviour, we collected USVs from wild-type male mice during different social contexts. Wild-type male mouse USVs were recorded during 2-min interactions with a variety of socially relevant sensory contexts including the presence of an awake female mouse (in the dark or light), female urine, an anaesthetized female mouse, male urine, or an anaesthetized male mouse. The flexibility of social vocalization is underscored by the longer and louder USV bouts triggered by awake behaving female mice compared to the USVs evoked by anaesthetized female mice even though much of the contextual sensory cues are similar. **i**, Latency to first USV evoked by different sensory contexts. **j**, Average inter vocalization intervals of USVs evoked by different sensory stimuli. Red bar denotes female context (live female mouse in either the dark with red light or bright light, female urine, anaesthetized female mouse); green bar denotes the male context (male urine or anaesthetized male mouse). Data are mean \pm s.e.m. $n = 20$ mice. **k**, Raster plot of USVs emitted while interacting with different sensory contexts. Each line is a single wild-type male. Average USV power is calculated by mean decibels in the 40–90-kHz band from raw recording.

[Source data](#)

Extended Data Fig. 9 Increasing LPOA^{ESR1} neuron activity generates more USV syllables without altering syllable identity.

a, Two sonograms (12-s long each) analysed for USV production. White bars (top of each 3-s line) indicate the production and duration of USV syllables automatically identified. In the top sonogram, there was little additional acoustic noise so USV syllables are easy to identify; in the bottom sonogram, although there is abundant low-frequency noise (from self-movement or from interactions with another individual during the USV recording), the white bars robustly identify USV syllables. **b**, To determine whether USV bout length is fixed or variable, we analysed the inter-USV vocalization intervals, and found a natural threshold of 2-s pauses as a basis to define the end of a USV bout²³. **c**, Number of USVs emitted after photostimulation of LPOA^{ESR1/ChR2} cells at 25 Hz or 50 Hz and 1–20-s duration. Data are mean ± s.e.m. $n = 16$ mice. **d**, Syllables maintain their identity and structure from 1–50-Hz photostimulation of LPOA^{ESR1/ChR2} neurons. **e**, Jensen–Shannon divergence score of USVs produced by 1–50-Hz photostimulation of LPOA^{ESR1/ChR2} cells compared to natural USVs during interaction with female urine or live female mice. Box plot denotes the minimum and maximum values and quantile (0.25, 0.75). Grey shading denotes the 95% confident interval of the control data. To compute P values, we randomly choose mice with no stimulation and mice with ChR2 stimulation and computed the Jensen–Shannon divergence score. This step was repeated 1,000 times to build a null distribution. We then computed the probability that each bootstrap exceeded the observed median at each stimulation frequency. We found that a stimulation frequency of only 5 Hz resulted in a significant P value. * $P = 0.036$, $n = 26$ mice. [Source data](#)

Extended Data Fig. 10 Circuit and intrinsic properties of PAG^{VGAT} neurons support USV persistence.

a, b, USVs emitted during photostimulation of LPOA^{VGAT/ChR2} cells with injection of saline as control (grey) or CNO (purple) to inhibit PAG^{VGAT/hM4Di} neurons on alternative days. **a**, Number of USVs emitted with 1 Hz 5s light stimulation. **b**, Raster plot of USVs emitted during and after photostimulation (blue bars). Each row is 30 s of a 230-s trial aligned to light stimuli applied every 40 s. Data are mean ± s.e.m. $n = 3$, 6 trials per mouse per test day. *** $P < 0.0001$, paired Wilcoxon test, two sided. ns,

not significant ($P > 0.05$). **c**, Representative image of co-expression of hM4Di-tdTomato with VGAT-ZsGreen cells in the PAG. Scale bar, 200 μm . $n = 2$ mice, 2 sections per mouse collected. **d**, Number of USVs emitted during increased frequency photostimulation in LPOA of male mice expressing LPOA^{VGAT/ChR2} and PAG^{VGAT/hM4Di} and injected with CNO or saline on alternative days. $n = 3$, 36 trials per condition. Data are mean \pm s.e.m. *** $P < 0.0001$, Wilcoxon test, two sided. **e**, Experimental design to express control virus (tdTomato) in the PAG of VGAT-Cre mice (Fig. 4e, f). **f**, Number of USVs emitted by photostimulating LPOA^{VGAT} cells under either CNO or saline conditions in mice expressing FLEX-tdTomato viral control (PAG^{VGAT/tdTomato}) (control). $n = 3$, 18 trials per condition. Data are mean \pm s.e.m. ns, not significant ($P > 0.05$), Wilcoxon test, two sided. **g**, Raster plot of USV bouts emitted during either CNO or saline test days under different stimulation frequency. Note that *Drosophila* courtship songs show similar feature separation across the circuit with songs evoked by pIP10 neurons tightly locked to stimulation (like the PAG USV-gate neurons) compared to calling generated by P1 neurons that persists beyond stimulation (as with the LPOA^{ESR1} neurons)⁵³. This suggests diverse social species use general circuit strategies to maintain persistent auditory responses that outlast the detection of sensory information. [Source data](#)

Supplementary information

[Reporting Summary](#)

[Video 1](#)

Female odour evokes USVs from males. Female odour (female urine) triggers the productions of USVs from a sexually naïve male. Upper: Video of male interacting with odour source. Lower: USV sonogram representing frequency, syllable type, and amplitude of USVs. USVs were transposed to audible range through MATLAB. Video and audio played in 3X speed.

[Video 2](#)

Photoactivation of LPOA^{Esr1} neurons triggers USVs. Sample video and USV sonogram during photostimulation LPOAEsr1 neurons. Same individual was given 5s 15ms light stimulation at 1Hz (No USVs), 5Hz, 10Hz (moderate USVs) and 50Hz (Strong USVs).

[Video 3](#)

Chemoinhibition of local PAG^{vGat} neurons decreases the threshold and prolongs USV bouts triggered by LPOA^{vGat} photostimulation. Sonograms of USVs produced by a single individual receiving 5s photo stimulation at 1Hz/25Hz on LPOAvGat neurons and chemoinhibition of PAGvGat neurons with CNO (upper) or control saline (lower).

[Peer Review File](#)

Source data

[Source Data Fig. 1](#)

[Source Data Fig. 2](#)

[Source Data Fig. 3](#)

[Source Data Fig. 4](#)

[Source Data Extended Data Fig. 1](#)

[Source Data Extended Data Fig. 2](#)

[Source Data Extended Data Fig. 3](#)

[Source Data Extended Data Fig. 4](#)

[Source Data Extended Data Fig. 5](#)

[Source Data Extended Data Fig. 6](#)

[Source Data Extended Data Fig. 7](#)

[Source Data Extended Data Fig. 8](#)

[Source Data Extended Data Fig. 9](#)

[Source Data Extended Data Fig. 10](#)

Rights and permissions

[Reprints and Permissions](#)

About this article



Check for
updates

Cite this article

Chen, J., Markowitz, J.E., Lilascharoen, V. *et al.* Flexible scaling and persistence of social vocal communication. *Nature* **593**, 108–113 (2021).
<https://doi.org/10.1038/s41586-021-03403-8>

[Download citation](#)

- Received: 20 March 2020
- Accepted: 26 February 2021
- Published: 31 March 2021
- Issue Date: 06 May 2021

- DOI: <https://doi.org/10.1038/s41586-021-03403-8>

Comments

By submitting a comment you agree to abide by our [Terms](#) and [Community Guidelines](#). If you find something abusive or that does not comply with our terms or guidelines please flag it as inappropriate.

[Access through your institution](#)

[Change institution](#)

[Buy or subscribe](#)

This article was downloaded by **calibre** from <https://www.nature.com/articles/s41586-021-03403-8>

| [Section menu](#) | [Main menu](#) |

- Article
- [Published: 31 March 2021](#)

An amygdala circuit that suppresses social engagement

- [Jeong-Tae Kwon^{1,2}](#),
- [Changhyeon Ryu](#) ORCID: [orcid.org/0000-0001-5207-9142](#)^{1,2} na1,
- [Hyeseung Lee^{1,2,4}](#) na1,
- [Alec Sheffield^{1,2}](#),
- [Jingxuan Fan](#) ORCID: [orcid.org/0000-0001-7860-4558](#)²,
- [Daniel H. Cho²](#),
- [Shivani Bigler](#) ORCID: [orcid.org/0000-0002-3342-1843](#)²,
- [Heather A. Sullivan³](#),
- [Han Kyung Choe²](#),
- [Ian R. Wickersham³](#),
- [Myriam Heiman^{1,2,4}](#) &
- [Gloria B. Choi](#) ORCID: [orcid.org/0000-0003-4050-8338](#)^{1,2}

[Nature](#) volume 593, pages114–118(2021)[Cite this article](#)

- 10k Accesses
- 151 Altmetric
- [Metrics details](#)

Subjects

- [Neural circuits](#)
- [Olfactory system](#)
- [Social behaviour](#)

- [Transporters in the nervous system](#)

Abstract

Innate social behaviours, such as mating and fighting, are fundamental to animal reproduction and survival¹. However, social engagements can also put an individual at risk². Little is known about the neural mechanisms that enable appropriate risk assessment and the suppression of hazardous social interactions. Here we identify the posteromedial nucleus of the cortical amygdala (COApm) as a locus required for the suppression of male mating when a female mouse is unhealthy. Using anatomical tracing, functional imaging and circuit-level epistatic analyses, we show that suppression of mating with an unhealthy female is mediated by the COApm projections onto the glutamatergic population of the medial amygdalar nucleus (MEA). We further show that the role of the COApm-to-MEA connection in regulating male mating behaviour relies on the neuromodulator thyrotropin-releasing hormone (TRH). TRH is expressed in the COApm, whereas the TRH receptor (TRHR) is found in the postsynaptic MEA glutamatergic neurons. Manipulating neural activity of TRH-expressing neurons in the COApm modulated male mating behaviour. In the MEA, activation of the TRHR pathway by ligand infusion inhibited mating even towards healthy female mice, whereas genetic ablation of TRHR facilitated mating with unhealthy individuals. In summary, we reveal a neural pathway that relies on the neuromodulator TRH to modulate social interactions according to the health status of the reciprocating individual. Individuals must balance the cost of social interactions relative to the benefit, as deficits in the ability to select healthy mates may lead to the spread of disease.

[Access through your institution](#)

[Change institution](#)

[Buy or subscribe](#)

Access options

[Subscribe to Journal](#)

Get full journal access for 1 year

\$199.00

only \$3.90 per issue

[Subscribe](#)

All prices are NET prices.

VAT will be added later in the checkout.

Tax calculation will be finalised during checkout.

Rent or Buy article

Get time limited or full article access on ReadCube.

from \$8.99

[Rent or Buy](#)

All prices are NET prices.

Additional access options:

- [Log in](#)
- [Access through your institution](#)
- [Learn about institutional subscriptions](#)

Fig. 1: COApm is activated by female mice treated with LPS.

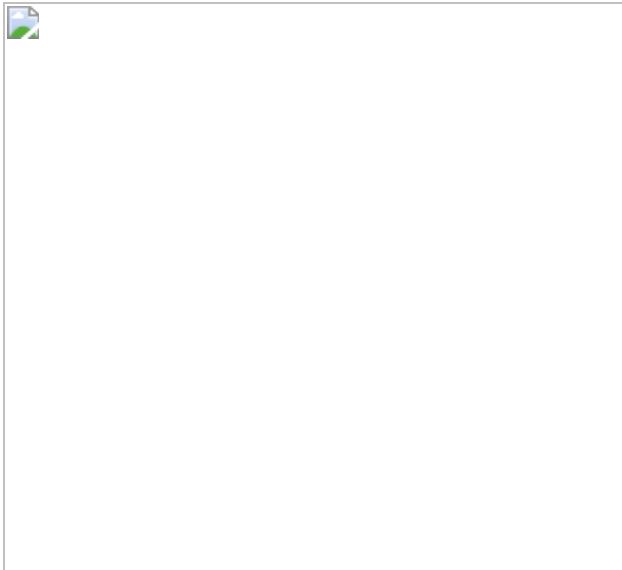


Fig. 2: COApm mediates suppression of mating behaviours towards unhealthy females.

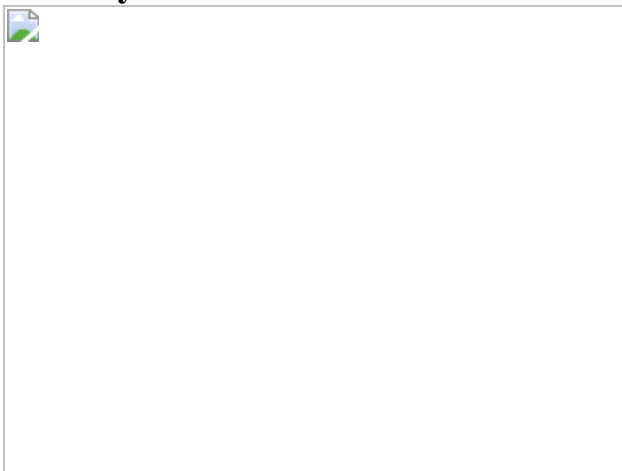


Fig. 3: COApm projections to MEA-Vglut2⁺ neurons mediate suppression of mating towards LPS females.



Fig. 4: Suppression of social behaviours engages COApm-TRH⁺ neurons.



Data availability

Source data are provided in the Supplementary Information. Sequencing data sets are publicly available in NCBI Gene Expression Omnibus (GEO) under accession [GSE167176](#). All data are available from the corresponding author upon request.

References

1. 1.

Tinbergen, N. *The Study of Instinct* (Oxford Univ. Press, 1951).

2. 2.

Altizer, S. et al. Social organization and parasite risk in mammals: integrating theory and empirical studies. *Annu. Rev. Ecol. Evol. Syst.* **34**, 517–547 (2003).

[Article](#) [Google Scholar](#)

3. 3.

Hart, B. L. Behavioral adaptations to pathogens and parasites: five strategies. *Neurosci. Biobehav. Rev.* **14**, 273–294 (1990).

[CAS](#) [PubMed](#) [Article](#) [PubMed Central](#) [Google Scholar](#)

4. 4.

Ehman, K. D. & Scott, M. E. Female mice mate preferentially with non-parasitized males. *Parasitology* **125**, 461–466 (2002).

[CAS](#) [PubMed](#) [Article](#) [PubMed Central](#) [Google Scholar](#)

5. 5.

Chen, P. & Hong, W. Neural circuit mechanisms of social behavior. *Neuron* **98**, 16–30 (2018).

[CAS](#) [PubMed](#) [PubMed Central](#) [Article](#) [Google Scholar](#)

6. 6.

Chamero, P. et al. Identification of protein pheromones that promote aggressive behaviour. *Nature* **450**, 899–902 (2007).

[ADS](#) [CAS](#) [PubMed](#) [Article](#) [PubMed Central](#) [Google Scholar](#)

7. 7.

Hashikawa, K., Hashikawa, Y., Falkner, A. & Lin, D. The neural circuits of mating and fighting in male mice. *Curr. Opin. Neurobiol.* **38**, 27–37 (2016).

[CAS](#) [PubMed](#) [PubMed Central](#) [Article](#) [Google Scholar](#)

8. 8.

Stowers, L., Holy, T. E., Meister, M., Dulac, C. & Koentges, G. Loss of sex discrimination and male–male aggression in mice deficient for TRP2. *Science* **295**, 1493–1500 (2002).

[ADS](#) [CAS](#) [PubMed](#) [Article](#) [PubMed Central](#) [Google Scholar](#)

9. 9.

Leybold, B. G. et al. Altered sexual and social behaviors in trp2 mutant mice. *Proc. Natl Acad. Sci. USA* **99**, 6376–6381 (2002).

[ADS](#) [CAS](#) [PubMed](#) [Article](#) [PubMed Central](#) [Google Scholar](#)

10. 10.

Medzhitov, R. Toll-like receptors and innate immunity. *Nat. Rev. Immunol.* **1**, 135–145 (2001).

[CAS](#) [PubMed](#) [Article](#) [PubMed Central](#) [Google Scholar](#)

11. 11.

Boillat, M. et al. The vomeronasal system mediates sick conspecific avoidance. *Curr. Biol.* **25**, 251–255 (2015).

[CAS](#) [PubMed](#) [Article](#) [PubMed Central](#) [Google Scholar](#)

12. 12.

Rivièvre, S., Challet, L., Fluegge, D., Spehr, M. & Rodriguez, I. Formyl peptide receptor-like proteins are a novel family of vomeronasal chemosensors. *Nature* **459**, 574–577 (2009).

[ADS](#) [PubMed](#) [Article](#) [CAS](#) [Google Scholar](#)

13. 13.

Liberles, S. D. et al. Formyl peptide receptors are candidate chemosensory receptors in the vomeronasal organ. *Proc. Natl Acad. Sci. USA* **106**, 9842–9847 (2009).

[ADS](#) [CAS](#) [PubMed](#) [Article](#) [Google Scholar](#)

14. 14.

Kavaliers, M., Choleris, E., Agmo, A. & Pfaff, D. W. Olfactory-mediated parasite recognition and avoidance: linking genes to behavior. *Horm. Behav.* **46**, 272–283 (2004).

[PubMed](#) [Article](#) [PubMed Central](#) [Google Scholar](#)

15. 15.

Scalia, F. & Winans, S. S. The differential projections of the olfactory bulb and accessory olfactory bulb in mammals. *J. Comp. Neurol.* **161**, 31–55 (1975).

[CAS](#) [PubMed](#) [Article](#) [PubMed Central](#) [Google Scholar](#)

16. 16.

Boehm, U. The vomeronasal system in mice: from the nose to the hypothalamus- and back! *Semin. Cell Dev. Biol.* **17**, 471–479 (2006).

[PubMed](#) [Article](#) [PubMed Central](#) [Google Scholar](#)

17. 17.

Choi, G. B. et al. Lhx6 delineates a pathway mediating innate reproductive behaviors from the amygdala to the hypothalamus. *Neuron* **46**, 647–660 (2005).

[CAS](#) [PubMed](#) [Article](#) [PubMed Central](#) [Google Scholar](#)

18. 18.

Li, Y. et al. Neuronal representation of social information in the medial amygdala of awake behaving mice. *Cell* **171**, 1176–1190 (2017).

[CAS](#) [PubMed](#) [PubMed Central](#) [Article](#) [Google Scholar](#)

19. 19.

Ishii, K. K. et al. A labeled-line neural circuit for pheromone-mediated sexual behaviors in mice. *Neuron* **95**, 123–137 (2017).

[CAS](#) [PubMed](#) [Article](#) [PubMed Central](#) [Google Scholar](#)

20. 20.

Hong, W., Kim, D. W. & Anderson, D. J. Antagonistic control of social versus repetitive self-grooming behaviors by separable amygdala neuronal subsets. *Cell* **158**, 1348–1361 (2014).

[CAS](#) [PubMed](#) [PubMed Central](#) [Article](#) [Google Scholar](#)

21. 21.

Wickersham, I. R., Finke, S., Conzelmann, K. K. & Callaway, E. M. Retrograde neuronal tracing with a deletion-mutant rabies virus. *Nat. Methods* **4**, 47–49 (2007).

[CAS](#) [PubMed](#) [Article](#) [PubMed Central](#) [Google Scholar](#)

22. 22.

Heiman, M. et al. A translational profiling approach for the molecular characterization of CNS cell types. *Cell* **135**, 738–748 (2008).

[CAS](#) [PubMed](#) [PubMed Central](#) [Article](#) [Google Scholar](#)

23. 23.

Suzuki, M., Sugano, H., Matsumoto, K., Yamamura, M. & Ishida, R. Synthesis and central nervous system actions of thyrotropin-releasing hormone analogues containing a dihydroorotic acid moiety. *J. Med. Chem.* **33**, 2130–2137 (1990).

[CAS](#) [PubMed](#) [Article](#) [PubMed Central](#) [Google Scholar](#)

24. 24.

Hart, B. L. Biological basis of the behavior of sick animals. *Neurosci. Biobehav. Rev.* **12**, 123–137 (1988).

[CAS](#) [PubMed](#) [Article](#) [PubMed Central](#) [Google Scholar](#)

25. 25.

Lopes, P. C., Block, P. & König, B. Infection-induced behavioural changes reduce connectivity and the potential for disease spread in wild mice contact networks. *Sci. Rep.* **6**, 31790 (2016).

[ADS](#) [CAS](#) [PubMed](#) [PubMed Central](#) [Article](#) [Google Scholar](#)

26. 26.

Van Kerckhove, K., Hens, N., Edmunds, W. J. & Eames, K. T. The impact of illness on social networks: implications for transmission and control of influenza. *Am. J. Epidemiol.* **178**, 1655–1662 (2013).

[PubMed](#) [PubMed Central](#) [Article](#) [Google Scholar](#)

27. 27.

Stockmaier, S., Bolnick, D. I., Page, R. A. & Carter, G. G. Sickness effects on social interactions depend on the type of behaviour and relationship. *J. Anim. Ecol.* **89**, 1387–1394 (2020).

[PubMed](#) [Article](#) [PubMed Central](#) [Google Scholar](#)

28. 28.

Fischer, S. & Ehlert, U. Hypothalamic-pituitary-thyroid (HPT) axis functioning in anxiety disorders. A systematic review. *Depress. Anxiety* **35**, 98–110 (2018).

[CAS](#) [PubMed](#) [Article](#) [PubMed Central](#) [Google Scholar](#)

29. 29.

Baumgartner, A. Thyroxine and the treatment of affective disorders: an overview of the results of basic and clinical research. *Int. J. Neuropsychopharmacol.* **3**, 149–165 (2000).

[CAS](#) [PubMed](#) [Article](#) [PubMed Central](#) [Google Scholar](#)

30. 30.

Krashes, M. J. et al. An excitatory paraventricular nucleus to AgRP neuron circuit that drives hunger. *Nature* **507**, 238–242 (2014).

[ADS](#) [CAS](#) [PubMed](#) [PubMed Central](#) [Article](#) [Google Scholar](#)

31. 31.

Chen, T. W. et al. Ultrasensitive fluorescent proteins for imaging neuronal activity. *Nature* **499**, 295–300 (2013).

[ADS](#) [CAS](#) [PubMed](#) [PubMed Central](#) [Article](#) [Google Scholar](#)

32. 32.

Zhang, F. et al. Optogenetic interrogation of neural circuits: technology for probing mammalian brain structures. *Nat. Protoc.* **5**, 439–456 (2010).

[CAS](#) [PubMed](#) [PubMed Central](#) [Article](#) [Google Scholar](#)

33. 33.

Ung, K. & Arenkiel, B. R. Fiber-optic implantation for chronic optogenetic stimulation of brain tissue. *J. Vis. Exp.* **68**, e50004 (2012).

[Google Scholar](#)

34. 34.

Armbruster, B. N., Li, X., Pausch, M. H., Herlitze, S. & Roth, B. L. Evolving the lock to fit the key to create a family of G protein-coupled receptors potently activated by an inert ligand. *Proc. Natl Acad. Sci. USA* **104**, 5163–5168 (2007).

[ADS](#) [PubMed](#) [Article](#) [CAS](#) [PubMed Central](#) [Google Scholar](#)

35. 35.

Pankevich, D. E., Baum, M. J. & Cherry, J. A. Olfactory sex discrimination persists, whereas the preference for urinary odorants from estrous females disappears in male mice after vomeronasal organ removal. *J. Neurosci.* **24**, 9451–9457 (2004).

[CAS](#) [PubMed](#) [PubMed Central](#) [Article](#) [Google Scholar](#)

36. 36.

McClure, C., Cole, K. L., Wulff, P., Klugmann, M. & Murray, A. J. Production and titering of recombinant adeno-associated viral vectors. *J. Vis. Exp.* **57**, e3348 (2011).

[Google Scholar](#)

37. 37.

Paxinos, G. & Franklin, K. B. J. *The Mouse Brain in Stereotaxic Coordinates* 2nd edn (Elsevier/Academic Press, 2004).

38. 38.

Gunaydin, L. A. et al. Natural neural projection dynamics underlying social behavior. *Cell* **157**, 1535–1551 (2014).

[CAS](#) [PubMed](#) [PubMed Central](#) [Article](#) [Google Scholar](#)

39. 39.

Byers, S. L., Wiles, M. V., Dunn, S. L. & Taft, R. A. Mouse estrous cycle identification tool and images. *PLoS ONE* **7**, e35538 (2012).

[ADS](#) [CAS](#) [PubMed](#) [PubMed Central](#) [Article](#) [Google Scholar](#)

40. 40.

Bankhead, P. et al. QuPath: Open source software for digital pathology image analysis. *Sci. Rep.* **7**, 16878 (2017).

[ADS](#) [PubMed](#) [PubMed Central](#) [Article](#) [CAS](#) [Google Scholar](#)

41. 41.

Cantu, D. A. et al. EZcalcium: open-source toolbox for analysis of calcium imaging data. *Front. Neural Circuits* **14**, 25 (2020).

[CAS](#) [PubMed](#) [PubMed Central](#) [Article](#) [Google Scholar](#)

42. 42.

Chan, K. Y. et al. Engineered AAVs for efficient noninvasive gene delivery to the central and peripheral nervous systems. *Nat. Neurosci.* **20**, 1172–1179 (2017).

[CAS](#) [PubMed](#) [PubMed Central](#) [Article](#) [Google Scholar](#)

43. 43.

Heiman, M., Kulicke, R., Fenster, R. J., Greengard, P. & Heintz, N. Cell type-specific mRNA purification by translating ribosome affinity purification (TRAP). *Nat. Protoc.* **9**, 1282–1291 (2014).

[CAS](#) [PubMed](#) [PubMed Central](#) [Article](#) [Google Scholar](#)

44. 44.

Love, M. I., Huber, W. & Anders, S. Moderated estimation of fold change and dispersion for RNA-seq data with DESeq2. *Genome Biol.* **15**, 550 (2014). 8

[PubMed](#) [PubMed Central](#) [Article](#) [CAS](#) [Google Scholar](#)

45. 45.

Hornung, V. et al. 5'-Triphosphate RNA is the ligand for RIG-I. *Science* **314**, 994–997 (2006).

[ADS](#) [PubMed](#) [Article](#) [PubMed Central](#) [Google Scholar](#)

46. 46.

Huang, K. W. & Sabatini, B. L. Single-cell analysis of neuroinflammatory responses following intracranial injection of G-deleted rabies viruses. *Front. Cell. Neurosci.* **14**, 65 (2020).

[CAS](#) [PubMed](#) [PubMed Central](#) [Article](#) [Google Scholar](#)

47. 47.

Chen, E. Y. et al. Enrichr: interactive and collaborative HTML5 gene list enrichment analysis tool. *BMC Bioinformatics* **14**, 128 (2013).

[PubMed](#) [PubMed Central](#) [Article](#) [Google Scholar](#)

48. 48.

Kuleshov, M. V. et al. Enrichr: a comprehensive gene set enrichment analysis web server 2016 update. *Nucleic Acids Res.* **44** (W1), W90–W97 (2016).

[CAS](#) [PubMed](#) [PubMed Central](#) [Article](#) [Google Scholar](#)

49. 49.

Choe, H. K. et al. Oxytocin mediates entrainment of sensory stimuli to social cues of opposing valence. *Neuron* **87**, 152–163 (2015).

[CAS](#) [PubMed](#) [PubMed Central](#) [Article](#) [Google Scholar](#)

[Download references](#)

Acknowledgements

We thank N. Soares, M. Andina, K. Ronayne and I. D. Mejia for assistance with experiments; B. Noro and M. Trombly for critical reading of the manuscript; J. Huh for his contribution to the conceptual development of the project; B. Lowell for generously sharing the *Trh*-Cre mouse line; and H. Choi for the fibre photometry setup. This work was supported by the National Institute of Mental Health grants R01 MH122270 and R01 MH106497 (G.B.C.), the JPB Foundation (M.H. and G.B.C), Simons Center for the Social Brain Postdoctoral Fellowship (J.-T.K. and H.K.C.) and the Picower Fellows (J.-T.K. and H.L.).

Author information

Author notes

1. These authors contributed equally: Changhyeon Ryu, Hyeseung Lee

Affiliations

1. Picower Institute for Learning and Memory, Massachusetts Institute of Technology, Cambridge, MA, USA

Jeong-Tae Kwon, Changhyeon Ryu, Hyeseung Lee, Alec Sheffield, Myriam Heiman & Gloria B. Choi

2. Department of Brain and Cognitive Sciences, Massachusetts Institute of Technology, Cambridge, MA, USA

Jeong-Tae Kwon, Changhyeon Ryu, Hyeseung Lee, Alec Sheffield, Jingxuan Fan, Daniel H. Cho, Shivani Bigler, Han Kyung Choe, Myriam Heiman & Gloria B. Choi

3. McGovern Institute for Brain Research, Massachusetts Institute of Technology, Cambridge, MA, USA

Heather A. Sullivan & Ian R. Wickersham

4. Broad Institute of MIT and Harvard, Cambridge, MA, USA

Hyeseung Lee & Myriam Heiman

Authors

1. Jeong-Tae Kwon

[View author publications](#)

You can also search for this author in [PubMed](#) [Google Scholar](#)

2. Changhyeon Ryu

[View author publications](#)

You can also search for this author in [PubMed](#) [Google Scholar](#)

3. Hyeseung Lee

[View author publications](#)

You can also search for this author in [PubMed](#) [Google Scholar](#)

4. Alec Sheffield

[View author publications](#)

You can also search for this author in [PubMed](#) [Google Scholar](#)

5. Jingxuan Fan

[View author publications](#)

You can also search for this author in [PubMed](#) [Google Scholar](#)

6. Daniel H. Cho

[View author publications](#)

You can also search for this author in [PubMed](#) [Google Scholar](#)

7. Shivani Bigler

[View author publications](#)

You can also search for this author in [PubMed](#) [Google Scholar](#)

8. Heather A. Sullivan

[View author publications](#)

You can also search for this author in [PubMed](#) [Google Scholar](#)

9. Han Kyung Choe

[View author publications](#)

You can also search for this author in [PubMed](#) [Google Scholar](#)

10. Ian R. Wickersham

[View author publications](#)

You can also search for this author in [PubMed](#) [Google Scholar](#)

11. Myriam Heiman

[View author publications](#)

You can also search for this author in [PubMed](#) [Google Scholar](#)

12. Gloria B. Choi

[View author publications](#)

You can also search for this author in [PubMed](#) [Google Scholar](#)

Contributions

J.-T.K. and G.B.C. conceptualized the study. J.-T.K., H.L., C.R., M.H. and G.B.C. designed the experiments and/or provided advice and technical expertise. J.-T.K., H.L., C.R., A.S., J.F., D.H.C., S.B., H.A.S. and H.K.C. performed the experiments. I.R.W. provided reagents. J.-T.K. and G.B.C. wrote the manuscript with inputs from the co-authors.

Corresponding author

Correspondence to [Gloria B. Choi](#).

Ethics declarations

Competing interests

The authors declare no competing interests.

Additional information

Peer review information *Nature* thanks Dayu Lin, Ruslan Medzhitov and the other, anonymous, reviewer(s) for their contribution to the peer review of this work.

Publisher's note Springer Nature remains neutral with regard to jurisdictional claims in published maps and institutional affiliations.

Extended data figures and tables

[Extended Data Fig. 1 Male mice avoid mounting sick females.](#)

a, b, Male mice were presented with a pair of oestrus female mice each injected intraperitoneally with either PBS (PBS female) or LPS (LPS female) (**a**). Mounting time during a 10-min test (**b**) ($n = 9$; from 2 independent experiments). **c**, Mounting time for male mice presented with two untreated, healthy females ($n = 8$; from 2 independent experiments). **d**, Investigation time of PBS and LPS females during a 10-min three-chamber assay ($n = 5$; from 2 independent experiments). **e–i**, These data are associated with Fig. [1a–e](#). Duration of other typical male behaviours while engaged in direct interactions with a PBS or LPS female (**e, f**). Percentage of individual female behaviours during males' mounting attempts (**g**) and the number of cage crossings (**h**). Representative traces of male and female behaviours during direct interactions (**i**). $**P < 0.01$, $***P < 0.001$ and $****P < 0.0001$ calculated by paired two-tailed *t*-test (**b**), two-way ANOVA with Sidak's post hoc test (**f, g**) and unpaired two-tailed *t*-test (**h**). Data are mean \pm s.e.m. *P*values are described in the Supplementary Statistical Information.

Extended Data Fig. 2 Role of the vomeronasal pathway in mounting behaviour.

a, Mounting time for males with a sham surgery (sham) or the VNO removed (VNOX) towards LPS females (sham, $n = 5$ and VNOX, $n = 7$; from 2 independent experiments). **b–d**, Virus encoding the anterograde trans-synaptic tracer (AAV₁-hSyn-Cre) was targeted to the AOB in Ai14 reporter mice that express tdTomato in a Cre-dependent manner (**b**). Representative images (**c**) and quantification (**d**) of trans-synaptically labelled tdTomato⁺ neurons in BST, MEA and COApM at the specified anterior-posterior axis ($n = 4$; from 3 independent experiments). Scale bars, 500 μ m. **e–g**, Virus encoding ChR2 (AAV₂-hSyn-hChR2-eYFP) was targeted to the AOB (**e, f**). **g**, Representative image of FOS expression in the COApM upon photoactivation of the AOB, from $n = 3$ mice. Scale bars, 500 μ m. **h**, These data are associated with Fig. [1g](#). Number of FOS-expressing neurons in the vomeronasal pathway after interaction with PBS or LPS females. $**P < 0.01$, $***P < 0.001$ and $****P < 0.0001$ calculated by unpaired two-tailed *t*-test (**a**), one-way ANOVA with Bonferroni's post hoc test (**d**) and two-way ANOVA with Sidak's post hoc test (**h**). Graph

indicates mean \pm s.e.m. P values are described in the Supplementary Statistical Information.

Extended Data Fig. 3 Investigation of LPS females induces neural activity in the COApm of males.

a–c, These data are associated with Fig. 1h–o. **a**, Representative image of GCaMP6s expression in the COApm. Scale bar, 300 μ m. **b**, Individual traces of COApm bulk fluorescence signal during interactions with a PBS or LPS female. **c**, Heat map of normalized COApm responses to PBS or LPS females. Each row represents a single investigation event.

Investigation events were pooled from 6 mice from 3 independent experiments. Time = 0 indicates initiation of investigation. **d, e**, Virus encoding GCaMP6s (AAV₁-Syn-GCaMP6s) was targeted to the COApm for fibre photometry recordings. Male mice were sequentially presented with an oestrus or dioestrus female in counterbalanced sessions.

Representative traces of COApm bulk fluorescence signal (**d**) and the mean z -score of the fluorescence during direct investigation of the oestrus or dioestrus female (**e**) (oestrus, $n = 5$ and dioestrus, $n = 5$; from 3 independent experiments). **f–j**, Male mounting behaviours towards an oestrus or dioestrus, healthy female. Percentage of male mounting (**f**), mounting time (**g**), number of mounts (**h**), latency to mount (**i**) and percentage of female partners with mating plugs (**j**) (oestrus, $n = 6$ and dioestrus, $n = 6$; from 2 independent experiments). **j**, $*P < 0.05$ calculated by chi-square test of independence. Data are mean \pm s.e.m. P values are described in the Supplementary Statistical Information.

Extended Data Fig. 4 LPS odour suppresses male mating behaviours.

a–c, Male mice were presented with PBS or LPS odour (**a**). Representative images (**b**) and quantification (**c**) of FOS expression in the COApm of males after exposure to PBS or LPS odour (PBS odour, $n = 6$ and LPS odour, $n = 8$; from 2 independent experiments). Scale bar, 500 μ m. **d, e**, Virus encoding GCaMP6s (AAV₁-Syn-GCaMP6s) was targeted to the COApm for fibre photometry recordings. Male mice were sequentially

presented with a PBS or LPS odour in counterbalanced sessions. Traces of COApm bulk fluorescence signal (solid line shows the average and shaded area indicates the s.e.m.) (**d**) and the mean *z*-score of the fluorescence during the first 20 s of direct investigation of the odour (**e**) ($n = 6$; from 3 independent experiments). **f–m**, Male mice were presented with a healthy female painted with PBS or LPS odour (**f**). Percentage of male mounting (**g**), mounting time (**h**), number of mounts (**i**), latency to mount (**j**) and duration of additional male behaviours while engaged in direct interactions with the female (**k**). Percentage of female behaviours in response to males' mounting attempts (**l**) and the number of cage crossings (**m**) (PBS odour, $n = 10$ and LPS odour, $n = 11$; from 2 independent experiments). * $P < 0.05$, ** $P < 0.01$ and *** $P < 0.0001$ calculated by unpaired two-tailed *t*-test (**c**, **h–j**), paired two-tailed *t*-test (**e**), chi-square test of independence (**g**) and two-way ANOVA with Sidak's post hoc test (**k**). Data are mean \pm s.e.m. *P* values are described in the Supplementary Statistical Information.

Extended Data Fig. 5 COApm mediates suppression of mating behaviours towards unhealthy females.

a–d, These data are associated with Fig. [2a–e](#). **a**, Representative image of ChR2 expression in the COApm. **b**, Total direct investigation time of healthy females in the presence (ON) and absence (OFF) of COApm photoactivation. Duration of self grooming (**c**) and percentage of photoactivation trials with self grooming (**d**). Scale bar, 1 mm. **e, f**, These data are associated with Fig. [2i–m](#). Representative image of hM4Di expression in the COApm (**e**) and total direct investigation time of LPS females (**f**). Scale bar, 1 mm. **g–k**, Additional control experiments for data in Fig. [2i–m](#). Male mice expressing inhibitory DREADD (AAV₂-hSyn-hM4D(G_i)-mCherry) in COApm were injected with either saline or CNO and tested for mounting behaviour towards LPS females (**g**). Percentage of male mounting (**h**), mounting time (**i**), number of mounts (**j**) and latency to mount (**k**) (saline, $n = 8$ and CNO, $n = 7$; from 2 independent experiments). **l–p**, Male mice expressing mCherry (AAV₂-hSyn-mCherry) or inhibitory DREADD (hM4Di, AAV₂-hSyn-hM4D(G_i)-mCherry) in COApm were injected with CNO and tested for mounting behaviour towards untreated, healthy oestrus females (**l**). Percentage of male mounting (**m**), mounting

time (**n**), number of mounts (**o**) and latency to mount (**p**) (mCherry, $n = 8$ and hM4Di, $n = 8$; from 2 independent experiments). **q–u**, Male mice expressing inhibitory DREADD (AAV₂-hSyn-hM4D(G_i)-mCherry) in COApm were injected with saline or CNO and tested for mounting behaviour towards untreated, healthy dioestrus females (**q**). Percentage of male mounting (**r**), mounting time (**s**), number of mounts (**t**), and latency to mount (**u**) (saline, $n = 6$ and CNO, $n = 6$; from 2 independent experiments). * $P < 0.05$, ** $P < 0.01$ calculated by unpaired two-tailed *t*-test (**c, i, j**). Data are mean ± s.e.m. *P* values are described in the Supplementary Statistical Information.

Extended Data Fig. 6 COApm neurons preferentially project to MEA-Vglut2⁺ neurons.

a, b, Virus encoding the anterograde tracer (AAV₂-hSyn-tdTomato) was targeted to the COApm. Total fluorescence intensity was measured in sub-regions receiving COApm axonal projections: MEA, BST, ventral hippocampus (HCv), lateral septum (LS), AOB and piriform cortex (PIR) ($n = 4$ mice; from 2 independent experiments). Scale bars, 500 μ m. **c**, Virus encoding the anterograde trans-synaptic tracer (AAV₁-hSyn-Cre) was targeted to the COApm of Ai14 reporter mice that express tdTomato in a Cre-dependent manner. Representative image of MEA post-synaptic neurons at AP –1.7 mm, from 3 independent experiments. Scale bar, 300 μ m. **d**, mRNA expression of *Vglut2* and *Vgat* in MEA (Image credit: Allen Institute). **e–g**, ChR2 (AAV₂-hSyn-ChR2-eYFP) was targeted to the COApm (**e**). Representative images of ChR2 expression in COApm (**f**) and FOS expression in MEA upon photoactivation of COApm (**g**) ($n = 3$; from 2 independent experiments). Scale bars, 300 μ m. **h, i**, Virus encoding GCaMP6s (AAV₁-Syn-GCaMP6s) was targeted to the MEA of Vglut2-Cre mice for fibre photometry recordings. Male mice were sequentially presented with a PBS or LPS female in counterbalanced sessions. Representative traces of MEA-vGlut2⁺ bulk fluorescence signal (**h**) and the mean *z*-score of the fluorescence during direct investigation of the PBS or LPS female (**i**) ($n = 3$; from 2 independent experiments). **i**, * $P < 0.05$ calculated by paired two-tailed *t*-test. Data are mean ± s.e.m. *P* values are described in the Supplementary Statistical Information.

Extended Data Fig. 7 COApm suppresses male mating behaviours by engaging MEA-Vglut2⁺ neurons.

These data are associated with Fig. 3f–i. Percentage of male mounting (a–d), number of mounts (e–h), latency to mount (i–l). Representative images of ChR2 expression in COApm (m) and hM4Di expression in MEA (n) of Vglut2-Cre mice with concurrent photoactivation of COApm-MEA projections and hM4Di-inhibition of MEA-Vglut2⁺ neurons. Scale bars, 500 µm. * $P < 0.05$, ** $P < 0.01$, *** $P < 0.001$ and **** $P < 0.0001$ calculated by chi-square test of independence (a–c) and unpaired two-tailed *t*-test (e–k). Data are mean ± s.e.m. *P* values are described in the Supplementary Statistical Information.

Extended Data Fig. 8 Summary of gene-expression profiling in COApm neurons projecting to MEA-Vglut2⁺ neurons.

a, A combination of AAV₁-Syn-FLEX-TTA and AAV-TRE-B19G, and RVΔG-L10a-eGFP were sequentially injected into the MEA of Vglut2-Cre mice to express L10a-eGFP in COApm neurons projecting to MEA-Vglut2⁺ neurons (COApm-proj). COApm tissue was collected and immediately used for TRAP analyses. Control mice were injected with AAV.PHP.eB-Syn-L10a-eGFP via retro-orbital injection in order to label COApm neurons with L10a-eGFP independently of their efferent projections (Total COApm). **b**, Volcano plot showing log₂-fold change plotted against –log₁₀ FDR for the labelled COApm neurons projecting to the MEA-Vglut2⁺ population (COApm-Proj.) compared to the total COApm. Differentially expressed genes that pass the threshold for the FDR are highlighted in red. **c**, Heat map showing COApm-differentially expressed genes that belong to the KEGG neuroactive ligand–receptor interaction pathway. *P* values are described in the Supplementary Statistical Information.

Extended Data Fig. 9 COApm-TRH[±] neurons mediate the suppression of male mating towards unhealthy females.

a–g, Trh-Cre male mice expressing tdTomato (AAV_{1/2}-Eflα-DO-DIO-tdTomato(tdT)-eGFP, Control) or ChR2 (AAV_{1/2}-Eflα-DO-ChR2-mCherry, ChR2) in Cre[–] neurons were tested for mating behaviours towards healthy females with COApm photoactivation (**a**). Representative images (**b**) and quantification (**c**) of FOS expression in COApm. Percentage of male mounting (**d**), mounting time (**e**), number of mounts (**f**), and latency to mount (**g**) with photoactivation of COApm-TRH[–] cells (control, $n = 5$ and ChR2, $n = 5$; from 2 independent experiments). Scale bars, 500 μm. **h–l**, Calcium imaging of MEA brain slices from Vglut2-Cre mice expressing GCaMP7f (AAV₁-hSyn-FLEX-GCaMP7f) in MEA-Vglut2⁺ neurons upon taltirelin (10 μM) application (**h**). **i**, Representative images of MEA slices before (–15 s) and after (+35 s) taltirelin application. Example traces of fluorescence signal from individual neurons (**j**) and the average of the fluorescence signal (solid line shows average and shaded area represents the s.e.m.) (**k**) upon taltirelin application. **l**, Area under the curve (AUC) of the average fluorescence signal from individual MEA slices binned every 30 s ($n = 6$ slices, from 3 mice). Scale bars, 50 μm. **m**, These data are associated with Fig. 4k–o. Total duration of direct investigation following microinjection of the TRH analogue taltirelin into MEA. * $P < 0.05$, ** $P < 0.01$ and *** $P < 0.001$ calculated by unpaired two-tailed *t*-test (**c, m**) and Friedman test with Dunn’s multiple comparisons test (**l**). Data are mean ± s.e.m. *P* values are described in the Supplementary Statistical Information.

Extended Data Fig. 10 Suppression of mating engages TRH-TRHR signalling in the COApm-MEA projection.

a, Schematic depicting the targeting construct used to generate the *Trhr* conditional-knockout mouse line. **b, c**, Representative images (AP –1.8 mm) (**b**) and quantification (**c**) of *Trhr* mRNA expression in the MEApv of *Trhr*^{fl/fl} mice with or without Cre expression (AAV₁-hSyn-Cre) (*Trhr*^{fl/fl}, $n = 3$ and *Trhr*^{fl/fl} with Cre, $n = 3$; from 2 independent experiments). Scale bars, 20 μm. **d–g**, In vivo recordings of MEA responses to COApm inputs in Trhr conditional-knockout mice. *Trhr*^{fl/fl} mice were injected with AAV₂-hSyn-ChR2-eYFP in COApm and either AAV₁-hSyn-GFP (GFP) or AAV₁-

hSyn-Cre (Cre) in MEApv. **d**, Local field potentials evoked by a 10-ms photoactivation were recorded from MEApv in anaesthetized mice using an optrode. **e**, Representative image of electrode localization. Representative waveforms (**f**) and amplitudes (baseline-to-negative peak) of MEApv responses evoked by photoactivation of COApM inputs (**g**) (GFP, $n = 6$ and Cre, $n = 6$; from 6 independent experiments). Scale bar, 300 μ m. *** $P < 0.001$ and **** $P < 0.0001$ calculated by unpaired two-tailed t -test (**c, g**). Data are mean \pm s.e.m. P values are described in the Supplementary Statistical Information.

Supplementary information

Supplementary Data

This file contains Supplementary Statistical Information.

Reporting Summary

Rights and permissions

Reprints and Permissions

About this article



Check for
updates

Cite this article

Kwon, JT., Ryu, C., Lee, H. *et al.* An amygdala circuit that suppresses social engagement. *Nature* **593**, 114–118 (2021).
<https://doi.org/10.1038/s41586-021-03413-6>

Download citation

- Received: 29 April 2020
- Accepted: 02 March 2021
- Published: 31 March 2021
- Issue Date: 06 May 2021
- DOI: <https://doi.org/10.1038/s41586-021-03413-6>

Comments

By submitting a comment you agree to abide by our [Terms](#) and [Community Guidelines](#). If you find something abusive or that does not comply with our terms or guidelines please flag it as inappropriate.

[Access through your institution](#)

[Change institution](#)

[Buy or subscribe](#)

This article was downloaded by **calibre** from <https://www.nature.com/articles/s41586-021-03413-6>

- Article
- [Published: 17 March 2021](#)

Ex utero mouse embryogenesis from pre-gastrulation to late organogenesis

- [Alejandro Aguilera-Castrejon](#) ORCID: [orcid.org/0000-0002-1339-7778^{1 na1 na2}](https://orcid.org/0000-0002-1339-7778),
- [Bernardo Oldak^{1 na1}](#),
- [Tom Shani](#) ORCID: [orcid.org/0000-0002-4878-2174¹](https://orcid.org/0000-0002-4878-2174),
- [Nadir Ghanem²](#),
- [Chen Itzkovich³](#),
- [Sharon Slomovich](#) ORCID: [orcid.org/0000-0002-1123-2400⁴](https://orcid.org/0000-0002-1123-2400),
- [Shadi Tarazi](#) ORCID: [orcid.org/0000-0002-4121-4289¹](https://orcid.org/0000-0002-4121-4289),
- [Jonathan Bayerl¹](#),
- [Valeriya Chugaeva¹](#),
- [Muneef Ayyash¹](#),
- [Shahd Ashouokhi¹](#),
- [Daoud Sheban¹](#),
- [Nir Livnat¹](#),
- [Lior Lasman¹](#),
- [Sergey Viukov¹](#),
- [Mirie Zerbib¹](#),
- [Yoseph Addadi](#) ORCID: [orcid.org/0000-0001-9827-0436⁵](https://orcid.org/0000-0001-9827-0436),
- [Yoach Rais⁶](#),
- [Saifeng Cheng⁶](#),
- [Yonatan Stelzer](#) ORCID: [orcid.org/0000-0001-9207-1479⁶](https://orcid.org/0000-0001-9207-1479),
- [Hadas Keren-Shaul⁷](#),
- [Raanan Shlomo⁸](#),

- [Rada Massarwa](#)^{1 na2 na3},
- [Noa Novershtern](#) [ORCID: orcid.org/0000-0002-2244-6877](#)^{1 na2},
- [Itay Maza](#) [ORCID: orcid.org/0000-0003-3877-6501](#)^{4,9 na2} &
- [Jacob H. Hanna](#) [ORCID: orcid.org/0000-0003-2042-9974](#)^{1 na2}

[*Nature*](#) volume **593**, pages119–124(2021)[Cite this article](#)

- 38k Accesses
- 1666 Altmetric
- [Metrics details](#)

Subjects

- [Embryology](#)

Abstract

The mammalian body plan is established shortly after the embryo implants into the maternal uterus, and our understanding of post-implantation developmental processes remains limited. Although pre- and peri-implantation mouse embryos are routinely cultured in vitro^{1,2}, approaches for the robust culture of post-implantation embryos from egg cylinder stages until advanced organogenesis remain to be established. Here we present highly effective platforms for the ex utero culture of post-implantation mouse embryos, which enable the appropriate development of embryos from before gastrulation (embryonic day (E) 5.5) until the hindlimb formation stage (E11). Late gastrulating embryos (E7.5) are grown in three-dimensional rotating bottles, whereas extended culture from pre-gastrulation stages (E5.5 or E6.5) requires a combination of static and rotating bottle culture platforms. Histological, molecular and single-cell RNA sequencing analyses confirm that the ex utero cultured embryos recapitulate in utero development precisely. This culture system is amenable to the introduction of a variety of embryonic perturbations and micro-manipulations, the results of which can be followed ex utero for up to six days. The establishment of a system for robustly growing normal mouse

embryos ex utero from pre-gastrulation to advanced organogenesis represents a valuable tool for investigating embryogenesis, as it eliminates the uterine barrier and allows researchers to mechanistically interrogate post-implantation morphogenesis and artificial embryogenesis in mammals.

[Access through your institution](#)

[Change institution](#)

[Buy or subscribe](#)

Access options

Subscribe to Journal

Get full journal access for 1 year

\$199.00

only \$3.90 per issue

[Subscribe](#)

All prices are NET prices.

VAT will be added later in the checkout.

Tax calculation will be finalised during checkout.

Rent or Buy article

Get time limited or full article access on ReadCube.

from \$8.99

[Rent or Buy](#)

All prices are NET prices.

Additional access options:

- [Log in](#)

- [Access through your institution](#)
- [Learn about institutional subscriptions](#)

Fig. 1: Ex utero culture system for growing mouse late-gastrulating embryos until advanced organogenesis.



Fig. 2: Defining conditions for recapitulating mouse gastrulation ex utero.

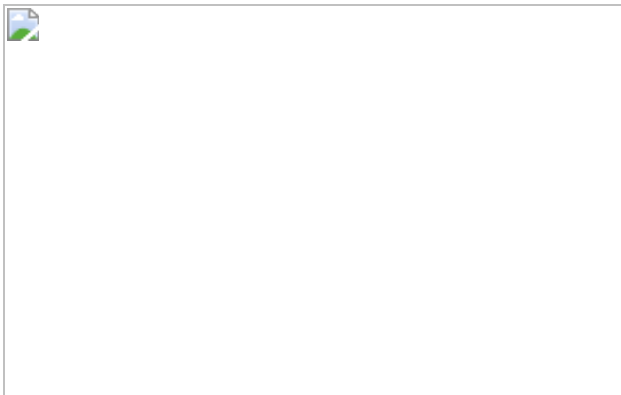
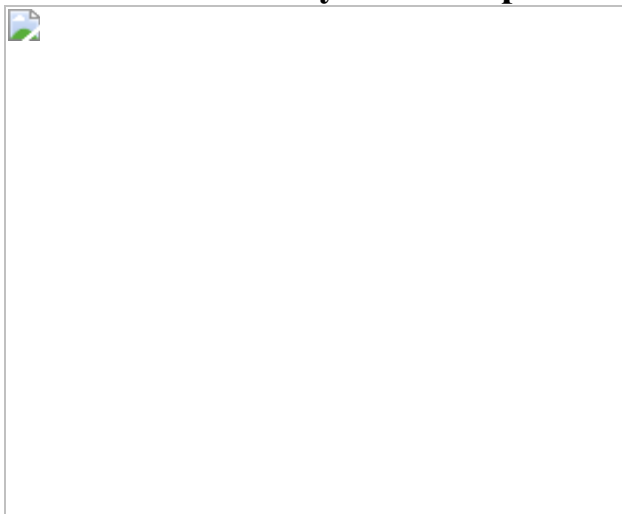


Fig. 3: Extending the mouse embryo ex utero culture system from pre-gastrulation to advanced organogenesis.



Fig. 4: Measuring functional outcomes of perturbations introduced into ex utero whole-embryo culture platform.



Data availability

Bulk and single-cell RNA-seq data have been deposited in the Gene Expression Omnibus (GEO) database under accession number [GSE149372](#). [Source data](#) are provided with this paper.

References

1. 1.

Bedzhov, I. & Zernicka-Goetz, M. Self-organizing properties of mouse pluripotent cells initiate morphogenesis upon implantation. *Cell* **156**, 1032–1044 (2014).

[CAS](#) [Article](#) [Google Scholar](#)

2. 2.

White, M. D. et al. Long-lived binding of Sox2 to DNA predicts cell fate in the four-cell mouse embryo. *Cell* **165**, 75–87 (2016).

[CAS](#) [Article](#) [Google Scholar](#)

3. 3.

New, D. A. T. Whole-embryo culture and the study of mammalian embryos during organogenesis. *Biol. Rev. Camb. Philos. Soc.* **53**, 81–122 (1978).

[CAS](#) [Article](#) [Google Scholar](#)

4. 4.

Huang, Q. et al. Intravital imaging of mouse embryos. *Science* **368**, 181–186 (2020).

[ADS](#) [CAS](#) [Article](#) [Google Scholar](#)

5. 5.

Nicholas, J. S. & Rudnick, D. The development of rat embryos in tissue culture. *Proc. Natl Acad. Sci. USA* **20**, 656–658 (1934).

[ADS](#) [CAS](#) [Article](#) [Google Scholar](#)

6. 6.

New, D. A. T. & Stein, K. F. Cultivation of mouse embryos in vitro. *Nature* **199**, 297–299 (1963).

[ADS](#) [CAS](#) [Article](#) [Google Scholar](#)

7. 7.

New, D. A. T., Coppola, P. T. & Terry, S. Culture of explanted rat embryos in rotating tubes. *J. Reprod. Fertil.* **35**, 135–138 (1973).

[CAS](#) [Article](#) [Google Scholar](#)

8. 8.

New, D. A. T. Development of explanted rat embryos in circulating medium. *Development* **17**, 513–525 (1967).

[CAS](#) [Article](#) [Google Scholar](#)

9. 9.

Beddington, R. S. Induction of a second neural axis by the mouse node. *Development* **120**, 613–620 (1994).

[CAS](#) [Article](#) [Google Scholar](#)

10. 10.

Parameswaran, M. & Tam, P. P. L. Regionalisation of cell fate and morphogenetic movement of the mesoderm during mouse gastrulation. *Dev. Genet.* **17**, 16–28 (1995).

[CAS](#) [Article](#) [Google Scholar](#)

11. 11.

Tam, P. P. Postimplantation mouse development: whole embryo culture and micro-manipulation. *Int. J. Dev. Biol.* **42**, 895–902 (1998).

[CAS](#) [PubMed](#) [Google Scholar](#)

12. 12.

Cantor, J. R. et al. Physiologic medium rewires cellular metabolism and reveals uric acid as an endogenous inhibitor of UMP synthase. *Cell* **169**, 258–272 (2017).

[CAS](#) [Article](#) [Google Scholar](#)

13. 13.

Nagamatsu, G., Shimamoto, S., Hamazaki, N., Nishimura, Y. & Hayashi, K. Mechanical stress accompanied with nuclear rotation is involved in the dormant state of mouse oocytes. *Sci. Adv.* **5**, eaav9960 (2019).

[ADS](#) [CAS](#) [Article](#) [Google Scholar](#)

14. 14.

Ueda, Y. et al. Intrauterine pressures adjusted by Reichert's membrane are crucial for early mouse morphogenesis. *Cell Rep.* **31**, 107637 (2020).

[CAS](#) [Article](#) [Google Scholar](#)

15. 15.

Downs, K. M. & Davies, T. Staging of gastrulating mouse embryos by morphological landmarks in the dissecting microscope. *Development* **118**, 1255–1266 (1993).

[CAS](#) [Article](#) [Google Scholar](#)

16. 16.

van Maele-Fabry, G., Delhaise, F. & Picard, J. J. Evolution of the developmental scores of sixteen morphological features in mouse

embryos displaying 0 to 30 somites. *Int. J. Dev. Biol.* **36**, 161–167 (1992).

[PubMed](#) [Google Scholar](#)

17. 17.

Stelzer, Y. et al. Parent-of-origin DNA methylation dynamics during mouse development. *Cell Rep.* **16**, 3167–3180 (2016).

[CAS](#) [Article](#) [Google Scholar](#)

18. 18.

McDole, K. et al. In toto imaging and reconstruction of post-implantation mouse development at the single-cell level. *Cell* **175**, 859–876 (2018).

[CAS](#) [Article](#) [Google Scholar](#)

19. 19.

Ibarra-Soria, X. et al. Defining murine organogenesis at single-cell resolution reveals a role for the leukotriene pathway in regulating blood progenitor formation. *Nat. Cell Biol.* **20**, 127–134 (2018).

[CAS](#) [Article](#) [Google Scholar](#)

20. 20.

Pijuan-Sala, B. et al. A single-cell molecular map of mouse gastrulation and early organogenesis. *Nature* **566**, 490–495 (2019).

[ADS](#) [CAS](#) [Article](#) [Google Scholar](#)

21. 21.

Cao, J. et al. The single-cell transcriptional landscape of mammalian organogenesis. *Nature* **566**, 496–502 (2019).

[ADS](#) [CAS](#) [Article](#) [Google Scholar](#)

22. 22.

Saito, T. & Nakatsuji, N. Efficient gene transfer into the embryonic mouse brain using in vivo electroporation. *Dev. Biol.* **240**, 237–246 (2001).

[CAS](#) [Article](#) [Google Scholar](#)

23. 23.

Beronja, S., Livshits, G., Williams, S. & Fuchs, E. Rapid functional dissection of genetic networks via tissue-specific transduction and RNAi in mouse embryos. *Nat. Med.* **16**, 821–827 (2010).

[CAS](#) [Article](#) [Google Scholar](#)

24. 24.

Morgani, S., Nichols, J. & Hadjantonakis, A. K. The many faces of pluripotency: in vitro adaptations of a continuum of in vivo states. *BMC Dev. Biol.* **17**, 7 (2017).

[Article](#) [Google Scholar](#)

25. 25.

Kojima, Y. et al. The transcriptional and functional properties of mouse epiblast stem cells resemble the anterior primitive streak. *Cell Stem Cell* **14**, 107–120 (2014).

[CAS](#) [Article](#) [Google Scholar](#)

26. 26.

Wu, J. et al. An alternative pluripotent state confers interspecies chimaeric competency. *Nature* **521**, 316–321 (2015).

[ADS](#) [CAS](#) [Article](#) [Google Scholar](#)

27. 27.

Huang, Y., Osorno, R., Tsakiridis, A. & Wilson, V. In vivo differentiation potential of epiblast stem cells revealed by chimeric embryo formation. *Cell Rep.* **2**, 1571–1578 (2012).

[CAS](#) [Article](#) [Google Scholar](#)

28. 28.

van Wilgenburg, B., Browne, C., Vowles, J. & Cowley, S. A. Efficient, long term production of monocyte-derived macrophages from human pluripotent stem cells under partly-defined and fully-defined conditions. *PLoS One* **8**, e71098 (2013).

[ADS](#) [Article](#) [Google Scholar](#)

29. 29.

Gafni, O. et al. Derivation of novel human ground state naive pluripotent stem cells. *Nature* **504**, 282–286 (2013).

[ADS](#) [CAS](#) [Article](#) [Google Scholar](#)

30. 30.

Harrison, S. E., Sozen, B., Christodoulou, N., Kyprianou, C. & Zernicka-Goetz, M. Assembly of embryonic and extraembryonic stem cells to mimic embryogenesis in vitro. *Science* **356**, eaal1810 (2017).

[Article](#) [Google Scholar](#)

31. 31.

Aguilera-Castrejon, A. & Hanna, J. H. Highly conducive ex utero mouse embryogenesis from pre-gastrulation to late organogenesis. *Protoc. Exch.* <https://doi.org/10.21203/rs.3.pex-1372/v1> (2021).

32. 32.

Renier, N. et al. iDISCO: a simple, rapid method to immunolabel large tissue samples for volume imaging. *Cell* **159**, 896–910 (2014).

[CAS](#) [Article](#) [Google Scholar](#)

33. 33.

Stuart, T. et al. Comprehensive integration of single-cell data. *Cell* **177**, 1888–1902 (2019).

[CAS](#) [Article](#) [Google Scholar](#)

34. 34.

Butler, A., Hoffman, P., Smibert, P., Papalexi, E. & Satija, R. Integrating single-cell transcriptomic data across different conditions, technologies, and species. *Nat. Biotechnol.* **36**, 411–420 (2018).

[CAS](#) [Article](#) [Google Scholar](#)

35. 35.

Aibar, S. et al. SCENIC: single-cell regulatory network inference and clustering. *Nat. Methods* **14**, 1083–1086 (2017).

[CAS](#) [Article](#) [Google Scholar](#)

36. 36.

Ritchie, M. E. et al. limma powers differential expression analyses for RNA-sequencing and microarray studies. *Nucleic Acids Res.* **43**, e47 (2015).

[Article](#) [Google Scholar](#)

[Download references](#)

Acknowledgements

This work was funded by Pascal and Ilana Mantoux; the European Research Council (ERC-CoG-2016 726497-Cellnaivety); the Flight Attendant Medical Research Council (FAMRI); an Israel Cancer Research Fund (ICRF) professorship; BSF; the Helen and Martin Kimmel Institute for Stem Cell Research; the Helen and Martin Kimmel Award for Innovative Investigation; the Israel Science Foundation (ISF); Minerva; the Sherman Institute for Medicinal Chemistry; the Nella and Leon Benoziyo Center for Neurological Diseases; the David and Fela Shapell Family Center for Genetic Disorders Research; the Weizmann–U. Michigan program; the Kekst Family Institute for Medical Genetics; the Dr. Beth Rom-Rymer Stem Cell Research Fund; the Edmond de Rothschild Foundations; the Zantker Charitable Foundation; and the Estate of Zvia Zeroni. We thank O. Reiner and T. Sapir for help with mouse embryo electroporations; the Crown Genomics institute of the Nancy and Stephen Grand Israel National Center for Personalized Medicine at the Weizmann Institute for support with scRNA-seq; and the Weizmann Institute management and board for providing critical financial and infrastructural support. We dedicate this paper to the memories of R. Massarwa and H. Garty.

Author information

Author notes

1. These authors contributed equally: Alejandro Aguilera-Castrejon, Bernardo Oldak
2. These authors jointly supervised this work: Alejandro Aguilera-Castrejon, Rada Massarwa, Noa Novershtern, Itay Maza, Jacob H. Hanna
3. Deceased: Rada Massarwa

Affiliations

1. Department of Molecular Genetics, Weizmann Institute of Science, Rehovot, Israel

Alejandro Aguilera-Castrejon, Bernardo Oldak, Tom Shani, Shadi Tarazi, Jonathan Bayerl, Valeriya Chugaeva, Muneef Ayyash, Shahd Ashouokhi, Daoud Sheban, Nir Livnat, Lior Lasman, Sergey Viukov, Mirie Zerbib, Rada Massarwa, Noa Novershtern & Jacob H. Hanna

2. Department of Obstetrics and Gynecology, Rambam Health Care Campus, Haifa, Israel

Nadir Ghanem

3. The Clinical Research Institute at Ramban (CRIR), Rambam Health Care Campus, Haifa, Israel

Chen Itzkovich

4. Bruce Rappaport Faculty of Medicine, Israel Institute of Technology - Technion, Haifa, Israel

Sharon Slomovich & Itay Maza

5. Department of Life Sciences Core Facilities, Weizmann Institute of Science, Rehovot, Israel

Yoseph Addadi

6. Department of Molecular Cell Biology, Weizmann Institute of Science, Rehovot, Israel

Yoach Rais, Saifeng Cheng & Yonatan Stelzer

7. Department of Life Sciences Core Facilities, Weizmann Institute of Science, Rehovot, Israel

Hadas Keren-Shaul

8. Arad Technologies Ltd, Ashdod, Israel

Raanan Shlomo

9. Gastroenterology Unit, Rambam Health Care Campus, Haifa, Israel

Itay Maza

Authors

1. Alejandro Aguilera-Castrejon

[View author publications](#)

You can also search for this author in [PubMed](#) [Google Scholar](#)

2. Bernardo Oldak

[View author publications](#)

You can also search for this author in [PubMed](#) [Google Scholar](#)

3. Tom Shani

[View author publications](#)

You can also search for this author in [PubMed](#) [Google Scholar](#)

4. Nadir Ghanem

[View author publications](#)

You can also search for this author in [PubMed](#) [Google Scholar](#)

5. Chen Itzkovich

[View author publications](#)

You can also search for this author in [PubMed](#) [Google Scholar](#)

6. Sharon Slomovich

[View author publications](#)

You can also search for this author in [PubMed](#) [Google Scholar](#)

7. Shadi Tarazi

[View author publications](#)

You can also search for this author in [PubMed](#) [Google Scholar](#)

8. Jonathan Bayerl

[View author publications](#)

You can also search for this author in [PubMed](#) [Google Scholar](#)

9. Valeriya Chugaeva

[View author publications](#)

You can also search for this author in [PubMed](#) [Google Scholar](#)

10. Muneef Ayyash

[View author publications](#)

You can also search for this author in [PubMed](#) [Google Scholar](#)

11. Shahd Ashouokhi

[View author publications](#)

You can also search for this author in [PubMed](#) [Google Scholar](#)

12. Daoud Sheban

[View author publications](#)

You can also search for this author in [PubMed](#) [Google Scholar](#)

13. Nir Livnat

[View author publications](#)

You can also search for this author in [PubMed](#) [Google Scholar](#)

14. Lior Lasman

[View author publications](#)

You can also search for this author in [PubMed](#) [Google Scholar](#)

15. Sergey Viukov

[View author publications](#)

You can also search for this author in [PubMed](#) [Google Scholar](#)

16. Mirie Zerbib

[View author publications](#)

You can also search for this author in [PubMed](#) [Google Scholar](#)

17. Yoseph Addadi

[View author publications](#)

You can also search for this author in [PubMed](#) [Google Scholar](#)

18. Yoach Rais

[View author publications](#)

You can also search for this author in [PubMed](#) [Google Scholar](#)

19. Saifeng Cheng

[View author publications](#)

You can also search for this author in [PubMed](#) [Google Scholar](#)

20. Yonatan Stelzer

[View author publications](#)

You can also search for this author in [PubMed](#) [Google Scholar](#)

21. Hadas Keren-Shaul

[View author publications](#)

You can also search for this author in [PubMed](#) [Google Scholar](#)

22. Raanan Shlomo

[View author publications](#)

You can also search for this author in [PubMed](#) [Google Scholar](#)

23. Rada Massarwa

[View author publications](#)

You can also search for this author in [PubMed](#) [Google Scholar](#)

24. Noa Novershtern

[View author publications](#)

You can also search for this author in [PubMed](#) [Google Scholar](#)

25. Itay Maza

[View author publications](#)

You can also search for this author in [PubMed](#) [Google Scholar](#)

26. Jacob H. Hanna

[View author publications](#)

You can also search for this author in [PubMed](#) [Google Scholar](#)

Contributions

A.A.-C. designed and conducted most of the wet lab, embryology, sequencing and imaging experiments, established the ex utero culture protocol and co-wrote the manuscript. B.O. conducted embryo injections, performed human microglia cultures and generated human–mouse chimeras, assisted in culture condition testing and processed cryosections. T.S. conducted bioinformatics analysis with N.N. supervising. R.M. helped to reproduce previously published protocols for ex utero culture and taught immunohistochemical protocols to our team. I.M. submitted Helsinki approval, collected cord blood and calibrated human cord serum production. N.G. recruited donors and performed cord blood extraction during caesarean sections. C.I. and S.S. assisted with human cord serum production. S.T. generated lentiviruses and assisted in embryo immunostaining and lentiviral infection of embryos. J.B., D.S. and S.V. performed tissue culture and bulk RNA sequencing of mouse pluripotent stem cells. V.C., S.A. and L.L. assisted with embryo immunostaining. N.L. performed characterization of cultured cells by qPCR. M.A. and H.K.-S.

assisted with library preparation and single-cell RNA sequencing. Y.A. assisted with light sheet microscopy and live imaging. Y.R., S.C. and Y.S. generated tdTomato reporter embryos and assisted with allele imprinting experiments. M.Z. assisted with embryo injections. R.S. assembled and maintained the gas-pressure regulator module. J.H.H. conceived the idea for this project, conceptually designed the gas regulator module, established the ex utero culture protocol, supervised execution of experiments and adequate analysis of data, and wrote the manuscript.

Corresponding authors

Correspondence to [Alejandro Aguilera-Castrejon](#) or [Itay Maza](#) or [Jacob H. Hanna](#).

Ethics declarations

Competing interests

J.H.H is an advisor to Biological Industries Ltd, and submitted a patent application that covers the roller and static culture conditions described herein (filed by J.H.H. and the Weizmann Institute of Science). R.S. is CEO of Arad Technologies Ltd. All other authors declare no competing interests.

Additional information

Peer review information *Nature* thanks Hiromitsu Nakauchi, Magdalena Zernicka-Goetz and the other, anonymous, reviewer(s) for their contribution to the peer review of this work.

Publisher's note Springer Nature remains neutral with regard to jurisdictional claims in published maps and institutional affiliations.

Extended data figures and tables

Extended Data Fig. 1 Optimized gas-regulating module for roller culture incubators.

a, Diagram depicting the configuration of the gas-mixing box for gas concentration and pressure regulation. N₂ and CO₂ enter the gas-mixing box and are mixed by a centrifugal blower. Gases are then injected into a water bottle inside the incubator by a pressure pump that allows control of the gas pressure in the gas-mixing box that is transmitted to the sealed embryo bottle apparatus. The voltage on the pressure transmitter controls the pressure generated by the pressure pump in the gas mixing box. Lph, litres per hour. **b, c**, Top and front views of the gas controller module. **d, e**, Picture displaying the localization of the main components in the gas regulation module (**d**; listed in **e**). **f**, Interior of the precision incubator system (by B.T.C. Engineering, Cullum Starr Ltd) showing the direction of the gas flow (white arrowheads). **g**, Image of day 3 (E10.5) embryos cultured in rotating bottles (yellow arrowheads).

Extended Data Fig. 2 Establishment and optimization of a mouse embryo ex utero culture from late gastrulation (E7.5) until advanced organogenesis (E11).

a, E7.5 embryo dissection overview (see [Methods](#)). **b**, Percentage of normally developed embryos under different gas pressures and glucose or oxygen concentrations. Blue numbers indicate the conditions that yielded the highest efficiency of embryo survival. Values in parentheses denote the number of embryos assessed per condition at every sampled time point. Embryos that were dissected, fixed or moved to other conditions are subtracted from the total. Representative bright-field images of embryos cultured under certain conditions are shown to the right. **c**, Efficiency of normal embryonic development evaluated in different mouse genetic backgrounds. Parental mouse lines are indicated on the left (female: male). Values in parentheses show the numbers of embryos evaluated. PYS, parietal yolk sac; RS, rat serum. Scale bars, 500 µm. [Source data](#)

Extended Data Fig. 3 Spatio-temporal expression patterns of ectoderm- and mesoderm-related lineage markers are

recapitulated in ex utero cultured embryos.

Maximum intensity projections of embryos developed in utero and ex utero, fixed and immunostained for SOX2, OTX2, TUJ1, PAX6, SOX9, Brachyury, CDX2 and MHC-II (myosin heavy chain-II) at the indicated stages. Blue, DAPI. Images are representative of a minimum of three biological replicates. Scale bars, 100 µm (E7.5), 200 µm (E8.5, E9.5), and 500 µm (E10.5, E11.5).

Extended Data Fig. 4 In vivo spatio-temporal expression patterns of endoderm-related lineage markers are recapitulated in cultured embryos.

Maximum intensity projections of embryos developed in utero and ex utero, fixed and immunostained for SOX17, FOXA2 and GATA4 at the indicated stages. Blue, DAPI. For SOX17, insets are enlargements of the dashed boxes. Representative immunohistochemistry (mid-section, sagittal plane) images are shown for FOXA2 and GATA4 at the last time point (far-right panels). Images represent a minimum of three biological replicates. Scale bars, 100 µm (E7.5), 200 µm (E8.5, E9.5), and 500 µm (E10.5, E11.5).

Extended Data Fig. 5 Ex utero culture of GFP-reporter transgenic embryos.

a, Bright-field and GFP fluorescence images of ex utero embryos in culture at the specified times expressing the GFP reporter following activation by *Wnt1-Cre* and *Isl1-Cre* lineage-specific reporter alleles. $n = 7$ and 10 embryos for *Wnt1-Cre* and *Isl1-Cre*, respectively. Embryos dissected out of the yolk sac at +Day 4 are shown in the far-right panel. Scale bars, 500 µm. **b**, Representative confocal images of in utero E11.5 and ex utero +Day 4 transgenic mouse embryos expressing GFP following activation by *Wnt1-Cre* and *Isl1-Cre* reporter alleles. Scale bars, 1 mm. **c**, GFP fluorescence and bright-field images of in utero E10.5 and ex utero +Day 3 IG-DMR-GFP reporter embryos. $n = 7$ in utero; $n = 7$ ex utero. Scale bars, 500 µm.

Extended Data Fig. 6 Devising a platform for culturing mouse embryos from the onset of gastrulation until advanced organogenesis.

a–o, Schematic protocols indicating the percentages of E6.5 embryos that had developed properly per day in each condition. The medium composition, static or roller culture, and oxygen concentration are specified for each protocol. Values in parentheses denote the number of embryos evaluated per condition. Embryos that were dissected, fixed or moved to other conditions are subtracted from the total. Representative bright-field images of embryos cultured under certain conditions are shown to the right. Numbers in blue indicate the protocol that yielded the highest efficiency of embryo survival and was subsequently used throughout the study. Scale bars, 500 µm.

Extended Data Fig. 7 Embryos grown ex utero since early gastrulation recapitulate the spatio-temporal expression profiles of lineage markers seen in utero.

a–c, Maximum intensity projections of embryos developed ex utero, fixed, and immunostained for eleven specific markers at the indicated time points. Blue, DAPI. Images are representative of a minimum of three biological replicates. Scale bars, 50 µm (E6.5), 100 µm (+Day 1), 200 µm (+Day 2/3), 500 µm (+Day 4/5).

Extended Data Fig. 8 Single-cell transcriptomic analysis of ex utero +Day 2 and +Day 4 cultured embryos compared to in utero E8.5 and E10.5 embryos.

a, Schematic illustration of the embryo culture protocol and sequenced time points. Early-gastrulating (E6.5) embryos grown ex utero were processed for 10x Genomics scRNA-seq after 2 or 4 days of culture. **b**, Violin plot indicating the number of unique molecular identifiers (UMIs) and genes obtained per condition at each time point. E8.5, median of 9,787 UMIs and 2,989 genes detected per cell; E10.5, median of 4,795 UMIs and 1,789 genes detected per cell. **c, d**, Lineage annotation at culture days +2 (**c**) and

+4 (**d**). Dot plots illustrating the area under the curve (AUC) enrichment value of overlapping cells across clusters and tissue lineages. Circle size denotes the magnitude of enrichment. Colours indicate *P* value (calculated from AUC). **e, f**, UMAP-based plots illustrating the normalized AUC assigned value of all individual cells for each lineage at culture days +2 (**e**) and +4 (**f**). **g**, Correlation of gene expression of the top 2,000 most variable genes per cluster between in utero E10.5 and ex utero +Day 4 embryos. Differentially expressed genes are named and shown as red dots. Clusters with the highest number of variable genes (range of 2–8 genes only per cluster) are encased in a red box. **h**, Pie charts depicting the proportional abundance of each cell cluster in both in utero and ex utero developed embryos at +Day 4/E10.5. Asterisks denote clusters with statistically significant differences between the two groups. Cluster 7, *P* = 0.004; cluster 8, *P* = 0.009; cluster 15, *P* = 0.001.

Extended Data Fig. 9 Changes in morphology and size in embryos developing ex utero from pre-gastrulation to the hindlimb formation stage.

a, Proportional increase in size of ex utero embryos grown from the onset of gastrulation (E6.5) to the 44-somite stage. Representative bright-field images of embryos cultured for 5 days are shown at each specific stage. Embryos without yolk sac are shown from day 3 to day 5. $n \geq 119$. **b**, Percentages of normal embryos in cultures started at E6.5. **c**, Diagram depicting the embryonic axis measured at each stage (length of the antero-posterior axis (A-P) for E6.5 to E8.5 and crown–rump length for later stages). **d**, Measurements of embryonic length at the indicated time points. Dots represent individual embryos; in utero, $n = 72, 25, 13, 19, 15, 38$ (left to right); ex utero, $n = 68, 29, 8, 19, 24$; **Mann–Whitney test; ns, not significant. **e**, Bright-field images of E5.5 embryos grown ex utero for 6 days until the 42-somite stage. Embryos cultured since E5.5 exhibit a mild developmental delay of about 2–4 pairs of somites when compared to those developed in utero; however, overall morphological development seemed to occur correctly. **f**, Percentages of normal embryos in cultures started at E5.5. **g**, Representative increase in size of embryos cultured from E5.5 to the hindlimb stage (6 days of culture). Embryos dissected at the beginning and end of culture are shown. **h**, Immunostaining of pre-

gastrulating (E5.5) embryos cultured for 6 days until the 42-somite stage. LEFTY1 and OCT4 immunostaining on a section of an E5.5 embryo (left); GATA4, MHC-II and SOX2 maximum intensity projection of an embryo at culture day 6 and stained (right). Scale bars, 50 µm (E5.5 embryos), 500 µm (all others). *n*, total number of embryos; *x*, number of experiments; all data represent mean ± s.e.m. Images are representative of a minimum of three embryos. [Source data](#)

Extended Data Fig. 10 Ex utero culture medium supplemented with HBS supports embryo development from early/late gastrulation until the hindlimb stage (E11).

a, b, Bright-field microscopy images of mouse embryos grown ex utero from E7.5 (**a**) or E6.5 (**b**) with HCS replaced by in-house-prepared and freshly isolated adult HBS. **c**, Percentages of normal and defective embryos in cultures started at E7.5 and E6.5. *n*, total number of cultured embryos; *x*, number of experiments. Data represent mean ± s.e.m. Scale bars, 500 µm. [Source data](#)

Extended Data Fig. 11 Ex utero manipulation of mouse embryonic development.

a, b, Percentages of developmentally normal (**a**) and GFP-expressing embryos (**b**) at 1–3 days after electroporation. **c**, Quantification of GFP⁺ cells in electroporated embryos at the indicated times. Dots represent individual embryos. **d, e**, Percentages of normally developed (**d**) and GFP⁺ embryos (**e**) after lentiviral transduction. Data represent mean ± s.e.m. **f**, Representative qPCR data showing the relative expression levels of mouse naive and primed markers in V6.5 mouse EpiS cells and formative EpiL cells, normalized to isogenic naive 2i/Lif ES cells. *n* = 3. **g**, Overlap in the transcriptional signature of differentially expressed genes measured by bulk RNA-seq in EpiS cells and ES cells used herein, compared to previously published datasets²⁶. *n* = 2. **h**, Top, generation of mouse chimeras using isogenic naive ES cells. Bottom, GFP, SOX2 and GATA4 immunofluorescence images of chimeric embryos generated with naive ESCs. **i**, Whole-mount immunostaining of GFP⁺ cells detected in embryos

injected with mouse EpiS cells or EpiL cells at E7.5, cultured ex utero for 1–4 days and stained for GFP, SOX2 and GATA4. Insets are enlargements of the dashed boxes. $n \geq 8$ embryos. **j**, Percentages of chimeric embryos (GFP^+ or tdT^+) after micro-injection and ex utero culture. **k**, Immunostaining of +Day 1 cultured embryos injected with EpiS cells and EpiL cells in the anterior or distal epiblast. Images represent a minimum of three biological replicates. **l**, Representative confocal images of mouse post-implantation chimeras generated by tdT^+ E7.5 *in vivo* epiblast orthotopic transplantation followed by ex utero culture for 1–4 days, stained for tdTomato, GATA4 or SOX9 and SOX2 or TUJ1. $n \geq 10$ embryos. **m**, tdT^+ embryos explanted at E7.5 and subjected to *in toto* live imaging of neural tube closure at E9.0. $n = 3$. **n**, Embryos cultured ex utero since E7.5 and exposed to vehicle or 1 mM valproic acid (VPA) from E8.5 to E9.5. $n = 6$. Inset shows magnification of the dashed box. Arrowheads, neural tube closure defects. Scale bars, 100 μm (**m**), 500 μm (all others). n , total number of embryos assessed; x , number of experiments. [Source data](#)

Extended Data Fig. 12 Generation of human–mouse microglia interspecies chimeric embryos.

a, Protocol for differentiation of microglia progenitors from humans ES cells as previously described²⁸. **b**, Flow cytometry dot plot to validate the identity of obtained microglia cells by co-expression of the microglia progenitor cell markers CD34^+ and CD43^+ . $n = 3$ independent experiments. **c**, Merged bright-field and fluorescence images of E7.5 embryos injected with GFP^+ human microglia progenitors at day 0. **d**, Representative immunofluorescence images of ex utero human microglia chimeric embryos 3 and 4 days after injection, labelled for GFP and TUJ1. The inset shows a magnification of the dashed box at day 4 identifying human nuclei (hNUMA), GFP and TUJ1. $n = 11$ embryos (day 3); $n = 8$ embryos (day 4). **e**, Quantification of GFP^+ cells detected in human–mouse microglia chimeric embryos (excluding GFP^+ cells found in the yolk sac). Dots represent individual embryos; $n = 11$ and 8 embryos for day 3 and day 4, respectively. **f**, Immunostaining for GFP and human TMEM119 in chimeric embryos. $n = 3$. **g**, Representative GFP immunofluorescence of a human microglia chimeric embryonic yolk sac and yolk sac vessel with circulating

human GFP⁺ cells. $n = 3$. Scale bars, 50 μm (f), 500 μm (all others). [Source data](#)

Supplementary information

Supplementary Information

This file contains Supplementary Video Legends, Supplementary Methods, Supplementary Discussion, and Supplementary References.

Reporting Summary

Supplementary Video 1

Ex utero mouse embryogenesis set-up. Part 1- Roller culture incubator with customized gas concentration and pressure regulation module for growing mouse embryos *ex utero*. Part 2- Media bottle exchange and transfer of an embryo into the roller culture system. Part 3- Setting up the roller culture incubator and gas regulation module.

Supplementary Video 2

Late-gastrulation to organogenesis *ex utero* roller culture. Representative snapshot bright field videos of E7.5 *ex utero* grown embryos after 1-4 days of culture.

Supplementary Video 3

Live embryo inside the culture bottle. Representative video of an embryo cultured in rotating bottles as seen by the naked eye.

Supplementary Video 4

Comparative light-sheet 3D reconstruction of *ex utero* and *in utero* embryos. E7.5 embryos grown 4 days *ex utero* and developmentally

matched *in utero* embryos immunostained for Otx2/MHC-II, Sox2, and Tuj1/Sox9.

Supplementary Video 5

Robust *in toto* live imaging from gastrulation to somitogenesis. Representative confocal live imaging for 58 hours of an *ex utero*-grown tdTomato⁺ embryo from early gastrulation (E6.5) to somitogenesis (E8.5).

Supplementary Video 6

Early-gastrulation to organogenesis *ex utero* embryo culture. Representative bright field snapshot videos of E6.5 *ex utero* grown embryos after 1-5 days of culture.

Supplementary Video 7

Pre-gastrulation to organogenesis *ex utero* embryo culture. Representative bright field snapshot videos of E5.5 *ex utero* grown embryos after 1-6 days of culture.

Supplementary Video 8

Imaging neural tube closure in cultured embryos. Long-term *in toto* live imaging of neural tube closure in cultured embryos. E7.5 tdTomato⁺ mouse embryo cultured *ex utero* until E9.0 and subjected to live confocal imaging.

Source data

Source Data Fig. 1

Source Data Fig. 2

Source Data Fig. 3

[**Source Data Fig. 4**](#)

[**Source Data Extended Data Fig. 2**](#)

[**Source Data Extended Data Fig. 9**](#)

[**Source Data Extended Data Fig. 10**](#)

[**Source Data Extended Data Fig. 11**](#)

[**Source Data Extended Data Fig. 12**](#)

Rights and permissions

[Reprints and Permissions](#)

About this article



Check for
updates

Cite this article

Aguilera-Castrejon, A., Oldak, B., Shani, T. *et al.* Ex utero mouse embryogenesis from pre-gastrulation to late organogenesis. *Nature* **593**, 119–124 (2021). <https://doi.org/10.1038/s41586-021-03416-3>

[Download citation](#)

- Received: 30 June 2020
- Accepted: 04 March 2021
- Published: 17 March 2021

- Issue Date: 06 May 2021
- DOI: <https://doi.org/10.1038/s41586-021-03416-3>

Comments

By submitting a comment you agree to abide by our [Terms](#) and [Community Guidelines](#). If you find something abusive or that does not comply with our terms or guidelines please flag it as inappropriate.

[Access through your institution](#)

[Change institution](#)

[Buy or subscribe](#)

This article was downloaded by **calibre** from <https://www.nature.com/articles/s41586-021-03416-3>

| [Section menu](#) | [Main menu](#) |

- Article
- [Published: 14 April 2021](#)

The antibiotic darobactin mimics a β-strand to inhibit outer membrane insertase

- [Hundeep Kaur^{1,na1}](#),
- [Roman P. Jakob](#) [ORCID: orcid.org/0000-0002-6451-8656^{1,na1}](#),
- [Jan K. Marzinek](#) [ORCID: orcid.org/0000-0002-5493-8753²](#),
- [Robert Green³](#),
- [Yu Imai³](#),
- [Jani Reddy Bolla](#) [ORCID: orcid.org/0000-0003-4346-182X^{4,5}](#),
- [Elia Agustoni](#) [ORCID: orcid.org/0000-0003-4003-7580¹](#),
- [Carol V. Robinson](#) [ORCID: orcid.org/0000-0001-7829-5505^{4,5}](#),
- [Peter J. Bond](#) [ORCID: orcid.org/0000-0003-2900-098X^{2,6}](#),
- [Kim Lewis](#) [ORCID: orcid.org/0000-0002-1621-7664³](#),
- [Timm Maier](#) [ORCID: orcid.org/0000-0002-7459-1363¹](#) &
- [Sebastian Hiller](#) [ORCID: orcid.org/0000-0002-6709-4684¹](#)

[Nature](#) volume 593, pages 125–129(2021) [Cite this article](#)

- 8044 Accesses
- 255 Altmetric
- [Metrics details](#)

Subjects

- [Antibiotics](#)

- [Cryoelectron microscopy](#)
- [Membrane structure and assembly](#)
- [X-ray crystallography](#)

Abstract

Antibiotics that target Gram-negative bacteria in new ways are needed to resolve the antimicrobial resistance crisis^{1,2,3}. Gram-negative bacteria are protected by an additional outer membrane, rendering proteins on the cell surface attractive drug targets^{4,5}. The natural compound darobactin targets the bacterial insertase BamA⁶—the central unit of the essential BAM complex, which facilitates the folding and insertion of outer membrane proteins^{7,8,9,10,11,12,13}. BamA lacks a typical catalytic centre, and it is not obvious how a small molecule such as darobactin might inhibit its function. Here we resolve the mode of action of darobactin at the atomic level using a combination of cryo-electron microscopy, X-ray crystallography, native mass spectrometry, in vivo experiments and molecular dynamics simulations. Two cyclizations pre-organize the darobactin peptide in a rigid β-strand conformation. This creates a mimic of the recognition signal of native substrates with a superior ability to bind to the lateral gate of BamA. Upon binding, darobactin replaces a lipid molecule from the lateral gate to use the membrane environment as an extended binding pocket. Because the interaction between darobactin and BamA is largely mediated by backbone contacts, it is particularly robust against potential resistance mutations. Our results identify the lateral gate as a functional hotspot in BamA and will allow the rational design of antibiotics that target this bacterial Achilles heel.

[Access through your institution](#)

[Change institution](#)

[Buy or subscribe](#)

Access options

Subscribe to Journal

Get full journal access for 1 year

\$199.00

only \$3.90 per issue

[Subscribe](#)

All prices are NET prices.

VAT will be added later in the checkout.

Tax calculation will be finalised during checkout.

Rent or Buy article

Get time limited or full article access on ReadCube.

from \$8.99

[Rent or Buy](#)

All prices are NET prices.

Additional access options:

- [Log in](#)
- [Access through your institution](#)
- [Learn about institutional subscriptions](#)

Fig. 1: Structural basis of darobactin function.

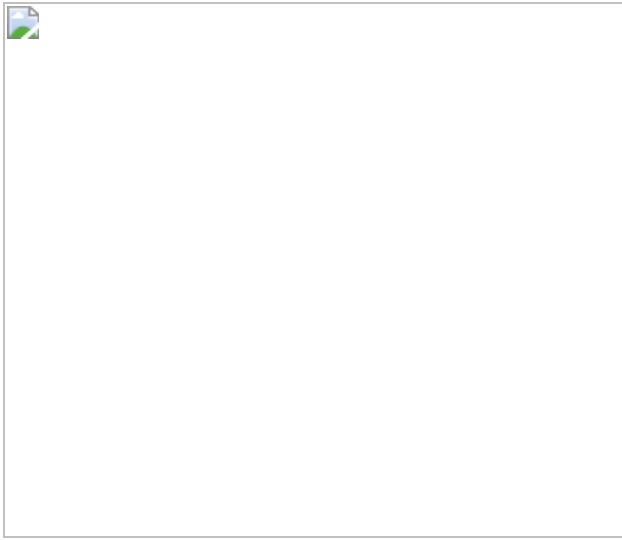


Fig. 2: The proteo-lipidic binding pocket of darobactin.

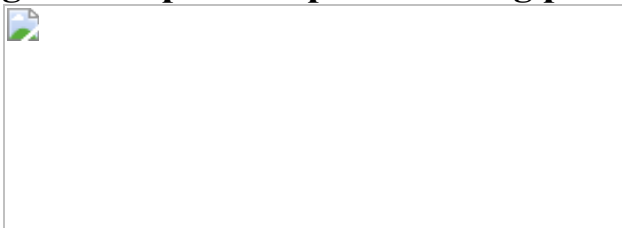


Fig. 3: Lipid dynamics of BamA–darobactin in the *E. coli* membrane.

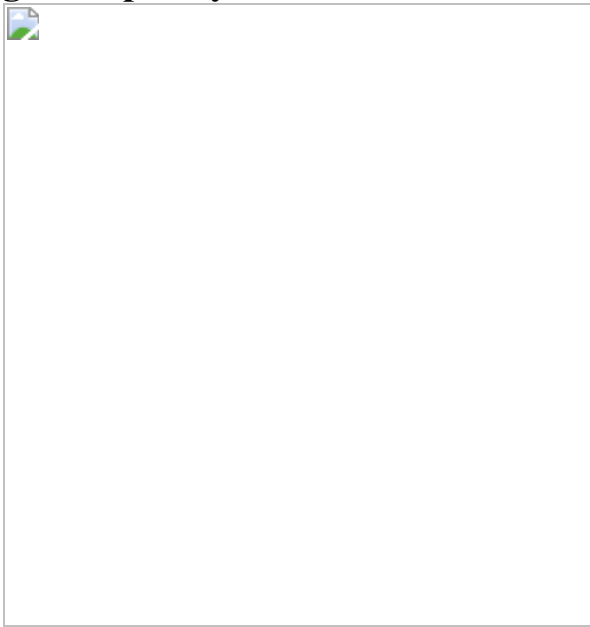
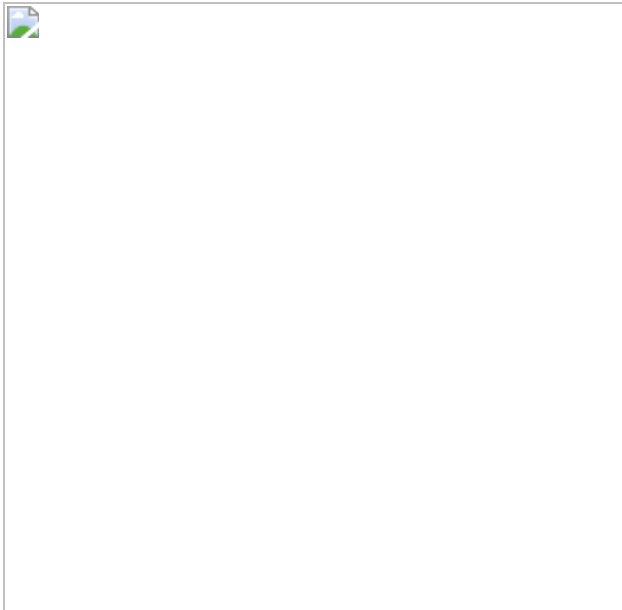


Fig. 4: Mechanism of darobactin action.



Data availability

The data that support the findings of this study are available from the corresponding author upon request. The atomic coordinates have been deposited in the RCSB Protein Data Bank and are available under the accession codes [7NRE](#) and [7NRF](#). The cryo-EM map has been deposited in the Protein Data Bank under accession code [7NRI](#) and EMDB accession code [12546](#). Mass spectrometry data have been deposited in figshare at <https://doi.org/10.6084/m9.figshare.12179784>. For the study, data were retrieved from the OMPdb (release Dec 1, 2020). [Source data](#) are provided with this paper.

Code availability

The codes developed for β -signal analysis have been deposited at <https://github.com/hiller-lab/kaur-jakob-2021>.

References

1. 1.

Brown, E. D. & Wright, G. D. Antibacterial drug discovery in the resistance era. *Nature* **529**, 336–343 (2016).

[ADS](#) [CAS](#) [PubMed](#) [Article](#) [PubMed Central](#) [Google Scholar](#)

2. 2.

Lewis, K. The science of antibiotic discovery. *Cell* **181**, 29–45 (2020).

[CAS](#) [PubMed](#) [Article](#) [PubMed Central](#) [Google Scholar](#)

3. 3.

Tacconelli, E. et al. Discovery, research, and development of new antibiotics: the WHO priority list of antibiotic-resistant bacteria and tuberculosis. *Lancet Infect. Dis.* **18**, 318–327 (2018).

[PubMed](#) [Article](#) [PubMed Central](#) [Google Scholar](#)

4. 4.

Epand, R. M., Walker, C., Epand, R. F. & Magarvey, N. A. Molecular mechanisms of membrane targeting antibiotics. *Biochim. Biophys. Acta* **1858**, 980–987 (2016).

[CAS](#) [PubMed](#) [Article](#) [PubMed Central](#) [Google Scholar](#)

5. 5.

Srinivas, N. et al. Peptidomimetic antibiotics target outer-membrane biogenesis in *Pseudomonas aeruginosa*. *Science* **327**, 1010–1013 (2010).

[ADS](#) [CAS](#) [PubMed](#) [Article](#) [PubMed Central](#) [Google Scholar](#)

6. 6.

Imai, Y. et al. A new antibiotic selectively kills Gram-negative pathogens. *Nature* **576**, 459–464 (2019).

[ADS](#) [CAS](#) [PubMed](#) [PubMed Central](#) [Article](#) [Google Scholar](#)

7. 7.

Bakelar, J., Buchanan, S. K. & Noinaj, N. The structure of the β -barrel assembly machinery complex. *Science* **351**, 180–186 (2016).

[ADS](#) [CAS](#) [PubMed](#) [PubMed Central](#) [Article](#) [Google Scholar](#)

8. 8.

Doyle, M. T. & Bernstein, H. D. Bacterial outer membrane proteins assemble via asymmetric interactions with the BamA β -barrel. *Nat. Commun.* **10**, 3358 (2019).

[ADS](#) [PubMed](#) [PubMed Central](#) [Article](#) [CAS](#) [Google Scholar](#)

9. 9.

Gu, Y. et al. Structural basis of outer membrane protein insertion by the BAM complex. *Nature* **531**, 64–69 (2016).

[ADS](#) [CAS](#) [PubMed](#) [Article](#) [PubMed Central](#) [Google Scholar](#)

10. 10.

Iadanza, M. G. et al. Lateral opening in the intact β -barrel assembly machinery captured by cryo-EM. *Nat. Commun.* **7**, 12865 (2016).

[ADS](#) [CAS](#) [PubMed](#) [PubMed Central](#) [Article](#) [Google Scholar](#)

11. 11.

Konovalova, A., Kahne, D. E. & Silhavy, T. J. Outer membrane biogenesis. *Annu. Rev. Microbiol.* **71**, 539–556 (2017).

[CAS](#) [PubMed](#) [PubMed Central](#) [Article](#) [Google Scholar](#)

12. 12.

Lee, J. et al. Formation of a β -barrel membrane protein is catalyzed by the interior surface of the assembly machine protein BamA. *eLife* **8**, e49787 (2019).

[PubMed](#) [PubMed Central](#) [Article](#) [Google Scholar](#)

13. 13.

Noinaj, N. et al. Structural insight into the biogenesis of β -barrel membrane proteins. *Nature* **501**, 385–390 (2013).

[ADS](#) [CAS](#) [PubMed](#) [PubMed Central](#) [Article](#) [Google Scholar](#)

14. 14.

Kaur, H. et al. Identification of conformation-selective nanobodies against the membrane protein insertase BamA by an integrated structural biology approach. *J. Biomol. NMR* **73**, 375–384 (2019).

[CAS](#) [PubMed](#) [Article](#) [PubMed Central](#) [Google Scholar](#)

15. 15.

Hartmann, J. B., Zahn, M., Burmann, I. M., Bibow, S. & Hiller, S. Sequence-specific solution NMR assignments of the β -barrel insertase BamA to monitor its conformational ensemble at the atomic level. *J. Am. Chem. Soc.* **140**, 11252–11260 (2018).

[CAS](#) [PubMed](#) [Article](#) [PubMed Central](#) [Google Scholar](#)

16. 16.

Ni, D. et al. Structural and functional analysis of the β -barrel domain of BamA from *Escherichia coli*. *FASEB J.* **28**, 2677–2685 (2014).

[CAS](#) [PubMed](#) [Article](#) [PubMed Central](#) [Google Scholar](#)

17. 17.

Hong, H., Park, S., Jiménez, R. H., Rinehart, D. & Tamm, L. K. Role of aromatic side chains in the folding and thermodynamic stability of integral membrane proteins. *J. Am. Chem. Soc.* **129**, 8320–8327 (2007).

[CAS](#) [PubMed](#) [Article](#) [PubMed Central](#) [Google Scholar](#)

18. 18.

Lee, A. G. Lipid–protein interactions in biological membranes: a structural perspective. *Biochim. Biophys. Acta* **1612**, 1–40 (2003).

[CAS](#) [PubMed](#) [Article](#) [PubMed Central](#) [Google Scholar](#)

19. 19.

Schulz, G. E. The structure of bacterial outer membrane proteins. *Biochim. Biophys. Acta* **1565**, 308–317 (2002).

[CAS](#) [PubMed](#) [Article](#) [PubMed Central](#) [Google Scholar](#)

20. 20.

Gruss, F. et al. The structural basis of autotransporter translocation by TamA. *Nat. Struct. Mol. Biol.* **20**, 1318–1320 (2013).

[CAS](#) [PubMed](#) [Article](#) [PubMed Central](#) [Google Scholar](#)

21. 21.

Chorev, D. S. et al. Protein assemblies ejected directly from native membranes yield complexes for mass spectrometry. *Science* **362**, 829–834 (2018).

[ADS](#) [CAS](#) [PubMed](#) [PubMed Central](#) [Article](#) [Google Scholar](#)

22. 22.

Wexler, H. M. Bacteroides: the good, the bad, and the nitty-gritty. *Clin. Microbiol. Rev.* **20**, 593–621 (2007).

[CAS](#) [PubMed](#) [PubMed Central](#) [Article](#) [Google Scholar](#)

23. 23.

Knowles, T. J., Scott-Tucker, A., Overduin, M. & Henderson, I. R. Membrane protein architects: the role of the BAM complex in outer membrane protein assembly. *Nat. Rev. Microbiol.* **7**, 206–214 (2009).

[CAS](#) [PubMed](#) [Article](#) [PubMed Central](#) [Google Scholar](#)

24. 24.

Noinaj, N., Rollauer, S. E. & Buchanan, S. K. The β-barrel membrane protein insertase machinery from Gram-negative bacteria. *Curr. Opin. Struct. Biol.* **31**, 35–42 (2015).

[CAS](#) [PubMed](#) [PubMed Central](#) [Article](#) [Google Scholar](#)

25. 25.

Robert, V. et al. Assembly factor Omp85 recognizes its outer membrane protein substrates by a species-specific C-terminal motif. *PLoS Biol.* **4**, e377 (2006).

[PubMed](#) [PubMed Central](#) [Article](#) [CAS](#) [Google Scholar](#)

26. 26.

Stubenrauch, C. et al. Effective assembly of fimbriae in *Escherichia coli* depends on the translocation assembly module nanomachine. *Nat. Microbiol.* **1**, 16064 (2016).

[CAS](#) [PubMed](#) [Article](#) [PubMed Central](#) [Google Scholar](#)

27. 27.

Höhr, A. I. C. et al. Membrane protein insertion through a mitochondrial β -barrel gate. *Science* **359**, eaah6834 (2018).

[PubMed](#) [PubMed Central](#) [Article](#) [CAS](#) [Google Scholar](#)

28. 28.

Xiao, L. et al. Structures of the β -barrel assembly machine recognizing outer membrane protein substrates. *FASEB J.* **35**, e21207 (2021).

[CAS](#) [PubMed](#) [PubMed Central](#) [Google Scholar](#)

29. 29.

Tomasek, D. et al. Structure of a nascent membrane protein as it folds on the BAM complex. *Nature* **583**, 473–478 (2020).

[ADS](#) [CAS](#) [PubMed](#) [PubMed Central](#) [Article](#) [Google Scholar](#)

30. 30.

Hart, E. M. et al. A small-molecule inhibitor of BamA impervious to efflux and the outer membrane permeability barrier. *Proc. Natl Acad. Sci. USA* **116**, 21748–21757 (2019).

[CAS](#) [PubMed](#) [Article](#) [PubMed Central](#) [Google Scholar](#)

31. 31.

Luther, A. et al. Chimeric peptidomimetic antibiotics against Gram-negative bacteria. *Nature* **576**, 452–458 (2019).

[ADS](#) [CAS](#) [PubMed](#) [Article](#) [PubMed Central](#) [Google Scholar](#)

32. 32.

Storek, K. M. et al. Monoclonal antibody targeting the β -barrel assembly machine of *Escherichia coli* is bactericidal. *Proc. Natl Acad. Sci. USA* **115**, 3692–3697 (2018).

[CAS](#) [PubMed](#) [Article](#) [PubMed Central](#) [Google Scholar](#)

33. 33.

Kaur, H., Grahl, A., Hartmann, J. B. & Hiller, S. Sample preparation and technical setup for NMR spectroscopy with integral membrane proteins. *Methods Mol. Biol.* **2127**, 373–396 (2020).

[CAS](#) [PubMed](#) [Article](#) [PubMed Central](#) [Google Scholar](#)

34. 34.

Kabsch, W. Xds. *Acta Crystallogr. D Biol. Crystallogr.* **66**, 125–132 (2010).

[CAS](#) [PubMed](#) [PubMed Central](#) [Article](#) [Google Scholar](#)

35. 35.

Evans, P. R. & Murshudov, G. N. How good are my data and what is the resolution? *Acta Crystallogr. D Biol. Crystallogr.* **69**, 1204–1214 (2013).

[CAS](#) [PubMed](#) [PubMed Central](#) [Article](#) [Google Scholar](#)

36. 36.

McCoy, A. J. et al. Phaser crystallographic software. *J. Appl. Crystallogr.* **40**, 658–674 (2007).

[CAS](#) [PubMed](#) [PubMed Central](#) [Article](#) [Google Scholar](#)

37. 37.

Emsley, P. & Cowtan, K. Coot: model-building tools for molecular graphics. *Acta Crystallogr. D Biol. Crystallogr.* **60**, 2126–2132 (2004).

[PubMed](#) [Article](#) [CAS](#) [PubMed Central](#) [Google Scholar](#)

38. 38.

Schüttelkopf, A. W. & van Aalten, D. M. PRODRG: a tool for high-throughput crystallography of protein-ligand complexes. *Acta Crystallogr. D Biol. Crystallogr.* **60**, 1355–1363 (2004).

[PubMed](#) [Article](#) [CAS](#) [PubMed Central](#) [Google Scholar](#)

39. 39.

Adams, P. D. et al. PHENIX: building new software for automated crystallographic structure determination. *Acta Crystallogr. D Biol. Crystallogr.* **58**, 1948–1954 (2002).

[PubMed](#) [Article](#) [CAS](#) [PubMed Central](#) [Google Scholar](#)

40. 40.

Chen, V. B. et al. MolProbity: all-atom structure validation for macromolecular crystallography. *Acta Crystallogr. D Biol. Crystallogr.* **66**, 12–21 (2010).

[CAS](#) [PubMed](#) [Article](#) [PubMed Central](#) [Google Scholar](#)

41. 41.

DeLano, W. L. Pymol: an open-source molecular graphics tool. *CCP4 Newslett. Prot. Crystallogr.* **40**, 82–92 (2002).

[Google Scholar](#)

42. 42.

Mastronarde, D. N. Automated electron microscope tomography using robust prediction of specimen movements. *J. Struct. Biol.* **152**, 36–51 (2005).

[PubMed](#) [Article](#) [PubMed Central](#) [Google Scholar](#)

43. 43.

Punjani, A., Rubinstein, J. L., Fleet, D. J. & Brubaker, M. A. cryoSPARC: algorithms for rapid unsupervised cryo-EM structure determination. *Nat. Methods* **14**, 290–296 (2017).

[CAS](#) [Article](#) [Google Scholar](#)

44. 44.

Pettersen, E. F. et al. UCSF Chimera—a visualization system for exploratory research and analysis. *J. Comput. Chem.* **25**, 1605–1612 (2004).

[CAS](#) [Article](#) [Google Scholar](#)

45. 45.

Afonine, P. V. et al. Real-space refinement in PHENIX for cryo-EM and crystallography. *Acta Crystallogr. D Struct. Biol.* **74**, 531–544 (2018).

[CAS](#) [PubMed](#) [PubMed Central](#) [Article](#) [Google Scholar](#)

46. 46.

Vranken, W. F. et al. The CCPN data model for NMR spectroscopy: development of a software pipeline. *Proteins* **59**, 687–696 (2005).

[CAS](#) [PubMed](#) [Article](#) [PubMed Central](#) [Google Scholar](#)

47. 47.

Piñeiro, Á. et al. AFFINImeter: A software to analyze molecular recognition processes from experimental data. *Anal. Biochem.* **577**, 117–134 (2019).

[PubMed](#) [Article](#) [CAS](#) [PubMed Central](#) [Google Scholar](#)

48. 48.

Kemmer, G. & Keller, S. Nonlinear least-squares data fitting in Excel spreadsheets. *Nat. Protocols* **5**, 267–281 (2010).

[CAS](#) [PubMed](#) [Article](#) [PubMed Central](#) [Google Scholar](#)

49. 49.

Zhao, H., Piszczek, G. & Schuck, P. SEDPHAT—a platform for global ITC analysis and global multi-method analysis of molecular interactions. *Methods* **76**, 137–148 (2015).

[CAS](#) [PubMed](#) [Article](#) [PubMed Central](#) [Google Scholar](#)

50. 50.

Sievers, F. et al. Fast, scalable generation of high-quality protein multiple sequence alignments using Clustal Omega. *Mol. Syst. Biol.* **7**, 539 (2011).

[PubMed](#) [PubMed Central](#) [Article](#) [Google Scholar](#)

51. 51.

Pei, J. & Grishin, N. V. AL2CO: calculation of positional conservation in a protein sequence alignment. *Bioinformatics* **17**, 700–712 (2001).

[CAS](#) [PubMed](#) [Article](#) [PubMed Central](#) [Google Scholar](#)

52. 52.

Datsenko, K. A. & Wanner, B. L. One-step inactivation of chromosomal genes in *Escherichia coli* K-12 using PCR products. *Proc. Natl Acad. Sci. USA* **97**, 6640–6645 (2000).

[ADS](#) [CAS](#) [Article](#) [PubMed](#) [Google Scholar](#)

53. 53.

Bennion, D., Charlson, E. S., Coon, E. & Misra, R. Dissection of β -barrel outer membrane protein assembly pathways through characterizing BamA POTRA 1 mutants of *Escherichia coli*. *Mol. Microbiol.* **77**, 1153–1171 (2010).

[CAS](#) [PubMed](#) [PubMed Central](#) [Article](#) [Google Scholar](#)

54. 54.

Ruiz, N., Wu, T., Kahne, D. & Silhavy, T. J. Probing the barrier function of the outer membrane with chemical conditionality. *ACS Chem. Biol.* **1**, 385–395 (2006).

[CAS](#) [PubMed](#) [Article](#) [PubMed Central](#) [Google Scholar](#)

55. 55.

Aoki, S. K. et al. Contact-dependent growth inhibition requires the essential outer membrane protein BamA (YaeT) as the receptor and the inner membrane transport protein AcrB. *Mol. Microbiol.* **70**, 323–340 (2008).

[CAS](#) [PubMed](#) [PubMed Central](#) [Article](#) [Google Scholar](#)

56. 56.

Marty, M. T. et al. Bayesian deconvolution of mass and ion mobility spectra: from binary interactions to polydisperse ensembles. *Anal. Chem.* **87**, 4370–4376 (2015).

[CAS](#) [PubMed](#) [PubMed Central](#) [Article](#) [Google Scholar](#)

57. 57.

Huang, J. et al. CHARMM36m: an improved force field for folded and intrinsically disordered proteins. *Nat. Methods* **14**, 71–73 (2017).

[CAS](#) [PubMed](#) [Article](#) [PubMed Central](#) [Google Scholar](#)

58. 58.

Vanommeslaeghe, K. et al. CHARMM general force field: a force field for drug-like molecules compatible with the CHARMM all-atom additive biological force fields. *J. Comput. Chem.* **31**, 671–690 (2010).

[CAS](#) [PubMed](#) [PubMed Central](#) [Google Scholar](#)

59. 59.

Jo, S., Kim, T., Iyer, V. G. & Im, W. CHARMM-GUI: a web-based graphical user interface for CHARMM. *J. Comput. Chem.* **29**, 1859–1865 (2008).

[CAS](#) [PubMed](#) [Article](#) [PubMed Central](#) [Google Scholar](#)

60. 60.

Lomize, M. A., Pogozheva, I. D., Joo, H., Mosberg, H. I. & Lomize, A. L. OPM database and PPM web server: resources for positioning of proteins in membranes. *Nucleic Acids Res.* **40**, D370–D376 (2012).

[CAS](#) [PubMed](#) [Article](#) [PubMed Central](#) [Google Scholar](#)

61. 61.

Van Der Spoel, D. et al. GROMACS: fast, flexible, and free. *J. Comput. Chem.* **26**, 1701–1718 (2005).

[Article](#) [CAS](#) [Google Scholar](#)

62. 62.

Jorgensen, W. L., Chandrasekhar, J., Madura, J. D., Impey, R. W. & Klein, M. L. Comparison of simple potential functions for simulating liquid water. *J. Chem. Phys.* **79**, 926–935 (1983).

[ADS](#) [CAS](#) [Article](#) [Google Scholar](#)

63. 63.

Essmann, U. et al. A smooth particle mesh Ewald method. *J. Chem. Phys.* **103**, 8577–8593 (1995).

[ADS](#) [CAS](#) [Article](#) [Google Scholar](#)

64. 64.

Hoover, W. G. Canonical dynamics: equilibrium phase-space distributions. *Phys. Rev. A* **31**, 1695–1697 (1985).

[ADS](#) [CAS](#) [Article](#) [Google Scholar](#)

65. 65.

Nose, S. A unified formulation of the constant temperature molecular-dynamics methods. *J. Chem. Phys.* **81**, 511–519 (1984).

[ADS](#) [CAS](#) [Article](#) [Google Scholar](#)

66. 66.

Parrinello, M. & Rahman, A. Polymorphic transitions in single crystals —a new molecular-dynamics method. *J. Appl. Phys.* **52**, 7182–7190 (1981).

[ADS](#) [CAS](#) [Article](#) [Google Scholar](#)

67. 67.

Castillo, N., Monticelli, L., Barnoud, J. & Tieleman, D. P. Free energy of WALP23 dimer association in DMPC, DPPC, and DOPC bilayers. *Chem. Phys. Lipids* **169**, 95–105 (2013).

[CAS](#) [PubMed](#) [Article](#) [PubMed Central](#) [Google Scholar](#)

68. 68.

Paramasivam, N., Habeck, M. & Linke, D. Is the C-terminal insertional signal in Gram-negative bacterial outer membrane proteins species-specific or not? *BMC Genomics* **13**, 510 (2012).

[CAS](#) [PubMed](#) [PubMed Central](#) [Article](#) [Google Scholar](#)

69. 69.

Tsirigos, K. D., Bagos, P. G. & Hamodrakas, S. J. OMPdb: a database of β -barrel outer membrane proteins from Gram-negative bacteria. *Nucleic Acids Res.* **39**, D324–D331 (2011).

[CAS](#) [PubMed](#) [Article](#) [PubMed Central](#) [Google Scholar](#)

70. 70.

Hunter, J. D. Matplotlib: a 2D graphics environment. *Comput. Sci. Eng.* **9**, 90–95 (2007).

[Article](#) [Google Scholar](#)

71. 71.

Tareen, A. & Kinney, J. B. Logomaker: beautiful sequence logos in Python. *Bioinformatics* **36**, 2272–2274 (2020).

[CAS](#) [PubMed](#) [Article](#) [PubMed Central](#) [Google Scholar](#)

[Download references](#)

Acknowledgements

We thank H. Bernstein and C. Bieniossek for expression plasmids, and T. Sharpe, T. Müntener and the Biozentrum Bio-EM lab for scientific support and discussions. The Scientific Computing Center at the University of Basel (sciCORE) and the National Supercomputing Centre Singapore (NSCC) are acknowledged for providing computational resources. This work was supported by the Swiss National Science Foundation (grants 167125,

185388 and 187170 to S.H. and R'Equip 177084 to T.M.), AntiResist: new approaches to combat antibiotic-resistant bacteria (51AU40_180541), the Medical Research Council (program grant MR/N020413/1 awarded to C.V.R.), the Bioinformatics Institute (BII) A*STAR and NRF (NRF2017NRF-CRP001-027 to P.J.B. and J.K.M.), and the NIH (grant P01 AI118687 to K.L.).

Author information

Author notes

1. These authors contributed equally: Hundeep Kaur, Roman P. Jakob

Affiliations

1. Biozentrum, University of Basel, Basel, Switzerland

Hundeep Kaur, Roman P. Jakob, Elia Agustoni, Timm Maier & Sebastian Hiller

2. Bioinformatics Institute (A*STAR), Singapore, Singapore

Jan K. Marzinek & Peter J. Bond

3. Antimicrobial Discovery Center, Department of Biology, Northeastern University, Boston, MA, USA

Robert Green, Yu Imai & Kim Lewis

4. Physical and Theoretical Chemistry Laboratory, University of Oxford, Oxford, UK

Jani Reddy Bolla & Carol V. Robinson

5. The Kavli Institute for Nanoscience Discovery, Oxford, UK

Jani Reddy Bolla & Carol V. Robinson

6. Department of Biological Sciences, National University of Singapore,
Singapore, Singapore

Peter J. Bond

Authors

1. Hundeep Kaur

[View author publications](#)

You can also search for this author in [PubMed](#) [Google Scholar](#)

2. Roman P. Jakob

[View author publications](#)

You can also search for this author in [PubMed](#) [Google Scholar](#)

3. Jan K. Marzinek

[View author publications](#)

You can also search for this author in [PubMed](#) [Google Scholar](#)

4. Robert Green

[View author publications](#)

You can also search for this author in [PubMed](#) [Google Scholar](#)

5. Yu Imai

[View author publications](#)

You can also search for this author in [PubMed](#) [Google Scholar](#)

6. Jani Reddy Bolla

[View author publications](#)

You can also search for this author in [PubMed](#) [Google Scholar](#)

7. Elia Agustoni

[View author publications](#)

You can also search for this author in [PubMed](#) [Google Scholar](#)

8. Carol V. Robinson

[View author publications](#)

You can also search for this author in [PubMed](#) [Google Scholar](#)

9. Peter J. Bond

[View author publications](#)

You can also search for this author in [PubMed](#) [Google Scholar](#)

10. Kim Lewis

[View author publications](#)

You can also search for this author in [PubMed](#) [Google Scholar](#)

11. Timm Maier

[View author publications](#)

You can also search for this author in [PubMed](#) [Google Scholar](#)

12. Sebastian Hiller

[View author publications](#)

You can also search for this author in [PubMed](#) [Google Scholar](#)

Contributions

C.V.R., K.L., T.M. and S.H. designed the study and supervised experiments. R.G. and Y.I. performed the microbiology experiments. J.R.B. performed the mass spectrometry experiments. H.K. and R.P.J. performed all other experiments. J.K.M. and P.J.B. ran simulations. E.A. performed sequence analysis. All authors analysed data and discussed the findings. H.K., K.L., T.M. and S.H. wrote the manuscript. All authors edited and approved the manuscript.

Corresponding authors

Correspondence to [Kim Lewis](#) or [Timm Maier](#) or [Sebastian Hiller](#).

Ethics declarations

Competing interests

The authors declare no competing interests.

Additional information

Peer review information *Nature* thanks Harris Bernstein, Susan Buchanan, John Rubinstein and the other, anonymous, reviewer(s) for their contribution to the peer review of this work.

Publisher's note Springer Nature remains neutral with regard to jurisdictional claims in published maps and institutional affiliations.

Extended data figures and tables

[Extended Data Fig. 1 Cryo-electron microscopy structure of the BAM–darobactin complex.](#)

a, Flow chart of data processing to generate the structure (see Methods). **b**, Purified BAM–darobactin sample used for cryo-EM structure determination analysed on SDS–PAGE. This experiment was repeated at least three times independently with similar results. **c**, Representative electron micrograph of BAM–darobactin. This experiment was repeated at least three times independently with similar results. **d**, Selected examples of 2D classes from cryoSPARC. **e**, Viewing direction distribution plot for the final 3D reconstruction. **f**, Fourier shell correlation (FSC) curves for unmasked, spherical, loose and tight masks, and corrected FSC curve for the final reconstruction, yielding a gold standard FSC resolution of 3.03 Å. **g**, Local resolution variations of the EM reconstruction. POTRA domains 1 and 2 are at a local resolution below 4.5 Å and are visualized only at a lower contour level where micelle density obscures the view onto the BamA

barrel. **h**, Plot of directional FSC (red; mean \pm s.d.) and histogram of per angle FSC (blue). FSC curve indicates a resolution of 3.15 Å. **i**, Overview of the cryo-EM reconstruction of the BAM complex. BAM is shown in ribbon representation and the coulomb potential map as blue mesh. Note that the density of POTRA domains P1 and P2 is below the display threshold chosen here because of motional averaging. **j–n**, Expanded local views, showing the map around selected atoms in stick representation from the directions and viewpoints indicated by arrows and letters in **i**.

Extended Data Fig. 2 Structural details of the cryo-EM and crystal structures of BAM.

a, Superposition of the BAM–darobactin cryo-EM structure (salmon) with the ligand-free BAM crystal structure (green, PDB 5D0O). **b**, Superposition of POTRA domains P1–P5 and the individual components BamB–BamE, as indicated. The dashed horizontal line indicates the pivot between P2 and P3 around which P1 and P2 are rotated by rigid-body movement. **c**, Superposition of the BamA β -barrel–darobactin crystal structure (salmon) with a closed-gate BamA β -barrel crystal structure (cyan, PDB 4N75). **d**, Crystallographic omit map for darobactin bound at the lateral gate region of the BamA β -barrel after refinement of the model without darobactin. The $2mF_o - DF_c$ map is shown at 1σ in slate and the $mF_o - DF_c$ difference map at $\pm 3\sigma$ level in green and red. Top, overview of an entire BamA barrel. Bottom left and right, expanded views without and with overlay of the refined model coordinates, respectively. The cyclizations of darobactin can clearly be observed at 2.3 Å resolution. **e**, Omit map for strands β 1 (top) and β 16 (bottom) of the BamA β -barrel visualized as in **d**. **f**, Superposition of the cryo-EM (Bordeaux and white for BamA and darobactin, respectively) and X-ray structures (salmon and blue). **g**, As in **f** for the ligand darobactin only.

Extended Data Fig. 3 Comparison of BamA β -barrel conformations in aqueous solution.

a, Comparison of 2D [^{15}N , ^1H]-TROSY fingerprint spectra of different BamA preparations in LDAO. Left, overlay of BamA- β fingerprint spectra

in the absence and presence of darobactin. Middle, overlay of fingerprint spectra of BamA- β -nanobodyF7 and BamA- β -darobactin. Right, overlay of fingerprint spectra of BamA⁺⁹ (BamA- β + C-terminal extension MENVALDFS) and BamA- β -darobactin complex. Bottom panels show expanded views of boxed areas in main spectra. **b**, Backbone amide chemical shift perturbations between the fingerprint spectra of BamA- β with and without darobactin (left, black), Bam- β -nanobodyF7 in comparison with BamA-darobactin (middle, blue) and BamA⁺⁹ in comparison with BamA-darobactin (right, purple). The dotted lines indicate the average chemical shift perturbation (CSP), which can be interpreted as a measure of dissimilarity between two spectra. **c**, Top, structures of the BamA β -barrel in various conformations of the gate region. Bottom, expanded views of part of the backbone showing hydrogen bonds between β 1 and β 16 or darobactin. From left to right: open gate (6QGW, red); closed gate (6QGX, blue); BamA⁺⁹ (6FSU, purple); and BamA-darobactin complex. **d**, In vivo functional assay of BamA barrel mutants and C-terminal extensions using JCM166 cells in the absence and presence of arabinose. fl-BamA^{MENVALDFS} and fl-BamA serve as a negative and positive controls, respectively. [Source data](#)

Extended Data Fig. 4 ITC of BamA β -barrel in detergent micelles and its variants titrated with darobactin.

Experiments were repeated independently twice with similar results.

Extended Data Fig. 5 MD simulations of BamA β -barrel.

a, Representative snapshots of lipid PE molecule (left) and PG molecule (right) anchored by Ile430 and Leu780 in the gate region. **b**, The most dominant conformation of BamA-darobactin showing contacts consistently observed between the BamA β -barrel and darobactin throughout the simulation sampling. **c**, Partial densities of all lipids (top-down view of the membrane); the white arrow highlights the darobactin-binding region. **d**, Partial densities of lipid phosphate groups (side view of the membrane). **e–g**, Structural drift and fluctuations of key β -strands around the darobactin-binding site. Time-dependent r.m.s.d. measured with respect to the initial

structure for backbone atoms of β -strands, after performing a least-squares fit. The resulting r.m.s.d. is shown for β 16 in ligand-free BamA (**e**), β 16 in BamA–darobactin complex (**f**), and hairpin β 1/ β 2 in BamA–darobactin complex (**g**).

Extended Data Fig. 6 Interaction of BAM complex with lipids in the absence and presence of bound darobactin.

a, Mass spectra of the BAM complex with different lipids (top, CL; middle, PG; bottom, PE). **b**, Deconvolution of the mass spectra in **a** indicates that all the subcomplexes have lipids bound. **c**, Relative intensities of lipid binding peaks from **a** suggest that the negatively charged PG and CL have higher affinity than PE. **d**, Mass spectra of BAM complex with lipids and darobactin. Bottom, PE and darobactin; top, PG and darobactin. Below, expanded view of a section of the 23+ charge state highlights the bound peaks; bar charts show relative ratio of darobactin binding. No significant increase in darobactin binding is observed in these two cases, suggesting that PE and PG lipids do not affect darobactin binding. **e**, Mass spectra of BAM complex with lipid mixtures (bottom, PE and CL; top, PG and CL) and darobactin. Below, expanded view of a section of the 23+ charge state with lipids, darobactin and their various combination binding peaks highlighted. Bar charts of relative peak intensities indicate that darobactin bound with CL is observed to a greater extent than bound alone or bound with PE or PG. This increase is even higher for 2 \times CL bound species and is slightly lower for PE or PG bound to 1 \times CL species. However, no change in darobactin binding is observed for PE and PG. Bars (**c–e**) represent mean \pm s.d., points show data from three independent experiments.

* $P < 0.05$; ** $P < 0.01$; *** $P < 0.001$; NS, not significant; two-tailed unpaired Student's *t*-test. Exact *P* values are indicated in the figures.

Extended Data Fig. 7 MD simulations of the effect of darobactin-resistance mutations on the BamA- β -darobactin interaction.

a, Left, representative snapshots with expanded views from a simulation with strain 1 bound to darobactin. Mutations G429V and G807V are shown

as yellow spheres at the α -carbon position. Right, time-dependent r.m.s.d. of β 16 backbone atoms relative to the initial structure. **b**, As in **a** for strain 2 (mutations E435K and G443D, cyan) and r.m.s.d. of hairpin β 1/ β 2. **c**, As in **a** for strain 3 (mutations T434A, Q445P and A705T, green) and r.m.s.d. of hairpin β 1/ β 2. In each panel, protein is shown in cartoon representation, darobactin as sticks (blue, carbon; red, oxygen; white, proton; navy, nitrogen). Hydrogen bonds are shown as black dotted lines.

Extended Data Fig. 8 Relatedness of predicted Gram-negative BamA proteins.

a, Sequence alignment of BamA sequence from Gram-negative bacteria. The region highlighted in yellow is the predicted interaction site of darobactin in sheet β 1. Right, these six-amino acid sequences from *A. baumannii* and *B. fragilis* were substituted into *E. coli* BamA for in vivo assays. **b**, Phylogenetic tree of full-length BamA sequences from various species of Gram-negative bacteria. Colours indicate branches belonging to the species specified next to the branch. Multiple alignments for the tree were carried out using CLUSTAL-W and the phylogenetic tree was derived using SEAVIEW software. **c**, Topology plot of BamA from *E. coli* with bound darobactin (blue). For the chimeric mutants, the red amino acids were exchanged with the local sequence from either *A. baumannii* or *B. fragilis*.

Extended Data Fig. 9 Comparison of BamA structures involved in molecular interactions and analysis of β -signals.

a, Overlay of the BamA subunit from the BAM–darobactin complex (salmon–blue; this work) with a BamA engaged with a substrate in a late-stage insertion intermediate state (green; PDB 6V05). The substrate has been omitted in this panel and the structures have been globally aligned to the protein backbone. **b**, Expanded view of the BamA β -barrel from **a** with strand β 16^{subs} of the substrate shown in purple. It is paired to strand β 1^{mem} of the catalytic BamA. Bold green and red arrows depict the directions of strand β 1, forming an ~90° angle. **c**, Expanded view of the gate region indicating the spatial proximity of the substrate and darobactin interaction

sites and their relative rotation of $\sim 90^\circ$. **d–f**, Comparison of the register of β 16 complementation to b1. **d**, In BamA–darobactin (salmon), residue Ile806 pairs with Tyr432. **e**, In the late-stage intermediate, Ile806 of the substrate BamA^{subs} (purple) pairs with Phe428 in catalyst BamA^{mem} (green), corresponding to a register shift of 4. **f**, Hypothetical position of the four C-terminal residues of substrate BamA, which are not resolved in the available electron density. When paired to β 1^{mem} in canonical antiparallel β -strand conformation, they locate exactly at the darobactin-binding site, with the C-terminal Trp810 at the position of Phe7 of darobactin. **g**, Frequency logo of known and putative β -signals from bacterial OMPs, coloured by amino acid type. Numbering refers to distance from the C terminus. **h**, Distribution of log-likelihood scores in three sets of sequences, as indicated. The score obtained by the darobactin sequence is indicated by a blue line. The percentile rank of darobactin within each of the three sets is given in parentheses. **i, j**, As in **g, h**, but based on amino acid chemistry. H, hydrophobic and non-polar residue; A, aromatic; N, neutral; C, charged; P, polar non-charged.

Extended Data Fig. 10 Interaction of β -signal peptides with BamA β -barrel in detergent micelles by ITC.

The first four panels show direct titration of each of the ten-amino acid β -signal peptides of BamA, BtuB, FhuA, and OmpF to the BamA β -barrel. The next five panels show a competition experiment with darobactin titrated to the BamA β -barrel in the presence of ten-amino acid β -signal peptides of OmpT (0.7 mM), BtuB (2.6 mM), OmpF (1.4 mM) and FhuA (1.1 mM) and a β -consensus-peptide (1.2 mM). The results from fitting of the data to the competition model are given in Supplementary Table 7.

Supplementary information

Supplementary Information

This file contains Supplementary Tables 1–8 and Supplementary Fig. 1.

Reporting Summary

Source data

[Source Data Fig. 2](#)

[Source Data Extended Data Fig. 3](#)

Rights and permissions

[Reprints and Permissions](#)

About this article



Check for
updates

Cite this article

Kaur, H., Jakob, R.P., Marzinek, J.K. *et al.* The antibiotic darobactin mimics a β -strand to inhibit outer membrane insertase. *Nature* **593**, 125–129 (2021). <https://doi.org/10.1038/s41586-021-03455-w>

[Download citation](#)

- Received: 06 May 2020
- Accepted: 15 March 2021
- Published: 14 April 2021
- Issue Date: 06 May 2021
- DOI: <https://doi.org/10.1038/s41586-021-03455-w>

Comments

By submitting a comment you agree to abide by our [Terms](#) and [Community Guidelines](#). If you find something abusive or that does not comply with our terms or guidelines please flag it as inappropriate.

[Access through your institution](#)

[Change institution](#)

[Buy or subscribe](#)

This article was downloaded by **calibre** from <https://www.nature.com/articles/s41586-021-03455-w>

| [Section menu](#) | [Main menu](#) |

Antibody resistance of SARS-CoV-2 variants B.1.351 and B.1.1.7

[Download PDF](#)

- Article
- [Published: 08 March 2021](#)

Antibody resistance of SARS-CoV-2 variants B.1.351 and B.1.1.7

- [Pengfei Wang¹](#), [na1](#),
- [Manoj S. Nair](#) [ORCID: orcid.org/0000-0002-5994-3957](#)¹, [na1](#),
- [Lihong Liu¹](#), [na1](#),
- [Sho Iketani](#) [ORCID: orcid.org/0000-0002-3733-9556](#)^{1,2}, [na1](#),
- [Yang Luo¹](#),
- [Yicheng Guo](#) [ORCID: orcid.org/0000-0001-5357-660X](#)¹,
- [Maple Wang¹](#),
- [Jian Yu¹](#),
- [Baoshan Zhang³](#),
- [Peter D. Kwong](#) [ORCID: orcid.org/0000-0003-3560-232X](#)^{3,4},
- [Barney S. Graham³](#),
- [John R. Mascola³](#),
- [Jennifer Y. Chang^{1,5}](#),
- [Michael T. Yin^{1,5}](#),
- [Magdalena Sobieszczuk^{1,5}](#),
- [Christos A. Kyratsous](#) [ORCID: orcid.org/0000-0002-2596-2906](#)⁶,
- [Lawrence Shapiro](#) [ORCID: orcid.org/0000-0001-9943-8819](#)^{1,4,7},
- [Zizhang Sheng¹](#),
- [Yaoxing Huang](#) [ORCID: orcid.org/0000-0001-6270-1644](#)¹ &
- [David D. Ho](#) [ORCID: orcid.org/0000-0003-1627-149X](#)^{1,2,5}

[Nature](#) volume 593, pages130–135(2021)[Cite this article](#)

- 137k Accesses
- 32 Citations
- 940 Altmetric

- [Metrics details](#)

Subjects

- [Infectious diseases](#)
- [SARS-CoV-2](#)
- [Vaccines](#)

Abstract

The COVID-19 pandemic has had widespread effects across the globe, and its causative agent, SARS-CoV-2, continues to spread. Effective interventions need to be developed to end this pandemic. Single and combination therapies with monoclonal antibodies have received emergency use authorization^{1,2,3}, and more treatments are under development^{4,5,6,7}. Furthermore, multiple vaccine constructs have shown promise⁸, including two that have an approximately 95% protective efficacy against COVID-19^{9,10}. However, these interventions were directed against the initial SARS-CoV-2 virus that emerged in 2019. The recent detection of SARS-CoV-2 variants B.1.1.7 in the UK¹¹ and B.1.351 in South Africa¹² is of concern because of their purported ease of transmission and extensive mutations in the spike protein. Here we show that B.1.1.7 is refractory to neutralization by most monoclonal antibodies against the N-terminal domain of the spike protein and is relatively resistant to a few monoclonal antibodies against the receptor-binding domain. It is not more resistant to plasma from individuals who have recovered from COVID-19 or sera from individuals who have been vaccinated against SARS-CoV-2. The B.1.351 variant is not only refractory to neutralization by most monoclonal antibodies against the N-terminal domain but also by multiple individual monoclonal antibodies against the receptor-binding motif of the receptor-binding domain, which is mostly due to a mutation causing an E484K substitution. Moreover, compared to wild-type SARS-CoV-2, B.1.351 is markedly more resistant to neutralization by convalescent plasma (9.4-fold) and sera from individuals who have been vaccinated (10.3–12.4-fold). B.1.351 and emergent variants^{13,14} with similar mutations in the spike protein present new challenges for monoclonal antibody therapies and threaten the protective efficacy of current vaccines.

[Download PDF](#)

Main

Considerable evolution of SARS-CoV-2 has occurred since its initial emergence, including the appearance of variants with a D614G mutation¹⁵ that have become

dominant. However, viruses with this mutation alone do not appear to be antigenically distinct¹⁶. SARS-CoV-2 B.1.1.7—which is also known as 501Y.V1 in the GR clade (Extended Data Fig. 1a)—was first detected in September 2020 in southeast England and rapidly became the dominant variant in the UK, possibly owing to its enhanced transmissibility¹¹. This strain has now spread to more than 50 countries and there are indications that it may be more virulent¹⁷. B.1.1.7 contains eight mutations in the spike gene in addition to the mutation causing the D614G substitution, including mutations that cause two deletions (Δ H69/ Δ V70 and Δ Y144) in the N-terminal domain (NTD), one substitution (N501Y) in the receptor-binding domain (RBD) and one substitution (P681H) near the furin cleavage site (Extended Data Fig. 1b). SARS-CoV-2 B.1.351—which is also known as 501Y.V2 in the GH clade (Extended Data Fig. 1a)—was first detected in late 2020 in Eastern Cape, South Africa¹². This variant has since become dominant locally, raising the possibility that it too has enhanced transmissibility. B.1.351 contains nine mutations in the spike gene in addition to the mutation causing the D614G substitution, including a cluster of mutations (for example, mutations leading to Δ 242– Δ 244 and R246I) in the NTD, three substitutions (K417N, E484K and N501Y) in the RBD and one substitution (A701V) near the furin cleavage site (Extended Data Fig. 1b). There is a growing concern that these new variants could impair the efficacy of current monoclonal antibody therapies or vaccines, because many of the mutations are found in the antigenic supersite in the NTD^{18,19} or in the ACE2-binding site (also known as the receptor-binding motif (RBM)) that is a major target of potent virus-neutralizing antibodies. We therefore address this concern by assessing the susceptibility of authentic B.1.1.7 and B.1.351 viruses to neutralization by 30 monoclonal antibodies, plasma from 20 patients convalescing from COVID-19 and sera from 22 individuals who received the Moderna or Pfizer vaccine. In addition, we created vesicular stomatitis virus (VSV)-based SARS-CoV-2 pseudoviruses that contain each of the individual mutations as well as one with all eight mutations of the B.1.1.7 variant (B.1.1.7 Δ 8) and another with all nine mutations of the B.1.351 variant (B.1.351 Δ 9). A total of 18 mutant pseudoviruses were made as previously described^{20,21}, and each was found to have a robust titre (Extended Data Fig. 1c) that was adequate for neutralization studies.

Monoclonal antibodies

We first assayed the neutralizing activity of 12 RBD monoclonal antibodies against the authentic B.1.1.7 and B.1.351 viruses compared with the original SARS-CoV-2 strain in Vero E6 cells, as previously described^{20,21}. Three monoclonal antibodies target the ‘inner side’, four target the RBM and five target the ‘outer side’ of the RBD. The footprints of these monoclonal antibodies on the RBD are shown in Fig. 1a and their neutralization profiles are shown in Fig. 1b. For neutralization of B.1.1.7, only the activities of 910-30²² and S309⁵ are substantially impaired. For neutralization of

B.1.351, however, the activities of 910-30, 2-15²⁰, LY-CoV555 (bamlanivimab)^{1,23}, C121²⁴ and REGN10933 (casirivimab)² are completely or markedly abolished. The four monoclonal antibodies that target the RBM are among the most potent SARS-CoV-2-neutralizing antibodies in clinical use or under development. Monoclonal antibodies directed to lower aspects of the inner side (2-36²⁰ and COVA1-16^{25,26}) or to the ‘outer side’ retain their activities against B.1.351, including 2-7^{20,27}, REGN10987 (imdevimab)², C135²⁴ and S309, which are in clinical use or under development. The results for the neutralization of B.1.1.7 and B.1.351 by these 12 monoclonal antibodies are summarized in Fig. 2a as fold increases or decreases in 50% inhibitory concentration (IC_{50}) relative to the wild-type virus. To understand the specific mutations in the spike gene that are responsible for the observed changes, we also tested the same panel of monoclonal antibodies against pseudoviruses B.1.1.7Δ8 and B.1.351Δ9, as well as those containing only single mutations found in B.1.1.7 or B.1.351. The results are displayed in Extended Data Fig. 3 and are summarized in Fig. 2a. There is general agreement in the results for B.1.1.7 and B.1.1.7Δ8, as well as the results for B.1.351 and B.1.351Δ9. The decreased activity of 910-30 against B.1.1.7 is mediated by the N501Y substitution, whereas the slightly impaired activity of S309 remains unexplained. The complete loss of activity of 2-15, LY-CoV555 and C121 against B.1.351 is mediated by the E484K substitution; the complete loss of activity of 910-30 is mediated by the K417N substitution; and the marked reduction in activity of REGN10933 is mediated by K417N and E484K, as has previously been reported²⁸. A structural explanation of how E484K disrupts the binding of 2-15, LY-CoV555 and REGN10933 is presented in Extended Data Fig. 4a.

Fig. 1: Susceptibility of B.1.1.7 and B.1.351 to neutralization by monoclonal antibodies.

 **figure1**

a, Footprints of neutralizing monoclonal antibodies on the RBD. Left, top view of SARS-CoV-2 spike with one RBD in the ‘up’ conformation (PDB: 6zgg). The RBD and NTD are coloured green and peach, respectively. The positions of the inner and outer sides are indicated on the up RBD with the ACE2-binding site coloured yellow. Right, the antibody footprints on the RBD. **b**, Neutralization of B.1.1.7, B.1.351 and wild-type (WA1) viruses by select RBD monoclonal antibodies. The horizontal dotted lines on each graph indicate 50% and 0% neutralization. The dashed outlines in **b** indicate the grouping of the monoclonal antibodies according to their epitopes shown

in **a**. Data are mean \pm s.e.m. of technical triplicates and represent one of two independent experiments. Neutralization by negative control monoclonal antibodies is shown in Extended Data Fig. 2a.

[Full size image](#)

Fig. 2: Susceptibility of B.1.1.7 and B.1.351 to neutralization by monoclonal antibodies (continued).

 figure2

a, Fold increase or decrease in IC₅₀ of neutralizing monoclonal antibodies against B.1.1.7, B.1.351, B.1.1.7Δ8, B.1.351Δ9 and single-mutation pseudoviruses relative to the wild-type (WT) virus, presented as a heat map in which darker colours indicate a greater change. MPI with a downward arrow indicates that the maximum percentage inhibition is substantially reduced, confounding IC₅₀ calculations. Red, resistance >3-fold; green, sensitization >3-fold. **b**, Neutralization of B.1.1.7, B.1.351 and wild-type

viruses by NTD-directed monoclonal antibodies, the footprints of which are delineated by the colour tracings in the inset. The horizontal dotted lines on each graph indicate 50% and 0% neutralization. Data are mean \pm s.e.m. of technical triplicates and represent one of two independent experiments. **c**, Changes in neutralization IC₅₀ of authorized or investigational therapeutic monoclonal antibodies against B.1.1.7, B.1.351 and wild-type (WA1) viruses (left) as well as B.1.1.7Δ8, B.1.351Δ9 and wild-type (D614G) pseudoviruses (right).

[Full size image](#)

We also assessed the neutralizing activity of six NTD-directed monoclonal antibodies against B.1.1.7, B.1.351 and wild-type viruses. Both B.1.1.7 and B.1.351 are markedly resistant to neutralization by antibodies 5-24 and 4-8²⁰, as well as by 4A8²⁹, all of which target the antigenic supersite in the NTD¹⁸ (Fig. 2b). The activities of 2-17, 4-19 and 5-7²⁰ are variably impaired, particularly against B.1.351. To understand the specific mutations that are responsible for the observed changes, we then tested these monoclonal antibodies against pseudoviruses containing only single mutations found in B.1.1.7 or B.1.351 (Extended Data Fig. 3). The results are summarized in Fig. 2a as a fold increase or decrease relative to the wild-type virus. We found that the resistance of B.1.1.7 to most NTD-directed monoclonal antibodies is largely conferred by ΔY144, whereas the resistance of B.1.351 is largely conferred by Δ242–Δ244 and/or R246I. Amino acid residues 144, 242–244 and 246 all fall within the NTD supersite^{18,19} (Fig. 2b; details are shown in Extended Data Fig. 4b).

We next tested the neutralizing activity of 12 additional RBD monoclonal antibodies, including ones from our own collection (1-20, 4-20, 2-4, 2-43, 2-30 and 2-38)²⁰ as well as CB6 (etesevimab)^{3,6}, COV2-2196 and COV2-2130⁷, Brii-196 and Brii-198⁴, and REGN10985. The results against B.1.1.7, B.1.351 and wild-type viruses are shown in Extended Data Fig. 5a, and the detailed findings against the single-mutation pseudoviruses are shown in Extended Data Fig. 3. The fold changes in neutralization IC₅₀ titres relative to the wild-type virus are tabulated in Extended Data Fig. 5b. Here, we discuss only the results for monoclonal antibodies in clinical development. The activity of CB6 is rendered inactive against B.1.351 because of the K417N substitution. Brii-196 and COV2-2130 are essentially unaffected by the new variants; the activities of Brii-198 and COV2-2196 are diminished by 14.6-fold and 6.3-fold, respectively, against B.1.351 but not against B.1.1.7.

We then examined, in a single experiment, the neutralizing activity of monoclonal antibody therapies in clinical use or under clinical investigation against B.1.1.7, B.1.351 and wild-type viruses, as well as against B.1.1.7Δ8, B.1.351Δ9 and wild-type pseudoviruses. The results for the single monoclonal antibodies LY-CoV555 and S309, as well as for combination regimens of REGN10933 and REGN10987, LY-CoV555

and CB6, Brii-196 and Brii-198, and COV2-2196 and COV2-2130, are shown in Extended Data Fig. 6 and summarized in Fig. 2c. LY-CoV555, alone or in combination with CB6, is no longer able to neutralize B.1.351. Although REGN10933 and REGN10987 and COV2-2196 and COV2-2130 are seemingly unaffected against variant pseudoviruses, there are noticeable decreases in their activity against the B.1.351 authentic virus. Although S309 and the combination of Brii-196 and Brii-198 are not significantly impaired, their potencies are noticeably lower (Fig. 2c). These findings suggest that antibody treatment of this virus might need to be modified in localities in which B.1.351 and related variants^{13,14} are prevalent, and highlight the importance of combination antibody therapy to address the expanding antigenic diversity of SARS-CoV-2.

Convalescent plasma

We obtained plasma from 20 patients convalescing from COVID-19 more than one month after documented SARS-CoV-2 infection in the spring of 2020. Each plasma sample was then assayed for neutralization against B.1.1.7, B.1.351 and wild-type viruses. Figure 3a shows that most (16 out of 20) plasma samples lost more than 2.5-fold neutralizing activity against B.1.351, while maintaining activity against B.1.1.7. Only plasma from P7, P10, P18 and P20 retain neutralizing activities similar to those against the wild-type virus. These results are summarized as fold increase or decrease in 50% inhibitory dilution (ID_{50}) in Fig. 3b. Furthermore, the magnitude of the drop in plasma neutralization is better seen in Fig. 3c, showing no loss of activity against B.1.1.7 but substantial loss against B.1.351 (9.4-fold).

Fig. 3: B.1.351 is more resistant to neutralization by convalescent plasma from patients.

 **figure3**

a, Neutralization results for 20 convalescent plasma samples (P1–P20) against B.1.1.7, B.1.351 and wild-type viruses. The horizontal dotted lines on each graph indicate 50% and 0% neutralization. Reciprocal plasma dilutions are given as 1: X , in which X is the value on the x axis. Data are mean \pm s.e.m. of technical triplicates. Neutralization by healthy donor plasma is shown in Extended Data Fig. 2b. **b**, Fold increase or decrease in neutralization ID₅₀ of B.1.1.7 and B.1.351 viruses, B.1.1.7Δ8, B.1.351Δ9 and single-mutation pseudoviruses relative to the wild-type virus presented as a heat map

in which darker colours indicate a greater change. Red, resistance >2.5-fold; green, sensitization >2.5-fold. **c**, Change in reciprocal plasma neutralization ID₅₀ values of convalescent plasma against B.1.1.7, B.1.351, B.1.1.7Δ8 and B.1.351Δ9 relative to the wild-type virus. Mean fold changes in ID₅₀ values relative to the wild-type virus are written above the *P* values. Statistical analysis was performed using a Wilcoxon matched-pairs signed-rank test. Two-tailed *P* values are reported.

[Full size image](#)

Every plasma sample was also tested against each mutant pseudovirus, and those findings are shown in Extended Data Fig. 7 and summarized in Fig. 3b,c. Eight samples show a decrease of more than 2.5-fold in neutralizing activity against B.1.1.7Δ8, in contrast to the results for neutralization of B.1.1.7. These discrepant results highlight a previous observation²⁰ that pseudovirus neutralization does not always faithfully recapitulate live virus neutralization. The loss of plasma neutralizing activity against B.1.351 could be largely attributed to the E484K substitution (Fig. 3b), which has been shown to attenuate the neutralizing activity of convalescent sera³⁰. Our findings here suggests that this mutation in the RBM is situated in an immunodominant epitope for most individuals infected with SARS-CoV-2. It is also interesting to note that sera such as P7, P10 and P18 contain neutralizing antibodies that are essentially unperturbed by the multitude of spike mutations found in these two new variants (Fig. 3b). A detailed analysis of the antibody repertoire of these samples against the viral spike could be informative.

Sera from vaccinated individuals

Sera were obtained from 12 participants of a phase-I clinical trial of the Moderna SARS-CoV-2 mRNA-1273 vaccine⁹ conducted at the NIH. These volunteers received two immunizations with the vaccine (100 µg) on days 0 and 28, and blood was collected on day 43. Additional sera from vaccinated individuals were obtained from 10 individuals who received the Pfizer BNT162b2 COVID-19 vaccine¹⁰ under emergency use authorization at the clinical dose on days 0 and 21. Blood was collected on day 28 or later.

Each serum sample from vaccinated individuals was assayed for neutralization against B.1.1.7, B.1.351 and wild-type viruses. Figure 4a shows no loss of neutralizing activity against B.1.1.7, whereas every sample lost activity against B.1.351. These results are quantified and tabulated as the fold increase or decrease in neutralization ID₅₀ titres in Fig. 4b, and the extent of the decrease in neutralizing activity is more evident in Fig. 4c. Overall, the neutralizing activity against B.1.1.7 was essentially

unchanged, but significantly lower against B.1.351 (12.4-fold for the Moderna vaccine; 10.3-fold for the Pfizer vaccine).

Fig. 4: B.1.351 is more resistant to neutralization by sera from individuals vaccinated with the Moderna or Pfizer vaccine.

 figure4

a, Neutralization profiles for 22 serum samples obtained from individuals who received the SARS-CoV-2 vaccine made by Moderna (V1–V12) or Pfizer (V13–V22) against B.1.1.7, B.1.351 and wild-type viruses. The horizontal dotted lines on each graph indicate 50% and 0% neutralization. Reciprocal serum dilutions are given as 1: X , in which X is the value on the x axis. Data are mean \pm s.e.m. of technical triplicates and represent one of two independent experiments. **b**, Fold change in serum neutralization ID₅₀ of B.1.1.7 and B.1.351 viruses, B.1.1.7Δ8, B.1.351Δ9 and single-mutation pseudoviruses relative to the wild-type virus, presented as a heat map in

which darker colours indicate greater change. Red, resistance >2.5-fold; green, sensitization >2.5-fold. **c**, Change in reciprocal serum ID₅₀ values for individuals who received the Moderna and Pfizer vaccines against B.1.1.7, B.1.351, B.1.1.7Δ8 and B.1.351Δ9 relative to the wild-type virus. Mean fold change in ID₅₀ relative to the wild-type virus is written above the *P* values. Statistical analysis was performed using a Wilcoxon matched-pairs signed-rank test. Two-tailed *P* values are reported.

[Full size image](#)

Every serum from vaccinated individuals was also tested against each mutant pseudovirus, and the results are presented in Extended Data Fig. 8 and summarized in Fig. 4b,c. No single mutation in B.1.1.7 had an appreciable effect on the neutralizing activity of sera from vaccinated individuals. The loss of neutralizing activity against B.1.351Δ9 is largely consistent with the loss in neutralization of the B.1.351 live virus. A major contributor to the resistance to neutralization of this variant virus appears to be the E484K substitution (Fig. 4b), indicating that this mutation in the RBM is situated in an immunodominant epitope recognized by all sera from the vaccinated individuals studied.

Discussion

Both SARS-CoV-2 variants B.1.1.7 and B.1.351 are raising concerns not only because of their increase transmissibility but also because of their extensive mutations in the spike gene that could lead to antigenic changes that are detrimental to monoclonal antibody therapies and protection afforded by vaccines. It is of equal concern that another variant known as P.1 or 501Y.V3 is increasing rapidly in Brazil and spreading far beyond^{13,14}. P.1 contains three substitutions (K417T, E484K and N501Y) at the same RBD residues as B.1.351. Much of our findings on B.1.351 would probably be similar for this emergent variant. N501Y is shared among viruses in these three lineages; although this mutation may confer enhanced binding to ACE2³¹, its antigenic effects are limited to a few monoclonal antibodies (Fig. 2a and Extended Data Fig. 5b), with no pronounced effects on the neutralizing activity of convalescent plasma or sera from vaccinated individuals (Figs. 3b, 4b), as other studies have also reported^{32,33,34}.

Our findings have relevance to the use of monoclonal antibody to treat or prevent SARS-CoV-2. Both B.1.1.7 and B.1.351 are resistant to neutralization by monoclonal antibodies directed against the NTD supersite (Fig. 2a,b and Extended Data Fig. 4b). More importantly, B.1.351 is resistant to a major group of potent monoclonal antibodies that target the RBM, including three regimens authorized for emergency use (Fig. 2a). LY-CoV555 alone and in combination with CB6 is inactive against B.1.351, and the activity of REGN10933 is impaired (Fig. 1b) although its

combination with REGN10987 retains much of the neutralization activity (Fig. 2c). Several other monoclonal antibodies in development are similarly impaired (Fig. 2a, c and Extended Data Fig. 5b) against this variant. Decisions on the use of these monoclonal antibodies will depend heavily on the local prevalence of B.1.351 or variants with an E484K substitution, thus highlighting the importance of viral genomic surveillance worldwide and proactive development of next-generation antibody therapeutics, including combinations that target antigenically distinct epitopes.

Convalescent plasma from patients infected with SARS-CoV-2 from early in the pandemic show no significant change in neutralizing activity against B.1.1.7, but the reduction against B.1.351 is remarkable (Fig. 3b,c). This relative resistance is mostly due to the E484K substitution, which is shared by the B.1.351 and P.1 variants^{12,13,14}. Again, in areas in which such viruses are common, one would have a concern about re-infection, as other studies are also suggesting^{35,36}. This apprehension is heightened by the recent observation from the Novavax vaccine trial in South Africa that recipients who received the placebo with previous SARS-CoV-2 infection were not protected against a subsequent exposure to B.1.351^{37,38}. Even more disturbing is the situation in Manaus, Brazil, where a second wave of infection due to P.1 is sweeping through a population that was already 76% seropositive owing to prior infection in the spring of 2020³⁹.

As for the ramifications of our findings for the protective efficacy of current SARS-CoV-2 vaccines, the neutralizing activity of sera from vaccinated individuals against B.1.1.7 is largely intact and no adverse effects on current vaccines are expected (Fig. 4c), consistent with conclusions that were reached by other studies^{34,40,41}. On the other hand, the loss in activity by 10.3–12.4-fold against B.1.351 is larger than results that were reported using mutant pseudoviruses^{34,42,43}. Taken together, the overall findings are troubling, particularly in light of recent reports that both the Novavax and Johnson & Johnson vaccines showed a substantial drop in efficacy in South Africa^{37,38}.

The recent emergence of B.1.1.7, B.1.351 and P.1 marks the beginning of SARS-CoV-2 antigenic drift. This conclusion is supported by the data presented here, illustrating how so many of these changes in the spike protein conferred resistance to antibody neutralization, and by studies reporting similar mutations in the spike gene selected by antibody pressure *in vivo*^{44,45,46}. Mutationally, this virus is going in a direction that could ultimately lead to escape from our current therapeutic and prophylactic interventions that are directed against the viral spike protein. If the rampant spread of the virus continues and more critical mutations accumulate, then we may be condemned to chasing after the evolving SARS-CoV-2 continually, as we have long done for influenza virus. Such considerations require that we stop virus transmission as quickly as is feasible, by redoubling our mitigation measures and by expediting vaccine rollout.

Methods

Data reporting

No statistical methods were used to predetermine sample size. The experiments were not randomized and the investigators were not blinded to allocation during experiments and outcome assessment.

Patients and vaccines

Plasma samples were obtained from patients (aged 34–79 years; mean, 54 years) convalescing from documented SARS-CoV-2 infection approximately one month after recovery or later. The patients were enrolled into an observational cohort study of patients convalescing from COVID-19 at the Columbia University Irving Medical Center (CUIMC) starting in the spring of 2020. The study protocol was approved by the CUIMC Institutional Review Board (IRB) and all participants provided written informed consent. From their documented clinical profiles, plasma samples from 10 patients with severe COVID-19 and plasma from 10 patients with a non-severe SARS-CoV-2 infection were selected for this study. Sera were obtained from 12 participants in a phase-I clinical trial of the Moderna SARS-CoV-2 mRNA-1273 vaccine conducted at the NIH, under a NIH IRB-approved protocol⁹. Sera were also obtained from 10 individuals followed in a CUIMC IRB-approved protocol to assess immunological responses to SARS-CoV-2 who received the Pfizer BNT162b2 COVID-19 vaccine as a part of the emergency use authorization.

Monoclonal antibodies

Monoclonal antibodies tested in this study were constructed and produced at Columbia University as previously described²⁰, except REGN10933, REGN10987, REGN10985, COV2-2196 and COV2-2130, which were provided by Regeneron Pharmaceuticals, Brii-196 and Brii-198, which were provided by Brii Biosciences and CB6, which was provided by B.Z. and P.D.K.

Authentic SARS-CoV-2 microplate neutralization

The SARS-CoV-2 viruses USA-WA1/2020 (WA1), USA/CA_CDC_5574/2020 (B.1.1.7) and hCoV-19/South Africa/KRISP-EC-K005321/2020 (B.1.351) were obtained from BEI Resources (NIAID, NIH) and propagated for one passage using Vero E6 cells. Virus infectious titres were determined by an end-point dilution and cytopathogenic effect assay on Vero E6 cells as previously described²⁰.

An end-point dilution microplate neutralization assay was performed to measure the neutralization activity of convalescent plasma samples, sera from vaccinated individuals and purified monoclonal antibodies. In brief, plasma and serum samples were subjected to successive fivefold dilutions starting from 1:100. Similarly, most monoclonal antibodies were serially diluted (fivefold dilutions) starting at $10 \mu\text{g ml}^{-1}$. Some clinical antibodies were tested from starting concentrations of $1 \mu\text{g ml}^{-1}$. Triplicates of each dilution were incubated with SARS-CoV-2 at a multiplicity of infection of 0.1 in EMEM with 7.5% inactivated fetal calf serum for 1 h at 37 °C. After incubation, the virus–antibody mixture was transferred onto a monolayer of Vero E6 cells grown overnight. The cells were incubated with the mixture for around 70 h. Cytopathogenic effects of viral infection were visually scored for each well in a blinded manner by two independent observers. The results were then converted into the percentage of neutralization at a given sample dilution or monoclonal antibody concentration, and the data (mean \pm s.e.m.) were plotted using a five-parameter dose–response curve in GraphPad Prism v.8.4.

Construction and production of variant pseudoviruses

The original pCMV3-SARS-CoV-2-spike plasmid was provided by P. Wang (Shandong University). Plasmids encoding the D614G variant, all of the single-mutation variants found in B.1.1.7 or B.1.351, the eight-mutation-combination variant (B.1.1.7Δ8) and nine-mutation-combination variant (B.1.351Δ9) were generated using the Quikchange II XL site-directed mutagenesis kit (Agilent). Recombinant Indiana VSV expressing different SARS-CoV-2 spike variants were generated as previously described^{20,21}. HEK293T cells were grown to 80% confluence before transfection with the spike gene using Lipofectamine 3000 (Invitrogen). Cells were cultured overnight at 37 °C with 5% CO₂ and VSV-G pseudo-typed ΔG-luciferase (G*ΔG-luciferase, Kerafast) was used to infect the cells in DMEM at an multiplicity of infection of 3 for 2 h before washing the cells with 1× DPBS three times. The next day, the transfection supernatant was collected and clarified by centrifugation at 300g for 10 min. Each viral stock was then incubated with 20% I1 hybridoma (anti-VSV-G; ATCC, CRL-2700) supernatant for 1 h at 37 °C to neutralize contaminating the VSV-G pseudo-typed ΔG-luciferase virus before measuring titres and making aliquots to be stored at –80 °C.

Pseudovirus neutralization assays

Neutralization assays were performed by incubating pseudoviruses with serial dilutions of monoclonal antibodies or heat-inactivated plasma or sera, and scored by the reduction in luciferase gene expression^{20,21}. In brief, Vero E6 cells were seeded in a 96-well plate at a concentration of 2×10^4 cells per well. Pseudoviruses were

incubated the next day with serial dilutions of the test samples in triplicate for 30 min at 37 °C. The mixture was added to cultured cells and incubated for an additional 24 h. The luminescence was measured by Luciferase Assay System (Promega). IC₅₀ was defined as the dilution at which the relative light units were reduced by 50% compared with the virus control wells (virus + cells) after subtraction of the background in the control groups with cells only. The IC₅₀ values were calculated using nonlinear regression in GraphPad Prism.

Reporting summary

Further information on research design is available in the [Nature Research Reporting Summary](#) linked to this paper.

Data availability

Materials used in this study will be made available but may require execution of a materials transfer agreement. All the data are provided in the paper or the Supplementary Information.

References

1. 1.

Chen, P. et al. SARS-CoV-2 neutralizing antibody LY-CoV555 in outpatients with COVID-19. *N. Engl. J. Med.* **384**, 229–237 (2021).

[CAS](#) [Article](#) [Google Scholar](#)

2. 2.

Hansen, J. et al. Studies in humanized mice and convalescent humans yield a SARS-CoV-2 antibody cocktail. *Science* **369**, 1010–1014 (2020).

[ADS](#) [CAS](#) [Article](#) [Google Scholar](#)

3. 3.

Gottlieb, R. L. et al. Effect of bamlanivimab as monotherapy or in combination with etesevimab on viral load in patients with mild to moderate COVID-19: a randomized clinical trial. *J. Am. Med. Assoc.* **325**, 632–644 (2021).

[CAS](#) [Article](#) [Google Scholar](#)

4. 4.

Ju, B. et al. Human neutralizing antibodies elicited by SARS-CoV-2 infection. *Nature* **584**, 115–119 (2020).

[ADS](#) [CAS](#) [Article](#) [Google Scholar](#)

5. 5.

Pinto, D. et al. Cross-neutralization of SARS-CoV-2 by a human monoclonal SARS-CoV antibody. *Nature* **583**, 290–295 (2020).

[ADS](#) [CAS](#) [Article](#) [Google Scholar](#)

6. 6.

Shi, R. et al. A human neutralizing antibody targets the receptor-binding site of SARS-CoV-2. *Nature* **584**, 120–124 (2020).

[ADS](#) [CAS](#) [Article](#) [Google Scholar](#)

7. 7.

Zost, S. J. et al. Potently neutralizing and protective human antibodies against SARS-CoV-2. *Nature* **584**, 443–449 (2020).

[CAS](#) [Article](#) [Google Scholar](#)

8. 8.

Krammer, F. SARS-CoV-2 vaccines in development. *Nature* **586**, 516–527 (2020).

[ADS](#) [CAS](#) [Article](#) [Google Scholar](#)

9. 9.

Anderson, E. J. et al. Safety and immunogenicity of SARS-CoV-2 mRNA-1273 vaccine in older adults. *N. Engl. J. Med.* **383**, 2427–2438 (2020).

[CAS](#) [Article](#) [Google Scholar](#)

10. 10.

Polack, F. P. et al. Safety and efficacy of the BNT162b2 mRNA COVID-19 vaccine. *N. Engl. J. Med.* **383**, 2603–2615 (2020).

[CAS Article](#) [Google Scholar](#)

11. 11.

Rambaut, A. et al. Preliminary genomic characterisation of an emergent SARS-CoV-2 lineage in the UK defined by a novel set of spike mutations.
<https://virological.org/t/preliminary-genomic-characterisation-of-an-emergent-sars-cov-2-lineage-in-the-uk-defined-by-a-novel-set-of-spike-mutations/563> (2020).

12. 12.

Tegally, H. et al. Emergence and rapid spread of a new severe acute respiratory syndrome-related coronavirus 2 (SARS-CoV-2) lineage with multiple spike mutations in South Africa. Preprint at
<https://doi.org/10.1101/2020.12.21.20248640> (2020).

13. 13.

Faria, N. R. et al. Genomic characterisation of an emergent SARS-CoV-2 lineage in Manaus: preliminary findings. Preprint at <https://virological.org/t/genomic-characterisation-of-an-emergent-sars-cov-2-lineage-in-manaus-preliminary-findings/586> (2021).

14. 14.

Naveca, F. et al. Phylogenetic relationship of SARS-CoV-2 sequences from Amazonas with emerging Brazilian variants harboring mutations E484K and N501Y in the spike protein. Preprint at <https://virological.org/t/phylogenetic-relationship-of-sars-cov-2-sequences-from-amazonas-with-emerging-brazilian-variants-harboring-mutations-e484k-and-n501y-in-the-spike-protein/585> (2021).

15. 15.

Korber, B. et al. Tracking changes in SARS-CoV-2 spike: evidence that D614G increases infectivity of the COVID-19 virus. *Cell* **182**, 812–827 (2020).

[CAS Article](#) [Google Scholar](#)

16. 16.

Hou, Y. J. et al. SARS-CoV-2 D614G variant exhibits efficient replication ex vivo and transmission in vivo. *Science* **370**, 1464–1468 (2020).

[ADS](#) [CAS](#) [PubMed](#) [PubMed Central](#) [Google Scholar](#)

17. 17.

Davies, N. G. et al. Increased hazard of death in community-tested cases of SARS-CoV-2 variant of concern 202012/01. Preprint at <https://doi.org/10.1101/2021.02.01.21250959> (2021).

18. 18.

Cerutti, G. et al. Potent SARS-CoV-2 neutralizing antibodies directed against spike N-terminal domain target a single supersite. *Cell Host Microbe* (in the press).

19. 19.

McCallum, M. et al. N-terminal domain antigenic mapping reveals a site of vulnerability for SARS-CoV-2. Preprint at <https://doi.org/10.1101/2021.01.14.426475> (2021).

20. 20.

Liu, L. et al. Potent neutralizing antibodies against multiple epitopes on SARS-CoV-2 spike. *Nature* **584**, 450–456 (2020).

[CAS](#) [Article](#) [Google Scholar](#)

21. 21.

Wang, P. et al. SARS-CoV-2 neutralizing antibody responses are more robust in patients with severe disease. *Emerg. Microbes Infect.* **9**, 2091–2093 (2020).

[CAS](#) [Article](#) [Google Scholar](#)

22. 22.

Banach, B. B. et al. Paired heavy and light chain signatures contribute to potent SARS-CoV-2 neutralization in public antibody responses. Preprint at <https://doi.org/10.1101/2020.12.31.424987> (2021).

23. 23.

Jones, B. E. et al. LY-CoV555, a rapidly isolated potent neutralizing antibody, provides protection in a non-human primate model of SARS-CoV-2 infection. Preprint at <https://doi.org/10.1101/2020.09.30.318972> (2020).

24. 24.

Robbiani, D. F. et al. Convergent antibody responses to SARS-CoV-2 in convalescent individuals. *Nature* **584**, 437–442 (2020).

[ADS](#) [CAS](#) [Article](#) [Google Scholar](#)

25. 25.

Brouwer, P. J. M. et al. Potent neutralizing antibodies from COVID-19 patients define multiple targets of vulnerability. *Science* **369**, 643–650 (2020).

[ADS](#) [CAS](#) [Article](#) [Google Scholar](#)

26. 26.

Liu, H. et al. Cross-neutralization of a SARS-CoV-2 antibody to a functionally conserved site is mediated by avidity. *Immunity* **53**, 1272–1280 (2020).

[CAS](#) [Article](#) [Google Scholar](#)

27. 27.

Cerutti, G. et al. Structural basis for accommodation of emerging B.1.351 and B.1.1.7 variants by two potent SARS-CoV-2 neutralizing antibodies. Preprint at <https://doi.org/10.1101/2021.02.21.432168> (2021).

28. 28.

Starr, T. N. et al. Prospective mapping of viral mutations that escape antibodies used to treat COVID-19. *Science* **371**, 850–854 (2021).

[ADS](#) [CAS](#) [Article](#) [Google Scholar](#)

29. 29.

Chi, X. et al. A neutralizing human antibody binds to the N-terminal domain of the spike protein of SARS-CoV-2. *Science* **369**, 650–655 (2020).

[ADS](#) [CAS](#) [Article](#) [Google Scholar](#)

30. 30.

Greaney, A. J. et al. Comprehensive mapping of mutations to the SARS-CoV-2 receptor-binding domain that affect recognition by polyclonal human serum antibodies. *Cell Host Microbe* <https://doi.org/10.1016/j.chom.2021.02.003> (2021).

31. 31.

Starr, T. N. et al. Deep mutational scanning of SARS-CoV-2 receptor binding domain reveals constraints on folding and ACE2 binding. *Cell* **182**, 1295–1310 (2020).

[CAS Article](#) [Google Scholar](#)

32. 32.

Xie, X. et al. Neutralization of SARS-CoV-2 spike 69/70 deletion, E484K and N501Y variants by BNT162b2 vaccine-elicited sera. *Nat. Med.* <https://doi.org/10.1038/s41591-021-01270-4> (2021).

33. 33.

Rees-Spear, C. et al. The impact of spike mutations on SARS-CoV-2 neutralization. Preprint at <https://doi.org/10.1101/2021.01.15.426849> (2021).

34. 34.

Wu, K. et al. mRNA-1273 vaccine induces neutralizing antibodies against spike mutants from global SARS-CoV-2 variants. Preprint at <https://doi.org/10.1101/2021.01.25.427948> (2021).

35. 35.

Cele, S. et al. Escape of SARS-CoV-2 501Y.V2 variants from neutralization by convalescent plasma. Preprint at <https://doi.org/10.1101/2021.01.26.21250224> (2021).

36. 36.

Wibmer, C. K. et al. SARS-CoV-2 501Y.V2 escapes neutralization by South African COVID-19 donor plasma. *Nat. Med.* <https://doi.org/10.1038/s41591-021-01285-x> (2021).

37. 37.

Wadman, M. & Cohen, J. Novavax vaccine delivers 89% efficacy against COVID-19 in U.K.—but is less potent in South Africa. *Science* <https://doi.org/10.1126/science.abg8101> (2021).

38. 38.

Callaway, E. & Mallapaty, S. Novavax offers first evidence that COVID vaccines protect people against variants. *Nature* **590**, 17 (2021).

[ADS](#) [CAS](#) [Article](#) [Google Scholar](#)

39. 39.

Sabino, E. C. et al. Resurgence of COVID-19 in Manaus, Brazil, despite high seroprevalence. *Lancet* **397**, 452–455 (2021).

[CAS](#) [Article](#) [Google Scholar](#)

40. 40.

Collier, D. et al. SARS-CoV-2 B.1.1.7 sensitivity to mRNA vaccine-elicited, convalescent and monoclonal antibodies. Preprint at <https://doi.org/10.1101/2021.01.19.21249840> (2021).

41. 41.

Muik, A. et al. Neutralization of SARS-CoV-2 lineage B.1.1.7 pseudovirus by BNT162b2 vaccine-elicited human sera. *Science* <https://doi.org/10.1126/science.abg6105> (2021).

42. 42.

Wang, Z. et al. mRNA vaccine-elicited antibodies to SARS-CoV-2 and circulating variants. *Nature* <https://doi.org/10.1038/s41586-021-03324-6> (2021).

43. 43.

Tada, T. et al. Neutralization of viruses with European, South African, and United States SARS-CoV-2 variant spike proteins by convalescent sera and BNT162b2 mRNA vaccine-elicited antibodies. Preprint at <https://doi.org/10.1101/2021.02.05.430003> (2021).

44. 44.

Kemp, S. A. et al. SARS-CoV-2 evolution during treatment of chronic infection. *Nature* <https://doi.org/10.1038/s41586-021-03291-y> (2021).

45. 45.

McCarthy, K. R. et al. Recurrent deletions in the SARS-CoV-2 spike glycoprotein drive antibody escape. *Science* <https://doi.org/10.1126/science.abf6950> (2021).

46. 46.

Choi, B. et al. Persistence and evolution of SARS-CoV-2 in an immunocompromised host. *N. Engl. J. Med.* **383**, 2291–2293 (2020).

[Article](#) [Google Scholar](#)

[Download references](#)

Acknowledgements

We thank S. Goff and B. DeKosky for helpful discussions. This study was supported by funding from Andrew and Peggy Cherng, Samuel Yin, Barbara Picower and the JPB Foundation, Brii Biosciences, Roger and David Wu, and the Bill and Melinda Gates Foundation.

Author information

Author notes

1. These authors contributed equally: Pengfei Wang, Manoj S. Nair, Lihong Liu, Sho Iketani

Affiliations

1. Aaron Diamond AIDS Research Center, Columbia University Vagelos College of Physicians and Surgeons, New York, NY, USA

Pengfei Wang, Manoj S. Nair, Lihong Liu, Sho Iketani, Yang Luo, Yicheng Guo, Maple Wang, Jian Yu, Jennifer Y. Chang, Michael T. Yin, Magdalena Sobieszczyk, Lawrence Shapiro, Zizhang Sheng, Yaoxing Huang & David D. Ho

2. Department of Microbiology and Immunology, Columbia University Irving Medical Center, New York, NY, USA

Sho Iketani & David D. Ho

3. Vaccine Research Center, National Institutes of Health, Bethesda, MD, USA

Baoshan Zhang, Peter D. Kwong, Barney S. Graham & John R. Mascola

4. Department of Biochemistry, Columbia University, New York, NY, USA

Peter D. Kwong & Lawrence Shapiro

5. Division of Infectious Diseases, Department of Internal Medicine, Columbia University Vagelos College of Physicians and Surgeons, New York, NY, USA

Jennifer Y. Chang, Michael T. Yin, Magdalena Sobieszczyk & David D. Ho

6. Regeneron Pharmaceuticals, Tarrytown, NY, USA

Christos A. Kyratsous

7. Zuckerman Mind Brain Behavior Institute, Columbia University, New York, NY, USA

Lawrence Shapiro

Authors

1. Pengfei Wang

[View author publications](#)

You can also search for this author in [PubMed](#) [Google Scholar](#)

2. Manoj S. Nair

[View author publications](#)

You can also search for this author in [PubMed](#) [Google Scholar](#)

3. Lihong Liu

[View author publications](#)

You can also search for this author in [PubMed](#) [Google Scholar](#)

4. Sho Iketani

[View author publications](#)

You can also search for this author in [PubMed](#) [Google Scholar](#)

5. Yang Luo

[View author publications](#)

You can also search for this author in [PubMed](#) [Google Scholar](#)

6. Yicheng Guo

[View author publications](#)

You can also search for this author in [PubMed](#) [Google Scholar](#)

7. Maple Wang

[View author publications](#)

You can also search for this author in [PubMed](#) [Google Scholar](#)

8. Jian Yu

[View author publications](#)

You can also search for this author in [PubMed](#) [Google Scholar](#)

9. Baoshan Zhang

[View author publications](#)

You can also search for this author in [PubMed](#) [Google Scholar](#)

10. Peter D. Kwong

[View author publications](#)

You can also search for this author in [PubMed](#) [Google Scholar](#)

11. Barney S. Graham

[View author publications](#)

You can also search for this author in [PubMed](#) [Google Scholar](#)

12. John R. Mascola

[View author publications](#)

You can also search for this author in [PubMed](#) [Google Scholar](#)

13. Jennifer Y. Chang

[View author publications](#)

You can also search for this author in [PubMed](#) [Google Scholar](#)

14. Michael T. Yin

[View author publications](#)

You can also search for this author in [PubMed](#) [Google Scholar](#)

15. Magdalena Sobieszczyk

[View author publications](#)

You can also search for this author in [PubMed](#) [Google Scholar](#)

16. Christos A. Kyratsous

[View author publications](#)

You can also search for this author in [PubMed](#) [Google Scholar](#)

17. Lawrence Shapiro

[View author publications](#)

You can also search for this author in [PubMed](#) [Google Scholar](#)

18. Zizhang Sheng

[View author publications](#)

You can also search for this author in [PubMed](#) [Google Scholar](#)

19. Yaoxing Huang

[View author publications](#)

You can also search for this author in [PubMed](#) [Google Scholar](#)

20. David D. Ho

[View author publications](#)

You can also search for this author in [PubMed](#) [Google Scholar](#)

Contributions

The study was conceptualized by D.D.H. The experiments were mainly carried out by P.W., M.S.N., Y.H., L.L. and S.I. with assistance from M.W. and J.Y. Structural interpretations were made by Y.G., Z.S., L.S. and P.D.K. B.Z., P.D.K. and C.A.K.

provided monoclonal antibodies. J.Y.C. and M.T.Y. provided plasma from patients convalescing from COVID-19. B.S.G. and J.R.M. provided sera from participants in the Moderna vaccine trial; J.Y.C. and M.S. provided sera from healthcare workers immunized with the Pfizer vaccine. Y.H. and Y.L. helped to supervise the study. The manuscript was written by D.D.H. with editing by P.W., P.D.K., L.S., Y.L. and was reviewed by, commented on and approved by all of the authors.

Corresponding authors

Correspondence to [Yaoxing Huang](#) or [David D. Ho](#).

Ethics declarations

Competing interests

P.W., L.L, J.Y., M.S.N., Y.H. and D.D.H. are inventors on a provisional patent application on monoclonal antibodies against SARS-CoV-2. D.D.H. is a member of the scientific advisory board of Brii Biosciences, which also has provided a grant to Columbia University to support this and other studies on SARS-CoV-2.

Additional information

Peer review information *Nature* thanks Jesse D. Bloom, Andreas Radbruch and the other, anonymous, reviewer(s) for their contribution to the peer review of this work.

Publisher's note Springer Nature remains neutral with regard to jurisdictional claims in published maps and institutional affiliations.

Extended data figures and tables

[Extended Data Fig. 1 Emerging SARS-CoV-2 variants identified in the UK and South Africa.](#)

a, Phylogenetic tree of SARS-CoV-2 variants, with B.1.351 and B.1.1.7 highlighted. **b**, Mutations in the viral spike protein identified in B.1.351 (SA) and B.1.1.7 (UK) in addition to D614G. **c**, Titres of wild-type (D614G) and 18 mutant SARS-CoV-2 pseudoviruses. VSV-based pseudoviruses were generated^{20,21} and viral particles were quantified and normalized to the expression of the nucleocapsid protein of VSV by western blot. Equal amounts of each pseudovirus were then used to infect Vero E6

cells and relative luciferase units (RLUs) were measured 16 h later. Data are mean ± s.e.m. of technical duplicates.

Extended Data Fig. 2 Neutralization profiles of negative control monoclonal antibodies and plasma from healthy donors.

a, b, Neutralization of two SARS-CoV-2 non-neutralizing monoclonal antibodies²⁰ (**a**) and healthy donor plasma against wild-type (WA1) live virus (**b**). **c**, Neutralization of plasma samples from two healthy donors against wild-type, B.1.1.7Δ8 and B.1.351Δ9 viruses, as well as single-mutation pseudoviruses. Data are mean ± s.e.m. of technical triplicates.

Extended Data Fig. 3 Neutralization profiles of monoclonal antibodies against wild-type, B.1.1.7Δ8 and B.1.351Δ9 viruses, as well as single-mutation pseudoviruses.

Data are mean ± s.e.m. of technical triplicates.

Extended Data Fig. 4 Structural explanations on how critical mutations affect monoclonal antibody activity.

a, E484 forms hydrogen bonds with monoclonal antibodies that target the RBM. E484K causes not only steric clashes but also a charge change at antibody-binding sites, and thus abolishes binding by these RBM-directed monoclonal antibodies. Steric clashes are shown by red plates. **b**, Mutations at or near the NTD antigenic supersite—comprising loops N1, N3 and N5—that is recognized by many potent NTD-directed monoclonal antibodies.

Extended Data Fig. 5 Neutralization susceptibility of B.1.1.7 and B.1.351 variants to additional SARS-CoV-2 RBD-directed monoclonal antibodies.

a, Neutralization of B.1.1.7, B.1.351 and wild-type viruses by additional RBD-directed monoclonal antibodies. Data are mean ± s.e.m. of technical triplicates. **b**, Fold increase or decrease in IC₅₀ of neutralizing monoclonal antibodies against B.1.1.7 and B.1.351, as well as mutant pseudoviruses, relative to the wild type. Red, resistance >3-fold; green, sensitization >3-fold.

Extended Data Fig. 6 Neutralization profiles of authorized or investigational therapeutic monoclonal antibodies against live viruses

and pseudoviruses.

a, Wild-type (WA1), B.1.1.7, and B.1.351 live viruses. **b**, Wild-type (D614G), B.1.1.7Δ8 and B.1.351Δ9 pseudoviruses. Data are mean ± s.e.m. of technical triplicates.

Extended Data Fig. 7 Neutralization profiles of plasma samples of 20 patients convalescing from COVID-19 against wild-type, B.1.1.7Δ8, B.1.351Δ9 and single-mutation pseudoviruses.

Data are mean ± s.e.m. of technical triplicates. Neutralization by plasma from healths donor is shown in Extended Data Fig. [2c](#).

Extended Data Fig. 8 Neutralization profiles of sera from vaccinated individuals against wild-type, B.1.1.7Δ8, B.1.351Δ9 and single-mutation pseudoviruses.

We tested 12 sera from individuals who received the Moderna vaccine (V1–V12) and 10 sera from individuals who received the Pfizer vaccine (V13–V22). Data are mean ± s.e.m. of technical triplicates.

Supplementary information

Reporting Summary

Rights and permissions

[Reprints and Permissions](#)

About this article



Check for
updates

Cite this article

Wang, P., Nair, M.S., Liu, L. *et al.* Antibody resistance of SARS-CoV-2 variants B.1.351 and B.1.1.7. *Nature* **593**, 130–135 (2021). <https://doi.org/10.1038/s41586-021-03837-w>

021-03398-2

[Download citation](#)

- Received: 25 January 2021
- Accepted: 25 February 2021
- Published: 08 March 2021
- Issue Date: 06 May 2021
- DOI: <https://doi.org/10.1038/s41586-021-03398-2>

Further reading

- [Severe acute respiratory syndrome coronavirus 2 escape mutants and protective immunity from natural infections or immunizations](#)
 - Antonino Di Caro
 - , Flavia Cunha
 - , Nicola Petrosillo
 - , Nicholas J. Beeching
 - , Oner Ergonul
 - , Eskild Petersen
 - & Marion P.G. Koopmans

Clinical Microbiology and Infection (2021)

- [Effects of SARS-CoV-2 on Cardiovascular System: The Dual Role of Angiotensin-Converting Enzyme 2 \(ACE2\) as the Virus Receptor and Homeostasis Regulator-Review](#)
 - Aneta Aleksova
 - , Giulia Gagno
 - , Gianfranco Sinagra
 - , Antonio Paolo Beltrami
 - , Milijana Janjusevic
 - , Giuseppe Ippolito
 - , Alimuddin Zumla
 - , Alessandra Lucia Fluca
 - & Federico Ferro

International Journal of Molecular Sciences (2021)

- **COVID vaccine efficacy against the B.1.351 (“South African”) variant—The urgent need to lay the groundwork for possible future challenge studies**

- Nir Eyal
- , Arthur Caplan
- & Stanley Plotkin

Human Vaccines & Immunotherapeutics (2021)

- **Involvement of KL-6 Biomarker in Interstitial Lung Disease Induced by SARS-CoV-2 Infection: A Systematic Review**

- Radu Crisan-Dabija
- , Adrian Covic
- , Criscentian Brinza
- , Iolanda Valentina Popa
- & Alexandru Burlacu

Applied Sciences (2021)

- **SARS-CoV-2 and other viruses in soil: an environmental outlook**

- Uttpal Anand
- , Francesco Bianco
- , S. Suresh
- , Vijay Tripathi
- , Avelino Núñez-Delgado
- & Marco Race

Environmental Research (2021)

Comments

By submitting a comment you agree to abide by our [Terms](#) and [Community Guidelines](#). If you find something abusive or that does not comply with our terms or guidelines please flag it as inappropriate.

[Download PDF](#)

This article was downloaded by **calibre** from <https://www.nature.com/articles/s41586-021-03398-2>

| [Section menu](#) | [Main menu](#) |

Sensitivity of SARS-CoV-2 B.1.1.7 to mRNA vaccine-elicited antibodies
[Download PDF](#)

- Article
- [Published: 11 March 2021](#)

Sensitivity of SARS-CoV-2 B.1.1.7 to mRNA vaccine-elicited antibodies

- [Dami A. Collier](#) ORCID: [orcid.org/0000-0001-5446-4423^{1,2,3 na1}](https://orcid.org/0000-0001-5446-4423),
- [Anna De Marco^{4 na1}](#),
- [Isabella A. T. M. Ferreira^{1,2 na1}](#),
- [Bo Meng^{1,2 na1}](#),
- [Rawlings P. Dahir](#) ORCID: [orcid.org/0000-0003-0521-2144^{1,2,3 na1}](https://orcid.org/0000-0003-0521-2144),
- [Alexandra C. Walls⁵](#),
- [Steven A. Kemp^{1,2,3}](#),
- [Jessica Bassi⁴](#),
- [Dora Pinto⁴](#),
- [Chiara Silacci-Fregni⁴](#),
- [Siro Bianchi](#) ORCID: [orcid.org/0000-0002-5100-8905⁴](https://orcid.org/0000-0002-5100-8905),
- [M. Alejandra Tortorici](#) ORCID: [orcid.org/0000-0002-2260-2577⁵](https://orcid.org/0000-0002-2260-2577),
- [John Bowen⁵](#),
- [Katja Culap](#) ORCID: [orcid.org/0000-0002-0956-0018⁴](https://orcid.org/0000-0002-0956-0018),
- [Stefano Jaconi⁴](#),
- [Elisabetta Cameroni⁴](#),
- [Gyorgy Snell⁶](#),
- [Matteo S. Pizzuto⁴](#),
- [Alessandra Franzetti Pellanda⁷](#),
- [Christian Garzoni⁷](#),
- [Agostino Riva](#) ORCID: [orcid.org/0000-0003-3171-3049⁸](https://orcid.org/0000-0003-3171-3049),
- [The CITIID-NIHR BioResource COVID-19 Collaboration](#),
- [Anne Elmer⁹](#),
- [Nathalie Kingston¹⁰](#),
- [Barbara Graves¹⁰](#),
- [Laura E. McCoy](#) ORCID: [orcid.org/0000-0001-9503-7946³](https://orcid.org/0000-0001-9503-7946),
- [Kenneth G. C. Smith](#) ORCID: [orcid.org/0000-0003-3829-4326^{1,2}](https://orcid.org/0000-0003-3829-4326),

- [John R. Bradley](#)^{2,10},
- [Nigel Temperton](#)¹¹,
- [Lourdes Ceron-Gutierrez](#)¹²,
- [Gabriela Barcenas-Morales](#)^{12,13},
- [The COVID-19 Genomics UK \(COG-UK\) Consortium](#),
- [William Harvey](#)¹⁴,
- [Herbert W. Virgin](#) ORCID: orcid.org/0000-0001-8580-7628⁶,
- [Antonio Lanzavecchia](#) ORCID: orcid.org/0000-0002-3041-7240⁴,
- [Luca Piccoli](#) ORCID: orcid.org/0000-0002-1085-6502⁴,
- [Rainer Doffinger](#) ORCID: orcid.org/0000-0002-9841-3617^{12,15},
- [Mark Wills](#)²,
- [David Veesler](#) ORCID: orcid.org/0000-0002-6019-8675⁵,
- [Davide Corti](#) ORCID: orcid.org/0000-0002-5797-1364^{4 na2} &
- [Ravindra K. Gupta](#) ORCID: orcid.org/0000-0001-9751-1808^{1,2,15,16,17,18 na2}

[Nature](#) volume **593**, pages 136–141 (2021) [Cite this article](#)

- 60k Accesses
- 11 Citations
- 537 Altmetric
- [Metrics details](#)

Subjects

- [SARS-CoV-2](#)
- [Vaccines](#)
- [Virology](#)

Abstract

Transmission of SARS-CoV-2 is uncontrolled in many parts of the world; control is compounded in some areas by the higher transmission potential of the B.1.1.7 variant¹, which has now been reported in 94 countries. It is unclear whether the response of the virus to vaccines against SARS-CoV-2 on the basis of the prototypic strain will be affected by the mutations found in B.1.1.7. Here we assess the immune responses of individuals after vaccination with the mRNA-based vaccine BNT162b2². We measured neutralizing antibody responses after the first and second immunizations using pseudoviruses that expressed the wild-type spike protein or a mutated spike

protein that contained the eight amino acid changes found in the B.1.1.7 variant. The sera from individuals who received the vaccine exhibited a broad range of neutralizing titres against the wild-type pseudoviruses that were modestly reduced against the B.1.1.7 variant. This reduction was also evident in sera from some patients who had recovered from COVID-19. Decreased neutralization of the B.1.1.7 variant was also observed for monoclonal antibodies that target the N-terminal domain (9 out of 10) and the receptor-binding motif (5 out of 31), but not for monoclonal antibodies that recognize the receptor-binding domain that bind outside the receptor-binding motif. Introduction of the mutation that encodes the E484K substitution in the B.1.1.7 background to reflect a newly emerged variant of concern (VOC 202102/02) led to a more-substantial loss of neutralizing activity by vaccine-elicited antibodies and monoclonal antibodies (19 out of 31) compared with the loss of neutralizing activity conferred by the mutations in B.1.1.7 alone. The emergence of the E484K substitution in a B.1.1.7 background represents a threat to the efficacy of the BNT162b2 vaccine.

[Download PDF](#)

Main

The BNT162b2 mRNA vaccine encodes the full-length trimerized spike protein of SARS CoV-2² and was designed against the Wuhan-1 isolate. Concerns have been raised as to whether vaccines will be effective against newly emergent SARS-CoV-2 variants, such as B.1.1.7 (N501Y.V1)³. In clinical studies of BNT162b2, the geometric mean titre (GMT) of neutralizing antibodies associated with 50% neutralization increased after the first dose and the vaccine provided high levels of protection against infection and severe disease after the second dose⁴.

Activity of vaccine and convalescent sera against B.1.1.7

Participants ($n = 37$) received the first dose of the BNT162b2 mRNA vaccine 3 weeks before blood was drawn for the collection of serum and peripheral blood mononuclear cells. The median age was 62 years (interquartile range, 47–84 years) and 35% of participants were female. Of these participants, 21 individuals also had a blood draw 3 weeks after receiving the second dose of the BNT162b2 mRNA vaccine. Serum IgG titres against nucleocapsid protein, the spike protein and the receptor-binding domain (RBD) of the spike protein were assayed (Extended Data Fig. 1a).

Using lentiviral pseudotyping, we studied the wild-type (wild-type spike bearing D614G) and mutant B.1.1.7 spike proteins (Fig. 1a) to measure the neutralization activity of vaccine-elicited sera. The vaccine sera exhibited a range of inhibitory dilutions that provided 50% neutralization (ID_{50}) (Fig. 1b,c). The GMT against the

wild-type spike protein after the second dose of vaccine was substantially higher than after the first dose (318 compared with 77) (Fig. [1b,e](#)). There was correlation between total spike IgG titres and serum neutralization titres (Extended Data Fig. [1b](#)). A broad range of T cell responses was measured by IFN γ FluoroSpot against SARS-CoV-2 peptides in samples from individuals who received the vaccine after the first dose. These cellular responses did not correlate with serum neutralization titres or IgG spike antibody titres (Extended Data Fig. [1c,d](#)).

Fig. 1: Neutralization by sera from the first and second dose of the BNT162b2 mRNA vaccine against wild-type and B.1.1.7 spike mutant SARS-CoV-2-pseudotyped viruses.

 [figure1](#)

a, Spike in the open conformation with a single erect RBD (Protein Data Bank (PDB): 6ZGG) is shown in the vertical view of the trimer axis. The locations of mutated residues are shown as red spheres, with deletions indicated in a dashed outline, and are labelled on the monomer with an erect RBD. **b–g**, The 50% serum neutralization titres of the first dose of the vaccine (**b, c**, $n = 37$), the second dose of the vaccine (**d, e**, $n = 21$) and convalescent sera (**f, g**, $n = 27$) against the wild-type (WT) spike protein and the spike protein of the variant B.1.1.7 (containing the N501Y, A570D, Δ H69/ Δ V70, Δ Y144, P681H, T716I, S982A and D1118H mutations). HS, human serum control. **b, d, f**, Mean fold changes in ID_{50} are indicated above the graphs. Data points of the same individual are connected by lines. Data are GMT \pm s.d. and individual values of two independent experiments each with two technical repeats. Two-tailed Wilcoxon

matched-pairs signed-rank test with no adjustment for multiple comparisons; ** $P < 0.01$, **** $P < 0.0001$. The cut-off for 50% neutralization was set to 4.

[Full size image](#)

We then generated mutated pseudoviruses carrying the spike protein with the N501Y and A570D substitutions and the H69/V70 deletion (Δ H69/ Δ V70). We observed a small increase in the ability of sera from individuals who were vaccinated or had recovered from COVID-19 to inhibit this triple-mutant virus (Extended Data Fig. 2a–c). We next included the full set of eight mutations in the spike protein that is present in the B.1.1.7 variant (Fig. 1a). Of the 29 sera with neutralization activity after the first dose, 20 showed evidence of a reduction in neutralization titres against the B.1.1.7 variant (Fig. 1b,c and Extended Data Fig. 3), with a fold change of 3.2 ± 5.7 (mean \pm s.d.). After the second dose, the GMT was markedly increased compared with the first-dose titres, with a fold change of 1.9 ± 0.9 (mean \pm s.d.) (Fig. 1d,e). Among sera from 27 individuals who had recovered from COVID-19, the GMT at 50% neutralization was 1,334 for the wild-type spike protein, which is significantly higher than the GMT after the second dose of the vaccine (Fig. 1f,g). The fold change in ID₅₀ for neutralization of the B.1.1.7 compared with wild-type (D614G) spike protein was 4.5 ± 8.7 (Fig. 1f,g and Extended Data Fig. 4).

The E484K substitution (Fig. 2a) has been reported as an escape mutation for several monoclonal antibodies⁵, and is present in the B.1.351 (501Y.V2) and P.1 (501Y.V3) lineages. As of 11 February 2021, 30 B.1.1.7 sequences also had the E484K substitution (Fig. 2c). Phylogenetic analysis suggests that there have been multiple independent acquisitions, with one lineage appearing to expand over time, indicating active transmission (Fig. 2b). This has resulted in Public Health England naming this a variant of concern (VOC 202102/02)⁶. We therefore generated pseudoviruses that carried the B.1.1.7 spike mutations with or without the additional E484K substitution and tested these against sera obtained after the first and second dose of the BNT162b2 mRNA vaccine as well as against convalescent sera. After the second vaccine dose, we observed a considerable loss of neutralizing activity for the pseudovirus with the B.1.1.7 spike mutations and E484K (Fig. 3d,e). The mean fold change for the E484K-containing B.1.1.7 spike variant was 6.7 compared with 1.9 for the B.1.1.7 variant, relative to the wild-type spike protein (Fig. 3a–c and Extended Data Fig. 5). Similarly, when we tested a panel of convalescent sera with a range of neutralization titres (Fig. 1f,g and Extended Data Fig. 5), we observed additional loss of activity against the mutant B.1.1.7 spike with E484K, with fold change of 11.4 relative to the wild-type spike protein (Fig. 3f,g and Extended Data Fig. 5).

Fig. 2: The E484K substitution was found in the background of B.1.1.7 and showed evidence of transmission.

 **figure2**

a, Representation of the spike RBM:ACE2 interface (PDB: 6M0J) with residues E484, N501 and K417 highlighted as spheres coloured by element. **b**, Maximum likelihood phylogeny of a subset of sequences from the UK with the E484K mutation (blue) and the B.1.1.7 lineage (green), with background sequences from the UK without RBD mutations shown in black. As of 11 February 2021, 30 sequences from the B.1.1.7 lineage (one cluster of 25 at the top of the phylogenetic tree) have acquired the E484K

substitution (red). **c**, Sequence accumulation over time in GISAID for UK sequences of the B.1.1.7 and other variants with or without E484K.

[Full size image](#)

Fig. 3: Neutralization potency of mRNA vaccine sera and convalescent sera (before SARS-CoV-2 B.1.1.7) against a pseudotyped virus with the spike mutations of the B1.1.7 lineage with or without E484K.

 figure3

All virus variants were in a spike(D614G) background. **a**, Example neutralization curves of vaccinated individuals (ID 5, 7, 18, 28). The inverse dilution is shown on a log scale. Data are mean \pm s.e.m. representative of two independent experiments each with two technical replicates. **b–g**, The 50% neutralization titres of each virus against sera derived after the first vaccine dose (**b**, **c**, $n = 37$), the second vaccine dose (**d**, **e**, $n = 21$) and for convalescent sera (**f**, **g**, $n = 20$) expressed as fold change relative to the wild-type virus. **b**, **d**, **f**, Mean fold changes in ID₅₀ are indicated above the graphs.

Data are mean \pm s.d. and individual values; error bars for negative values are not shown. **c**, **e**, **g**, Data are the mean fold change of two technical replicates and are representative of two independent experiments. Data points of the same individual are connected by lines. **b**, **d**, **f**, Two-tailed paired Student's *t*-test; **P* < 0.05, ***P* < 0.01, ****P* < 0.0001; NS, not significant. The cut-off for 50% neutralization was set to 4.

[Full size image](#)

Monoclonal antibody activity against B.1.1.7

We tested 60 monoclonal antibodies isolated from 15 individuals who had recovered from SARS-CoV-2 infection in early 2020 with an in vitro pseudotyped neutralization assay against the B.1.1.7 spike protein (Supplementary Table 1). Out of 60 monoclonal antibodies, 20 (33.3%) showed a greater than twofold loss of neutralizing activity against the B.1.1.7 variant compared to wild-type SARS-CoV-2 (Fig. 4a, b and Extended Data Fig. 6). The B.1.1.7 mutant virus fully escaped neutralization by 8 out of 10 monoclonal antibodies (80%) that target the N-terminal domain (NTD) (Fig. 4c). Of the 31 monoclonal antibodies that target the receptor-binding motif (RBM), 5 (16.1%) showed more than 100-fold decrease in B.1.1.7 neutralization, and additional 6 monoclonal antibodies (19.4%) had a partial 2–10-fold reduction (Fig. 4d). Finally, all RBD-specific non-RBM-targeting monoclonal antibodies that were tested fully retained neutralizing activity against B.1.1.7 (Fig. 4e).

Fig. 4: Neutralization and binding by a panel of NTD- and RBD-specific monoclonal antibodies against wild-type, B.1.1.7 and RBD-mutant SARS-CoV-2 viruses.

 **figure4**

a, Neutralization of pseudotyped SARS-CoV-2–murine leukemia virus (MLV) carrying wild-type spike (spike(D614G)) (grey), spike from B.1.1.7 (blue) or a triple-mutant spike protein (TM, carrying RBD mutations K417N, E484K and N501Y) (red) by three selected monoclonal antibodies (S2E12, S2X333 and S2H14) from one representative experiment. Data are mean \pm s.d. of two technical replicates. **b**, Neutralization of SARS-CoV-2–MLVs carrying wild-type spike (spike(D614G)), spike from B.1.1.7 or a triple-mutant spike protein (spike(N501Y, E484K, K417N)) by 60 monoclonal antibodies targeting the NTD ($n = 10$), RBM ($n = 31$) or non-RBM sites in the RBD ($n = 19$). Data are the mean 50% inhibitory concentration (IC_{50}) values (ng ml $^{-1}$) of $n = 2$ independent experiments. **c–e**, Neutralization by NTD-specific (**c**), RBM-specific (**d**) and non-RBM-specific (**e**) monoclonal antibodies is shown as the mean IC_{50} values (top) and mean fold change in B.1.1.7 (blue) or the triple mutant

(spike(N501Y, E484K, K417N)) (red) relative to the wild-type virus (bottom). The orange line shows the threshold for non-neutralizing titres. Top, data are mean \pm s.d. IC₅₀ values from two independent experiments. Bottom, data are mean \pm s.d. fold change from two independent experiments. **f–h**, The kinetics of the binding of monoclonal antibodies to wild-type (black), N501Y (blue) and E484K (red) RBD as measured by biolayer interferometry. **f**, The four RBM-targeting monoclonal antibodies with no reduced binding to the RBD with N501Y or E484K are shown. **g**, **h**, Area under the curve (AUC) (**g**) and the fold change in the area under the curve (**h**) of 50 monoclonal antibodies tested against the wild-type, N501Y and E484K RBD. Monoclonal antibodies with a more than 1.3-fold (cut-off indicated by the orange line) change in area under the curve are shown in blue and red; orange dots show non-RBM-specific monoclonal antibodies.

[Full size image](#)

To address the role of the N501Y substitution in B.1.1.7 in the neutralization escape from RBM-specific antibodies, we tested the binding of 50 RBD-specific monoclonal antibodies to the wild-type and N501Y-mutant RBD by biolayer interferometry (Fig. [4f](#) and Extended Data Fig. [7](#)). The 5 RBM-specific monoclonal antibodies that did not neutralize the B.1.1.7 variant (Fig. [4d](#)) showed a complete loss of binding to the N501Y-mutant RBD (Fig. [4g,h](#)), demonstrating a role for this mutation as an escape mechanism for certain RBM-targeting monoclonal antibodies.

To assess the effect of E484K on this panel of monoclonal antibodies, we generated a triple-mutant SARS-CoV-2 pseudotype virus carrying the K417N, E484K and N501Y mutations (spike(N501Y, E484K, K417N)). The inclusion of the K417N substitution was prompted by the observation that substitutions at this position have been found in five sequences from recent viral isolates within the B.1.1.7 lineage (K417 to Asn, Glu or Arg). This is in keeping with the convergent evolution of the virus to an RBD containing N501Y, E484K and K417N or K417T as evidenced by the B.1.351 and P.1 lineages. Notably, mutations at K417 are reported to escape neutralization by monoclonal antibodies, including the recently approved monoclonal antibody LY-CoV016^{[5,7](#)}. Out of the 60 monoclonal antibodies tested, 20 (33.3%) showed a loss of neutralizing activity against the spike(N501Y, E484K, K417N) mutant of more than 10-fold compared to wild-type SARS-CoV-2 (Fig. [4a,b](#) and Extended Data Fig. [6](#)), and of these 19 are RBM-specific monoclonal antibodies. As above, we addressed the role of the E484K substitution in the escape from RBM-specific antibodies by testing the binding of 50 RBD-specific monoclonal antibodies to the RBD of the wild-type and E484K-mutant spike protein by biolayer interferometry (Fig. [4f](#) and Extended Data Fig. [8](#)). Out of the 19 RBM-specific monoclonal antibodies that showed reduced or loss of neutralization of the spike(N501Y, E484K, K417N) mutant (Fig. [4d](#)), 16 showed a complete or partial loss of binding to the RBD of the E484K mutant (Fig.

[4g, h](#)), which is consistent with findings that E484K is an important mutation for viral escape^{[8,9,10](#)}. In addition, 3 of these 16 monoclonal antibodies also lost the ability to bind to an RBD containing the N501Y substitution, indicating that a fraction of RBM-specific antibodies are sensitive to both the N501Y and E484K substitutions.

Similarly, 3 of the 19 monoclonal antibodies that lost neutralization against the spike(N501Y, E484K, K417N) mutant (S2D8, S2H7 and S2X128) were previously shown to lose binding and neutralization to the K417V mutant, and are here shown to be sensitive to either the N501Y or the E484K substitution.

Binding of the RBD of the B.1.1.7 variant to ACE2

Using biolayer interferometry, we found that human ACE2 bound to the RBD of the B.1.1.7 variant with an affinity of 22 nM compared to an affinity of 133 nM for the wild-type RBD (Extended Data Fig. [9](#)), in agreement with our previous deep-mutational scanning measurements using dimeric ACE2^{[11](#)}. Although ACE2 bound with comparable on rates to both RBDs, the observed dissociation rate constant was slower for B.1.1.7 than for the wild-type RBD (Extended Data Table [1](#)). These findings could explain the efficient ongoing transmission of this newly emergent SARS-CoV-2 lineage and the possibly reduced opportunity for antibody binding. To understand the effect of the mutations in the triple mutant (K417N, E484K and N501Y), we evaluated the binding of ACE2 to the immobilized RBD of spike(N501Y, E484K, K417N). We determined an ACE2-binding affinity of 64 nM for the RBD of spike(N501Y, E484K, K417N), driven by a faster off rate than observed for the RBD of the B.1.1.7 variant but slower than for the wild-type RBD. We propose that the K417N mutation is slightly detrimental to ACE2 binding, which explains the intermediate affinity determined for the RBD of spike(N501Y, E484K, K417N) compared to the B.1.1.7 and wild-type RBDs, probably as a result of disrupting the salt bridge formed with ACE2 residue D30.

Discussion

Serum neutralizing activity is a correlate of protection for other respiratory viruses, including influenza^{[12](#)} and respiratory syncytial virus, for which prophylaxis with monoclonal antibodies has been used in at-risk groups^{[13,14](#)}. Neutralizing antibody titres seemed to be highly correlated with vaccine protection against SARS-CoV-2 rechallenge in nonhuman primates^{[15,16](#)}.

This study reports on neutralization by sera collected after both the first and second doses of the BNT162b2 vaccine. The participants of this study were older adults, in line with the targeting of this age group in the initial rollout of the vaccination campaign in the UK. We demonstrate that neutralization of a pseudovirus containing

the spike protein with the full set of mutations that is present in the B.1.1.7 variant showed a small reduction using sera from individuals who received the BNT162b2 vaccine that was more marked after the first dose than the second dose. This could be related to the increased breadth, potency and/or concentration of antibodies after the boost dose. Other studies have reported a small reduction in neutralization against the B.1.1.7 variant in individuals vaccinated with two doses of BNT162b2¹⁷ and mRNA-1273¹⁸. The reduced neutralizing activity observed with polyclonal antibodies elicited by mRNA vaccines observed in this study is further supported by the loss of neutralizing activity observed with human monoclonal antibodies directed against both the RBD and, to a major extent, the NTD.

Multiple variants, including the 501Y.V2 and B.1.1.7 lineages, have multiple mutations as well as deletions in the NTD, most of which are located in a site of vulnerability that is targeted by all known NTD-specific neutralizing antibodies^{19,20}. The role of NTD-specific neutralizing antibodies might be underestimated, in part by the use of neutralization assays based on target cells that overexpress ACE2 receptors. NTD-specific monoclonal antibodies were suggested to interfere with viral entry based on other accessory receptors, such as DC-SIGN and L-SIGN²¹, and their neutralization potency was found to be dependent on different in vitro culture conditions¹⁹. The observation that 9 out of 10 NTD-specific neutralizing antibodies did not show a complete or near-complete loss of neutralizing activity against B.1.1.7 indicates that this new variant may have also evolved to escape from this class of antibodies, which may have a yet unrecognized role in protective immunity. Taken together, the presence of multiple escape mutations in the NTD is supportive of the hypothesis that this region of the spike, in addition to the RBM, is also under immune pressure.

Worryingly, we have shown that there are multiple B.1.1.7 sequences in the UK that contain the E484K substitution with early evidence of transmission as well as independent acquisitions. We measured a further reduction in neutralization titres by vaccine sera when E484K was present alongside the B.1.1.7 spike mutations. A recent study¹⁸ has also shown that variants carrying the E484K substitution resulted in a 3–6-fold reduction in neutralization by sera from individuals who received the mRNA-1273 vaccine. Consistently, in this study we found that approximately 50% of the RBM-specific monoclonal antibodies tested lost neutralizing activity against SARS-CoV-2 carrying E484K. E484K has been shown to affect neutralization by monoclonal antibodies or convalescent sera, especially in combination with N501Y and K417N^{8,22,23,24}.

Vaccines are a key part of a long-term strategy to bring SARS-CoV-2 transmission under control. Our data suggest that vaccine escape by the virus of current spike-directed vaccines designed against the Wuhan-1 strain will be inevitable, particularly given that E484K is emerging independently and recurrently on a B.1.1.7 (501Y.V1)

background, and given the rapid global spread of B.1.1.7. Other major variants with E484K such as 501Y.V2 and V3 are also spreading regionally. This should be mitigated by designing next-generation vaccines with mutated spike sequences and using alternative viral antigens.

Methods

Data reporting

No statistical methods were used to predetermine sample size. The experiments were not randomized and the investigators were not blinded to allocation during experiments and outcome assessment.

Participant recruitment and ethics

Participants who had received the first dose of the BNT162b2 vaccine and individuals with COVID-19 were consented into the COVID-19 cohort of the NIHR Bioresource. The study was approved by the East of England–Cambridge Central Research Ethics Committee (17/EE/0025).

SARS-CoV-2 serology by multiplex particle-based flow cytometry

Recombinant SARS-CoV-2 nucleocapsid, spike and RBD proteins were covalently coupled to distinct carboxylated bead sets (Luminex) to form a triplex and were analysed as previously described²⁵. Specific binding was reported as the mean fluorescence intensity.

Generation of spike mutants

Amino acid substitutions were introduced into the D614G pCDNA_SARS-CoV-2_S plasmid as previously described²⁶ using the QuikChange Lightening Site-Directed Mutagenesis kit, following the manufacturer's instructions (Agilent Technologies). Sequences were checked by Sanger sequencing.

The plasmid encoding the B.1.1.7 or triple-mutant (spike(N501Y, E484K, K417N)) SARS-CoV-2 spike glycoprotein was used to produce SARS-CoV-2-MLVs based on overlap extension PCR as follows. In brief, a modification of the overlap extension PCR protocol²⁷ was used to introduce the eight mutations of the B.1.1.7 lineage or the three mutations of the triple mutant (spike(N501Y, E484K, K417N)) in the SARS-CoV-2 spike gene. In a first step, nine DNA fragments with overlapping sequences were amplified by PCR from a plasmid (phCMV1, Genlantis) encoding the full-length

SARS-CoV-2 spike gene (BetaCoV/Wuhan-Hu-1/2019; accession number, mn908947). The mutations (Δ H69/ Δ V70, Δ 144, N501Y, A570D, D614G, P681H, S982A, T716I and D1118H or K417N, E484K and N501Y) were introduced by amplification with primers with a similar melting temperature. Deletion of the C-terminal 21 amino acids was introduced to increase surface expression of the recombinant spike protein²⁸. Next, three contiguous overlapping fragments were fused by a first overlap PCR using the most external primers of each set, resulting in three larger fragments with overlapping sequences. A final overlap PCR was performed on the three large fragments using the most external primers to amplify the full-length spike gene and the flanking sequences including the restriction sites KpnI and NotI. This fragment was digested and cloned into the expression plasmid phCMV1. For all PCR reactions the Q5 Hot Start High Fidelity DNA polymerase (New England Biolabs) was used according to the manufacturer's instructions and adapting the elongation time to the size of the amplicon. After each PCR step, the amplified regions were separated on an agarose gel and purified using an Illustra GFX PCR DNA and Gel Band Purification Kit (Merck).

Pseudotype virus preparation

Viral vectors were prepared by transfection of HEK293T cells using the Fugene HD transfection reagent (Promega). HEK293T cells were transfected with a mixture of 11 μ l of Fugene HD, 1 μ g of pCDNAD19spike-HA, 1 μ g of p8.91 HIV-1 Gag-Pol expression vector^{29,30} and 1.5 μ g of pCSFLW (expressing the firefly luciferase reporter gene with the HIV-1 packaging signal)³¹. Viral supernatants were collected at 48 h and 72 h after transfection, filtered through a 0.45- μ m filter and stored at -80°C . The 50% tissue culture infectious dose of the SARS-CoV-2 pseudovirus was determined using the Steady-Glo Luciferase assay system (Promega).

Serum and plasma pseudotype neutralization assay

Spike pseudotype assays have been shown to have similar characteristics to neutralization tests using fully infectious wild-type SARS-CoV-2³². Virus neutralization assays were performed on HEK293T cells that were transiently transfected with ACE2 and TMPRSS2 using a SARS-CoV-2 spike pseudotyped virus that expressed luciferase³³. Pseudotyped virus was incubated with a serial dilution of heat-inactivated human serum samples or sera from individuals who were vaccinated in duplicate for 1 h at 37°C . Virus-only and cell-only controls were also included. Then, freshly trypsinized HEK293T ACE2- and TMPRSS2-expressing cells were added to each well. After incubation for 48 h in a 5% CO_2 environment at 37°C , luminescence was measured using the Steady-Glo or Bright-Glo Luciferase assay system (Promega). Neutralization was calculated relative to virus-only controls.

Dilution curves are shown as the mean \pm s.e.m. neutralization. ID₅₀ values were calculated in GraphPad Prism. The ID₅₀ values within groups were summarized as the GMT and statistical comparisons between groups were made with Wilcoxon ranked-sign tests. In addition, the effects of the mutations on the neutralizing effect of the sera were expressed as fold change in ID₅₀ of the wild-type compared to mutant pseudotyped virus. Statistical difference in the mean fold change between groups was determined using a two-tailed Student's *t*-test.

IFN γ FluoroSpot assays

Frozen peripheral blood mononuclear cells (PBMCs) were rapidly thawed, and the freezing medium was diluted into 10 ml of TexMACS medium (Miltenyi Biotech), centrifuged and resuspended in 10 ml of fresh medium with 10 U ml⁻¹ DNase (Benzonase, Merck-Millipore via Sigma-Aldrich), PBMCs were incubated at 37 °C for 1 h, followed by centrifugation and resuspension in fresh medium supplemented with 5% human serum (Sigma-Aldrich) before being counted. PBMCs were stained with 2 μ l of each antibody: anti-CD3–fluorescein isothiocyanate (FITC), clone UCHT1; anti-CD4–phycoerythrin (PE), clone RPA-T4; anti-CD8a–peridinin-chlorophyll protein-cyanine 5.5 (PerCP-Cy5.5), clone RPA-8a (all BioLegend, London, UK), LIVE/DEAD Fixable Far Red Dead Cell Stain Kit (Thermo Fisher Scientific). PBMC phenotyping was performed on the BD Accuri C6 flow cytometer. Data were analysed with FlowJo v.10 (Becton Dickinson). In brief, 1.5–2.5 \times 10⁵ PBMCs were incubated in precoated Fluorospot plates (Human IFN γ FLUOROSPOT (Mabtech)) in triplicate with peptide mixes specific to spike, nucleocapsid and membrane proteins of SARS-CoV-2 (final peptide concentration 1 μ g ml⁻¹ per peptide, Miltenyi Biotech) and an unstimulated and positive control mix (containing anti-CD3 (Mabtech), *Staphylococcus* Enterotoxin B, phytohaemagglutinin (all Sigma-Aldrich)) at 37 °C in a humidified CO₂ atmosphere for 48 h. The cells and medium were decanted from the plate and the assay was developed following the manufacturer's instructions. Developed plates were read using an AID iSpot reader (Oxford Biosystems) and counted using AID EliSpot v.7 software (Autoimmun Diagnostika). All data were then corrected for background cytokine production and expressed as spot-forming units per million PBMCs or CD3⁺ T cells.

Antibody discovery and recombinant expression

Human monoclonal antibodies were isolated from plasma cells or memory B cells of donors who are immune to SARS-CoV or SARS-CoV-2 as previously described^{34,35,36,37}. Recombinant antibodies were expressed in ExpiCHO cells at 37 °C and 8% CO₂. Cells were transfected using ExpiFectamine. Transfected cells were supplemented 1 day after transfection with ExpiCHO Feed and ExpiFectamine CHO

Enhancer. The cell culture supernatant was collected 8 days after transfection and filtered through a 0.2- μ m filter. Recombinant antibodies were affinity purified on an ÄKTA xpress FPLC device using 5-ml HiTrap MabSelect PrismA columns followed by buffer exchange to histidine buffer (20 mM histidine, 8% sucrose, pH 6) using HiPrep 26/10 desalting columns.

Pseudovirus neutralization assay using monoclonal antibodies

MLV-based SARS-CoV-2 S-glycoprotein-pseudotyped viruses were prepared as previously described³⁵. HEK293T/17 cells were cotransfected with a plasmid encoding the wild-type, B.1.1.7 or triple-mutant (spike(N501Y, E484K, K417N)) SARS-CoV-2 spike glycoprotein, an MLV Gag-Pol packaging construct and the MLV transfer vector encoding a luciferase reporter using X-tremeGENE HP transfection reagent (Roche) according to the manufacturer's instructions. Cells were cultured for 72 h at 37 °C with 5% CO₂ before collection of the supernatant. VeroE6 cells stably expressing human TMPRSS2 were cultured in Dulbecco's modified Eagle's medium (DMEM) containing 10% fetal bovine serum, 1% penicillin–streptomycin (100 IU ml⁻¹ penicillin, 100 μ g ml⁻¹), 8 μ g ml⁻¹ puromycin and plated into 96-well plates for 16–24 h. Pseudovirus with a serial dilution of monoclonal antibodies was incubated for 1 h at 37 °C and then added to the wells after washing twice with DMEM. After 2–3 h, DMEM containing 20% fetal bovine serum and 2% penicillin–streptomycin was added to the cells. After 48–72 h of infection, Bio-Glo (Promega) was added to the cells and incubated in the dark for 15 min before the luminescence was read using a Synergy H1 microplate reader (BioTek). Measurements were done in duplicate and relative luciferase units were converted to the percentage of neutralization and plotted with a nonlinear regression model to determine the IC₅₀ values using GraphPad Prism software (v.9.0.0).

Antibody binding measurements using biolayer interferometry

Monoclonal antibodies (Supplementary Table 1) were diluted to 3 μ g ml⁻¹ in kinetic buffer (PBS supplemented with 0.01% BSA) and immobilized on Protein A Biosensors (FortéBio). Antibody-coated biosensors were incubated for 3 min with a solution containing 5 μ g ml⁻¹ of wild-type, N501Y or E484K SARS-CoV-2 RBD in kinetic buffer, followed by a 3-min dissociation step. Changes in the molecules bound to the biosensors caused a shift in the interference pattern that was recorded in real time using an Octet RED96 system (FortéBio). The binding response over time was used to calculate the area under the curve using GraphPad Prism software (v.9.0.0).

Production of SARS-CoV-2 and B.1.1.7 RBDs and human ACE2

The SARS-CoV-2 RBD (BEI NR-52422) construct was synthesized by GenScript into CMVR with an N-terminal mu-phosphatase signal peptide, a C-terminal octa-histidine tag (GHHHHHHHH) and an avi tag. The boundaries of the construct are $_{328}\text{RFPN}_{331}$ (N terminus) and $_{528}\text{KKST}_{531}$ (C terminus)³⁸. The B.1.1.7 RBD gene was synthesized by GenScript into pCMVR with the same boundaries and construct details with a mutation at N501Y. These plasmids were transiently transfected into Expi293F cells using Expi293F expression medium (Life Technologies) at 37 °C 8% CO₂ while rotating at 150 rpm. The cultures were transfected using PEI cultivated for 5 days. Supernatants were clarified by centrifugation (10 min at 4,000g) before loading onto a nickel-NTA column (GE Healthcare). Purified protein was biotinylated overnight using BirA (Biotin ligase) before size-exclusion chromatography into PBS. Human ACE2–Fc (residues 1–615 with a C-terminal thrombin cleavage site and human Fc tag) was synthesized by Twist. Clarified supernatants were affinity-purified using a Protein A column (GE Life Sciences) that was directly neutralized and buffer exchanged. The Fc tag was removed by thrombin cleavage in a reaction mixture containing 3 mg of recombinant ACE2–Fc ectodomain and 10 µg of thrombin in 20 mM Tris-HCl pH 8.0, 150 mM NaCl and 2.5 mM CaCl₂. The reaction mixture was incubated at 25 °C overnight and reloaded on a Protein A column to remove uncleaved protein and the Fc tag. The cleaved protein was further purified by gel filtration using a Superdex 200 column 10/300 GL (GE Life Sciences) equilibrated in PBS.

Protein affinity measurements using biolayer interferometry

Biotinylated RBDs (from wild-type spike, spike(N501Y) or spike(N501Y, E484K, K417N)) were immobilized at 5 ng µl in undiluted 10× Kinetics Buffer (Pall) to SA sensors until a load level of 1.1 nm. A dilution series of either monomeric ACE2 or Fab in undiluted kinetics buffer starting at 1,000 to 50 nM was used for 300–600 s to determine protein–protein affinity. The data were baseline subtracted and the plots fitted using the Pall FortéBio/Sartorius analysis software (v.12.0). Data were plotted in Graphpad Prism (v.9.0.2).

Phylogenetic analysis

All complete and low-coverage-excluded SARS-CoV-2 sequences were downloaded from the GISAID database (<http://gisaid.org/>)³⁹ on 11 February 2021. All sequences were realigned to the SARS-CoV-2 reference strain MN908947.3, using MAFFT v.7.475 with automatic flavour selection and the --keeplength --addfragments options⁴⁰. Sequences were then deduplicated. Major SARS-CoV-2 clade memberships were assigned to all sequences using the Nextclade server v.0.12 (<https://clades.nextstrain.org/>).

Maximum likelihood phylogenetic trees were produced using the above curated dataset using IQ-TREE v.2.1.2⁴¹. Evolutionary model selection for trees was inferred using ModelFinder¹⁰ and trees were estimated using the GTR + F + I model with 1,000 ultrafast bootstrap replicates⁴². All trees were visualized with Figtree v.1.4.4 (<http://tree.bio.ed.ac.uk/software/figtree/>) and manipulated and coloured with ggtree v.2.2.4. Phylogenies were rooted on the SARS-CoV-2 reference sequence (MN908947.3) and nodes arranged in descending order.

Statistical analysis

Linear regression was used to explore the association between the antibody response, T cell response and serum neutralization in Stata 13. The Pearson correlation coefficient was reported.

Neutralization data analysis

Neutralization was calculated relative to virus-only controls. Dilution curves were presented as a mean ± s.e.m. neutralization. IC₅₀ values were calculated in GraphPad Prism. The ID₅₀ values within groups were summarized as a GMT and statistical comparisons between groups were made using Wilcoxon ranked-sign tests. In addition, the effects of the mutations on the neutralizing effect of the sera were expressed as the fold change in ID₅₀ of the wild-type compared to the mutant pseudotyped virus. Statistical difference in the mean fold change between groups was determined using a two-tailed Student's t-test.

IFNγ FluoroSpot assay data analysis

The association between the spike-associated T cell response, spike-specific antibody response and serum neutralization was determined using linear regression. The Pearson correlation coefficients between these variables were determined using Stata 13.

Reporting summary

Further information on research design is available in the [Nature Research Reporting Summary](#) linked to this paper.

Data availability

The neutralization and biolayer interferometry data shown in Fig. 4 and Extended Data Figs. 6–8 can be found in the Source Data for Fig. 4. All sequences are publicly available and were downloaded from <http://gisaid.org>. Deduplicated and subsampled data are freely available at https://github.com/StevenKemp/sequence_files/blob/main/vaccinepaper/with_background_and_subsampled_deduped_aligned_UKonly_484_vui.fasta.gz. Other data are available from the corresponding authors on request. Source data are provided with this paper.

References

1. 1.

Volz, E. et al. Transmission of SARS-CoV-2 lineage B.1.1.7 in England: insights from linking epidemiological and genetic data. Preprint at <https://doi.org/10.1101/2020.12.30.20249034> (2021).

2. 2.

Mulligan, M. J. et al. Phase I/II study of COVID-19 RNA vaccine BNT162b1 in adults. *Nature* **586**, 589–593 (2020).

[ADS](#) [CAS](#) [Article](#) [Google Scholar](#)

3. 3.

Kemp, S. A. et al. Recurrent emergence and transmission of a SARS-CoV-2 spike deletion H69/V70. Preprint at <https://doi.org/10.1101/2020.12.14.422555> (2021).

4. 4.

Polack, F. P. et al. Safety and efficacy of the BNT162b2 mRNA COVID-19 vaccine. *N. Engl. J. Med.* **383**, 2603–2615 (2020).

[CAS](#) [Article](#) [Google Scholar](#)

5. 5.

Wang, P. et al. Antibody resistance of SARS-CoV-2 variants B.1.351 and B.1.1.7. *Nature* <https://doi.org/10.1038/s41586-021-03398-2> (2021).

6. 6.

Public Health England. *PHE statement on Variant of Concern and new Variant Under Investigation*. <https://www.gov.uk/government/news/phe-statement-on-variant-of-concern-and-new-variant-under-investigation> (2021).

7. 7.

Thomson, E. C. et al. Circulating SARS-CoV-2 spike N439K variants maintain fitness while evading antibody-mediated immunity. *Cell* **184**, 1171–1187 (2021).

[CAS Article](#) [Google Scholar](#)

8. 8.

Greaney, A. J. et al. Comprehensive mapping of mutations in the SARS-CoV-2 receptor-binding domain that affect recognition by polyclonal human plasma antibodies. *Cell Host Microbe* <https://doi.org/10.1016/j.chom.2021.02.003> (2021).

9. 9.

Andreano, E. et al. SARS-CoV-2 escape in vitro from a highly neutralizing COVID-19 convalescent plasma. Preprint at <https://doi.org/10.1101/2020.12.28.424451> (2020).

10. 10.

Kalyaanamoorthy, S., Minh, B. Q., Wong, T. K. F., von Haeseler, A. & Jermiin, L. S. ModelFinder: fast model selection for accurate phylogenetic estimates. *Nat. Methods* **14**, 587–589 (2017).

[CAS Article](#) [Google Scholar](#)

11. 11.

Starr, T. N. et al. Deep mutational scanning of SARS-CoV-2 receptor binding domain reveals constraints on folding and ACE2 binding. *Cell* **182**, 1295–1310 (2020).

[CAS Article](#) [Google Scholar](#)

12. 12.

Verschoor, C. P. et al. Microneutralization assay titres correlate with protection against seasonal influenza H1N1 and H3N2 in children. *PLoS ONE* **10**, e0131531

(2015).

[Article](#) [Google Scholar](#)

13. 13.

Kulkarni, P. S., Hurwitz, J. L., Simões, E. A. F. & Piedra, P. A. Establishing correlates of protection for vaccine development: considerations for the respiratory syncytial virus vaccine field. *Viral Immunol.* **31**, 195–203 (2018).

[CAS Article](#) [Google Scholar](#)

14. 14.

Goddard, N. L., Cooke, M. C., Gupta, R. K. & Nguyen-Van-Tam, J. S. Timing of monoclonal antibody for seasonal RSV prophylaxis in the United Kingdom. *Epidemiol. Infect.* **135**, 159–162 (2007).

[CAS Article](#) [Google Scholar](#)

15. 15.

Mercado, N. B. et al. Single-shot Ad26 vaccine protects against SARS-CoV-2 in rhesus macaques. *Nature* **586**, 583–588 (2020).

[ADS](#) [CAS Article](#) [Google Scholar](#)

16. 16.

McMahan, K. et al. Correlates of protection against SARS-CoV-2 in rhesus macaques. *Nature* **590**, 630–634 (2021).

[ADS](#) [CAS Article](#) [Google Scholar](#)

17. 17.

Muik, A. et al. Neutralization of SARS-CoV-2 lineage B.1.1.7 pseudovirus by BNT162b2 vaccine-elicited human sera. *Science*
<https://doi.org/10.1126/science.abg6105> (2021).

18. 18.

Wu, K. et al. mRNA-1273 vaccine induces neutralizing antibodies against spike mutants from global SARS-CoV-2 variants. Preprint at

<https://doi.org/10.1101/2021.01.25.427948> (2021).

19. 19.

McCallum, M. et al. N-terminal domain antigenic mapping reveals a site of vulnerability for SARS-CoV-2. Preprint at <https://doi.org/10.1101/2021.01.14.426475> (2021).

20. 20.

Suryadevara, N. et al. Neutralizing and protective human monoclonal antibodies recognizing the N-terminal domain of the SARS-CoV-2 spike protein. Preprint at <https://doi.org/10.1101/2021.01.19.427324> (2021).

21. 21.

Soh, W. T. et al. The N-terminal domain of spike glycoprotein mediates SARS-CoV-2 infection by associating with L-SIGN and DC-SIGN. Preprint at <https://doi.org/10.1101/2020.11.05.369264> (2020).

22. 22.

Tegally, H. et al. Detection of a SARS-CoV-2 variant of concern in South Africa. *Nature* <https://doi.org/10.1038/s41586-021-03402-9> (2021).

23. 23.

Greaney, A. J. et al. Complete mapping of mutations to the SARS-CoV-2 spike receptor-binding domain that escape antibody recognition. *Cell Host Microbe* **29**, 44–57 (2020).

[Article](#) [Google Scholar](#)

24. 24.

Weisblum, Y. et al. Escape from neutralizing antibodies by SARS-CoV-2 spike protein variants. *eLife* **9**, e61312 (2020).

[CAS](#) [Article](#) [Google Scholar](#)

25. 25.

Xiong, X. et al. A thermostable, closed SARS-CoV-2 spike protein trimer. *Nat. Struct. Mol. Biol.* **27**, 934–941 (2020).

[CAS](#) [Article](#) [Google Scholar](#)

26. 26.

Gregson, J. et al. Human immunodeficiency virus-1 viral load is elevated in individuals with reverse-transcriptase mutation M184V/I during virological failure of first-line antiretroviral therapy and is associated with compensatory mutation L74I. *J. Infect. Dis.* **222**, 1108–1116 (2019).

[Article](#) [Google Scholar](#)

27. 27.

Forloni, M., Liu, A. Y. & Wajapeyee, N. Creating insertions or deletions using overlap extension polymerase chain reaction (PCR) mutagenesis. *Cold Spring Harb. Protoc.* <https://doi.org/10.1101/pdb.prot097758> (2018).

28. 28.

Case, J. B. et al. Neutralizing antibody and soluble ACE2 inhibition of a replication-competent VSV-SARS-CoV-2 and a clinical isolate of SARS-CoV-2. *Cell Host Microbe* **28**, 475–485 (2020).

[CAS](#) [Article](#) [Google Scholar](#)

29. 29.

Naldini, L., Blömer, U., Gage, F. H., Trono, D. & Verma, I. M. Efficient transfer, integration, and sustained long-term expression of the transgene in adult rat brains injected with a lentiviral vector. *Proc. Natl Acad. Sci. USA* **93**, 11382–11388 (1996).

[ADS](#) [CAS](#) [Article](#) [Google Scholar](#)

30. 30.

Gupta, R. K. et al. Full-length HIV-1 Gag determines protease inhibitor susceptibility within in-vitro assays. *AIDS* **24**, 1651–1655 (2010).

[CAS](#) [Article](#) [Google Scholar](#)

31. 31.

Kemp, S. A. et al. SARS-CoV-2 evolution during treatment of chronic infection. *Nature* <https://doi.org/10.1038/s41586-021-03291-y> (2021).

32. 32.

Schmidt, F. et al. Measuring SARS-CoV-2 neutralizing antibody activity using pseudotyped and chimeric viruses. *J. Exp. Med.* **217**, e20201181 (2020).

[Article](#) [Google Scholar](#)

33. 33.

Mlcochova, P. et al. Combined point of care nucleic acid and antibody testing for SARS-CoV-2 following emergence of D614G spike variant. *Cell Rep. Med.* **1**, 100099 (2020).

[Article](#) [Google Scholar](#)

34. 34.

Corti, D. et al. A neutralizing antibody selected from plasma cells that binds to group 1 and group 2 influenza A hemagglutinins. *Science* **333**, 850–856 (2011).

[ADS](#) [CAS](#) [Article](#) [Google Scholar](#)

35. 35.

Pinto, D. et al. Cross-neutralization of SARS-CoV-2 by a human monoclonal SARS-CoV antibody. *Nature* **583**, 290–295 (2020).

[ADS](#) [CAS](#) [Article](#) [Google Scholar](#)

36. 36.

Tortorici, M. A. et al. Ultrapotent human antibodies protect against SARS-CoV-2 challenge via multiple mechanisms. *Science* **370**, 950–957 (2020).

[ADS](#) [CAS](#) [Article](#) [Google Scholar](#)

37. 37.

Piccoli, L. et al. Mapping neutralizing and immunodominant sites on the SARS-CoV-2 spike receptor-binding domain by structure-guided high-resolution serology. *Cell* **183**, 1024–1042 (2020).

[CAS](#) [Article](#) [Google Scholar](#)

38. 38.

Walls, A. C. et al. Elicitation of potent neutralizing antibody responses by designed protein nanoparticle vaccines for SARS-CoV-2. *Cell* **183**, 1367–1382 (2020).

[CAS](#) [Article](#) [Google Scholar](#)

39. 39.

Shu, Y. & McCauley, J. GISAID: global initiative on sharing all influenza data — from vision to reality. *Euro Surveill.* **22**, 30494 (2017).

[Article](#) [Google Scholar](#)

40. 40.

Katoh, K. & Standley, D. M. MAFFT multiple sequence alignment software version 7: improvements in performance and usability. *Mol. Biol. Evol.* **30**, 772–780 (2013).

[CAS](#) [Article](#) [Google Scholar](#)

41. 41.

Minh, B. Q. et al. IQ-TREE 2: new models and efficient methods for phylogenetic inference in the genomic era. *Mol. Biol. Evol.* **37**, 1530–1534 (2020).

[CAS](#) [Article](#) [Google Scholar](#)

42. 42.

Minh, B. Q., Nguyen, M. A. & von Haeseler, A. Ultrafast approximation for phylogenetic bootstrap. *Mol. Biol. Evol.* **30**, 1188–1195 (2013).

[CAS](#) [Article](#) [Google Scholar](#)

[Download references](#)

Acknowledgements

We thank the Cambridge University Hospitals NHS Trust Occupational Health Department; the NIHR Cambridge Clinical Research Facility and staff at CUH; E. Lim and G. Okecha; J. Voss for the gift of HeLa cells that stably express ACE2. R.K.G. is supported by a Wellcome Trust Senior Fellowship in Clinical Science (WT108082AIA). L.E.M. is supported by a Medical Research Council Career Development Award (MR/R008698/1). S.A.K. is supported by the Bill and Melinda Gates Foundation via PANGEA grant OPP1175094. D.A.C. is supported by a Wellcome Trust Clinical PhD Research Fellowship. K.G.C.S. is the recipient of a Wellcome Investigator Award (200871/Z/16/Z). This research was supported by the National Institute for Health Research (NIHR) Cambridge Biomedical Research Centre, the Cambridge Clinical Trials Unit (CCTU) and the NIHR BioResource. This study was supported by the National Institute of General Medical Sciences (R01GM120553 to D.V.), the National Institute of Allergy and Infectious Diseases (DP1AI158186 and HHSN272201700059C to D.V.), a Pew Biomedical Scholars Award (D.V.), an Investigators in the Pathogenesis of Infectious Disease Awards from the Burroughs Wellcome Fund (D.V.) and Fast Grants (D.V.). The views expressed are those of the authors and not necessarily those of the NIHR or the Department of Health and Social Care. I.A.T.M.F. is funded by a SANTHE award (DEL-15-006).

Author information

Author notes

1. These authors contributed equally: Dami A. Collier, Anna De Marco, Isabella A. T. M. Ferreira, Bo Meng, Rawlings P. Datir
2. These authors jointly supervised this work: Davide Corti, Ravindra K. Gupta

Affiliations

1. Cambridge Institute of Therapeutic Immunology & Infectious Disease, Cambridge, UK

Dami A. Collier, Isabella A. T. M. Ferreira, Bo Meng, Rawlings P. Datir, Steven A. Kemp, Kenneth G. C. Smith & Ravindra K. Gupta

2. Department of Medicine, University of Cambridge, Cambridge, UK

Dami A. Collier, Isabella A. T. M. Ferreira, Bo Meng, Rawlings P. Datir, Steven A. Kemp, Stephen Baker, Gordon Dougan, Christoph Hess, Paul J. Lehner, Paul A. Lyons, Nicholas J. Matheson, James E. D. Thaventhiran, Michael P. Weekes, Ben Bullman, Kelvin Hunter, Federica Mescia, Nicole Pond, Laura

Bergamaschi, Ariana Betancourt, Georgie Bower, Chiara Cossetti, Madeline Epping, Andrew Hinch, Veronika Romashova, Lori Turner, Kenneth G. C. Smith, John R. Bradley, Catherine Ludden, Ewan M. Harrison, Dinesh Aggarwal, Alessandro M. Carabelli, Michael H. Spencer Chapman, Chris Ruis, Sharon J. Peacock, Beth Blane, Sophia T. Girgis, Katherine L. Bellis, Nazreen F. Hadjirin, Leanne M. Kermack, Michael R. Chapman, Sophie Palmer, Carol M. Churcher, Ellena Brooks, Kim S. Smith, Katerina Galai, Georgina M. McManus, Danielle Leek, Sushmita Sridhar, Sally Forrest, Claire Cormie, Harmeet K. Gill, Joana Dias, Ellen E. Higginson, Mailis Maes, Jamie Young, Elias Allara, Clare Pearson, Mark Wills & Ravindra K. Gupta

3. Division of Infection and Immunity, University College London, London, UK

Dami A. Collier, Rawlings P. Datir, Steven A. Kemp, Stephen Baker, Gordon Dougan, Christoph Hess, Paul J. Lehner, Paul A. Lyons, Nicholas J. Matheson, Charlotte Summers, James E. D. Thaventhiran, Mark Toshner, Benjamin J. Dunmore, Stefan Gräf, Josh Hodgson, Christopher Huang, Kelvin Hunter, Ekaterina Legchenko, Cecilia Matara, Jennifer Martin, Federica Mescia, Ciara O'Donnell, Linda Pointon, Nicole Pond, Joy Shih, Rachel Sutcliffe, Tobias Tilly, Carmen Treacy, Zhen Tong, Jennifer Wood, Laura Bergamaschi, Ariana Betancourt, Georgie Bower, Chiara Cossetti, Aloka De Sa, Madeline Epping, Andrew Hinch, Sarah Jackson, Isobel Jarvis, Daniel Lewis, Joe Marsden, Georgina Okecha, Ommar Omarjee, Marianne Perera, Nathan Richoz, Veronika Romashova, Natalia Savinykh Yarkoni, Rahul Sharma, Lori Turner, Eckart M. D. D. De Bie, Katherine Bunclark, Michael Mackay, Mayurun Selvan, Laura E. McCoy & M. Estee Torok

4. Humabs Biomed SA, a subsidiary of Vir Biotechnology, Bellinzona, Switzerland

Anna De Marco, Jessica Bassi, Dora Pinto, Chiara Silacci-Fregni, Siro Bianchi, Katja Culap, Stefano Jaconi, Elisabetta Cameroni, Matteo S. Pizzuto, Antonio Lanzavecchia, Luca Piccoli & Davide Corti

5. Department of Biochemistry, University of Washington, Seattle, WA, USA

Alexandra C. Walls, M. Alejandra Tortorici, John Bowen & David Veesler

6. Vir Biotechnology, San Francisco, CA, USA

Gyorgy Snell & Herbert W. Virgin

7. Clinic of Internal Medicine and Infectious Diseases, Clinica Luganese Moncucco, Lugano, Switzerland

Alessandra Franzetti Pellanda & Christian Garzoni

8. Division of Infectious Diseases, Luigi Sacco Hospital, University of Milan, Milan, Italy

Agostino Riva

9. NIHR Cambridge Clinical Research Facility, Cambridge, UK

Anne Elmer

10. NIHR Bioresource, Cambridge, UK

Nathalie Kingston, Barbara Graves & John R. Bradley

11. University of Kent, Canterbury, UK

Nathalie Kingston, Stefan Gräf, John Allison, Helen Butcher, Daniela Caputo, Debbie Clapham-Riley, Eleanor Dewhurst, Anita Furlong, Barbara Graves, Jennifer Gray, Tasmin Ivers, Mary Kasanicki, Emma Le Gresley, Rachel Linger, Sarah Meloy, Francesca Muldoon, Nigel Ovington, Sofia Papadia, Isabel Phelan, Hannah Stark, Kathleen E. Stirrups, Paul Townsend, Neil Walker, Jennifer Webster & Nigel Temperton

12. Department of Clinical Biochemistry and Immunology, Addenbrooke's Hospital, Cambridge, UK

Lourdes Ceron-Gutierrez, Gabriela Barcenas-Morales & Rainer Doffinger

13. Laboratorio de Inmunología, UNAM, Cuautitlán, Mexico

Gabriela Barcenas-Morales

14. Institute of Biodiversity, University of Glasgow, Glasgow, UK

William Harvey

15. Department of Haematology, University of Cambridge, Cambridge, UK

Nathalie Kingston, Willem H. Owehand, Stefan Gräf, Luca Stefanucci, Jonathan Stephens, John Allison, Nigel Ovington, Kathleen E. Stirrups, Paul

Townsend, Neil Walker, Chris Jackson, Rainer Doffinger & Ravindra K. Gupta

16. University of KwaZulu Natal, Durban, South Africa

Ravindra K. Gupta

17. Africa Health Research Institute, Durban, South Africa

Ravindra K. Gupta

18. Department of Infectious Diseases, Cambridge University Hospitals NHS Trust, Cambridge, UK

Ravindra K. Gupta

19. Department of Biomedicine, University Basel and University Hospital Basel, Basel, Switzerland

Christoph Hess

20. Botnar Research Centre for Child Health (BRCCH), University Basel & ETH Zurich, Basel, Switzerland

Christoph Hess

21. Cambridge Clinical Research Centre, NIHR Clinical Research Facility, Cambridge University Hospitals NHS Foundation Trust, Addenbrooke's Hospital, Cambridge, UK

Caroline Saunders, Ashlea Bucke, Jo Calder, Laura Canna, Jason Domingo, Anne Elmer, Stewart Fuller, Sarah Hewitt, Jane Kennet, Sherly Jose, Jenny Kourampa, Anne Meadows, Jane Price, Cherry Publico, Rebecca Rastall, Carla Ribeiro, Jane Rowlands, Valentina Ruffolo & Hugo Tordesillas

22. Heart and Lung Research Institute, Cambridge, UK

Charlotte Summers & Mark Toshner

23. Royal Papworth Hospital NHS Foundation Trust, Cambridge, UK

Charlotte Summers, Mark Toshner, Ali Ansaripour, Alice Michael, Lucy Mwaura, Caroline Patterson & Gary Polwarth

24. Addenbrooke's Hospital, Cambridge, UK

Charlotte Summers, Petra Polgarova, Giovanni di Stefano & Mary Kasanicki

25. MRC Toxicology Unit, School of Biological Sciences, University of Cambridge, Cambridge, UK

James E. D. Thaventhiran

26. Department of Medicine, Cardiff University, Cardiff, UK

Julie Harris, Criona O'Brien, Thomas R. Connor, Anna Price, Joel Southgate, Christine Kitchen, Huw Gulliver, Ian Merrick, Martyn Guest, Robert Munn, Angela Marchbank, Trudy Workman, William Fuller & Catherine Bresner

27. Cambridge Institute for Medical Research, Cambridge, UK

Stuart Fawke

28. Department of Veterinary Medicine, Cambridge, UK

Emma Jones

29. Department of Biochemistry, University of Cambridge, Cambridge, UK

Marta Wylot

30. Cancer Research UK, Cambridge Institute, University of Cambridge, Cambridge, UK

Richard Grenfell & Mateusz Strezlecki

31. Department of Obstetrics & Gynaecology, The Rosie Maternity Hospital, Cambridge, UK

Oisin Huhn

32. Centre for Enzyme Innovation, University of Portsmouth (PORT), Portsmouth, UK

Francesca Nice, Samuel C. Robson & Angela H. Beckett

33. Institute of Microbiology and Infection, University of Birmingham, Birmingham, UK

Masa Josipovic, Nicholas J. Loman, Sam Nicholls, Claire McMurray, Alan McNally, Joshua Quick, Radoslaw Poplawski, Joanne Stockton & Will Rowe

34. Department of Surgery, Addenbrooke's Hospital, Cambridge, UK

Sabrina Rossi & Cissy Yong

35. Biochemistry and Molecular Genetics, University of Colorado School of Medicine, Aurora, CO, USA

Sarah Spencer

36. Cambridge and Peterborough Foundation Trust, Fulbourn Hospital, Fulbourn, UK

Codie Fahey & Rachel Michel

37. Australian National Phenome Centre, Murdoch University, Murdoch, Western Australia, Australia

Sze-How Bong

38. Centre for Molecular Medicine and Innovative Therapeutics, Health Futures Institute, Murdoch University, Perth, Western Australia, Australia

Jerome D. Coudert

39. Centre of Computational and Systems Medicine, Health Futures Institute, Murdoch University, Perth, Western Australia, Australia

Elaine Holmes

40. Department of Public Health and Primary Care, School of Clinical Medicine, University of Cambridge, Cambridge, UK

Helen Butcher, Daniela Caputo, Debbie Clapham-Riley, Eleanor Dewhurst, Anita Furlong, Barbara Graves, Jennifer Gray, Tasmin Ivers, Emma Le Gresley, Rachel Linger, Sarah Meloy, Francesca Muldoon, Sofia Papadia, Isabel Phelan, Hannah Stark & Jennifer Webster

41. Public Health Wales NHS Trust, Cardiff, UK

Thomas R. Connor, Sally Corden, Catherine Moore, Joanne Watkins, Matthew Bull, Nicole Pacchiarini, Simon Cottrell, Sara Rey, David Heyburn, Chris Williams, Malorie Perry, Noel Craine, Alec Birchley, Alexander Adams, Amy Plimmer, Bree Gatica-Wilcox, Caoimhe McKerr, Ember Hilvers, Hannah Jones, Hibo Asad, Jason Coombes, Johnathan M. Evans, Laia Fina, Lauren Gilbert, Lee Graham, Michelle Cronin, Sara Kumziene-Summerhayes, Sarah

Taylor, Sophie Jones, Joel Southgate, Giri Shankar, Rachel Jones, Robin Howe, Alisha Davies, Elen De Lacy, Fatima Downing, Sue Edwards, Laura Gifford, Mari Morgan & Amy Gaskin

42. Nuffield Department of Medicine, University of Oxford, Oxford, UK

Tanya Golubchik, David Bonsall & Christophe Fraser

43. Department of Virology, King's College London, London, UK

Rocio T. Martinez Nunez & Themoula Charalampous

44. Department of Pathogen Genomics, Wellcome Sanger Institute, London, UK

Ian Johnston, David K. Jackson, Ewan M. Harrison, Sonia Goncalves, Rich Livett, Roberto Amato, Jeff Barrett, Dinesh Aggarwal, Cordelia F. Langford, John Sillitoe, Dominic Kwiatkowski, Mara Lawniczak, Alex Alderton, Inigo Martincorena, Andrew R. Bassett, Cristina V. Ariani, Michael H. Spencer Chapman, Laura Letchford, Steve Palmer, Danni Weldon, Naomi R. Park, Karen Oliver, Steven Leonard, Jillian Durham, Robert Davies, Mathew A. Beale, Katherine L. Bellis, Matthew J. Dorman, Eleanor Drury, Leanne Kane, Sally Kay, Samantha McGuigan, Rachel Nelson, Liam Prestwood, Shavanti Rajatileka, Robin J. Moll, Marina Gourtovaia, Gerry Tonkin-Hill, Kevin Lewis, Jaime M. Tovar-Corona, Keith James, Jon-Paul Keatley, John Danesh, Michael R. Chapman, Charlotte Beaver, Luke Foulser, Sushmita Sridhar, Dorota Jamrozy, Stephanie Lo, Minal Patel, Emma Betteridge, Ben W. Farr, Scott Goodwin, Michael A. Quail, Carol Scott, Lesley Shirley, Scott A. J. Thurston, Diana Rajan, Iraad F. Bronner, Louise Aigrain, Nicholas M. Redshaw, Stefanie V. Lensing, Shane McCarthy, Alex Makunin, James Bonfield, Christoph Puethe, Andrew Whitwham & Jennifer Liddle

45. Department of Medicine, University of Brighton, Brighton, UK

Colin P. Smith, Giselda Bucca & Andrew R. Hesketh

46. Genomics Innovation Department, Guy's and St Thomas' NHS Foundation Trust, London, UK

Ali R. Awan & Chloe L. Fisher

47. Department of Infectious Diseases, Cambridge University Hospitals NHS Foundation Trust, Cambridge, UK

M. Estee Torok & William L. Hamilton

48. Department of Microbiology, Cambridge University Hospitals NHS Foundation Trust, Cambridge, UK

M. Estee Torok & William L. Hamilton

49. Department of Medicine, University Hospital Southampton NHS Foundation Trust, Southampton, UK

Kordo Saeed, Jacqui A. Prieto, Siona Silveira, Emanuela Pelosi, Eleri Wilson-Davies, Adhyana I. K. Mahanama, Buddhini Samaraweera & Sarah Jeremiah

50. School of Medicine, Department of Medicine, University of Southampton, Southampton, UK

Kordo Saeed

51. School of Health Sciences, Department of Medicine, University of Southampton, Southampton, UK

Jacqui A. Prieto

52. Department of Clinical Infection & Diagnostics Research, St Thomas' Hospital and Kings College London, London, UK

Luke B. Snell & Amita Patel

53. Belfast Health & Social Care Trust, Belfast, UK

Derek J. Fairley, James P. McKenna & Tanya Curran

54. Department of Medicine, Queen's University Belfast, Belfast, UK

Derek J. Fairley, David A. Simpson, Declan T. Bradley, Zoltan Molnar, Thomas Thompson & Erwan Acheson

55. Deep Seq Department, School of Life Sciences, Queens Medical Centre, University of Nottingham, Nottingham, UK

Matthew W. Loose, Nadine Holmes, Christopher Moore, Matthew Carlile, Victoria Wright, Fei Sang & Johnny Debebe

56. East Kent Hospitals University NHS Foundation Trust, Canterbury, UK

Samuel Moses & Hannah Lowe

57. Department of Medicine, University of Kent, Canterbury, UK

Samuel Moses

58. Hub for Biotechnology in the Built Environment, Northumbria University, Newcastle-Upon-Tyne, UK

Darren L. Smith, Matthew Bashton & Gregory R. Young

59. Department of Medicine, Northumbria University, Newcastle-Upon-Tyne, UK

Darren L. Smith, Matthew Bashton, Andrew Nelson, Gregory R. Young, Clare M. McCann & Wen C. Yew

60. NU-OMICS, Northumbria University, Newcastle-upon-Tyne, UK

Darren L. Smith, Andrew Nelson & Clare M. McCann

61. Centre for Genomic Pathogen Surveillance, University of Oxford, Oxford, UK

David M. Aanensen, Anthony P. Underwood, Corin A. Yeats, Khalil Abudahab, Ben E. W. Taylor & Mirko Menegazzo

62. Clinical Microbiology and Public Health Laboratory, Public Health England, Cambridge, UK

Martin D. Curran & Surendra Parmar

63. Public Health England, London, UK

Dinesh Aggarwal, Husam Osman, Meera Chand, Sharon J. Peacock, Esther Robinson, Peter Muir, Ian B. Vipond, Andrew Bosworth, Hannah M. Pymont, Stephanie Hutchings, Alicia Thornton, Richard Myers, Ian Harrison, Chloe Bishop, Vicki Chalker, Richard Hopes, Nicholas W. Machin, Shazaad S. Y. Ahmad, Angie Lackenby, Tamyo Mbisa, Steven Platt, Shahjahan Miah, David Bibby, Carmen Manso, Jonathan Hubb, Gavin Dabrera, Mary Ramsay, Daniel Bradshaw, Ulf Schaefer, Natalie Groves, Eileen Gallagher, David Lee, David Williams, Nicholas Ellaby, Hassan Hartman, Nikos Manesis, Vineet Patel, Juan Ledesma, Katherine A. Twohig, Elias Allara & Clare Pearson

64. MRC–University of Glasgow Centre for Virus Research, Glasgow, UK

James G. Shepherd, Emma C. Thomson, David L. Robertson, Kathy K. Li, Rajiv N. Shah, Natasha G. Jesudason, Ana da Silva Filipe, Igor Starinskij, Richard J. Orton, Joseph Hughes, Sreenu Vattipally, Joshua B. Singer, Patawee Asamaphan, Marc O. Niebel, Lily Tong, Alice Broos, Daniel Mair, Jenna Nichols, Stephen N. Carmichael, Kyriaki Nomikou, Elihu Aranday-Cortes, Natasha Johnson & Seema Nickbakhsh

65. University of Sheffield, Sheffield, UK

Matthew D. Parker, Thushan I. de Silva, Dennis Wang, Matthew Wyles, Danielle C. Groves, Peijun Zhang, Marta Gallis, Stavroula F. Louka, Benjamin B. Lindsey, Timothy M. Freeman, Nikki Smith, Alexander J. Keeley, David G. Partridge, Mohammad Raza, Cariad Evans, Kate Johnson, Adrienn Angyal, Luke R. Green, Paul J. Parsons, Rachel M. Tucker, Rebecca Brown & Max Whiteley

66. Portsmouth Hospitals University NHS Trust, Portsmouth, UK

Sharon Glaysher, Anoop J. Chauhan, Scott Elliott, Kelly Bicknell, Sarah Wyllie, Allyson Lloyd & Robert Impey

67. School of Pharmacy and Biomedical Sciences, University of Portsmouth (PORT), Portsmouth, UK

Katie F. Loveson, Salman Goudarzi, Christopher Fearn, Kate Cook, Hannah Dent & Hannah Paul

68. NHS Lothian, Edinburgh, UK

Kate E. Templeton, Martin P. McHugh, Rebecca Dewar & Elizabeth Wastenge

69. University of Edinburgh, Edinburgh, UK

Kate E. Templeton, Andrew Rambaut, Stefan Rooke, Áine O'Toole, Thomas Williams, Verity Hill, Carlos E. Balcazar, Michael D. Gallagher, Kathleen A. Williamson & Thomas D. Stanton

70. Department of Medicine, University of Oxford, Oxford, UK

Dominic Kwiatkowski

71. Quadram Institute Bioscience, Norwich, UK

Justin O'Grady, Andrew J. Page, Gemma L. Kay, Nabil-Fareed Alikhan, Alexander J. Trotter, Leonardo de Oliveira Martins, Alison E.

Mather, Lizzie Meadows, David J. Baker, Steven Rudder, Alp Aydin & Thanh Le-Viet

72. Department of Medicine, University of East Anglia, Norwich, UK

Justin O'Grady & Rose K. Davidson

73. Public Health Scotland, Glasgow, UK

Matthew T. G. Holden, Sharif Shaaban & Seema Nickbakhsh

74. Heartlands Hospital, Birmingham, UK

Husam Osman, Esther Robinson, Andrew Bosworth & Li Xu-McCrae

75. Department of Medicine, Oxford University Hospitals NHS Foundation Trust, Oxford, UK

Monique Andersson, Anita Justice, Timothy Peto, David Eyre & Derrick Crook

76. Department of Medicine, Brighton and Sussex University Hospitals NHS Trust, Brighton, UK

Mohammed O. Hassan-Ibrahim, Cassandra S. Malone & Benjamin J. Cogger

77. Department of Medicine, University of Warwick, Warwick, UK

Chrystala Constantnidou, Meera Unnikrishnan, Richard Stark, Sascha Ott, Laura Baxter, Mohammad T. Alam, Jeffrey K. J. Cheng, Hannah E. Bridgewater, Lucy R. Frost, Grace Taylor-Joyce & Paul E. Brown

78. Department of Medicine, University of Liverpool, Liverpool, UK

Alistair C. Darby, Julian A. Hiscox, Steve Paterson, Miren Iturriza-Gomara, Anita O. Lucaci, Sam T. Haldenby, Kathryn A. Jackson, Lance Turtle, Edith E. Vamos, Margaret Hughes, Lucille Rainbow, Richard Eccles, Charlotte Nelson, Mark Whitehead, Richard Gregory, Matthew Gemmell, Claudia Wierzbicki & Hermione J. Webster

79. Department of Medicine, Imperial College London, London, UK

Erik M. Volz, Manon Ragonnet-Cronin, Fabricia F. Nascimento, David Jorgensen, Olivia Boyd, Lily Geidelberg, Aileen Rowan, Graham P. Taylor, Igor Siveroni & Rob Johnson

80. Department of Zoology, University of Oxford, Oxford, UK

Oliver G. Pybus, Louis du Plessis, Alex E. Zarebski, Jayna Raghwani, Moritz U. G. Kraemer, Stephen W. Attwood, Sarah Francois, Tetyana I. Vaslyeva, Marina Escalera Zamudio & Bernardo Gutierrez

81. Newcastle Hospitals NHS Foundation Trust, Newcastle-upon-Tyne, UK

Yusri Taha, Jennifer Collins, Gary Eltringham, Brendan A. I. Payne, Shirelle Burton-Fanning & Sheila Waugh

82. Division of Virology, Department of Pathology, University of Cambridge, Cambridge, UK

Aminu S. Jahun, Myra Hosmillo, Grant Hall, Yasmin Chaudhry, Malte L. Pinckert & Iliana Georgana

83. University Hospitals Coventry and Warwickshire, Coventry, UK

Sarojini Pandey, Dimitris Gramatopoulos, Lisa Berry & Katie Jones

84. University of Exeter, Exeter, UK

Ben Temperton, Stephen L. Michell, Aaron R. Jeffries, Jane A. H. Masoli, Bridget A. Knight, Christopher R. Jones, Claire M. Bewshea, Sian Ellard, Michelle L. Michelsen, Joanna Warwick-Dugdale, Robin Manley, Audrey Farbos, James W. Harrison, Christine M. Sambles & David J. Studholme

85. University College London, London, UK

Sunando Roy, Judith Breuer, Rachel J. Williams, Mark Kristiansen, Charlotte A. Williams, John A. Hartley, Adam P. Westhorpe, Riaz Jannoo, Helen L. Lowe, Angeliki Karamani, Leah Ensell, Marius Cotic & Nadua Bayzid

86. Wellcome Centre for Human Genetics, Nuffield Department of Medicine, University of Oxford, Oxford, UK

Mariateresa de Cesare, John A. Todd, David Buck, Angie Green, Amy Trebes & George MacIntyre-Cockett

87. Betsi Cadwaladr University Health Board, Betsi Cadwaladr, UK

Helen Adams

88. School of Biological Sciences, University of Portsmouth (PORT), Portsmouth, UK

Yann Bourgeois & Garry P. Scarlett

89. Warwick Medical School and Institute of Precision Diagnostics, Pathology, UHCW NHS Trust, Warwick, UK

Dimitris Gramatopoulos

90. Centre for Clinical Infection and Diagnostics Research, Department of Infectious Diseases, Guy's and St Thomas' NHS Foundation Trust, London, UK

Jonathan Edgeworth, Rahul Batra, Themoula Charalampous & Gaia Nebbia

91. Great Ormond Street Hospital for Children NHS Foundation Trust, London, UK

Judith Breuer, Kathryn Ann Harris, Julianne Rose Brown, Nathaniel Storey, Divya Shah, Laura Atkinson & Jack C. D. Lee

92. Cardiff and Vale University Health Board, Cardiff, UK

Michaela John, Sian Morgan, Joshua Maksimovic, Karla Spellman, Kathryn McCluggage, Robert Beer & Safiah Afifi

93. Turnkey Laboratory, University of Birmingham, Birmingham, UK

Alan McNally, Angus Best, Benita Percival, Jeremy Mirza, Oliver Megram, Megan Mayhew, Liam Crawford, Fiona Ashcroft, Emma Moles-Garcia & Nicola Cumley

94. Gloucestershire Hospitals NHS Foundation Trust, Gloucester, UK

John Boyes

95. Microbiology Department, Wye Valley NHS Trust, Hereford, UK

Venkat Sivaprakasam, Fenella Halstead & Wendy Hogsden

96. Sandwell and West Birmingham NHS Trust, Birmingham, UK

Tranprit Salluja, Melisa Louise Fenton, Ashok Dadrah & Amanda Symmonds

97. Norfolk and Norwich University Hospital, Norwich, UK

Samir Dervisevic, Emma J. Meader, Rachael Stanley & Lindsay Coupland

98. Royal Devon and Exeter NHS Foundation Trust, Exeter, UK

Jane A. H. Masoli, Bridget A. Knight, Christopher R. Jones, Sian Ellard & Cressida Auckland

99. Barking, Havering and Redbridge University Hospitals NHS Trust, Barking, UK

Cherian Koshy & Amy Ash

100. Queen Elizabeth Hospital, Birmingham, UK

Anna Casey & Liz Ratcliffe

101. Department of Microbiology, Kettering General Hospital, Kettering, UK

Thomas Davis, Sahar Eldirdiri & Anita Kenyon

102. Clinical Microbiology, University Hospitals of Leicester NHS Trust, Leicester, UK

Christopher Holmes, Paul Bird, Thomas Helmer, Karlie Fallon & Julian Tang

103. Imperial College Hospitals NHS Trust, London, UK

Paul Anthony Randell, Alison Cox, Pinglawathee Madona, Alison Holmes, James Price, Siddharth Mookerjee & Frances Bolt

104. North West London Pathology, London, UK

Paul Anthony Randell, Alison Cox & Pinglawathee Madona

105. Royal Free NHS Trust, London, UK

Tabitha W. Mahungu, Dianne Irish-Tavares, Tanzina Haque, Jennifer Hart & Eric Witele

106. South Tees Hospitals NHS Foundation Trust, Newcastle-upon-Tyne, UK

Steven Liggett, Paul Baker, Stephen Bonner & Sarah Essex

107. North Cumbria Integrated Care NHS Foundation Trust, Carlisle, UK

Clive Graham, Edward Barton, Debra Padgett & Garren Scott

108. North Tees and Hartlepool NHS Foundation Trust, Stockton-on-Tees, UK

Emma Swindells & Jane Greenaway

109. County Durham and Darlington NHS Foundation Trust, Durham, UK

Sharon Campbell, Veena Raviprakash, Nicola Sheriff, Victoria Blakey & Lesley-Anne Williams

110. Virology, School of Life Sciences, Queens Medical Centre, University of Nottingham, Nottingham, UK

Patrick C. McClure, Joseph G. Chappell, Theocharis Tsoleridis & Jonathan Ball

111. Clinical Microbiology Department, Queens Medical Centre, Nottingham, UK

Gemma Clark, Carl Jones, Wendy Smith, Manjinder Khakh, Vicki M. Fleming, Michelle M. Lister, Hannah C. Howson-Wells, Louise Berry, Tim Boswell, Amelia Joseph & Iona Willingham

112. PathLinks, Northern Lincolnshire & Goole NHS Foundation Trust, Scunthorpe, UK

Tim J. Sloan, Nichola Duckworth & Sarah Walsh

113. Basingstoke Hospital, Basingstoke, UK

Jessica Lynch, Emma Wise, Nathan Moore, Matilde Mori, Nick Cortes & Stephen Kidd

114. University of Surrey, Guildford, UK

Jessica Lynch, Emma Wise, Nathan Moore, Matilde Mori, Nick Cortes & Stephen Kidd

115. Cambridge University Hospitals NHS Foundation Trust, Cambridge, UK

Ben Warne

116. Swansea University, Swansea, UK

Ronan A. Lyons

117. Ministry of Health, Colombo, Sri Lanka

Adhyana I. K. Mahanama & Buddhini Samaraweera

118. Cambridge Stem Cell Institute, University of Cambridge, Cambridge, UK

Nicola Reynolds & Michelle Wantoch

119. Liverpool Clinical Laboratories, Liverpool, UK

Jenifer Mason, Trevor I. Robinson, Elaine O'Toole, Joanne Watts, Cassie Breen & Angela Cowell

120. NIHR Health Protection Research Unit in HCAI and AMR, Imperial College London, London, UK

Alison Holmes, James Price, Siddharth Mookerjee & Frances Bolt

121. Health Data Research UK Cambridge, Cambridge, UK

Michael R. Chapman

122. Hampshire Hospitals NHS Foundation Trust, Winchester, UK

Gabrielle Vernet & Rebecca Williams

123. Public Health Agency, London, UK

Declan T. Bradley & Tim Wyatt

124. Department of Infection Biology, Faculty of Infectious & Tropical Diseases, London School of Hygiene & Tropical Medicine, London, UK

Francesc Coll

125. University of Birmingham, Birmingham, UK

Alex Richter & Andrew Beggs

126. West of Scotland Specialist Virology Centre, NHS Greater Glasgow and Clyde, Glasgow, UK

Rory N. Gunson

127. NHS Greater Glasgow and Clyde, Glasgow, UK

Amanda Bradley, Alasdair Maclean, Guy Mollett & Rachel Blacow

128. National Infection Service, PHE and Leeds Teaching Hospitals Trust, Leeds, UK

Antony D. Hale, Louissa R. Macfarlane-Smith, Katherine L. Harper & Holli Carden

129. Manchester University NHS Foundation Trust, Manchester, UK

Nicholas W. Machin, Shazaad S. Y. Ahmad & Ryan P. George

130. Guy's and St Thomas' Hospitals, London, UK

Adela Alcolea-Medina

131. Viapath, Guy's and St Thomas' NHS Foundation Trust, and King's College Hospital NHS Foundation Trust, London, UK

Adela Alcolea-Medina, Alberto C. Cerda, Tammy V. Merrill & Rebekah E. Wilson

132. Health Services Laboratories, London, UK

Lisa J. Levett, Judith Heaney, Wendy Chatterton & Monika Pusok

133. Maidstone and Tunbridge Wells NHS Trust, Maidstone, UK

Graciela Sluga

134. Gateshead Health NHS Foundation Trust, Gateshead, UK

Jonathan Moore & Susanne Stonehouse

135. Norfolk County Council, Norwich, UK

Louise Smith

136. East Suffolk and North Essex NHS Foundation Trust, Ipswich, UK

Luke Bedford

137. Department of Medicine, University of Southampton, Southampton, UK

Matilde Mori

138. Microbiology Department, Princess Alexandra Hospital, Harlow, UK

Nick Levene & Lynn Monaghan

139. Sheffield Teaching Hospitals, Sheffield, UK

David G. Partridge, Mohammad Raza, Cariad Evans & Kate Johnson

140. Institute of Biodiversity, Animal Health & Comparative Medicine, Glasgow, UK

Katherine L. Smollett

141. Department of Infectious Diseases, King's College London, London, UK

Adrian W. Signell, Gilberto Betancor & Harry D. Wilson

142. Guy's and St Thomas' BRC, London, UK

Flavia Flaviani

143. Wellcome Sanger Centre, Hinxton, UK

Steven Rushton, Sarah O'Brien, Irina Abnizova, Louise Aigrain, Alex Alderton, Mozam Ali, Laura Allen, Roberto Amato, Ralph Anderson, Cristina Ariani, Siobhan Austin-Guest, Sendu Bala, Jeffrey Barrett, Andrew Bassett, Kristina Battleday, James Beal, Mathew Beale, Charlotte Beaver, Sam Bellany, Tristram Bellerby, Katie Bellis, Duncan Berger, Matt Berriman, Emma Betteridge, Paul Bevan, Simon Binley, Jason Bishop, Kirsty Blackburn, James Bonfield, Nick Boughton, Sam Bowker, Timothy Brendler-Spaeth, Iraad Bronner, Tanya Brooklyn, Sarah Kay Buddenborg, Robert Bush, Catarina Caetano, Alex Cagan, Nicola Carter, Joanna Cartwright, Tiago Carvalho Monteiro, Liz Chapman, Tracey-Jane Chillingworth, Peter Clapham, Richard Clark, Adrian Clarke, Catriona Clarke, Daryl Cole, Elizabeth Cook, Maria Coppola, Linda Cornell, Clare Cornwell, Craig Corton, Abby Crackett, Alison Cranage, Harriet Craven, Sarah Craw, Mark Crawford, Tim Cutts, Monika Dabrowska, Matt Davies, Robert Davies, Joseph Dawson, Callum Day, Aiden Densem, Thomas Dibling, Cat Dockree, David Dodd, Sunil Dogga, Matthew Dorman, Gordon Dougan, Martin Dougherty, Alexander Dove, Lucy Drummond, Eleanor Drury, Monika Dudek, Jillian Durham, Laura Durrant, Elizabeth Easthope, Sabine Eckert, Pete Ellis, Ben Farr, Michael Fenton, Marcella Ferrero, Neil Flack, Howard Fordham, Grace Forsythe, Luke Foulser, Matt Francis, Audrey Fraser, Adam Freeman, Anastasia Galvin, Maria Garcia-Casado, Alex Gedny, Sophia Girgis, James Glover, Sonia Goncalves, Scott Goodwin, Oliver Gould, Marina Gourtovaia, Andy Gray, Emma Gray, Coline Griffiths, Yong Gu, Florence Guerin, Will Hamilton, Hannah Hanks, Ewan Harrison, Alexandria Harrott, Edward Harry, Julia Harvison, Paul

Heath, Anastasia Hernandez-Koutoucheva, Rhiannon Hobbs, Dave Holland, Sarah Holmes, Gary Hornett, Nicholas Hough, Liz Huckle, Lena Hughes-Hallet, Adam Hunter, Stephen Inglis, Sameena Iqbal, Adam Jackson, David Jackson, Keith James, Dorota Jamrozy, Carlos Jimenez Verdejo, Ian Johnston, Matthew Jones, Kalyan Kallepally, Leanne Kane, Keely Kay, Sally Kay, Jon Keatley, Alan Keith, Alison King, Lucy Kitchin, Matt Kleanthous, Martina Klimekova, Petra Korlevic, Ksenia Krasheninnikova, Dominic Kwiatkowski, Greg Lane, Cordelia Langford, Adam Laverack, Katharine Law, Mara Lawniczak, Stefanie Lensing, Steven Leonard, Laura Letchford, Kevin Lewis, Amanah Lewis-Wade, Jennifer Liddle, Quan Lin, Sarah Lindsay, Sally Linsdell, Rich Livett, Stephanie Lo, Rhona Long, Jamie Lovell, Jon Lovell, Catherine Ludden, James Mack, Mark Maddison, Aleksei Makunin, Irfan Mamun, Jenny Mansfield, Neil Marriott, Matt Martin, Inigo Martincorena, Matthew Mayho, Shane McCarthy, Jo McClintock, Samantha McGuigan, Sandra McHugh, Liz McMinn, Carl Meadows, Emily Mobley, Robin Moll, Maria Morra, Leanne Morrow, Kathryn Murie, Sian Nash, Claire Nathwani, Plamena Naydenova, Alexandra Neaverson, Rachel Nelson, Ed Nerou, Jon Nicholson, Tabea Nimz, Guillaume G. Noell, Sarah O'Meara, Valeriu Ohan, Karen Oliver, Charles Olney, Doug Ormond, Agnes Oszlanczi, Steve Palmer, Yoke Fei Pang, Barbora Pardubska, Naomi Park, Aaron Parmar, Gaurang Patel, Minal Patel, Maggie Payne, Sharon Peacock, Arabella Petersen, Deborah Plowman, Tom Preston, Liam Prestwood, Christoph Puethe, Michael Quail, Diana Rajan, Shavanti Rajatileka, Richard Rance, Suzannah Rawlings, Nicholas Redshaw, Joe Reynolds, Mark Reynolds, Simon Rice, Matt Richardson, Connor Roberts, Katrina Robinson, Melanie Robinson, David Robinson, Hazel Rogers, Eduardo Martin Rojo, Daljit Roopra, Mark Rose, Luke Rudd, Ramin Sadri, Nicholas Salmon, David Saul, Frank Schwach, Carol Scott, Phil Seekings, Lesley Shirley, John Sillitoe, Alison Simms, Matt Sinnott, Shanthi Sivadasan, Bart Siwek, Dale Sizer, Kenneth Skeldon, Jason Skelton, Joanna Slater-Tunstill, Lisa Sloper, Nathalie Smerdon, Chris Smith, Christen Smith, James Smith, Katie Smith, Michelle Smith, Sean Smith, Tina Smith, Leighton Sneade, Carmen Diaz Soria, Catarina Sousa, Emily Souster, Andrew Sparkes, Michael Spencer-Chapman, Janet Squares, Robert Stanley, Claire Steed, Tim Stickland, Ian Still, Mike Stratton, Michelle Strickland, Allen Swann, Agnieszka Swiatkowska, Neil Sycamore, Emma Swift, Edward Symons, Suzanne Szluha, Emma Taluy, Nunu Tao, Katy Taylor, Sam Taylor, Stacey Thompson, Mark Thompson, Mark Thomson, Nicholas Thomson, Scott Thurston, Gerry Tonkin-Hill, Dee Toombs, Benjamin Topping, Jaime Tovar-Corona, Daniel Ungureanu, James Uphill, Jana Urbanova, Philip Jansen Van, Valerie Vancollie, Paul Voak, Danielle Walker, Matthew Walker, Matt Waller, Gary Ward, Charlie Weatherhogg, Niki

Webb, Danni Weldon, Alan Wells, Eloise Wells, Luke Westwood, Theo Whipp, Thomas Whiteley, Georgia Whitton, Andrew Whitwham, Sara Widaa, Mia Williams, Mark Wilson & Sean Wright

Authors

1. Dami A. Collier

[View author publications](#)

You can also search for this author in [PubMed](#) [Google Scholar](#)

2. Anna De Marco

[View author publications](#)

You can also search for this author in [PubMed](#) [Google Scholar](#)

3. Isabella A. T. M. Ferreira

[View author publications](#)

You can also search for this author in [PubMed](#) [Google Scholar](#)

4. Bo Meng

[View author publications](#)

You can also search for this author in [PubMed](#) [Google Scholar](#)

5. Rawlings P. Datin

[View author publications](#)

You can also search for this author in [PubMed](#) [Google Scholar](#)

6. Alexandra C. Walls

[View author publications](#)

You can also search for this author in [PubMed](#) [Google Scholar](#)

7. Steven A. Kemp

[View author publications](#)

You can also search for this author in [PubMed](#) [Google Scholar](#)

8. Jessica Bassi

[View author publications](#)

You can also search for this author in [PubMed](#) [Google Scholar](#)

9. Dora Pinto

[View author publications](#)

You can also search for this author in [PubMed](#) [Google Scholar](#)

10. Chiara Silacci-Fregni

[View author publications](#)

You can also search for this author in [PubMed](#) [Google Scholar](#)

11. Siro Bianchi

[View author publications](#)

You can also search for this author in [PubMed](#) [Google Scholar](#)

12. M. Alejandra Tortorici

[View author publications](#)

You can also search for this author in [PubMed](#) [Google Scholar](#)

13. John Bowen

[View author publications](#)

You can also search for this author in [PubMed](#) [Google Scholar](#)

14. Katja Culap

[View author publications](#)

You can also search for this author in [PubMed](#) [Google Scholar](#)

15. Stefano Jaconi

[View author publications](#)

You can also search for this author in [PubMed](#) [Google Scholar](#)

16. Elisabetta Cameroni

[View author publications](#)

You can also search for this author in [PubMed](#) [Google Scholar](#)

17. Gyorgy Snell

[View author publications](#)

You can also search for this author in [PubMed](#) [Google Scholar](#)

18. Matteo S. Pizzuto

[View author publications](#)

You can also search for this author in [PubMed](#) [Google Scholar](#)

19. Alessandra Franzetti Pellanda

[View author publications](#)

You can also search for this author in [PubMed](#) [Google Scholar](#)

20. Christian Garzoni

[View author publications](#)

You can also search for this author in [PubMed](#) [Google Scholar](#)

21. Agostino Riva

[View author publications](#)

You can also search for this author in [PubMed](#) [Google Scholar](#)

22. Anne Elmer

[View author publications](#)

You can also search for this author in [PubMed](#) [Google Scholar](#)

23. Nathalie Kingston

[View author publications](#)

You can also search for this author in [PubMed](#) [Google Scholar](#)

24. Barbara Graves

[View author publications](#)

You can also search for this author in [PubMed](#) [Google Scholar](#)

25. Laura E. McCoy

[View author publications](#)

You can also search for this author in [PubMed](#) [Google Scholar](#)

26. Kenneth G. C. Smith

[View author publications](#)

You can also search for this author in [PubMed](#) [Google Scholar](#)

27. John R. Bradley

[View author publications](#)

You can also search for this author in [PubMed](#) [Google Scholar](#)

28. Nigel Temperton

[View author publications](#)

You can also search for this author in [PubMed](#) [Google Scholar](#)

29. Lourdes Ceron-Gutierrez

[View author publications](#)

You can also search for this author in [PubMed](#) [Google Scholar](#)

30. Gabriela Barcenas-Morales

[View author publications](#)

You can also search for this author in [PubMed](#) [Google Scholar](#)

31. William Harvey

[View author publications](#)

You can also search for this author in [PubMed](#) [Google Scholar](#)

32. Herbert W. Virgin

[View author publications](#)

You can also search for this author in [PubMed](#) [Google Scholar](#)

33. Antonio Lanzavecchia

[View author publications](#)

You can also search for this author in [PubMed](#) [Google Scholar](#)

34. Luca Piccoli

[View author publications](#)

You can also search for this author in [PubMed](#) [Google Scholar](#)

35. Rainer Doffinger

[View author publications](#)

You can also search for this author in [PubMed](#) [Google Scholar](#)

36. Mark Wills

[View author publications](#)

You can also search for this author in [PubMed](#) [Google Scholar](#)

37. David Veesler

[View author publications](#)

You can also search for this author in [PubMed](#) [Google Scholar](#)

38. Davide Corti

[View author publications](#)

You can also search for this author in [PubMed](#) [Google Scholar](#)

39. Ravindra K. Gupta

[View author publications](#)

You can also search for this author in [PubMed](#) [Google Scholar](#)

Consortia

The CITIID-NIHR BioResource COVID-19 Collaboration

- Principal investigators

- Stephen Baker
- , Gordon Dougan
- , Christoph Hess
- , Nathalie Kingston
- , Paul J. Lehner
- , Paul A. Lyons
- , Nicholas J. Matheson
- , Willem H. Owehand
- , Caroline Saunders
- , Charlotte Summers
- , James E. D. Thaventhiran
- , Mark Toshner
- & Michael P. Weekes

- CRF & volunteer research nurses

- Ashlea Bucke
- , Jo Calder
- , Laura Canna
- , Jason Domingo
- , Anne Elmer
- , Stewart Fuller
- , Julie Harris
- , Sarah Hewitt
- , Jane Kennet
- , Sherly Jose
- , Jenny Kourampa
- , Anne Meadows
- , Criona O'Brien
- , Jane Price
- , Cherry Publico
- , Rebecca Rastall
- , Carla Ribeiro
- , Jane Rowlands
- , Valentina Ruffolo
- & Hugo Tordesillas

- **Sample logistics**

- Ben Bullman
- , Benjamin J. Dunmore
- , Stuart Fawke
- , Stefan Gräf
- , Josh Hodgson
- , Christopher Huang
- , Kelvin Hunter
- , Emma Jones
- , Ekaterina Legchenko
- , Cecilia Matara
- , Jennifer Martin
- , Federica Mescia
- , Ciara O'Donnell
- , Linda Pointon
- , Nicole Pond
- , Joy Shih
- , Rachel Sutcliffe
- , Tobias Tilly
- , Carmen Treacy

- , Zhen Tong
- , Jennifer Wood
- & Marta Wylot

- **Sample processing & data acquisition**

- Laura Bergamaschi
- , Ariana Betancourt
- , Georgie Bower
- , Chiara Cossetti
- , Aloka De Sa
- , Madeline Epping
- , Stuart Fawke
- , Richard Grenfell
- , Andrew Hinch
- , Oisin Huhn
- , Sarah Jackson
- , Isobel Jarvis
- , Daniel Lewis
- , Joe Marsden
- , Francesca Nice
- , Georgina Okecha
- , Ommar Omarjee
- , Marianne Perera
- , Nathan Richoz
- , Veronika Romashova
- , Natalia Savinykh Yarkoni
- , Rahul Sharma
- , Luca Stefanucci
- , Jonathan Stephens
- , Mateusz Strezlecki
- & Lori Turner

- **Clinical data collection**

- Eckart M. D. D. De Bie
- , Katherine Bunclark
- , Masa Josipovic
- , Michael Mackay

- , Federica Mescia
- , Sabrina Rossi
- , Mayurun Selvan
- , Sarah Spencer
- & Cissy Yong

- **Royal Papworth Hospital ICU**

- Ali Ansaripour
- , Alice Michael
- , Lucy Mwaura
- , Caroline Patterson
- & Gary Polwarth

- **Addenbrooke's Hospital ICU**

- Petra Polgarova
- & Giovanni di Stefano

- **Cambridge & Peterborough Foundation Trust**

- Codie Fahey
- & Rachel Michel

- **ANPC & Centre for Molecular Medicine & Innovative Therapeutics**

- Sze-How Bong
- , Jerome D. Coudert
- & Elaine Holmes

- **NIHR BioResource**

- John Allison
- , Helen Butcher
- , Daniela Caputo

- , Debbie Clapham-Riley
- , Eleanor Dewhurst
- , Anita Furlong
- , Barbara Graves
- , Jennifer Gray
- , Tasmin Ivers
- , Mary Kasanicki
- , Emma Le Gresley
- , Rachel Linger
- , Sarah Meloy
- , Francesca Muldoon
- , Nigel Ovington
- , Sofia Papadia
- , Isabel Phelan
- , Hannah Stark
- , Kathleen E. Stirrups
- , Paul Townsend
- , Neil Walker
- & Jennifer Webster

The COVID-19 Genomics UK (COG-UK) Consortium

- **Funding acquisition, leadership & supervision, metadata curation, project administration, samples & logistics, sequencing & analysis, software & analysis tools and visualization**
 - Samuel C. Robson
- **Funding acquisition, leadership & supervision, metadata curation, project administration, samples & logistics, sequencing & analysis and software & analysis tools**
 - Nicholas J. Loman
 - & Thomas R. Connor

- **Leadership & supervision, metadata curation, project administration, samples & logistics, sequencing & analysis, software & analysis tools and visualization**
 - Tanya Golubchik
- **Funding acquisition, metadata curation, samples & logistics, sequencing & analysis, software & analysis tools and visualization**
 - Rocio T. Martinez Nunez
- **Funding acquisition, leadership & supervision, metadata curation, project administration and samples & logistics**
 - Catherine Ludden
- **Funding acquisition, leadership & supervision, metadata curation, samples & logistics and sequencing & analysis**
 - Sally Corden
- **Funding acquisition, leadership & supervision, project administration, samples & logistics and sequencing & analysis**
 - Ian Johnston
 - & David Bonsall
- **Funding acquisition, leadership & supervision, sequencing & analysis, software & analysis tools and visualization**
 - Colin P. Smith
 - & Ali R. Awan
- **Funding acquisition, samples & logistics, sequencing & analysis, software & analysis tools and visualization**

- Giselda Bucca
- **Leadership & supervision, metadata curation, project administration, samples & logistics and sequencing & analysis**
- M. Estee Torok
- **Leadership & supervision, metadata curation, project administration, samples & logistics and visualization**
- Kordo Saeed
- & Jacqui A. Prieto
- **Leadership & supervision, metadata curation, project administration, sequencing & analysis and software & analysis tools**
- David K. Jackson
- **Metadata curation, project administration, samples & logistics, sequencing & analysis and software & analysis tools**
- William L. Hamilton
- **Metadata curation, project administration, samples & logistics, sequencing & analysis and visualization**
- Luke B. Snell
- **Funding acquisition, leadership & supervision, metadata curation and samples & logistics**
- Catherine Moore

- **Funding acquisition, leadership & supervision, project administration and samples & logistics**
 - Ewan M. Harrison
- **Leadership & supervision, metadata curation, project administration and samples & logistics**
 - Sonia Goncalves
- **Leadership & supervision, metadata curation, samples & logistics and sequencing & analysis**
 - Derek J. Fairley
 - , Matthew W. Loose
 - & Joanne Watkins
- **Leadership & supervision, metadata curation, samples & logistics and software & analysis tools**
 - Rich Livett
- **Leadership & supervision, metadata curation, samples & logistics and visualization**
 - Samuel Moses
- **Leadership & supervision, metadata curation, sequencing & analysis and software & analysis tools**
 - Roberto Amato
 - , Sam Nicholls
 - & Matthew Bull

- **Leadership & supervision, project administration, samples & logistics and sequencing & analysis**
 - Darren L. Smith
- **Leadership & supervision, sequencing & analysis, software & analysis tools and visualization**
 - Jeff Barrett
 - & David M. Aanensen
- **Metadata curation, project administration, samples & logistics and sequencing & analysis**
 - Martin D. Curran
 - , Surendra Parmar
 - , Dinesh Aggarwal
 - & James G. Shepherd
- **Metadata curation, project administration, sequencing & analysis and software & analysis tools**
 - Matthew D. Parker
- **Metadata curation, samples & logistics, sequencing & analysis and visualization**
 - Sharon Glaysher
- **Metadata curation, sequencing & analysis, software & analysis tools and visualization**
 - Matthew Bashton
 - , Anthony P. Underwood
 - , Nicole Pacchiarini

- & Katie F. Loveson
- **Project administration, sequencing & analysis, software & analysis tools and visualization**
- Alessandro M. Carabelli
- **Funding acquisition, leadership & supervision and metadata curation**
- Kate E. Templeton

- **Funding acquisition, leadership & supervision and project administration**
 - Cordelia F. Langford
 - , John Sillitoe
 - , Thushan I. de Silva
 - & Dennis Wang
- **Funding acquisition, leadership & supervision and sequencing & analysis**
 - Dominic Kwiatkowski
 - , Andrew Rambaut
 - , Justin O’Grady
 - & Simon Cottrell
- **Leadership & supervision, metadata curation and sequencing & analysis**
 - Matthew T. G. Holden
 - & Emma C. Thomson
- **Leadership & supervision, project administration and samples & logistics**
 - Husam Osman
 - , Monique Andersson
 - , Anoop J. Chauhan
 - & Mohammed O. Hassan-Ibrahim
- **Leadership & supervision, project administration and sequencing & analysis**
 - Mara Lawniczak

- **Leadership & supervision, samples & logistics and sequencing & analysis**
 - Alex Alderton
 - , Meera Chand
 - , Chrystala Constantinidou
 - , Meera Unnikrishnan
 - , Alistair C. Darby
 - , Julian A. Hiscox
 - & Steve Paterson
- **Leadership & supervision, sequencing & analysis and software & analysis tools**
 - Inigo Martincorena
 - , David L. Robertson
 - , Erik M. Volz
 - , Andrew J. Page
 - & Oliver G. Pybus
- **Leadership & supervision, sequencing & analysis and visualization**
 - Andrew R. Bassett
- **Metadata curation, project administration and samples & logistics**
 - Cristina V. Ariani
 - , Michael H. Spencer Chapman
 - , Kathy K. Li
 - , Rajiv N. Shah
 - , Natasha G. Jesudason
 - & Yusri Taha
- **Metadata curation, project administration and sequencing & analysis**

- Martin P. McHugh
- & Rebecca Dewar
- **Metadata curation, samples & logistics and sequencing & analysis**
 - Aminu S. Jahun
 - , Claire McMurray
 - , Sarojini Pandey
 - , James P. McKenna
 - , Andrew Nelson
 - , Gregory R. Young
 - , Clare M. McCann
 - & Scott Elliott
- **Metadata curation, samples & logistics and visualization**
 - Hannah Lowe
- **Metadata curation, sequencing & analysis and software & analysis tools**
 - Ben Temperton
 - , Sunando Roy
 - , Anna Price
 - , Sara Rey
 - & Matthew Wyles
- **Metadata curation, sequencing & analysis and visualization**
 - Stefan Rooke
 - & Sharif Shaaban
- **Project administration, samples & logistics and sequencing & analysis**
 - Mariateresa de Cesare

- **Project administration, samples & logistics and software & analysis tools**
 - Laura Letchford
- **Project administration, samples & logistics and visualization**
 - Siona Silveira
 - , Emanuela Pelosi
 - & Eleri Wilson-Davies
- **Samples & logistics, sequencing & analysis and software & analysis tools**
 - Myra Hosmillo
- **Sequencing & analysis, software & analysis tools and visualization**
 - Áine O'Toole
 - , Andrew R. Hesketh
 - , Richard Stark
 - , Louis du Plessis
 - , Chris Ruis
 - , Helen Adams
 - & Yann Bourgeois
- **Funding acquisition & leadership and supervision**
 - Stephen L. Michell
 - , Dimitris Gramatopoulos
 - , Jonathan Edgeworth
 - , Judith Breuer
 - , John A. Todd
 - & Christophe Fraser
- **Funding acquisition and project administration**

- David Buck
- & Michaela John
- **Leadership & supervision and metadata curation**
 - Gemma L. Kay
- **Leadership & supervision and project administration**
 - Steve Palmer
 - , Sharon J. Peacock
 - & David Heyburn
- **Leadership & supervision and samples & logistics**
 - Danni Weldon
 - , Esther Robinson
 - , Alan McNally
 - , Peter Muir
 - , Ian B. Vipond
 - , John Boyes
 - , Venkat Sivaprakasam
 - , Tranprit Salluja
 - , Samir Dervisevic
 - & Emma J. Meader
- **Leadership & supervision and sequencing & analysis**
 - Naomi R. Park
 - , Karen Oliver
 - , Aaron R. Jeffries
 - , Sascha Ott
 - , Ana da Silva Filipe
 - , David A. Simpson
 - & Chris Williams

- **Leadership & supervision and visualization**

- Jane A. H. Masoli

- **Metadata curation and samples & logistics**

- Bridget A. Knight
 - , Christopher R. Jones
 - , Cherian Koshy
 - , Amy Ash
 - , Anna Casey
 - , Andrew Bosworth
 - , Liz Ratcliffe
 - , Li Xu-McCrae
 - , Hannah M. Pymont
 - , Stephanie Hutchings
 - , Lisa Berry
 - , Katie Jones
 - , Fenella Halstead
 - , Thomas Davis
 - , Christopher Holmes
 - , Miren Iturriza-Gomara
 - , Anita O. Lucaci
 - , Paul Anthony Randell
 - , Alison Cox
 - , Pinglawathee Madona
 - , Kathryn Ann Harris
 - , Julianne Rose Brown
 - , Tabitha W. Mahungu
 - , Dianne Irish-Tavares
 - , Tanzina Haque
 - , Jennifer Hart
 - , Eric Witele
 - , Melisa Louise Fenton
 - , Steven Liggett
 - , Clive Graham
 - , Emma Swindells

- , Jennifer Collins
- , Gary Eltringham
- , Sharon Campbell
- , Patrick C. McClure
- , Gemma Clark
- , Tim J. Sloan
- , Carl Jones
- & Jessica Lynch

- **Metadata curation and sequencing & analysis**

- Ben Warne
- , Steven Leonard
- , Jillian Durham
- , Thomas Williams
- , Sam T. Haldenby
- , Nathaniel Storey
- , Nabil-Fareed Alikhan
- , Nadine Holmes
- , Christopher Moore
- , Matthew Carlile
- , Malorie Perry
- , Noel Craine
- , Ronan A. Lyons
- , Angela H. Beckett
- , Salman Goudarzi
- , Christopher Fearn
- , Kate Cook
- , Hannah Dent
- & Hannah Paul

- **Metadata curation and software & analysis tools**

- Robert Davies

- **Project administration and samples & logistics**

- Beth Blane
- , Sophia T. Girgis
- , Mathew A. Beale
- , Katherine L. Bellis
- , Matthew J. Dorman
- , Eleanor Drury
- , Leanne Kane
- , Sally Kay
- , Samantha McGuigan
- , Rachel Nelson
- , Liam Prestwood
- , Shavanti Rajatileka
- , Rahul Batra
- , Rachel J. Williams
- , Mark Kristiansen
- , Angie Green
- , Anita Justice
- , Adhyana I. K. Mahanama
- & Buddhini Samaraweera

- **Project administration and sequencing & analysis**
 - Nazreen F. Hadjirin
 - & Joshua Quick
- **Project administration and software & analysis tools**
 - Radoslaw Poplawski
- **Samples & logistics and sequencing & analysis**
 - Leanne M. Kermack
 - , Nicola Reynolds
 - , Grant Hall
 - , Yasmin Chaudhry
 - , Malte L. Pinckert

- , Iliana Georgana
- , Robin J. Moll
- , Alicia Thornton
- , Richard Myers
- , Joanne Stockton
- , Charlotte A. Williams
- , Wen C. Yew
- , Alexander J. Trotter
- , Amy Trebes
- , George MacIntyre-Cockett
- , Alec Birchley
- , Alexander Adams
- , Amy Plimmer
- , Bree Gatica-Wilcox
- , Caoimhe McKerr
- , Ember Hilvers
- , Hannah Jones
- , Hibo Asad
- , Jason Coombes
- , Johnathan M. Evans
- , Laia Fina
- , Lauren Gilbert
- , Lee Graham
- , Michelle Cronin
- , Sara Kumziene-Summerhayes
- , Sarah Taylor
- , Sophie Jones
- , Danielle C. Groves
- , Peijun Zhang
- , Marta Gallis
- & Stavroula F. Louka

- **Samples & logistics and software & analysis tools**
 - Igor Starinskij
- **Sequencing & analysis and software & analysis tools**

- Chris Jackson
- , Marina Gourtovaia
- , Gerry Tonkin-Hill
- , Kevin Lewis
- , Jaime M. Tovar-Corona
- , Keith James
- , Laura Baxter
- , Mohammad T. Alam
- , Richard J. Orton
- , Joseph Hughes
- , Sreenu Vattipally
- , Manon Ragonnet-Cronin
- , Fabricia F. Nascimento
- , David Jorgensen
- , Olivia Boyd
- , Lily Geidelberg
- , Alex E. Zarebski
- , Jayna Raghwani
- , Moritz U. G. Kraemer
- , Joel Southgate
- , Benjamin B. Lindsey
- & Timothy M. Freeman

- **Software & analysis tools and visualization**

- Jon-Paul Keatley
- , Joshua B. Singer
- , Leonardo de Oliveira Martins
- , Corin A. Yeats
- , Khalil Abudahab
- , Ben E. W. Taylor
- & Mirko Menegazzo

- **Leadership & supervision**

- John Danesh

- , Wendy Hogsden
- , Sahar Eldirdiri
- , Anita Kenyon
- , Jenifer Mason
- , Trevor I. Robinson
- , Alison Holmes
- , James Price
- , John A. Hartley
- , Tanya Curran
- , Alison E. Mather
- , Giri Shankar
- , Rachel Jones
- , Robin Howe
- & Sian Morgan

- **Metadata curation**

- Elizabeth Wastenge
- , Michael R. Chapman
- , Siddharth Mookerjee
- , Rachael Stanley
- , Wendy Smith
- , Timothy Peto
- , David Eyre
- , Derrick Crook
- , Gabrielle Vernet
- , Christine Kitchen
- , Huw Gulliver
- , Ian Merrick
- , Martyn Guest
- , Robert Munn
- , Declan T. Bradley
- & Tim Wyatt

- **Project administration**

- Charlotte Beaver
- , Luke Foulser
- , Sophie Palmer
- , Carol M. Churcher
- , Ellena Brooks
- , Kim S. Smith
- , Katerina Galai
- , Georgina M. McManus
- , Frances Bolt
- , Francesc Coll
- , Lizzie Meadows
- , Stephen W. Attwood
- , Alisha Davies
- , Elen De Lacy
- , Fatima Downing
- , Sue Edwards
- , Garry P. Scarlett
- , Sarah Jeremiah
- & Nikki Smith

- **Samples & logistics**

- Danielle Leek
- , Sushmita Sridhar
- , Sally Forrest
- , Claire Cormie
- , Harmeet K. Gill
- , Joana Dias
- , Ellen E. Higginson
- , Mailis Maes
- , Jamie Young
- , Michelle Wantoch
- , Dorota Jamrozy
- , Stephanie Lo
- , Minal Patel
- , Verity Hill
- , Claire M. Bewshea

- , Sian Ellard
- , Cressida Auckland
- , Ian Harrison
- , Chloe Bishop
- , Vicki Chalker
- , Alex Richter
- , Andrew Beggs
- , Angus Best
- , Benita Percival
- , Jeremy Mirza
- , Oliver Megram
- , Megan Mayhew
- , Liam Crawford
- , Fiona Ashcroft
- , Emma Moles-Garcia
- , Nicola Cumley
- , Richard Hopes
- , Patawee Asamaphan
- , Marc O. Niebel
- , Rory N. Gunson
- , Amanda Bradley
- , Alasdair Maclean
- , Guy Mollett
- , Rachel Blacow
- , Paul Bird
- , Thomas Helmer
- , Karlie Fallon
- , Julian Tang
- , Antony D. Hale
- , Louissa R. Macfarlane-Smith
- , Katherine L. Harper
- , Holli Carden
- , Nicholas W. Machin
- , Kathryn A. Jackson
- , Shazaad S. Y. Ahmad
- , Ryan P. George
- , Lance Turtle

- , Elaine O'Toole
- , Joanne Watts
- , Cassie Breen
- , Angela Cowell
- , Adela Alcolea-Medina
- , Themoula Charalampous
- , Amita Patel
- , Lisa J. Levett
- , Judith Heaney
- , Aileen Rowan
- , Graham P. Taylor
- , Divya Shah
- , Laura Atkinson
- , Jack C. D. Lee
- , Adam P. Westhorpe
- , Riaz Jannoo
- , Helen L. Lowe
- , Angeliki Karamani
- , Leah Ensell
- , Wendy Chatterton
- , Monika Pusok
- , Ashok Dadrah
- , Amanda Symmonds
- , Graciela Sluga
- , Zoltan Molnar
- , Paul Baker
- , Stephen Bonner
- , Sarah Essex
- , Edward Barton
- , Debra Padgett
- , Garren Scott
- , Jane Greenaway
- , Brendan A. I. Payne
- , Shirelle Burton-Fanning
- , Sheila Waugh
- , Veena Raviprakash
- , Nicola Sheriff

- , Victoria Blakey
- , Lesley-Anne Williams
- , Jonathan Moore
- , Susanne Stonehouse
- , Louise Smith
- , Rose K. Davidson
- , Luke Bedford
- , Lindsay Coupland
- , Victoria Wright
- , Joseph G. Chappell
- , Theocharis Tsoleridis
- , Jonathan Ball
- , Manjinder Khakh
- , Vicki M. Fleming
- , Michelle M. Lister
- , Hannah C. Howson-Wells
- , Louise Berry
- , Tim Boswell
- , Amelia Joseph
- , Iona Willingham
- , Nichola Duckworth
- , Sarah Walsh
- , Emma Wise
- , Nathan Moore
- , Matilde Mori
- , Nick Cortes
- , Stephen Kidd
- , Rebecca Williams
- , Laura Gifford
- , Kelly Bicknell
- , Sarah Wyllie
- , Allyson Lloyd
- , Robert Impey
- , Cassandra S. Malone
- , Benjamin J. Cogger
- , Nick Levene
- , Lynn Monaghan

- , Alexander J. Keeley
- , David G. Partridge
- , Mohammad Raza
- , Cariad Evans
- & Kate Johnson

- **Sequencing & analysis**

- Emma Betteridge
- , Ben W. Farr
- , Scott Goodwin
- , Michael A. Quail
- , Carol Scott
- , Lesley Shirley
- , Scott A. J. Thurston
- , Diana Rajan
- , Iraad F. Bronner
- , Louise Aigrain
- , Nicholas M. Redshaw
- , Stefanie V. Lensing
- , Shane McCarthy
- , Alex Makunin
- , Carlos E. Balcazar
- , Michael D. Gallagher
- , Kathleen A. Williamson
- , Thomas D. Stanton
- , Michelle L. Michelsen
- , Joanna Warwick-Dugdale
- , Robin Manley
- , Audrey Farbos
- , James W. Harrison
- , Christine M. Sambles
- , David J. Studholme
- , Angie Lackenby
- , Tamyo Mbisa
- , Steven Platt
- , Shahjahan Miah

- , David Bibby
- , Carmen Manso
- , Jonathan Hubb
- , Gavin Dabrera
- , Mary Ramsay
- , Daniel Bradshaw
- , Ulf Schaefer
- , Natalie Groves
- , Eileen Gallagher
- , David Lee
- , David Williams
- , Nicholas Ellaby
- , Hassan Hartman
- , Nikos Manesis
- , Vineet Patel
- , Juan Ledesma
- , Katherine A. Twohig
- , Elias Allara
- , Clare Pearson
- , Jeffrey K. J. Cheng
- , Hannah E. Bridgewater
- , Lucy R. Frost
- , Grace Taylor-Joyce
- , Paul E. Brown
- , Lily Tong
- , Alice Broos
- , Daniel Mair
- , Jenna Nichols
- , Stephen N. Carmichael
- , Katherine L. Smollett
- , Kyriaki Nomikou
- , Elihu Aranday-Cortes
- , Natasha Johnson
- , Seema Nickbakhsh
- , Edith E. Vamos
- , Margaret Hughes
- , Lucille Rainbow

- , Richard Eccles
- , Charlotte Nelson
- , Mark Whitehead
- , Richard Gregory
- , Matthew Gemmell
- , Claudia Wierzbicki
- , Hermione J. Webster
- , Chloe L. Fisher
- , Adrian W. Signell
- , Gilberto Betancor
- , Harry D. Wilson
- , Gaia Nebbia
- , Flavia Flaviani
- , Alberto C. Cerda
- , Tammy V. Merrill
- , Rebekah E. Wilson
- , Marius Cotic
- , Nadua Bayzid
- , Thomas Thompson
- , Erwan Acheson
- , Steven Rushton
- , Sarah O'Brien
- , David J. Baker
- , Steven Rudder
- , Alp Aydin
- , Fei Sang
- , Johnny Debebe
- , Sarah Francois
- , Tetyana I. Vasylyeva
- , Marina Escalera Zamudio
- , Bernardo Gutierrez
- , Angela Marchbank
- , Joshua Maksimovic
- , Karla Spellman
- , Kathryn McCluggage
- , Mari Morgan
- , Robert Beer

- , Safiah Afifi
- , Trudy Workman
- , William Fuller
- , Catherine Bresner
- , Adrienn Angyal
- , Luke R. Green
- , Paul J. Parsons
- , Rachel M. Tucker
- , Rebecca Brown
- & Max Whiteley

- **Software & analysis tools**

- James Bonfield
- , Christoph Puethe
- , Andrew Whitwham
- , Jennifer Liddle
- , Will Rowe
- , Igor Siveroni
- , Thanh Le-Viet
- & Amy Gaskin

- **Visualization**

- Rob Johnson

- **Wellcome Sanger Centre**

- Irina Abnizova
- , Louise Aigrain
- , Alex Alderton
- , Mozam Ali
- , Laura Allen
- , Roberto Amato
- , Ralph Anderson
- , Cristina Ariani

- , Siobhan Austin-Guest
- , Sendu Bala
- , Jeffrey Barrett
- , Andrew Bassett
- , Kristina Battleday
- , James Beal
- , Mathew Beale
- , Charlotte Beaver
- , Sam Bellany
- , Tristram Bellerby
- , Katie Bellis
- , Duncan Berger
- , Matt Berriman
- , Emma Betteridge
- , Paul Bevan
- , Simon Binley
- , Jason Bishop
- , Kirsty Blackburn
- , James Bonfield
- , Nick Boughton
- , Sam Bowker
- , Timothy Brendler-Spaeth
- , Iraad Bronner
- , Tanya Brooklyn
- , Sarah Kay Buddenborg
- , Robert Bush
- , Catarina Caetano
- , Alex Cagan
- , Nicola Carter
- , Joanna Cartwright
- , Tiago Carvalho Monteiro
- , Liz Chapman
- , Tracey-Jane Chillingworth
- , Peter Clapham
- , Richard Clark
- , Adrian Clarke
- , Catriona Clarke

- , Daryl Cole
- , Elizabeth Cook
- , Maria Coppola
- , Linda Cornell
- , Clare Cornwell
- , Craig Corton
- , Abby Crackett
- , Alison Cranage
- , Harriet Craven
- , Sarah Craw
- , Mark Crawford
- , Tim Cutts
- , Monika Dabrowska
- , Matt Davies
- , Robert Davies
- , Joseph Dawson
- , Callum Day
- , Aiden Densem
- , Thomas Dibling
- , Cat Dockree
- , David Dodd
- , Sunil Dogga
- , Matthew Dorman
- , Gordon Dougan
- , Martin Dougherty
- , Alexander Dove
- , Lucy Drummond
- , Eleanor Drury
- , Monika Dudek
- , Jillian Durham
- , Laura Durrant
- , Elizabeth Easthope
- , Sabine Eckert
- , Pete Ellis
- , Ben Farr
- , Michael Fenton
- , Marcella Ferrero

- , Neil Flack
- , Howard Fordham
- , Grace Forsythe
- , Luke Foulser
- , Matt Francis
- , Audrey Fraser
- , Adam Freeman
- , Anastasia Galvin
- , Maria Garcia-Casado
- , Alex Gedny
- , Sophia Girgis
- , James Glover
- , Sonia Goncalves
- , Scott Goodwin
- , Oliver Gould
- , Marina Gourtovaia
- , Andy Gray
- , Emma Gray
- , Coline Griffiths
- , Yong Gu
- , Florence Guerin
- , Will Hamilton
- , Hannah Hanks
- , Ewan Harrison
- , Alexandria Harrott
- , Edward Harry
- , Julia Harvison
- , Paul Heath
- , Anastasia Hernandez-Koutoucheva
- , Rhiannon Hobbs
- , Dave Holland
- , Sarah Holmes
- , Gary Hornett
- , Nicholas Hough
- , Liz Huckle
- , Lena Hughes-Hallet
- , Adam Hunter

- , Stephen Inglis
- , Sameena Iqbal
- , Adam Jackson
- , David Jackson
- , Keith James
- , Dorota Jamrozy
- , Carlos Jimenez Verdejo
- , Ian Johnston
- , Matthew Jones
- , Kalyan Kallepally
- , Leanne Kane
- , Keely Kay
- , Sally Kay
- , Jon Keatley
- , Alan Keith
- , Alison King
- , Lucy Kitchin
- , Matt Kleanthous
- , Martina Klimekova
- , Petra Korlevic
- , Ksenia Krasheninnkova
- , Dominic Kwiatkowski
- , Greg Lane
- , Cordelia Langford
- , Adam Laverack
- , Katharine Law
- , Mara Lawniczak
- , Stefanie Lensing
- , Steven Leonard
- , Laura Letchford
- , Kevin Lewis
- , Amanah Lewis-Wade
- , Jennifer Liddle
- , Quan Lin
- , Sarah Lindsay
- , Sally Linsdell
- , Rich Livett

- , Stephanie Lo
- , Rhona Long
- , Jamie Lovell
- , Jon Lovell
- , Catherine Ludden
- , James Mack
- , Mark Maddison
- , Aleksei Makunin
- , Irfan Mamun
- , Jenny Mansfield
- , Neil Marriott
- , Matt Martin
- , Inigo Martincorena
- , Matthew Mayho
- , Shane McCarthy
- , Jo McClintock
- , Samantha McGuigan
- , Sandra McHugh
- , Liz McMinn
- , Carl Meadows
- , Emily Mobley
- , Robin Moll
- , Maria Morra
- , Leanne Morrow
- , Kathryn Murie
- , Sian Nash
- , Claire Nathwani
- , Plamena Naydenova
- , Alexandra Neaverson
- , Rachel Nelson
- , Ed Nerou
- , Jon Nicholson
- , Tabea Nimz
- , Guillaume G. Noell
- , Sarah O'Meara
- , Valeriu Ohan
- , Karen Oliver

- , Charles Olney
- , Doug Ormond
- , Agnes Oszlanczi
- , Steve Palmer
- , Yoke Fei Pang
- , Barbora Pardubska
- , Naomi Park
- , Aaron Parmar
- , Gaurang Patel
- , Minal Patel
- , Maggie Payne
- , Sharon Peacock
- , Arabella Petersen
- , Deborah Plowman
- , Tom Preston
- , Liam Prestwood
- , Christoph Puethe
- , Michael Quail
- , Diana Rajan
- , Shavanti Rajatileka
- , Richard Rance
- , Suzannah Rawlings
- , Nicholas Redshaw
- , Joe Reynolds
- , Mark Reynolds
- , Simon Rice
- , Matt Richardson
- , Connor Roberts
- , Katrina Robinson
- , Melanie Robinson
- , David Robinson
- , Hazel Rogers
- , Eduardo Martin Rojo
- , Daljit Roopra
- , Mark Rose
- , Luke Rudd
- , Ramin Sadri

- , Nicholas Salmon
- , David Saul
- , Frank Schwach
- , Carol Scott
- , Phil Seekings
- , Lesley Shirley
- , John Sillitoe
- , Alison Simms
- , Matt Sinnott
- , Shanthi Sivadasan
- , Bart Siwek
- , Dale Sizer
- , Kenneth Skeldon
- , Jason Skelton
- , Joanna Slater-Tunstill
- , Lisa Sloper
- , Nathalie Smerdon
- , Chris Smith
- , Christen Smith
- , James Smith
- , Katie Smith
- , Michelle Smith
- , Sean Smith
- , Tina Smith
- , Leighton Sneade
- , Carmen Diaz Soria
- , Catarina Sousa
- , Emily Souster
- , Andrew Sparkes
- , Michael Spencer-Chapman
- , Janet Squares
- , Robert Stanley
- , Claire Steed
- , Tim Stickland
- , Ian Still
- , Mike Stratton
- , Michelle Strickland

- , Allen Swann
- , Agnieszka Swiatkowska
- , Neil Sycamore
- , Emma Swift
- , Edward Symons
- , Suzanne Szluha
- , Emma Taluy
- , Nunu Tao
- , Katy Taylor
- , Sam Taylor
- , Stacey Thompson
- , Mark Thompson
- , Mark Thomson
- , Nicholas Thomson
- , Scott Thurston
- , Gerry Tonkin-Hill
- , Dee Toombs
- , Benjamin Topping
- , Jaime Tovar-Corona
- , Daniel Ungureanu
- , James Uphill
- , Jana Urbanova
- , Philip Jansen Van
- , Valerie Vancollie
- , Paul Voak
- , Danielle Walker
- , Matthew Walker
- , Matt Waller
- , Gary Ward
- , Charlie Weatherhogg
- , Niki Webb
- , Danni Weldon
- , Alan Wells
- , Eloise Wells
- , Luke Westwood
- , Theo Whipp
- , Thomas Whiteley

- , Georgia Whitton
- , Andrew Whitwham
- , Sara Widaa
- , Mia Williams
- , Mark Wilson
- & Sean Wright

Contributions

D.C., R.K.G. and D.A.C. conceived the study. R.K.G., D.A.C., L.E.M., J. Bassi, M.W., L.C.-G., G.B.-M., R.D., B.G., N.K., A.E., M.S.P., D.V., L.P., A.D.M., J.R.B. and D.C. designed the study and experiments. B.M., D.A.C., N.T., R.P.D., I.A.T.M.F., A.C.W., L.C.-G., S.A.K. and G.B.-M. performed experiments. R.K.G., D.A.C., B.M., R.D., I.A.T.M.F., A.C.W., L.E.M., J. Bassi, K.G.C.S. and D.V. interpreted data. A.D.M., and C.S.F. carried out pseudovirus neutralization assays. D.P. produced pseudoviruses. M.S.P., L.P., W.H., D.V. and D.C. designed the experiments. M.A.T., J. Bassi and S.J. expressed and purified the proteins. K.C., S.J. and E.C. sequenced and expressed antibodies. E.C. and K.C. performed mutagenesis to create mutant expression plasmids. A.C.W. and S.B. performed binding assays. A.R., A.F.P. and C.G. contributed to the recruitment of donors and collection of samples related to the isolation of monoclonal antibodies. H.W.V., G.S., A.L., D.V., L.P., D.V. and D.C. analysed the data and prepared the manuscript with input from all authors.

Corresponding authors

Correspondence to [Davide Corti](#) or [Ravindra K. Gupta](#).

Ethics declarations

Competing interests

A.D.M., J. Bassi, D.P., C.S.F., S.B., K.C., N.S., E.C., G.S., S.J., A.L., H.W.V., M.S.P., L.P. and D.C. are employees of Vir Biotechnology and may hold shares in Vir Biotechnology. H.W.V. is a founder of PierianDx and

Casma Therapeutics. Neither company provided funding for this work or is performing related work. D.V. is a consultant for Vir Biotechnology. The Veesler laboratory has received a sponsored research agreement from Vir Biotechnology. R.K.G. has received consulting fees from UMOVIS Lab, Gilead and ViiV. The other authors declare no competing interests.

Additional information

Peer review information *Nature* thanks the anonymous reviewers for their contribution to the peer review of this work. Peer reviewer reports are available.

Publisher's note Springer Nature remains neutral with regard to jurisdictional claims in published maps and institutional affiliations.

Extended data figures and tables

Extended Data Fig. 1 Immune responses three weeks after first dose of the BNT162b2 vaccine against SARS-CoV-2.

a, Serum IgG responses against the N protein, spike protein and the RBD of the spike protein of participants who received one vaccine dose (light green) or two vaccine doses (dark green), patients who had recovered from COVID-19 (red) and healthy control individuals (grey) were measured by a flow-cytometry-based Luminex assay. $n = 25$. MFI, mean fluorescence intensity. Data are $\text{GMT} \pm \text{s.d.}$ (lines and error bars) of two technical repeats and individual values (circles). **b**, Relationship between serum IgG responses, measured by flow cytometry, and serum neutralization ID_{50} . $n = 25$. **c**, Relationship between serum neutralization ID_{50} and T cell responses against SARS-CoV-2 by IFN γ FluoroSpot. $n = 24$. SFU, spot-forming units. **d**, Relationship between serum IgG responses and T cell responses. $n = 23$. **b-d**, Simple linear regressions are shown with Pearson correlation (r), P value (p) and regression coefficient/slope (β).

Extended Data Fig. 2 Neutralization by the first dose of the BNT162b2 vaccine and convalescent sera against the wild-type and mutant (N501Y, A570D, ΔH69/ΔV70) SARS-CoV-2-pseudotyped viruses.

a, b, Dilution of the vaccine sera for 50% neutralization against the wild-type and spike mutant (N501Y, A570D, ΔH69/ΔV70) viruses. **b**, Data are GMT ± s.d. (lines and error bars) of two independent experiments with two technical repeats and individual values (circles). Two-tailed Wilcoxon matched-pairs signed-rank test with no adjustment for multiple comparisons; *** $P < 0.001$. **c, d**, Dilution of convalescent sera for 50% neutralization against the wild-type and spike mutant (N501Y, A570D, ΔH69/ΔV70) viruses. Data are GMT ± s.d. (dotted lines and error bars) of a representative experiment with two technical repeats and individual values (circles). Two-tailed Wilcoxon matched-pairs signed-rank test with no adjustment for multiple comparisons; ns, not significant. **e**, Representative curves of \log_{10} -transformed inverse dilutions of convalescent sera against the percentage of neutralization for the wild-type and spike mutant (N501Y, A570D, ΔH69/ΔV70) viruses. In cases in which a curve is shifted to the right the virus is less sensitive to the neutralizing antibodies in the serum. Data are mean ± s.e.m. of two technical replicates. Data are representative of two independent experiments. The cut-off for 50% neutralization was set to 4 (dotted lines in **a, b**). **a, c**, Data points of the same individual are connected by lines.

Extended Data Fig. 3 Representative neutralization curves of sera from individuals vaccinated with the BNT162b2 vaccine against pseudotyped virus bearing eight mutations in the spike protein that are present in the B.1.1.7 variant compared with the wild-type virus.

All virus variants were in a spike(D614G) background. The \log_{10} -transformed inverse dilutions of the sera are shown against the percentage of neutralization. In cases in which a curve is shifted to the right the virus is less sensitive to the neutralizing antibodies in the serum. Data are for the

first dose of vaccine (D1). Data are mean \pm s.e.m. representative of two independent experiments each with two technical replicates.

Extended Data Fig. 4 Representative neutralization curves of convalescent sera against wild-type and B.1.1.7 spike-mutant SARS-CoV-2 pseudotyped viruses.

The \log_{10} -transformed inverse dilutions of the sera are shown against the percentage of neutralization. In cases in which a curve is shifted to the right the virus is less sensitive to the neutralizing antibodies in the serum. Data are mean \pm s.e.m. representative of two independent experiments each with two technical replicates.

Extended Data Fig. 5 Neutralization potency of mRNA vaccine sera and convalescent sera (before SARS-CoV-2 B.1.1.7) against pseudotyped virus bearing spike mutations in the B.1.1.7 lineage with and without the E484K substitution in the RBD.

All virus variants were in a spike(D614G) background. Neutralization potency of the sera from the first (left; $n = 37$) and the second (middle, $n = 21$) vaccine dose and of convalescent plasma (CP) (right; $n = 27$) against wild-type SARS-CoV-2, the B.1.1.7 variant with spike(N501Y, A570D, Δ H69/ Δ V70, Δ 144, P681H, T716I, S982A, D1118H) and the B.1.1.7 variant with spike(N501Y, A570D, Δ H69/ Δ V70, Δ 144, P681H, T716I, S982A, D1118H) and the additional E484K substitution. Data are GMT \pm s.d. representative of two independent experiments each with two technical repeats. Wilcoxon matched-pairs signed-rank test; ** $P < 0.01$, *** $P < 0.001$, **** $P < 0.0001$.

Extended Data Fig. 6 Neutralization of the wild-type spike(D614G), B.1.1.7 spike and spike(N501Y, E484K, K417N) proteins of the SARS-CoV-2-pseudotyped virus by a panel of 57 monoclonal antibodies.

a–c, Neutralization of the wild-type spike (black), B.1.1.7 spike (blue) and spike(N501Y, E484K, K417N) (TM) (red) SARS-CoV-2–MLV by 9 NTD-targeting (**a**), 29 RBM-targeting (**b**) and 19 non-RBM-targeting (**c**) monoclonal antibodies. Data are mean ± s.d. of two technical replicates from one representative experiment.

Extended Data Fig. 7 Kinetics of binding to the RBD of wild-type and spike(N501Y) SARS-CoV-2 for 43 RBD-specific monoclonal antibodies.

a–b, a, b, Binding to the RBD of wild-type (black) and spike(N501Y) (blue) SARS-CoV-2 by 22 RBM-targeting (**a**) and 21 non-RBM-targeting (**b**) monoclonal antibodies. An antibody of irrelevant specificity was included as a negative control.

Extended Data Fig. 8 Kinetics of binding to the RBD of wild-type and spike(E484K) SARS-CoV-2 for 46 RBD-specific monoclonal antibodies.

a, b, Binding to the RBD of wild-type (black) and spike(E484K) (red) SARS-CoV-2 by 27 RBM-targeting (**a**) and 19 non-RBM-targeting (**b**) monoclonal antibodies. An antibody of irrelevant specificity was included as a negative control.

Extended Data Fig. 9 Binding of human ACE2 to the RBDs of the wild-type SARS-CoV-2 spike, spike(N501Y) and spike(N501Y, E484K, K417N) proteins.

a–c, Biolayer interferometry binding analysis of the human ACE2 (huACE2) ectodomain (residues 1–615) to immobilized RBD of wild-type SARS-CoV-2 (**a**) and the RBD of B.1.1.7 spike(N501Y) (**b**) and spike (N501Y, E484K, K417N) proteins (**c**). Black lines correspond to a global fit of the data using a 1:1 binding model.

Extended Data Table 1 Kinetic analysis of human ACE2 binding to RBDs of SARS-CoV-2

[Full size table](#)

Supplementary information

[Supplementary Table 1](#)

Neutralization, V gene usage and other properties of tested mAbs.

[Reporting Summary](#)

[Supplementary Table 2](#)

GISAID acknowledgements.

[Peer Review File](#)

Rights and permissions

[Reprints and Permissions](#)

About this article



Check for
updates

Cite this article

Collier, D.A., De Marco, A., Ferreira, I.A.T.M. *et al.* Sensitivity of SARS-CoV-2 B.1.1.7 to mRNA vaccine-elicited antibodies. *Nature* **593**, 136–141 (2021). <https://doi.org/10.1038/s41586-021-03412-7>

[Download citation](#)

- Received: 26 January 2021

- Accepted: 01 March 2021
- Published: 11 March 2021
- Issue Date: 06 May 2021
- DOI: <https://doi.org/10.1038/s41586-021-03412-7>

Further reading

- **Will SARS-CoV-2 variants of concern affect the promise of vaccines?**
 - Ravindra K. Gupta
- Nature Reviews Immunology (2021)
- **Molecular Aspects Concerning the Use of the SARS-CoV-2 Receptor Binding Domain as a Target for Preventive Vaccines**
 - Yury Valdes-Balbin
 - , Darielys Santana-Mederos
 - , Françoise Paquet
 - , Sonsire Fernandez
 - , Yanet Climent
 - , Fabrizio Chiodo
 - , Laura Rodríguez
 - , Belinda Sanchez Ramirez
 - , Kalet Leon
 - , Tays Hernandez
 - , Lila Castellanos-Serra
 - , Raine Garrido
 - , Guang-Wu Chen
 - , Dagmar Garcia-Rivera
 - , Daniel G. Rivera

- & Vicente Verez-Bencomo

ACS Central Science (2021)

- **The Challenge of Emerging SARS-CoV-2 Mutants to Vaccine Development**

- Rong Li
- , Jun Liu
- & Hui Zhang

Journal of Genetics and Genomics (2021)

- **BNT162b2 vaccination effectively prevents the rapid rise of SARS-CoV-2 variant B.1.1.7 in high-risk populations in Israel**

- Ariel Munitz
- , Matan Yechezkel
- , Yoav Dickstein
- , Dan Yamin
- & Motti Gerlic

Cell Reports Medicine (2021)

- **Pandemic moves and countermoves: vaccines and viral variants**

- Rogier W Sanders
- & Menno D de Jong

The Lancet (2021)

Comments

By submitting a comment you agree to abide by our [Terms](#) and [Community Guidelines](#). If you find something abusive or that does not comply with our terms or guidelines please flag it as inappropriate.

[Download PDF](#)

This article was downloaded by **calibre** from <https://www.nature.com/articles/s41586-021-03412-7>

| [Section menu](#) | [Main menu](#) |

Escape of SARS-CoV-2 501Y.V2 from neutralization by convalescent plasma

[Download PDF](#)

- Article
- [Published: 29 March 2021](#)

Escape of SARS-CoV-2 501Y.V2 from neutralization by convalescent plasma

- [Sandile Cele^{1,2}](#),
- [Inbal Gazy^{2,3,4}](#),
- [Laurelle Jackson¹](#),
- [Shi-Hsia Hwa^{1,5}](#),
- [Hourriyah Tegally³](#),
- [Gila Lustig⁶](#),
- [Jennifer Giandhari³](#),
- [Sureshnee Pillay³](#),
- [Eduan Wilkinson³](#),
- [Yeshnee Naidoo³](#),
- [Farina Karim^{1,2}](#),
- [Yashica Ganga¹](#),
- [Khadija Khan¹](#),
- [Mallory Bernstein¹](#),
- [Alejandro B. Balazs⁷](#),
- [Bernadett I. Gosnell⁸](#),
- [Willem Hanekom^{1,5}](#),
- [Mahomed-Yunus S. Moosa⁸](#),
- [Network for Genomic Surveillance in South Africa](#),
- [COMMIT-KZN Team](#),
- [Richard J. Lessells](#) ORCID: [orcid.org/0000-0003-0926-710X^{3,6}](https://orcid.org/0000-0003-0926-710X),
- [Tulio de Oliveira](#) ORCID: [orcid.org/0000-0002-3027-5254^{3,6,9}](https://orcid.org/0000-0002-3027-5254) &
- [Alex Sigal](#) ORCID: [orcid.org/0000-0001-8571-2004^{1,2,10}](https://orcid.org/0000-0001-8571-2004)

[Nature](#) volume 593, pages142–146(2021)[Cite this article](#)

- 28k Accesses

- 7 Citations
- 555 Altmetric
- [Metrics details](#)

Subjects

- [SARS-CoV-2](#)
- [Viral evolution](#)

Abstract

SARS-CoV-2 variants of concern (VOC) have arisen independently at multiple locations^{1,2} and may reduce the efficacy of current vaccines that target the spike glycoprotein of SARS-CoV-2³. Here, using a live-virus neutralization assay, we compared the neutralization of a non-VOC variant with the 501Y.V2 VOC (also known as B.1.351) using plasma collected from adults who were hospitalized with COVID-19 during the two waves of infection in South Africa, the second wave of which was dominated by infections with the 501Y.V2 variant. Sequencing demonstrated that infections of plasma donors from the first wave were with viruses that did not contain the mutations associated with 501Y.V2, except for one infection that contained the E484K substitution in the receptor-binding domain. The 501Y.V2 virus variant was effectively neutralized by plasma from individuals who were infected during the second wave. The first-wave virus variant was effectively neutralized by plasma from first-wave infections. However, the 501Y.V2 variant was poorly cross-neutralized by plasma from individuals with first-wave infections; the efficacy was reduced by 15.1-fold relative to neutralization of 501Y.V2 by plasma from individuals infected in the second wave. By contrast, cross-neutralization of first-wave virus variants using plasma from individuals with second-wave infections was more effective, showing only a 2.3-fold decrease relative to neutralization of first-wave virus variants by plasma from individuals infected in the first wave. Although we tested only one plasma sample from an individual infected with a SARS-CoV-2 variant with only the E484K substitution, this plasma sample potently neutralized both variants. The observed effective neutralization of first-wave virus by plasma from individuals infected with 501Y.V2 provides preliminary evidence that vaccines based on VOC sequences could retain activity against other circulating SARS-CoV-2 lineages.

[Download PDF](#)

Main

Through genomic surveillance of SARS-CoV-2, a number of new variants have been identified with multiple mutations in the spike glycoprotein. We recently described the emergence of the 501Y.V2 variant in South Africa, which is characterized by substitutions (K417N, E484K and N501Y) in the receptor-binding domain (RBD) of the spike protein as well as by substitutions and a deletion in the N-terminal domain (NTD)¹. This variant was first detected in October 2020, and has rapidly become the dominant variant in South Africa with a frequency in January 2021 of 97% according to GISAID (<https://www.gisaid.org/hcov19-mutation-dashboard/>).

The RBD is the main target of neutralizing antibodies elicited by infection with SARS-CoV-2, with the remaining activity directed against the NTD^{4,5}. All three amino acid residues associated with the substitutions in the RBD in 501Y.V2 interact directly with the human angiotensin-converting enzyme 2 (ACE2) receptor⁶. The E484 residue specifically is a hotspot for the binding of highly potent neutralizing antibodies⁶. In a number of separate in vitro studies using monoclonal antibodies, mutations that cause substitutions at E484 have emerged as immune escape mutations and conferred broad cross-resistance to panels of monoclonal antibodies and to convalescent plasma neutralization^{7,8,9,10}. The E484K substitution also emerged during the passaging of live SARS-CoV-2 in Vero E6 cells in the presence of convalescent plasma, leading to a substantial reduction in neutralization¹¹. Using a deep mutation-scanning approach to determine the effect of individual mutations on neutralization by polyclonal sera, substitutions at E484 were associated with the largest decreases in neutralization¹².

South Africa has experienced two waves of SARS-CoV-2 infections to date (<https://coronavirus.jhu.edu/map.html>). The first wave peaked in July 2020 and consisted of viral variants that usually showed the D614G substitution but had none of the defining mutations of 501Y.V2. These variants have been almost completely replaced by 501Y.V2 variants in the second wave of infections in South Africa, which peaked in January 2021.

Coinciding with our initial report, there have been multiple studies that showed that 501Y.V2 decreases the neutralization capacity of polyclonal antibodies that have been elicited by infection with non-VOC SARS-CoV-2 or by vaccination^{13,14,15,16,17,18,19,20,21,22}. This decrease ranges from relatively moderate^{13,14,15,16} to severe^{17,18,19,20,21,22}. Notably, three clinical trials performed in South Africa during the second wave, which include infections with 501Y.V2, reported considerable decreases in vaccine efficacy. The NVX-CoV2373 subunit vaccine (Novavax) showed a decrease in efficacy from 89.3% to 49.4% (<https://ir.novavax.com/news-releases/news-release-details/novavax-covid-19-vaccine->

[demonstrates-893-efficacy-uk-phase-3](#)). This trial also reported no differences in infection frequency between SARS-CoV-2-seropositive and SARS-CoV-2-seronegative participants in the placebo arm, indicating that infection with variants other than 501Y.V2 does not protect against re-infection with 501Y.V2. Details of the seroprevalence testing are not available at the time of publication of this study. The adenovirus-vectored single-dose vaccine (Johnson and Johnson) showed a reduced efficacy from 72% in the USA to 57% in South Africa (<https://www.jnj.com/johnson-johnson-announces-single-shot-janssen-covid-19-vaccine-candidate-met-primary-endpoints-in-interim-analysis-of-its-phase-3-ensemble-trial>). Importantly, the ChAdOx1 AZD1222 chimpanzee adenovirus-vectored vaccine (AstraZeneca) showed only 10% efficacy against the 501Y.V2 variant, compared with an efficacy of 75% against earlier variants in South Africa³. The rollout of this vaccine in South Africa is currently paused.

Here, using a live-virus neutralization assay, we measured the degree to which the 501Y.V2 virus variant compromises neutralization elicited by natural infection with variants other than 501Y.V2 circulating in South Africa. We also measured the degree to which the earlier variants could escape the neutralizing response elicited by 501Y.V2 virus (Fig. 1a). We used plasma samples from our ongoing longitudinal cohort that tracks cases of COVID-19 who were enrolled at hospitals in Durban, South Africa²³. We sampled participants weekly for the first month after enrolment. At each time point, a blood draw and combined nasopharyngeal and oropharyngeal swab were performed to obtain both plasma and the infecting virus. Swabs positive for SARS-CoV-2 were sequenced.

Fig. 1: Study design and sequences of SARS-CoV-2 variants.

 **figure1**

a, We obtained convalescent plasma and sequenced the matching infecting virus from individuals with COVID-19 during the first and second waves of SARS-CoV-2 infections in South Africa. A variant that lacked the mutations in the RBD and NTD of 501Y.V2 was expanded from one participant infected in the first wave of infections in South Africa, and 501Y.V2 was expanded from a participant at the beginning of the second wave. Live-virus neutralization was assessed using a focus-forming assay. Conditions were: neutralization of non-VOC virus by plasma elicited against first-wave, non-VOC virus, neutralization of 501Y.V2 virus by plasma elicited against 501Y.V2 virus, neutralization of 501Y.V2 virus by plasma elicited against first-wave non-VOC virus, and neutralization of non-VOC virus by plasma elicited against 501Y.V2. **b**, Top, phylogenetic relationships and mutations in the virus sequences. Variants that elicited the antibody immunity in the plasma samples are highlighted in green boxes. Variants that were expanded are highlighted in magenta boxes. The y axis denotes the time of sampling. Bottom, substitutions and deletions that are present in the spike protein of the SARS-CoV-2 expanded variants used in the live-virus neutralization assay. See Supplementary Table 1 for a complete list of mutations in the viral genomes of variants that elicited plasma immunity and the expanded variants.

[Full size image](#)

We chose plasma from 14 participants from the first wave of infections in South Africa for whom the infecting virus was successfully sequenced (Methods). Plasma samples were from blood drawn approximately one month after the onset of symptoms (Extended Data Table 1), close to the peak in the antibody response²⁴. Of the 14 participants, 13 did not show mutations in the RBD or NTD of the infecting virus. A

single participant sampled in October 2020 showed the escape mutation that leads to the E484K substitution in the absence of the other changes associated with 501Y.V2 (Supplementary Table 1). We had fewer participants from the second wave of infection at the time of writing as most participants had not yet reached the time point for sampling of one month after the onset of symptoms. The participants from the second wave in this study were infected in late December 2020 or early January 2021 (Fig. 1b and Extended Data Table 1). We were able to sequence the virus from three participants of the second wave for which the obtained sequences enabled variant calling, two of which had good coverage of the spike gene (Fig. 1b and Supplementary Table 1). In all cases, the infecting variant was 501Y.V2. It is extremely likely that 501Y.V2 was also the infecting variant for the rest of the participants from the second wave of infections, given the complete dominance of this variant in January 2021. For each participant from the second wave, our clinical team conducted a telephone interview and examined clinical records to determine whether the participant was also infected during the first wave of infections in South Africa. None of the participants showed evidence of being previously infected.

We expanded a first-wave virus (Methods) from one participant during the first wave of infections as well as a 501Y.V2 virus from a sample obtained during the second wave in November 2020 through our genomic surveillance programme (Fig. 1b). We used a microneutralization live-virus focus-forming assay²⁵, which relies on a methylcellulose overlay to limit cell-free spread of the virus. This results in a local infection focus that represents one infectious unit of the virus. The focus is detected by an anti-SARS-CoV-2 spike antibody (Methods). We normalized the number of foci to the number of foci in the absence of plasma on the same plate to obtain the transmission index (Tx)²⁶. This controls for the experimental variability in the input virus dose between experiments. We mixed the virus with serially diluted plasma, then added the mixture to Vero E6 cells and counted the number of infection foci after 28 h using automated image analysis (Fig. 2a, Methods and Extended Data Fig. 1a).

Fig. 2: Neutralization of first-wave and 501Y.V2 variants by convalescent plasma elicited by first-wave and 501Y.V2 infections.

 **figure2**

a, Focus formation by first-wave and 501Y.V2 virus variants. To obtain similar focus sizes, the incubation time with 501Y.V2 was reduced to 18 h. Scale bar, 2 mm. **b, c**, A representative focus-forming assay using plasma from participant 039-13-0015, who was infected with a first-wave variant (**b**), and participant 039-02-0033, who was infected with 501Y.V2 (**c**). Columns are plasma dilutions—which range from 1:25 to 1:1,600—a plasma pool from three uninfected individuals (control) and a no-plasma control (no plasma). **d**, Quantified neutralization per participant for the first-wave virus variants (left two plots) and 501Y.V2 (right two plots). Red points are neutralization by the A02051 neutralizing antibody (NAb), grey points show

neutralization by the plasma pool from uninfected individuals (control), green points indicate neutralization by plasma from the participant who was infected with the S(E484K)-mutant virus, orange points are neutralization by plasma from participants who were infected by first-wave variants, and blue points are neutralization by plasma from participants who were infected with 501Y.V2. Data are mean and s.e.m. of 3–4 independent experiments per plasma sample of participants convalescing from infection with the first-wave ($n = 14$) or 501Y.V2 ($n = 6$) virus variants or 10 independent experiments for A02051 and uninfected plasma controls. Solid lines of the corresponding colour are fitted values using a sigmoidal equation. From left to right, the plots show the following analyses. First plot, neutralization of the first-wave virus by the neutralizing antibody A02051 ($\text{PRNT}_{50} = 6.5 \text{ ng ml}^{-1}$; 95% confidence intervals, $3.9\text{--}9.1 \text{ ng ml}^{-1}$) and control plasma. Second plot, neutralization of first-wave virus by plasma from participants convalescing from infection with first-wave or 501Y.V2 viruses. Third plot, neutralization of the 501Y.V2 variant by the neutralizing antibody A02051 ($\text{PRNT}_{50} = 3.5 \text{ ng ml}^{-1}$ ($2.9\text{--}4.1 \text{ ng ml}^{-1}$)) and control plasma. Fourth plot, neutralization of the 501Y.V2 variant by plasma from participants convalescing from infection with first-wave or 501Y.V2 viruses. e, Decrease in PRNT_{50} in cross-neutralization. Left, neutralization of first-wave or 501Y.V2 virus variants by first-wave plasma. Right, neutralization of 501Y.V2 or first-wave virus variants by second-wave plasma. The fold change was calculated as PRNT_{50} of the homologous virus/ PRNT_{50} of the heterologous virus and ranged from 3.2 to 41.9 for first-wave plasma, and from 1.6 to 7.2 for second-wave plasma. The fold change in PRNT_{50} elicited by the S(E484K)-mutant virus was excluded.

[Full size image](#)

There was a clear reduction in the neutralization capacity of plasma from participants with first-wave infections against 501Y.V2 relative to the neutralization of the homologous, first-wave variant (Extended Data Fig. 1). 501Y.V2 also showed larger foci, which is probably caused by a larger number of cells being infected by one infected cell or by more rapid infection cycles (Fig. 2a, Extended Data Fig. 1a). To compare foci of a similar size, we reduced the incubation time of cells infected with 501Y.V2 to 18 h (Fig. 2a). To investigate whether plasma from first-wave samples had any effects on the 501Y.V2 variant, we tested more-concentrated plasma (Fig. 2b). To rule out infection-saturation effects, we obtained a positive-control monoclonal antibody with a similar neutralization efficacy against first-wave and 501Y.V2 variants. We then repeated the experiments (Extended Data Figs. 2–4 show representative neutralization experiments for plasma from each participant).

We observed the same trend in neutralization capacity as with the first set of experiments: there was a decrease in the number of foci when plasma elicited against

first-wave infections was added to the homologous, first-wave virus. This decrease was strongly attenuated in neutralization of the 501Y.V2 variant (Fig. 2b). When second-wave, 501Y.V2-elicited plasma was used, it effectively neutralized the homologous, 501Y.V2 variant (Fig. 2c). In contrast to plasma elicited against first-wave variants, substantial cross-neutralization of first-wave virus was observed with second-wave, 501Y.V2-elicited plasma. Some of the foci of the first-wave variant were smaller at higher antibody concentrations (Fig. 2c and Extended Data Figs. 2–4), which is possibly indicative of some antibody-mediated reduction in cell-to-cell spread in the Vero E6 cell line.

The data from the focus-forming assay at each dilution approximated a normal distribution (Extended Data Fig. 5) and we therefore used parametric statistics to describe these data. We fitted the data for each participant to a sigmoidal function²⁷ with the dilution required to inhibit 50% of the infection (ID_{50}) as the only free parameter (Methods). For clarity, we plotted the data for each neutralization experiment as the percentage neutralization¹⁷ ($(1 - Tx) \times 100\%$) (Methods), with neutralization represented by the 50% plaque reduction neutralization titre¹⁶ ($PRNT_{50}$), the reciprocal of the ID_{50} .

The Genscript BS-R2B2 rabbit monoclonal neutralizing antibody (hereafter referred to by its catalogue number, A02051) was used as a positive control in each experiment (Extended Data Figs. 2–4). This antibody showed a similar neutralization response between variants (Fig. 2d) and was used to test that the number and size of the foci were not saturating in each experiment. We also used a plasma pool from three study participants who did not have any indications of infection with SARS-CoV-2, and this plasma pool did not appreciably neutralize either variant (Fig. 2d).

We then quantified the neutralization of the homologous virus as well as cross-neutralization between variants. Infection with the first-wave virus was neutralized by plasma elicited by first-wave virus variants, with some variability in neutralization capacity between participants who had been infected with a first-wave variant. The first-wave virus was also cross-neutralized by second-wave, 501Y.V2-elicited plasma (Fig. 2d). There was overlap between the neutralization capacity of the non-VOC variant by plasma induced by infection with first-wave and second-wave viruses. By contrast, when the 510Y.V2 variant was used as the infecting virus, there was a clear separation between the neutralization capacity of plasma from the homologous second wave (Fig. 2d) compared with plasma from the heterologous first wave. Whereas the homologous plasma effectively neutralized the 501Y.V2 variant, cross-neutralization mediated by plasma elicited by first-wave variants was weaker, which is consistent with what is apparent when viewing the raw number of foci (Fig. 2b and Extended Data Figs. 2–4). Plasma elicited by the variant with the E484K substitution alone

showed a much stronger neutralization efficacy of both the first-wave and 501Y.V2 virus variants relative to any of the other plasma samples (Fig. 2d).

The PRNT₅₀ values showed a strong reduction in cross-neutralization by first-wave plasma of the 501Y.V2 virus (Fig. 2e). Excluding the plasma elicited by the virus with the E484K substitution alone, which showed a very high PRNT₅₀ for both variants, the PRNT₅₀ of plasma elicited by first-wave virus infections decreased by between 3.2- and 41.9-fold against the 501Y.V2 variant relative to the non-VOC virus. By contrast, the decrease in PRNT₅₀ in cross-neutralization of the first-wave virus by second-wave, 501Y.V2-elicited plasma was more attenuated. In this case, the decrease ranged between 1.6- and 7.2-fold relative to the homologous 501Y.V2 virus (Fig. 2e).

As the data approximated a normal distribution (Extended Data Fig. 5), we derived the mean neutralization between participants infected with first-wave (excluding the plasma elicited by the E484K-only virus) and second-wave virus variants (Fig. 3). In both cases, neutralization showed a separation across all dilutions tested between the homologous and heterologous virus variants, for which cross-neutralization was always lower than neutralization of the virus from the same wave (Fig. 3a, b).

However, the separation was less pronounced for the cross-neutralization of first-wave virus by 501Y.V2-elicited plasma (Fig. 3a) relative to cross-neutralization of 501Y.V2 virus by first-wave plasma (Fig. 3b). To quantify the homologous versus cross-neutralization capacity, we repeated the sigmoidal fit to the combined participant means and obtained the combined PRNT₅₀. For neutralization of first-wave virus with first-wave plasma, the PRNT₅₀ was 344.0 (fit 95% confidence intervals, 275.4–458.0) (Fig. 3c, top left blue entry). For neutralization of the homologous, 501Y.V2 virus with second-wave plasma (Fig. 3c, bottom right blue entry), the PRNT₅₀ was 619.7 (517.8–771.5). Therefore, 501Y.V2 elicited a robust antibody response in the participants tested. For cross-neutralization, neutralization of 501Y.V2 virus by first-wave plasma (Fig. 3c, bottom left yellow entry) was strongly attenuated across participants, with PRNT₅₀ = 41.1 (32.7–55.5). By contrast, cross-neutralization of first-wave virus by second-wave plasma (Fig. 3c, top right yellow entry) was more effective at PRNT₅₀ = 149.7 (132.1–172.8). The 95% confidence intervals did not overlap between any of the conditions.

Fig. 3: Cross-neutralization of first infection wave and 501Y.V2 virus across all participants.

 **figure3**

Neutralization of the virus from the first wave (**a**) or 501Y.V2 (**b**). Sigmoidal fits were performed to the means of plasma neutralization results from the first wave (red points) and second wave (blue points) across all participants excluding a participant with plasma immunity elicited by SARS-CoV-2 with only the E484K substitution. Data are mean \pm s.d. of $n = 13$ plasma donors infected with a first-wave virus and $n = 6$ plasma donors infected with a second-wave virus. **c**, Plasma PRNT₅₀ as a function of plasma source (columns) and infecting viral variant (rows). Blue rectangles highlight homologous (HM) neutralization for which virus and infection wave are matched; yellow rectangles highlight heterologous, cross-neutralization (HT) for which virus and plasma are from different infection waves.

[Full size image](#)

The fold decrease in neutralization of 501Y.V2 by first-wave plasma compared to the homologous first-wave virus was 8.4. The fold decrease in neutralization of first-wave virus by second-wave plasma compared to the homologous virus was 4.1. However, the absolute neutralization capacity of 501Y.V2-elicited plasma against the first-wave virus decreased by only 2.3-fold compared with the capacity of first-wave plasma. By contrast, the absolute neutralization capacity decreased by 15.1-fold when 501Y.V2 was cross-neutralized by first-wave plasma (Fig. 3).

The importance of these results is that 501Y.V2 is poorly neutralized by plasma elicited by non-VOC virus. However, plasma elicited by infection with 501Y.V2 not only effectively neutralized the 501Y.V2 virus, but also more successfully cross-neutralized the earlier variant (Fig. 2). This level of cross-neutralization is within the lower part of the neutralization capacity range elicited by the BNT162b2 mRNA vaccine (Pfizer)^{13,14,16}. Owing to the potentially higher immunogenicity of the 501Y.V2 variant indicated by the high PRNT₅₀ of 501Y.V2-elicited plasma, this plasma does not greatly underperform compared with the plasma elicited by earlier variants of SARS-CoV-2 when neutralizing these earlier variants.

The larger focus size of the 501Y.V2 variant relative to first-wave virus variants is unlikely to influence results. We performed 501Y.V2 infections with larger foci using the same infection incubation time as the first-wave virus as well as 501Y.V2 infections with a focus size that was similar to the first-wave virus using a shorter incubation time of 501Y.V2 infection. The results showed similar trends. Furthermore, neutralization by the monoclonal antibody control indicated that the system could effectively read out unsaturated neutralization for both variants (Fig. 2d and Extended Data Figs. 2–4). 501Y.V2 variants vary in some of their mutations. The variant that we used has an L18F substitution in the NTD that currently occurs in about a quarter of the 501Y.V2 variants (GISAID). Other 501Y.V2 mutation patterns require further investigation. An important question in the interpretation of the results is whether the participants infected during the second wave were also infected during the first wave of infections. Our clinical team conducted telephone interviews and investigated the clinical charts and found no evidence of a previous SARS-CoV-2 infection. Although a previous infection could still be missed despite these measures, we believe it is unlikely to have occurred in all of the participants with a second-wave infection. Furthermore, although we and others have measured plasma neutralization, how well this correlates with protection against SARS-CoV-2 at the mucosal surface where the initial infection takes place remains unclear.

The plasma elicited by the virus with the E484K substitution alone showed the strongest neutralization against both the first-wave and 501Y.V2 virus variants relative to any of the other plasma samples that we tested (Fig. 2). Because we only found one participant in this category, this result is difficult to interpret: it may be due to the high

immunogenicity of the mutant or because of participant-specific factors. Our clinical data do not show prolonged SARS-CoV-2 shedding in this participant or other any unusual features (Extended Data Table 1). This result highlights the importance of sequencing the infecting virus and requires further investigation.

The recent results from the vaccine trials of Novavax, Johnson and Johnson and AstraZeneca in South Africa indicate that the 501Y.V2 variant may lead to a decrease in vaccine efficacy. The loss of neutralization capacity against infection with 501Y.V2 that we quantified among the vaccinated participants in the AstraZeneca trial³ shows that loss of neutralization may be associated with a loss of vaccine efficacy. Loss of vaccine efficacy may also be mediated by escape from T cell immunity, although this is less likely because of the diversity of HLA alleles in the population, which may curtail the ability of an escape variant that evolved in one individual to escape T cell immunity in another²⁸. If the loss of vaccine efficacy proves to require vaccine redesign, the results presented here may be the first indication that a vaccine designed to target 501Y.V2 may also be effective at targeting other SARS-CoV-2 variants.

Methods

Data reporting

No statistical methods were used to predetermine sample size. The experiments were not randomized and the investigators were not blinded to allocation during experiments and outcome assessment.

Ethical statement

Nasopharyngeal and oropharyngeal swab samples and plasma samples were obtained from 20 hospitalized adults with PCR-confirmed SARS-CoV-2 infection who were enrolled in a prospective cohort study approved by the Biomedical Research Ethics Committee (BREC) at the University of KwaZulu–Natal (reference BREC/00001275/2020). The 501Y.V2 variant was obtained from a residual nasopharyngeal and oropharyngeal sample used for routine SARS-CoV-2 diagnostic testing by the National Health Laboratory Service through our SARS-CoV-2 genomic surveillance programme (BREC approval reference BREC/00001510/2020).

Whole-genome sequencing, genome assembly and phylogenetic analysis

cDNA synthesis was performed on the extracted RNA using random primers followed by gene-specific multiplex PCR using the ARTIC V.3 protocol (<https://www.protocols.io/view/covid-19-artic-v3-illumina-library-construction-an->

[bibtkann](#)). In brief, extracted RNA was converted to cDNA using the Superscript IV First Strand synthesis system (Life Technologies) and random hexamer primers. SARS-CoV-2 whole-genome amplification was performed by multiplex PCR using primers designed using Primal Scheme (<http://primal.zibraproject.org/>) to generate 400-bp amplicons with an overlap of 70 bp that covers the 30 kb SARS-CoV-2 genome. PCR products were cleaned up using AmpureXP purification beads (Beckman Coulter) and quantified using the Qubit dsDNA High Sensitivity assay on the Qubit 4.0 instrument (Life Technologies). We then used the Illumina Nextera Flex DNA Library Prep kit according to the manufacturer's protocol to prepare indexed paired-end libraries of genomic DNA. Sequencing libraries were normalized to 4 nM, pooled and denatured with 0.2 N sodium acetate. Then, a 12-pM sample library was spiked with 1% PhiX (a PhiX Control v.3 adaptor-ligated library was used as a control). We sequenced libraries on a 500-cycle v.2 MiSeq Reagent Kit on the Illumina MiSeq instrument (Illumina). We assembled paired-end fastq reads using Genome Detective 1.126 (<https://www.genomedetective.com>) and the Coronavirus Typing Tool. We polished the initial assembly obtained from Genome Detective by aligning mapped reads to the reference sequences and filtering out low-quality mutations using the bcftools 1.7-2 mpileup method. Mutations were confirmed visually with BAM files using Geneious software (Biomatters). All of the sequences were deposited in GISAID (<https://www.gisaid.org/>). We retrieved all SARS-CoV-2 genotypes from South Africa from the GISAID database as of 11 January 2021 ($n = 2,704$). We initially analysed genotypes from South Africa against the global reference dataset ($n = 2,592$) using a custom pipeline based on a local version of NextStrain. The pipeline contains several Python scripts that manage the analysis workflow. It performs alignment of genotypes in MAFFT, phylogenetic tree inference in IQ-Tree20, tree dating and ancestral state construction and annotation (<https://github.com/nextstrain/ncov>).

Cells

Vero E6 cells (ATCC CRL-1586, obtained from Cellonex in South Africa) were propagated in complete DMEM with 10% fetal bovine serum (Hyclone) containing 1% each of HEPES, sodium pyruvate, l-glutamine and nonessential amino acids (Sigma-Aldrich). Vero E6 cells were passaged every 3–4 days. H1299 cells were propagated in complete RPMI with 10% fetal bovine serum containing 1% each of HEPES, sodium pyruvate, l-glutamine and nonessential amino acids. H1299 cells were passaged every second day. HEK-293 (ATCC CRL-1573) cells were propagated in complete DMEM with 10% fetal bovine serum containing 1% each of HEPES, sodium pyruvate, l-glutamine and nonessential amino acids. HEK-293 cells were passaged every second day. Cell lines have not been authenticated. The cell lines have been tested for mycoplasma contamination and are mycoplasma negative.

H1299-E3 cell line for first-passage SARS-CoV-2 expansion

The H1299-H2AZ clone with nuclear-labelled YFP was constructed to overexpress human ACE2 as follows. Vesicular stomatitis virus G protein (VSVG)-pseudotyped lentivirus containing the human ACE2 was generated by co-transfecting HEK-293T cells with the pHAGE2-EF1alnt-ACE2-WT plasmid along with the lentiviral helper plasmids HDM-VSVG, HDM-Hgpm2, HDM-tat1b and pRC-CMV-Rev1b using the TransIT-LT1 (Mirus) transfection reagent. Supernatant containing the lentivirus was collected 2 days after infection, filtered through a 0.45- μ m filter (Corning) and used to spinfect H1299-H2AZ at 1,000 rcf for 2 h at room temperature in the presence of 5 μ g ml⁻¹ polybrene (Sigma-Aldrich). ACE2-transduced H1299-H2AZ cells were then subcloned at single-cell density in 96-well plates (Eppendorf) in conditioned medium derived from confluent cells. After 3 weeks, wells were trypsinized (Sigma-Aldrich) and plated in two replicate plates. The first plate was used to determine infectivity and the second plate was used as stock. The first plate was screened for the fraction of mCherry-positive cells per cell clone after infection with SARS-CoV-2 mCherry-expressing spike-pseudotyped lentiviral vector 1610-pHAGE2/EF1a Int-mCherry3-W produced by transfecting the cells as described above. Screening was performed using a Metamorph-controlled (Molecular Devices) Nikon TiE motorized microscope (Nikon Corporation) with a 20 \times /0.75 NA phase objective, 561 laser line, and 607-nm emission filter (Semrock). Images were captured using an 888 EMCCD camera (Andor). Temperature (37 °C), humidity and CO₂ (5%) were controlled using an environmental chamber (OKO Labs). The clone with the highest fraction of mCherry expression was expanded from the stock plate and denoted H1299-E3. This clone was used in the expansion assays.

Virus expansion

All work with live virus was performed in Biosafety Level 3 containment using protocols for SARS-CoV-2 approved by the Africa Health Research Institute Biosafety Committee. For first-wave virus, a T25 flask (Corning) was seeded with Vero E6 cells at 2 \times 10⁵ cells per ml and incubated for 18–20 h. After one DPBS wash, the subconfluent cell monolayer was inoculated with 500 μ l universal transport medium diluted 1:1 with growth medium and filtered through a 0.45- μ m filter. Cells were incubated for 1 h. The flask was then filled with 7 ml of complete growth medium and checked daily for cytopathogenic effects. After infection for 4 days, supernatants of the infected culture were collected, centrifuged at 300 rcf for 3 min to remove cell debris and filtered using a 0.45- μ m filter. Viral supernatant was aliquoted and stored at -80 °C. For 501Y.V2 variants, we used ACE2-expressing H1299-E3 cells for the initial isolation followed by passaging in Vero E6 cells. ACE2-expressing H1299-E3 cells were seeded at 1.5 \times 10⁵ cells per ml and incubated for 18–20 h. After one DPBS wash, the subconfluent cell monolayer was inoculated with 500 μ l universal transport

medium diluted 1:1 with growth medium and filtered through a 0.45- μ m filter. Cells were incubated for 1 h. Wells were then filled with 3 ml complete growth medium. After 8 days of infection, cells were trypsinized, centrifuged at 300 rcf for 3 min and resuspended in 4 ml growth medium. Then, 1 ml was added to Vero E6 cells that had been seeded at 2×10^5 cells per ml 18–20 h earlier in a T25 flask (approximately 1:8 donor-to-target cell dilution ratio) for cell-to-cell infection. The coculture of ACE2-expressing H1299-E3 and Vero E6 cells was incubated for 1 h and the flask was then filled with 7 ml of complete growth medium and incubated for 6 days. The viral supernatant was aliquoted and stored at –80 °C or further passaged in Vero E6 cells as described above. Two isolates were expanded, 501Y.V2.HV001 and 501Y.V2.HVdF002. The second isolate showed fixation of mutations in the furin cleavage site during expansion in Vero E6 cells and was not used except for data presented in Extended Data Fig. 1.

Microneutralization using the focus-forming assay

For plasma from donors infected with first-wave virus variants, we first quantified IgG targeting the spike RBD by enzyme-linked immunosorbent assay (ELISA) using the monoclonal antibody CR3022 (used at fourfold serial dilutions from 1,000 ng ml^{–1} to 0.244 ng ml^{–1}) as a quantitative standard ($n = 13$ excluding participant 039-13-0103, for whom ELISA data were not available). The mean concentration was 23.7 ± 19.1 μ g ml^{–1} (range, 5.7–62.6 μ g ml^{–1}). In comparison, control samples from donors who were not infected with SARS-CoV-2 had a mean of 1.85 ± 0.645 μ g ml^{–1}. To quantify neutralization, Vero E6 cells were plated in an 96-well plate (Eppendorf or Corning) at 30,000 cells per well 1 day before infection. Notably, before infection approximately 5 ml sterile water was added between wells to prevent wells at the edge drying more rapidly, which we have observed to cause edge effects (lower number of foci). Plasma was separated from EDTA-anticoagulated blood by centrifugation at 500 rcf for 10 min and stored at –80 °C. Aliquots of plasma samples were heat-inactivated at 56 °C for 30 min and clarified by centrifugation at 10,000 rcf for 5 min, after which the clear middle layer was used for experiments. Inactivated plasma was stored in single-use aliquots to prevent freeze–thaw cycles. For experiments, plasma was serially diluted twofold from 1:100 to 1:1,600; this is the concentration that was used during the virus–plasma incubation step before addition to cells and during the adsorption step. As a positive control, the GenScript A02051 anti-spike monoclonal antibody was added at concentrations listed in the figures. Virus stocks were used at approximately 50 focus-forming units per microwell and added to diluted plasma; antibody–virus mixtures were incubated for 1 h at 37 °C, 5% CO₂. Cells were infected with 100 μ l of the virus–antibody mixtures for 1 h, to allow adsorption of virus. Subsequently, 100 μ l of a 1× RPMI 1640 (Sigma-Aldrich, R6504), 1.5% carboxymethylcellulose (Sigma-Aldrich, C4888) overlay was added to the wells without removing the inoculum. Cells were fixed at 28 h after infection using 4%

paraformaldehyde (Sigma-Aldrich) for 20 min. For staining of foci, a rabbit anti-spike monoclonal antibody (BS-R2B12, GenScript A02058) was used at $0.5 \mu\text{g ml}^{-1}$ as the primary detection antibody. Antibody was resuspended in a permeabilization buffer containing 0.1% saponin (Sigma-Aldrich), 0.1% BSA (Sigma-Aldrich) and 0.05% Tween-20 (Sigma-Aldrich) in PBS. Plates were incubated with primary antibody overnight at 4°C , then washed with wash buffer containing 0.05% Tween-20 in PBS. Secondary goat anti-rabbit horseradish peroxidase (Abcam ab205718) antibody was added at $1 \mu\text{g ml}^{-1}$ and incubated for 2 h at room temperature with shaking. The TrueBlue peroxidase substrate (SeraCare 5510-0030) was then added at $50 \mu\text{l}$ per well and incubated for 20 min at room temperature. Plates were then dried for 2 h and imaged using a Metamorph-controlled Nikon TiE motorized microscope with a $2\times$ objective. Automated image analysis was performed using a custom script in MATLAB v.2019b (Mathworks), in which focus detection was automated and did not involve user curation. Image segmentation steps were stretching the image from minimum to maximum intensity, local Laplacian filtering, image complementation, thresholding and binarization. Two plasma donors initially measured from the second infection wave in South Africa did not have detectable neutralization of either 501Y.V2 or the first-wave variant and were not included in the study.

Statistics and fitting

All statistics and fitting were performed using MATLAB v.2019b. Neutralization data were fit to

$$Tx = \frac{1}{1 + (D / (D - 50))},$$

where Tx is the number of foci normalized to the number of foci in the absence of plasma on the same plate at dilution D . To visualize the data, we used percentage neutralization, calculated as $(1 - Tx) \times 100\%$. Negative values ($Tx > 1$, enhancement) were presented as 0% neutralization. Data were fitted to a normal distribution using the function `normplot` in MATLAB v.2019b, which compared the distribution of the Tx data to the normal distribution (see <https://www.mathworks.com/help/stats/normplot.html>).

Reporting summary

Further information on research design is available in the [Nature Research Reporting Summary](#) linked to this paper.

Data availability

Sequence data that support the findings of this study have been deposited in GISAID with accession codes listed in Supplementary Table 1. Raw images are available from the corresponding authors upon reasonable request.

Code availability

The sequence analysis and visualization pipeline is available on GitHub (<https://github.com/nextstrain/ncov>). Image analysis and curve fitting scripts in MATLAB v.2019b are available on GitHub (<https://github.com/sigallab/NatureMarch2021>).

References

1. 1.

Tegally, H. et al. Detection of a SARS-CoV-2 variant of concern in South Africa. *Nature* <https://doi.org/10.1038/s41586-021-03402-9> (2021).

[Article](#) [Google Scholar](#)

2. 2.

Faria, N. R. et al. Genomics and epidemiology of a novel SARS-CoV-2 lineage in Manaus, Brazil. Preprint at <https://doi.org/10.1101/2021.02.26.21252554> (2021).

3. 3.

Madhi, S. A. et al. Efficacy of the ChAdOx1 nCoV-19 COVID-19 vaccine against the B.1.351 variant. *N. Engl. J. Med.* <https://doi.org/10.1056/NEJMoa2102214> (2021).

[Article](#) [PubMed](#) [PubMed Central](#) [Google Scholar](#)

4. 4.

Piccoli, L. et al. Mapping neutralizing and immunodominant sites on the SARS-CoV-2 spike receptor-binding domain by structure-guided high-resolution serology. *Cell* **183**, 1024–1042 (2020).

[CAS](#) [Article](#) [Google Scholar](#)

5. 5.

McCallum, M. et al. N-terminal domain antigenic mapping reveals a site of vulnerability for SARS-CoV-2. *Cell* <https://doi.org/10.1016/j.cell.2021.03.028> (2021).

6. 6.

Barnes, C. O. et al. SARS-CoV-2 neutralizing antibody structures inform therapeutic strategies. *Nature* **588**, 682–687 (2020).

[ADS](#) [CAS](#) [Article](#) [Google Scholar](#)

7. 7.

Baum, A. et al. Antibody cocktail to SARS-CoV-2 spike protein prevents rapid mutational escape seen with individual antibodies. *Science* **369**, 1014–1018 (2020).

[ADS](#) [CAS](#) [Article](#) [Google Scholar](#)

8. 8.

Greaney, A. J. et al. Complete mapping of mutations to the SARS-CoV-2 spike receptor-binding domain that escape antibody recognition. *Cell Host Microbe* **29**, 44–57 (2021).

[CAS](#) [Article](#) [Google Scholar](#)

9. 9.

Weisblum, Y. et al. Escape from neutralizing antibodies by SARS-CoV-2 spike protein variants. *eLife* **9**, e61312 (2020).

[CAS](#) [Article](#) [Google Scholar](#)

10. 10.

Liu, Z. et al. Identification of SARS-CoV-2 spike mutations that attenuate monoclonal and serum antibody neutralization. *Cell Host Microbe* **29**, 477–488 (2021).

[CAS](#) [Article](#) [Google Scholar](#)

11. 11.

Andreano, E. et al. SARS-CoV-2 escape in vitro from a highly neutralizing Covid-19 convalescent plasma. Preprint at <https://doi.org/10.1101/2020.12.28.424451> (2020).

12. 12.

Greaney, A. J. et al. Comprehensive mapping of mutations in the SARS-CoV-2 receptor-binding domain that affect recognition by polyclonal human plasma antibodies. *Cell Host Microbe* **29**, 463–476 (2021).

[CAS Article](#) [Google Scholar](#)

13. 13.

Xie, X. et al. Neutralization of SARSCoV-2 spike 69/70 deletion, E484K and N501Y variants by BNT162b2 vaccine-elicited sera. *Nat. Med.* <https://doi.org/10.1038/s41591-021-01270-4> (2021).

14. 14.

Wang, Z. et al. mRNA vaccine-elicited antibodies to SARS-CoV-2 and circulating variants. *Nature* <https://doi.org/10.1038/s41586-021-03324-6> (2021).

15. 15.

Wu, K. et al. Serum neutralizing activity elicited by mRNA-1273 vaccine. *N. Engl. J. Med.* <https://doi.org/10.1056/NEJMc2102179> (2021).

16. 16.

Liu, Y. et al. Neutralizing activity of BNT162b2-elicited serum. *N. Engl. J. Med.* <https://doi.org/10.1056/NEJMc2102017> (2021).

17. 17.

Garcia-Beltran, W. F. et al. Multiple SARS-CoV-2 variants escape neutralization by vaccine-induced humoral immunity. *Cell* <https://doi.org/10.1016/j.cell.2021.03.013> (2021).

18. 18.

Wibmer, C. K. et al. SARS-CoV-2 501Y.V2 escapes neutralization by South African COVID-19 donor plasma. *Nat. Med.* <https://doi.org/10.1038/s41591-021-01285-x> (2021).

19. 19.

Hoffmann, M. et al. SARS-CoV-2 variants B.1.351 and B.1.1.248: escape from therapeutic antibodies and antibodies induced by infection and vaccination. Preprint at <https://doi.org/10.1101/2021.02.11.430787> (2021).

20. 20.

Planas, D. et al. Sensitivity of infectious SARS-CoV-2 B.1.1.7 and B.1.351 variants to neutralizing antibodies. *Nat. Med.* <https://doi.org/10.1038/s41591-021-01318-5> (2021).

21. 21.

Skelly, D. T. et al. Vaccine-induced immunity provides more robust heterotypic immunity than natural infection to emerging SARS-CoV-2 variants of concern. Preprint at <https://doi.org/10.21203/rs.3.rs-226857/v1> (2021).

22. 22.

Wang, P. et al. Antibody resistance of SARS-CoV-2 variants B.1.351 and B.1.1.7. *Nature* <https://doi.org/10.1038/s41586-021-03398-2> (2021).

23. 23.

Karim, F. et al. HIV infection alters SARSCoV-2 responsive immune parameters but not clinical outcomes in COVID-19 disease. Preprint at <https://doi.org/10.1101/2020.11.23.20236828> (2020).

24. 24.

Gaebler, C. et al. Evolution of antibody immunity to SARS-CoV-2. *Nature* **591**, 639–644 (2021).

[ADS](#) [CAS](#) [Article](#) [Google Scholar](#)

25. 25.

Case, J. B., Bailey, A L., Kim, A. S., Chen, R. E. & Diamond, M. S. Growth, detection, quantification, and inactivation of SARS-CoV-2. *Virology* **548**, 39–48 (2020).

[CAS](#) [Article](#) [Google Scholar](#)

26. 26.

Sigal, A. et al. Cell-to-cell spread of HIV permits ongoing replication despite antiretroviral therapy. *Nature* **477**, 95–98 (2011).

[ADS](#) [CAS](#) [Article](#) [Google Scholar](#)

27. 27.

Shen, L. et al. Dose-response curve slope sets class-specific limits on inhibitory potential of anti-HIV drugs. *Nat. Med.* **14**, 762–766 (2008).

[CAS](#) [Article](#) [Google Scholar](#)

28. 28.

Tarke, A. et al. Comprehensive analysis of T cell immunodominance and immunoprevalence of SARS-CoV-2 epitopes in COVID-19 cases. *Cell. Rep. Med.* **2**, 100204 (2021).

[Article](#) [Google Scholar](#)

[Download references](#)

Acknowledgements

This work was supported by the Bill and Melinda Gates Investment INV-018944 (A.S.) and by the South African Medical Research Council and the Department of Science and Innovation (T.d.O.).

Author information

Affiliations

1. Africa Health Research Institute, Durban, South Africa

Sandile Cele, Laurelle Jackson, Shi-Hsia Hwa, Farina Karim, Yashica Ganga, Khadija Khan, Mallory Bernstein, Willem Hanekom, Philip Goulder, Sashin Harilall, Guy Harling, Kobus Herbst, Thandeka Khoza, Nigel Klein, Henrik Kløverpris, Alasdair Leslie, Mohlopheni Marakalala, Matilda Mazibuko, Ntombifuthi Mthabela, Zaza Ndhlovu, Thumbi Ndung'u, Dirhona Ramjit, Hylton Rodel, Theresa Smit, Adrie Steyn, Emily Wong & Alex Sigal

2. School of Laboratory Medicine and Medical Sciences, University of KwaZulu-Natal, Durban, South Africa

Sandile Cele, Inbal Gazy, Farina Karim & Alex Sigal

3. KwaZulu-Natal Research Innovation and Sequencing Platform (KRISP), School of Laboratory Medicine and Medical Sciences, University of KwaZulu-Natal, Durban, South Africa

Inbal Gazy, Hourriyah Tegally, Jennifer Giandhari, Sureshnee Pillay, Eduan Wilkinson, Yeshnee Naidoo, Vagner Fonseca, Emmanuel James San, Richard J. Lessells & Tulio de Oliveira

4. Department of Biochemistry and Molecular Biology, The Institute for Medical Research Israel-Canada, Hadassah Medical School, The Hebrew University of Jerusalem, Jerusalem, Israel

Inbal Gazy

5. Division of Infection and Immunity, University College London, London, UK

Shi-Hsia Hwa, Willem Hanekom, Henrik Kløverpris, Alasdair Leslie, Mohlopheni Marakalala, Thumbi Ndung'u & Hylton Rodel

6. Centre for the AIDS Programme of Research in South Africa (CAPRISA), Durban, South Africa

Gila Lustig, Koleka Mlisana, Carolyn Williamson, Kogie Naidoo, Nesri Padayatchi, Richard J. Lessells & Tulio de Oliveira

7. Ragon Institute of MGH, Harvard and MIT, Cambridge, MA, USA

Alejandro B. Balazs & Zaza Ndhlovu

8. Department of Infectious Diseases, Nelson R. Mandela School of Clinical Medicine, University of KwaZulu-Natal, Durban, South Africa

Bernadett I. Gosnell & Mahomed-Yunus S. Moosa

9. Department of Global Health, University of Washington, Seattle, WA, USA

Tulio de Oliveira

10. Max Planck Institute for Infection Biology, Berlin, Germany

Thumbi Ndung'u & Alex Sigal

11. National Health Laboratory Service, Port Elizabeth, South Africa

Shareef Abrahams & Oluwakemi Laguda-Akingba

12. Laboratorio de Flavivirus, Fundacao Oswaldo Cruz, Rio de Janeiro, Brazil

Luiz Carlos Junior Alcantara & Marta Giovanetti

13. Division of Medical Virology, Department of Pathology, University of Cape Town, Cape Town, South Africa

Arghavan Alisoltani-Dehkordi

14. Division of Biomedical Sciences, University of California Riverside School of Medicine, Riverside, CA, USA

Arghavan Alisoltani-Dehkordi, Adam Godzik & Arash Iranzadeh

15. National Institute for Communicable Diseases, National Health Laboratory Service, Johannesburg, South Africa

Mushal Allam, Jinal N. Bhiman, Arshad Ismail, Thabo Mohale, Anne von Gottberg, Sibongile Walaza & Constantinos Kurt Wibmer

16. School of Pathology, Faculty of Health Sciences, University of the Witwatersrand, Johannesburg, South Africa

Jinal N. Bhiman, Allison J. Glass & Anne von Gottberg

17. Centre for Infectious Disease Epidemiology and Research, University of Cape Town, Cape Town, South Africa

Mary-Ann Davies

18. Western Cape Government: Health, Cape Town, South Africa

Mary-Ann Davies

19. Division of Medical Virology, Institute of Infectious Disease and Molecular Medicine, University of Cape Town, Cape Town, South Africa

Deelan Doolabh, Darren Martin, Innocent Mudau, Lynn Tyers & Carolyn Williamson

20. Division of Medical Virology at NHLS Tygerberg Hospital, Faculty of Medicine and Health Sciences, Stellenbosch University, Cape Town, South Africa

Susan Engelbrecht, Wolfgang Preiser & Gert Van Zyl

21. Department of Molecular Pathology, Lancet Laboratories, Johannesburg, South Africa

Allison J. Glass

22. Division of Virology, NHLS Universitas Academic Laboratories, University of The Free State, Bloemfontein, South Africa

Dominique Goedhals

23. Division of Medical Virology, NHLS Groote Schuur Hospital, University of Cape Town, Cape Town, South Africa

Diana Hardie, Marvin Hsiao, Stephen Korsman, Gert Marais & Carolyn Williamson

24. Institute for Genomics and Evolutionary Medicine, Temple University, Philadelphia, PA, USA

Sergei L. Kosakovsky Pond & Steven Weaver

25. Department of Laboratory Medicine and Pathology, Faculty of Health Sciences, Walter Sisulu University, Mthatha, South Africa

Oluwakemi Laguda-Akingba

26. Department of Zoology, University of Oxford, Oxford, UK

Jose Lourenco

27. Computational Biology Division, Department of Integrative Biomedical Sciences, University of Cape Town, Cape Town, South Africa

Darren Martin

28. Department of Quality Leadership, Netcare Hospitals, Johannesburg, South Africa

Caroline Maslo

29. National Health Laboratory Service, Johannesburg, South Africa

Koleka Mlisana

30. Discipline of Virology, School of Laboratory Medicine and Medical Sciences, University of KwaZulu–Natal, Durban, South Africa

Nokukhanya Msomi

31. Virology Department, Inkosi Albert Luthuli Central Hospital, National Health Laboratory Service, Durban, South Africa

Nokukhanya Msomi

32. Centre for Quantum Technology, University of KwaZulu–Natal, Durban, South Africa

Francesco Petruccione

33. National Institute for Theoretical Physics (NITheP), University of KwaZulu–Natal, Durban, South Africa

Francesco Petruccione

34. Structural Biology Research Unit, Department of Integrative Biomedical Sciences, University of Cape Town, Rondebosch, South Africa

Bryan Trevor Sewell

35. School of Public Health, Faculty of Health Sciences, University of the Witwatersrand, Johannesburg, South Africa

Sibongile Walaza

36. Molecular Diagnostics Services, Durban, South Africa

Denis York

37. Department of Paediatrics and Child Health, University of KwaZulu–Natal, Durban, South Africa

Moherndran Archary & Prakash Jeena

38. Department of Cardiothoracic Surgery, University of KwaZulu–Natal, Durban, South Africa

Kaylesh J. Dullabh & Rajhmun Madansein

39. Department of Paediatrics, University of Oxford, Oxford, UK

Philip Goulder

40. Institute for Global Health, University College London, London, UK

Guy Harling

41. Department of Neurosurgery, University of KwaZulu–Natal, Durban, South Africa

Rohen Harrichandparsad

42. South African Population Research Infrastructure Network, Durban, South Africa

Kobus Herbst

43. Institute of Child Health, University College London, London, UK

Nigel Klein

44. Department of Immunology and Microbiology, University of Copenhagen, Copenhagen, Denmark

Henrik Kløverpris

45. College of Health Sciences, University of KwaZulu–Natal, Durban, South Africa

Mosa Moshabela

46. HIV Pathogenesis Programme, The Doris Duke Medical Research Institute, University of KwaZulu–Natal, Durban, South Africa

Thumbi Ndung'u

47. Department of Pulmonology and Critical Care, University of KwaZulu–Natal, Durban, South Africa

Kennedy Nyamande

48. Department of Neurology, University of KwaZulu–Natal, Durban, South Africa

Vinod Patel

49. Division of Infectious Diseases, University of Alabama at Birmingham,
Birmingham, AL, USA

Adrie Steyn & Emily Wong

Authors

1. Sandile Cele

[View author publications](#)

You can also search for this author in [PubMed](#) [Google Scholar](#)

2. Inbal Gazy

[View author publications](#)

You can also search for this author in [PubMed](#) [Google Scholar](#)

3. Laurelle Jackson

[View author publications](#)

You can also search for this author in [PubMed](#) [Google Scholar](#)

4. Shi-Hsia Hwa

[View author publications](#)

You can also search for this author in [PubMed](#) [Google Scholar](#)

5. Houriiyah Tegally

[View author publications](#)

You can also search for this author in [PubMed](#) [Google Scholar](#)

6. Gila Lustig

[View author publications](#)

You can also search for this author in [PubMed](#) [Google Scholar](#)

7. Jennifer Giandhari

[View author publications](#)

You can also search for this author in [PubMed](#) [Google Scholar](#)

8. Sureshnee Pillay

[View author publications](#)

You can also search for this author in [PubMed](#) [Google Scholar](#)

9. Eduan Wilkinson

[View author publications](#)

You can also search for this author in [PubMed](#) [Google Scholar](#)

10. Yeshnee Naidoo

[View author publications](#)

You can also search for this author in [PubMed](#) [Google Scholar](#)

11. Farina Karim

[View author publications](#)

You can also search for this author in [PubMed](#) [Google Scholar](#)

12. Yashica Ganga

[View author publications](#)

You can also search for this author in [PubMed](#) [Google Scholar](#)

13. Khadija Khan

[View author publications](#)

You can also search for this author in [PubMed](#) [Google Scholar](#)

14. Mallory Bernstein

[View author publications](#)

You can also search for this author in [PubMed](#) [Google Scholar](#)

15. Alejandro B. Balazs

[View author publications](#)

You can also search for this author in [PubMed](#) [Google Scholar](#)

16. Bernadett I. Gosnell

[View author publications](#)

You can also search for this author in [PubMed](#) [Google Scholar](#)

17. Willem Hanekom

[View author publications](#)

You can also search for this author in [PubMed](#) [Google Scholar](#)

18. Mahomed-Yunus S. Moosa

[View author publications](#)

You can also search for this author in [PubMed](#) [Google Scholar](#)

19. Richard J. Lessells

[View author publications](#)

You can also search for this author in [PubMed](#) [Google Scholar](#)

20. Tulio de Oliveira

[View author publications](#)

You can also search for this author in [PubMed](#) [Google Scholar](#)

21. Alex Sigal

[View author publications](#)

You can also search for this author in [PubMed](#) [Google Scholar](#)

Consortia

Network for Genomic Surveillance in South Africa

- Shareef Abrahams
- , Luiz Carlos Junior Alcantara
- , Arghavan Alisoltani-Dehkordi
- , Mushal Allam
- , Jinal N. Bhiman
- , Mary-Ann Davies
- , Deelan Doolabh
- , Susan Engelbrecht
- , Vagner Fonseca
- , Marta Giovanetti
- , Allison J. Glass
- , Adam Godzik
- , Dominique Goedhals
- , Diana Hardie
- , Marvin Hsiao
- , Arash Iranzadeh
- , Arshad Ismail

- , Stephen Korsman
- , Sergei L. Kosakovsky Pond
- , Oluwakemi Laguda-Akingba
- , Jose Lourenco
- , Gert Marais
- , Darren Martin
- , Caroline Maslo
- , Koleka Mlisana
- , Thabo Mohale
- , Nokukhanya Msomi
- , Innocent Mudau
- , Francesco Petruccione
- , Wolfgang Preiser
- , Emmanuel James San
- , Bryan Trevor Sewell
- , Lynn Tyers
- , Gert Van Zyl
- , Anne von Gottberg
- , Sibongile Walaza
- , Steven Weaver
- , Constantinos Kurt Wibmer
- , Carolyn Williamson
- & Denis York

COMMIT-KZN Team

- Moherndran Archary
- , Kaylesh J. Dullabh
- , Philip Goulder
- , Sashin Harilall
- , Guy Harling
- , Rohen Harrichandparsad
- , Kobus Herbst
- , Prakash Jeena
- , Thandeka Khoza
- , Nigel Klein
- , Henrik Kløverpris
- , Alasdair Leslie
- , Rajhmun Madansein
- , Mohlopheni Marakalala
- , Matilda Mazibuko
- , Mosa Moshabela

- , Ntombifuthi Mthabela
- , Kogie Naidoo
- , Zaza Ndhlovu
- , Thumbi Ndung'u
- , Kennedy Nyamande
- , Nesri Padayatchi
- , Vinod Patel
- , Dirhona Ramjit
- , Hylton Rodel
- , Theresa Smit
- , Adrie Steyn
- & Emily Wong

Contributions

A.S., T.d.O. and R.J.L. conceived the study with input from A.B.B. A.S., T.d.O., S.C., S.-H.H. and L.J. designed the study and experiments. S.C., I.G., J.G., Y.N., S.P. and A.S. performed experiments. A.S., T.d.O., S.C., H.T., E.W., G.L., M.-Y.S.M., B.I.G. and R.J.L. analysed and interpreted data. F.K., K.K., Y.G., M.B., B.I.G., M.-Y.S.M. and S.C. set up and managed the cohort. A.S., T.d.O., R.J.L., W.H., A.B.B. and S.C. prepared the manuscript with input from all authors.

Corresponding authors

Correspondence to [Tulio de Oliveira](#) or [Alex Sigal](#).

Ethics declarations

Competing interests

The authors declare no competing interests.

Additional information

Peer review information *Nature* thanks Andreas Radbruch and the other, anonymous, reviewer(s) for their contribution to the peer review of this work. Peer reviewer reports are available.

Publisher's note Springer Nature remains neutral with regard to jurisdictional claims in published maps and institutional affiliations.

Extended data figures and tables

Extended Data Fig. 1 Neutralization of first-wave and 501Y.V2 variants by convalescent plasma from first-wave infections using equal infection incubation times.

a, A representative focus-forming assay using plasma from participant 039-13-0015. **b, c**, Plasma neutralization of first-wave virus (**b**) and 501Y.V2 variants (501Y.V2.HV001 and 501Y.V2.HVdF002) (**c**). Coloured circles represent mean \pm s.e.m. from 8 independent neutralization experiments using plasma from $n = 6$ participants convalescing from an infection with first-wave variants in the first peak of the pandemic in South Africa. Correspondingly coloured lines are fits of the sigmoidal equation with ID₅₀ as the fitted parameter. Data from both 501Y.V2 variants were combined to obtain a more accurate fit as neutralization of 501Y.V2 virus infection was low in the range of plasma concentrations used. The matched infections with first-wave virus that were done in parallel with each 501Y.V2 variant were also combined. One experiment was removed in the process of quality control owing to plate edge effects, which were subsequently corrected by adding sterile water between wells. Black points represent a pool of plasma from three uninfected control individuals. The transmission index (Tx) is the number of foci in the presence of the plasma dilution normalized to the number of foci in the absence of plasma. **d**, Plasma ID₅₀ values and ratios for first-wave and 501Y.V2 variants. Knockout (KO) was scored as ID₅₀ > 1. ND, not defined. **e**, Plasma neutralization of all first-wave and all 501Y.V2 variants combined. Data are mean \pm s.e.m. across all plasma donors ($n = 6$) from 8 independent neutralization experiments.

Extended Data Fig. 2 Neutralization of first-wave and 501Y.V2 variants by convalescent plasma: representative experiments of the first set of participant plasma tested.

Top, neutralization of first-wave virus. Bottom, neutralization of 501Y.V2. Rows are plasma dilutions, ranging from 1:25 to 1:1,600. The last three columns comprise plasma from a pool of uninfected participants, the no-plasma control and no-virus control, respectively. The first column is the neutralizing antibody A2051, with antibody concentrations in ng ml⁻¹ (magenta). First-wave plasma donors are marked with a red line.

Extended Data Fig. 3 Neutralization of first-wave and 501Y.V2 variants by convalescent plasma: representative experiments of the second set of participant plasma tested.

Top, neutralization of first-wave virus. Bottom, neutralization of 501Y.V2. Rows are plasma dilutions, ranging from 1:25 to 1:1,600. The last three columns comprise plasma from a pool of uninfected participants, the no-plasma control and no-virus control, respectively. The first column is the neutralizing antibody A2051, with antibody concentrations in ng ml⁻¹ (magenta). First-wave plasma donors are marked with a red line; second-wave plasma donors are marked with a blue line; and the plasma donor who was infected with SARS-CoV-2 with the E484K substitution only is marked with a green line.

Extended Data Fig. 4 Neutralization of first-wave and 501Y.V2 variants by convalescent plasma: representative experiments of the third set of participant plasma tested.

Top, neutralization of first-wave virus. Bottom, neutralization of 501Y.V2. Rows are plasma dilutions, ranging from 1:25 to 1:1,600. The last three columns comprise plasma from a pool of uninfected participants, the no-plasma control and no-virus control, respectively. The first column is the neutralizing antibody A2051, with antibody concentrations in ng ml⁻¹ (magenta). First-wave plasma donors are marked with a red line and second-wave plasma donors are marked with a blue line.

Extended Data Fig. 5 Fit of combined data for each plasma dilution to a normal distribution.

The function normplot in MATLAB v.2019b was used to assess the fit of the data (blue crosses) to a normal distribution (solid red line). For each plot, one data point is the Tx result for one experiment for one participant at the specified dilution. The number of total experiments per viral variant was $n = 42$ for first-wave plasma and $n = 21$ for second-wave plasma. Lack of pronounced curvature of the data in the range of the solid line indicates that the data are a reasonably good fit to a normal distribution. See <https://www.mathworks.com/help/stats/normplot.html> for additional information.

Extended Data Table 1 Plasma donor characteristics
[Full size table](#)

Supplementary information

Supplementary Table 1

Mutation profile for the genomes of the outgrown viruses and for the infecting viruses of convalescent plasma donors.

Reporting Summary

Peer Review File

Rights and permissions

Reprints and Permissions

About this article



Check for
updates

Cite this article

Cele, S., Gazy, I., Jackson, L. *et al.* Escape of SARS-CoV-2 501Y.V2 from neutralization by convalescent plasma. *Nature* **593**, 142–146 (2021).
<https://doi.org/10.1038/s41586-021-03471-w>

Download citation

- Received: 21 January 2021
- Accepted: 18 March 2021
- Published: 29 March 2021
- Issue Date: 06 May 2021
- DOI: <https://doi.org/10.1038/s41586-021-03471-w>

Further reading

- **Persistence of immunoglobulin G after natural infection with SARS-CoV-2**
 - Nina Kreuzberger
 - , Caroline Hirsch
 - , Kanika Vanshylla

- , Veronica Di Cristanziano
- , Elena Dorando
- , Zahra Khosravi
- , Miriam Neidhardt
- , Susanne Salomon
- , Ina Monsef
- , Berit Lange
- & Nicole Skoetz

Cochrane Database of Systematic Reviews (2021)

- **Temporal Dominance of B.1.1.7 over B.1.354 SARS-CoV-2 Variant: A Hypothesis Based on Areas of Variant Co-Circulation**

- Evangelia Georgia Kostaki
- , Ioulia Tseti
- , Sotirios Tsiodras
- , George N. Pavlakis
- , Petros P. Sfikakis
- & Dimitrios Paraskevis

Life (2021)

- **Will SARS-CoV-2 variants of concern affect the promise of vaccines?**

- Ravindra K. Gupta

Nature Reviews Immunology (2021)

- **Cross-Reactive Neutralizing Antibody Responses Elicited by SARS-CoV-2 501Y.V2 (B.1.351)**

- Thandeka Moyo-Gwete
- , Mashudu Madzivhandila
- , Zanele Makhado
- , Frances Ayres
- , Donald Mhlanga
- , Brent Oosthuysen
- , Bronwen E. Lambson
- , Prudence Kgagudi
- , Houriiyah Tegally

- , Arash Iranzadeh
- , Deelan Doolabh
- , Lynn Tyers
- , Lionel R. Chinhoyi
- , Mathilda Mennen
- , Sango Skelem
- , Gert Marais
- , Constantinos K. Wibmer
- , Jinal N. Bhiman
- , Veronica Ueckermann
- , Theresa Rossouw
- , Michael Boswell
- , Tullio de Oliveira
- , Carolyn Williamson
- , Wendy A. Burgers
- , Ntobeko Ntusi
- , Lynn Morris
- & Penny L. Moore

New England Journal of Medicine (2021)

- **Age, Disease Severity and Ethnicity Influence Humoral Responses in a Multi-Ethnic COVID-19 Cohort**

- Muneerah Smith
- , Houari B. Abdesselem
- , Michelle Mullins
- , Ti-Myen Tan
- , Andrew J. M. Nel
- , Maryam A. Y. Al-Nesf
- , Ilham Bensmail
- , Nour K. Majbour
- , Nishant N. Vaikath
- , Adviti Naik
- , Khalid Ouararhni
- , Vidya Mohamed-Ali
- , Mohammed Al-Maadheed
- , Darien T. Schell
- , Seanantha S. Baros-Steyl
- , Nur D. Anuar
- , Nur H. Ismail
- , Priscilla E. Morris

- , Raja N. R. Mamat
- , Nurul S. M. Rosli
- , Arif Anwar
- , Kavithambigai Ellan
- , Rozainanee M. Zain
- , Wendy A. Burgers
- , Elizabeth S. Mayne
- , Omar M. A. El-Agnaf
- & Jonathan M. Blackburn

Viruses (2021)

Comments

By submitting a comment you agree to abide by our [Terms](#) and [Community Guidelines](#). If you find something abusive or that does not comply with our terms or guidelines please flag it as inappropriate.

[Download PDF](#)

Associated Content

Collection

[**Coronavirus**](#)

This article was downloaded by **calibre** from <https://www.nature.com/articles/s41586-021-03471-w>

| [Section menu](#) | [Main menu](#) |

- Article
- [Published: 07 April 2021](#)

CAR directs T cell adaptation to bile acids in the small intestine

- [Mei Lan Chen](#)^{1,2} na1,
- [Xiangsheng Huang](#)³ na1,
- [Hongtao Wang](#)³,
- [Courtney Hegner](#)^{1,2},
- [Yujin Liu](#)¹,
- [Jinsai Shang](#)⁴ nAff12,
- [Amber Eliason](#) ORCID: orcid.org/0000-0001-8765-686X¹,
- [Huitian Diao](#)^{1,2},
- [HaJeung Park](#)⁵,
- [Blake Frey](#)⁶,
- [Guohui Wang](#)³,
- [Sarah A. Mosure](#)^{1,2,4,7},
- [Laura A. Solt](#) ORCID: orcid.org/0000-0001-8807-0342^{1,2,7},
- [Douglas J. Kojetin](#) ORCID: orcid.org/0000-0001-8058-6168^{2,4,7},
- [Alex Rodriguez-Palacios](#)^{8,9},
- [Deborah A. Schady](#)¹⁰,
- [Casey T. Weaver](#)⁶,
- [Matthew E. Pipkin](#)^{1,2},
- [David D. Moore](#) ORCID: orcid.org/0000-0002-5151-9748¹¹ nAff13 &
- [Mark S. Sundrud](#) ORCID: orcid.org/0000-0002-4249-0525^{1,2}

[Nature](#) volume **593**, pages 147–151 (2021) [Cite this article](#)

- 6262 Accesses

- 112 Altmetric
- [Metrics details](#)

Subjects

- [Chronic inflammation](#)
- [Mucosal immunology](#)

Abstract

Bile acids are lipid-emulsifying metabolites synthesized in hepatocytes and maintained in vivo through enterohepatic circulation between the liver and small intestine¹. As detergents, bile acids can cause toxicity and inflammation in enterohepatic tissues². Nuclear receptors maintain bile acid homeostasis in hepatocytes and enterocytes³, but it is unclear how mucosal immune cells tolerate high concentrations of bile acids in the small intestine lamina propria (siLP). CD4⁺ T effector (T_{eff}) cells upregulate expression of the xenobiotic transporter MDR1 (encoded by *Abcb1a*) in the siLP to prevent bile acid toxicity and suppress Crohn's disease-like small bowel inflammation⁴. Here we identify the nuclear xenobiotic receptor CAR (encoded by *Nrl13*) as a regulator of MDR1 expression in T cells that can safeguard against bile acid toxicity and inflammation in the mouse small intestine. Activation of CAR induced large-scale transcriptional reprogramming in T_{eff} cells that infiltrated the siLP, but not the colon. CAR induced the expression of not only detoxifying enzymes and transporters in siLP T_{eff} cells, as in hepatocytes, but also the key anti-inflammatory cytokine IL-10. Accordingly, CAR deficiency in T cells exacerbated bile acid-driven ileitis in T cell-reconstituted *Rag1*^{-/-} or *Rag2*^{-/-} mice, whereas pharmacological activation of CAR suppressed it. These data suggest that CAR acts locally in T cells that infiltrate the small intestine to detoxify bile acids and resolve inflammation. Activation of this program offers an unexpected strategy to treat small bowel Crohn's disease and defines lymphocyte sub-specialization in the small intestine.

[Access through your institution](#)

[Change institution](#)
[Buy or subscribe](#)

Access options

Subscribe to Journal

Get full journal access for 1 year

\$199.00

only \$3.90 per issue

[Subscribe](#)

All prices are NET prices.

VAT will be added later in the checkout.

Tax calculation will be finalised during checkout.

Rent or Buy article

Get time limited or full article access on ReadCube.

from \$8.99

[Rent or Buy](#)

All prices are NET prices.

Additional access options:

- [Log in](#)
- [Access through your institution](#)
- [Learn about institutional subscriptions](#)

Fig. 1: CAR regulates MDR1 expression in CD4⁺ T cells.

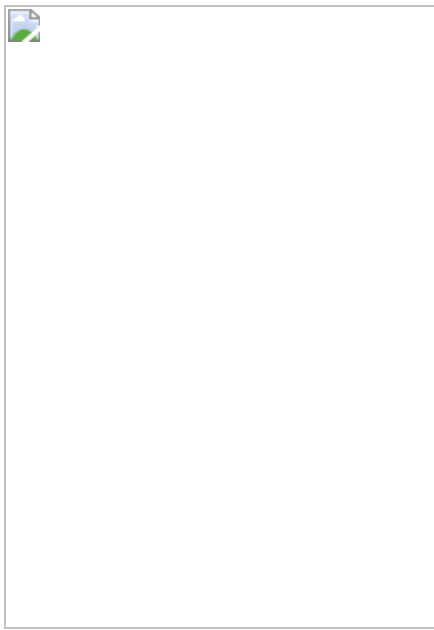


Fig. 2: CAR preferentially regulates T cell gene expression in the small intestine.

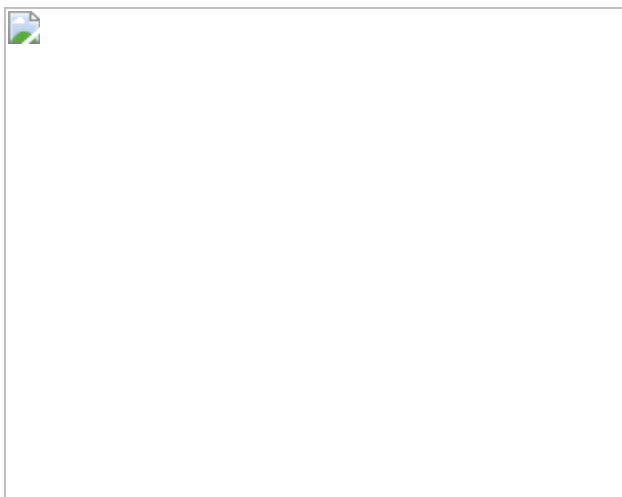


Fig. 3: CAR promotes IL-10 expression.

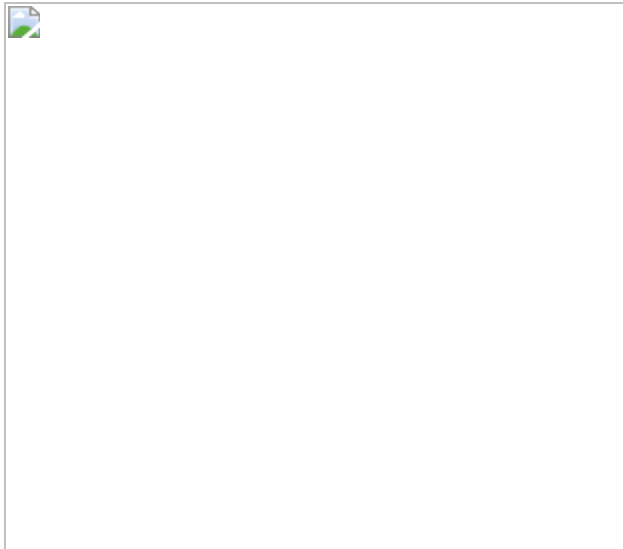
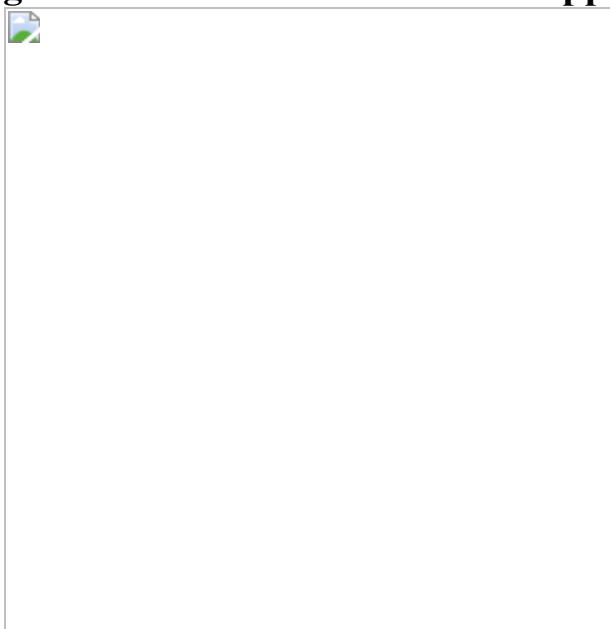


Fig. 4: CAR activation in T cells suppresses bile acid-driven ileitis.



Data availability

RNA-seq data for mouse ([GSE149218](#)) and human ([GSE149219](#)) CD4⁺ T cells described here are publicly available at the NCBI Gene Expression Omnibus (GEO) repository (series no. [GSE149220](#)). Sequence and other information related to shRNAmir retroviral constructs used in the pooled in vivo RNAi screen (related to Fig. 1, Extended Data Fig. 1), as well as complete gene lists derived from differential gene expression analyses of wild-type and *Nrl1i3*^{-/-} T_{eff} cells (related to Figs. 2a–d, [3a–c](#)) and statistical

analysis of differences between in vitro-polarized wild-type and *Nrl1i3*^{-/-} CD4⁺ T cells (related to Fig. 3*h, i*), are available in the Supplementary Information. Other relevant data are available from the corresponding authors upon reasonable request. Previously generated ChIP-seq and RNA-seq datasets analysed in this study include GEO accession numbers [GSE104734](#), [GSE112199](#), [GSE92940](#) and [GSE21670](#). Datasets obtained from the Molecular Signature Database (MSigDB; <https://www.gsea-msigdb.org/>) derive from GEO accession numbers [GSE14308](#) and [GSE21379](#). [Source data](#) are provided with this paper.

References

1. 1.

Hofmann, A. F. & Hagey, L. R. Key discoveries in bile acid chemistry and biology and their clinical applications: history of the last eight decades. *J. Lipid Res.* **55**, 1553–1595 (2014).

[CAS](#) [PubMed](#) [PubMed Central](#) [Article](#) [Google Scholar](#)

2. 2.

Poupon, R., Chazouillères, O. & Poupon, R. E. Chronic cholestatic diseases. *J. Hepatol.* **32** (Suppl. 1), 129–140 (2000).

[CAS](#) [PubMed](#) [Article](#) [PubMed Central](#) [Google Scholar](#)

3. 3.

Arab, J. P., Karpen, S. J., Dawson, P. A., Arrese, M. & Trauner, M. Bile acids and nonalcoholic fatty liver disease: Molecular insights and therapeutic perspectives. *Hepatology* **65**, 350–362 (2017).

[PubMed](#) [Article](#) [PubMed Central](#) [Google Scholar](#)

4. 4.

Cao, W. et al. The xenobiotic transporter Mdr1 enforces T cell homeostasis in the presence of intestinal bile acids. *Immunity* **47**, 1182–1196 (2017).

[CAS](#) [PubMed](#) [PubMed Central](#) [Article](#) [Google Scholar](#)

5. 5.

Lazar, M. A. Maturing of the nuclear receptor family. *J. Clin. Invest.* **127**, 1123–1125 (2017).

[PubMed](#) [PubMed Central](#) [Article](#) [Google Scholar](#)

6. 6.

Chen, R. et al. In vivo RNA interference screens identify regulators of antiviral CD4⁺ and CD8⁺ T cell differentiation. *Immunity* **41**, 325–338 (2014).

[CAS](#) [PubMed](#) [PubMed Central](#) [Article](#) [Google Scholar](#)

7. 7.

Ludescher, C. et al. Detection of activity of P-glycoprotein in human tumour samples using rhodamine 123. *Br. J. Haematol.* **82**, 161–168 (1992).

[CAS](#) [PubMed](#) [Article](#) [PubMed Central](#) [Google Scholar](#)

8. 8.

Zhang, J., Huang, W., Qatanani, M., Evans, R. M. & Moore, D. D. The constitutive androstane receptor and pregnane X receptor function coordinately to prevent bile acid-induced hepatotoxicity. *J. Biol. Chem.* **279**, 49517–49522 (2004).

[CAS](#) [PubMed](#) [Article](#) [PubMed Central](#) [Google Scholar](#)

9. 9.

Cerveny, L. et al. Valproic acid induces CYP3A4 and MDR1 gene expression by activation of constitutive androstane receptor and pregnane X receptor pathways. *Drug Metab. Dispos.* **35**, 1032–1041 (2007).

[CAS](#) [PubMed](#) [Article](#) [PubMed Central](#) [Google Scholar](#)

10. 10.

Wei, P., Zhang, J., Egan-Hafley, M., Liang, S. & Moore, D. D. The nuclear receptor CAR mediates specific xenobiotic induction of drug metabolism. *Nature* **407**, 920–923 (2000).

[ADS](#) [CAS](#) [PubMed](#) [Article](#) [PubMed Central](#) [Google Scholar](#)

11. 11.

Evans, R. M. & Mangelsdorf, D. J. Nuclear receptors, RXR, and the big bang. *Cell* **157**, 255–266 (2014).

[CAS](#) [PubMed](#) [PubMed Central](#) [Article](#) [Google Scholar](#)

12. 12.

Staudinger, J. L. et al. The nuclear receptor PXR is a lithocholic acid sensor that protects against liver toxicity. *Proc. Natl Acad. Sci. USA* **98**, 3369–3374 (2001).

[ADS](#) [CAS](#) [PubMed](#) [Article](#) [PubMed Central](#) [Google Scholar](#)

13. 13.

Ostanin, D. V. et al. T cell transfer model of chronic colitis: concepts, considerations, and tricks of the trade. *Am. J. Physiol. Gastrointest. Liver Physiol.* **296**, G135–G146 (2009).

[CAS](#) [PubMed](#) [Article](#) [Google Scholar](#)

14. 14.

Arnold, M. A. et al. Colesevelam and colestipol: novel medication resins in the gastrointestinal tract. *Am. J. Surg. Pathol.* **38**, 1530–1537 (2014).

[PubMed](#) [Article](#) [Google Scholar](#)

15. 15.

Dawson, P. A., Lan, T. & Rao, A. Bile acid transporters. *J. Lipid Res.* **50**, 2340–2357 (2009).

[CAS](#) [PubMed](#) [PubMed Central](#) [Article](#) [Google Scholar](#)

16. 16.

Cui, J. Y. & Klaassen, C. D. RNA-seq reveals common and unique PXR- and CAR-target gene signatures in the mouse liver transcriptome. *Biochim. Biophys. Acta* **1859**, 1198–1217 (2016).

[CAS](#) [PubMed](#) [PubMed Central](#) [Article](#) [Google Scholar](#)

17. 17.

Niu, B. et al. In vivo genome-wide binding interactions of mouse and human constitutive androstane receptors reveal novel gene targets. *Nucleic Acids Res.* **46**, 8385–8403 (2018).

[CAS](#) [PubMed](#) [PubMed Central](#) [Article](#) [Google Scholar](#)

18. 18.

De Calisto, J. et al. T-cell homing to the gut mucosa: general concepts and methodological considerations. *Methods Mol. Biol.* **757**, 411–434 (2012).

[PubMed](#) [Article](#) [CAS](#) [Google Scholar](#)

19. 19.

Maglich, J. M. et al. Identification of a novel human constitutive androstane receptor (CAR) agonist and its use in the identification of CAR target genes. *J. Biol. Chem.* **278**, 17277–17283 (2003).

[CAS](#) [PubMed](#) [Article](#) [Google Scholar](#)

20. 20.

Ramesh, R. et al. Pro-inflammatory human Th17 cells selectively express P-glycoprotein and are refractory to glucocorticoids. *J. Exp. Med.* **211**, 89–104 (2014).

[CAS](#) [PubMed](#) [PubMed Central](#) [Article](#) [Google Scholar](#)

21. 21.

Moore, L. B. et al. Pregnane X receptor (PXR), constitutive androstane receptor (CAR), and benzoate X receptor (BXR) define three pharmacologically distinct classes of nuclear receptors. *Mol. Endocrinol.* **16**, 977–986 (2002).

[CAS](#) [PubMed](#) [Article](#) [PubMed Central](#) [Google Scholar](#)

22. 22.

Karwacz, K. et al. Critical role of IRF1 and BATF in forming chromatin landscape during type 1 regulatory cell differentiation. *Nat. Immunol.* **18**, 412–421 (2017).

[CAS](#) [PubMed](#) [PubMed Central](#) [Article](#) [Google Scholar](#)

23. 23.

Gagliani, N. et al. Coexpression of CD49b and LAG-3 identifies human and mouse T regulatory type 1 cells. *Nat. Med.* **19**, 739–746 (2013).

[CAS](#) [PubMed](#) [Article](#) [PubMed Central](#) [Google Scholar](#)

24. 24.

Korn, T., Bettelli, E., Oukka, M. & Kuchroo, V. K. IL-17 and Th17 cells. *Annu. Rev. Immunol.* **27**, 485–517 (2009).

[CAS](#) [PubMed](#) [Article](#) [PubMed Central](#) [Google Scholar](#)

25. 25.

Maynard, C. L. et al. Regulatory T cells expressing interleukin 10 develop from Foxp3^+ and Foxp3^- precursor cells in the absence of interleukin 10. *Nat. Immunol.* **8**, 931–941 (2007).

[CAS](#) [PubMed](#) [Article](#) [PubMed Central](#) [Google Scholar](#)

26. 26.

Sano, T. et al. An IL-23R/IL-22 circuit regulates epithelial serum amyloid A to promote local effector Th17 responses. *Cell* **163**, 381–393 (2015).

[CAS](#) [PubMed](#) [PubMed Central](#) [Article](#) [Google Scholar](#)

27. 27.

Wan, Q. et al. Cytokine signals through PI-3 kinase pathway modulate Th17 cytokine production by CCR6^+ human memory T cells. *J. Exp. Med.* **208**, 1875–1887 (2011).

[CAS](#) [PubMed](#) [PubMed Central](#) [Article](#) [Google Scholar](#)

28. 28.

Yadava, K. et al. Natural Tr1-like cells do not confer long-term tolerogenic memory. *eLife* **8**, e44821 (2019).

[CAS](#) [PubMed](#) [PubMed Central](#) [Article](#) [Google Scholar](#)

29. 29.

Barrat, F. J. et al. In vitro generation of interleukin 10-producing regulatory CD4⁺ T cells is induced by immunosuppressive drugs and inhibited by T helper type 1 (Th1)- and Th2-inducing cytokines. *J. Exp. Med.* **195**, 603–616 (2002).

[CAS](#) [PubMed](#) [PubMed Central](#) [Article](#) [Google Scholar](#)

30. 30.

Song, X. et al. Microbial bile acid metabolites modulate gut ROR γ ⁺ regulatory T cell homeostasis. *Nature* **577**, 410–415 (2020).

[CAS](#) [PubMed](#) [Article](#) [PubMed Central](#) [Google Scholar](#)

31. 31.

Knott, S. R. V. et al. A computational algorithm to predict shRNA potency. *Mol. Cell* **56**, 796–807 (2014).

[CAS](#) [PubMed](#) [PubMed Central](#) [Article](#) [Google Scholar](#)

32. 32.

Fellmann, C. et al. An optimized microRNA backbone for effective single-copy RNAi. *Cell Rep.* **5**, 1704–1713 (2013).

[CAS](#) [PubMed](#) [PubMed Central](#) [Article](#) [Google Scholar](#)

33. 33.

Kim, J. J., Shajib, M. S., Manocha, M. M. & Khan, W. I. Investigating intestinal inflammation in DSS-induced model of IBD. *J. Vis. Exp.* **60**, 3678 (2012).

[Google Scholar](#)

34. 34.

Berg, D. J. et al. Enterocolitis and colon cancer in interleukin-10-deficient mice are associated with aberrant cytokine production and CD4⁺ TH1-like responses. *J. Clin. Invest.* **98**, 1010–1020 (1996).

[CAS](#) [PubMed](#) [PubMed Central](#) [Article](#) [Google Scholar](#)

35. 35.

Langmead, B. & Salzberg, S. L. Fast gapped-read alignment with Bowtie 2. *Nat. Methods* **9**, 357–359 (2012).

[CAS](#) [PubMed](#) [PubMed Central](#) [Article](#) [Google Scholar](#)

36. 36.

Zhang, Y. et al. Model-based analysis of ChIP-Seq (MACS). *Genome Biol.* **9**, R137 (2008).

[PubMed](#) [PubMed Central](#) [Article](#) [CAS](#) [Google Scholar](#)

37. 37.

Robinson, J. T. et al. Integrative genomics viewer. *Nat. Biotechnol.* **29**, 24–26 (2011).

[CAS](#) [PubMed](#) [PubMed Central](#) [Article](#) [Google Scholar](#)

38. 38.

Patro, R., Duggal, G., Love, M. I., Irizarry, R. A. & Kingsford, C. Salmon provides fast and bias-aware quantification of transcript expression. *Nat. Methods* **14**, 417–419 (2017).

[CAS](#) [PubMed](#) [PubMed Central](#) [Article](#) [Google Scholar](#)

39. 39.

Subramanian, A. et al. Gene set enrichment analysis: a knowledge-based approach for interpreting genome-wide expression profiles.

Proc. Natl Acad. Sci. USA **102**, 15545–15550 (2005).

[ADS](#) [CAS](#) [Article](#) [Google Scholar](#)

40. 40.

Mootha, V. K. et al. PGC-1 α -responsive genes involved in oxidative phosphorylation are coordinately downregulated in human diabetes. *Nat. Genet.* **34**, 267–273 (2003).

[CAS](#) [PubMed](#) [Article](#) [PubMed Central](#) [Google Scholar](#)

41. 41.

Durant, L. et al. Diverse targets of the transcription factor STAT3 contribute to T cell pathogenicity and homeostasis. *Immunity* **32**, 605–615 (2010).

[CAS](#) [PubMed](#) [PubMed Central](#) [Article](#) [Google Scholar](#)

42. 42.

Ritchie, M. E. et al. limma powers differential expression analyses for RNA-sequencing and microarray studies. *Nucleic Acids Res.* **43**, e47 (2015).

[PubMed](#) [PubMed Central](#) [Article](#) [CAS](#) [Google Scholar](#)

43. 43.

Wei, G. et al. Global mapping of H3K4me3 and H3K27me3 reveals specificity and plasticity in lineage fate determination of differentiating CD4+ T cells. *Immunity* **30**, 155–167 (2009).

[PubMed](#) [PubMed Central](#) [Article](#) [CAS](#) [Google Scholar](#)

44. 44.

Yusuf, I. et al. Germinal center T follicular helper cell IL-4 production is dependent on signaling lymphocytic activation molecule receptor (CD150). *J. Immunol.* **185**, 190–202 (2010).

[CAS](#) [PubMed](#) [PubMed Central](#) [Article](#) [Google Scholar](#)

45. 45.

Suino, K. et al. The nuclear xenobiotic receptor CAR: structural determinants of constitutive activation and heterodimerization. *Mol. Cell* **16**, 893–905 (2004).

[CAS](#) [PubMed](#) [PubMed Central](#) [Article](#) [Google Scholar](#)

[Download references](#)

Acknowledgements

We thank Core Facility staff at Scripps Florida and Baylor College of Medicine for technical support, and P. Dawson and A. Rao for discussions. This work was supported by Scripps Florida via the State of Florida (M.S.S.), the R. P. Doherty Jr.–Welch Chair in Science Q-0022 at Baylor College of Medicine (D.D.M.), National Institute of Health grants R21AI119728 (M.S.S.), R01AI118931 (M.S.S.), U19AI109976 (M.E.P.), P01AI145815 (M.E.P.), R01DK113789 (C.T.W.) and F30DK127865 (B.F.), and Crohn’s and Colitis Foundation (CCF) grants (Senior Research Award no. 422515 (M.S.S.) and Litwin IBD pioneer award no. 572171 (H.W.)).

Author information

Author notes

1. Jinsai Shang

Present address: Bioland Laboratory, Guangzhou Regenerative Medicine and Health Guangdong Laboratory, Guangzhou, China

2. David D. Moore

Present address: Department of Nutritional Sciences and Toxicology,
University of California Berkeley, Berkeley, CA, USA

3. These authors contributed equally: Mei Lan Chen, Xiangsheng Huang

Affiliations

1. Department of Immunology and Microbiology, The Scripps Research Institute, Jupiter, FL, USA

Mei Lan Chen, Courtney Hegner, Yujin Liu, Amber Eliason, Huitian Diao, Sarah A. Mosure, Laura A. Solt, Matthew E. Pipkin & Mark S. Sundrud

2. The Skaggs Graduate School of Chemical and Biological Sciences, The Scripps Research Institute, Jupiter, FL, USA

Mei Lan Chen, Courtney Hegner, Huitian Diao, Sarah A. Mosure, Laura A. Solt, Douglas J. Kojetin, Matthew E. Pipkin & Mark S. Sundrud

3. Section of Gastroenterology, Hepatology, and Nutrition, Department of Pediatrics, Baylor College of Medicine and Texas Children's Hospital, Houston, TX, USA

Xiangsheng Huang, Hongtao Wang & Guohui Wang

4. Department of Integrative Structural and Computational Biology, The Scripps Research Institute, Jupiter, FL, USA

Jinsai Shang, Sarah A. Mosure & Douglas J. Kojetin

5. X-ray Crystallography Core Facility, The Scripps Research Institute, Jupiter, FL, USA

HaJeung Park

6. Department of Pathology, University of Alabama at Birmingham,
Birmingham, AL, USA

Blake Frey & Casey T. Weaver

7. Department of Molecular Medicine, The Scripps Research Institute,
Jupiter, FL, USA

Sarah A. Masure, Laura A. Solt & Douglas J. Kojetin

8. Division of Gastroenterology and Liver Disease, School of Medicine,
Case Western Reserve University, Cleveland, OH, USA

Alex Rodriguez-Palacios

9. University Hospitals Research and Education Institute, University
Hospitals Cleveland Medical Center, Cleveland, OH, USA

Alex Rodriguez-Palacios

10. Department of Pathology and Immunology, Baylor College of
Medicine and Texas Children's Hospital, Houston, TX, USA

Deborah A. Schady

11. Department of Molecular and Cellular Biology, Baylor College of
Medicine, Houston, TX, USA

David D. Moore

Authors

1. Mei Lan Chen

[View author publications](#)

You can also search for this author in [PubMed](#) [Google Scholar](#)

2. Xiangsheng Huang

[View author publications](#)

You can also search for this author in [PubMed](#) [Google Scholar](#)

3. Hongtao Wang

[View author publications](#)

You can also search for this author in [PubMed](#) [Google Scholar](#)

4. Courtney Hegner

[View author publications](#)

You can also search for this author in [PubMed](#) [Google Scholar](#)

5. Yujin Liu

[View author publications](#)

You can also search for this author in [PubMed](#) [Google Scholar](#)

6. Jinsai Shang

[View author publications](#)

You can also search for this author in [PubMed](#) [Google Scholar](#)

7. Amber Eliason

[View author publications](#)

You can also search for this author in [PubMed](#) [Google Scholar](#)

8. Huitian Diao

[View author publications](#)

You can also search for this author in [PubMed](#) [Google Scholar](#)

9. HaJeung Park

[View author publications](#)

You can also search for this author in [PubMed](#) [Google Scholar](#)

10. Blake Frey

[View author publications](#)

You can also search for this author in [PubMed](#) [Google Scholar](#)

11. Guohui Wang
[View author publications](#)

You can also search for this author in [PubMed](#) [Google Scholar](#)

12. Sarah A. Masure
[View author publications](#)

You can also search for this author in [PubMed](#) [Google Scholar](#)

13. Laura A. Solt
[View author publications](#)

You can also search for this author in [PubMed](#) [Google Scholar](#)

14. Douglas J. Kojetin
[View author publications](#)

You can also search for this author in [PubMed](#) [Google Scholar](#)

15. Alex Rodriguez-Palacios
[View author publications](#)

You can also search for this author in [PubMed](#) [Google Scholar](#)

16. Deborah A. Schady
[View author publications](#)

You can also search for this author in [PubMed](#) [Google Scholar](#)

17. Casey T. Weaver
[View author publications](#)

You can also search for this author in [PubMed](#) [Google Scholar](#)

18. Matthew E. Pipkin
[View author publications](#)

You can also search for this author in [PubMed](#) [Google Scholar](#)

19. David D. Moore

[View author publications](#)

You can also search for this author in [PubMed](#) [Google Scholar](#)

20. Mark S. Sundrud

[View author publications](#)

You can also search for this author in [PubMed](#) [Google Scholar](#)

Contributions

Study design: M.L.C., X.H., H.W., J.S., H.P., B.F., L.A.S., D.J.K., A.R.-P., D.A.S., C.T.W., M.E.P., D.D.M. and M.S.S. Data generation: M.L.C., X.H., H.W., C.H., Y.L., J.S., A.E. and S.A.M. Bioinformatics: M.L.C., H.D., G.W., A.R.-P. and M.E.P. Manuscript: M.L.C., X.H., C.H., A.E., D.J.K., A.R.-P., C.T.W., M.E.P., D.D.M. and M.S.S. Principal investigators: L.A.S., D.J.K., A.R.-P., D.A.S., C.T.W., M.E.P., D.D.M. and M.S.S.

Corresponding authors

Correspondence to [David D. Moore](#) or [Mark S. Sundrud](#).

Ethics declarations

Competing interests

M.S.S. is a consultant to Sigilon Therapeutics and Sage Therapeutics.

Additional information

Peer review information *Nature* thanks Richard Blumberg and the other, anonymous, reviewer(s) for their contribution to the peer review of this work.

Publisher's note Springer Nature remains neutral with regard to jurisdictional claims in published maps and institutional affiliations.

Extended data figures and tables

Extended Data Fig. 1 Nuclear receptor-dependent regulation of effector T cell persistence and MDR1 expression in vivo.

a, Left, abundance of shRNAmirs in ex vivo-isolated spleen and in vitro-transduced (input) T_{eff} cells. shRNAmirs with one normalized read or fewer in both ex vivo spleen and input T_{eff} cell pools were considered ‘poorly represented’ (highlighted green). Well-represented shRNAmirs with ≤ 10 -fold change between ex vivo spleen and input T_{eff} cell pools (between blue lines) were considered for downstream analysis. Right, abundance of shRNAmirs, filtered for minimal effects on in vivo T_{eff} cell persistence, in ex vivo-isolated $MDR1^{hi}$ ($Rh123^{lo}$) and $MDR1^{lo}$ ($Rh123^{hi}$) siLP T_{eff} cells.

b, Mean \pm s.e.m. \log_2 [fold change in abundance] of shRNAmirs against *Cd19* ($n = 3$), *Abcb1a* ($n = 2$), *Nrl1i3* ($n = 5$), *Thra* ($n = 6$) and *Esrra* ($n = 3$) in FVB/N wild-type $Rh123^{lo}$ ($MDR1^{hi}$) versus $Rh123^{hi}$ ($MDR1^{lo}$) T_{eff} cells (sorted as in Fig. 1a) recovered from spleens or siLP of transferred FVB/N.*Rag1^{-/-}* mice. **a, b**, Data incorporate shRNAmir abundance, determined by DNA-seq, in two independent screens using pooled spleens and siLP from 10 transferred FVB/N.*Rag1^{-/-}* mice per screen. **c**, Top, schematic of the mouse *Nrl1i3* locus. Positions of seed sequences for *Nrl1i3*-specific shRNAmirs are shown. Untranslated regions (UTRs) are indicated by open boxes. Bottom, ex vivo Rh123 efflux, determined by flow cytometry, in FVB/N wild-type T_{eff} cells transduced with ametrine-expressing retroviruses containing control (shCD8a) or one of five *Nrl1i3*-specific shRNAmirs re-isolated from spleens of FVB/N.*Rag1^{-/-}* mice six weeks after T cell transfer. Rh123 efflux in transduced (ametrine $^+$; red) cells is overlaid with that in bystander untransduced (ametrine $^-$; blue) T_{eff} cells from the same mouse. Background Rh123 efflux in untransduced T_{eff} cells treated with the MDR1 inhibitor elacridar is shown in grey. Representative of at least ten mice per group analysed in three independent experiments. **d**,

Mean \pm s.e.m. normalized ex vivo Rh123 efflux in FVB/N wild-type spleen T_{eff} cells expressing control (shCd8a; $n = 11$) or Nr1i3-specific shRNAmirs (shNr1i3.1 ($n = 10$), shNr1i3.2 ($n = 10$), shNr1i3.3 ($n = 12$), shNr1i3.4 ($n = 10$) and shNr1i3.5 ($n = 10$)), determined by flow cytometry as in **c**. Rh123 efflux was normalized to control shCd8a-expressing T_{eff} cells after calculating the change (Δ) in Rh123 mean fluorescence intensity (MFI) between bystander transduced (ametrine⁺) and untransduced (ametrine⁻) T_{eff} cells. * $P = 0.049$, ** $P = 0.003$, *** $P = 0.0006$, one-way ANOVA with Dunnett's correction for multiple comparisons. **e**, Mean \pm s.e.m. relative *Abcb1a*, *Nr1i3*, and *Cyp2b10* expression determined by qPCR in FVB/N spleen T_{eff} cells FACS-sorted from FVB/N.*Rag1*^{-/-} recipient mice expressing either a negative control shRNAmir against CD8 (shCd8a; $n = 8$), or the indicated shRNAmirs against CAR (shNr1i3.1 ($n = 8$), shNr1i3.2 ($n = 8$), shNr1i3.3 ($n = 8$), shNr1i3.4 ($n = 8$) and shNr1i3.5 ($n = 8$). $P < 0.05$ versus shCd8a-expressing cells (one-way ANOVA with Tukey's correction for multiple comparisons) are shown. **f**, Median log₂[fold change] in shRNAmir abundance between FVB/N wild-type ex vivo-isolated spleen and in vitro-transduced (input) T_{eff} cells. **a**, **f**, shRNAmir abundance reflects the mean number of normalized reads, by DNA-seq, in the indicated T_{eff} subsets obtained in two independent screens, each using cells transferred into 10 FVB/N.*Rag1*^{-/-} mice. **g**, Ex vivo Rh123 efflux, determined by flow cytometry, in CD45.1 wild-type (B6; blue) or CD45.2 (red) CAR-deficient (B6.Nr1i3^{-/-}), PXR-deficient (B6.Nr1i2^{-/-}) or CAR/PXR double-deficient (B6.Nr1i3^{-/-}Nr1i2^{-/-}) T_{eff} cells (gated as in Extended Data Fig. [6a](#)) recovered from spleens of B6.*Rag1*^{-/-} mice six weeks after co-transfer of mixed naive T cells. Background Rh123 efflux in CD45.1 B6 T_{eff} cells treated with the MDR1 inhibitor elacridar is shown in grey. Representative of a total of seven mice per group analysed in two independent experiments. **h**, Mean \pm s.e.m. normalized Rh123 efflux in congenically transferred CD45.1 wild-type (B6; $n = 7$) or CD45.2 CAR-deficient (B6.Nr1i3^{-/-}; $n = 7$), PXR-deficient (B6.Nr1i2^{-/-}; $n = 7$) or CAR/PXR double-deficient (B6.Nr1i3^{-/-}Nr1i2^{-/-}; $n = 7$) spleen T_{eff} cells, determined by flow cytometry as in **g**. * $P < 0.019$, ** $P < 0.002$, one-way ANOVA with Tukey's correction for multiple comparisons. **i**, Mean \pm s.e.m. relative *Abcb1a* expression determined by ex vivo qPCR in CD45.1 wild-

type (B6; $n = 5$) or CD45.2 CAR-deficient (B6.*Nrl1i3*^{-/-}; $n = 5$), PXR-deficient (B6.*Nrl1i2*^{-/-}; $n = 4$) or CAR/PXR double-deficient (B6.*Nrl1i3*^{-/-}*Nrl1i2*^{-/-}; $n = 5$) spleen T_{eff} cells as in **g**. $P < 0.05$ versus wild-type (B6) T_{eff} cells (one-way ANOVA with Tukey's correction for multiple comparisons) are shown. [Source data](#)

Extended Data Fig. 2 Inhibition of bile acid reabsorption rescues ileitis induced by CAR-deficient T cells in reconstituted *Rag*^{-/-} mice.

a, Mean ± s.e.m. weight loss of co-housed B6.*Rag2*^{-/-} mice transplanted with wild-type (B6; blue; $n = 15$) or CAR-deficient (B6.*Nrl1i3*^{-/-}; red; $n = 13$) naive CD4⁺ T cells and treated with 2% (w:w) cholestyramine (CME) beginning three weeks after T cell transfer. NS, not significant by two-way ANOVA. **b**, Top, H&E-stained sections of colons or terminal ilea from B6.*Rag2*^{-/-} mice reconstituted with wild-type or CAR-deficient T cells and treated with or without CME as in **a**. Representative of 12 mice per group analysed in 3 independent experiments. Magnification, 10×; scale bars, 100 μm. Bottom, mean ± s.e.m. histology scores ($n = 12$) for colons or terminal ilea as in **a**. NS, not significant by unpaired two-tailed Student's *t*-test. **c**, Mean ± s.e.m. weight loss ($n = 16$ per group) of co-housed B6.*Rag1*^{-/-} mice with or without ASBT (encoded by *Slc10a2*) after reconstitution with wild-type (B6) or CAR-deficient (B6.*Nrl1i3*^{-/-}) naive CD4⁺ T cells. ** $P = 0.005$ (CAR-deficient T cell transfer into control versus *Slc10a2*^{-/-}*Rag1*^{-/-} recipients), two-way ANOVA. **d**, Top, H&E-stained colon or terminal ileum sections from control or ASBT-deficient B6.*Rag1*^{-/-} mice reconstituted with wild-type or CAR-deficient T cells as in **c**. Representative of five mice per group. Bottom, mean ± s.e.m. histology scores for colons or terminal ilea ($n = 5$) as above. P values (one-way ANOVA with Tukey's correction for multiple comparisons) are listed. NS, not significant. [Source data](#)

Extended Data Fig. 3 Shared features of CAR-dependent gene expression in mucosal T cells and hepatocytes.

a, Overlap between genes induced in B6 wild-type mouse hepatocytes by in vivo treatment with TC or PCN, relative to vehicle (CO, corn oil). **b**, Enrichment of genes induced by TC, but not PCN, in mouse hepatocytes (as in **a**), within those reduced in CAR-deficient ($B6.NrIi3^{-/-}$) versus wild-type (B6) siLP T_{eff} cells from week-3 congenically co-transferred $RagI^{-/-}$ mice (as in Fig. 2a–c). Nominal P values compare observed NESs to the null distribution for 1,000 permutations. **c**, Differential gene expression, determined by DESeq2 and shown as a volcano plot, between CAR-deficient ($B6.NrIi3^{-/-}$) and wild-type (B6) siLP T_{eff} cells re-isolated from transferred $B6.RagI^{-/-}$ mice, as in Fig. 2a. Genes induced by TC, but not PCN, treatment in mouse hepatocytes (as in **a**; purple), bound by CAR in ChIP-seq analysis of hepatocytes from TC-treated mice (blue), or both (red) are highlighted. Chi-square P values are indicated. **d**, CAR occupancy, determined by ChIP-seq, at representative loci whose expression is regulated by CAR in both mucosal T cells and hepatocytes within mouse hepatocytes ectopically expressing epitope-tagged mouse (m) or human (h) CAR proteins and re-isolated from mice after treatment with TC or CITCO. *False discovery rate (FDR) $q < 0.05$ determined using MACS2 base settings.

Extended Data Fig. 4 CAR promotes effector T cell persistence in the presence of small intestinal bile acids.

a, Percentages of live $CD44^{hi}$ wild-type (B6; $CD45.1^+$; blue) or CAR-deficient ($B6.NrIi3^{-/-}$; $CD45.1^-$; red) T_{eff} cells, determined by flow cytometry and gated as in Extended Data Fig. 6a, in tissues from reconstituted $B6.RagI^{-/-}$ mice over time. Numbers indicate percentages; representative of five mice per tissue and time point. **b**, Fitness, defined as mean \pm s.e.m. \log_2 [fold change (F.C.)] of CAR-deficient ($B6.NrIi3^{-/-}$) versus wild-type (B6) T_{eff} cell percentages ($n = 5$) in tissues from congenically co-transferred $RagI^{-/-}$ mice over time, determined by flow cytometry as in **a**. **c**, Percentage of wild-type (B6, $CD45.1^+$; blue) and CAR-deficient ($B6.NrIi3^{-/-}$, $CD45.1^-$; red) naive ($CD62L^{hi}$) $CD4^+$ T cells after sorting and mixing, and before in vivo transfer into $RagI^{-/-}$ mice (input T_{naive}); representative of three mixtures used for analysing resulting

T_{eff} cells at 2, 4 or 6 weeks after transfer. **d**, Equal numbers of CD45.1 wild-type (B6; blue) and CD45.2 CAR-deficient (B6.*Nrl1i3*^{-/-}; red) naive CD4⁺ T cells were transferred together into co-housed *Rag1*^{-/-} mice with or without the ileal bile acid reuptake transporter ASBT (gene symbol *Slc10a2*). The resulting T_{eff} cells from siLP were analysed two weeks after T cell transfer via flow cytometry. **e**, Percentages of live CD44^{hi} wild-type (B6; CD45.1⁺; blue) or CAR-deficient (B6.*Nrl1i3*^{-/-}; CD45.1⁻; red) T_{eff} cells, determined by flow cytometry and gated as in Extended Data Fig. 6a, in siLP from week-2 reconstituted B6.*Rag1*^{-/-} mice. Numbers indicate percentages; representative of 8–10 mice analysed over two independent experiments. **f**, Mean ± s.e.m. absolute numbers of live CD45.1 wild-type (B6; left) or CD45.2 CAR-deficient (B6.*Nrl1i3*^{-/-}; right) T_{eff} cells, determined by ex vivo flow cytometry as in e, from siLP two weeks after mixed T cell transfer into control (*Slc10a2*^{+/+}; blue; $n = 8$) or ASBT-deficient (*Slc10a2*^{-/-}; red; $n = 10$) *Rag1*^{-/-} recipients. Fold changes in cell numbers recovered from ASBT-deficient versus control recipients, as well as P values (two-tailed unpaired Student's *t*-test), are indicated. [Source data](#)

Extended Data Fig. 5 Preferential CAR expression and function in human T_{eff} cells expressing small bowel homing receptors.

a, FACS-based identification of human CD4⁺ T cell subsets in PBMCs from healthy adult human donors. Right, expression of integrin α4 (α4 int.) in gated naive (grey), T_{reg} (blue), and T_{eff} (red) T cells. **b**, Expression of integrin β7 (β7 int.) and CCR9 in total naive CD4⁺ T cells, or in α4 int. with or without T_{reg} or T_{eff} subsets (gated as in a). Representative of seven independent experiments using PBMCs from different donors. **c**, Percentages of α4⁺β7⁺CCR9⁺ naive T, T_{reg} , and T_{eff} cells, determined by flow cytometry as in a, b. Individual data points for seven independent experiments are shown and connected by lines. P values (one-way ANOVA with Tukey's correction for multiple comparisons) are shown. **d**, Ex vivo Rh123 efflux in CD4⁺ T cell subsets (gated as in a, b) in the presence (grey) or absence (red) of the selective MDR1 inhibitor elacridar. Representative of seven experiments. **e**, Mean ± s.e.m. percentages ($n = 7$) of Rh123^{lo}

(MDR1⁺) T_{eff} subsets, determined by flow cytometry as in **d**. *P* values (one-way ANOVA with Tukey's correction for multiple comparisons) are shown. **f**, Mean ± s.e.m. ex vivo expression, determined by qPCR, of *NR1I3* (*n* = 12), *ABCB1* (*n* = 12) and *CYP2B6* (*n* = 10) in α4⁻β7⁻CCR9⁻ and α4⁺β7⁺CCR9⁺ naive T, T_{reg} and T_{eff} cells, FACS-sorted as in **a**, **b**. *P* values (one-way ANOVA with Tukey's correction for multiple comparisons) are shown. **g**, Mean ± s.e.m. relative *CYP2B6* expression (*n* = 5), determined by qPCR, in CD4⁺ T cell subsets (as in **f**) stimulated ex vivo in the presence of titrating concentrations of CITCO. Gene expression analysed 24 h after activation. ****P* < 0.0001 by two-way ANOVA. **h**, Mean ± s.e.m. normalized *ABCB1* or *CYP2B6* expression, determined by RNA-seq and presented as TPM, in FACS-sorted α4⁺β7⁺CCR9⁺ T_{eff} cells stimulated in vitro with or without CITCO. Data from four independent RNA-seq experiments using cells sorted from different healthy adult donors; *P* values (paired two-tailed Student's *t*-test) are indicated. **i**, Identification of CD4⁺ naive (T_{naive}; CD25⁻CD45RO⁻; grey) or T_{eff} (CD25⁻CD45RO⁺; red) cells, by flow cytometry, from healthy adult human PBMCs. For improved purity of T_H1, T_H2, T_H17 and T_H17.1 cells, CCR10-expressing T_H22 cells were excluded. CCR6 expression in naive T (grey) or non-T_H22 T_{eff} cells (red) is shown on the right; CCR6⁺ or CCR6⁻ T_{eff} cells were gated to enrich for T_H17 or non-T_H17 lineages, respectively. **j**, Expression of CCR4 and CXCR3 in CCR6⁻ (non-T_H17; left) or CCR6⁺ (T_H17; right) T_{eff} cells identifies enriched CCR6⁻CCR4^{lo}CXCR3^{hi} (T_H1; orange), CCR6⁻CCR4^{hi}CXCR3^{lo} (T_H2; blue), CCR6⁺CCR4^{hi}CXCR3^{lo} (T_H17; green), and CCR6⁺CCR4^{lo}CXCR3^{hi} (T_H17.1; red) subsets. **k**, Expression of integrin α4 (α4 int.; top) in T_H2, T_H1, T_H17 and T_H17.1 human T_{eff} cells gated as in **a**, **b**. Expression of integrin β7 (β7 int.) and CCR9 within α4 int⁻ (middle) or α4 int⁺ (bottom) T_H2, T_H1, T_H17 or T_H17.1 cells gated as above. **i–k**, Representative of nine independent experiments using PBMCs from different healthy adult donors. **l**, Percentages (*n* = 9) of α4⁺β7⁺CCR9⁺ cells (gated as in **a**, **b**) amongst ex vivo T_H1, T_H2, T_H17 and T_H17.1 T_{eff} cells (gated as in **i–k**). Data from independent donors are connected by lines; *P* values (one-way ANOVA with Tukey's correction for multiple

comparisons) are shown. **m**, MDR1-dependent Rh123 efflux in the indicated T_H1, T_H2, T_H17 and T_H17.1 T_{eff} subsets gated by expression of α4 int., β7 int., and/or CCR9 in the presence (grey) or absence (red) of elacridar. Representative of eight independent experiments using PBMCs from different donors. **n**, Mean ± s.e.m. percentages ($n = 8$) of Rh123^{lo} (MDR1⁺) cells within T_H1, T_H2, T_H17 and T_H17.11 T_{eff} subsets gated according to expression of α4 int., β7 int., and/or CCR9 as in e. P values (one-way ANOVA with Tukey's correction for multiple comparisons) are indicated; **** $P < 0.0001$. N.D., not detected; NS, not significant. [Source data](#)

Extended Data Fig. 6 TCPOBOP promotes CAR-dependent gene expression in ex vivo-isolated effector T cells.

a, Top left, equal numbers of CD45.1 wild-type (B6; blue) and CD45.2 CAR-deficient (B6.*Nrl1i3*^{-/-}; red) naive CD4⁺ T cells were transferred together into B6.*Rag1*^{-/-} mice. The resulting T_{eff} cells were FACS-purified from spleen after 3 weeks. Right, sequential gating strategy for re-isolating wild-type and CD45.2 CAR-deficient spleen T_{eff} cells. Bottom left, mean ± s.e.m. relative expression of *Abcb1a* ($n = 4$), *Cyp2b10* ($n = 4$), and *Il10* ($n = 3$), determined by qPCR, in ex vivo-isolated wild-type (B6) or CAR-deficient (B6.*Nrl1i3*^{-/-}) spleen T_{eff} cells. These cells were used for ex vivo stimulation experiments with or without small-molecule ligands (**b**, **c**). P values (paired two-tailed Student's *t*-test) are indicated. **b**, Mean ± s.e.m. relative expression of *Abcb1a* ($n = 4$), *Cyp2b10* ($n = 4$), and *Il10* ($n = 3$), by qPCR, in wild-type (B6) or CAR-deficient T_{eff} cells isolated from transferred *Rag1*^{-/-} mice (as in **a**), and stimulated ex vivo with anti-CD3 and anti-CD28 antibodies in the presence or absence of TC (10 μM), the mCAR inverse agonist And (10 μM), or both. P values (one-way ANOVA with Tukey's correction for multiple comparisons) are indicated; **** $P < 0.0001$. **c**, Mean ± s.e.m. relative expression of *Abcb1a*, *Cyp2b10*, and *Il10* ($n = 5$), determined by qPCR, in wild-type (B6) or CAR-deficient (B6.*Nrl1i3*^{-/-}) T_{eff} cells isolated and stimulated as in **a**, **b** in the presence or absence of TC (10 μM) or PCN (10 μM). Data are presented as fold change in mRNA abundance relative to vehicle-treated cells (DMSO for TC;

ethanol for PCN). **** $P < 0.0001$, one-way ANOVA with Dunnett's correction for multiple comparisons. NS, not significant. [Source data](#)

Extended Data Fig. 7 Characteristics of endogenous intestinal metabolites that activate the CAR LBD.

a, Mean ± s.e.m. activation (triplicate samples) of recombinant hRXR α LBD homodimers, determined by TR-FRET in the presence of TC (blue) or 9-*cis* retinoic acid (RA; red). Median effective concentration (EC_{50}) of 9-*cis* RA-dependent hRXR α LBD homodimer activation is indicated. Representative of more than five independent experiments. **b**, Mean ± s.e.m. activation ($n = 3$) of hRXR α LBD homodimers, determined by TR-FRET as in **a**, in the presence of titrating concentrations of siLC, bile, cLC or serum from wild-type B6 mice. NS, not significant by one-way ANOVA with Dunnett's correction for multiple comparisons. **c**, Mean ± s.e.m. activation ($n = 3$) of CAR–RXR LBD heterodimers, determined by TR-FRET, in the presence of titrating concentrations of siLC isolated from wild-type B6 mice housed under specific pathogen-free (SPF) or germ-free (GF) conditions and pre-treated with or without cholestyramine (CME) to deplete free bile acids. **** $P < 0.0001$, one-way ANOVA with Dunnett's correction for multiple comparisons. **a–c**, The bars for each tissue extract indicate dilution series (left to right): diluent (PBS) alone; 0.01%, 0.1%, 1%. Data are shown from three independent experiments using extracts from different wild-type mice, with each concentration from each individual mouse run in triplicate. **d**, Mean ± s.e.m. TR-FRET signals ($n = 3$) of CAR–RXR LBD heterodimers in the presence of titrating concentrations of individual bile acid (BA) species. NS, not significant by one-way ANOVA with Dunnett's correction for multiple comparisons. The bars for bile acids indicate concentrations (left to right): vehicle (DMSO), 10 μ M, 100 μ M, 1,000 μ M. Data are shown from three independent experiments, in which each bile acid concentration was run in triplicate. [Source data](#)

Extended Data Fig. 8 CAR promotes IL-10 expression in mucosal T_{eff} cells and regulates T_{R1} and T_{H17} cell development in the small intestine.

a, Equal numbers of CD45.1 wild-type (B6; blue) and CD45.2 CAR-deficient (B6.*Nrl1i3*^{-/-}; red) naive CD4⁺ T cells were transferred together into *Rag1*^{-/-} mice. The resulting T_{eff} cells were analysed using surface and intracellular flow cytometry after ex vivo stimulation with PMA and ionomycin at 2, 4, and 6 weeks from spleen, MLN, siLP, or cLP. Gating hierarchy is shown from a representative sample of MLN mononuclear cells at two weeks after T cell transfer. **b**, Intracellular IL-10 and IFN γ expression, determined by flow cytometry, in wild-type (B6, blue; left) and CAR-deficient (B6.*Nrl1i3*^{-/-}, red; right) non-T_H17 T_{eff} cells, gated as in **a**, from tissues of T cell-reconstituted B6.*Rag1*^{-/-} mice over time. Numbers indicate percentages; representative of five mice per tissue and time point. **c, d**, Mean \pm s.e.m. percentages (**c**) or numbers (**d**) ($n = 5$) of IL-10-expressing wild-type (B6, left) or CAR-deficient (B6.*Nrl1i3*^{-/-}, right) T_{eff} cells, determined by ex vivo flow cytometry as in **a, b** from tissues of transferred B6.*Rag1*^{-/-} mice over time. **e**, Specificity of IL-10 intracellular staining, as validated by analysis of IL-10 production by CD45.1 wild-type (B6; blue) or CD45.2 *Il10*^{-/-} (red) T_{eff} cells isolated from spleen or siLP of congenically co-transferred *Rag1*^{-/-} mice. Representative of six mice analysed over two independent experiments. **f**, Expression of ROR γ t and IL-17A, determined by intracellular FACS analysis as in Extended Data Fig. [8a](#), in wild-type (B6) or CAR-deficient (B6.*Nrl1i3*^{-/-}) CD4⁺ T_{eff} cells from tissues of reconstituted *Rag1*^{-/-} mice two weeks after mixed T cell transfer. Numbers indicate percentages; representative of five mice per tissue and time point. **g**, Mean \pm s.e.m. percentages of ($n = 5$) wild-type (B6; blue) or CAR-deficient (B6.*Nrl1i3*^{-/-}; red) ROR γ t⁺IL-17A⁻ T_{eff} cells, determined by intracellular flow cytometry as in **a**. * $P = 0.029$, paired two-tailed Student's *t*-test. **h**, Expression of ROR γ t and IL-17A, determined by intracellular FACS analysis, in wild-type (B6) or *Il10*^{-/-} T_{eff} cells from tissues of reconstituted *Rag1*^{-/-} mice two weeks after mixed T cell transfer. Numbers indicate percentages; representative of five mice per tissue and time point. **i**, Mean \pm s.e.m. percentages of ($n = 7$) wild-type (B6; blue) or *Il10*^{-/-} (red) ROR γ t⁺IL-17A⁻ T_{eff} cells, determined by intracellular flow cytometry as in **c**. * $P = 0.033$, ** $P = 0.0099$, paired two-tailed Student's *t*-test. [Source data](#)

Extended Data Fig. 9 CAR expression and function in mucosal Teff cells is increased in response to intestinal inflammation.

a, Percentages of CD3⁺CD4⁺ T cells in tissues from *Rag1*^{-/-} mice transplanted with congenic mixtures of wild-type and CAR-deficient naive CD4⁺ T cells over time, determined by flow cytometry. Representative of five mice per tissue and time point. **b**, Mean ± s.e.m. absolute numbers of CD3⁺CD4⁺ T_H cells ($n = 5$) in tissues from transferred B6.*Rag1*^{-/-} mice over time, determined by flow cytometry as in **a**. **c**, Mean ± s.e.m. relative ex vivo *Nr1i3*, *Abcb1a*, *Cyp2b10*, and *Il10* gene expression ($n = 3$), determined by qPCR, in wild-type (B6) CD4⁺ T_{eff} cells (sorted as in Extended Data Fig. 8a) from spleens of transferred B6.*Rag1*^{-/-} mice over time. **d**, Top, expression of FOXP3 and ROR γ t, determined by intracellular staining after ex vivo (PMA + ionomycin) stimulation, in CD4⁺CD44^{hi} cells from spleen (left) or siLP (right) of wild-type (B6, blue) or CAR-deficient (B6.*Nr1i3*^{-/-}, red) mice injected with isotype control (IgG) or soluble anti-CD3. Bottom, expression of IL-10 and IL-17A in wild-type or CAR-deficient spleen or siLP T cell subsets from mice treated with isotype control (IgG) or anti-CD3 antibodies. Cells were gated and analysed by flow cytometry as above. Numbers indicate percentages; representative of three mice per group and genotype analysed over two independent experiments. **e**, **f**, Mean ± s.e.m. percentages of IL-10-expressing T cell subsets ($n = 3$), gated and analysed by ex vivo flow cytometry as in **a**, in spleen (**e**) or siLP (**f**) T_H cell subsets from wild-type (B6, blue) or CAR-deficient (B6.*Nr1i3*^{-/-}, red) mice injected with isotype control (IgG) or anti-CD3 antibody. *P* values (unpaired Student's *t*-test) are indicated; NS, not significant. [Source data](#)

Extended Data Fig. 10 TCPOBOP protection against bile acid-induced ileitis requires CAR expression in T cells.

a, Mean ± s.e.m. weight loss ($n = 5$ per group) of co-housed B6.*Rag2*^{-/-} mice transplanted with CAR-deficient (B6.*Nr1i3*^{-/-}) CD4⁺ naive T cells and maintained on a cholic acid-supplemented diet with (CA/TC) or without (CA/Veh) TC treatment. Weights are shown relative to three weeks

after transfer, when TC treatments were initiated. NS, not significant; two-way ANOVA. **b**, H&E-stained sections of terminal ilea or colons from B6.*Rag2*^{-/-} mice reconstituted with CAR-deficient T cells and treated as above and as indicated. Representative of five mice per group analysed in two independent experiments. Magnification, 10×; scale bars, 100 µm. **c**, Mean ± s.e.m. histology scores for colons and terminal ilea as in **b**. NS, not significant by unpaired two-tailed Student's *t*-test. [Source data](#)

Supplementary information

[Supplementary Tables](#)

This file contains Supplementary Tables 1–3.

[Reporting Summary](#)

Source data

[Source Data Fig. 1](#)

[Source Data Fig. 2](#)

[Source Data Fig. 3](#)

[Source Data Fig. 4](#)

[Source Data Extended Data Fig. 1](#)

[Source Data Extended Data Fig. 2](#)

[Source Data Extended Data Fig. 4](#)

[Source Data Extended Data Fig. 5](#)

[**Source Data Extended Data Fig. 6**](#)

[**Source Data Extended Data Fig. 7**](#)

[**Source Data Extended Data Fig. 8**](#)

[**Source Data Extended Data Fig. 9**](#)

[**Source Data Extended Data Fig. 10**](#)

Rights and permissions

[Reprints and Permissions](#)

About this article



Check for
updates

Cite this article

Chen, M.L., Huang, X., Wang, H. *et al.* CAR directs T cell adaptation to bile acids in the small intestine. *Nature* **593**, 147–151 (2021).
<https://doi.org/10.1038/s41586-021-03421-6>

[Download citation](#)

- Received: 18 April 2019
- Accepted: 04 March 2021
- Published: 07 April 2021
- Issue Date: 06 May 2021

- DOI: <https://doi.org/10.1038/s41586-021-03421-6>

Comments

By submitting a comment you agree to abide by our [Terms](#) and [Community Guidelines](#). If you find something abusive or that does not comply with our terms or guidelines please flag it as inappropriate.

[Access through your institution](#)

[Change institution](#)

[Buy or subscribe](#)

This article was downloaded by **calibre** from <https://www.nature.com/articles/s41586-021-03421-6>

| [Section menu](#) | [Main menu](#) |

Amendments & Corrections

- [**Author Correction: Rebuilding marine life**](#) [16 April 2021]
Author Correction •
- [**Author Correction: Synthesis and breakdown of universal metabolic precursors promoted by iron**](#) [17 April 2021]
Author Correction •
- [**Author Correction: Slower decay of landfalling hurricanes in a warming world**](#) [19 April 2021]
Author Correction •

Author Correction: Rebuilding marine life

[Download PDF](#)

- Author Correction
- [Published: 16 April 2021](#)

Author Correction: Rebuilding marine life

- [Carlos M. Duarte](#) [ORCID: orcid.org/0000-0002-1213-1361](#)^{1,2,3},
- [Susana Agusti](#) [ORCID: orcid.org/0000-0003-0536-7293](#)¹,
- [Edward Barbier](#) [ORCID: orcid.org/0000-0002-5354-3995](#)⁴,
- [Gregory L. Britten](#)⁵,
- [Juan Carlos Castilla](#)⁶,
- [Jean-Pierre Gattuso](#) [ORCID: orcid.org/0000-0002-4533-4114](#)^{7,8,9},
- [Robinson W. Fulweiler](#) [ORCID: orcid.org/0000-0003-0871-4246](#)^{10,11},
- [Terry P. Hughes](#) [ORCID: orcid.org/0000-0002-5257-5063](#)¹²,
- [Nancy Knowlton](#)¹³,
- [Catherine E. Lovelock](#) [ORCID: orcid.org/0000-0002-2219-6855](#)¹⁴,
- [Heike K. Lotze](#) [ORCID: orcid.org/0000-0001-6258-1304](#)¹⁵,
- [Milica Predragovic](#)¹,
- [Elvira Poloczanska](#)¹⁶,
- [Callum Roberts](#) [ORCID: orcid.org/0000-0003-2276-4258](#)¹⁷ &
- [Boris Worm](#)¹⁵

Nature volume **593**, pages E1–E2 (2021) [Cite this article](#)

- 1112 Accesses
- 3 Altmetric
- [Metrics details](#)

Subjects

- [Conservation biology](#)
- [Marine biology](#)

The [Original Article](#) was published on 01 April 2020

[Download PDF](#)

Correction to: *Nature* <https://doi.org/10.1038/s41586-020-2146-7> Published online 01 April 2020

Following publication of this Article, correspondence with colleagues and subsequent analysis uncovered discrepancies between the spreadsheet containing data from the RAM Legacy Stock Assessment Database we used for this analysis and the content of the database, which is now publicly available¹. In particular, a set of numerical entries for ‘spawning stock biomass’ and ‘total stock biomass’ are numerically incorrect or missing in the spreadsheet analysed for the paper. We have been unable to trace back the origin of these differences. As the updated database has now been published online¹, we wish to ensure reproducibility by correcting the published record to be consistent with the publicly available database.

We have re-run all analyses that use the data in question. This included recalculating: (1) the proportions of stocks in ‘increasing/decreasing/no change’ biomass categories (Fig. 3a and Supplementary Fig. [S2.3](#) of the original Article); (2) the aggregate B/B_{MSY} time series across all global stocks (Fig. 4a of the original Article); (3) the recovery probabilities for individual stocks currently depleted below B_{MSY} (Fig. 4b of the original Article); and (4) the validation of the B_{MSY} approximation in cases where assessment-estimated B_{MSY} values are not available (Supplementary Fig. [S2.2](#) of the original Article). We made a methodological modification to the way the aggregate B/B_{MSY} was calculated for the original Fig. 4a. We originally weighted each stock by their observed biomass value per year; we now weight by the mean annual biomass calculated across years. The motivation for the original choice was to weight stocks according to their contribution to global biomass. In the corrected database, the time series for Japanese sardine now inappropriately dominates the original calculations. The Japanese sardine is one of the largest stocks in the database. Its stock assessment (as now reflected in the RAM Legacy Stock Assessment Database¹) gives an estimate for B/B_{MSY} that exceeded 30.0 during the 1980s and declines to a value of 0.1 in the early 2000s. This represents an overly influential outlier in the database, absent from the previous dataset, in which the vast majority of stocks vary with B/B_{MSY} between 0.01 and 2.0, and very rarely over 3.0 or 4.0. This variation, combined with the large overall size of the stock, make the original weighting untenable because it produces a global aggregate trend that mirrors Japanese sardine through the 1980s and is unrepresentative of the global fishery. Weighting by mean annual biomass was the simplest modification. Calculating the weights in this way achieves the intended goal

of weighting stocks according to their contribution to global biomass, while removing the extreme dominance of single large stocks. Because the number of affected stocks is small relative to the total number of analysed stocks (<10%), other trends remained unchanged, or required small numerical updates.

The changes affect Figs. 3a, 4, Supplementary Figs. [S2.2](#), [S2.3](#) and Supplementary Table [S1](#) of the original Article. Figures 3a, 4, and Supplementary Figs. [S2.2](#) and [S2.3](#) have been redrawn. Figure [1](#) of this Amendment shows the original and corrected Fig. 3a side by side, for transparency. The proportions of species in the pie chart categories shifted slightly with the corrected database. The data continue to show that the proportion of increasing stocks has improved after year 2000. Figure [2](#) of this Amendment shows the original and corrected Fig. 4, for transparency. The number of stocks with biomass below the biomass supporting the maximum sustainable yield (B_{MSY}) increased from $n = 172$ in the original paper to $n = 194$ using the corrected database. The recovery histograms were re-computed using the updated list of stocks. The updated list of stocks is given in Supplementary Table [S1](#). The legend of Fig. 4 has been updated to reflect the sample size and version number of the corrected database. In the redrawn Fig. 4a, the updated calculations raise the average value of the mean globally aggregated B/B_{MSY} time series above where it was originally displayed, primarily owing to the treatment of Japanese sardine. These changes do not alter any of our conclusions or the main text of the Article. All text and conclusions are based on the ability to recover depleted individual stocks (Fig. 4b), which does not involve the global aggregate calculations. The recovery of individual stocks is calculated from stock-specific growth rates and fishing pressure, and the probability of recovering all depleted stocks is calculated by combining the stock-specific recovery probabilities.

Fig. 1: This figure shows the original and corrected Fig. 3a of the original Article.



The original, incorrect Fig. 3a is on the left and the corrected Fig. 3a is on the right.

[Full size image](#)

Fig. 2: This figure shows the original and corrected Fig. 4 of the original Article



[Full size image](#)

Supplementary Table [S1](#) also now contains three additional columns, to clarify more precisely the selection criteria; specifically, we added indicators for the availability of total biomass (TB), total catch (TC), and the most recent estimate of the biomass relative to the target (TB/TB_{MSY}). The simulations continue to show that recovery to 2050 is highly probable and that the probability of recovery increases as fishing pressure decreases. For Supplementary Fig. [S2.2](#), we re-calculated the metrics used to validate our B_{MSY} approximation for cases where the assessment does not provide an estimate. The validation continues to show that $B_{MSY} = 0.5\max(B)$ approximates the assessment B_{MSY} well.

A copy of RAM Legacy 4.491 and the code we used to perform and visualize the B/B_{MSY} calculations is available at the public GitHub page <https://github.com/gregbritten/duarte-etal-correction>. The [Supplementary Information](#) of this Amendment is the originally published, incorrect [Supplementary Information](#) of the original Article, for transparency to our readers. Figures 3 and 4 and the [Supplementary Information](#) of the original Article have been corrected online.

Supplementary Information is available in the online version of this Amendment.

References

1. 1.

RAM Legacy Stock Assessment Database version RAMLDB v4.491,
<http://zenodo.org/record/3676088> (2020).

[Download references](#)

Author information

Affiliations

1. Red Sea Research Center (RSRC), King Abdullah University of Science and Technology, Thuwal, Saudi Arabia

Carlos M. Duarte, Susana Agusti & Milica Predragovic

2. Arctic Research Centre, Department of Biology, Aarhus University, Aarhus, Denmark

Carlos M. Duarte

3. Computational Bioscience Research Center (CBRC), King Abdullah University of Science and Technology, Thuwal, Saudi Arabia

Carlos M. Duarte

4. Department of Economics, Colorado State University, Fort Collins, CO, USA

Edward Barbier

5. Department of Earth, Atmospheric, and Planetary Sciences, Massachusetts Institute of Technology, Cambridge, MA, USA

Gregory L. Britten

6. Departamento de Ecología, Facultad de Ciencias Biológicas and Centro Interdisciplinario de Cambio Global, Pontificia Universidad Católica de Chile, Santiago, Chile

Juan Carlos Castilla

7. Laboratoire d'Océanographie de Villefranche, Sorbonne Université, CNRS, Villefranche-sur-Mer, France

Jean-Pierre Gattuso

8. Institute for Sustainable Development and International Relations, Sciences Po, Paris, France

Jean-Pierre Gattuso

9. Monegasque Association on Ocean Acidification, Prince Albert II of Monaco Foundation, Monaco, Monaco

Jean-Pierre Gattuso

10. Department of Earth & Environment, Boston University, Boston, MA, USA

Robinson W. Fulweiler

11. Department of Biology, Boston University, Boston, MA, USA

Robinson W. Fulweiler

12. Australian Research Council Centre of Excellence for Coral Reef Studies, James Cook University, Townsville, Queensland, Australia

Terry P. Hughes

13. National Museum of Natural History, Smithsonian Institution, Washington, DC, USA

Nancy Knowlton

14. School of Biological Sciences, The University of Queensland, St Lucia, Queensland, Australia

Catherine E. Lovelock

15. Department of Biology, Dalhousie University, Halifax, Nova Scotia, Canada

Heike K. Lotze & Boris Worm

16. Alfred Wegener Institute, Integrative Ecophysiology, Bremerhaven, Germany

Elvira Poloczanska

17. Department of Environment and Geography, University of York, York, UK

Callum Roberts

Authors

1. Carlos M. Duarte

[View author publications](#)

You can also search for this author in [PubMed](#) [Google Scholar](#)

2. Susana Agusti

[View author publications](#)

You can also search for this author in [PubMed](#) [Google Scholar](#)

3. Edward Barbier

[View author publications](#)

You can also search for this author in [PubMed](#) [Google Scholar](#)

4. Gregory L. Britten

[View author publications](#)

You can also search for this author in [PubMed](#) [Google Scholar](#)

5. Juan Carlos Castilla

[View author publications](#)

You can also search for this author in [PubMed](#) [Google Scholar](#)

6. Jean-Pierre Gattuso

[View author publications](#)

You can also search for this author in [PubMed](#) [Google Scholar](#)

7. Robinson W. Fulweiler

[View author publications](#)

You can also search for this author in [PubMed](#) [Google Scholar](#)

8. Terry P. Hughes

[View author publications](#)

You can also search for this author in [PubMed](#) [Google Scholar](#)

9. Nancy Knowlton

[View author publications](#)

You can also search for this author in [PubMed](#) [Google Scholar](#)

10. Catherine E. Lovelock

[View author publications](#)

You can also search for this author in [PubMed](#) [Google Scholar](#)

11. Heike K. Lotze

[View author publications](#)

You can also search for this author in [PubMed](#) [Google Scholar](#)

12. Milica Predragovic

[View author publications](#)

You can also search for this author in [PubMed](#) [Google Scholar](#)

13. Elvira Poloczanska

[View author publications](#)

You can also search for this author in [PubMed](#) [Google Scholar](#)

14. Callum Roberts
[View author publications](#)

You can also search for this author in [PubMed](#) [Google Scholar](#)

15. Boris Worm
[View author publications](#)

You can also search for this author in [PubMed](#) [Google Scholar](#)

Corresponding author

Correspondence to [Carlos M. Duarte](#).

Supplementary information

[Supplementary Information](#)

This file contains the original incorrect Supplementary Information.

Rights and permissions

[Reprints and Permissions](#)

About this article



Check for
updates

Cite this article

Duarte, C.M., Agusti, S., Barbier, E. *et al.* Author Correction: Rebuilding marine life. *Nature* **593**, E1–E2 (2021). <https://doi.org/10.1038/s41586-021-03271-2>

[Download citation](#)

- Published: 16 April 2021
- Issue Date: 06 May 2021

- DOI: <https://doi.org/10.1038/s41586-021-03271-2>

Comments

By submitting a comment you agree to abide by our [Terms](#) and [Community Guidelines](#). If you find something abusive or that does not comply with our terms or guidelines please flag it as inappropriate.

[Download PDF](#)

This article was downloaded by **calibre** from <https://www.nature.com/articles/s41586-021-03271-2>

| [Section menu](#) | [Main menu](#) |

Author Correction: Synthesis and breakdown of universal metabolic precursors promoted by iron

[Download PDF](#)

- Author Correction
- [Published: 17 April 2021](#)

Author Correction: Synthesis and breakdown of universal metabolic precursors promoted by iron

- [Kamila B. Muchowska](#)¹,
- [Sreejith J. Varma](#)¹ &
- [Joseph Moran](#)¹

[Nature](#) volume 593, page E3(2021) [Cite this article](#)

- 759 Accesses
- 2 Altmetric
- [Metrics details](#)

Subjects

- [Iron](#)
- [Chemical origin of life](#)

The [Original Article](#) was published on 01 May 2019

[Download PDF](#)

Correction to: *Nature* <https://doi.org/10.1038/s41586-019-1151-1> Published online 01 May 2019

In the [Supplementary Information](#) of this Letter, the following additions and corrections have been made: Gas chromatography–mass spectrometry (GC–MS) traces of control experiments without Fe²⁺ have been added as Supplementary Figs. [S30](#) and [S31](#). Supplementary Table [S5](#) has been added to present the data obtained in the additional control experiments mentioned above. Some misaligned entries have been corrected in Supplementary Tables [S2](#) and [S4](#) and numerical values in these tables are now expressed in scientific notation for clarity. None of these changes affects the data plots, results, or conclusions of the original paper. The [Supplementary Information](#) of the original Article has been corrected online. The [Supplementary Information](#) of this Amendment contains the old, incorrect [Supplementary information](#) for transparency.

Supplementary information is available in the online version of this Amendment.

Author information

Affiliations

1. Université de Strasbourg, CNRS, ISIS, Strasbourg, France

Kamila B. Muchowska, Sreejith J. Varma & Joseph Moran

Authors

1. Kamila B. Muchowska

[View author publications](#)

You can also search for this author in [PubMed](#) [Google Scholar](#)

2. Sreejith J. Varma

[View author publications](#)

You can also search for this author in [PubMed](#) [Google Scholar](#)

3. Joseph Moran

[View author publications](#)

You can also search for this author in [PubMed](#) [Google Scholar](#)

Corresponding author

Correspondence to [Joseph Moran](#).

Supplementary information

[This file contains the incorrect, as-published Supplementary Information \(Materials and Methods, Supplementary References, Supplementary Figures 1–29 and Supplementary Tables 1–4\).](#)

Rights and permissions

[Reprints and Permissions](#)

About this article



Check for
updates

Cite this article

Muchowska, K.B., Varma, S.J. & Moran, J. Author Correction: Synthesis and breakdown of universal metabolic precursors promoted by iron. *Nature* **593**, E3 (2021). <https://doi.org/10.1038/s41586-021-03383-9>

[Download citation](#)

- Published: 17 April 2021
- Issue Date: 06 May 2021
- DOI: <https://doi.org/10.1038/s41586-021-03383-9>

Comments

By submitting a comment you agree to abide by our [Terms](#) and [Community Guidelines](#). If you find something abusive or that does not comply with our terms or guidelines please flag it as inappropriate.

[Download PDF](#)

This article was downloaded by **calibre** from <https://www.nature.com/articles/s41586-021-03383-9>

| [Section menu](#) | [Main menu](#) |

Author Correction: Slower decay of landfalling hurricanes in a warming world
[Download PDF](#)

- Author Correction
- [Published: 19 April 2021](#)

Author Correction: Slower decay of landfalling hurricanes in a warming world

- [Lin Li ORCID: orcid.org/0000-0003-3764-729X¹](#) &
- [Pinaki Chakraborty ORCID: orcid.org/0000-0001-7393-6684¹](#)

Nature volume 593, pages E4–E11 (2021) [Cite this article](#)

- 448 Accesses
- 4 Altmetric
- [Metrics details](#)

Subjects

- [Atmospheric dynamics](#)
- [Climate-change impacts](#)

The [Original Article](#) was published on 11 November 2020

[Download PDF](#)

Correction to: *Nature* <https://doi.org/10.1038/s41586-020-2867-7> Published online 11 November 2020

In the Article, we studied 71 landfall events. For each event, we analysed the data of hurricane intensities and locations corresponding to the first four synoptic times past landfall (0000 utc, 0600 utc, 1200 utc and 1800 utc). From the intensities, we computed the decay timescale, and from the locations, we computed the translation

speed, coastline-perpendicular translation speed, and latitude and longitude of the centroid. For five landfall events (Jerry in 1989; Georges in 1998; Ivan in 2004; Dolly in 2008; and Richard in 2010), we mistakenly analysed the data for one asynoptic time by considering it as synoptic (see the times marked in boldface in Table 1 of this Amendment). As a result, the reported values of the decay timescale, translation speed, coastline-perpendicular translation speed, and latitude and longitude of the centroid for these five landfall events are incorrect. This affects Fig. 1b, c, e, f, Fig. 3, Extended Data Fig. 1b, d, f, Extended Data Fig. 2a, b, d, e, Extended Data Fig. 3, Extended Data Table 2, Extended Data Table 3b, c, Supplementary Data and the Source Data for Fig. 1 of the original Article, and these figures and tables have all been corrected online. Correspondingly, many of the numerical values reported in the original Article have minor changes; for example, in the legend to Fig. 1, the correlation, r , between the decay timescale and SST has changed from 0.73 to 0.72; in the footnote to Extended Data Table 2, the text ‘two-sided 95% CI of the corresponding slope’ has changed to ‘two-sided 95% CI (93% CI for the two cases marked with an asterisk) of the corresponding slope’; and many numerical values in the ‘Hurricane tracks and decay’ section of the Methods have changed slightly. Figures 1–7 of this Amendment show the incorrect, as-published versions next to the corrected versions, for transparency. The Supplementary Information of this Amendment contains the incorrect, as-published versions of the Supplementary Data and the Source Data for Fig. 1 of the original Article, for transparency. In the corrected analysis, we discarded the data corresponding to the asynoptic time and instead analysed the data for the first four synoptic times past landfall (see the rightmost column in Table 1 of this Amendment). The resulting changes in the values of the decay timescale and other parameters do not affect our discussions and conclusions. We apologize for the error and thank Kelvin Chan for bringing this error to our attention. The original Article has been corrected online.

Table 1 Synoptic and asynoptic times used in the original and corrected analyses
[Full size table](#)

Fig. 1: This figure shows the incorrect, as-published version and the corrected version of Fig. 1b, c, e and f of the original Article.



(Note that the error does not affect the span of τ in Fig. 1b; the difference in the spans of the original and corrected versions shown here is because the abscissa in the original version was incorrect owing to a separate error during production, now also corrected here.).

[Full size image](#)

Fig. 2: This figure shows the incorrect, as-published version and the corrected version of Fig. 3 of the original Article.

figure2

[Full size image](#)

Fig. 3: This figure shows the incorrect, as-published version and the corrected version of Extended Data Fig. 1b, d and f of the original Article.

 [figure3](#)

[Full size image](#)

Fig. 4: This figure shows the incorrect, as-published version and the corrected version of Extended Data Fig. 2a, b, d and e of the original Article.



[Full size image](#)

Fig. 5: This figure shows the incorrect, as-published version and the corrected version of Extended Data Fig. 3 of the original Article.



[Full size image](#)

Fig. 6: This figure shows the incorrect, as-published version and the corrected version of Extended Data Table 2 of the original Article.



[Full size image](#)

Fig. 7: This figure shows the incorrect, as-published version and the corrected version of Extended Data Table 3b and c of the original Article.



[Full size image](#)

Author information

Affiliations

1. Fluid Mechanics Unit, Okinawa Institute of Science and Technology Graduate University, Okinawa, Japan

Lin Li & Pinaki Chakraborty

Authors

1. Lin Li

[View author publications](#)

You can also search for this author in [PubMed](#) [Google Scholar](#)

2. Pinaki Chakraborty

[View author publications](#)

You can also search for this author in [PubMed](#) [Google Scholar](#)

Corresponding author

Correspondence to [Pinaki Chakraborty](#).

Rights and permissions

[Reprints and Permissions](#)

About this article



Check for
updates

Cite this article

Li, L., Chakraborty, P. Author Correction: Slower decay of landfalling hurricanes in a warming world. *Nature* **593**, E4–E11 (2021). <https://doi.org/10.1038/s41586-021-03321-9>

[Download citation](#)

- Published: 19 April 2021
- Issue Date: 06 May 2021
- DOI: <https://doi.org/10.1038/s41586-021-03321-9>

Comments

By submitting a comment you agree to abide by our [Terms](#) and [Community Guidelines](#). If you find something abusive or that does not comply with our terms or guidelines please flag it as inappropriate.

[Download PDF](#)

This article was downloaded by **calibre** from <https://www.nature.com/articles/s41586-021-03321-9>

| [Section menu](#) | [Main menu](#) |